Magmatic Architecture of Hotspot Volcanism and Large Igneous Provinces

by

Tushar Mittal

A dissertation submitted in partial satisfaction of the

requirements for the degree of

Doctor of Philosophy

in

Earth and Planetary Science

in the

Graduate Division

of the

University of California, Berkeley

Committee in charge:

Professor Mark A. Richards, Chair
Professor Michael Manga
Professor Paul R. Renne
Professor James R. Graham

Spring 2020

Abstract

Magmatic Architecture of Hotspot Volcanism and Large Igneous Provinces

by

Tushar Mittal

Doctor of Philosophy in Earth and Planetary Science

University of California, Berkeley

Professor Mark A. Richards, Chair

Volcanoes are an important part of the Earth system - supplying volatiles (e.g., H_2O, CO_2, SO_2) to the atmosphere, as well as nutrients to the oceans (e.g., Fe, other trace elements), and producing subaerial and submarine topography. In particular, flood basalt events are some of the largest magmatic events in Earth history, with intrusion and eruption of millions of km^3 of basaltic magma over a short time period ($\sim$ 1-5 Ma). They are hypothesized to be the result of the emergence of a mantle plume head - which frequently forms the start of a hotspot track. Flood basalt eruptions are associated with significant perturbations to the Earth's climate and biosphere, including mass extinctions. This link is generally hypothesized to be due to the emission of climatically active volatiles, such as CO_2 and SO_2. In this thesis, I utilize fluid dynamics and mechanical theory from Earth-science, astrophysical, and engineering sub-disciplines to develop intermediate-complexity models for hotspot volcanism and flood basalt eruptions.

I analyze how the mantle partial melt gets mobilized and transported in the asthenosphere before feeding the crustal magmatic system. For this, I used natural modern day occurrences of where a mantle plume interacts with a nearby mid-ocean ridge e.g., Galápagos and Iceland. My results suggest that plume-ridge interaction in general, possibly including transport of plume-derived material along ridge axes (e.g., Iceland), may involve transport in high-melt-fraction channels, as opposed to just solid-state mantle flow. With regards to the crustal magmatic system, I analyze how the loss of volatiles from a magma reservoir affects the magmatic overpressure responsible for driving ground deformation and eruptions. I developed a fully coupled poro-thermo-elastic framework to account for both the flow of volatiles as well as associated effects on the stress state of the crust and calculate an analytical solution for spherical geometry.

I utilize these ideas to understand the eruptive dynamics and magmatic architecture of continental flood basalts (CFB). I used a new volume-averaged visco-elastic mechanical model for an ellipsoidal magma reservoir coupled to a dike-shaped erodible conduit to calculate

how eruptive fluxes (km^3/year) and volumes vary as a function of reservoir geometry and crustal properties for a single magma reservoir, as well as multiple connected reservoirs. I found that the presence of just a few large crustal magma reservoirs is inconsistent with observational constraints. Instead, I propose that CFB eruptions are fed from a number of smaller ($\sim 10^2$ - $10^{3.5}$ km^3) interconnected magma reservoirs present throughout the crust consistent with the paradigm of a trans-crustal magmatic system.

This work has important implications for interpreting a CFB's potential to cause environmental change.

Contents

Acknowledgments

I would like to thank Prof. Mark Richards for supervision, ideas, and support. I strongly appreciate him providing me the freedom to explore my interests and work on a variety of topics in addition to my primary thesis work. Thanks also to Profs. Michael Manga, Paul Renne, Steve Self, and Bruce Buffet for significant help and support during my Ph.D. work. Many thanks to Prof. Bruce Marsh for continued support and discussions during my research career. Thanks to the staff, postdocs, PhD students, and undergraduates at UC Berkeley. Finally, thanks to my parents, brother and sister-in-law, and Isabel for many discussions and constant support.

Chapter 1

Introduction

Volcanoes are an important part of the Earth system - supplying volatiles (e.g. H_2O, CO_2, SO_2) to the atmosphere, as well as nutrients to the oceans (e.g. Fe, other trace elements), and producing subaerial and submarine topography. Volcanic processes influence the ocean-atmosphere system over a large variety of spatial and temporal scales: from < 1 yr for a large sub-aerial volcanic eruption to ~ 1 million years for the eruption of a flood basalt such as the Deccan Traps.

Flood basalt events are some of the largest magmatic events in Earth history, with intrusion and eruption of millions of km^3 of basaltic magma over a short time period ($\sim$ 1-5 Ma). They are hypothesized to be the result of the emergence of a mantle plume head - which frequently forms the start of a hot-spot track. These processes are significant to our understanding of plate tectonics and long-term rock cycling. In addition to their geological significance, flood basalt eruptions are associated with significant perturbations to the Earth's climate and biosphere, including mass extinctions. This link is generally hypothesized to be due to the emission of climatically active volatiles, such as CO_2 and SO_2.

These volatiles can be released during eruptions or passively from the magma chamber. The amount of gases released passively is determined by the properties of the host rock, which are altered by the emplacement of a magma chamber. It is important to understand these processes and hence the flux of passively emitted volatiles, because the environmental effects of these gases can be different than those released during eruptions. The rate of magmatic volatile loss also has an effect on the eruptibility of magma since the buoyancy of the melt-crystal-volatile mixture is an important source of magmatic overpressure. Thus the processes controlling magmatic volatile loss from a magma reservoir, along with the number and the size of individual magma chambers, determines the eruptive tempo of flood basalts.

In this thesis, I investigate the link between geophysical processes and the ocean-atmosphere system by a) developing idealized models and b) analyzing large observational datasets to validate these models. Specifically, I have utilized fluid dynamics and mechanical theory from Earth-science, astrophysical, and engineering sub-disciplines to develop intermediate-complexity models for flood basalt eruptions and their climatic influence.

In Chapter 2, I analyze how the mantle partial melt gets mobilized and transported in the asthenosphere before feeding the crustal magmatic system. For this, I used natural modern day occurrences of where a mantle plume interacts with a nearby mid-ocean ridge e.g., Galápagos and Iceland. This interaction is typified by trace element and isotopic signatures demonstrating the "contamination" of normal ridge composition by relatively enriched plume material. Another common signature of plume-ridge interaction is volcanic lineaments linking ridges and nearby plumes, perhaps most conspicuously the Wolf-Darwin lineament (WDL) at Galápagos and the Rodrigues Ridge (RR) at La Réunion. These volcanic lineaments are observed in multiple plume-ridge settings, each with a different plume buoyancy flux, plume composition, and plate spreading rate; hence, we these environments are natural laboratories to better understand sub-lithospheric melt transport and extraction.

Subsequently in Chapter 3, I analyze how the loss of volatiles from a magma reservoir affects the magmatic overpressure responsible for driving ground deformation and eruptions. Although the high-temperature metamorphic aureole around a magma chamber is typically considered to have low permeability, recent theoretical, experimental, and field studies have highlighted the role of transient permeability in magmatic systems. Also, direct measurements suggest that passive degassing is a significant component of total volatile loss in both basaltic and silicic volcanoes. Consequently, the effective permeability of the crust when magma is present in the system can be many orders of magnitude larger than that of exhumed rock samples. We develop a fully coupled poro-thermo-elastic framework to account for both the flow of volatiles as well as associated effects on the stress state of the crust as well as magma eruptibility.

Finally, in Chapter 4, I utilize the ideas developed in Chapters 2 & 3 to understand the eruptive dynamics and magmatic architecture of continental flood basalts. A typical CFB is emplaced in hundreds of individual eruptive episodes lasting decades to centuries with lava flow volumes of 10^3- 10^4 km^3. These large volumes have logically led to CFB models invoking large magma reservoirs ($> 10^5$-10^6 km^3) within the crust or at Moho depth. Since there are currently no active CFB provinces, we must rely on observations of past CFBs with varying degrees of surface exposure to develop and test models. In the last few decades, significant improvements in geochronological, geochemical, paleomagnetic, volcanological, and paleoproxy measurements have provided high-resolution constraints on CFB eruptive tempo - the volume, duration, and frequency of individual eruptive episodes - for the Deccan Traps flood basalt province. I compiled a variety of observations to test against the predictions of existing models and develop a new model for CFB magmatic architecture using new mechanical and thermal models for magma reservoirs.

Chapter 2

Plume-ridge Interaction via Melt Channelization at Galápagos and Other Near-ridge Hotspot Provinces

2.1 Introduction

Mid-ocean ridges and oceanic hot-spots (associated with mantle plumes) are two of the principal regions of magma generation and volcanic activity on the Earth. Although, they are generally considered to represent different regimes of mantle upwelling, these two systems are not always isolated from each other (e.g., J. Schilling, 1991; Ito & Lin, 1995; Ito, Lin, & Graham, 2003; Dyment, Lin, & Baker, 2007; Whittaker et al., 2015). A number of mantle plumes are located on or near mid-ocean ridges either at present, e.g., Galápagos (J.-G. Schilling, Kingsley, & Devine, 1982), Azores (Cannat et al., 1999), Iceland (J. Schilling, 1973), Tristan da Cunha (J. G. Schilling, Thompson, Kingsley, & Humphris, 1985), Easter-Salas y Gómez (Kingsley & Schilling, 1998), or in the past, e.g., Kerguelen (Sreejith & Krishna, 2015). A nearby ($\leq$ 1600 km) plume may lead to higher mantle temperatures and more fertile mantle geochemistry beneath the ridge (e.g., for Galápagos - J.-G. Schilling, Fontignie, Blichert-Toft, Kingsley, & Tomza, 2003; Ingle et al., 2010). The consequent excess melting along with direct melt transport from the plume to the ridge increases the thickness of the oceanic crust and modifies both the structure and composition of the underlying lithosphere (e.g., J. Schilling, 1973, 1991; J. Canales, Ito, Detrick, & Sinton, 2002).

Nearby mantle plumes also impart a strong geochemical signature to ridge volcanics due to their different geochemistry, as compared to typical mid-ocean ridge basalts (MORB). In particular, erupted lavas at plume-influenced ridge segments are enriched in incompatible elements and show a distinct (generally enriched) isotopic signature, suggesting direct transfer of material from the mantle plume instead of a purely thermal effect (J.-G. Schilling et al., 2003; Shorttle, MacLennan, & Jones, 2010; Kelley, Kingsley, & Schilling, 2013, see also the review by); W. M. White (2010) and references therein). Geophysical and geochemical

observations show that the maximum plume-ridge separation for active interaction is ~ 1600 km (Ito & Lin, 1995; Mittelstaedt & Ito, 2005; Whittaker et al., 2015). Since plumes may have influenced a significant fraction (15-20%) of the mid-oceanic ridges (Ito et al., 2003), this process has an important affect on the oceanic plate structure and composition.

Plume-ridge interaction is expected to be strongest when a plume is located on or is very close to the spreading ridge (e.g., Iceland; J. Schilling, 1973; Shorttle et al., 2010). Nevertheless, it can be difficult to identify this interaction from amongst the behaviors of the plume and the ridge system in isolation. In contrast, the primary domains of plume-related volcanism and spreading ridge volcanism are spatially separated in near-ridge plumes, such as the Galápagos and La Réunion, by an intermediate region where interaction features can be clearly observed. In many near-ridge plumes, this spatial region of interaction is typified by non-age progressive volcanic lineaments with the most prominent examples associated with mantle plumes in the Galápagos (Figures 2.1 and 2.2, Morgan, 1978; K. Harpp & Geist, 2002), La Réunion (Figure 2.3, Morgan, 1978; Dyment et al., 2007), Louisville (Figure 2.4 Small, 1995; Géli et al., 1998; Vlastélic & Dosso, 2005), Kerguelen, Foundation seamounts (O'Connor, Stoffers, & Wijbrans, 2004; Maia, Dyment, & Jouannetaud, 2005), Easter-Salas y Gómez (Kingsley & Schilling, 1998), and the Mid-Pac Mountains (Line Islands, Mittelstaedt & Ito, 2005).

The lineaments (either continuous ridges or chains of islands and seamounts) represent volcanic volumes much smaller than the magma erupted at either the spreading ridge or the associated mantle plume. However, they are surprisingly a common characteristic feature of plume-ridge interaction regions (Morgan, 1978; Mittelstaedt & Ito, 2005; Sleep, 2008). Due to the thin overlying lithosphere (as a consequence of a young plate age), these subsidiary volcanic structures likely represent the surface expression of otherwise un-sampled small amounts of melt. Therefore, if the model we propose here of sub-lithospheric melt channelization is correct, the volcanic lineaments associated with off-axis plume-ridge interaction provide unique environments to develop and test models for sub-lithospheric magma and mantle dynamics with regional scale geological features.

Many models have been proposed (e.g., K. Harpp & Geist, 2002, see Section 2.2.3 for details) to explain the lineaments, especially the Wolf-Darwin volcanic lineament (WDL, Figure 2.1) in the Galápagos. In this study, we first evaluate these models using recent geophysical observations. Our primary focus in this study is the Galápagos region since there exists a wealth of geophysical and geochemical data-sets characterizing the lineament region (e.g., K. S. Harpp & White, 2001; K. Harpp & Geist, 2002; Mittelstaedt et al., 2012; Mittelstaedt, Soule, Harpp, & Fornari, 2014; K. S. Harpp, Wirth, et al., 2014). In addition, the plume-ridge interaction region has a relatively well-constrained regional tectonic history along with substantial information on the location, geochemistry, and ridge expression of the Galápagos plume (e.g., J.-G. Schilling et al., 1982; D. S. Wilson & Hey, 1995; Meschede & Barckhausen, 2000; Ito, Lin, & Gable, 1997; J. Canales et al., 2002; J.-G. Schilling et al., 2003; J. Sinton, Detrick, Canales, Ito, & Behn, 2003; Blacic, Ito, Canales, Detrick, & Sinton, 2004; Christie, Werner, Hauff, Hoernle, & Hanan, 2005; Ingle et al., 2010; Colman et al.,

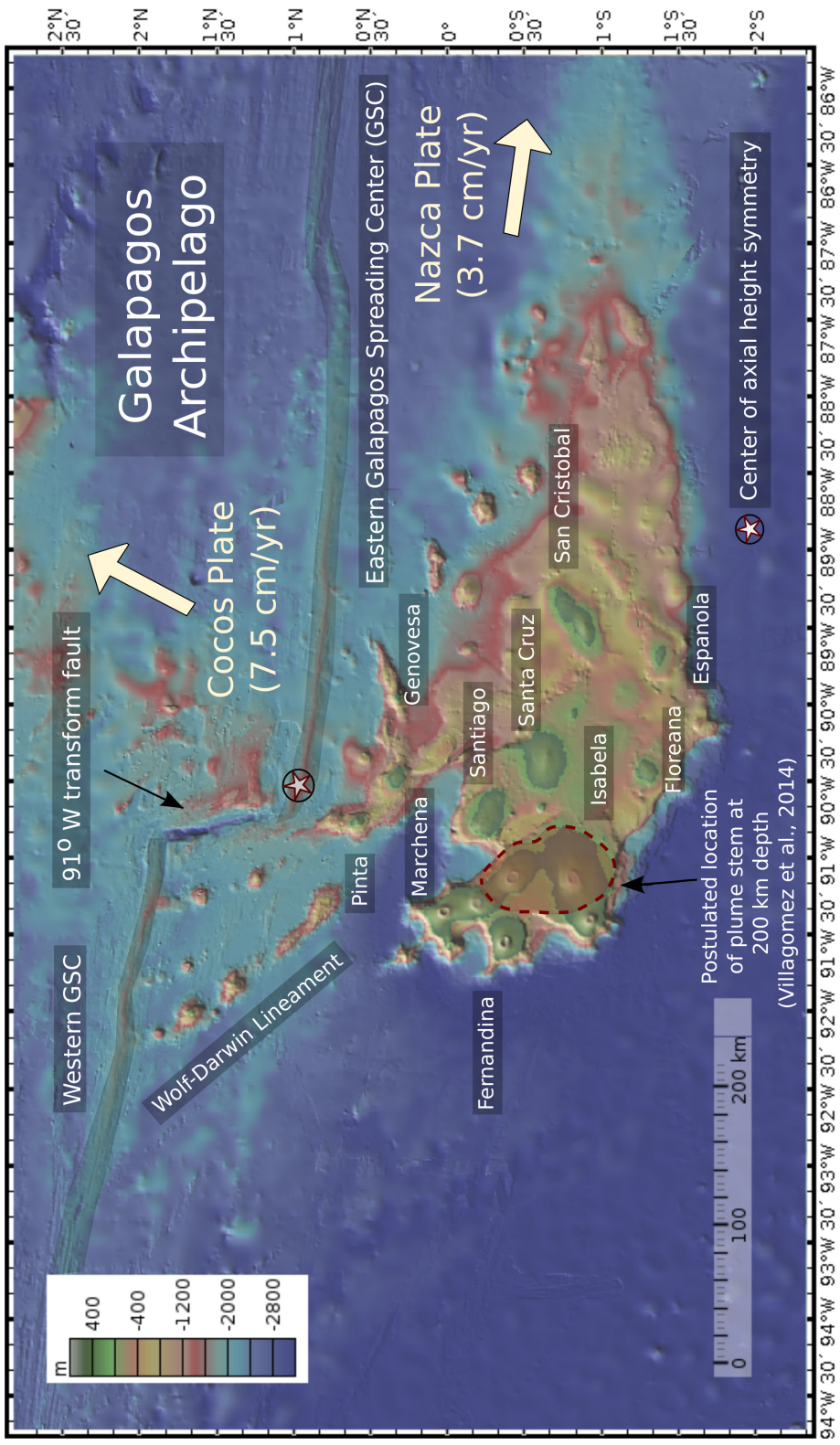
Galapagos Archipelago
Cocos Plate (7.5 cm/yr)
Nazca Plate (3.7 cm/yr)
Eastern Galapagos Spreading Center (GSC)
Western GSC
91° W transform fault
Wolf-Darwin Lineament
Pinta
Marchena
Genovesa
Santiago
Santa Cruz
San Cristobal
Isabela
Floreana
Espanola
Fernandina
Postulated location of plume stem at 200 km depth (Villagomez et al., 2014)
Center of axial height symmetry
m
400
-400
-1200
-2000
-2800
0
100
200 km
2°N 30′
2°N
1°N 30′
1°N
0°N 30′
0°
0°S 30′
1°S
1°S 30′
2°S
94°W 30′ 94°W 93°W 30′ 93°W 92°W 30′ 92°W 91°W 30′ 91°W 90°W 30′ 90°W 89°W 30′ 89°W 88°W 30′ 88°W 87°W 30′ 87°W 86°W 30′ 86°W

Figure 2.1

Figure 2.1 *(previous page)*: Bathymetric map of the Galápagos region. The bathymetric base map is obtained from GeoMapApp [Haxby et al., 2010; Ryan et al., 2009]. We use the deep-hotspot reference frame Morgan et al. (2007) to estimate the plate velocities (Thick white arrows)

2012; S. A. Gibson, Geist, & Richards, 2015). Since we find inconsistencies between the model predictions and observations, we argue that the current models lack some physical processes that are crucial to explain the volcanic lineaments in plume-ridge interaction environments. In particular, we propose that the volcanic lineaments are the surface expression of localized melt channels (either a high-porosity, two-phase aggregate, or an open melt-filled channel) in the asthenosphere formed due to instabilities in a two-phase partially-molten system with the channels transporting melt from the mantle plume to the ridge. Our proposed model for the WDL and other lineaments is conceptually similar to the model proposed in S. A. Gibson et al. (2015) based on geochemical observations and builds upon their ideas.

We first discuss some conspicuous plume-ridge interaction features in the Galápagos, especially the WDL, and the key geochemical and geophysical observables in Section 2.2. In Section 2.3, we describe the various models proposed to explain the lineaments and discuss their shortcomings as motivation for an alternative approach. We propose our model for the WDL and other volcanic lineaments in Section 2.4, followed by a scaling analysis in Section 2.5, to demonstrate the thermodynamic feasibility of our proposal. We discuss some observational support for our model, limitations and future extensions of our calculations, and application to other lineaments in Section 2.6.

2.2 Plume-ridge interaction in Galápagos

The Galápagos Islands are a group of volcanic islands located about 200-300 km south of a spreading ridge - Galápagos Spreading Center (GSC, spreading rate $\sim$ 5 cm/yr, Mittelstaedt et al., 2012; D. S. Wilson & Hey, 1995) - separating the Cocos and the Nazca Plates (Figure 2.1). The islands and the underlying volcanic platform represent the current surface expression of the Galápagos mantle plume. On the other hand, the age-progressive Carnegie and Cocos aseismic ridges on respectively the Nazca and the Cocos plates represent the long term activity of the plume. Results from seismic tomography (Villagómez, Toomey, Geist, Hooft, & Solomon, 2014) show that the plume is centered beneath Fernandina and Isabela Islands, the most volcanically active islands in the archipelago.

The two primary expressions of plume-ridge interaction in the Galápagos region are the geochemical and geophysical anomalies along the GSC compared to a typical ridge (see S. A. Gibson et al., 2015, for a review) and the volcanic lineaments located between the GSC and the current location of the mantle plume (See Figure 2.1). The lineament volca-

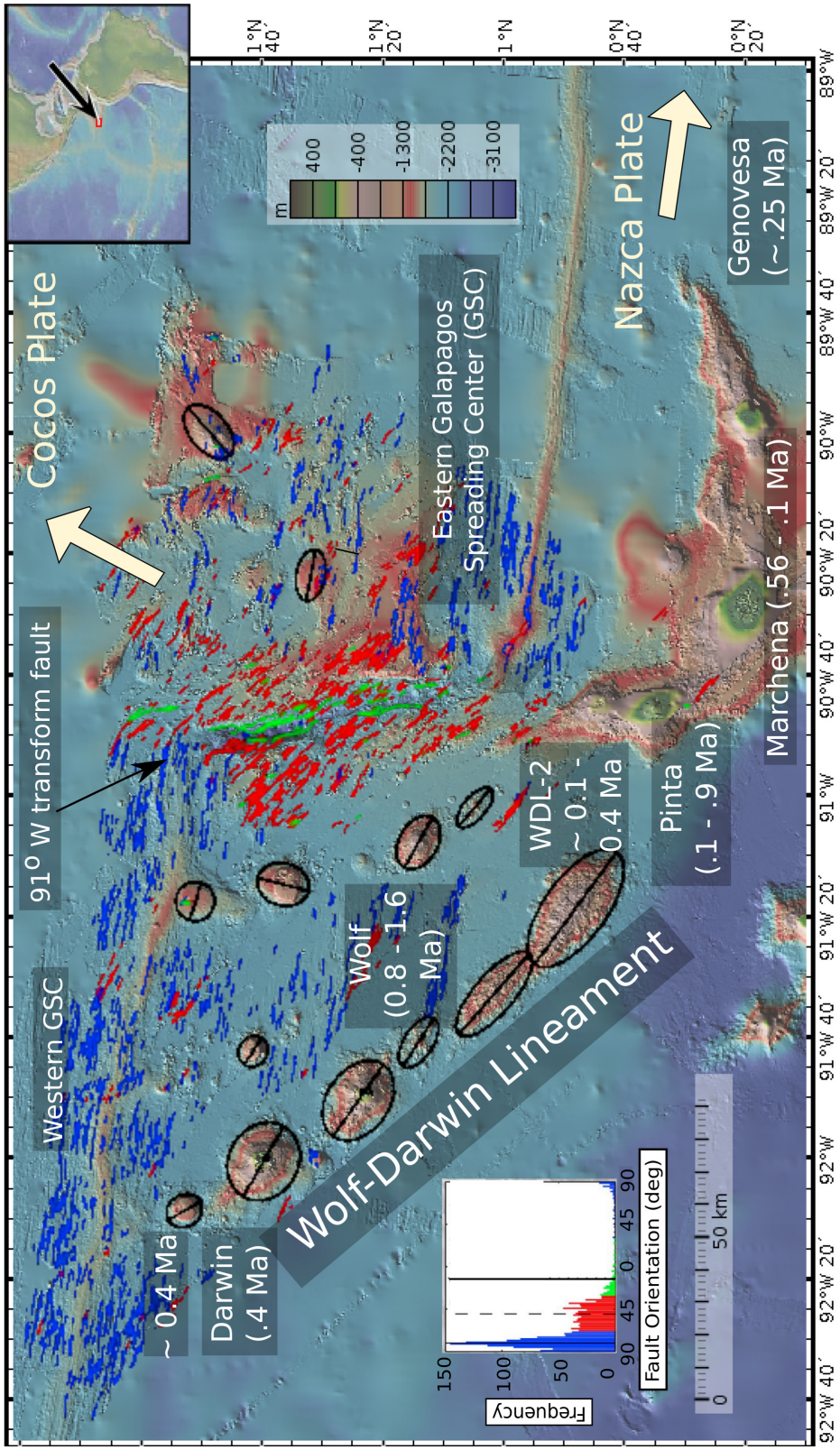
Cocos Plate
Nazca Plate
91° W transform fault
Western GSC
Eastern Galapagos Spreading Center (GSC)
~ 0.4 Ma
Darwin (.4 Ma)
Wolf (0.8 - 1.6 Ma)
WDL-2 ~ 0.1 - 0.4 Ma
Pinta (.1 - .9 Ma)
Marchena (.56 - .1 Ma)
Genovesa (~.25 Ma)
Wolf-Darwin Lineament
m
400
-400
-1300
-2200
-3100
Frequency
Fault Orientation (deg)
50 km
1°N 40'
1°N 20'
1°N
0°N 40'
0°N 20'
92°W 40'
92°W 20'
92°W
91°W 40'
91°W 20'
91°W
90°W 40'
90°W 20'
90°W
89°W 40'
89°W 20'
89°W

Figure 2.2

Figure 2.2 *(previous page)*: A zoomed in bathymetric map of the Northern Galaapagos Volcanic Province (NGVP) showing the Wolf-Darwin lineament (WDL). The ages for the1002islands/seamounts in NGVP have been compiled from White et al.[1993]; Sinton et al.[1996]; Harpp et al.[2014b]. The bathymetric base map is obtained from GeoMapApp [Haxby et al., 2010; Ryan et al., 2009]. The red and blue dashed lines show the faults mapped by Mittelstaedt et al., (2012) using a high-resolution bathymetric, magnetic, and gravity survey. All faults with orientations close to 90° are marked as blue lines while faults with $\sim 45°$ orientations are colored red - see inset for fault orientation frequency distribution. The black ovals show the orientation of individual seamounts along the lineaments.

noes include several isolated islands (Wolf, Darwin, Genovesa, Marchena, and Pinta) and seamounts as well as the striking Wolf-Darwin lineament (see Figures 2.1 and 2.2 for a bathymetric map).

2.2.1 Galápagos Spreading Center

The most obvious expression of plume-ridge interaction in the Galápagos region is found along the GSC, which has a minimum hotspot-GSC distance of $\sim$ 200 km. The closest $\sim$ 800-km-long section of the GSC (between 87° and 95° W) is characterized by bathymetry much shallower (less than 2,500 m water depth) than that observed for ridges with similar spreading rate and no nearby plumes (Figure 2.1). The excess magmatism along this section of the GSC is also evidenced by the transition of ridge morphology from a valley-and-ridge domain to an axial high as the plume-GSC separation decreases (J. Sinton et al., 2003; Christie et al., 2005). The shallowest region of the GSC is located at approximately 90.5°W with a bathymetric depth of $\sim$ 1500 m compared to $\sim$ 3500 m depth of non-plume influenced segments of the GSC (See Figure 2.1). In addition, a large oblique transform fault - the Galápagos Transform Fault (GTF) - occurs at 90.7 °W along the GSC with maximum seafloor depth approaching approximately 3,300 m (See Figure 2.2). The plume influence along the GSC is geochemically manifested through more enriched incompatible element ratios (e.g., La/Sm) and radiogenic isotope ratios (Pb, Sr, Hf, Nd) with decreasing distance to the plume center due to increasing plume contribution (J.-G. Schilling et al., 1982, 2003; Ingle et al., 2010; S. A. Gibson et al., 2015).

2.2.2 Wolf-Darwin lineament

The WDL is a bathymetric high in the seafloor between the GSC and the Galápagos platform (Figures 2.1 and 2.2). It includes Wolf and Darwin Islands as well a couple of large elongate seamounts, all located on relatively young, thin, near-ridge lithosphere. The WDL and the WGSC intersect at approximately 92.2°W, substantially west of the seismically

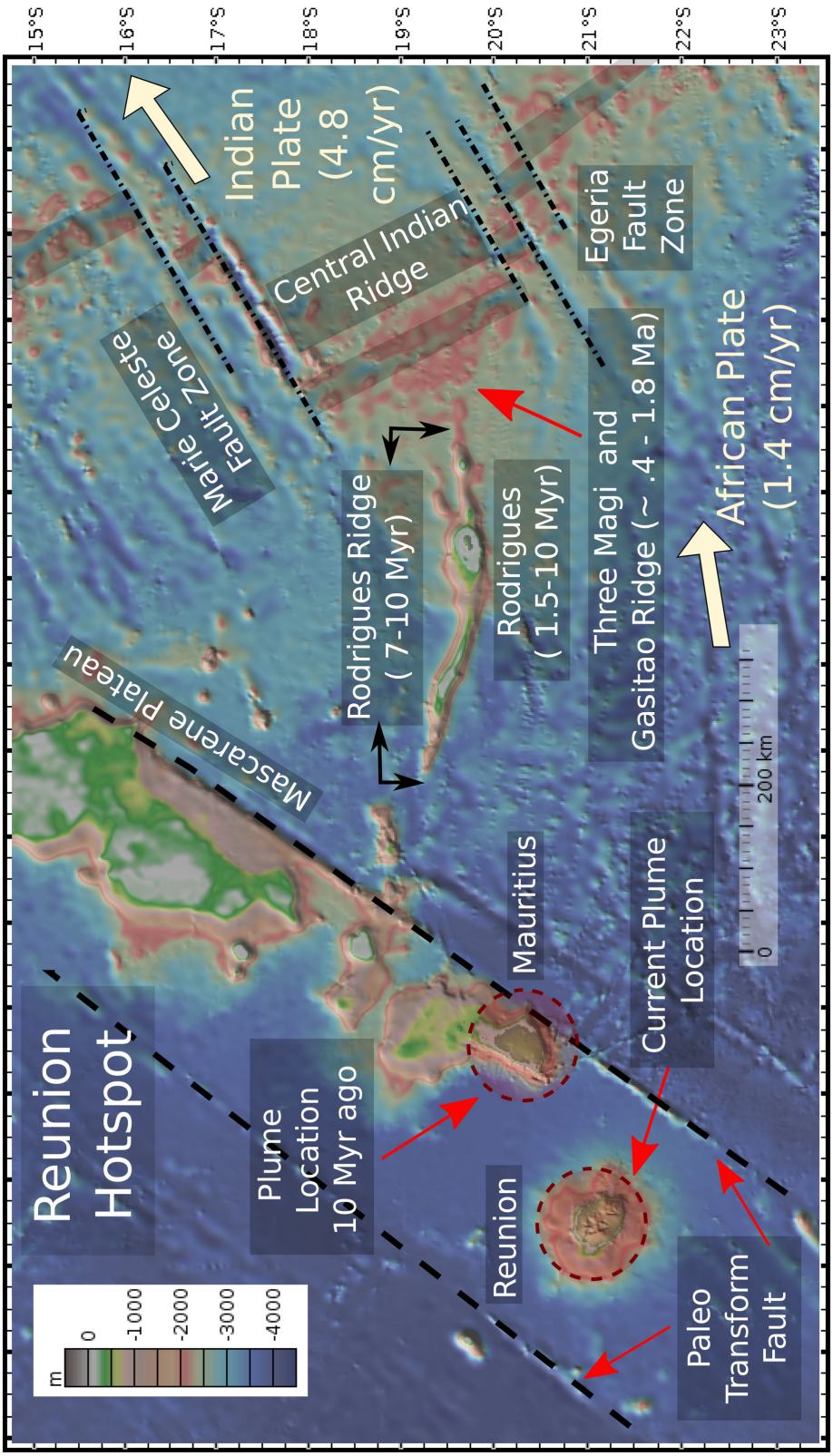
Reunion Hotspot
Plume Location 10 Myr ago
Reunion
Mauritius
Paleo Transform Fault
Current Plume Location
African Plate (1.4 cm/yr)
Three Magi and Gasitao Ridge (~ .4 - 1.8 Ma)
Rodrigues (1.5-10 Myr)
Rodrigues Ridge (7-10 Myr)
Mascarene plateau
Marie Celeste Fault Zone
Central Indian Ridge
Indian Plate (4.8 cm/yr)
Egeria Fault Zone
m
0
-1000
-2000
-3000
-4000
200 km
15°S
16°S
17°S
18°S
19°S
20°S
21°S
22°S
23°S
53°E
54°E
55°E
56°E
57°E
58°E
59°E
60°E
61°E
62°E
63°E
64°E
65°E
66°E
67°E
68°E

Figure 2.3

Figure 2.3 *(previous page)*: Bathymetric map of La Reunion hotspot - Rodrigues ridge with ages from McDougall et al.[1965]; McDougall[1971]; Duncan[1990]; Dyment et al.[2001, 2007];Moore et al.[2011]. We suggest that the Rodrigues ridge is analogous to the Wolf-Darwin lineament in the Galapagos and is formed by a similar process. The bathymetric base map is obtained from GeoMapApp [Haxby et al., 2010; Ryan et al.,2009]. We use the Seton et al.[2012] plate reconstruction model to estimate the plate velocities (Thick white arrows).

inferred plume location. In addition, the intersection is a local bathymetric high along the WGSC.

Darwin Island is a small island (less than 2 km across) which has been inferred to be a remnant of a much larger submarine volcano (K. S. Harpp, Wirth, et al., 2014). It is located at the northern end of the WDL, $\sim$ 50 km south of the GSC (see Figure 2.2). There are only two published K-Ar for Darwin lavas - 0.39 $\pm$ 0.15 Ma and 0.41 $\pm$ 0.16 Ma (W. M. White, McBirney, & Duncan, 1993). Wolf Island is the other island along WDL and is located southeast of Darwin Island. Analogous to Darwin, Wolf Island is an severly eroded volcano approximately 3 km long by 1 km wide (K. S. Harpp, Wirth, et al., 2014). The two K-Ar dates for Wolf Island lavas are 0.88 $\pm$ 0.13 Ma and 1.6 $\pm$ 0.07 Ma (W. M. White et al., 1993). It is noteworthy that one of these dates is older than any lavas currently dated in all of Northern Galápagos Volcanic Province (NGVP) (C. W. Sinton, Christie, & Duncan, 1996; K. S. Harpp, Hall, & Jackson, 2014). However, the sparse sampling precludes us from building a robust time-sequence of volcanism along WDL.

An important feature of the WDL volcanoes is the volcanoes are consistently younger than the underlying ocean crust. For instance, Wolf Island is at about 1.6 Ma old on 2-3.5 Ma crust whereas Darwin Island is approximately 0.4 Ma old on 1.5-2 Ma crust (D. S. Wilson & Hey, 1995; Mittelstaedt et al., 2012). Additionally, the WDL volcanoes do not exhibit any age progression (see Figure 2.2, K. S. Harpp, Wirth, & Korich, 2002a). Therefore, the current data suggests that these islands were formed close to their current locations, not at the GSC. A similar pattern with regards to the age of volcanism is observed for Rodrigues and Hollister ridges - Figures 2.3 and 2.4 respectively with ages for Rodrigues ridge (RR) from McDougall, Upton, and Wadsworth (1965); McDougall (1971); Duncan (1990); Dyment et al. (2001, 2007); J. Moore et al. (2011) and Hollister ridge (HR) from Vlastélic and Dosso (2005). Geochemically, the lavas on Wolf and Darwin Islands show some plume influence with contributions from both the high $^{207}Pb/^{204}Pb$-$^{208}Pb/^{204}Pb$ source and depleted upper mantle (K. S. Harpp & White, 2001; Vidito, Herzberg, Gazel, Geist, & Harpp, 2013). The mantle potential temperature beneath the WGSC is lower than under either WDL-2 or the plume center (J. Canales et al., 2002; Cushman, Sinton, Ito, & Eaby Dixon, 2004; Villagomez, Toomey, Hooft, & Solomon, 2007; S. A. Gibson & Geist, 2010), thus showing mantle cooling away from the plume center. Both of these observations suggest a transfer of mass between

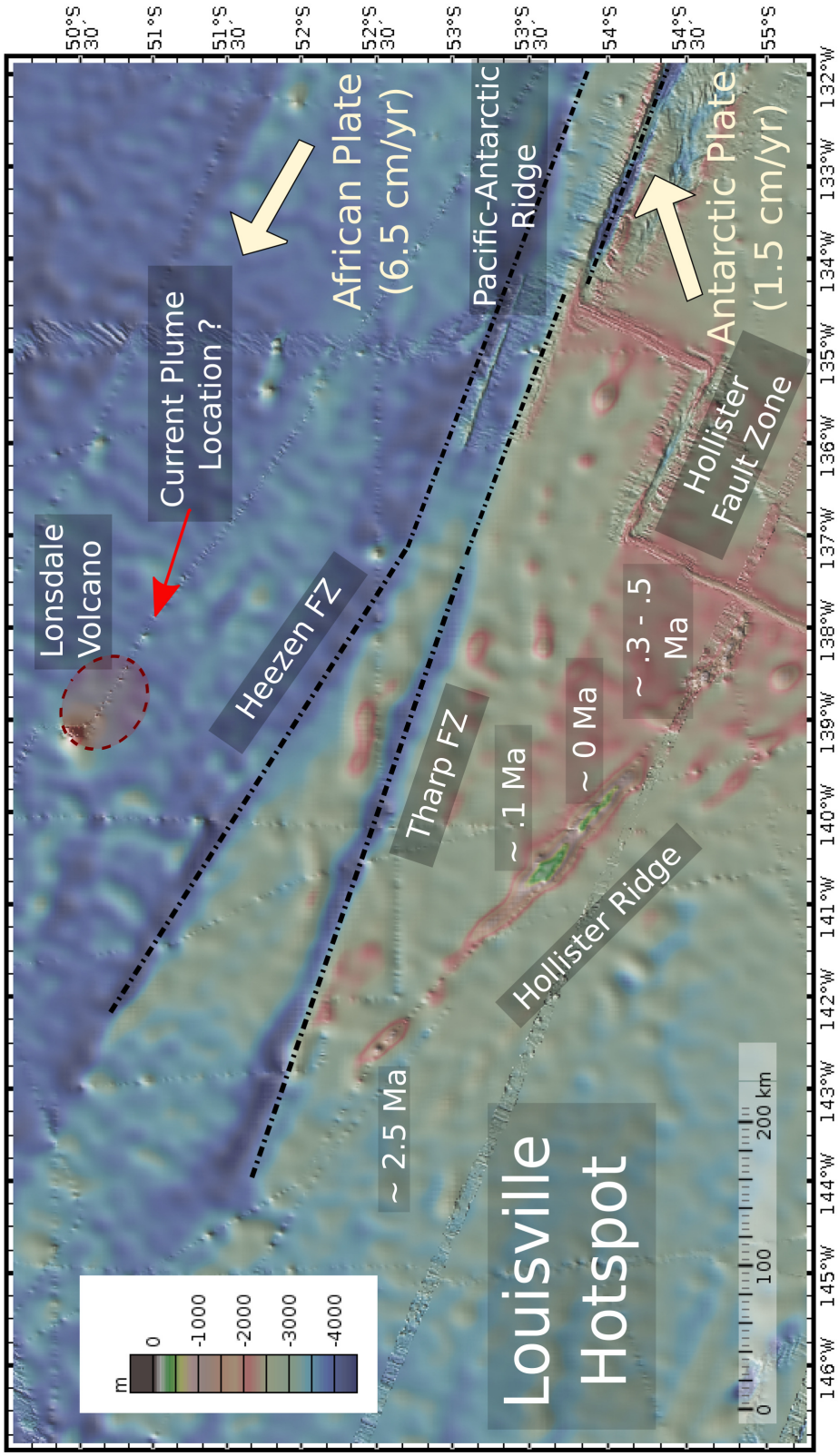
Lonsdale Volcano
Current Plume Location ?
African Plate (6.5 cm/yr)
Pacific-Antarctic Ridge
Antarctic Plate (1.5 cm/yr)
Hollister Fault Zone
Heezen FZ
Tharp FZ
~ 2.5 Ma
~ .1 Ma
~ 0 Ma
~ .3 - .5 Ma
Hollister Ridge
Louisville Hotspot
m
0
-1000
-2000
-3000
-4000
0
100
200 km
50°S 30′
51°S
51°S 30′
52°S
52°S 30′
53°S
53°S 30′
54°S
54°S 30′
55°S
146°W
145°W
144°W
143°W
142°W
141°W
140°W
139°W
138°W
137°W
136°W
135°W
134°W
133°W
132°W

Figure 2.4

Figure 2.4 *(previous page)*: Bathymetric map of Louisville Hotspot - Hollister ridge with ages from Vlastelic and Dosso[2005]. We suggest that the Hollister ridge is analogous to the Wolf-Darwin lineament in the Galápagos and is formed by a similar process. The bathymetric base map is obtained from GeoMapApp [Haxby et al., 2010; Ryan et al.,2009]. We use the Seton et al.[2012] plate reconstruction model to estimate the plate velocities (Thick white arrows)

the mantle plume (located beneath the Fernandina and Isabela islands) and the spreading center $\sim$ 250 km to the north, with the lineament volcanoes being the by-product surface expression.

2.2.3 Crustal Structure in Northern Galápagos Volcanic Province

High-resolution bathymetric, magnetic, and gravity surveys of the Northern Galápagos Volcanic Province (NGVP) by Mittelstaedt et al. (2012) and Mittelstaedt et al. (2014), as well as earlier work by J. Canales et al. (2002), have provided information on the crustal and lithospheric structure of the oceanic plate in the region encompassing the Wolf-Darwin lineament (See top panel in Figure 2.9 for the crustal thickness map). Specifically, (Mittelstaedt et al., 2014) find that the free-air gravity anomalies associated with the Galápagos lineaments are best fit using a flexure model with a spatially variable subsurface load likely corresponding to volcanic underplating beneath each seamount. Plate flexure models and mantle Bouger anomaly (MBA) inversions also suggest that the thermal thickness of the lithosphere is relatively uniform across the NGVP (Mittelstaedt et al., 2014). Hence, the slope of base of the lithosphere towards the ridge in the NGVP may be smaller than predicted from a standard plate cooling model due to the thermal influence of the plume. However, degeneracies between elastic thickness and crustal and lithospheric density structure make it difficult to ascertain the precise lithosphere/asthenosphere boundary slope.

Besides the lineaments, another strong influence on NGVP crustal structure is the oblique orientation of the GTF relative to plate spreading. In Figure 2.2, we show the results of fault density mapping in the NGVP based on a high-resolution bathymetric survey (Mittelstaedt et al., 2012). To first order, the fault density near the GTF appears to larger than along the NGVP (excluding the ridge axis). Since the oblique opening of the GTF (about 8 mm/yr) leads to an accumulation of normal strain, the mapped fault may accommodate some this strain (Mittelstaedt et al., 2012). In the figure, faults with orientations close to 90° are marked as blue lines while faults with $\sim$ 45° orientations are colored red. Looking at the histogram (Figure 2.2), we can see that most of the faults are not oriented parallel to WDL.

2.3 Models for lineament formation during plume-ridge interaction

Volcanic lineaments such as the WDL are enigmatic because they cannot be explained using either a simple mantle plume-plate motion model or currently preferred models for plume-ridge interaction. In the context of a fixed mantle plume sheared by overlying plate motion, it is challenging to explain the formation of the off-axis volcanic lineaments since the lineament direction does not match the direction of Nazca Plate's motion (towards the east) over the Galápagos hotspot (K. Harpp & Geist, 2002; R. Werner, Hoernle, Barckhausen, & Hauff, 2003; Morgan & Morgan, 2007).

Typically, plume-ridge interaction is modeled as an consequence of pancake-type solid-state flow of the plume towards the ridge up the topographic gradient. Although this model reasonably explains the along-axis width of plume-ridge interaction zones as a function of varying ridge spreading rate and changing plume volume flux (Feighner & Richards, 1995; Ribe, 1996; Ito & Lin, 1995; Ito et al., 2003), additional physical processes are needed to produce narrow volcanic lineaments such as the WDL, the RR, and the HR. This is supported by recent 3-D numerical simulations of purely solid-state flow by Ito and Bianco (2014) for the Galápagos plume with no narrow regions of melt accumulation as required to form lineaments. Furthermore, these simulations have difficulties in matching the detailed spatial pattern of geochemical variations. It must be noted that since Ito and Bianco (2014) do not explicitly model melt transport in the mantle, it is possible that some melt accumulation occurs underneath the mantle. However, we would contend that the results hints at the role of other processes which could both be responsible for localized lineament formation and could affect geochemistry without fundamentally altering the larger plume-ridge interaction scale that the existing models predict well (S. A. Gibson et al., 2015).

Two types of alternative models have been proposed to explain the presence of the volcanic lineaments - channelized solid-state flow of mantle plume material to the ridge (Morgan, 1978; Vogt, 1976, 1983), and lithospheric faulting in concert with localized mantle upwelling (or extraction of pre-existing melt) to produce lineament volcanism. In the following sections, we briefly discuss these models and highlight some geophysical observations that indicate their shortcomings. Our main focus for this section is to ascertain if models with significant additional complexity due to a two-phase partially-molten system are justified given the current state of observations.

2.3.1 Solid-State flow channelization

Morgan (1978) proposed that plume-ridge interaction-related lineaments such as the WDL are due to a channel at the base of the lithosphere thermally eroded due to the ridge-ward plume flow. In this model, the island/seamount formation occurs when this channel intersects the ridge axis. Consequently, one should expect a seamount age both identical to the seafloor age and systematically increasing away from the ridge axis. Additionally, the

lineament track should match the vectorial difference between the spreading center motion away from the hotspot and the plate motion (Mittelstaedt et al., 2012). Although the trace of the WDL approximately matches this latter prediction (K. Harpp & Geist, 2002), the age progression does not (see Figure 2.2, ages from W. M. White et al., 1993; C. W. Sinton et al., 1996; K. S. Harpp, Hall, & Jackson, 2014). Furthermore, other less prominent lineaments in the NGVP, which were presumably formed by the same mechanism as the WDL, don't have the right vector trace. The lack of age-progressive volcanism along the WDL also precludes the seamount lineaments originating from small-scale-convection-related channelized asthenospheric return flow (e.g., Harmon, Forsyth, & Scheirer, 2006), or shear-driven upwelling (Ballmer, Conrad, Smith, & Harmon, 2013). We note however that processes responsible for transporting melt from the asthenosphere to the seafloor are not well understood and can bias observations *vis-a-vis* expectations with regards to age progression.

Another model commonly proposed to explain the volcanic lineaments is a Saffman-Taylor type viscous fingering instability (Saffman & Taylor, 1958) of the hotter and lower viscosity plume material flowing into the higher viscosity upper mantle (Snyder & Tait, 1995; Weeraratne, Parmentier, & Forsyth, 2003; Nissanka, Weeraratne, & Parmentier, 2014). However, 3-D numerical simulations by Sleep (2008) to test this hypothesis have demonstrated that it is implausibly difficult to produce narrow enough three-dimensional viscous fingers. The advancing fingers tend to spread perpendicular to the flow direction with time due to the buoyancy of the plume material with respect to the background mantle. In addition, (Pollard, Muller, & Dockstader, 1975) have shown that flow as a continuous sheet is preferable to transport as thin fingers in a high-viscosity medium since more mechanical energy is dissipated through dilation and deformation by thin fingers. Consequently, narrow fingers would experience increased viscous drag compared to a sheet flow. The results of simulations in Sleep (2008) are also consistent with field observations of much smaller scale magmatic fingers in sheet intrusions, wherein typical well-isolated finger lengths are not very large ($\sim$ 10 m, Pollard et al., 1975) and the magmatic fingers typically widen and coalesce as the flow progresses (Schofield, Brown, Magee, & Stevenson, 2012; Magee, Muirhead, et al., 2016a). Hence, both numerical simulations as well as observational analogs predict a relation between the width and length of the lineaments that does not correspond to the geometry of WDL or other lineaments. The difficulty in forming narrow solid state channels further makes the Morgan/Vogt hypotheses less likely, even if the other points discussed above are ignored.

2.3.2 Lithospheric extension model

K. Harpp and Geist (2002) proposed a model for the lineaments (and volcanism in the NGVP in general) wherein the volcanics is a consequence of tensional stresses arising from the slightly oblique orientation of the GTF ($\sim 15^\circ$) relative to the Nazca plate motion. They hypothesized that the strain in this region will be partitioned between strike-slip motion along the fault and extension arising from the inside ridge-fault corner at 90.7° W along the GSC (Taylor, Crook, & Sinton, 1994). Since there are two sources of hot mantle upwelling in

this region – the GSC and the Galápagos plume, pre-existing partial melt in the mantle can erupt to the surface and form volcanic centers along regional deviatoric stresses trajectories. Thus the regional stress field due to the GTF would be expected to be the primary influence on the location of volcanoes across the NGVP. Since the K. Harpp and Geist (2002) paper, a variety of new geophysical datasets have been collected along with new numerical simulations of relevant systems. Here, we briefly discuss some of these results, highlighting potential inconsistencies between observations and predictions of the lithospheric extension model. Our primary motivation for this discussion is not to argue that lithospheric extension has no role in lineament formation, but rather to highlight aspects suggesting a more significant role for other physical processes.

1. The orientation of the majority of mapped faults in the NGVP does not correspond to the orientation of the WDL (see Figure 2.1, fault locations from Mittelstaedt et al., 2012). Instead the faults are either parallel to the spreading ridge or slightly oblique to the Galápagos Transform Fault, but not parallel to the WDL. This is shown by the histogram in the inset of Figure 2.2, which illustrates the number density of the faults as a function of their angle measured perpendicular to the WGSC. We note that the observed fault density may be affected by voluminous volcanism covering up faults as well as influence of heating due to magma transport. The faults may also have been buried by sediments. We may still expect an increasing or constant density of mapped faults throughout NGVP with an orientation parallel to the WDL. However, this can be biased by some fraction due to strongly varying orientations of the lithospheric stresses (Mittelstaedt & Ito, 2005).

2. The region around the Galapagos Transform Fault has an anomalously large density of faults and may be the region in the NGVP with maximum extension (Mittelstaedt et al., 2014). Hence, given the broad region of thermal and geochemical anomalies expected due to mixing of the plume material with the upwelling mantle, the most extensive volcanism may be expected along this region. The northern GTF is instead a strong topographic low with depths as great as $\sim$ 3300 m below sea level, and little indication of anomalous volcanism (Figure 2.2; note that this is not true for the southern GTF as the active plume is approached). Furthermore, the Rodrigues Ridge, Hollister Ridge, and the Mid-Pac Mountains/ridges intersect large transform faults along their path from the plume location to the spreading ridge (Figures 2.3 and 2.4). The lineament orientations however don't seem to be strongly influenced by the presence the transform fractures as one might have expected nor do we see any volcanism along the transform faults.

3. Mittelstaedt et al. (2012) have done numerical calculations of melt production due to mantle upwelling as a consequence of extension along the WDL. They show the insufficient amount of melt is produced to account for even the surface volcanic expression of the WDL, leaving aside the significant intrusive volcanism inferred from bathymetric

and gravity mapping by Mittelstaedt et al. (2014). Numerical results from Karakas and Dufek (2015) modeling the effect of extension incorporating both mantle-derived and crustal melts confirm the conclusions of Mittelstaedt et al. (2012). Their results also show that the small amount of melt generated by extension would provide insufficient heat flux to melt any appreciable amount of existing lithosphere. Thus, both the results indicate a significant mismatch between the volcanic volume predicted by lithospheric extension and what is actually observed.

4. The analysis of gravity measurements using plate-flexure models indicates the presence of a large (4-10 times the extruded volume), but localized volume of under-plated magmatic material underneath the NGVP lineaments (Mittelstaedt et al., 2014). This is challenging, though not impossible, to explain in the lithospheric extension model, wherein a broader region of partial melt and underplating may be expected, given the large-scale thermal and compositional anomaly of the plume. Similarly, the expression of the lineament track extends along a very confined path up until its intersection with the spreading ridge, with a corresponding signature in topography and gravity. Both of these observations suggest a very spatially localized region of excess melt production or transport.

5. The seismicity of the Galápagos region (all magnitude 3 and above earthquakes in the ISC Bulletin catalogue -][Figure 2.5 - top panel International Seismological Centre, 2013) as well as other plume-ridge interaction regions - La Réunion and Louisville (See Figure 2.5, earthquakes from the same ISC catalogue) - indicates a relative paucity of earthquakes along the WDL or any of the other lineaments compared to their corresponding ridges. This suggests that these features are not primarily active fractures induced by lithospheric extensional faulting though the heating of the crust and the lithosphere due volcanism may have reduced the seismicity. Simulations of the thermal and mechanical behavior of oceanic transform faults by Roland, Behn, and Hirth (2010) show that a $\sim$100 km transform zone would have a seismogenic width of order 10-20 km surrounding the transform zone, which is consistent with the seismicity observations. We would note that there are some seismic events located along the lineaments and it is possible that the lack of seismicity maybe be potentially explained by lack of activity along the lineaments.

We note that detailed modeling work is required to precisely quantify the above statements and compare with observations. In particular, cooler mantle temperature beneath the transform fault may partially/completely account for the lack of volcanism while silent slip due to cracking involving fluids and serpentinization may account for some of the lack of seismicity elsewhere. Similarly, the seismicity in some lineament regions may be underrepresented due to gaps in coverage. Analogously, the confined surface expression of the lineaments may be partially due to lithospheric and crustal melt transport processes. However, considering the mismatches in aggregate, we believe that it is difficult for the lithospheric

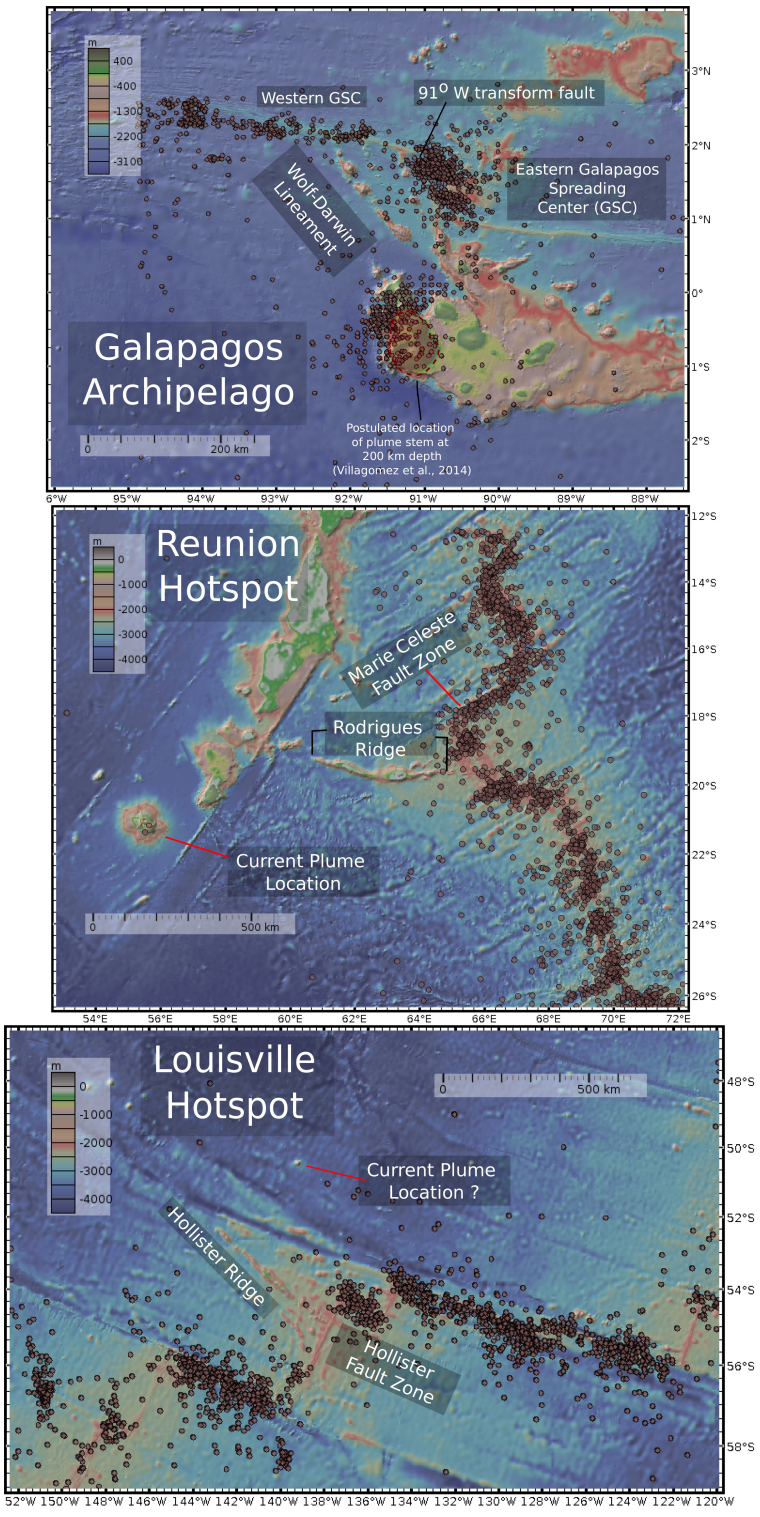
Western GSC
91° W transform fault
Eastern Galapagos Spreading Center (GSC)
Wolf-Darwin Lineament
Galapagos Archipelago
Postulated location of plume stem at 200 km depth (Villagomez et al., 2014)
200 km
Reunion Hotspot
Marie Celeste Fault Zone
Rodrigues Ridge
Current Plume Location
500 km
Louisville Hotspot
Current Plume Location ?
Hollister Ridge
Hollister Fault Zone
500 km

Figure 2.5

Figure 2.5 *(previous page)*: Earthquakes of magnitude 3 and above in the ISC Bulletin catalogue [International Seismological Centre, 2013] for the Galápagos, Réunion, and Louisville hotspot regions. There is a clear lack of seismicity along any of the lineaments, thus suggesting that these are not principally due to lithospheric extension.

extension model to explain the WDL and other lineaments on its own, and that additional physical processes are needed.

2.3.3 Other models

Besides the models discussed above, some additional processes have also been suggested as being important in plume-ridge interaction. In particular, Braun and Sohn (2003) proposed a model for plume-ridge interaction wherein melt from the mantle plume is transported to the nearby ridge through a high permeability melt channel - a sheet, rather than a cylindrical pipe - at the base of the lithosphere. Specifically, they postulated the presence of a ridgeward sloping high-porosity 'decompaction channel' at the base of the lithosphere collecting melt from the underlying mantle (D. W. Sparks & Parmentier, 1991; Spiegelman, 1993b). The primary problem with this model is that it provides no explanation for why there are narrow volcanic lineaments without invoking additional thermo-viscous fingering instabilities as in Helfrich (1995). Furthermore, if the lithospheric slope in the NGVP is less steep than what is expected based on plate cooling models (Mittelstaedt et al., 2014), melt transport along the base of the lithosphere may be less efficient.

Mittelstaedt and Ito (2005) suggested that the stress pattern induced on the Nazca plate due the buoyancy of the mantle plume interacting with the Galápagos transform fault-GSC boundary can explain the shape of the NGVP lineaments, including WDL. Using a numerical thin-plate model, they found that the depth integrated stresses in the NGVP lithosphere do indeed have the right pattern to explain the lineaments. Furthermore, the calculations predicted an age progression for the lineaments since it is easiest to fracture close to the ridge axis where the tensile stress would equal the lithospheric yield stress. Subsequently, the volcanism would be expected to propagate towards the plume along the spatial stress pattern. However, this prediction is in conflict with the lack of an age progression along the volcanic lineaments (see Figure 2, main text). Furthermore, the Rodrigues Ridge volcanic lineament at La Réunion cuts across a large paleo-transform fault that limits the plume swell's spatial extent (Figure 2.3, see (Lénat, Merle, & Lespagnol, 2009) for further discussion). Thus, further calculations are required to confirm whether the shape of the ridge for La Réunion hotspot due to depth-integrated stresses would match observations.

Another possible model for the Galápagos lineaments is the deflection of the mantle plume by a low-viscosity asthenosphere layer with significant return flow driven by plate motion and mid-ocean ridge pressure drop (M. A. Richards & Griffiths, 1988; R. C. Kerr, Meriaux,

& Lister, 2008). We estimated the deflection of the mantle plume due to this return flow assuming a radially layered mantle viscosity model and using a propagator-matrix method for mantle flow calculations (Hager & O'Connell, 1981). We did not find any reasonable viscosity and plume structure parameters that allowed a significant deflection of the plume channel given the current plume ridge separation for the Galápagos. Hence, we conclude that deflection of the plume by asthenospheric return flow is not a likely mechanism for explaining the WDL and other similar lineaments.

Finally,S. A. Gibson et al. (2015) analyzed the geochemistry of Galápagos and GSC basalts using Principal Component analysis and found that the ridge sections closest to the plume (i.e. EGSC) exhibit an enrichment signature which is well explained by addition of a deep plume component. Physically, they proposed that either a single deep $\sim$ 175 km wide, NE trending confined solid-state channel or a collection of deep melt channels is required to transport hydrous melt component from the plume to the ridge. Additionally, S. A. Gibson et al. (2015) proposed that the plume-to-ridge transport in Galápagos has been anchored to a ridge section even with increasing plume-ridge distance over the past 5 Ma (Mittelstaedt et al., 2014). Our proposed model for WDL and other lineaments in the next section is conceptually similar to the S. A. Gibson et al. (2015) model, and expands upon these ideas more quantitatively.

2.4 Proposed model for lineament formation - Melt channelization

We have explored what we believe is a crucial missing component in most previous models – melt transport from plume to ridge, likely in the form of melt channels. We envision that the melt could be transported as either a high-porosity, two-phase aggregate, or an open melt-filled channel. The concept of melt channelization is based on the various instabilities which can lead to localization of the melt flow in two-phase porous melt mantle flow. In the following sections, we describe our conceptual model for melt channelization in Galápagos, followed by a discussion of the physical mechanisms that may lead to melt channelization and the nature of our hypothesized channels.

2.4.1 Melt channelization in Galápagos

We propose the following model for the formation of the Wolf-Darwin lineament (and other NGVP lineaments) in the Galápagos: these lineaments are a direct surface expression of sub-lithospheric melt channels transporting melt from the mantle plume to the spreading ridge beneath a young, thin lithosphere (see Figure 2.6 and Figure 2.7). The locus of the lineaments including the WDL itself, as well as the Pinta, Marchena, and Genovesa related ridges, is located northward of the inferred plume center (See Figure 2.6 for the trace of the lineaments J. Sinton et al., 2003; Villagómez et al., 2014).

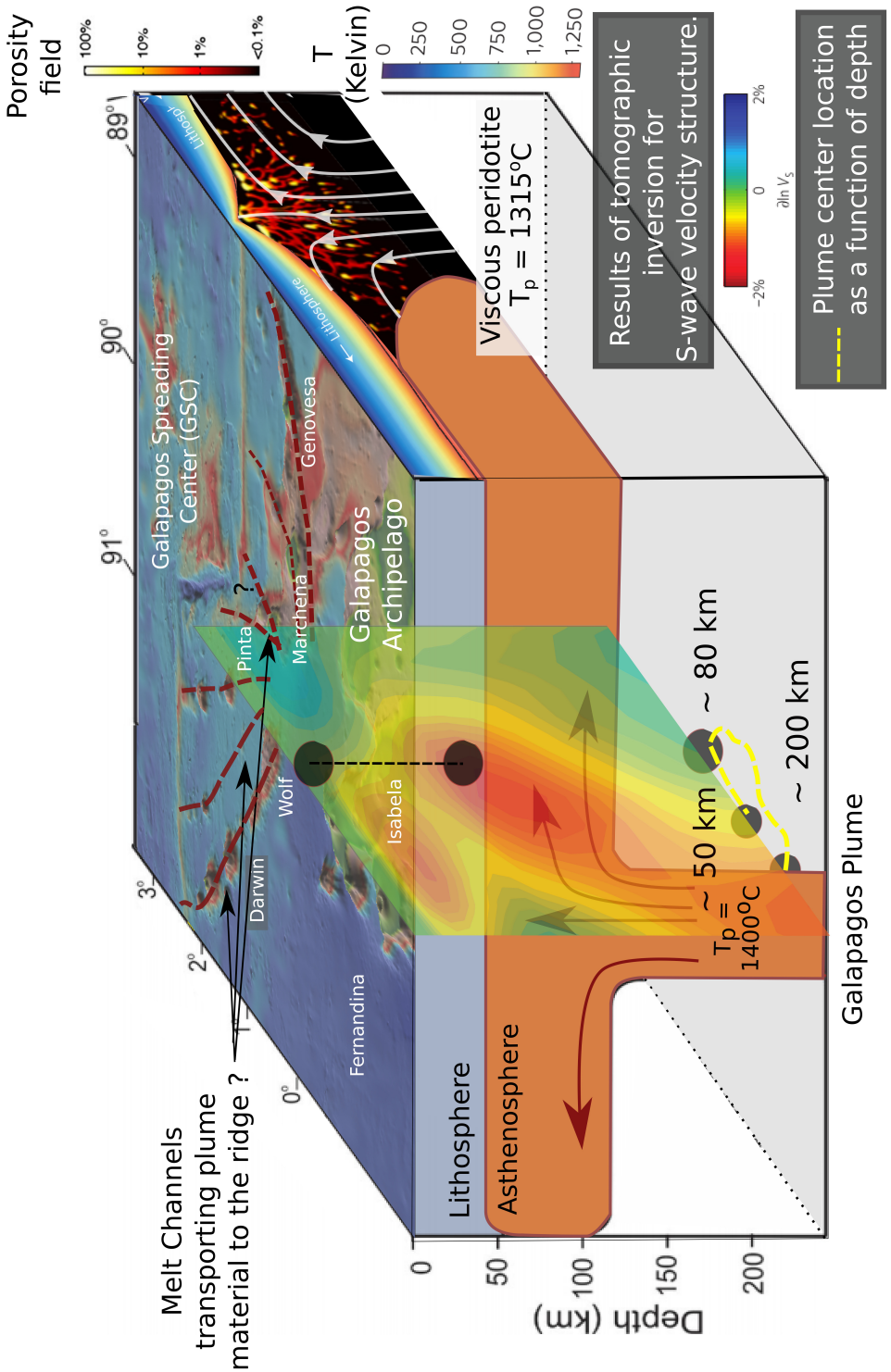
Porosity field
100%
10%
1%
<0.1%
T (Kelvin)
0
250
500
750
1,000
1,250
Viscous peridotite
Tp = 1315°C
Results of tomographic inversion for S-wave velocity structure.
2%
0
-2%
∂ln Vs
Plume center location as a function of depth
Galapagos Spreading Center (GSC)
Lithosphere
Lithosphere
Galapagos Archipelago
Genovesa
Marchena
Pinta
?
Wolf
Darwin
Isabela
Fernandina
89°
90°
91°
3°
2°
0°
Melt Channels transporting plume material to the ridge ?
Lithosphere
Asthenosphere
~ 50 km
~ 80 km
~ 200 km
Tp = 1400°C
Galapagos Plume
Depth (km)
0
50
100
150
200

Figure 2.6

Figure 2.6 *(previous page)*: A 3D schematic illustration of the proposed model for Galápagos lineaments. We show the position of the mantle plume and the hypothesized melt channels forming the lineaments. In addition, the asthenosphere - lithosphere cut-out at the upper right side of the diagram shows results from a 2D two-phase flow simulation for an isolated mid-ocean ridge by Katz and Weatherley, [2012]. The high-porosity regions in the figure denote channelized flow akin to our proposed melt channels. We also include a North-South cross-section at 91° W of the S-wave tomographic model of Villagomez et al.[2014]. We have plotted the location of the plume center as a function of depth (black circles at the base of the figure). This clearly shows a deflection of the plume stem towards the ridge at intermediate depths ($\sim$ 70 - 100 km). Analogously, the two black points connected by a dashed line show the connection between the plume center's location at $\sim$ 80 km depth and its surface projection. Note that this central location at intermediate depths is located north east of Isabela island and is close to the location of the convergence of the lineaments. We suggest that this convergence point at the asthenospheric plume center may represent the source location of melt channels forming lineaments. The estimates for ambient mantle and plume temperatures are from Gibson and Geist [2010] while the bathymetry is from GeoMapApp [Haxby et al., 2010; Ryan et al., 2009]

2.4.1.1 Source location of melt channels

We hypothesize that the melt channels are sourced from the upper, northwardly deflected section of the plume at relatively large depths ($\sim$ 60 - 100 km). A deep source location of the melt channels is required to explain the geochemical observations of plume-derived volatile-rich melts at the GSC (S. A. Gibson et al., 2015). The addition of even small weight percentages of water and carbon dioxide has been shown to lower the solidus temperature in multiple experiments (e.g., Hirschmann, Asimow, Ghiorso, & Stolper, 1999; Dasgupta, Hirschmann, & Smith, 2007) and thus increase the depth where mantle melting initiates. Consequently, the hydrous phases in the plume would melt first and the residual plume material flowing towards the ridge would become depleted in those components (T. Keller & Katz, 2016). In addition, substantial mixing with melt produced above the dry peridotite solidus in the plume would decrease volatile fraction of the melt (T. Keller, Katz, & Hirschmann, 2017). Thus, melt supplied to the GSC can retain substantial H_2O only if the melt channels are sourced from greater depths as proposed.

The proposed source location and initiation depth of the melt channels is also consistent with the results of seismic tomography from Villagómez et al. (2014), who find that the plume is tilted towards the ridge at about 60 - 100 km depths. To illustrate this point, we show a slice from their tomographic model in Figure 2.6. The black circles at the base of the figure represent projected locations of the plume center at various depths ($\sim$ 40, 80, and 200 km) and suggest a deflection of the plume stem towards the ridge at intermediate depths.

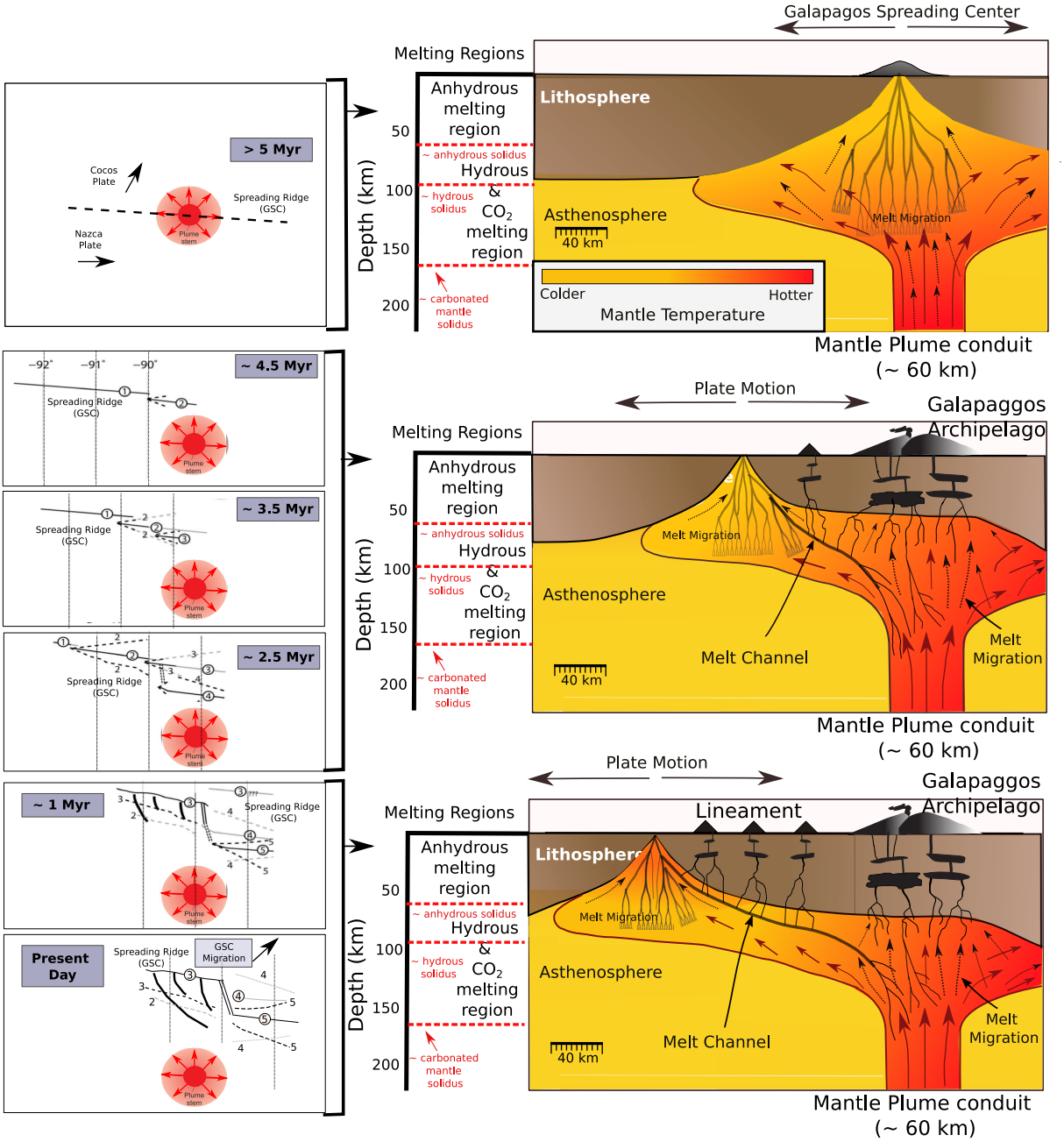
Galapagos Spreading Center
Melting Regions
Anhydrous melting region
~ anhydrous solidus
Hydrous & CO_2 melting region
~ hydrous solidus
~ carbonated mantle solidus
Depth (km)
50
100
150
200
Lithosphere
Asthenosphere
40 km
Melt Migration
Colder
Hotter
Mantle Temperature
Mantle Plume conduit (~ 60 km)
> 5 Myr
Cocos Plate
Nazca Plate
Spreading Ridge (GSC)
Plume stem
~ 4.5 Myr
~ 3.5 Myr
~ 2.5 Myr
~ 1 Myr
Present Day
GSC Migration
Plate Motion
Galapaggos Archipelago
Melt Channel
Lineament

Figure 2.7

Figure 2.7 *(previous page)*: A schematic showing the relative locations of the Galápagos Spreading Center (GSC) and the mantle plume over time and the corresponding process of melt channelization and lineament formation. The GSC has migrated continuously to the north of the plume over the past 5 Ma along with multiple small ridge jumps (50 - 100 km) towards the plume ; the plume location is fixed in all plots (figure modified from Mittelstaedt et al., 2012). The left panels show the relative ridge and plume locations with corresponding cross-sections perpendicular to the ridge on the right. The illustration of melt flow and channelization is shown schematically with a channel network as well as dashed black arrows. On the other hand, the flow of the solid mantle is indicated schematically by red arrows. As the plume-ridge separation increases, only a few active melt channels can transport melt to the ridge, and the channels also become "stretched" while their slopes become shallower. Eventually, melt is periodically transported from the channel to the surface to form lineaments.

Analogously, the two black points connected by a dashed line illustrate the connection between plume center's location at $\sim$ 80 km depth and its surface projection. We consider this link preliminary since existing seismic tomography studies of the Galápagos do not have station coverage across the NGVP and GSC. Consequently, the structure of the plume in the region close to the ridge is still uncertain.

In our model, the bulk of melt transported to the WDL and the GSC is produced beneath the main Galápagos archipelago, instead of in the shallow mantle in the intermediate region between the plume and the ridge. We argue that this direct transport is a crucial component of plume-ridge interaction, and may even be primarily responsible for the geophysical and geochemical influence of the plume on the ridge segments closest to the hot-spot (S. A. Gibson et al., 2015). We show a schematic cross-section of the proposed melt channels in a 2D slice perpendicular to the spreading ridge in Figure 2.7 (bottom right panel).

2.4.1.2 Role of ridge migration

To understand the current disposition of the lineaments, it is also necessary to consider the time-evolution of the relative location of the Galápagos spreading center and the mantle plume. In particular, plate reconstructions based on seafloor magnetic mapping in the NGVP by Mittelstaedt et al. (2012) (with previous work by (D. S. Wilson & Hey, 1995)) suggest that over the past 5 Ma, the GSC has continuously migrated away from the plume (see Figure 2.7a-f for reconstructions with the plume location fixed over time). As a consequence, the melt channel network beneath the spreading ridge, which may extend up to 50-100 km away from the ridge, would get stretched over time and remain connected to the plume utilizing pre-existing older melt channels (see results of a two-phase flow simulation from R. F. Katz and Weatherley (2012) for a spreading ridge not influenced by a plume in Figure

2.6). In addition, sections of the GSC have also had small ($\sim$ 50-100 km each) ridge jumps towards the plume (See Figure 2.7a-f) due to the weakening of the crust due to the plume (Mittelstaedt, Ito, & Van Hunen, 2011). Since these ridge jumps periodically decreased the plume-ridge distance, they further enhanced the ability of melt channels to transport plume melt to the ridge. We propose that, in aggregate, over time a few melt channels would come to dominate transport and remain active, and that these are eventually expressed as volcanic lineaments at the surface.

A schematic representation of this process is shown in Figure 2.7 with the left panels showing the relative location of the plume and the GSC in plan view and the right panels illustrating the formation and extension of melt channels. The top right panel in Figure 2.7 shows the location of the melt channelization when the plume is located under the ridge followed by panels with increasing plume-ridge separation. We note that a similar concept was suggested by S. A. Gibson et al. (2015), and we are elaborating upon it here. In our model, the volcanic construction of the islands and seamounts along the lineaments would have initiated only after the plume was sufficiently far away from the ridge such that the active melt channels were shallower and had an opportunity to dike through the lithosphere, instead of feeding eruptions at the spreading ridge only (see schematic in Figure 2.7).

Physically, we expect the maximum distance over which a melt channel can transport melt without freezing to be proportional to the melt flux carried in the channel (see next section for scalings that justify this assertion). Hence, over time only the largest melt flux-carrying channels survive. A similar result is obtained when considering the melt flow in the channel as a Darcy porous flow. The Darcy melt flux in a melt channel is directly proportional to mantle hydraulic permeability (K) and inversely proportional to melt viscosity (e.g., McKenzie, 1984), and the effective K for an array of cylindrical channels is proportional to pipe radius (R) to the fourth power (R^4) (Phillips, 1991). The strong dependence of permeability on thickness of the conduits means that melt is focused preferentially into the thickest conduits (Zhao, Hobbs, & Ord, 2008) and the thinner conduits are starved of melt and collapse in thickness (freeze-out). Thus, we propose that initially closely-spaced channels would tend to coalesce into higher melt-flux channels and get stretched over longer distances with increasing plume-ridge separation.

2.4.2 Formation of melt channels

In our preceding discussion of melt channelization in the context of volcanic lineaments, we have not specified any particular physical mechanism responsible for channel formation. The primary physical rationale for melt channelization is the extensive work over the past couple of decades which has been shown that the two-phase melt flow equations in the mantle have solutions leading to melt channelization (i.e. localization of melt flow in preferential regions) by a variety of mechanisms (e.g., Richter & McKenzie, 1984; Scott & Stevenson, 1984; Spiegelman, 1993c, 1993a; Stevenson, 1989; Aharonov, Whitehead, Kelemen, & Spiegelman, 1995; Aharonov, Spiegelman, & Kelemen, 1997; Spiegelman, Kelemen, & Aharonov, 2001;

Liang & Peng, 2010; Hewitt, 2010). Complementarily, numerical simulations by Spiegelman and McKenzie (1987); Ghods and Arkani-Hamed (2000); R. F. Katz and Weatherley (2012); Weatherley and Katz (2012); Crowley, Katz, Huybers, Langmuir, and Park (2015), and Weatherley and Katz (2015) have found that melt channelization may also occur on a tectonic scale. In addition, there is geological evidence that melt producing oceanic crust is not always in equilibrium with asthenospheric mantle which it passed through (Braun & Kelemen, 2002). Also, the melt transport time from the point of generation to surface eruption has been estimated to order thousands of years for some mid-ocean ridges using U-Th series data (see reviews by Peate & Hawkesworth, 2005; Elliott & Spiegelman, 2013). Both of these observations are difficult to reconcile with purely melt percolation in a porous medium and require the presence of some form of melt channels which can are chemically isolated from their surrounding mantle and have high permeability (Spiegelman & Kelemen, 2003; Kelemen, Hirth, Shimizu, Spiegelman, & Dick, 1997; Braun & Kelemen, 2002; Kohlstedt & Holtzman, 2009).

Although, it would require calculations beyond the scope of this paper to ascertain the dominant mode of channelization instability for the mantle plume-spreading interaction case, we highlight some thermo-fluid instability mechanisms which we think are likely candidates for focusing melt. One of the most extensively studied of such instabilities is the reactive infiltration instability (RII) (Chadam, Merino, & Ortoleva, 1986; Ortoleva, Chadam, Merino, & Sen, 1987; Aharonov et al., 1995; Spiegelman et al., 2001). The physical mechanism for RII is the increasing solubility of clinopyroxene (cpx) in the melt with decreasing pressures (i.e., towards the surface). Consequently, as the basaltic melt migrates upward through the melting column, it can dissolve more cpx from the peridotitic mantle. The dissolution leads to increased melt permeability of the mantle locally which in turn enhances local melt flux. Since it is easier to maintain a stronger solubility gradient with higher melt flux, regions with larger flux dissolve more cpx and thus lead to a positive feedback eventually forming melt rich channels. For typical mantle properties and models include both mass and energy conservation, Hewitt (2010) and Weatherley and Katz (2012) show that adding a small spatially variable fraction of an additional mantle component with a lower solidus temperature leads to spatial variations in melting. These variations can act as sites where high-porosity channels can initiate and eventually lead to channelization on a tectonic scale (R. F. Katz & Weatherley, 2012).

Analogously, T. Keller and Katz (2016) and T. Keller et al. (2017) show that the flux of deep, low-viscosity, low-degree, volatile-rich melt (usually CO_2 or H_2O rich melt) toward the volatile-free ("dry") solidus also leads to an instability physically akin to the RII. As volatile enriched melts, with lower solidus temperature than the surrounding mantle (e.g., Hirschmann et al., 1999; Dasgupta et al., 2007), flows up from deeper depths, it promotes local melting of anhydrous peridotic component. Consequently, there is an increase in the local permeability and hence a positive feedback on melt flux. Since mantle plume source material is typically more volatile enriched than MORB, and observations suggest H_2O transport from the plume to the ridge (e.g., S. A. Gibson et al., 2015), we consider the

volatile flux-induced RII as a promising mechanism for initiation of melt channelization in the asthenosphere.

2.4.3 Nature of melt channels

In our conceptual model, we expect the melt channels to be more akin to a Poiseuille-type pipe flow rather than porous percolating flow through the residual mantle (as proposed by Braun & Sohn, 2003). In order for our model to be feasible, we require melt flow velocities to be large enough such that the melt is not in exact thermodynamic equilibrium with the surrounding mantle. This likely requires local porosities of at least a few percent (more likely order 10s of percent) in order to have large enough melt permeability. We would however acknowledge that additional theoretical work is required to test this assertion and ascertain the dynamic conditions where melt and the surrounding mantle are not in thermodynamic equilibrium.

Stability analysis of the two-phase mantle flow equations by Hewitt (2010), as well as experiments (Pec, Holtzman, Zimmerman, & Kohlstedt, 2015; Holtzman, Groebner, Zimmerman, Ginsberg, & Kohlstedt, 2003) show that in two-phase flow instabilities, the local melt fraction (porosity) in the sheet or finger-like channels can be much much higher than the surrounding mantle and may locally even reach unity. Thus, our model requirement may be potentially satisfied for mantle melt transport. We acknowledge that the details of the process of melt localization are dependent on the form of the chosen mantle rheology and inclusion of factors such as temperature, pressure, grain size, water content, melt fraction, shear modulus anisotropy, and compaction-decompaction asymmetry (e.g., Stevenson, 1989; Holtzman et al., 2003; J. A. D. Connolly & Podladchikov, 2007; T. Keller, May, & Kaus, 2013; Takei & Katz, 2013; Yarushina, Podladchikov, & Connolly, 2015a; Veveakis, Regenauer-Lieb, & Weinberg, 2015; J. A. D. Connolly & Podladchikov, 2015; Turner et al., 2015; Taylor-West & Katz, 2015; Baltzell, Parmentier, Liang, & Tirupathi, 2015). Hence, further work is required to ascertain the most likely values of melt fractions in melt channels and whether it reaches a value high enough such that the mantle would be better modeled as a high-porosity, two-phase dis-aggregated material rather than fluid percolation through a solid medium.

2.5 Scaling Relationships

In this initial study, we test the plausibility of our proposed model using simple scaling relations for the behavior of channelized flow of the plume material towards the ridge. Numerically simulating two-phase flow with appropriate resolution (< 100 m) at a reasonable tectonic scale for plume-ridge interaction is computationally challenging, so a full numerical model will await future studies.

We estimate analytically the horizontal distance over which a melt channel can thermodynamically persist in the sub-solidus mantle (L_p, see Figure 2.8 – top panel). If the

background mantle potential temperature is either above or at solidus (the melting region), even melt in thermodynamic equilibrium with the rock matrix will be transported without any freezing. The sub-solidus region would always be smaller than the actual plume center-ridge distance since there is a broad region of melting both around the plume center as well as the mid-ocean ridge location. We illustrate this in Figures 2.7 (redder colors indicate regions of higher melt generation) and 2.8. Detailed 3D numerical simulations with realistic rheology are needed to precisely quantify the sub-solidus region. Hence, our estimates of L_p are a minimal estimate of the permissible plume-ridge interaction distance.

2.5.1 Thermodynamic feasibility

We estimate the maximum length (L_p) over which a cylindrical melt channel can be sustained thermodynamically by modeling the temperature evolution of a cylindrical heat source in an infinite medium at uniform temperature T_m (see Figure 2.8, top panels).

In the following sections, we consider the end-member scenario of an open melt-filled channel (i.e. $\phi = 1$) for calculating the thermal viability of melt transport. However, this choice is not particularly restrictive since both Darcy flow through a porous media and Poiseuille-type pipe flow are proportional to imposed pressure gradients - $\mathrm{v}_{pipe} \propto (R_p^2/\eta_m)dp/dz$ while $\mathrm{v}_{darcy} \propto (k/\eta_m)dp/dz$ (R_p, η_m, and k are the pipe radius, fluid viscosity, and fluid permeability respectively). Hence, one can obtain the same radially averaged velocity with an appropriate choice of permeability, pipe radius, and fluid viscosity. Although the actual flow profile of the melt in a two-phase aggregate would indeed be very different, we are only interested in aggregate properties for our scaling analysis. Thus, we would emphasize that our conceptual model is completely applicable for melt transported as a high-porosity, two-phase aggregate instead of an open melt channel as long our parameter choices for R_p and η_m are thought of as 'effective' parameters. We partially consider the influence of this effect in our estimates by considering values of the magma dynamic viscosity (η_m) orders of magnitude larger than that of pure melt.

We use three different approximations to model the cylindrical heat source: an instantaneous heat pulse with equal power per unit length, a continuous heat flux source with equal power per unit length, and steady-state pressure-driven flow in a rigid channel. Only the third model includes latent heat effects. In all the models, we parametrise our calculations in terms of prescribed melt volume flux into the pipe, since that is an observationally constrained quantity (based on the volume of associated extrusive volcanism and the amount of underplated material). We choose these three models since they provide reasonable end-member scenarios for the thermal evolution of a melt channel. The top left panel of Figure 2.8 shows how the scaling analysis fits in the context of our schematic model. We list all the variables used in the subsequent section and their representative values in Table 2.2.

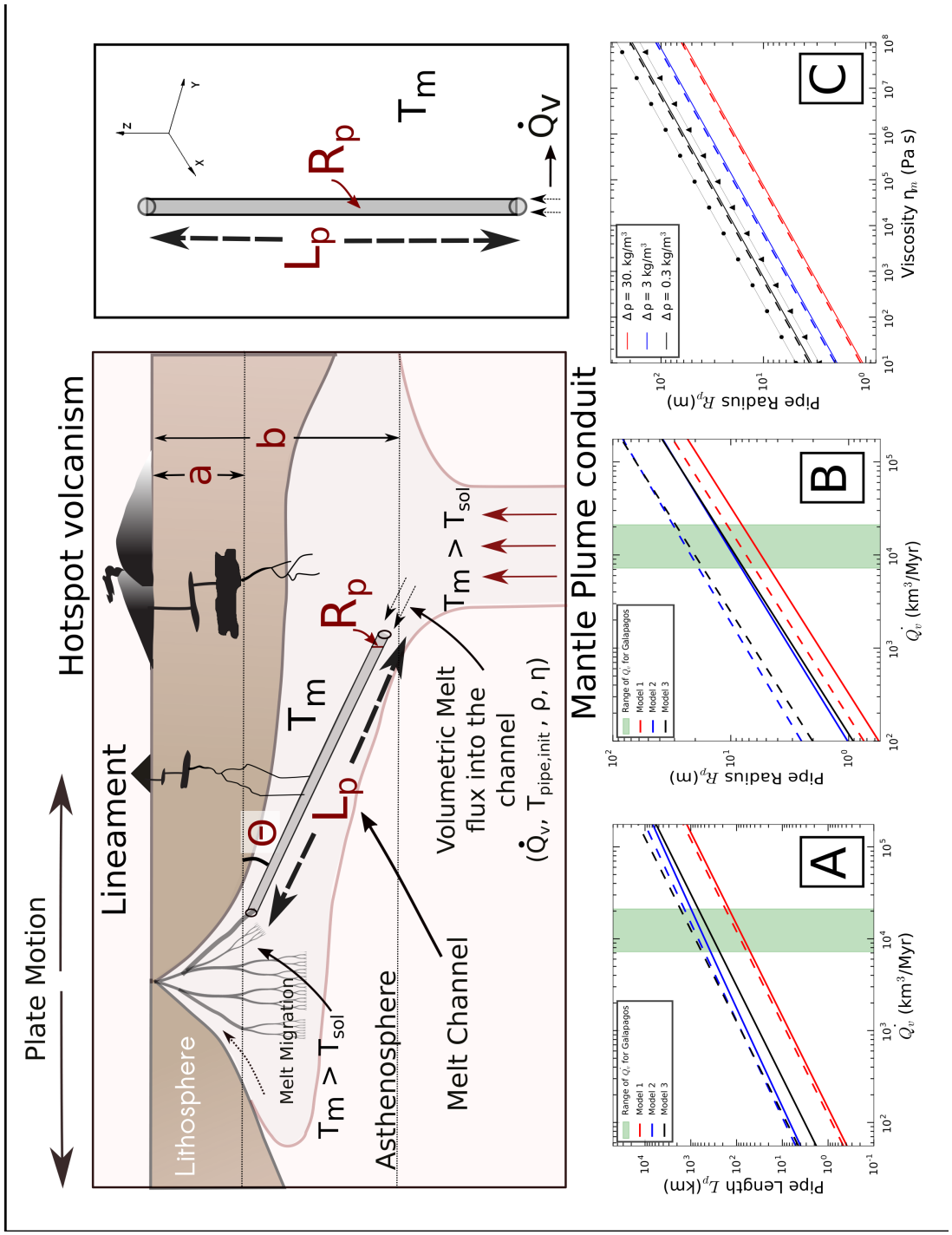
Plate Motion
Hotspot volcanism
Lineament
Lithosphere
Melt Migration
Tm > Tsol
Asthenosphere
a
b
Θ
Tm
Lp
Rp
Melt Channel
Volumetric Melt flux into the channel
(Q̇v, Tpipe,init , ρ, η)
Tm > Tsol
Mantle Plume conduit
Tm
Lp
Rp
Q̇V
A
B
C
Pipe Length Lp(km)
Pipe Radius Rp(m)
Q̇v (km³/Myr)
Viscosity ηm (Pa s)
Range of Q̇v for Galapagos
Model 1
Model 2
Model 3
Δρ = 30. kg/m³
Δρ = 3 kg/m³
Δρ = 0.3 kg/m³

Figure 2.8

Figure 2.8 *(previous page)*: A schematic showing the setup for the scaling analysis models and the primary variables as well as some scaling results. In the top left figure, the geodynamic setup is the same as in Figure 7 for direct comparison, while the top right panel shows the idealized case for models 1 and 2. In the **Bottom left** (labeled 'A'), we show the scaling results for L_p as a function of $\dot{Q}_v$ with the appropriate values for the Galápagos highlighed. The dashed and solid lines show results when varying one additional parameter that affects the results most (See Section 2.5.2 for details). In the **Bottom middle** (labeled 'B'), we show the results for R_p (R_{eff} for steady state model) as a function of $\dot{Q}_v$. In this figure, solid line represents results for nominal values (See Table 2.2) while dashed lines show the pipe radius required for critical Brinkman number $Br_c \sim 1$. Since $R_{p,c} > R_p$, our choice of neglecting viscous heating for our conservative estimates is reasonable. Finally, the **Bottom right** (labeled 'C'), shows the influence of viscosity, τ_m, $\Delta\rho$, and $(b-a)$ on R_p in the instantaneous heat pulse model (See Section 2.5.3 for details of parameter choices). In panels 'A' and 'B', instantaneous heat pulse model is Model 1, constant heat flux source model is Model 2, and the steady state model is Model 3. The particular parameter choices for the figures are described in the main text (Section 2.5.3).

2.5.1.1 Heat flow - cylindrical pipe

In all three models, we model the channel as a cylindrical pipe of radius R_p and length L_p. In this section, we define relationships that apply to all the models. First, the conductive heat flux out of the pipe at any time t is

$$\dot{Q}_{h,out}(t) = K_c \left.\frac{dT}{dr}\right|_{r=R_p} * (2\pi R_p L_p) \tag{2.1}$$

while heat flux into the pipe due to inflow of melt is

$$\dot{Q}_{h,in} = \dot{Q}_v \rho C_p \Delta T_{init} \tag{2.2}$$

Here, K_c is the thermal conductivity of the melt, ρ is the melt density, C_p is the specific heat capacity of melt, $\dot{Q}_v$ is the melt volumetric flux into the pipe, and ΔT_{init} is the initial length and flux averaged temperature excess of the melt relative to the surrounding mantle. Also, $\left.\frac{dT}{dr}\right|_{r=R_p}$, is the radial temperature gradient at $r = R_p$ averaged over the length of the channel.

Assuming Poiseuille flow in a cylindrical pipe, the volumetric flux will be $\dot{Q}_v \sim \frac{dP}{dz}\frac{R_p^4}{8\eta_m}$ where $\frac{dP}{dz}$ is the pressure gradient driving the flow and η_m is the magma dynamic viscosity. Since the primary driving force for the flow is the buoyancy of the melt with respect to the surrounding mantle, we assume that the total pressure drop is :

$$\Delta P = \Delta\rho g_x L_p \tag{2.3}$$

Here, $\Delta\rho$ is the density difference between the melt and solid mantle and $g_x = g\sin(\theta)$ is the component of gravity along the pipe direction. We approximate $\sin(\theta) \sim (b-a)/L_p$ where 'b' and 'a' correspond to the depths at the which the melt channel is initiated and terminated, respectively (see Figure 2.8 – top left panel). Hence,

$$\dot{Q}_v = (\Delta\rho g(b-a))R_p^4/(8\eta_m L_p) \tag{2.4}$$

In order to compare the relative importance of heat advection relative to diffusion ($u_{pipe}R_p/\kappa$), we use a non-dimensional number - Péclet number Pe :

$$Pe = \frac{\Delta P R_p^3}{8\kappa\eta_m L_p} \tag{2.5}$$

where κ is thermal diffusivity ($\kappa = \frac{K_c}{\rho C_p}$).

An order of magnitude estimate of the channel length L_p can be calculated using the fact that for a fluid parcel the typical conductive cooling timescale (τ) is R_p^2/κ and hence $L_p \sim \tau u_{pipe}$. However, the mean flow velocity in a cylindrical pipe (u_{pipe}) is $\sim \dot{Q}_v/R_p^2$. Hence, $L_p \sim \dot{Q}_v/\kappa$. The models in the subsequent sections refine this estimate by considering heat transport more carefully. Still, qualitatively the scaling results are similar (See Figure 2.8A and Eqn 2.10).

2.5.1.2 Instantaneous heat pulse source

We first model radial heat flux from a pipe by representing it as an impulse heat source placed along the z-axis in an infinite medium with temperature T_m (see Figure 2.8 – top right panel). Conceptually, this model represents a case where a cylindrical pipe filled with a fluid with an average temperature excess of ΔT_{init} relative to surroundings is allowed to cool radially by conduction. We then calculate the heat flow out of the pipe and equate it with the heat flow into the pipe. As the pipe length increases, the net heat loss increases and eventually exceeds input, thus freezing the pipe. Since we use a constant ΔT_{init} along the pipe, our results would be applicable if the heat transfer for a fluid parcel is dominated by advection rather than diffusion (Pe >> 1) and hence ΔT_{init} can remain above the solidus for an appreciable distance. We will check this assumption *a posteriori* for our parameters of interest.

The heat energy per unit length emitted at $t = 0$ is Q_0/L_p with $Q_0 = \rho C_p \Delta T_{init}(\pi R_p^2 L_p)$. The temperature field $T(r,t)$ at any subsequent time t will be (Carslaw & Jaeger, 1959; Taler & Duda, 2006) :

$$T(r,t) - T_m = \frac{Q_0}{\rho C_p L_p}\frac{1}{4\pi\kappa t}\exp(-\frac{r^2}{4\kappa t}) \tag{2.6}$$

$$\Rightarrow \frac{T(r,t)-T_m}{\Delta T_{init}} = \frac{R_p^2}{4\kappa t}\exp(-\frac{r^2}{4\kappa t}) \tag{2.7}$$

where $r^2 = x^2 + y^2$ and . The time averaged $\overline{dT/dr}|_{(r=R_p)}$ averaged from $t = 0$ to an arbitrary time $t = t_m$ is

$$\left.\frac{\overline{dT}}{dr}\right|_{r=R_p} = \frac{\Delta T_{init} R_p}{2\kappa t_m} \exp(-\frac{R_p^2}{4\kappa t_m}) \tag{2.8}$$

Equating the time averaged advective heat flux into and the conductive heat flux out of the pipe Eqns. (2.1), (2.2), and (2.8), the maximum pipe length L_p over which melt can be transported is obtained by setting

$$\dot{Q}_{h,in} = \dot{Q}_{h,out} \tag{2.9}$$

$$\Rightarrow L_p = \frac{\dot{Q}_v}{\pi\kappa} \frac{\tau_m}{\exp(-\frac{1}{4\tau_m})} \quad \text{where } \tau_m = \frac{\kappa t_m}{R_p^2} \tag{2.10}$$

Since most of the heat loss occurs on a typical diffusion timescale, we assume that $t_m \leq R_p^2/\kappa$ as a conservative estimate. Thus, we expect $\tau_m \leq 1$. Although the model described above is for an infinitesimal line source (the heat flux source is deposited only along the center of the pipe instead uniformly across the pipe radius), we have found that accounting for the finite size of the pipe affects the final results only minimally ($< 30\%$ difference) but adds significant complexity to the scaling relationships.

Thus, the pipe radius will be (using Eqns. (2.4) and (2.10))

$$R_p = \sqrt{\dot{Q}_v} \left[\frac{8\eta_m}{\pi\kappa} \frac{\tau_m}{\exp(-\frac{1}{4\tau_m})} \frac{1}{\Delta\rho g(b-a)} \right]^{1/4} \tag{2.11}$$

$$\Rightarrow R_p = \sqrt{L_p} \left[\frac{8\eta_m \pi\kappa}{\Delta\rho g(b-a)} \frac{\exp(-\frac{1}{4\tau_m})}{\tau_m} \right]^{1/4} \tag{2.12}$$

Since we only have an initial heat source and have not included latent heat effects, this model represents a conservative limit for the maximum pipe length L_p (Eqn. 2.10).

2.5.1.3 Constant heat flux source

We also constrain the maximum permissible pipe length using a slightly different approach that accounts for the long time duration of the channel flow ($t_f = [0.5 - 2]$ Ma) envisioned in our conceptual model. Physically, this model better accounts for the fact that over time, the mantle around the channel would not have a uniform temperature T_m but will be slightly hotter. Consequently, the radial heat loss out of the pipe will decrease and a larger transport distance will be permissible. We again approximate the melt transport in the pipe using the same type of heat source as in the calculations above, but now considering a constant heat source instead of an instantaneous source. Mathematically, this simply implies a convolution

of the temperature solutions with time lags integrated from time = 0 to t. As in the previous section, the model is valid if Pe >> 1.

The temperature profile for this model at any time t is given by (Carslaw & Jaeger, 1959; Taler & Duda, 2006) :

$$T(r,t) - T_m = \frac{\dot{Q}_{h,in}}{\rho C_p L_p} \frac{1}{4\pi\kappa} Ei(-\frac{r^2}{4\kappa t}) \tag{2.13}$$

$$\Rightarrow \frac{T(r,t) - T_m}{\Delta T_{init}} = \frac{\dot{Q}_v}{L_p} \frac{1}{4\pi\kappa} Ei(-\frac{r^2}{4\kappa t}) \tag{2.14}$$

where Ei is the exponential integral (Weisstein, 2002).

Since we are interested in heat flux from the pipe a long time (t_f) after its setup, we approximate a value for the radial temperature gradient $\frac{dT}{dr}$ by considering $T(r,t) - T_m = \Delta T_{init}/2$. The next step is to find the appropriate value of r to use in $\frac{dT}{dr} = \Delta T_{init}/2r$. It is important to note that r will generally not be equivalent to R_p. First, we use Eqn. (2.14) with $T(r,t) - T_m = \Delta T_{init}/2$ to get an appropriate value for L_p at $t = t_f$:

$$\frac{L_p}{2} = \frac{\dot{Q}_v}{4\pi\kappa} Ei(-\frac{r^2}{4\kappa t_f}) \tag{2.15}$$

Using a heat flux balance in and out of a cylindrical region of radius r (Eqns. 2.1 and 2.2), we obtain another estimate for pipe length L_p :

$$L_p = \frac{\dot{Q}_v}{2\pi\kappa} \frac{dr}{dT} \frac{\Delta T_{init}}{R_p} \tag{2.16}$$

$$\Rightarrow L_p = \frac{\dot{Q}_v}{\pi\kappa} \frac{r}{R_p} \tag{2.17}$$

We scale r with R_p, and hence we can represent r as $r/R_p = f(L_p, \dot{Q}_v)$ where $f(L_p, \dot{Q}_v)$ is an arbitrary function. Thus we get :

$$L_p = \frac{\dot{Q}_v}{\pi\kappa} f \tag{2.18}$$

$$\Rightarrow f = \frac{\pi\kappa L_p}{\dot{Q}_v} \tag{2.19}$$

Using this relationship for f and substituting r in Eqn. (2.15), we get

$$\frac{L_p}{2} = \frac{\dot{Q}_v}{4\pi\kappa} Ei(-\frac{R_p^2 L_p^2 \pi^2 \kappa}{4 t_f {\dot{Q}_v}^2}) \tag{2.20}$$

In addition, the flux through a cylindrical pipe due to buoyancy is given by Eqn. 2.4. Hence, given a value for $\dot{Q}_v$ (and other constants in Table 2.2), we can use Eqns. (2.4) and (2.20) to calculate the corresponding L_p and R_p. For all our calculations, we choose $t_f = 1$ Myr. A different value for t_f does not affect the results as long as $t_f > 0.1$ Myr.

2.5.1.4 Steady state model

As an alternative to the two estimates described above, we also consider the model discussed in Lister and Dellar (1996) for the solidification of a cylindrical channel. Their paper considers the fluid-mechanical problem of solidification of axisymmetric flow in an initially cylindrical channel (radius R_p) embedded in a cold rigid solid. The effective pipe radius and melt flow rates can evolve along the pipe radius and the latent heat term is included in their thermodynamic calculations. Solving the full problem numerically, Lister and Dellar (1996) map out the parameter values for which a melt channel can remain open in steady state (the radius of the liquid portion of the pipe is stable given the flow into the pipe). Here, we use their results to estimate the maximum possible value of L_p.

The primary non-dimensional model parameters in the Lister and Dellar (1996) model are the dimensionless solidification temperature Θ, modified Péclet number Pe_m, and Stefán Number S :

$$S = \frac{L_l}{C_p \Delta T_{init}} \tag{2.21}$$

$$\Theta = \frac{T_{solidus} - T_m}{\Delta T_{init}} \tag{2.22}$$

$$Pe_m = \frac{\Delta P R_p^4}{\kappa \eta_m L_p^2} \tag{2.23}$$

where L_l is the latent heat($\sim$ 4x10^5 J/kg for mantle rocks).

Using the definition of ΔP and $\dot{Q}_v$ - Eqns. (2.3) and (2.4), we can parametrize ΔP in terms of $\dot{Q}_v$ as :

$$\Delta P = \frac{8 \eta_m \dot{Q}_v L_p}{R_{eff}^4} \tag{2.24}$$

where R_{eff} is the mean radius of the pipe in steady state and replaces R_p in Eqn. (2.4). Physically, R_{eff} represents the portion of mean radius of the pipe section open for liquid flow. Hence, it is always smaller than the original pipe radius R_p in steady state since some of the melt freezes along the pipe edges, decreasing the effective radius. This is confirmed by full numerical simulations in Lister and Dellar (1996).

The critical value of L_p in this model is then :

$$L_p = \sqrt{\frac{\Delta P R_p^4}{\kappa \eta_m Pe_c(S, \Theta)}} \tag{2.25}$$

$$\Rightarrow L_p = \frac{8 \dot{Q}_v}{\kappa Pe_c(S, \Theta)} \frac{R_p^4}{R_{eff}^4} \tag{2.26}$$

where Pe_c is the critical modified Péclet number. If Pe_m is smaller than a critical value (Pe_c) then the channel becomes blocked at the downstream end and flow ceases. Hence,

using Pe_c allows us to estimate the maximum distance over which the channel can remain open in steady state.

Using typical parameters for our melt channels (see Table 2.2, please see discussion in next section), we get S $\sim$ 10-30 and $\Theta \sim$ 0.5 - 0.75 with the corresponding critical Péclet number, $Pe_c \sim$ 10 - 60 (from Lister & Dellar, 1996) with $R_{eff}/R_p \sim$ [0.6-0.8]. We calculate the value of the original pipe radius (R_p) in the model by using the calculated critical value of L_p, the definition of L_p in terms of ΔP, and other parameters (using Eqn. (2.26)) along with Eqn. (2.3).

2.5.2 Estimates for Galápagos

The main variables in our models are $\dot{Q}_v$, ΔT_{init}, and $\Delta\rho$. For estimating the parameter values, we used a value of $\Delta T_{init} = 20K$ along with $T_{pipe,init} - T_{solidus} = 5 - 10K$. This is physically meant to represent a melt channel initially close to thermodynamic equilibrium with the surrounding super/at soldius mantle (Hewitt & Fowler, 2009) and flowing through a sub-solidus mantle with $T_{solidus} - T_m = 10 - 15K$. In the particular case of the instantaneous heat pulse source model, we calculate τ_m as the time at which the center of the pipe has a temperature $\frac{T(R_p,t)-T_m}{\Delta T_{init}} \sim [.5-.75]$. Using Eqn. 2.7, this condition implies that $\tau_m \sim [.3-.5]$. A larger value for τ_m is likely more representative since our conceptual model envisions a pipe flow continuing over $\sim$ 2 Ma - this would increase the temperature of the ambient mantle (along with the direct influence of the plume head) and reduce the initial rapid heat flux included in our transient model. As we show later in this section, the exact choice of these values does not strongly affect our results.

As we discussed in Section 2.4.2, we do not know the precise mechanism for achieving lateral transport of melt in the asthenospheric region. In typical two-phase flow simulations (e.g., R. F. Katz & Weatherley, 2012; T. Keller & Katz, 2016), the melt channels are predominantly buoyancy driven and hence tend to be vertically oriented with a minor influence of shear terms, except very close to the ridge (Spiegelman & McKenzie, 1987; Kohlstedt, Zimmerman, & Mackwell, 2009). In contrast, we are proposing that the WDL is a surface representation of a narrow tilted cylindrical melt channel. We thus hypothesize that a melt channel becomes tilted as the ridge migrates away from the quasi-fixed plume (see Figure 2.7 for a diagramatic description of this model). This model would likely require that the melt velocity is small enough to not ignore the lateral pathway and flow vertically due to buoyancy. Physically, this implies that we have 'magmastatic' conditions – the fluid pressure in the melt channel is close to the lithospheric pressure. As a consequence, the net pressure gradient driving melt flow would be only a part of the melt buoyancy $\Delta\rho g$. The magmastatic condition in melt channels has also been suggested by Hewitt and Fowler (2009) based on the requirement for geophysically reasonable flow velocities in the melt channels, and is thus a plausible assumption. Hence, we choose a range of $\Delta\rho \sim$ 0.3 - 30 kg/m^3 for our calculations, noting that this parameter primarily affects pipe radius, not pipe length. We would contend that more theoretical work on flow in melt channels is required to precisely address

the extent of the 'magmastatic' condition and thus our chosen values are representative, but not absolute.

Finally, the primary observable constraint on our model is $\dot{Q}_v$, the magma volume flux into the pipe. We use estimates of residual crustal thickness and extrusive volcanism along the Wolf-Darwin lineament from Mittelstaedt et al. (2014) as well as the excess magma supply at WGSC from McClinton, White, Colman, and Sinton (2013) to establish :

$\dot{Q}_v \sim$ [6,000 - 18,000 km^3] over 1.8 Myr (Wolf-Darwin)

$\sim$ [7,000 - 20,000 km^3] over 1.8 Myr (WGSC)

2.5.3 Scaling Results

Using estimates from the previous section and other parameter values listed in Table 2.2, we can estimate L_p in the three models. For the instantaneous heat pulse model, L_p depends linearly on $\dot{Q}_v$ and weakly on τ_m. Similarly, the L_p in the constant heat flux source model is primarily influenced by $\dot{Q}_v$ although there is a weak dependence on melt viscosity (η_m), $\Delta\rho$, and $(b-a)$. Finally, the value of L_p in the steady state model is a function of only $\dot{Q}_v$, Pe_c, and R_p/R_{eff} with the latter estimated using the numerical results from Lister and Dellar (1996) in the relevant parameter region.

In Figure 2.8A, we show the results of the three models for a range of input melt fluxes while varying one additional parameter that affects the results most. In particular, we choose $\tau_m = 0.3$ (red solid line) and $\tau_m = 0.5$ (red dashed line) for the instantaneous heat pulse model, $\eta_m = 1\text{x}10^6$ Pa-s (blue solid line) and $\eta_m = 1\text{x}10^2$ Pa-s (blue dashed line) for the constant heat flux source model, and $Pe_c = 60$ (black solid line,$R_{eff}/R_p = 0.6$) and $Pe_c = 10$ (black dashed line, $R_{eff}/R_p = 0.75$) for the steady state model. For the other parameters, we use a constant value of $\Delta\rho = 3$ kg/m^3 and $(b-a) = 20$ km. We highlight the appropriate range of appropriate $\dot{Q}_v$ for the Galápagos in the figure.

In contrast to L_p, the estimates for R_p are dependent on additional parameters e.g. $\dot{Q}_v$, η_m, $\Delta\rho$, and $(b-a)$. We illustrate this dependence using a set of two figures. Firstly, we fix η_m, $\Delta\rho$, and $(b-a)$ to their nominal values of $1\text{x}10^4$ Pa-s, 3 kg/m^3, and 20 km respectively along with $R_{eff}/R_p = 0.7$, $Pe_c = 20$, and $\tau_m = 0.5$. See Table 2.2 for the list of parameters. Figure 2.8B shows the estimates for R_p as a function of $\dot{Q}_v$ for the three models (R_{eff} for steady state model). The typical pipe radius for $\dot{Q}_v$ for WDL is of order 10-100 m.

We also show the role of some of the other parameters on R_p by fixing $\dot{Q}_v$ and varying η_m as well as $\Delta\rho$ and τ_m in Figure 2.8C for the instantaneous heat pulse model (with $\dot{Q}_v = 38{,}000$ km^3 over 1.8 Myr). As we discussed at the beginning of Section 2.5, we can partially account for the effects of a high-porosity two phase aggregate instead of an open melt channel by assuming a larger value of η_m than is reasonable for volatile-enriched melt. We show results for $\Delta\rho = 0.3$ kg/m^3 (black), 3 kg/m^3(blue), and 30 kg/m^3(red) with each $\tau_m = 0.3$ (solid lines) and 0.5 (dashed lines). As shown by the figure, $\Delta\rho$ has a strongest influence on the pipe radius. However, $(b-a)$ also has a comparable influence. We show this by considering

$\Delta\rho = 0.3$ kg/m^3, $\tau_m = 0.3$, and either $(b-a) = 5$ km (black circles) or $(b-a) = 40$ km (black triangles). The principal dependence on $\Delta\rho$ is also true for the other two models. For instance, Pe_c and R_{eff}/R_p do not influence R_p as much as $\Delta\rho$ in the steady state model.

Using the nominal parameters discussed above, we obtain $L_p \sim 50 - 220$ km and $R_p \sim 2 - 40$ m for the instantaneous heat pulse model. Analogously, for the constant heat flux source model, we estimate $L_p \sim 350 - 1400$ km and $R_p \sim 4 - 60$ m. Finally, we find that the steady state model with $R_{eff}/R_p \sim 0.6 - 0.8$ predicts $L_p \sim 240 - 1700$ km and $R_p \sim 3 - 60$ m. We also calculated the Péclet number (Pe) for all the models above and it is always ≥ 100 thus ensuring that we are in the correct parameter region for our scalings to be valid.

We would like to note that the estimate for L_p calculated above is made assuming that all the flux $\dot{Q}_v$ feeds a single pipe. In case, this flux is distributed among a few pipes, for instance three pipes each feeding a lineament in NGVP, the maximum distance would reduce by a concomitant factor of three. However, for the case of Galápagos, it would still imply a large enough L_p to transport melt between the plume and the ridge.

Model	L_p	R_p
Instantaneous linear heat pulse	50 - 220 km	2-40 m
Constant heat flux source	350 - 1400 km	4 - 60 m
Steady state model	240 - 1700 km	R_{eff} = 3-50 m

Table 2.1: Summary of results

2.5.4 Additional remarks on the validity of models

The primary conclusion of our scaling analysis is that a melt channel of a length corresponding to that of the Wolf-Darwin lineament (as well as other plume-ridge lineaments) is thermodynamically feasible. All three approaches (Table 2.1) give consistent estimates for L_p and R_p despite very different assumptions, especially considering the fact the instantaneous heat pulse model provides only a lower bound. Additionally, the longest scale permissible is on the order of 1500 km, which is in fact the maximum distance over which plumes and ridges are observed to interact. This latter result is of course dependent on the exact parameter choices, and a full numerical model may be required to ascertain the maximum distance after which plume-ridge interaction ceases.

Another conclusion of our analysis is that the typical magma flow velocities for our chosen parameter ($u_m \sim 4\text{x}10^{-5}$ - $5\text{x}10^{-2}$ m/s using $\dot{Q}_v$ and estimated R_p) would be much larger than the plate-related flow velocities ($\sim$ cm/yr). Consequently, we expect the channels to persist in spite of overlying lithospheric plate movement. We plan to address the effect of the consequent non-hydrostatic pressures due to deformation or compaction of the mantle matrix (McKenzie, 1984) as well as dynamic forcing at the boundary of the partially molten region (Ribe, 1986) in detail in a future study.

Additionally, the small $Re \leq 1\text{x}10^{-4}$ suggests that the flow of magma in the pipes would not be turbulent. Finally, we note that none of the models discussed above include viscous heating. The critical pipe radius that corresponds to the onset of thermal runaway due to viscous heating is typically (Fialko & Rubin, 1998, 1999):

$$R_{p,c} = \left[\frac{Br_c(S,\Theta)\eta_m K_c \Delta T_{init}}{(dP/dz)^2}\right]^{1/4} \tag{2.27}$$

$$\Rightarrow R_{p,c} = \left[\frac{Br_c(S,\Theta)\eta_m K_c \Delta T_{init}}{(\Delta\rho g(b-a)/L_p)^2}\right]^{1/4} \tag{2.28}$$

where dP/dz is the pressure gradient due to melt buoyancy and Br is the Brinkman number - the ratio of viscous heating to conductive heat loss. For a critical Brinkman number $Br_c \sim 1$ and typical parameters for our melt channels (see Table 2.2), including a value for L_p we can find a $R_{p,c}$. This is shown in Figure 2.8B (dashed lines) assuming L_p is equal to the maximum permissible distance at a given $\dot{Q}_v$. We can see that it is reasonable to neglect viscous heating for our conservative estimates since $R_{p,c} > R_p$. However, since $R_{p,c}$ is a strong function of L_p, a pipe length smaller than the maximum value would reduce $R_{p,c}$. Hence, once established, viscous heating may further help to keep the melt channel open.

We again emphasize here that our computed melt velocities and pipe radius (R_p) are much more sensitive to η_m as compared to L_p (See Figure 2.8). Thus, we can easily obtain a larger value for R_p and a slower melt/aggregate velocity (u_m) by increasing the effective viscosity (η_m) which can be significantly greater than actual magma viscosity, depending on the actual porosities in melt channels (See the discussion in sections 2.4.3 and 2.5.1).

2.6 Discussion

The focus of this paper is to explain certain enigmatic volcanic lineaments in regions of plume-ridge interaction; we are interested in these volumetrically small features because they provide an opportunity to test models of plume-ridge interaction processes in general. In the following sections, we discuss some specific aspects of the volcanic lineaments and spreading ridges that provide additional support for our proposed model of melt channelization, as well as highlighting the limitations of the model and directions for future work.

2.6.1 Observations in the NGVP

An analysis of crustal thickness variations in the NGVP from inversion of gravity data by Mittelstaedt et al. (2014) provides interesting observational evidence supporting our proposed model of direct melt transport from the plume to the ridge. Mittelstaedt et al. (2014) found that the regions of excess crustal thickness/underplated material are localized just beneath the lineaments (see Figure 2.9; note that smoothing during gravity inversion tends to artificially broaden the regions with thicker crust). In particular, the largest topographic

features along WDL (Wolf Island, Darwin Island, and WDL-2) also have the thickest inferred crust ($\sim$ 11 - 12.5 km vs 8 km for non-lineament regions). This suggests that the regions of melting in the sub-lithospheric mantle that feed the lineaments must be narrow (as expected from melt channels), and that the sharpness of the lineaments is not just a surface expression bias. We acknowledge that lithospheric and crustal melt transport process can also lead to melt focusing partly explaining the observations. Also, we do not expect a exact one-on-one relationship between surface and asthenospheric width of the lineaments.

We therefore consider some of the processes relevant for melt transport from the asthenosphere to the surface, particularly the influence of diking and volcanic loading. On a local scale, diking would relieve some of the tensional stresses and in concert with the load of the volcanic edifice help focus stress near the ends of the seamounts and lead to their elongate growth (Hieronymus & Bercovici, 2001; K. Harpp & Geist, 2002; Heimisson, Hooper, & Sigmundsson, 2015). On a more regional scale, the loading of the crust by volcanic edifices and shallow magma chambers would help focus dikes towards the volcano and thus determine the surface location of volcanics. However, eventually the weight of the edifice will introduce much larger bending stresses than the integrated tension (Dahm, 2000; Karlstrom, Dufek, & Manga, 2009a; Maccaferri, Bonafede, & Rivalta, 2011) and will inhibit crustal magma transport (Hieronymus & Bercovici, 2001; Tibaldi, 2008; Bistacchi, Tibaldi, Pasquarè, & Rust, 2012) leading to increasing volume of under-plating at the Moho *vis-a-vis* extrusive volcanism. An interesting consequence of such a volcanic construction sequence is that if a large structure such as Wolf island with significant excess crustal thickness is formed first, the resulting compressive stresses on the lithosphere will start to dominate the local pattern of lithospheric tension and hence establish the location of adjacent volcanoes.

For the WDL, we found that at least locally, the Wolf island, which has the oldest age (0.8 - 1.6 Myr, W. M. White et al., 1993) among WDL seamounts, may significantly impact the local lithospheric stress field in comparison with plume shear and uplift, effect of the nearby ridge and transform and changing lithospheric thickness (comparing the load of the volcanic edifice with estimates from numerical models in (Mittelstaedt & Ito, 2005)). Thus, the subsequent volcanoes along the WDL would form along a narrow lineament, as is observed in the WDL, only if the melt source in the asthenospheric mantle is spatially localized (as in a melt channel). A similar conclusion also holds for other volcanic lineaments in NGVP. We would caution the reader that additional future work is required to confirm these preliminary conclusions with models including all the sources of lithospheric stresses consistently. A very similar (and stronger) argument can be made when considering other plume-ridge systems like Rodrigues ridge.

This modeling work thus provides additional evidence that the melt source in the mantle feeding the lineaments is spatially localized and appears to preclude broader underlying solid-state flow channels in the asthenosphere. We are currently working on more realistic models of lithospheric and crustal melt transport and will address this issue in more detail in a future study.

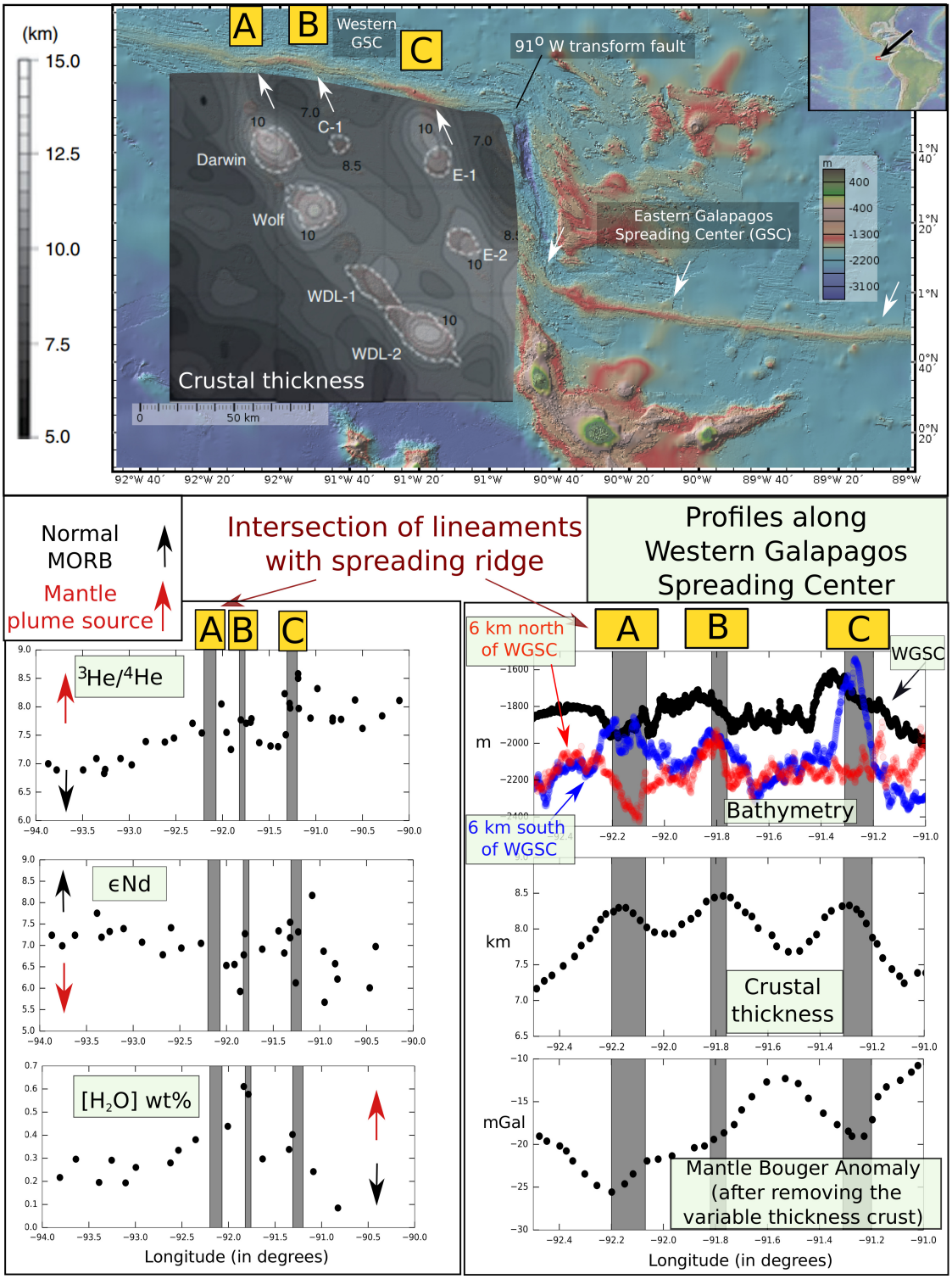
(km)
15.0
12.5
10.0
7.5
5.0
A
B
C
Western GSC
91° W transform fault
Darwin
Wolf
C-1
E-1
E-2
WDL-1
WDL-2
Crustal thickness
0
50 km
Eastern Galapagos Spreading Center (GSC)
m
400
-400
-1300
-2200
-3100
92°W 40´
92°W 20´
92°W
91°W 40´
91°W 20´
91°W
90°W 40´
90°W 20´
90°W
89°W 40´
89°W 20´
89°W
1°N 40´
1°N 20´
1°N
0°N 40´
0°N 20´
Normal MORB
Mantle plume source
Intersection of lineaments with spreading ridge
Profiles along Western Galapagos Spreading Center
3He/4He
ϵNd
[H2O] wt%
Longitude (in degrees)
6 km north of WGSC
6 km south of WGSC
WGSC
Bathymetry
m
Crustal thickness
km
mGal
Mantle Bouger Anomaly (after removing the variable thickness crust)
Longitude (in degrees)

Figure 2.9

Figure 2.9 *(previous page)*: *Top* : Bathymetric map of the NGVP overlaid with crustal thickness estimates (gray-scale) based on an inversion of mantle bouger anomalies (MBA)[Haxby et al., 2010;Ryan et al., 2009;Mittelstaedt et al., 2014]. The actual widths of thicker crustal regions are likely smaller than shown in the plot due to inversion smoothing and MBA filtering. *Bottom* : The crustal thickness estimates along the ridge are from Mittelstaedt et al., [2014], while MBA along the ridge is reproduced from Canales et al., [2002]. The grey bands 'A','B', and 'C' indicate the intersection of the lineaments with the spreading ridge, with 'A' being the WDL-ridge intersection. Several relevant geochemical datasets have been plotted using data described in Schilling et al.[2003], Cushman et al.[2004], Ingle et al.[2010] and Graham et al.[2014]

2.6.2 Observations along the GSC

Our proposed model of melt channelization satisfies the constraints from ^{238}U–^{230}Th–^{226}Ra and ^{231}Pa–^{235}U disequilibrium data for the GSC presented by Kokfelt, Lundstrom, Hoernle, Hauff, and Werner (2005). Since we envision a very melt rich channel, the estimated flow velocities based on the results of our scaling analysis in the previous section are of order $10^{-2} - 10^{-5}$ m/s ($\sim \dot{Q}_v/R_p^2$). This melt flow velocity would be large enough to satisfy the maximum melt transport times of 35 kyr, especially given the uncertainties regarding the extent of U-series fractionation throughout the melt column - e.g. equilibrium vs dynamic melting models (see review by Elliott & Spiegelman, 2013). As we discussed in Section 2.4.3, the velocities stated above would be a few orders of magnitude smaller if the effective melt viscosity is larger. However, it will still not be difficult to satisfy the U-series disequilibrium constraint.

Another observation hinting at melt channelization from the plume to the ridge beneath the lineaments is the localized excursions in bathymetry and crustal thickness (up to 500 m) along the WGSC at the intersections between the lineaments (including WDL) and the WGSC (see Figure 2.9, bathymetry data from GeoMapApp - Haxby, Melkonian, Coplan, Chan, & Ryan, 2010; Ryan et al., 2009). We suggest that the very localized peaks are indicative of excess melt presence at the lineament-ridge intersections. In addition, there is a strong minimum in residual mantle Bouger anomaly (after removing the effect of excess crustal thickness) at 92.15° W, the intersection between the WGSC and the WDL (see Figure 2.9, data from J. Canales et al., 2002). Modeling of gravity and geoid data by J. Canales et al. (2002) suggests that a modest mantle density reduction of 8 - 19 kg/m^3 at this location is required to explain the observations.

Finally, the GSC exhibits small scale tectonic segmentation. We consider any substantial lateral offsets along the spreading axis as constituting a tectonic segment (J. Sinton et al., 2003; Christie et al., 2005). Remarkably, each segment typically bounds a lineament - ridge intersection and the segment endpoints are generally local bathymetric lows of at least 50

m (S. M. White et al., 2008). We also find that $^3He/^4He$ isotopes, H_2O wt% (Figure 2.9, data from Cushman et al., 2004; Graham et al., 2014) as well as other geochemical tracers (S. A. Gibson et al., 2015) show subtle localized excursions wherever the GSC intersects with a volcanic lineament (WDL and others). Although the datasets for each of these observations suffer from sparse sampling and other possible biases, they suggest excursions at GSC-lineament intersections and warrant further work. In addition, we would like to note that the absolute value of the $^3He/^4He$ is at least a factor of few smaller than the corresponding value for the plume center (Graham et al., 2014). This is potentially in tension with our proposal of deep melt transport since He is expected to be relatively incompatible similar to H_2O. Additional geochemical work - both samples and modeling is however required to explicitly compare the observations with expectations and include the subtleties of He partitioning and transport (See e.g., W. M. White, 2010).

The above described observations, especially bathymetry and crustal thickness, are difficult to explain in the context of passive upwelling of fertile mantle beneath ridges without invoking crustal processes focusing melt, but they are naturally explained in a model of localized narrow melt channels transporting hydrous plume-derived melt to the spreading ridge in the asthenosphere [See S. A. Gibson et al. (2015) for a more detailed discussion of the geochemistry supporting this hypothesis]. In our model, the lineaments are just stochastic surface expressions of these channels with a majority of the melt transported to the ridge. The evidence for localized melt transport is more robust when considering geophysical datasets, whereas geochemical proxies for plume derived material such as ϵ_{Nd} have more intrinsic scatter, potentially reflecting stronger influence of melt mixing, crustal magmatic processes and finite length scales of individual eruptive fissures and lava flow fields (Shorttle et al., 2010; Colman et al., 2012).

Another unrelated observation – the small scale variation in geochemistry across closely located islands such as Pinta, Genovesa, and Marchena (K. S. Harpp & White, 2001; K. S. Harpp, Wirth, et al., 2014) – is easier to explain through melt channelization than non-channelized melt percolation through a porous medium. However, a more detailed discussion of the geochemical consequences of melt channelization and why each of the islands have a different geochemistry is beyond the scope of this study. The melt channelization processes may also play a role in determining the offset of the axial high on the EGSC to the east of the GTF (see Figure 2.1, and the discussion in Weatherley and Katz (2010); Montesi, Behn, Hebert, Lin, and Barry (2011); H. Bai and Montési (2015)).

2.6.3 Dual scales of plume-ridge interaction at the GSC

In the Galápagos-GSC system, the influence of the plume as traced by crustal thickness variations along the GSC shows two distinct scales. Along the WGSC, the gradient of crustal thickening changes significantly with decreasing plume-ridge separation with 94°W denoting the approximate location of a sharp gradient change. West of 94°W, the crust thickness increases eastward (i.e. towards the plume) at a rate of ∼130 m per 100 km (J. Canales

et al., 2002). In contrast, towards the east of 94°W, the thickness increases much more rapidly - ∼620 m per 100 km(J. Canales et al., 2002). Furthermore, a large fraction of the total crustal thickness increase (above the typical mid-ocean plate thickness) occurs to the east of 94°W - ∼2 km (east) vs ∼200 m (west)(J. Canales et al., 2002). Since increases in crustal thickness are a direct consequence of increased magma supply to the ridge segment, the above-described pattern along WGSC suggests that the plume influence is concentrated mainly within ∼250 km of the GTF with regards to direct magma supply.

This interpretation is supported by multichannel seismic (MCS) reflection imaging of a shallower axial melt lens (AML) – 1.0 - 2.5 km below sea floor – east of 92° 30'W compared to 2.5 - 4.5 km depth west of this region (Blacic et al., 2004). Furthermore, a seismic refraction experiment focused on three WGSC segments (each representing a non-plume, intermediate, and strongly influenced spreading segment) found increasing melt fraction in the sub-crustal magma reservoirs with decreasing plume-ridge separation (J. P. Canales, Dunn, Ito, Detrick, & Sallares, 2014). Only the ridge segment centered close to WDL - WGSC intersection, and hence closest to the plume location, shows evidence for intermediate-depth melt reservoirs at ∼ 4 km above the Moho, indicating larger magma supply (Blacic, Ito, Shah, Canales, & Lin, 2008; J. P. Canales et al., 2014). In contrast, the compositional influence (as measured by ϵNd, Pb, and Sr isotopes) of the plume material on the GSC extends to a much larger distance (∼ 500 km on either side of the GTF, J.-G. Schilling et al., 2003). This is typically interpreted as signifying the width of the plume-ridge interaction process and is well-predicted by solid-state flow models (see review by Ito et al., 2003). However, the major, minor and trace element lava compositions along the GSC exhibit a more localized region of plume influence on a length scale comparable to that discussed in the above paragraph (∼ 200 km either side of GTF). Specifically, these higher-magma-supply regions have on average lower MgO, CaO, higher K_2O,Na_2O,Ti_2O, La/Sm, Sm/Yb, and more variable, but on average slightly lower eruption temperatures (J. Sinton et al., 2003; Cushman et al., 2004; Christie et al., 2005; Shorttle et al., 2010; Colman et al., 2012).

We propose that these observations may be indicative of dual-modes of influence of the plume on the nearby ridge. This idea was also discussed by S. A. Gibson et al. (2015) for the Galápagos region; we are primarily refining it here and including the lineaments in the same physical framework. In this dual-mode model, the first component is the standard solid-state flow of fertile and hotter plume material towards the ridge. This leads to a generally increased melt production during passive upwelling beneath the GSC. We propose that this component is responsible for the large scale topographic swell as well as the isotopic differences along the ridge since this scale is well predicted by standard plume-ridge interaction models. However, in our melt- channelization picture, there is an additional component of plume-ridge interaction - the direct transport of melt to the ridge, which leads to enhanced crustal thickness and enrichment in regions closest to the plume center. The combination of melt channels from the plume to the ridge, as well as deep channels beneath the ridge itself (as proposed for the Reykajnes ridge by Vogt, 1974, , see also); S. A. Gibson et al. (2015)), would explain the lack of influence of the large transform fault at 90.7°W on along-axis

$^3He/^4He$ and some variations in elemental compositions. We see evidence for this feature in many other plume-ridge interaction systems also and have a manuscript in preparation. In detail, the values of some geochemical tracers of plume influence (e.g., Pb, Hf, and Nd isotopes) exhibit a single peak while K_2O, TiO_2, La/Sm, and K/Ti have two peaks (e.g., J.-G. Schilling et al., 2003; J. Sinton et al., 2003; Cushman et al., 2004; Christie et al., 2005) when plotted along the GSC from the west to the east. The two peaks include a western peak (between 91°40'W and 92°10'W) and an eastern peak (between 90.7° transform fault and 91°30' W). However, the relative strength of the two peaks varies and these conclusions are sensitive to data coverage (ridge basalt samples are not always uniformly distributed along the ridge) and the chosen threshold for peak detection above noise. Overall, we suggest that the finer details of melt-transport would express themselves in regions closest to the nearby plume, whereas at longer wavelengths solid state plume-ridge interaction is dominant. Additionally, this hypothesis would partially address the problem of the expected low level of mixing between the ambient mantle and mantle plumes in solid-state flow models (e.g., Albers & Christensen, 2001).

2.6.4 Other observational features

In the Galápagos-GSC system, the crustal thickness along the GSC increases more steeply within ∼200 km of the GTF (J. Canales et al., 2002) while the scale of the plume's compositional influence (as measured by ϵNd, Pb, and Sr isotopes) extends to a much larger distance (∼ 500 km on either side of the GTF, J.-G. Schilling et al., 2003). We propose that these observations may be indicative of dual-modes of influence of the plume on the nearby ridge as also suggested by S. A. Gibson et al. (2015). The first component is the classical solid-state flow of plume material towards the ridge responsible for the large scale topographic swell as well as the geochemical (isotopic) influence of the plume. In addition, there is also channelized transport of melt to the ridge leading to enhanced crustal thickness and enrichment in regions closest to the plume center.

2.6.5 Model Predictions for other lineaments

Rodrigues Ridge (RR, Figure 2.3), is an approximately 500 km long, quasi-linear ridge representing the interaction of the Réunion plume with the Central Indian Ridge. Although the age of Rodrigues Island is perhaps young - 1.5 Myr (McDougall et al., 1965), the underlying Rodrigues Ridge is much older - 8 to 10 Myr (Duncan, 1990) without any age progression. Although the plume-ridge separation is ∼ 1000 km currently, it was smaller in the past when the Rodrigues ridge started forming. In addition, there is a set of additional smaller volcanic ridges extending from the end of the Rodrigues Ridge to the CIR - the *en-échelon* Three Magi Ridges and the Gasitao Ridge (Figure 2.3, (Dyment et al., 2001)). Extensive geochemical work along the section of CIR intersecting with the lineaments has shown that there is an active interaction of the ridge with the plume with the principal region

of interaction between ∼19° and 20°S along the CIR axis (e.g., Murton, Tindle, Milton, & Sauter, 2005; Nauret et al., 2006; Füri et al., 2011).

Hollister Ridge (HR, Figure 2.4) is a ∼ 450 km long bathymetric high, quasi-linear structure representing the interaction of the Louisville hotspot with the Pacific-Antarctic Ridge (PAR) (e.g., Small, 1995; Géli et al., 1998). There is strong isotopic evidence for direct interaction between the plume and the ridge (Vlastélic & Dosso, 2005). Furthermore, the plume influence is maximal close to where the Hollister Ridge intersects with PAR (Castillo, Natland, Niu, & Lonsdale, 1998). The influence of the plume on the ridge is also evident geophysically from the rapid migration of the PAR (∼ 50 mm/yr) toward the likely location of the Louisville hot spot (marked on Figure 2.4) and a 15-20 km ridge in that direction about 3-4 Myr ago (Small, 1995). Within the context of the plume-ridge interaction models, the Louisville-PAR system is particularly interesting due to the presence of the Eltanin fault system (Heezen and Tharp fault zones) in between the proposed plume-ridge interaction trace. However, there is no significant volcanism observed along the very long fracture zone. Another unique feature of this system is the strong age difference between the oceanic plate age underneath the hotspot (∼ 50 Myr) and the Hollister ridge (∼ 0-10 Myr) (Müller et al., 2016) and hence a strong difference in the oceanic lithosphere thickness. The ages of the different seamounts are shown on Figure 2.4 - they are always younger than the underlying plate age.

Although the primary focus of our study has been Galápagos, our model for lineament formation should be applicable to other plume-ridge systems. In general, our model predicts that analogous to the NGVP, the crustal thickness beneath the lineaments related to plume-ridge interaction should only be locally enhanced. Hence, high resolution gravity and seismic datasets for other plume-ridge systems, especially Rodrigues Ridge and Hollister Ridge, might be able to test our model. Similarly, crustal thickness estimates as well as closely-sampled geochemical datasets along other mid-ocean ridges influenced by nearby plumes might show an influence of melt channels akin to what we observe for the WGSC and lineament intersections (see Figure 5 from the main text).

We would however note that as we emphasized in the main text, the tectonic history (e.g. plate thickness, ridge migration, etc) has a strong effect on the exact structure and formation of lineament volcanoes. For example, the sharp decrease in the lithospheric thickness across the Tharp FZ near the Louisville hotspot would strongly deflect the asthenospheric flow of the mantle plume and the structure and organization of melt channels. Similarly, the long term interaction of the Réunion plume with the Central Indian ridge (> 10 Myr timespan) would affect the location and stability of melt channels. In addition, akin to the Galápagos, the tectonic environment may affect the surface expression of the lineament as is evidenced by the effect on ridge orientation due to the intersection of the lineament with the Marie Celeste Fracture Zone. It is unclear how this would affect melt channels. Hence, focused studies for each region (akin to what we do here for WDL) are required to test whether our model or previously proposed models can explain the lineaments.

2.6.6 Melt extraction and seamount spacing

The seamounts and ridges which make up the volcanic lineaments typically have a distinctive elongate structure (Smith & Cann, 1992; K. Harpp & Geist, 2002; K. S. Harpp, Wirth, & Korich, 2002b). As a specific example, Genovesa Island in Galápagos is the sub-aerial portion of a > 60 km long, ridge-like seamount (K. S. Harpp et al., 2002b). This suggests that some of the models discussed in Section 2.2.3 may have a secondary role in lineament formation. For instance, the elongation of individual seamounts is generally a better match to the fracture orientations in the NGVP than to the overall direction of the lineaments, suggesting that regional lithospheric stresses exercise a strong control on seamount morphology (see Figure 2). Within the context of our model, we expect that although the trend of the lineament is set-up by the underlying melt channel, locally magma can dike its way through the lithosphere in regions of high integrated tension due to lithospheric extension or dynamic stresses from the plume (as modelled by Mittelstaedt & Ito, 2005). Similar processes - intersection between a melt-rich region and a preexisting fracture - have been argued to be important for extracting melt in some transform faults regions (Hebert & Montési, 2011; H. Bai & Montési, 2015).

In addition to the shape of individual seamounts, another intriguing aspect of plume-ridge lineaments is the dichotomy in the style of seamounts, with WDL and Hollister ridges being composed of individual volcanoes in contrast to Rodrigues Ridge, which is laterally very continuous. In a similar vein, there are several volcanic lineaments in the Galápagos, whereas Réunion and Louisville exhibit only a single conspicuous plume-ridge interaction (lineament) feature. Furthermore, individual lineaments in a system like Galápagos may be active at different times, with Genovesa island having a peak activity age of ~ 250 kyr (K. S. Harpp, Hall, & Jackson, 2014) in contrast with Wolf island's age between 0.8 - 1.6 Myr (W. M. White et al., 1993).

Our model can only qualitatively explain these differences. As we discussed in section 2.4.2, we expect that the number of active melt channels should decrease as plume-ridge separation increases based on the requirement for the thermodynamic stability of channels. Hence, it is more likely that regions where the ridge and the plume are close (such as Galápagos) have multiple lineaments of varying intensity, whereas other regions with larger distances such as La Réunion have only a single high melt flux lineament connecting the plume and the spreading ridge. Without detailed simulations, we cannot predict quantitatively the spacing over time and how interactions among multiple sub-lithospheric melt channels affect their evolution and surface expression.

We do however expect that the mechanism of melt extraction from the channel to the surface is among the primary controls on this process. Hence, this suggests that one important component is currently missing from our proposed model - how does melt move from the melt channels to form lineament volcanoes, and how does the channel remain stable in spite of episodic melt removal ? One possible mechanism is Rayleigh-Taylor (RT) instability of the buoyant melt in the channel. To ascertain the likelihood of instability, we calculate

the Rayleigh number - $Ra = (g\Delta\rho a^3)/(\kappa\nu_{amb})$ where a is the radius of the channel and ν_{amb} is the viscosity of the ambient mantle. Experiments by R. C. Kerr et al. (2008) show that a $Ra_c \sim 100 - 200$ is required for RT instability - effectively the melt diapir must rise fast enough to not lose its driving buoyancy by heat diffusion. For typical parameters of our proposed melt channels – $a \sim 10$ m, $\nu_{amb} \sim 1\text{x}10^{18}$ Pa s, and $\Delta\rho \sim 3kg/m^3$ – Ra is $\sim 1\text{x}10^{-7}$. Hence, Rayleigh-Taylor instability induced melt diapirs are unlikely to be the dominant mechanisms for melt removal from the channels. Other potential ways to transport melt from the sub-lithospheric channel include porous media percolation of small quantities of melt, compaction waves (e.g., J. A. D. Connolly & Podladchikov, 2007; Cai & Bercovici, 2016), variations of melt flux in the channel leading to instabilities due to differential pressure changes, and interactions between melt channels and radial dikes (Havlin, Parmentier, & Hirth, 2013; T. Keller et al., 2013). A detailed discussion of these processes and their implications for lava geochemistry is beyond the scope of this paper.

2.6.7 Avenues for future work

Although our proposed model can account some un-explained features of plume-ridge lineaments, we readily acknowledge that it is incomplete since we do not explicitly address melt transport from the melt channels to the surface. We discuss some of the possible mechanisms such as Rayleigh-Taylor (RT) instability of the buoyant melt in the section above. A more consistent physical picture of our model may be a network of melt channels of varying lengths that are focused into mutual alignment between the plume and the ridge and a few of these periodically feed crustal growth along a lineament both by crustal under-accretion as well as by extrusion in seamount volcanism. There are also some other intriguing observational features that hint at additional complexity. In particular, the lineament seamounts have elongate morphologies and there is a dichotomy in the style of seamounts, with WDL and Hollister ridges being composed of individual volcanoes in contrast to Rodrigues Ridge, which is laterally very continuous. Since melt extraction processes may significantly influence the surface observables, future work should try to address how melt moves from the melt channels to the surface to build a consistent model scenario.

In addition, we do not know the exact mechanism for achieving lateral transport of melt in the asthenospheric region (see Section 2.4.2 for more discussion). In particular, future work is required to assess whether melt channels would get tilted sufficiently either as a consequence of solid-state plume flow towards the ridge or due to continuous ridge migration (as proposed here) and if the magmastatic pressure assumption is reasonable.

Finally, our model of deep melt transport has potential geochemical implications for a variety of isotope ratios (e.g. $^3\text{He}/^4\text{He}$) as well as rare earth and major elements compositions of erupted lavas both at the lineament volcanics and the GSC. Future work on these aspects could help provide confirmation of our model or highlight inconsistencies.

2.7 Conclusions

The interaction of an active mantle plume and a nearby mid-ocean ridge is a fairly common geologic phenomenon occurring at near-ridge hotspots such as the Galápagos, La Réunion, Louisville, and Iceland. The signatures of this interaction provide us with an opportunity to understand fundamental transport processes associated with both plumes and ridges, and to test our models with extensive geochemical and geophysical data-sets. A unique and common feature of plume-ridge interaction is the presence of volcanic lineaments linking plumes and ridges, with the Wolf-Darwin lineament in the Galápagos being a particularly well-studied example. Although these features have been known for decades, proposed models such as solid-state viscous fingering or generation of melt due to lithospheric extension and faulting appear to be inconsistent with a variety of evidence.

We propose that these commonly-observed lineaments are a consequence of melt channelization in the asthenosphere due to two-phase instabilities. A few of the melt channels (See the discussion in section 2.4.3 about their structure) are able to sustain plume-ridge connections as the ridge migrates away from the plume, and to occasionally erupt along the path to form volcanic islands and ridges. Simple analytical estimates show that this model is thermodynamically feasible, with the maximum distance for melt transport being almost linearly proportional to melt flux $\dot{Q}_v$. Plume-ridge distances over which these melt channels can be maintained are estimated to be order 1000-1500 km, consistent with the longest observed volcanic lineaments. This model builds directly upon a recent study of geochemical trends along the GSC by S. A. Gibson et al. (2015) that argues for a large scale ($\sim$ 100 km), confined, northeasterly oriented, deep ridgeward flow of plume material.

Within the context of our proposed model, a number of unexplained features of plume-ridge interaction are naturally explained (see Figures 2.9), including variation in excess crustal thickness and mantle Bouger anomaly along the WGSC. In addition, melt transport in channels can easily satisfy the U-series based constraint of 35,000 yrs for the transport time between the plume and the GSC (Kokfelt et al., 2005). Although the inclusion of coupled two-phase mantle magma flow dynamics in our model introduces significant additional complexity, the observational data strongly suggest that two-phase transport is required. Previous theoretical and experimental studies of melt dynamics suggest that channelization is a relatively common phenomenon, and is likely to be the norm rather than the exception. Melt channelization can have an important influence on the observed pattern of geochemistry and the surface expression of sub-lithospheric melt generation (S. A. Gibson et al., 2015). In particular, the melt source region for observed volcanism may not be directly beneath the mantle melt column, as is assumed for porous media melt percolation within typical solid-state mantle flow models. Volcanic lineaments are observed in multiple plume-ridge settings, each with a different plume buoyancy flux, plume composition, and plate spreading rate; hence, we have multiple natural laboratories to test our proposed model, and to better understand sub-lithospheric melt transport and extraction.

Variable	Description	Characteristic Value	Units
L_p	Maximum channel length		km
R_p	Pipe radius		m
R_{eff}	Mean radius of the pipe in steady state		m
T_m	Uniform background temperature		Kelvin
$T(r,t)$	Temperature field in the pipe (spatial and time varying)		Kelvin
$\dot{Q}_{h,out}(t)$	Conductive heat flux out of the pipe		J/s
$\dot{Q}_{h,in}(t)$	Heat flux into the pipe		J/s
$\dot{Q}_v$	Melt volumetric flux into the pipe		m^3/s
dP/dz	Pressure gradient driving the flow due to melt buoyancy		Pa/m
ρ	Mantle density	2800	kg/m^3
$\Delta\rho$	Density difference between the melt and mantle	0.3 - 30	kg/m^3
t_m	Characteristic time (for Instantaneous heat pulse model). It is defined as the time when $\frac{T(R_p,t)-T_m}{\Delta T_{init}} \sim 0.5$ - .75 in Eqn. 2.7		s
τ_m	Dimensionless time (Instantaneous linear heat pulse model)	0.3 - 0.5	
η_m	Magma dynamic viscosity	10^2 - 10^5	Pa-s
C_p	Mantle specific heat capacity	1200	J/kg/K
K_c	Thermal conductivity	3.6	W/m/K
κ	Mantle thermal diffusivity	10^{-6}	m^2/s
b	Depth at the melt channel is initiated	70	km
a	Depth at the melt channel is terminated	50	km
L_l	Latent heat of solidification	4x10^5	J/kg
g	Gravitational acceleration	9.8	m/s^2

ΔT_{init}	Initial excess temperature of the melt relative to the surrounding mantle	20	Kelvin
$T_{pipe,init} - T_{solidus}$	Initial excess temperature of the melt relative to the mantle solidus	5-10	Kelvin
$T_{solidus} - T_m$	Initial temperature difference between mantle solidus and surrounding mantle	10-15	Kelvin

Table 2.2: Summary of variables and values, where applicable.

Chapter 3

Volatile degassing from magma chambers as a control on volcanic eruptions

3.1 Introduction

Volatiles (H_2O, CO_2, and various sulphur and halogen species) play an essential role in modulating the evolution of magmatic systems, and affect the occurrence, style, and duration of individual eruptive episodes, as well as the thermal and chemical evolution of the magma through interaction with the overlying crustal hydrothermal system. Although surface eruptions release a large amount of magmatic fluids into the environment, observations over the past few decades (e.g., Edmonds and Wallace (2017); Ilyinskaya et al. (2018)) suggest that passive degassing during quiescent (non-eruptive) periods can also release a significant amount of volatiles. This passive volatile transport to the surface and within the magmatic system can occur through the volcano-tectonic features such as conduits, faults, and fractured regions with high permeability, as well as the hydrothermal system. Thus, a magmatic reservoir behaves partially as an open system with regards to magmatic volatiles.

This open-system nature of the magmatic system can have a significant impact on its structure, as suggested by observations of heat transport near mid-ocean ridges (Pirajno & Van Kranendonk, 2005; Stein & Stein, 1994), deformation around volcanic conduits (R. Brown, Kavanagh, Sparks, Tait, & Field, 2007; Busby-Spera & White, 1987; Delaney & Pollard, 1981; Delaney, 1982; Elsworth & Voight, 1996; M. Townsend, Pollard, Johnson, & Culha, 2015), transport of economically valuable metals (Koide & Bhattacharji, 1975), and geothermal energy (Barbier, 2002). The influx of volatiles from the magma reservoir as well as the associated heat transport can lead to rapid changes in the stress state of the pre-existing rock matrix and pore fluid (Huppert & Woods, 2002; D. Norton & Knight, 1977; D. L. Norton, 1984; Wohletz, 1986). This stress change, in turn, leads to changes in background fluid flow pattern and host rock permeability and porosity (S. Ingebritsen &

Sanford, 1999; S. Ingebritsen & Manning, 2010), as evidenced by the common occurrence of veins and fractures in metamorphic aureoles surrounding magmatic intrusions and dikes (Cucci, Di Luccio, Esposito, & Ventura, 2017; Stober & Bucher, 2015; M. R. Townsend, 2018).

A large number of studies have analyzed, both analytically and numerically, how changes in permeability affect fluid flow and heat loss from magma reservoirs (Dutrow & Norton, 1995; Hayba & Ingebritsen, 1997; Weis, Driesner, & Heinrich, 2012; Peiffer, Wanner, & Lewicki, 2018; D. Norton & Taylor Jr, 1979). In addition, extensive work has been done concerning the mechanisms responsible for changes in permeability (Germanovich, Lowell, & Astakhov, 2001; Lowell, Van Cappellen, & Germanovich, 1993; Taron & Elsworth, 2009; Taron, Elsworth, & Min, 2009) - both increases due to fracturing as well as reductions due to deformation and precipitation. Finally, from a magma reservoir perspective, previous studies have shown that magmatic volatiles play a vital role in modulating the temporal evolution of magma and the buildup of overpressure required for eruption (Degruyter & Huber, 2014; Karlstrom & Richards, 2011). However, few studies have incorporated a direct coupling of magmatic and hydrothermal systems, modulated by the magmatic volatiles (Black & Manga, 2017; Girona, Costa, & Schubert, 2015; Iguchi, Saito, Nishi, & Tameguri, 2002; Simakin & Botcharnikov, 2001). The loss of volatiles will significantly affect the fluid pressure within the volcanic system, leading to depressurization of the magma reservoir over time as well as affecting the stress state of the background crust.

In this study, we will explore how the two-way coupling of the hydrothermal-magmatic system affects the eruption dynamics and the thermo-hydro-mechanical response of the crust. We note that some recent studies (Girona, Costa, Newhall, & Taisne, 2014; Girona et al., 2015) have shown, using primarily mechanical models, that passive degassing has an essential effect on the pressure buildup of magmatic reservoirs in the context of open-vent conduit systems. Our study extends this analysis to more a general magmatic architecture, and also incorporates a more comprehensive thermo-mechanical model for the temporal evolution of melt, especially the release of magmatic volatiles as the magma crystallizes or ascends to shallower depths.

We first discuss observations of passive degassing in volcanic systems (Section 3.2), followed by a discussion of the mechanisms that may produce the increased transient permeability required to explain the observations (Section 3.3). We then describe the general outline of our model in Section 3.4 followed by the crustal as well as the magma chamber components of our model in Sections 2.5 & 2.6 and the model results in Section 3.7. Finally, we discuss the implications of our results in the context of a regime plot for volcanic eruptions and magmatic degassing.

3.2 Observations of passive degassing

Over the past few decades, a variety of geophysical, geological, and geochemical studies have shown the importance of passive degassing as a crucial component of magmatic systems. The clearest constraints on magmatic volatile degassing come from direct measurements of SO_2 and CO_2. Carn, Fioletov, McLinden, Li, and Krotkov (2017) calculated the global SO_2 flux from volcanoes during 2005-2015 using satellite remote sensing measurements and found that the total global annual SO_2 passively degassed is typically an order of magnitude larger than volatile release during eruptions, except during a couple of years with large eruptions. Similarly, when considering the global fluxes of H_2O, CO_2, S, and Cl from subduction zones, Shinohara (2013) concluded that explosive eruptions contributed less than $\sim$ 15 % to the total volatile fluxes. Direct measurements of soil CO_2 from a variety of volcanic environments Burton, Sawyer, and Granieri (2013); Inguaggiato et al. (2013); Viveiros et al. (2010) confirm this general result. In particular, many geologic regions with limited to no recent active volcanism (e.g., Apennines : Italy Chiodini et al. (2004); French Massif Central : Gal, Leconte, and Gadalia (2018); sections of the East African Rift Valley Hunt, Zafu, Mather, Pyle, and Barry (2017); H. Lee et al. (2016)) show evidence for significant passive volatile fluxes derived from deep magma sources.

This passive degassing process is dynamic and can be variable over a variety of time-scales ranging from hours to centuries (and potentially longer). Specifically, multiple volcanic systems show variations in diffuse volcanic CO_2 emissions as well as the SO_2/CO_2 ratio on hourly to decadal scale (e.g.,Christopher et al. (2015); Chiodini et al. (2016); De Moor et al. (2016)). These changes have been interpreted to represent varying influx of magmatic gases into the hydrothermal system, changes in crustal permeability, magma and/or magmatic fluid injection from deeper sources, or meteorological forcing (Burton et al., 2013; Hernández et al., 2001; Hildreth, 2017; Lewicki et al., 2014; Pichavant, Le Gall, & Scaillet, 2018; Rogie, Kerrick, Sorey, Chiodini, & Galloway, 2001; C. Werner et al., 2014). These interpretations are further supported by observations of fluid associated volcano-tectonic earthquakes which are frequently co-located with the resistivity anomalies and the peripheries of the geophysically imaged deeper magma reservoirs (e.g.,Long Valley, California Peacock, Mangan, McPhee, and Wannamaker (2016)). As a specific example, Shelly, Ellsworth, and Hill (2016) resolved numerous episodes of upward-migrating seismic activity through an analysis of a month-long earthquake swarm in 2014 in the Long Valley Caldera. They concluded that the upward migration of hypo-centers was very likely a consequence of an expanding fluid-pressure pulse due to fluid loss from the magma reservoir.

Finally, field observations of thermal aureoles of many magmatic plutons clearly show that they are intensely fractured and veined (Achtziger-Zupančič, Loew, & Mariéthoz, 2017; Gruen, Heinrich, & Schroeder, 2010; Mair, Goldfarb, Johnson, Hart, & Marsh, 2006), indicative of the presence of some high-permeability pathways and volatile loss from magmatic systems. This conclusion is supported by the analysis of fluid inclusions (e.g., $\delta^{18}O$, thermobarometry) from veins in porphyry copper deposits which show evidence of interaction be-

tween a near-lithostatically pressured magmatic two-phase fluid mixture and meteoric water under near-hydrostatic fluid pressures (Hedenquist, Arribas, & Reynolds, 1998; Fournier, 1999; Weis et al., 2012). The field observations additionally indicate that these processes occurred multiple times, as evidenced by successive generations of cross-cutting veins (Gerdes, Baumgartner, & Person, 1995; Gruen et al., 2010; Redmond & Einaudi, 2010; C. J. Wilson, Moore, Luzin, & Salvemini, 2017) and high precision dating (Chiaradia, Schaltegger, & Spikings, 2014).

In conclusion, there are a variety of independent observations that indicate the ubiquity and importance of passive degassing of volatiles from crustal magma reservoirs over long time-scales. Hence, the permeability of the crust surrounding the magmatic system must be finite in order to facilitate this volatile flow. In the next section, we discuss some physical processes that can modify the crustal permeability surrounding magma reservoirs.

3.3 Transient Permeability

In the context of modeling the pressurization of a magma reservoir due to magma recharge and volatile exsolution as magma crystallizes, most previous studies have assumed that the crust surrounding the magma reservoir has effectively zero permeability ($< 10^{-20}$ m^2) on long timescales (e.g.,Black and Manga (2017), though Paonita, Caracausi, Martelli, and Rizzo (2016) do include variable crustal permeability). However, the crustal rock permeability is a non-zero time varying quantity, as has been long recognized by a host of hydrologists, economic geologists, and metamorphic petrologists (R. Sibson, Moore, & Rankin, 1975; R. H. Sibson, 1987; Titley, 1990; R. Hanson, 1992; R. B. Hanson, 1997; Dutrow & Norton, 1995; S. F. Cox, 2002; Yardley, Baumgartner, Handy, Hirth, & Hovius, 2007; Cathles & Adams, 2005; S. Ingebritsen & Gleeson, 2017; S. E. Ingebritsen & Appold, 2012; Henley & McNabb, 1978; Fournier, 1999; Weis et al., 2012; Weis, 2015). Recent compilations of deep crustal permeability measurements (S. Ingebritsen & Gleeson, 2017; Achtziger-Zupančič, Loew, & Mariéthoz, 2017) clearly show that the permeability-depth profiles of tectonically quiescent and active regions are markedly different with much larger permeability in active regions. Besides, in-situ measurements of permeability in volcanic systems from drilling projects (Ikeda, Kajiwara, Omura, & Hickman, 2008; Reinsch et al., 2017; Fridhleifsson et al., 2017) and lab experiments also suggest non-negligible permeability even at temperatures higher than the brittle-ductile transition ($\sim>$ 500°C) (Watanabe, Numakura, et al., 2017; Watanabe, Egawa, Sakaguchi, Ishibashi, & Tsuchiya, 2017).

In practice, the concept of transient permeability introduces a theoretical challenge in modeling magmatic systems, since both the spatial and temporal scales at which permeability is being enhanced and subsequently reduced are small compared to those for magma reservoir evolution (mm-cm scale vs km scale; days-yrs compared to kyr-Ma). Additionally, the permeability is a function of not only the porosity of the medium but also the pore geometry (size, connectivity, crack shapes), alteration, multi-phase fluid properties, temperature, and pressure (e.g., M. Heap, Farquharson, Baud, Lavallée, and Reuschlé (2015);

M. J. Heap and Kennedy (2016); M. J. Heap, Violay, Wadsworth, and Vasseur (2017); Burgisser, Chevalier, Gardner, and Castro (2017); Kushnir, Martel, Champallier, and Arbaret (2017); Colombier et al. (2017); Vasseur and Wadsworth (2017); Pimienta, Sarout, Esteban, David, and Clennell (2017); Parmigiani, Degruyter, Leclaire, Huber, and Bachmann (2017)). Consequently, variations in these properties lead to a multitude of mechanisms for both increase and decrease of transient permeability, some of which can be strongly non-linear. In the following, we discuss some of these mechanisms with a focus on the variety of mechanisms and the corresponding length and time-scales over which they might act. Our primary goal in this section is to ascertain what are the plausible range of values for time-averaged permeability (motivated by higher transient permeability) that we can use to probe the two-way interaction between the magma reservoir and the crustal system.

3.3.1 Permeability enhancing processes

One common way to produce transient permeability is the emplacement of dikes, sills, and other hydro-fractures which lead to the development of damage zones and permeable pathways at their periphery (Weinberger, Lyakhovsky, Baer, & Agnon, 2000; R. Brown et al., 2007). Another mechanism to increase permeability is to increase the crustal fluid pore pressure enough such that the local stresses exceed the tensile strength of the rock (R. H. Sibson, 2017). This pore pressure increase can be achieved by the production of volatiles by metamorphic reactions (Nabelek, 2009; Nabelek, Bédard, & Rainbird, 2014; Rozhko, Podladchikov, & Renard, 2007) or rapid increase of the fluid temperature by intruding magma (Das, Zhang, Schaubs, & Cleary, 2014). The high pore pressure front will subsequently propagate outward, creating more fractures and consequently enhancing permeability over a wide area (Dutrow & Norton, 1995). The above-described processes can increase permeability over 10s of m scales to even kilometers (for the case of dikes), but the actual permeability distribution is likely going to be relatively heterogeneous and dependent on the crustal rheological properties.

Other processes that can produce transient permeability include filter pressing - the low-density volatile phase forces melt through the locked crystal network (Sisson & Bacon, 1999); deviatoric thermal-elastic stresses due to differential thermal expansion and the elastic response of the mineral assemblage in a rock (Joanne & Teng-fong, 1986; Regenauer-Lieb & Yuen, 2004); porosity waves initiated by the visco-poroelastic response of the crust (recurrence time of order 1-10 years, J. A. Connolly and Podladchikov (2015)); and dissolution of crustal rock by magmatic volatiles e.g, dissolution of carbonate samples by an aqueous carbon dioxide solution (Vanorio & Kanitpanyacharoen, 2015). The length-scales for most of these processes are dependent on details of the magmatic-hydrothermal system and are hence difficult to ascertain. With regards to timescales, observations from volcanic systems with high frequency geophysical and geochemical monitoring suggests that the typical time scale for magmatic fluid injection is of order 1 month - 10 years (e.g., Campi Flegrei - Chiodini et al. (2017); Long Valley Caldera - Peiffer et al. (2018); Shelly et al. (2016); Cascade volcanoes

- Crankshaw et al. (2018)).

3.3.2 Permeability decreasing processes

There are also competing mechanisms which can reduce the permeability of crustal rocks. The most common processes are the closure of fractures by ductile deformation and precipitation. The Maxwell time-scale for ductile flow is $\sim \eta/E$ where η is the crustal viscosity, and E is the elastic Young's modulus. For a typical value of 10^{19} Pa s for η and 10 GPa for E, the Maxwell time-scale is $\sim$ 30 years. In general, the stress relaxation by ductile flow is a time-dependent, slow process and is coupled to the stress history of the magmatic reservoir with typical time-scales of decades for reasonable strains.

With regards to precipitation, natural magmatic fluids contain solutes such as silica whose solubility is strongly pressure-temperature dependent. Thus, the fractures responsible for enhanced permeability can be closed off by precipitation of quartz and calcite (Mayer et al., 2015; Vignaroli et al., 2015) as volatile ascend and cool. However, estimating the timescale of permeability decrease by precipitation is challenging because the permeability is not just a simple function of porosity for rough fractures (Molins, Trebotich, Steefel, & Shen, 2012; T. A. Jones & Detwiler, 2016). There are various forms of feedback processes - the heat generated by reactions, heterogeneous kinetics, and crystal growth, and the feedback between fluid flow rates and reaction kinetics - that need to be accounted for to calculate the permeability evolution correctly. As an example, the feedback between change in fracture aperture and precipitation can focus flow into higher velocity, low reactivity channels. This feedback can increase the time to completely seal a fracture from 2 months to 20 years (T. A. Jones & Detwiler, 2016).

Nevertheless, an order of magnitude estimate for fracture sealing timescale due to mineral precipitation is 100-600 yr for anhydrite precipitation (Larson, Houghton, Lowell, Farough, & Meile, 2015; Lowell et al., 1993) and 2-3 years for mineralization of carbonate minerals in basalt by injected CO_2 (CarbFix site in Iceland - Matter et al. (2016)). A similar sealing time-scale (1-3 years) is estimated based on the observations of permeability decrease in faults after large earthquakes (Manga et al., 2012). S. Ingebritsen and Manning (2010) inferred from modeling crustal-scale permeability that enhanced permeability in dynamic geologic environments may decay over a time scale of 1-1000 year.

3.3.3 Estimates of transient permeability

In general, the very approximate time scales of permeability production are generally comparable/shorter than the time-scales for closing fractures. Consequently, we should expect a non-zero permeability around magmatic reservoirs in a time-averaged sense. We note that the effective permeability of a medium is strongly influenced by macro-fractures, and a single fracture can increase permeability from $5\text{x}10^{-19}$ m^2 to 10^{-14} m^2 (at 20 MPa background pressure) for a low porosity rock (Lamur et al., 2017).

We readily acknowledge that for a given magmatic system, the choice of which process for permeability increase/decrease dominates depends on a host of factors, including but not limited to, magmatic fluid composition, fracturing history, and fluid-rock interaction, background tectonics, and critically, the temporal history of the system (see discussion in Manga et al. (2012)). For instance, if a new batch of magma is emplaced in a cold crust, thermal fluid pressurization and volatile production by metamorphism is a likely mechanism for enhancing crustal permeability. However, in a mature magmatic system, these processes would not be as relevant since the thermal aureole would be well developed and the ductile flow is faster in a hotter crust. Eventually, once the magmatic flux decreases and the system cools down, the thermal contraction and influx of fluids during cooling can produce sufficient stresses to induce fracturing (Olive & Crone, 2018).

In conclusion, the likely range of time-averaged permeability surrounding magmatic reservoirs from field studies (e.g.,fractures around Palisade sill Matter, Goldberg, Morin, and Stute (2006)), lab experiments, and geochemical proxies (e.g.,observed distribution of δ18O values) is 10^{-19} - 10^{-16} m^2 (Kushnir et al., 2017; Muraoka et al., 1998; Violay, Heap, Acosta, & Madonna, 2017) with a weak depth dependence for geologically active regions (Achtziger-Zupančič, Loew, & Hiller, 2017). In hydrothermally influenced fault systems with sealed microfactures, the typical paleo-permeability has been estimated to be of order 10^{-13} to 10^{-14} m^2 (Gomila, Arancibia, Mitchell, Cembrano, & Faulkner, 2016; Nippress & Rietbrock, 2007). The mean permeability estimates for subductional orogons at $\sim$ 2 km is 10^{-16} m^2, two orders of magnitude larger than passive orogens (Achtziger-Zupančič, Loew, & Hiller, 2017). A similarly high permeability of 10^{-17} to 10^{-16} m^2 has been estimated for disturbed, seismically active deep crust (S. Ingebritsen & Manning, 2010) as well as for magmatic systems using a variety of geophysical and geochemical proxies (R. B. Hanson, 1997). Dipple and Ferry (1992) estimate a permeability of 10^{-15} to 10^{-19} m^2 for fault zone metamorphism (see S. Ingebritsen and Manning (2010) for a detailed discussion of the permeability estimates). In aggregate, a range of 10^{-19} - 10^{-16} m^2 is a plausible range of values for time-averaged permeability near a magmatic reservoir.

3.4 Magmatic system Model

In order to assess the role of transient permeability on the dynamics of a magma reservoir, we need to couple the crustal response with the magma reservoir thermo-chemical evolution. In particular, we need to include the response of the fluid occupying the pore spaces in the crust. Consequently, in this study, we describe a model for the solid crust as a two-phase medium with a fluid component that can flow by porous media flow along with a thermal evolution equation for the medium. In the following section (Section 3.5), we will first briefly describe this coupled (visco)-thermo-poro-elasticity theory followed by a description of the spherically symmetric cavity solution. We then couple this crustal model with a simplified magma reservoir box model (described in Section 3.6) for understanding how magma reservoir-crustal interaction affects the ability of magma to erupt to the surface with

non-zero time-averaged crustal permeability.

The primary difference in our calculations compared to many previous studies is that we consider the magma reservoir to be a partially open system with regards to interaction with the overlying crust. Although this is qualitatively similar to some of the modeling work by Huppert and Woods (2002); Paonita et al. (2016); Weis et al. (2012), our study incorporates a more realistic thermo-chemical box model for the magma reservoir evolution. We want to stress that in this study, we are exploring an end-member wherein the primary controlling factor for the volatile loss is the crustal permeability. In contrast, some other open system models have considered the other end-member wherein the rate-limiting factor for gas loss comes from the internal dynamics in the chamber (e.g., Degruyter, Parmigiani, Huber, and Bachmann (2019); Parmigiani et al. (2017); Parmigiani, Faroughi, Huber, Bachmann, and Su (2016) and references therein). We compare our results with the internal dynamics end-member in Section 3.8 and discuss the implications for volatile loss from magmatic systems.

3.5 Crustal Response Model

An accurate representation of the stress state of the crust is essential since it exerts a first-order control on the ability of a magma reservoir to produce dikes and erupt to the surface (R. B. Hanson, 1996; S. E. Ingebritsen & Appold, 2012; Rubin, 1995; Taisne, Tait, & Jaupart, 2011). Besides, we need a multi-physics framework that accounts for both the visco-elastic response of the solid matrix to changes in temperature and boundary stresses as well as the fluid flow through the pore spaces in the crustal rock.

The challenge for modeling these processes is that the temperature evolution, deformation of a visco-poroelastic solid, and porous media fluid flow in the crust is inherently coupled. In order to illustrate these couplings, we can consider a simple case wherein a sudden temperature change is imposed at the boundary of a spherical cavity embedded in an infinite medium consisting of a solid and a fluid component (see Figure 1). The resulting temperature gradients in the medium surrounding the cavity cause thermal stresses leading to deformation of the medium. This deformation, in turn, affects the pore pressure of the fluid in the medium, leading to fluid flow and heat advection. Furthermore, if the fluid has a higher thermal expansion coefficient than the solid, as is typically the case for geomaterials saturated with water, the temperature change will lead to thermal pore pressurization. In the case of slow fluid flow in the medium because of low permeability, this excess pore pressure will induce stresses on the solid matrix and can place it effectively into tension. Thus the net stress of the crustal medium, which ultimately controls brittle material failure, as well as the fluid flow is a coupled phenomenon.

3.5.1 Model Assumptions

In order to make the problem analytically tractable and understandable, we make some simplifying assumptions in the presented model. Firstly, we assume constant material prop-

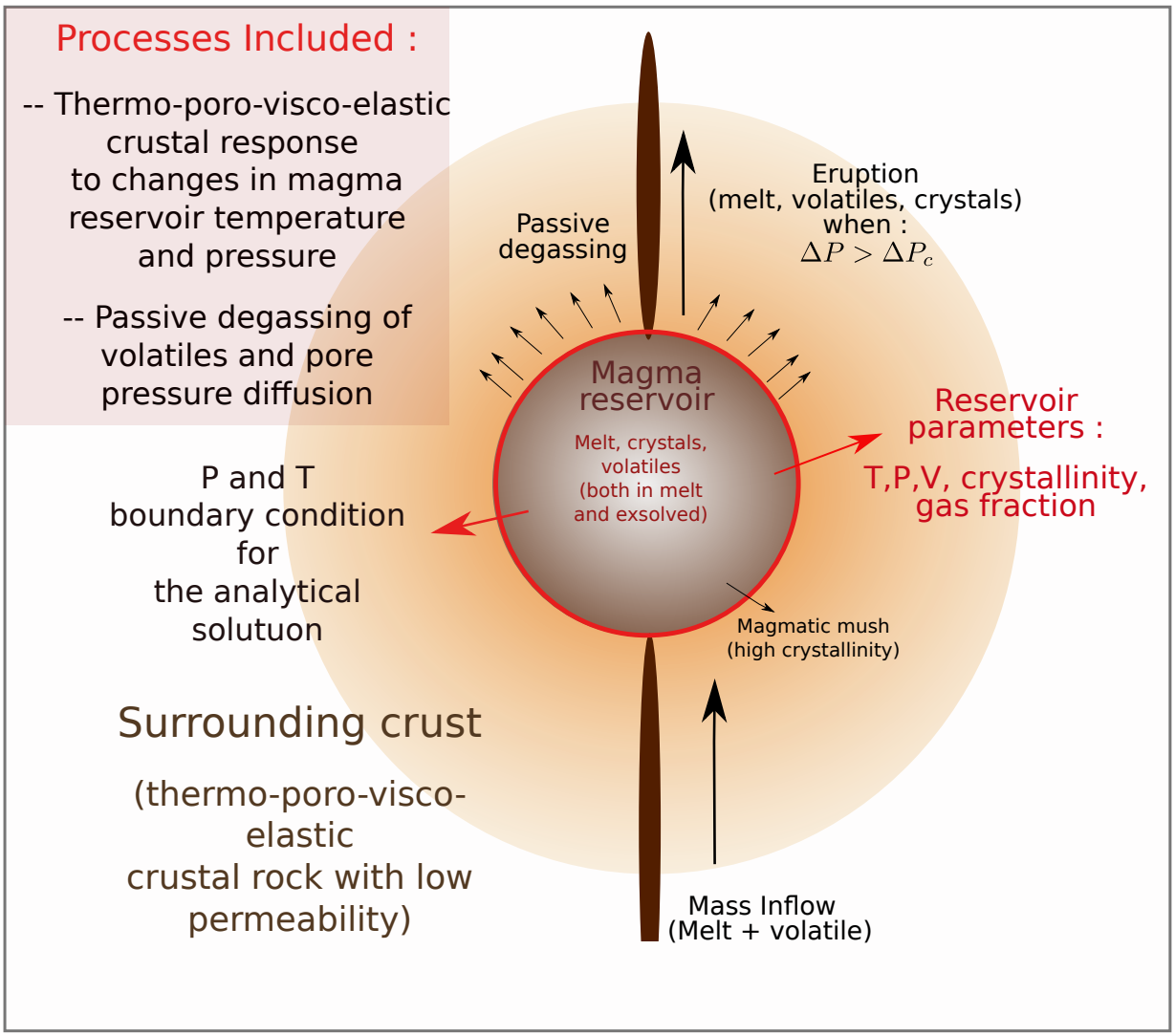

Figure 3.1: Schematic description of the crustal-magma reservoir model developed in this study as well as the processes included in the magma reservoir and crustal domain.

erties for the crustal region, including permeability. Although observations and models as discussed in the previous sections (Section 3.2 and 3.3) clearly show that there will be short-term temporal variability in porosity, permeability, fluid viscosity, and other microphysical parameters, including this in a self-consistent manner make the equations extremely non-linear and less amenable for a wide parameter space exploration. Furthermore, it is unclear how to properly parameterize the various competing mechanism for permeability increase and decrease. Instead, we assume a non-zero averaged permeability and perform calculations for a wide range of parameters in order to quantify the influence of different parameter choices on our results. We similarly drop the heat advection term in our equation set to similarly avoid non-linearities in our model. For self-consistency, we confirm that for our chosen parameter ranges, the Peclet number (the ratio of advective to conductive heat transfer) is always less than unity in order to justify neglecting advective heat transport. We would note that in natural magmatic systems, strong convective hydrothermal systems will be set-up in the regions where the permeability is large enough ($\sim> 10^{-16}$ m^2, Dutrow and Norton (1995)).

Secondly, we do not include the full viscous relaxation term in our coupled crustal model. Although it is not difficult to include a viscous term in our coupled thermo-poro-elasticity theory from a theoretical perspective, visco-elasticity transforms our spherical cavity solutions from a closed form analytical form (for an elastic case) to an expensive numerical form. Consequently, we have included only a simplified viscous crustal response in our final magma reservoir model by keeping the viscous relaxation term in Degruyter and Huber (2014) (DH model, see details in Section 3.6).

Thirdly, we assume that the volatile flux out of the magma chamber and into the crust is monophase and we consequently do not include any phase change terms in our equations. We readily acknowledge that in real magmatic systems, the magmatic volatiles may be in both gaseous and liquid phases depending on their composition and the pressure-temperature conditions (Hayba & Ingebritsen, 1997). However, explicitly including both phases is challenging not only from a model complexity perspective, but more critically, more a material properties perspective. The multiphase flow process of relevance at the pore scale for such systems is not well understood and is an area of active research (Armstrong et al., 2016). Thus, the relative permeability between the phases is a function of uncertain porous media structure, and non-equilibrium kinetics in the region surrounding the magmatic reservoir and its inclusion will lead to additional uncertain model parameters. Although we anticipate that the details of our model results may change for the multiphase case due to differences in effective fluid viscosity and material properties, we have tried to make conservative choices for material parameters as much as possible. As a result, we think that our simplified model captures the first-order physical influence of transient permeability and future models can include multiphase flow as the micro-scale physics becomes better constrained. Furthermore, proper multiphase behavior will have to be included in the DH style box model in order to have a consistent set of assumptions.

Fourthly, we consider an idealized setup of a magma reservoir as a spherical cavity em-

bedded in an infinite crustal medium (see Figure 1 for a schematic) fully saturated with an aqueous fluid. Although observations from geophysical surveys, field studies, and measurements of diffusion profiles in crystals (Cashman, Sparks, & Blundy, 2017) over the past decade strongly indicate that the idea of a single large magma reservoir is simplistic, we would argue that it is still a useful first step with regards to understanding the dynamics of the coupled system. Similarly, the assumption of a fully volatile saturated crust is likely a simplification and in reality may be spatio-temporally heterogeneous. However, it is unclear what the appropriate saturation state is for an upper crustal magmatic system with lots of passive degassing and a hydrothermal system especially when considering the role of deep fluids (Manning, 2018). Consequently, we have chosen a spherical shape for the reservoir in a fully saturated crust since it allows simplification of the coupled equation set, derivation of an analytical solution, and coupling with the pre-existing DH box model.

Lastly, we do not include the gravitational terms in our final solution since addition of gravity breaks the symmetry of the problem, and introduces significant additional mathematical complexity. We readily acknowledge that since the magmatic volatiles are buoyant, they would not be degassed in a radially symmetric pattern and this will influence the spatial stress field around the magma reservoir. Nevertheless, given the significant simplifications in our geometry, material properties, and the 0D box model, we would contend that our model can be used to analyze the first order poro-thermo-elastic influence of fluids on the magma reservoir stability with additional complexity reserved for future studies. We would note that since our solutions (fluid pressure and elastic stresses) are defined with respect to a reference stress state (lithostatic stress), we are including the large scale effect of gravity in our model.

3.5.2 Coupled Thermo-poro-elasticity

The four primary variables describing the physical state of the crustal system are :

- u_i : Solid displacement
- $\hat{P}_f$: Difference in fluid pore pressure relative to the reference initial pressure
- $\Theta = T - T_0$: Difference in temperature of the porous medium relative to the reference initial temperature (T_0)
- $q^d = \phi(v^f - v^s)$: Darcy fluid flux which is equal to the porosity (ϕ) multiplied by the velocity difference between the fluid (v^f) and solid components (v^s)

In addition, we also need a few other derived variables for representing the conversation equations in a compact form :

- $\epsilon_{ij} = \frac{1}{2}(u_{i,j} + u_{j,i})$: Strain tensor - a symmetric second order tensor
- σ_{ij} : Total stress tensor

- $e = \epsilon_{kk}$: First invariant of the strain tensor which represent the change of volume per unit volume of the material
- $e_{ij} = \epsilon_{ij} - (e/3)\delta_{ij}$: Deviatoric strain tensor

Here δ_{ij} is the Kronecker delta function. In the following, we use the subscript i and ij to represent the vector components x,y,& z and tensor components (nine combinations of x,y, z) respectively. The various spatial derivatives are represented as follows - $u_{i,j}$ implies $\sum_{j=x,y,z} \partial u_i/\partial j$. For compactness, we also use the Einstein summation convention for summing over repeated indices.

The primary assumption underlying our coupled Thermo-poro-elastic formalism is that the infinitesimal theory of elasticity is applicable. Hence, the total strains must be small ($\sim$ few %) in the application of interest. Consequently, the quadratic terms can be neglected and strain tensor ϵ_{ij} is reduced to the linear form. We also assume that the fluid and solid are in local thermodynamic equilibrium and hence have the same temperatures. This simplification is justified since we are modeling the fluid component as being distributed in microscopic pore spaces in the medium. Hence the timescale for diffusive temperature equilibration between the solid and the fluid components is small compared to the macroscopic fluid flow time-scale. We refer the reader to A. Cheng (2016) for a detailed derivation of thermo-poro-elasticity as our final equations closely follow their results with some minor adjustments to make the sign conventions consistent. In particular, we use the typical pressure convention in all our equations wherein pressure is positive for compression and negative for tension which opposite to that for the stress tensor.

We first start with describing the elastic response of the medium to mechanical loads as well as changes in temperature and fluid pore pressure. The thermo-poro-elastic (total) stress tensor can be represented as :

$$\sigma_{ij} = 2G_b(\epsilon_{ij} - \frac{e}{3}\delta_{ij}) + K_b e\delta_{ij} - 3K_b\alpha_{Th,d}\Theta\delta_{ij} - \alpha_B\hat{P}_f\delta_{ij} \tag{3.1}$$

Here $G_b = \mu$ is the shear modulus, K_b is the drained bulk modulus, and $\alpha_{Th,d}$ is the drained coefficient of linear thermal expansion for the porous medium frame. For the contexts of interest to us, bulk values imply properties averaged over a representative volume of the porous media. The temperature and pore pressure terms are multiplied by a δ_{ij} function since thermal and pore pressure induced strains are assumed to have no shear component. Finally, α_B is the Biot-Willis factor - the ratio of the fluid volume gained in a porous frame to the volume change of that frame while maintaining a drained (constant fluid pressure) condition. Terzaghi's effective stress is a special case where $\alpha_B = 1$.

Since the primary application for thermo-poro-elasticity are problems where the stress or strain are evolving over time, we need a momentum conservation equation to model this change. The corresponding momentum equation is called the Navier equation and is, in essence, equivalent to Newton 2nd law of motion. The Navier equation is (neglecting inertial

terms) :

$$\sigma_{ij,j} = 0 \tag{3.2}$$

$$2G_b(\frac{1}{2}u_{i,kk} + \frac{1}{6}e_{,i}) + K_b e_{,i} - 3\alpha_{Th,d}(K_b)(\Theta)_{,i} - \alpha_B(\hat{P}_f)_{,i} = 0 \tag{3.3}$$

We next need an equation to model the fluid flow relative to the solid frame. We use the Darcy's law to calculate fluid flow due to gradients in pore pressure and hydraulic head (z^h) (fluid momentum conservation equation) :

$$q_i^d = \phi(v_i^f - v_i^s) = -\frac{k^m}{\eta_f}\nabla(\hat{P}_f + \rho_f g z^h) \tag{3.4}$$

Here k^m is the hydraulic permeability and η_f is the fluid viscosity. Generally, $v^f >> v^s$ for most relevant applications of interest.

The temperature evolution of the medium can be modelled using a modified diffusion equation for Θ (energy conservation equation) :

$$(k_b^c\Theta_{,i})_{,i} = m_d^{''}T_0\frac{\partial\Theta}{\partial t} - Q_h + 3K_b\alpha_{Th,d}T_0\frac{\partial e}{\partial t} - 3T_0\alpha_{Th,e}\frac{\partial\hat{P}_f}{\partial t} \tag{3.5}$$

Here $m_d^{''}$ is the drained thermoelastic constitutive constant (see more details in Appendix A), and k_b^c is the effective bulk thermal conductivity. Besides the standard terms for heat transfer by conduction, we have included additional terms to account for entropy changes during expansion of the solid matrix ($\alpha_{Th,d}$ term) and the fluid ($\alpha_{Th,e}$ term). In addition, Q_h represents heat sources/sinks.

Finally, we can obtain a constitutive equation for pore pressure change by considering the net amount of fluid entering the solid matrix of the medium per unit volume of the solid frame. This continuity equation for the fluid pore pressure is :

$$-\frac{\rho_f}{M_B}\frac{\partial\hat{P}_f}{\partial t} = \rho_f\nabla\cdot(q^d) + \rho_f\alpha_B\frac{\partial e}{\partial t} - Q_f - 3\alpha_{Th,e}\rho_f\frac{\partial\Theta}{\partial t} \tag{3.6}$$

Here, the pore pressure evolves with time due to pressure diffusion by fluid flow (first term on the right hand side), deformation of the porous media (second term), sources/sinks of fluids (third term), and temporal changes in temperature (fourth term). In these equations, M_B is the Biot modulus and $\alpha_{Th,e}$ is the coefficient of linear thermal expansion for variation in fluid content at constant frame volume. We thus have a final equation set for the evolution of u_i, q_d, Θ, and $\hat{P}_f$: Eqns. 3,4,5, and 6 respectively. A more detailed description of the various material parameters and their inter-relationships is described in the Appendix A.

3.5.3 Spherical Cavity solution

In order to understand how the thermo-poro-elastic behaviour of the crust affects the evolution of the magmatic reservoir, we consider a 1D spherical cavity of radius (R_0) embedded

in an infinite medium (see Figure 1 for a schematic) fully saturated with an aqueous fluid. Since our model system has spherical symmetry, all the variables are primarily a function of the radial coordinate r and time t only. Due to the chosen symmetry, the displacement is non-zero only in the radial direction -

$$u_R = u_R(R,t)\ ;\ u_\phi = u_\theta = 0 \tag{3.7}$$

$$\text{with } \sigma_{\theta\theta} = \sigma_{\phi\phi} \tag{3.8}$$

The Navier equation for this system will be hence be simplified to :

$$(K_b + \frac{4G_b}{3})(\frac{\partial^2 u_R}{\partial R^2} + \frac{2}{R}\frac{\partial u_R}{\partial R} - \frac{2u_R}{R^2}) - 3K_b\alpha_{Th,d}\frac{\partial \Theta}{\partial R} - \alpha_B\frac{\partial \hat{P}_f}{\partial R} = 0 \tag{3.9}$$

with e (total volumetric displacement) being equal to :

$$e = \frac{\partial u_R}{\partial R} + \frac{2u_R}{R} \tag{3.10}$$

Hence, Eqn 3.9 can be re-written as :

$$(K_b + \frac{4G_b}{3})\frac{\partial e}{\partial R} - 3K_b\alpha_{Th,d}\frac{\partial \Theta}{\partial R} - \alpha_B\frac{\partial \hat{P}_f}{\partial R} = 0 \tag{3.11}$$

Integrating the above equation from R_0 to ∞, we get :

$$e = \frac{\alpha_B}{K_b + \frac{4G_b}{3}}\hat{P}_f + \frac{3K_b\alpha_{Th,d}}{K_b + \frac{4G_b}{3}}\Theta + F_s^1 \tag{3.12}$$

Here where F_s^1 is an integration constant (potentially a function of time) which can be determined using the boundary conditions. Thus, we get :

$$F_s^1 = (e^\infty - \frac{\alpha_B}{K_b + \frac{4G_b}{3}}\hat{P}_f^\infty + \frac{3K_b\alpha_{Th,d}}{K_b + \frac{4G_b}{3}}\Theta^\infty) \tag{3.13}$$

where e^∞, Θ^∞, and $\hat{P}_f^\infty$ refer to the values for the volumetric strain, temperature, and pressure change at the $R -> \infty$ limit.

Using this result, we can re-write the coupled pore pressure and temperature equations (Eqns 5 & 6) as a set of coupled diffusion equations with source terms :

$$\frac{\partial \hat{P}_f}{\partial t} - \frac{c}{R^2}\frac{\partial}{\partial R}(R^2\frac{\partial \hat{P}_f}{\partial R}) = \alpha_e\frac{\partial \Theta}{\partial t} - \frac{3\alpha_B}{S}\frac{\partial F_s^1}{\partial t} \tag{3.14}$$

$$\frac{\partial \Theta}{\partial t} - \frac{c_a}{R^2}\frac{\partial}{\partial R}(R^2\frac{\partial \Theta}{\partial R}) = \alpha_p\frac{\partial \hat{P}_f}{\partial t} - \frac{3\alpha_d}{S_a}\frac{F_s^1}{\partial t} \tag{3.15}$$

Once we have a solution for $\hat{P}_f$ and Θ with the appropriate boundary conditions, we can calculate σ_{rr},$\sigma_{\phi\phi}$, and u_R as follows :

$$u_r = \frac{\eta}{R^2 G_b}\int R^2 \hat{P}(R,t)dR + \frac{\eta_d}{R^2 G_b}\int R^2 \Theta(R,t)dR + \frac{F_s^2}{R^2} \tag{3.16}$$

$$\sigma_{rr} = -\frac{4\eta}{R^3}\int R^2 \hat{P}(R,t)dR - \frac{\eta_d}{R^3}\int R^2 \Theta(R,t)dR - \frac{4G_b}{R^3}F_s^2 \tag{3.17}$$

$$\sigma_{\phi\phi} = \frac{2\eta}{R^3}\int R^2 \hat{P}(R,t)dR + \frac{2\eta_d}{R^3}\int R^2 \Theta(R,t)dR + \frac{2G_b}{R^3}F_s^2 - 2\eta\hat{P}(R,t) - 2\eta_d\Theta(R,t) \tag{3.18}$$

Here η_d, η, c, c_a, S, and S_a are constants depending on the microphysical properties of the medium (see Appendix A for their expressions in terms of the parameters defined in the previous section B. Bai (2006); Ghassemi, Nygren, and Cheng (2008)). $F_s^2(t)$ is another integration constant to be determined by the boundary conditions of a specific problem. We would note that in the above, we have simplified the equations by setting $F_s^1 = 0$ since that is the only relevant case for this study (see discussion in next section for why this is reasonable).

The coupled equations for $\hat{P}_f$ and Θ can be solved analytically using Laplace transforms (with $F_s^1 = 0$). In the following equations, we use the $\sim$ symbol as a superscript to represent variables in the Laplace domain (for e.g.,$\hat{P}_f$ is represented by $\widetilde{P_f}$)

$$-\frac{s}{c}\widetilde{P_f} + \frac{1}{R^2}\frac{\partial}{\partial R}(R^2\frac{\partial\widetilde{P_f}}{\partial R}) = -\frac{s\alpha_e}{c}\partial\widetilde{\Theta} \tag{3.19}$$

$$-\frac{s}{c_a}\widetilde{\Theta} + \frac{1}{R^2}\frac{\partial}{\partial R}(R^2\frac{\partial\widetilde{\Theta}}{\partial R}) = -\frac{s\alpha_p}{c_a}\partial\widetilde{P_f} \tag{3.20}$$

The general solution of these equations is :

$$\widetilde{P_f} = \frac{C_1(c-c_a-C_Q)}{2c\alpha_p}\frac{e^{-\lambda_1\sqrt{s}R}}{R} + \frac{C_2(c-c_a+C_Q)}{2c\alpha_p}\frac{e^{-\lambda_2\sqrt{s}R}}{R} \tag{3.21}$$

$$\widetilde{\Theta} = C_1\frac{e^{-\lambda_1\sqrt{s}R}}{R} + C_2\frac{e^{-\lambda_2\sqrt{s}R}}{R} \tag{3.22}$$

We can now use the relevant boundary conditions to solve for the appropriate values of the constants C_1 and C_2. If we consider a purely elastic medium, the inverse transform can be done analytically to obtain a closed form solution.

3.5.3.1 Boundary Conditions

For our problem of interest, we consider two sets of boundary conditions. We specify either the temperature and pressure (Type 1) or the heat and fluid flux (Type 2) at the

spherical cavity wall. Since our simplified equation set is linear, we can combine these two end-member boundary conditions to calculate the coupled magma reservoir-crustal evolution. The solutions for all variables asymptote to zero values at infinity for both boundary types. This boundary condition is a reasonable assumption since the stress-strain, $\hat{P}_f$, and Θ are all defined as deviations with respect to a steady state background. Thus, as long as our magma reservoir is not close to the surface, the deviations will all asymptote to zero far away from the reservoir.

If we have the solutions for $\Theta(R,t)$ and $\hat{P}(R,t)$, we can calculate the value of $F_s^2(t)$ using a boundary condition for the radial stress (σ_{rr}). We typically fix the radial stress in the crust to be equal to the pressure inside the magma reservoir minus the lithostatic reference pressure at the magma reservoir-crust interface. This boundary condition is reasonable since the fluid pressure and the stress they are equal inside the magma reservoir in the DH box model.

Since it is easier to analytically solve the equations with step function boundary conditions (i.e., Heavyside functions) in the Laplace domain, our boundary conditions are step functions in temperature/pressure/flux at time t =0 instead of more commonly used delta functions in time. However, we can still obtain a final solution for any arbitrary boundary forcing by appropriately combining the linear solutions over time.

First, when $R = R_0, \hat{P}_f = P_1, \Theta = T_1$ (Type 1 boundary), then the final Laplace domain solution (for elasticity) is :

$$\widetilde{\Theta} = \frac{1}{2c_Q s}\left(A_1 \frac{e^{-\lambda_1\sqrt{s}(R-R_0)}}{R} - A_2 \frac{e^{-\lambda_2\sqrt{s}(R-R_0)}}{R}\right) \tag{3.23}$$

$$\widetilde{P} = \frac{1}{4cc_Q s\alpha_p}\left(A_3 \frac{e^{-\lambda_1\sqrt{s}(R-R_0)}}{R} - A_4 \frac{e^{-\lambda_2\sqrt{s}(R-R_0)}}{R}\right) \tag{3.24}$$

$$A_1 = T_1 R_0(c - c_a + C_Q) - 2P_1\alpha_p c R_0 \tag{3.25}$$

$$A_2 = T_1 R_0(c - c_a - C_Q) - 2P_1\alpha_p c R_0 \tag{3.26}$$

$$A_3 = (T_1 R_0(c - c_a + C_Q) - 2P_1\alpha_p c R_0)(c - c_a - C_Q) \tag{3.27}$$

$$A_4 = (T_1 R_0(c - c_a + C_Q) - 2P_1\alpha_p c R_0)(c - c_a + C_Q) \tag{3.28}$$

leading to the final time domain solution (for the elastic case) :

$$\Theta(R,t) = \frac{1}{2c_Q R}\left[A_1 \mathrm{erfc}\left(\frac{-\lambda_1(R-R_0)}{2\sqrt{t}}\right) - A_2 \mathrm{erfc}\left(\frac{-\lambda_2(R-R_0)}{2\sqrt{t}}\right)\right] \tag{3.29}$$

$$\hat{P}_f(R,t) = \frac{1}{4cc_Q\alpha_p R}\left[A_3 \mathrm{erfc}\left(\frac{-\lambda_1(R-R_0)}{2\sqrt{t}}\right) - A_4 \mathrm{erfc}\left(\frac{-\lambda_2(R-R_0)}{2\sqrt{t}}\right)\right] \tag{3.30}$$

For the flux boundary condition (Type 2 boundary), when $R = R_0, d\hat{P}_f/dR = P_1', d\Theta/dR =$

$T_1^{'}$, the final Laplace domain solution is :

$$\widetilde{\Theta} = -\frac{R_0}{2c_Q sR}\Big[A_1\frac{e^{-\lambda_1\sqrt{s}(R-R_0)}}{\lambda_1\sqrt{s}R_0+1} - A_2\frac{e^{-\lambda_2\sqrt{s}(R-R_0)}}{\lambda_2\sqrt{s}R_0+1}\Big] \tag{3.31}$$

$$\widetilde{P} = \frac{R_0}{4cc_Q\alpha_p sR}(-A_3\frac{e^{-\lambda_1\sqrt{s}(R-R_0)}}{\lambda_1\sqrt{s}R_0+1} + A_4\frac{e^{-\lambda_2\sqrt{s}(R-R_0)}}{\lambda_2\sqrt{s}R_0+1}) \tag{3.32}$$

$$A_1 = T_1^{'}R_0(c-c_a+C_Q) - 2P_1^{'}\alpha_p cR_0 \tag{3.33}$$

$$A_2 = T_1^{'}R_0(c-c_a-C_Q) - 2P_1^{'}\alpha_p cR_0 \tag{3.34}$$

$$A_3 = (T_1^{'}R_0(c-c_a+C_Q) - 2P_1^{'}\alpha_p cR_0)(c-c_a-C_Q) \tag{3.35}$$

$$A_4 = (T_1^{'}R_0(c-c_a-C_Q) - 2P_1^{'}\alpha_p cR_0)(c-c_a+C_Q) \tag{3.36}$$

leading to the final time domain solution (for the elastic case):

$$\Theta(R,t) = -\frac{R_0}{2c_Q R}\Big[A_1(-\exp(\frac{t}{(\lambda_1 R_0)^2}+\frac{R-R_0}{R_0})\mathrm{erfc}(\frac{\sqrt{t}}{\lambda_1 R_0}+ \tag{3.37}$$

$$\frac{\lambda_1(R-R_0)}{2\sqrt{t}}) + \mathrm{erfc}(\frac{\lambda_1(R-R_0)}{2\sqrt{t}})) \tag{3.38}$$

$$-A_2(-\exp(\frac{t}{(\lambda_2 R_0)^2}+\frac{R-R_0}{R_0})\mathrm{erfc}(\frac{\sqrt{t}}{\lambda_2 R_0}+$$

$$\frac{\lambda_2(R-R_0)}{2\sqrt{t}}) + \mathrm{erfc}(\frac{\lambda_2(R-R_0)}{2\sqrt{t}}))\Big] \tag{3.39}$$

$$\hat{P}_f(R,t) = \frac{R_0}{4cc_Q\alpha_p R}\Big[- A_3(-\exp(\frac{t}{(\lambda_1 R_0)^2}+ \tag{3.40}$$

$$\frac{R-R_0}{R_0})\mathrm{erfc}(\frac{\sqrt{t}}{\lambda_1 R_0}+\frac{\lambda_1(R-R_0)}{2\sqrt{t}})+ \tag{3.41}$$

$$\mathrm{erfc}(\frac{\lambda_1(R-R_0)}{2\sqrt{t}})) \tag{3.42}$$

$$+A_4(-\exp(\frac{t}{(\lambda_2 R_0)^2}+\frac{R-R_0}{R_0})\mathrm{erfc}(\frac{\sqrt{t}}{\lambda_2 R_0}+\frac{\lambda_2(R-R_0)}{2\sqrt{t}}) + \mathrm{erfc}(\frac{\lambda_2(R-R_0)}{2\sqrt{t}}))\Big]$$

With these solutions, we have an analytic solution for how the crust surrounding a spherical magma reservoir will respond to changes in perturbations at the cavity interface ($R = R_0$).

3.6 Magma Chamber Box model

We next couple our thermo-poro-elastic crustal model with a simplified magma reservoir box model to understand how this coupling affects the magma eruptibility for non-zero time-averaged crustal permeability. We use a modified version of the volume integrated

model developed by Degruyter and Huber (2014) (DH model). The model includes chamber averaged evolution equations for conservation of mass and energy, along with simplified phase equilibrium parameterizations. Consequently, the model allows self-consistent calculation of the pressure (P), temperature (T), and volume, and the crystal, melt, and volatile-gas (ϵ_g) fractions in the magma reservoir. We refer the reader to Degruyter and Huber (2014)for a detailed description of the model and the various assumptions/choices. In the following, we describe the specific changes we have implemented in the DH model.

3.6.1 Modifications to the DH model

Our main modification to the DH model is to introduce a two-way coupling between the magmatic and the crustal components. The volatile and the melt phases in the magma chamber are expected to have the same pressure (modulo a small surface tension term) since they are two fluids in contact with each other. The fluid saturated crust outside the magma reservoir also has the same aqueous phase. Since there is a non-zero passive degassing and transient permeability (see sections 2.2 and 2.3), the magmatic volatiles and crustal fluid must be in contact with each other.

In our model, we allow the magmatic volatiles to flow between the magmatic reservoir and the surrounding crust with a non-zero permeability. This fluid flow, along with the pressure and temperature variations at the magmatic reservoir-crustal interface, modifies the crustal stress state and the pore fluid pressure gradients. The fluid flow also influences the pressure evolution inside the magmatic reservoir and hence the thermo-chemical evolution of the magmatic system. The primary control on the volatile flow direction and rate is the fluid pore pressure difference between the magma body and the surrounding crust. Thus, although the magma reservoir impacts the surrounding crust, the (visco)-thermo-poro-elastic crustal stress state also exerts a first-order control on the magmatic system leading to a two-way coupling between the two components.

In order to allow for this physical process, we use our coupled thermo-poro-elastic solution from the previous section as the external boundary for the DH model instead of using a simplified thermo-visco-elastic, non-porous crust. The consequent changes to the DH model equations are as follows :

- Replace the term $\frac{\Delta P}{\eta}$ with $\frac{\Delta P^1}{\eta} + F(\epsilon_g)\frac{k^m}{\eta_f}\frac{\partial^2 \Delta P^2}{\partial r^2}$ in equations 14,16, 20, and 32 from the DH model (Degruyter & Huber, 2014). η is the crustal viscosity in a radial shell ($\sim 0.1R_0$) surrounding the magma reservoir (same as the DH model). The other terms are :

$$\begin{aligned} \Delta P &= (P - P_{lith}) \\ \Delta P^1 &= (P - P_{lith} - P_{mean,crust}) \\ \Delta P^2 &= (P - P_{lith} - P_{fluid,crust}) \end{aligned} \tag{3.43}$$

Here, $P_{mean,crust}$ and $P_{fluid,crust}$ are the mean σ_{rr} and fluid pore pressure averaged over same radial shell ($\sim 0.1R_0$) as is used to calculate the mean viscosity. We would like to remind the reader that the solutions from our crustal model are all calculated as deviations from a background lithostatic state. We calculate the ΔP^2 gradient terms using a first order Taylor expansion. Finally, since the our model is only valid when there is a volatile phase in the magmatic reservoir, we apply a threshold function $F(\epsilon_g)$ which is unity if $\epsilon_g > 0.02$ and zero otherwise.

- Since there is flux of volatiles across the magma reservoir-crust interface, we include an additional degassing mass flux term $\dot{M}^{dg}_{out}$. This term is defined as

$$\dot{M}^{dg}_{out} = 4\pi R_0^2 \epsilon_g \rho_g \frac{k^m}{\eta_f} \frac{d\Delta P^2}{dr} \tag{3.44}$$

  There is also a consequent modification to the $\dot{H}_{out}$ equation (Eqn 23, DH model) with an additional term added :

$$\dot{H}_{out} = F(\epsilon_g) c_g T \dot{M}^{dg}_{out} + \dot{H}_{cool} + c_{out} T_{out} \dot{M}_{out} \tag{3.45}$$

At every time-step during the solution of the coupled ODE model, we use the analytical solution to calculate the crustal pore pressure, temperature, and stress field. Since the pore pressure (P_f) and temperature (T) should be continuous across the magma reservoir-crust interface, we use the solution for a Type 1 boundary with the P_f and T at boundary equal to the pressure and temperature inside the reservoir at the previous time-step. In addition, pressure gradient in the crustal shell surrounding the magma reservoir can be non-zero. Consequently, there is a potentially a fluid flux into/out of the chamber and a consequent enthalpy flux. Since we explicitly neglected the advection term in the temperature equation, we need to account for this additional heat flux from the chamber. We do this by using the Type 2 boundary condition solution, with the boundary condition being a heat flux term equivalent to the enthalpy transport by passively degassed magmatic fluids per unit area ($(c_g T \dot{M}^{dg}_{out})/(4\pi R_0^2 k_b^c)$). Hence, our model introduces a two-way coupling between the magmatic and the crustal components.

We account for viscous relaxation in our modified model by keeping the viscous relaxation term in the original DH model (see above). Analogous to the original DH model, we use our crustal temperature solution to calculate the mean temperature in a radial shell for estimating the temperature-dependent viscosity. We solved our combined ODE-analytical solution system using a Python-based simulation package - Assimulo (Andersson, Führer, & Åkesson, 2015) with a variable-order, variable multi-step integration algorithm with event detection: CVODE (SUNDIALS package, Hindmarsh et al. (2005)).

In the similar way as the DH model (this was done as a post-processing step), we calculate a buoyancy overpressure term for the magma reservoir ($P_{buoy} = g(\rho - \rho_{crust})R_0$) where ρ is the average magma (melt + crystal + volatiles) density, ρ_{crust} is the crustal density, and R_0 is the

chamber radius. This term contributes to the critical overpressure (above the background lithostatic pressure) that is required to initiate tensile failure of the crust and magmatic dike formation. As noted in Section 3.5.1, we have neglected gravity in our spherically symmetric model and hence the model is inadequate for analyzing the detailed spatial stress pattern around the magma reservoir and does not consider any large scale gravitational flow of the crustal region. Consequently, we include magma buoyancy in a very simplified manner analogous to previous studies (e.g., Caricchi, Annen, Blundy, Simpson, and Pinel (2014a)) :

$$\Delta P_{ovp} = (P - P_{lith}) + P_{buoy} \tag{3.46}$$

3.6.2 Initial Conditions and parameters

In all of our calculations, the initial fluid pressure profile and stress profile is assumed to be lithostatic. The presence of extensive veining around magma reservoir as well as analysis of mineral assemblages has been argued to be evidence that lithostatic pressure conditions are present at great depths. Observations from deep boreholes around the world also corroborate this conclusion (Barton, Zoback, & Moos, 1995; Hsieh & Bredehoeft, 1981). Furthermore, the observation in Long Valley Caldera that the stress directions, as measured by borehole breakouts and earthquake source mechanisms, are very variable indicates that the fractures are critically stressed and pore-fluid pressure is nearly lithostatic (Moos & Zoback, 1993). Since our focus in this study is principally upon the dynamical influence of pore pressure within 100's of m of the magmatic-hydrothermal system interface, we consider that a background lithostatic stress state is a reasonable starting condition.

Analogously, we chose a conductive geotherm as the reference for the temperature solutions wherein we specify the initial crustal reference temperature and depth(or lithostatic pressure) with the surface temperature fixed to 300° K. Although magmatic systems are sites of active hydrothermal systems and hence advective heat transport is essential on large scales, the typical permeabilities for which advective heat transport dominates heat transport are of order 10^{-16} m^2 (and larger) (S. E. Ingebritsen & Appold, 2012). Since we are focused on the near-magma region, the permeabilities are expected to be lower than this threshold averaged over long time durations (see discussion in transient permeability section). We also note that in an active hydrothermal system, there exists a lateral pressure gradient from the margin of the magma reservoir from lithostatic to hydrostatic (Afanasyev, Blundy, Melnik, & Sparks, 2018; Weis et al., 2012; Zencher, Bonafede, & Stefansson, 2006). This pressure gradient will lead to more efficient fluid flow away from the magma body, thus helping diffuse pressure away faster and resulting in greater heat loss. At least to first order, both of these effects would amplify the feedbacks we find in our results. Hence, our assumptions are generally conservative, and we expect our general conclusions to be valid for realistic physical systems.

A critical tensile stress in the crust surrounding the magma reservoir is required to initiate diking and eruptions (Rubin, 1995). In the context of our model, this tensile stress can be approximated by the overpressure (ΔP_{ovp}, Eqn 3.46) in the magma reservoir. We choose

a critical tensile stress threshold (P_c) between 10-40 MPa (nominal value of 20 MPa), a range similar to what has been used in previous studies (Rubin, 1995; Black & Manga, 2017; Caricchi et al., 2014a; Degruyter & Huber, 2014). This critical threshold is broadly consistent with field estimates for the tensile strength of rocks in dyke propagation (Benson et al., 2012; Gudmundsson, 2011; Gudmundsson, Lecoeur, Mohajeri, & Thordarson, 2014). We used the International Association for the Properties of Water and Steam 1995 equation of state (IAPWS-95; (Wagner & Pruß, 2002)) to calculate the thermo-physical properties of aqueous fluids at appropriate depths and temperature. Since our semi-analytical solutions are only valid for constant micro-physical constants, we chose a reference temperature ($T_{ref} = 750$K) and pressure (lithostatic pressure at the depth of the magma reservoir) to calculate these values. We performed calculations with different reference temperatures to ascertain if doing so affects the results and found that as long as the temperatures/pressures were high enough ($\geq 600^\circ$ K at 50-200 MPa), our conclusions are robust.

We use two end-member material constants for modeling the crustal response - Westerly Granite (WG) and Berea Sandstone (BS) (A. Cheng (2016) - Table 3.4 and 11.2; Appendix A). We chose these two materials since they represent end-members for upper-crustal granitic and sedimentary compositions that would be appropriate for mid-upper crustal magmatic systems. In addition, both of these materials are commonly used standards in rock mechanics and hence have well-characterized micro-physical parameters.

We follow the DH model for input parameterizations of the melting curve, equation of state of the gas phase, solubility curve, crustal viscosity (with the same corresponding parameters), and other parameters (unless otherwise explicitly stated). Although there are potentially more accurate melting and solubility models (e.g.,AlphaMelts : Ghiorso, Hirschmann, Reiners, and Kress (2002), PerpleX : J. Connolly (2009)], we chose to use the same models since multiple studies (Degruyter & Huber, 2014; Degruyter, Huber, Bachmann, Cooper, & Kent, 2017; Parmigiani et al., 2017; M. Townsend, Huber, Degruyter, & Bachmann, 2019) have characterized the behavior of the DH model. Our focus in this study is to illustrate a specific physical process, and the DH model serves a useful test-bed to do so in a transparent manner.

Variable	Description	Units
ϵ_{ij}	strain tensor	Unitless
e	first invariant of the strain tensor $= \epsilon_{kk}$	Unitless
e_{ij}	deviatoric strain tensor $\epsilon_{ij} - (e/3)\delta_{ij}$	Unitless
u_i	displacement	m
σ_{ij}	stress tensor	Pa
Θ	T - T_0	K
T_0	Reference temperature	K
Q_h	intensity of applied heat source per unit volume	W/m^3
ϕ	porosity	unitless
$\hat{P}_f$	Change in fluid pore pressure	Pa
z^h	Hydraulic pressure head	m
v_f	Fluid velocity	m/s
v_s	Solid velocity (du_i/dt)	m/s
q_d	Darcy flux ($\phi(v_f - v_s)$)	m/s
Q_f	Fluid source/sink	$kg/m^3/s$
α_{Th}	Linear thermal expansivity coefficient	K^{-1}
$\alpha_{Th,s}$	Linear thermal expansivity coefficient solid grains	K^{-1}
$\alpha_{Th,f}$	Linear thermal expansivity coefficient fluid	K^{-1}
$G = \mu$	Shear modulus	Pa
λ	Láme parameter (K - 2G/3)	Pa
K	Bulk Modulus ($= \lambda + (2/3)\mu$)	Pa
E	Young's Modulus ($= 2G(1 + \nu)$)	Pa
k^c_{ij}	thermal conductivity tensor	W/m/K
c_p	specific heat capacity at constant strain	J/kg/K
$c_{p,s}$	specific heat capacity at constant strain, solid	J/kg/K
$c_{p,f}$	specific heat capacity at constant strain, fluid	J/kg/K
c_d	drained specific heat at constant strain	J/kg/K

κ_{th}	thermal diffusivity (= $k^c/rho_0/c_p$)	m^2/s
η	coefficient of viscosity (= $\sigma_{II}/(\dot{e}_{ij})$)	Pa s
k^m	Permeability of the matrix y	m^2
ρ_s	Solid mass density	kg/m^3
ρ_f	Fluid mass density	kg/m^3
ρ_b	bulk density of the medium	kg/m^3
g	Gravitational acceleration	m/s^2
α_B	Biot-Willis factor	
K_b	Bulk Modulus of the porous media when dry/fluid pressure is constant	Pa
K_s	Bulk Modulus of solid grains	Pa
K_f	Bulk Modulus of the fluid	Pa
c_b	Bulk compressibility of porous media ($1/K_b$)	1/Pa

Table 3.1: Summary of variables and units

3.7 Results

In the following, we first describe the behavior of our thermo-poro-elastic solution with a specified boundary forcing. We subsequently discuss our results for the coupled magma reservoir-crustal model and follow up with a regime plot describing the model behavior for the various input parameter choices.

K	2.5 x 10^{10}	8.00x 10^9	Pa
K_s	4.5 x 10^{10}	3.60x 10^{10}	Pa
ϕ	1x 10^{-2}	1.50x 10^{-1}	
M_B	5.59x 10^{10}	7.09x 10^9	Pa
K_u	3.60x 10^{10}	9.40x 10^9	Pa
S	2.23x 10^{-11}	1.53x 10^{-10}	1/Pa
c	4.94x 10^{-5}	7.17x 10^{-6}	m^2
c_d	2.30x 10^6	1.76x 10^6	J/m^3 K
$k_{T,s}$	2.79	2.24	W/m/K
k_T	2.77	1.99	W/m/K
κ_T	1.20x 10^{-6}	1.13x 10^{-6}	m^2/s
m_d	3.07x 10^3	2.35x 10^3	J/m^3

β_s	2.40x 10^{-5}	4.50x 10^{-6}	1/K
β_ν	1.41x 10^{-5}	2.15x 10^{-4}	1/K
β_e	2.48x 10^{-5}	2.17x 10^{-4}	1/K
β_c	1.89x 10^{-5}	2.16x 10^{-4}	1/K
α_e	8.46x 10^5	1.41x 10^6	N/m^2 K
α_d	6.00x 10^5	3.60x 10^4	N/m^2 K
η_d	2.00x 10^5	1.35x 10^4	N/m^2 K
η	1.48x 10^{-1}	1.67x 10^{-1}	N/m^2 K
S_a	3.07x 10^3	2.35x 10^3	J/m^3
c_a	1.20x 10^{-6}	1.13x 10^{-6}	m^2/s
α_p	6.13x 10^{-9}	9.19x 10^{-8}	m^3 K^{-1} J^{-1}
$k_{T,f}$	5.86x 10^{-1}	5.86x 10^{-1}	W/m/K
β_f	1.44x 10^{-3}	1.44x 10^{-3}	K^{-1}
K_f	1.21x 10^9	1.21x 10^9	Pa
η_{fl}	9.09x 10^{-5}	9.09x 10^{-5}	Pa s
$k^{m,ref}$	1.00x 10^{-19}	1.00x 10^{-19}	m^2

Table 3.2: Summary of Material values - Westerly Granite (WG), Berea Sandstone (BS)

3.7.1 Analytical Model results

We can illustrate the coupling terms in our thermo-poro-elastic solution using time-invariant boundary perturbations in temperature and pressure (Type 1 boundary). First, we consider a scenario with an initial zero background temperature and pressure and a temperature perturbation of 400° K applied at the cavity interface (at R= R_0 = 2 km, $T_1 = 400°K, P_1 = 0$ MPa). This example is physically representative of a magma body (e.g. sill or a dyke) close to its solidus (∼900° K) being emplaced very rapidly in the crust with a temperature of 500 ° K. Additionally, we here assume that there is no feedback between the magma body and the surrounding fluids such that the magma pressure remains lithostatic. The solutions from Eqns. 3.30 are shown in Figure 2 (Panel A) for for Westerly Granite with distance from the spherical cavity along the x-axis and time along the y-axis. The results show that since we do not include advective heat transport, the temperature solution is primarily conductive.

However, these results also illustrate the strong coupling between temperature and pore fluid pressure wherein the higher thermal expansion coefficient of the fluid leads to pressurization. This pressure diffuses out radially, with an expected strong influence of permeability. We find that for characteristic permeabilities greater than 10^{-18} m^2, the thermally induced pore pressure diffuses relatively rapidly and does not lead to significant increases in pres-

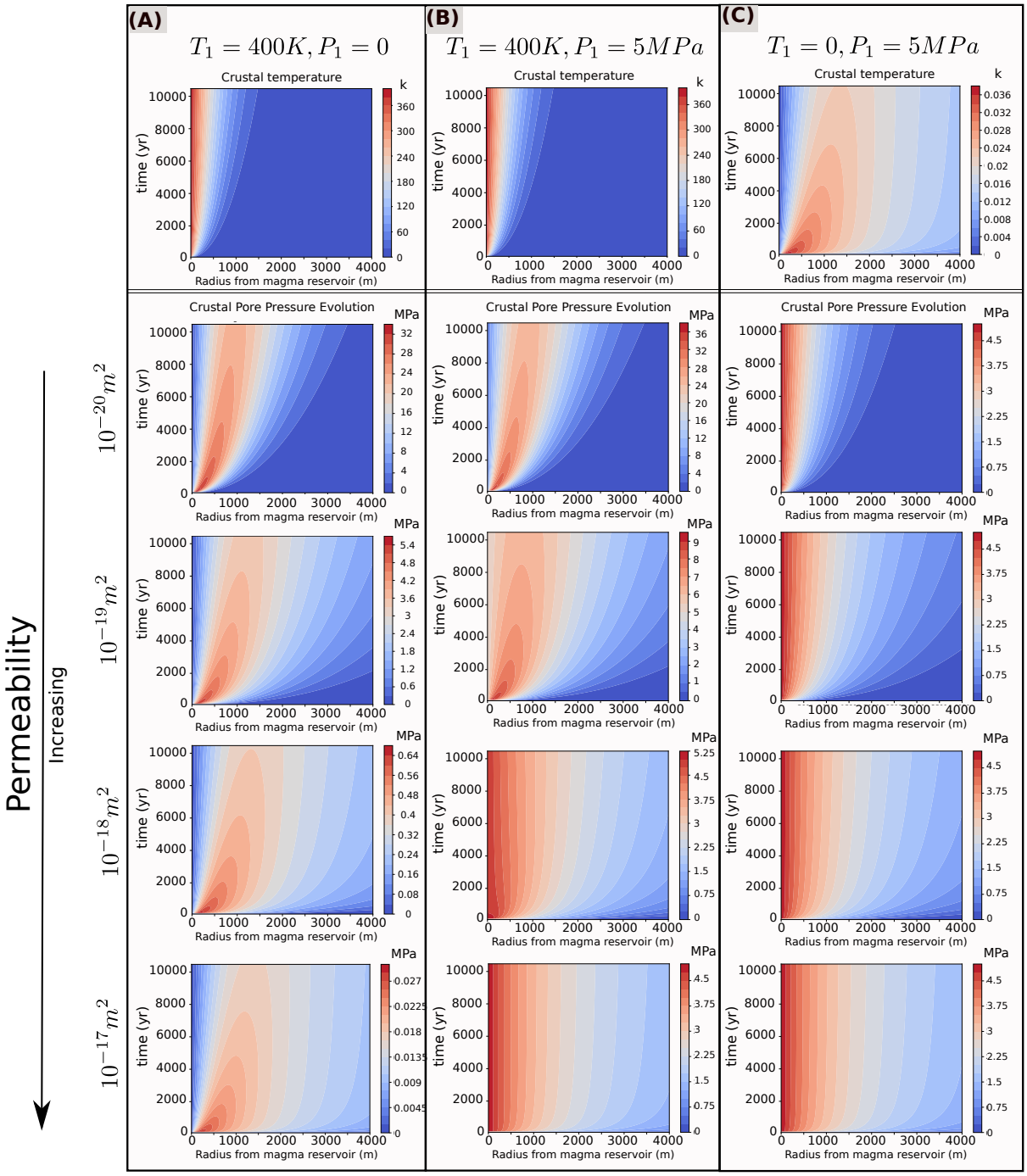
(A)
$T_1 = 400K, P_1 = 0$
(B)
$T_1 = 400K, P_1 = 5MPa$
(C)
$T_1 = 0, P_1 = 5MPa$
Crustal temperature
Crustal Pore Pressure Evolution
time (yr)
Radius from magma reservoir (m)
k
MPa
Permeability
Increasing
$10^{-20}m^2$
$10^{-19}m^2$
$10^{-18}m^2$
$10^{-17}m^2$

Figure 3.2

Figure 3.2 *(previous page)*: Results for the coupled thermo-poro-elastic solution (Eqns. 3.30) with Westerly Granite physical properties for three different set of boundary conditions (temperature boundary condition, pressure boundary condition, and mixed boundary condition). Each sub-figure shows the pressure/temperature field with increasing distance from the magma reservoir along the X-axis and time along the Y-axis. For each boundary condition, we show a set of solutions with varying crustal permeabilities from 10^{-17} to 10^{-20} m^2. The results clearly illustrate the faster diffusion of pore pressures at higher permeabilities.

sure compared to the rock tensile strength. We can further illustrate this transition using a mixed boundary : temperature perturbation of 400° K and pressure perturbation of 5 MPa ($T_1 = 400°K, P_1 = 5$ MPa; Figure 2[Panel B]). As discussed earlier, a critical overpressure of ~ 20 MPa is required to lead to tensile failure and diking. Since injection of new magma from depth into a magmatic body can in certain cases lead to increase in pressure above this threshold (e.g., see results later; Degruyter and Huber (2014)), it is reasonable to consider a slightly smaller pressure increase for a magmatic body. Here, the transition from thermal pore pressure dominated regime to boundary pressurization regime occurs at a permeability of about 10^{-18} m^2. Finally, when the thermal effect is, i.e. the boundary condition is purely a pressure perturbation ($T_1 = 0, P_1 = 5$MPa; Figure 2[Panel C]), the pore fluid pressure diffuses out into the crust with a rate that depends on the crustal permeability. Additionally, the temperature field with this boundary condition is effectively isothermal, illustrating that the temperature evolution is mostly uncoupled from pressure evolution (for a non-advective case).

We repeat these calculations for Berea Sandstone material parameters in Figure 3. The Sandstone has higher porosity (10-15 % vs 1 % for the Granite) as well as lower bulk and shear modulus (see Table 2 for the parameters). As a consequence, the thermoelastic effective stress coefficient ($\alpha_{Th,e}$) in the pore pressure diffusion equation (Eqn 3.6) is much larger for Berea Sandstone vis-à -vis Westerly Granite. Thus, the thermally induced pore pressure increase is much larger compared to that for Westerly Granite (see Figure 3, Panel A vs Figure 2, Panel A). Additionally, the pore pressure diffusion is faster in Westerly Granite than in Berea Sandstone (see Figure 3 vs Figure 2). In the pressure evolution equation (Eqn 3.6), if we ignore the temperature and stress changes as well as fluid /source terms, we recover a simple diffusion equation (substituting Eqn 3.4 for q^d:

$$\frac{1}{M_B}\frac{\partial \hat{P}_f}{\partial t} = \frac{k^m}{\eta_f}\nabla^2(\hat{P}_f)$$

where the pressure diffusivity (in analogy with thermal diffusion equation) is $\kappa_{pd} = \frac{k^m M_B}{\eta_f}$. The value of the Biot modulus (M_B) for granite is much higher than that for the sandstone (Table 2), and hence pressure diffuses faster. Physically, the Biot modulus is the inverse of the storage coefficient which represents how much fluid volume is gained by a poroelastic

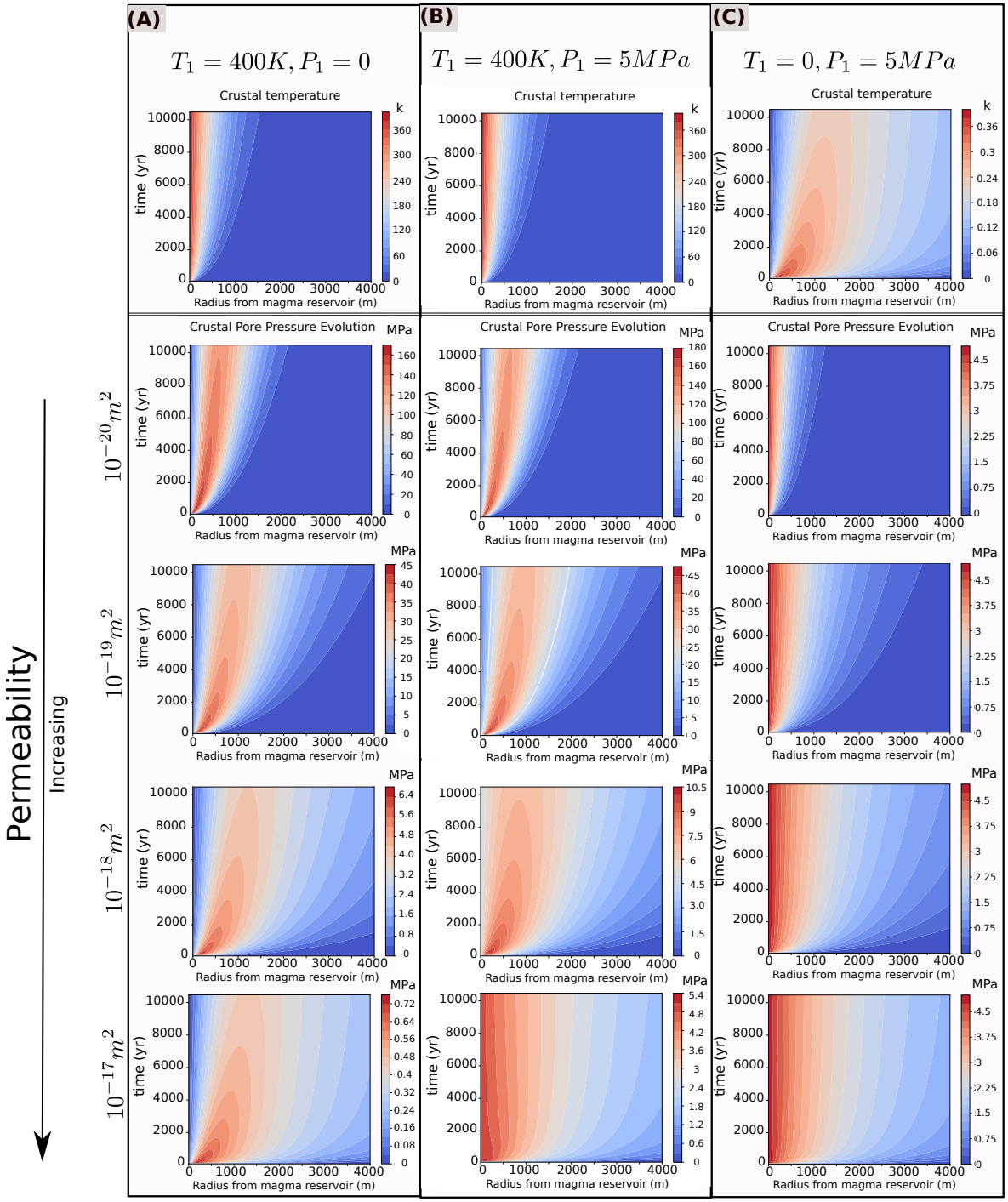
(A)
$T_1 = 400K, P_1 = 0$
(B)
$T_1 = 400K, P_1 = 5MPa$
(C)
$T_1 = 0, P_1 = 5MPa$
Crustal temperature
Crustal Pore Pressure Evolution
time (yr)
Radius from magma reservoir (m)
k
MPa
Permeability
Increasing
$10^{-20}m^2$
$10^{-19}m^2$
$10^{-18}m^2$
$10^{-17}m^2$

Figure 3.3

Figure 3.3 *(previous page)*: Results for the coupled thermo-poro-elastic solution (Eqns. 3.30) with Berea Sandstone physical properties for three different set of boundary conditions (temperature boundary condition, pressure boundary condition, and mixed boundary condition). Each sub-figure shows the pressure/temperature field with increasing distance from the magma reservoir along the X-axis and time along the Y-axis. For each boundary condition, we show a set of solutions with varying crustal permeabilities from 10^{-17} to 10^{-20} m^2. The results illustrate that changing the material properties has a significant effect on both the amplitude and the spatial distribution of pore pressure in the crust surrounding a magma reservoir.

frame (per unit frame volume) for a unit increase of pore pressure. The lower bulk and shear modulus of Sandstone enhances the storage coefficient and thus reduces M_B.

Finally, we also analyze the stress field - radial (σ_{rr}) and circumferential ($\sigma_{\theta\theta}$) for the temperature boundary condition (Figure 2, Panel A). The Cauchy stress tensor ($\sigma_{ij}(x, y, z)$) is the sum of forces applied to the solid and the fluid phases, divided by the total surface area of the cross section, without differentiating the contribution by the individual phases. Consequently, the stress (σ''_{ij}) experienced by the solid matrix (effective stress) is the difference between the total stress and the pore pressure :

$$\sigma''_{ij} = \sigma_{ij} + \alpha_B \hat{P}_f \delta_{ij}$$

In Figure 4, we show these effective stress fields (positive for tension and negative for compression) for three different permeabilities with Westerly Granite material properties. As a consequence of the higher thermal compression of the medium near the cavity wall where the temperature gradients are largest, the effective radial and circumferential stress are negative (compression) - Figure 4 (Panels B and C). However, the increase in pore pressure (Figure 4, Panel A) can partially counteract this effect leading to tensile (positive) effective stress in a radial band which moves outward over time with pressure diffusion. Since the pressure diffuses faster for higher permeability, the peak pore fluid pressures are reduced at higher permeabilities (10^{-20} m^2 vs 10^{-18} m^2). Consequently, the peak tensile stresses that the solid matrix experiences decrease with increasing permeability. In Figure 5, we repeat this calculation with the same boundary condition but using material parameters for Berea Sandstone. We also find that the peak effective tensile stresses are larger for Berea Sandstone due to the higher values of thermally induced fluid pore pressure. In addition, the tensile stresses persist for a longer duration due to slower diffusion in comparison with Westerly Granite.

We note that our maximum calculated effective pressures in Figures 4 and 5 can be comparable/larger than the tensile strength of rocks ($\sim$ 20 MPa), see discussion in the previous section). We can use the Mohr-Coulomb and Griffith's failure criteria to assess

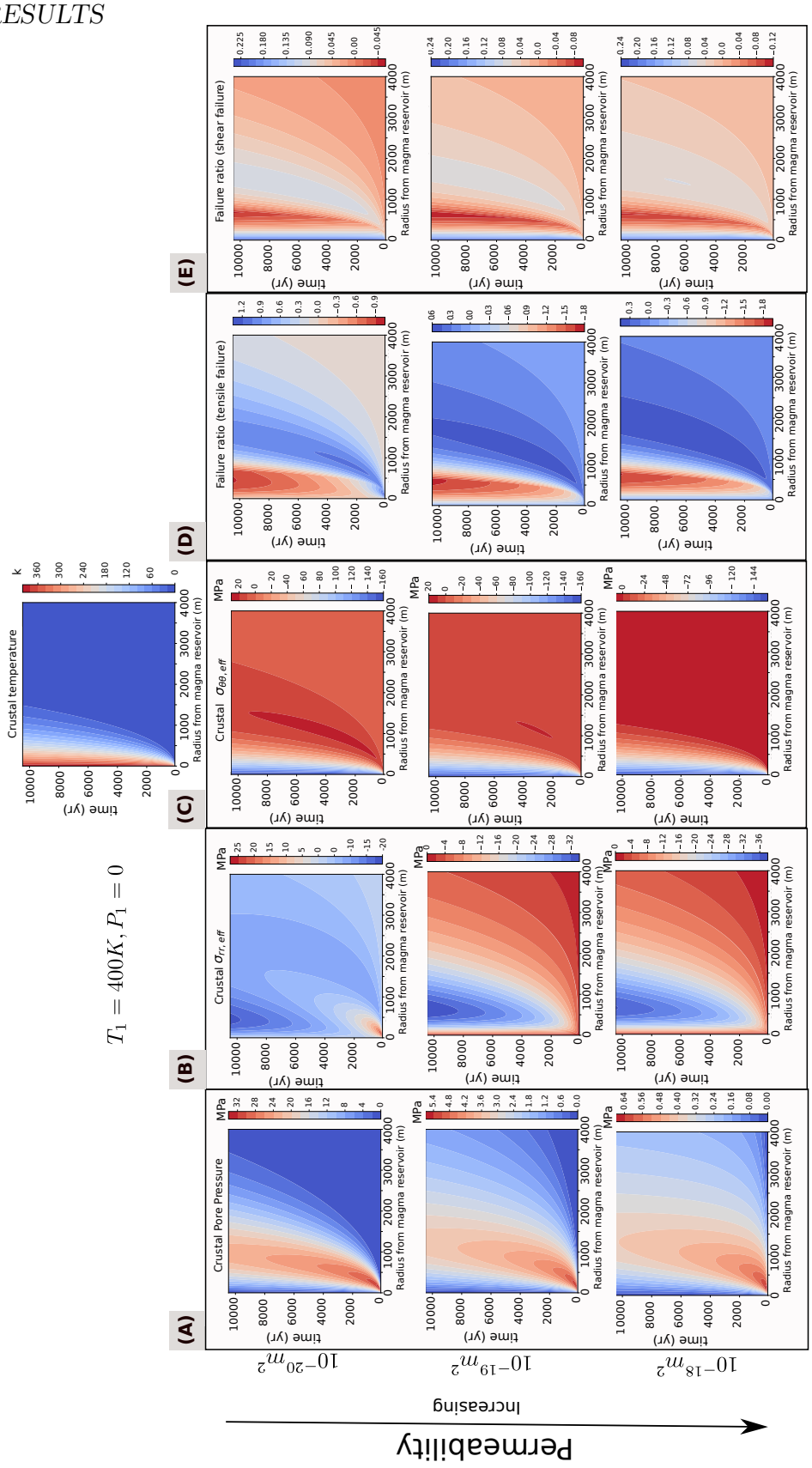
Permeability
Increasing
$10^{-18}m^2$
$10^{-19}m^2$
$10^{-20}m^2$
$T_1 = 400K, P_1 = 0$
(A)
(B)
(C)
(D)
(E)
Crustal Pore Pressure
Crustal $\sigma_{rr,eff}$
Crustal $\sigma_{\theta\theta,eff}$
Failure ratio (tensile failure)
Failure ratio (shear failure)
Crustal temperature
time (yr)
Radius from magma reservoir (m)
MPa
K

Figure 3.4

Figure 3.4 *(previous page)*: Results for the coupled thermo-poro-elastic solution (Eqns. 3.30) with Westerly Granite physical properties for temperature boundary condition and three permeabilities. Each sub-figure shows the pore pressure/radial (σ_{rr}); circumferential ($\sigma_{\theta\theta}$) effective stress field as well as failure criterion with increasing distance from the magma reservoir along the X-axis and time along the Y-axis. We denote tensile effective stress fields as positive and compressive stresses as negative.

whether the crustal material should fail, and if so, in what form - shear bands or tensile fractures. The Mohr-Coulomb criterion for shear failure is (Paterson & Wong, 2005) :

$$\tau_{st} - \sigma_m^{''} sin(\phi_{fr}) = C_{ch} cos(\phi_{fr}) \tag{3.47}$$

$$R_f^S = \frac{(\tau_{st} - \sigma_m^{''} sin(\phi_{fr}))}{C_{ch} cos(\phi_{fr})} \tag{3.48}$$

where ϕ_{fr} is the fraction angle ($\sim 30^\circ$) and C_{ch} is the cohesive strength of the rock. τ_{st} is the effective deviatoric stress and $\sigma_m^{''}$ is the mean effective stress. They are respectively defined as :

$$\tau_{st} = \sqrt{(\sigma_{rr}^{''} - \sigma_{\theta\theta}^{''})^2/4 + \sigma_{r\theta}^{''}} \tag{3.49}$$

$$\sigma_m^{''} = (\sigma_{rr}^{''} + \sigma_{\theta\theta}^{''})/2 \tag{3.50}$$

Finally, R_f^S is a ratio which quantifies how close a material is to shear failure with values greater than one indicative of failure.

The Griffith's failure criterion for tensile fracturing due to fluid over pressure is (Murrell, 1964; Rozhko et al., 2007) :

$$\tau_{st} - \sigma_m^{''} = \sigma_T \tag{3.51}$$

$$R_f^T = \frac{(\tau_{st} - \sigma_m^{''})}{\sigma_T} \tag{3.52}$$

where $\sigma_T = P_c$ is the tensile strength of the rock. We use $P_c = 20$MPa (see discussion in the previous section) and $C = 200$MPa which is representative of a fractured rock (Hoek, Carranza-Torres, & Corkum, 2002). Analogous to R_f^S, R_f^T is a ratio which quantifies how close a material is to tensile failure with values greater than one indicative of failure.

In Figure 4 and 5 respectively, we calculate these two failure criteria ratios (R_f^S and R_f^T) for each permeability using the corresponding effective stresses (Panels D and E). We find that at low permeabilities (10^{-20} m^2 for granite and 10^{-19} - 10^{-20} m^2 for sandstone, the tensile failure criterion is satisfied while the shear failure criterion is not. Furthermore, as expected based on the stress fields, the region with tensile failure radially expands outward

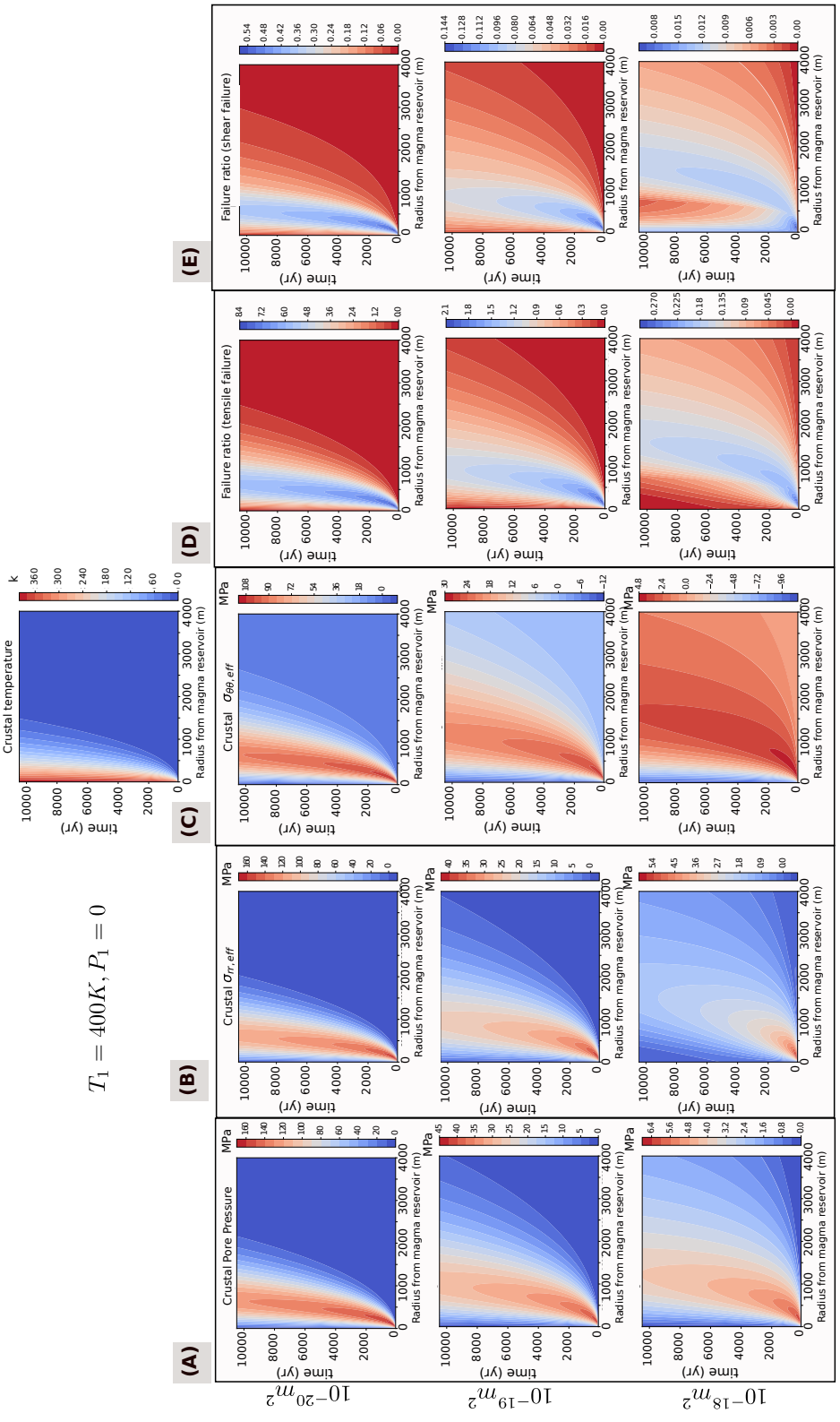
Permeability
increasing
$10^{-18}m^2$
$10^{-19}m^2$
$10^{-20}m^2$
$T_1 = 400K, P_1 = 0$
(A)
(B)
(C)
(D)
(E)
Crustal Pore Pressure
Crustal $\sigma_{rr,eff}$
Crustal $\sigma_{\theta\theta,eff}$
Failure ratio (tensile failure)
Failure ratio (shear failure)
Crustal temperature
time (yr)
Radius from magma reservoir (m)
MPa
k

Figure 3.5

Figure 3.5 *(previous page)*: Results for the coupled thermo-poro-elastic solution (Eqns. 3.30) with Berea Sandstone physical properties for temperature boundary condition and three permeabilities. Each sub-figure shows the pore pressure/radial (σ_{rr}); circumferential ($\sigma_{\theta\theta}$) effective stress field as well as failure criterion with increasing distance from the magma reservoir along the X-axis and time along the Y-axis. We denote tensile effective stress fields as positive and compressive stresses as negative.

with pore pressure diffusion. Hence, we expect that near the magma reservoir interface, tensile fracturing due to high pore pressurization is more likely than shear failures if the crust is porous and fluid saturated before the intrusion. In addition, we note that the tensile fractures formed in the surrounding crust will, in practice, lead to enhancement of permeability and permeabilities of order 10^{-18} m^2 are required to prevent large fluid overpressures (over lithostatic). The simple scenario illustrated in Figures 4 and 5 highlights how the thermo-poro-elastic couplings and time-varying changes in temperature and pressure may potentially help create and maintain non-zero transient permeability in the magmatic-hydrothermal systems. We acknowledge that a more realistic, time-varying boundary condition is required to properly test this hypothesis.

In conclusion, our analytical thermo-poro-elastic solutions illustrate the importance of the various couplings in determining the crustal fluid pore-pressure, stress fields, and the likelihood of tensile or shear failure. In addition, the crustal response for different materials can be different due to the different material poroelastic constants as illustrated by our two end members - Westerly Granite and Berea Sandstone.

3.7.2 Magma Chamber results

In order to illustrate the characteristic behavior of the coupled system, we use a model setup with a magma reservoir radius (R_0) of 1000 m, a mass inflow rate of 10 kg/s, 200 MPa lithostatic pressure, and Westerly granite material properties. The reference crustal temperature at the depth of the magma reservoir was set to 500° K, with the temperature increasing linearly with depth from the surface temperature of 300° K.

At first, we do not include any pore pressure or passive degassing volatile flux terms in the model, thus effectively reducing it to the original DH formalism. The magma over-pressure (with the buoyancy component not included), magma temperature, crystal fraction, and gas fraction for this scenario are plotted with orange lines in Figure 6. The main feature of note for the model output is that over time the magma pressure increases due to both magma recharge and volatile exsolution from the melt as the magma reservoir cools ("second boiling"). Once the pressure (with buoyancy included) reaches a critical threshold, $P_c = 20$ MPa, dikes are expected to initiate from the magma reservoir leading to an eruption in the model with an assumed constant outflow rate of 100 kg/s during the eruption. As

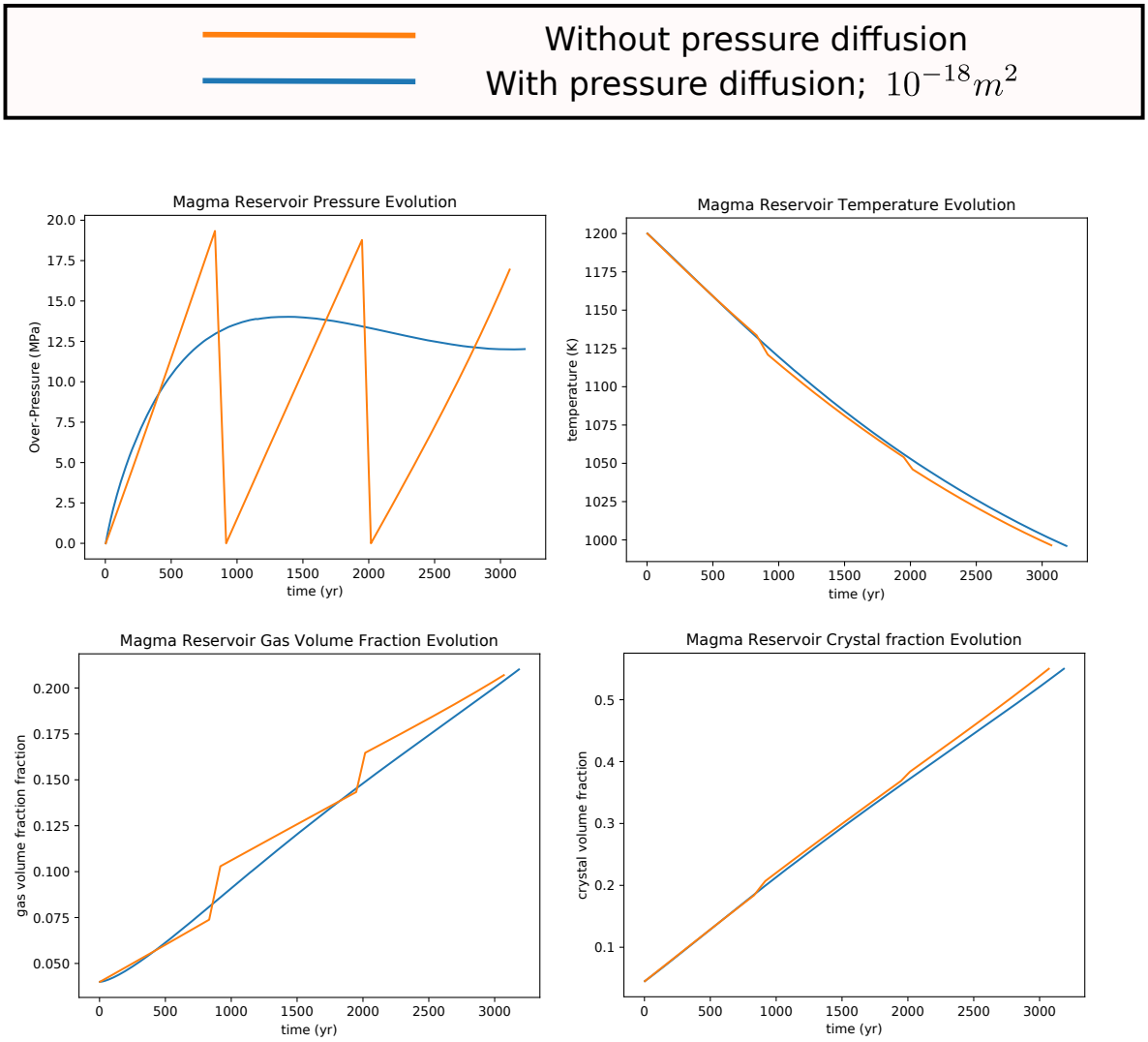

Figure 3.6: Model calculation for the coupled crustal magma reservoir model. Each panel respectively shows the results for evolution of magmatic over-pressure, magma temperature, crystal fraction, and gas fraction for two sets of calculations - a) without pore pressure diffusion in the surrounding crust (orange curves) and b) with coupled crustal poro-visco-thermo-elastic response (blue) with permeability of 10^{-18} m^2.

mass (melt and volatiles) is removed from the magma reservoir, the pressure in the magma chamber drops back to the original lithostatic pressure.

Next, we keep the model parameters the same as above, but allow pressure diffusion out (and into) the chamber due to interaction with the surrounding crust, along with the corresponding volatile enthalpy fluxes. The results of this model are shown with the blue colored lines in Figure 6 for a crustal permeability of 10^{-18} m^2. We find a drastic change in the model behavior, with the magma pressure never reaching the critical threshold required to initiate volcanic eruptions to the surface. This model solution is a direct consequence of the two-way interaction of the magma reservoir and the crustal fluids, wherein increasing temperatures and pressures in the magma reservoir lead to pressurization of the surrounding crust. This extra fluid pore pressure (above the lithostatic background) diffuses out into the crust and prevents a large buildup of pressure inside the magma reservoir. We show the pore pressure, effective radial stress, and temperature fields in the crust over time in Figure 8.

The pore pressure diffusion is to first order a function of crustal permeability (k^m) since the pressure diffusivity κ_{pd} is directly proportional to k^m. This result is illustrated clearly by model results (Figure 7) where we kept all the parameters the same as previously, but systematically vary the permeability from 10^{-20} to 10^{-17} m^2. The results show that with decreasing permeability, the influence of pore pressure diffusion on the magma chamber pressure decreases. *The critical permeability required to prevent eruptions is approximately* 10^{-18} m^2 *for these model parameters.* In Figure 8, the corresponding crustal pore pressure, effective radial stress, and temperature fields for each permeability solution are shown. These results show the clear effect of volcanic eruptions on the crustal pore pressure field wherein the rapid decreases in magma chamber pressure during eruptions lead to pressure diffusion into the chamber (through the flow of some crustal fluids). Thus, the inclusion of pore pressure can influence the duration of an eruption, even if the pressure diffusion is insufficient to prevent the buildup of magmatic pressure. We find that in our models, the total fluid flux out of the magma reservoir during its life history is generally small and the consequent enthalpy flux has a small impact on the temperature evolution. This result is partially a consequence of our choosing low enough crustal permeabilities to prevent significant advective transport and convection as required for the validity of our analytical solutions. We note that for very low permeability (Figure 8, Panels A and B), the effective radial stress in the crust is in tension near the magma reservoir interface. As a consequence, the tensile stresses should lead to fracturing and increased transient permeability (see the results of the previous section for a more detailed discussion of the relevant processes). Thus, if the crust does have very low permeabilities, to begin with, the permeability would initially increase immediately after the initial magma emplacement and enhance the effectiveness of pore pressure diffusion.

3.7.3 Scaling results

We performed model calculations for a range of initial magma reservoir sizes (100 - 2000 m), and mass inflow rates of 10^{-1} to 10^{2} kg/s (equivalent to $\sim 10^{-6}$ to 10^{-3} km^3/yr

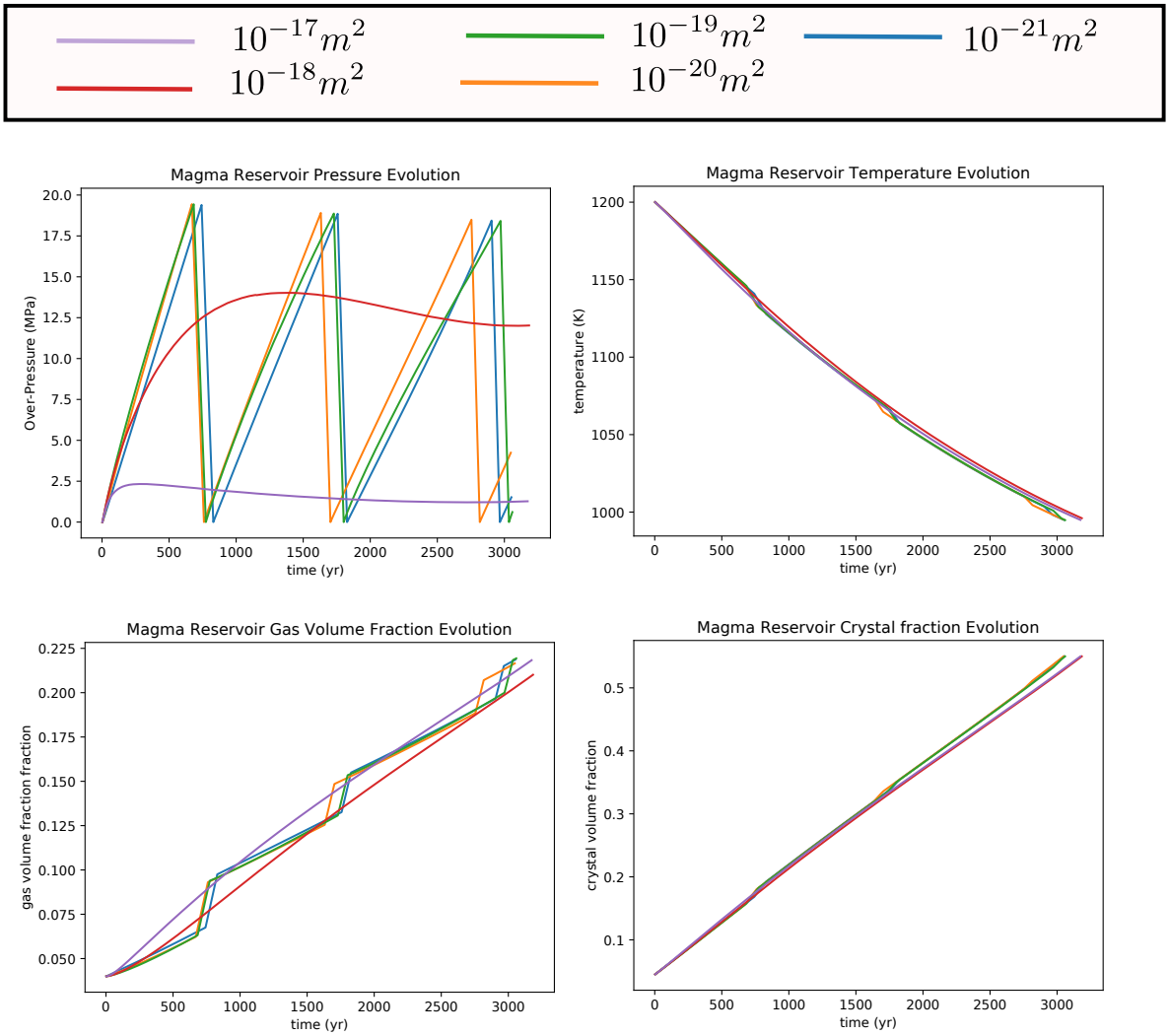

Figure 3.7: Model calculation for the coupled crustal magma reservoir model for five different sets of crustal permeabilities ranging from 10^{-17} to 10^{-21} m^2. Each panel respectively shows the results for evolution of magmatic over-pressure, magma temperature, crystal fraction, and gas fraction for the model with crustal permeability being the only different input variable.

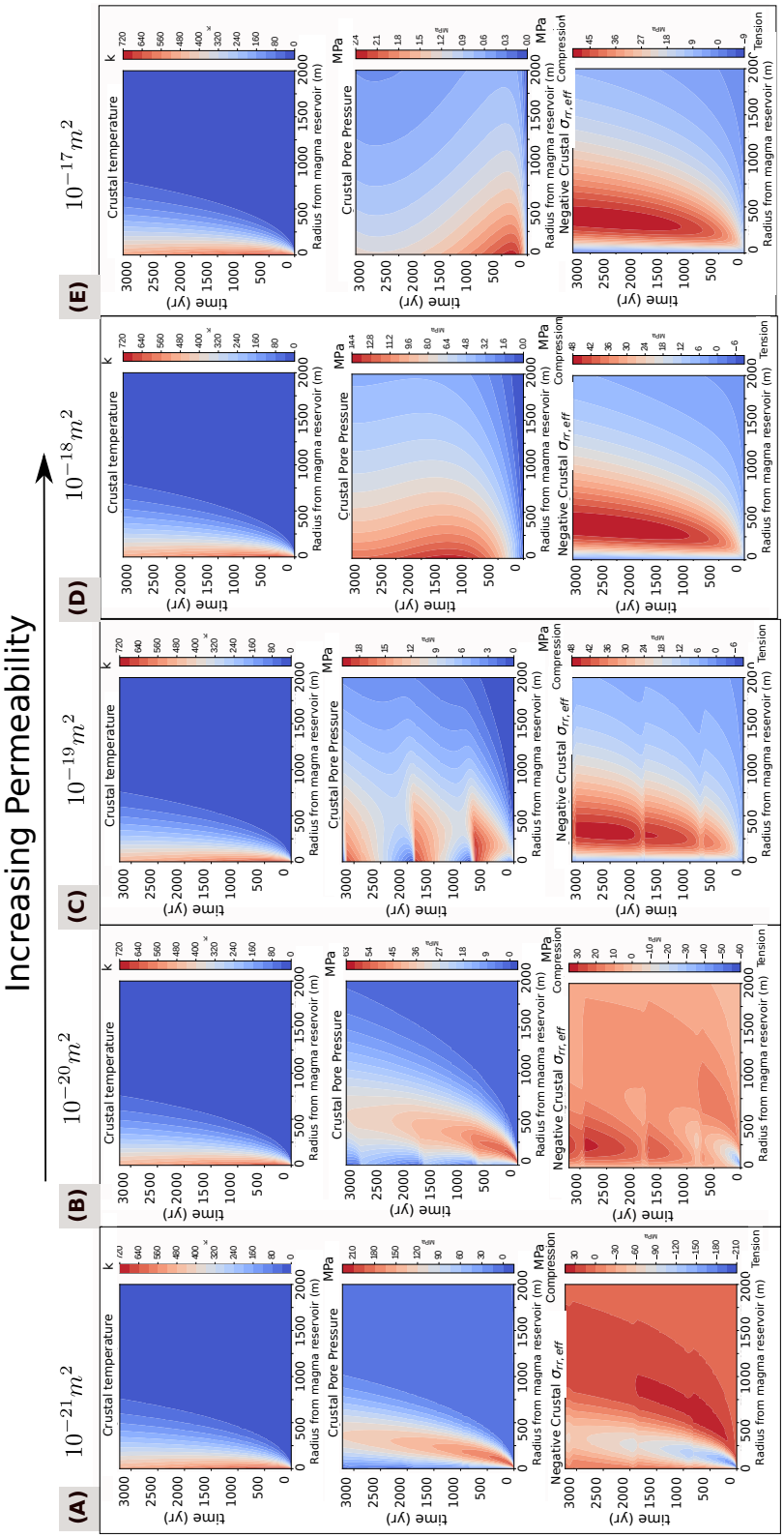
Increasing Permeability
(A)
$10^{-21}m^2$
(B)
$10^{-20}m^2$
(C)
$10^{-19}m^2$
(D)
$10^{-18}m^2$
(E)
$10^{-17}m^2$
Crustal temperature
Crustal Pore Pressure
Negative Crustal $\sigma_{rr,eff}$
time (yr)
Radius from magma reservoir (m)
k
MPa
Compression
Tension

Figure 3.8

Figure 3.8 *(previous page)*: Time-distance plots (akin to Figures 4-5) showing the model output for crustal pore pressure, effective radial stress, and temperature fields for every corresponding permeability solution in Figure 7 and Westerly Granite properties. The results clearly illustrate that with decreasing permeability, the corresponding crustal pore pressure diffusion decreases. However, the regions of the crustal effective stress field are increasingly put in tension due to the thermo-poro-elastic stresses. We denote tensile effective stress fields as negative and compressive stresses as positive in these plots.

estimated from Coleman, Gray, and Glazner (2004); Crisp (1984); S. M. White, Crisp, and Spera (2006). We also varied the crustal permeability between 10^{-21} to 10^{-17} m^2, as well as the crustal lithology (Berea Sandstone and Westerly Granite). In the aggregate, we found that the model behavior, with regards to whether a magma reservoir would lead to eruptions before freezing, is controlled by four primary timescales.

These timescales are the thermal cooling timescale (t_{cool}), elastic pressurization by magma recharge timescale (t_{inj}), viscous relaxation timescale (t_{viscous}), and pressure diffusion timescale ($t_{\text{press,diff}}$). These timescales are defined as :

$$t_{\text{cool}} = \frac{R_0^2}{\kappa_{th}} \tag{3.53}$$

$$t_{\text{inj}} = \frac{V_0 \rho_0}{\dot{M}_{in}} \tag{3.54}$$

$$t_{\text{viscous}} = \frac{\eta_{visc,0}}{P_c} \tag{3.55}$$

$$t_{\text{press,diff}} = \frac{L^2}{\kappa_{pd}} \tag{3.56}$$

where R_0, V_0, and ρ_0 are the initial magma chamber size, volume, and density respectively. $\eta_{visc,0}$ is the mean crustal viscosity, κ_{th} is the thermal diffusivity, and κ_{pd} is the pore pressure diffusivity. Finally, L is a characteristic length-scale for pressure diffusion and is physically equal to spatial scale over which the crustal permeability increases sufficiently to allow active hydrothermal circulation and hydrostatic fluid pressures. In our calculations, we set $L = R_0$ the radius of the magma reservoir. However, we would note that L may be smaller than R_0 in natural systems as evidenced by observation from drilling projects (Ikeda et al., 2008; Reinsch et al., 2017) of active hydrothermal flows and convective temperature profiles in close vicinity to the magma body. Our pressure diffusion timescale is analogous to the pressure diffusion timescale in Liao, Soule, and Jones (2018) wherein they consider melt transport between a molten magma reservoir and its surrounding poroelastic mush.

Degruyter and Huber (2014) found that their model results could be described by a regime plot of the first three time-scales. The inclusion of a two-way interaction between the crust and the magma chamber in our model necessitates the inclusion of an additional

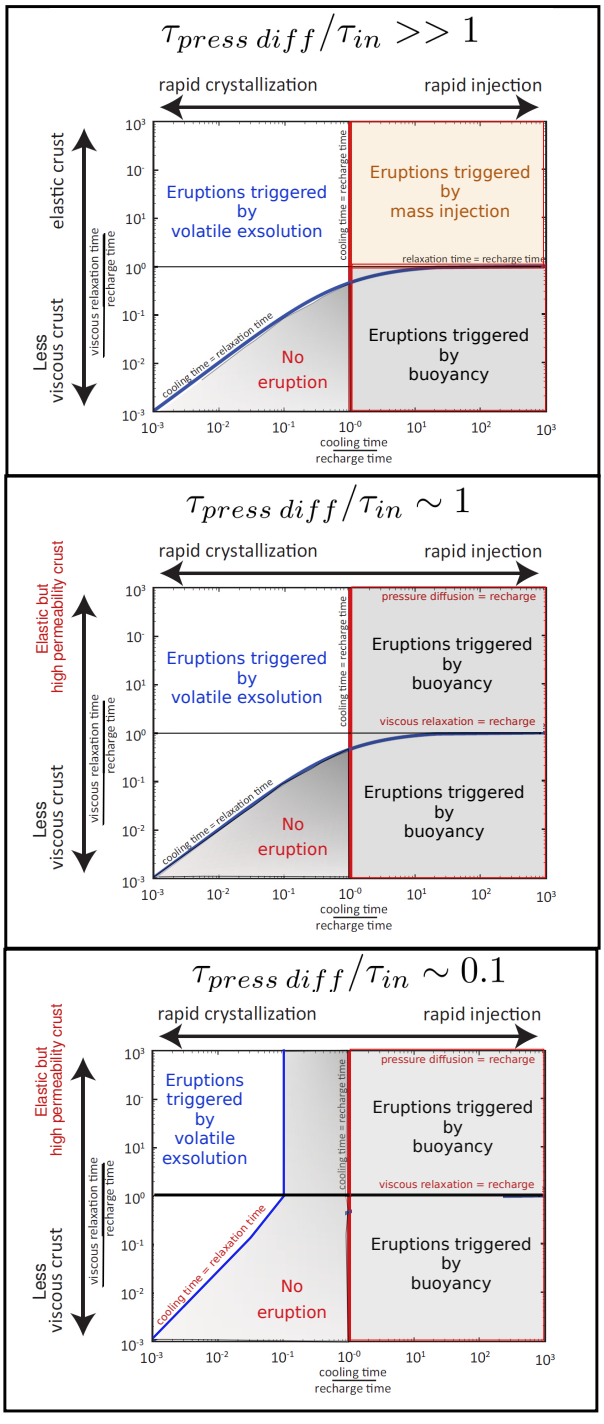
$\tau_{press\ diff}/\tau_{in} >> 1$
rapid crystallization
rapid injection
elastic crust
Less viscous crust
viscous relaxation time / recharge time
Eruptions triggered by volatile exsolution
Eruptions triggered by mass injection
cooling time = recharge time
relaxation time = recharge time
cooling time = relaxation time
No eruption
Eruptions triggered by buoyancy
cooling time / recharge time
$\tau_{press\ diff}/\tau_{in} \sim 1$
Elastic but high permeability crust
pressure diffusion = recharge
viscous relaxation = recharge
$\tau_{press\ diff}/\tau_{in} \sim 0.1$

Figure 3.9

Figure 3.9 *(previous page)*: Regime diagram showing three 2-dimensional slices through the full 3D regime space spanned by the non-dimensional timescales $X_1 = t_{\rm cool}/t_{\rm inj}$, $X_2 = t_{\rm viscous}/t_{\rm inj}$, and $X_3 = t_{\rm press,diff}/t_{\rm inj}$.

timescale ($t_{\rm press,diff}$). Overall, the model behaviour can be described in a 3-dimensional regime plot consisting with the three variables being : $X_1 = t_{\rm cool}/t_{\rm inj}$, $X_2 = t_{\rm viscous}/t_{\rm inj}$, and $X_3 = t_{\rm press,diff}/t_{\rm inj}$. In our modified DH model, there are four primary outcomes (see Degruyter and Huber (2014); Jellinek and DePaolo (2003); Karlstrom and Richards (2011) and references therein for a detailed discussion of these eruption regimes) :

- **No Eruption**: If the pressure inside the magma reservoir never reaches the critical threshold, no eruption occurs. In the context of our model, if X_1 is less than unity (i.e., cooling time is smaller than recharge), and X_1 is greater than X_2 or X_3 (i.e., cooling time is slower than either viscous relaxation or pressure diffusion time), we find that no eruptions occur. Physically, this occurs since there are relaxation mechanisms that can dissipate any over-pressure generated as a consequence of "second boiling" in the magma reservoir with cooling.

- **Eruption by Second Boiling**: An eruption can occur if the pressure inside the magma reservoir reaches the critical threshold due to exsolution of volatiles due to decreasing solubility in a cooling magma body. This eruption trigger mechanism is dominant when X_1 is less than unity, and X_1 is smaller than both X_2 and X_3 (i.e., cooling time is faster than both viscous relaxation and pressure diffusion times). Since neither viscous relaxation in the crust nor pressure diffusion is fast enough, a few eruptions can occur before the magma body becomes rheologically locked ($\sim$ 55 % crystallinity) if the initial melt contains enough dissolved volatiles to begin with.

- **Eruption by Recharge** : Another eruption mechanism is the elastic pressure increase due to magma recharge ($\dot{M}_{in}$). In order for this process to operate, we require X_1 to be greater than unity, and both X_2 and X_3 to be greater than unity as well. Analogous to eruption by second boiling, neither viscous relaxation nor pressure diffusion is fast enough to relax pressurization by recharge. Since the cooling time-scale is smaller than the recharge timescale, there is a continuous injection of enthalpy into the system by fresh magma. As a consequence, this mechanism can lead to long-lived volcanic centers.

- **Eruption by Buoyancy**: A final endogenous eruption mechanism is that of increased pressure in the magma reservoir due to the buoyancy of the volatile-melt (and maybe crystal) mixture with respect to the surrounding crust, with volatiles being the dominant contributors. The region of the parameter space where this process will operate

is when X_1 is greater than unity (slow cooling), and either X_2 or X_3 is less than unity. Since buoyancy pressure cannot be relaxed by viscous deformation of the crust (Black & Manga, 2017), $X_2 < 1$ enables continuous buildup of volatiles in the magma body without an eruption. Analogously, $X_3 < 1$ also prevents eruptions from causing rapid volatile loss and allows for a build-up of buoyancy. However, the pressure diffusion and associated volatile loss from the magma chamber can hamper eruptions by volatile buoyancy. An additional requirement for this process is that the ratio of volatile mass flux into the chamber ($\dot{M}_{in,vol}$) to that passively degassed is greater than one. The degassed volatile mass flux is :

$$\dot{M}_{out,vol} = \Big(\frac{k^m}{\eta_{fl}}\frac{\Delta P_{gr}}{L}\Big) A_{dg}\rho_{fl} \tag{3.57}$$

where ΔP_{gr} is the typical pore pressure change (or buoyancy pressure) over the characteristic length-scale L. A_{dg} is the area over which passive degassing is active and ρ_{fl} is the typical density of the degassed magmatic fluids. Thus, eruptions by volatile derived buoyancy require $X_4 = \dot{M}_{in,vol}/\dot{M}_{out,vol}$ to be greater than one, at least for substantial timescales.

In Figure 9, we show a few 2-dimensional slices through the full regime space with each of the four eruptive outcomes illustrated. An important conclusion of these regime plots is that the addition of pore pressure diffusion timescale leads to both a restriction of the parameter choices where eruptions can occur as well as an increasing role of volatile buoyancy for driving eruptions. However, the degassing of volatiles into the surrounding crust unsurprisingly reduces the efficiency of the buoyancy-driven eruptions and may lead to longer accumulation timescales than previously thought. This conclusion is consistent with the results by (Black & Manga, 2017) who found that gas escape efficiency is much higher when crustal permeability is non-zero (of order 10^{-18} m^2 and larger) and this adversely affects the ability of a magma chamber to erupt.

3.8 Discussion

3.8.1 Relevance of volatile degassing

Our results for our coupled magma reservoir-crustal model highlight the importance of pore pressure diffusion as an important mechanism in controlling whether a magma body will erupt or solidify in the crust to form a pluton. In order to assess how relevant this process will be for terrestrial magmatic systems, we can estimate the typical values of permeabilities required for $t_{\text{press,diff}} \sim t_{\text{inj}}$. Using a range of $\dot{M}_{in} = 10^{-3}$km^3/yr (S. M. White et al., 2006), a magma chamber size of 1 km, and a length scale L of 1 km, we get a required pore pressure diffusivity of $\sim$ 7x10^{-6} m^2/s. Using values for M_B and η_{fl} from Table 2, this translates to a permeability of $\sim 10^{-20}$ m^2 for Westerly Granite and $\sim 10^{-19}$ m^2 for Berea Sandstone.

These permeabilities are compatible with the range of the permeabilities estimated from various geophysical, observational, and theoretical estimates (see Section 3.3). A similar (and smaller) order of magnitude estimate for required permeabilities is obtained upon comparing cooling and viscous relaxation timescales with the pressure diffusion timescale. Hence, we argue that pore pressure diffusion is an important process that must be accounted for when considering the dynamics of a natural magmatic system. We would like to note that the short-term magma recharge rate can far exceed the long-term average recharge rates (Menand, Annen, & de Saint Blanquat, 2015) increasing the likelihood of the recharge-driven eruption triggering mechanism significantly.

3.8.2 Influence of crustal mush structure

In this study, the magma chamber has a uniform temperature, pressure, and other microphysical properties. However, a real magmatic reservoir will have a spatio- temperature profile as well as concomitant changes in crystal, melt, and gas fractions in the solidification fronts (B. D. Marsh, 2004; Montagna, Papale, & Longo, 2015; Papale, Montagna, & Longo, 2017). As a consequence, the rheological response of the magma reservoir will be more complicated than has been modeled here. Similarly, the effective permeability for a volatile phase in the crustal zone is going to be spatio-temporally variable. We contend that adding this structure will affect how and when an eruption initiates from a magma reservoir. An analysis of the full coupled spatially variable thermo-poro-viscoelastic response of a crustal-magmatic system with radially varying permeability (and other material constants) is far beyond the scope of this study.

3.8.3 Internal vs External control for passive degassing

In our model framework, the volatile loss rate from the magma reservoir is externally controlled by the time-averaged crustal permeability. However, another end-member is to consider the rate limiting step being the supply of volatiles to the magma reservoir - crust interface. As an example, Parmigiani et al. (2016) showed that bubbles might accumulate slowly in the crystal-poor magma caps since sufficient amount of volatiles must be exsolved in the deeper melt regions to be able to form percolation channels through the high crystallinity mush regions. In this picture, the relative permeability of the gaseous phase is important besides the mush permeability.

A few studies (e.g., Degruyter et al. (2019); Jackson, Blundy, and Sparks (2018); Parmigiani et al. (2017); R. Sparks et al. (2019); J. Solano, Jackson, Sparks, Blundy, and Annen (2012) and references therein) have modeled the evolving permeability structure within a magmatic system and considered the implications for volatile loss. As a specific example, we can consider the Parmigiani et al. (2017) study. In this study, the authors used Lattice Boltzmann (LB) calculations to calculate the net fluid permeability (multiplication of mush permeability and volatile phase relative permeability) of a magmatic mush with less than 70 % crystallinity. They found that the net permeability at $>$ 70 % crystallinity mush is

expected to substantially decrease since bubbles may get trapped between individual crystals preventing free flow (Parmigiani et al., 2017). Using these LB permeability results, Parmigiani et al. (2017) and Degruyter et al. (2019) included a volatile degassing term in a modified DH box model with collective bubble rise for <40 % crystalline fraction and channelized flow between 40 % and 70 % crystal fraction. In this higher crystallinity range (40-70 %), they obtained a net permeability of order 10^{-9} to 10^{-13} m^2. In contrast, when crystal fraction is < 40 %, the permeability is a bit lower since the collective bubble rise is slow and convection within the magma reservoir may hinder volatiles flow. These studies found that in most cases, a substantial amount (up to $\sim$ 50%) of volatiles are outgassed passively (Degruyter et al., 2019) with the rate and composition of the magmatic volatile potentially a strong function of the internal dynamics. Additionally, a common outcome of these model runs is an under/lithostatic pressure in the magma reservoir instead of the typical overpressure required to initiate diking (Degruyter et al., 2019; Parmigiani et al., 2017).

We posit that some of these model results may be influenced by assuming that the background crust remains at a lithostatic pressure distribution irrespective of the magnitude passive degassing. As we discussed based on field and geochemical observations of magmatic systems (see Section 3.3), we expect the crustal permeability in the zone surrounding the magma reservoir to be non-zero. However, it may potentially be many magnitudes lower than the net permeability for magmatic volatiles in the substantial parts of the mush. Consequently, the diffusion of pressure through the mush region inside the magma reservoir can be many order of magnitude faster than crustal pore pressure diffusion and the long term evolution of interest here. Thus, we think that the model in our study is complementary to magma chamber models considering the internal processes only. In addition, we anticipate that the first order result regarding the relevance of pore pressure diffusion into the crust is a robust conclusion. We also want to note that in our model, the region of the magma reservoir that can erupt is the region where the crystallinity is less than/ or close to the critical locking crystal fraction of 55% (B. D. Marsh, 1989). Thus, in the context of our modeling, the regions of the magma chamber with much higher crystallinity may even be considered part of the "crustal" domain with low permeability and pressure diffusion.

We readily acknowledge that in order to model the thermo-chemical evolution of a magmatic body accurately, we eventually need to consider a coupling between both : a) the internal dynamics of the volatile loss within a magmatic system and the internal spatio-temporal permeability changes, and b) the thermo-poro-visco-elastic response of the surrounding crust (Edmonds & Woods, 2018; Edmonds, Cashman, Holness, & Jackson, 2019; Liao et al., 2018; Parmigiani et al., 2017). In addition, more work is required to ascertain how to properly parameterize the internal volatile flow dynamics which critically depend on the crystallinity (and maybe its spatial gradients) in a 0D box model where the parameters are averaged over the whole magma reservoir.

3.8.4 Implications for magmatic architecture

With increasing observations, our understanding of magmatic systems has transitioned from that of large, isolated magma chambers to a network of interconnected regions of melt and volatiles in the crust that undergo complex interactions leading up to eruptions (Cashman et al., 2017; Hildreth, 1981; B. D. Marsh, 2004). In such an interconnected system, the role of volatiles becomes increasingly important since they are the most mobile phase and can lead to substantial heat advection (Bachmann & Bergantz, 2006) affecting the mush rheology and composition. In addition, hydrothermal circulation can have a significant impact on the cooling rate of the magma body (Cathles, 1977; Gerdes, Baumgartner, & Person, 1998; Hayba & Ingebritsen, 1997) and is likely to influence the petrological evolution and lifetime of magma reservoirs. Within this context, our results in this study have two important implications: First the introduction of an additional timescale - pore pressure diffusion time - allows for a physically-motivated assessment of how volatile loss from a magma pocket affects its eruptibility. Although, we have mostly discussed volatile loss as a negative influence on the likelihood of eruptions, continuous volatile loss from deeper systems can in turn flux volatiles into the magma reservoirs at shallower depths and enhance their likelihood of eruption, either by providing a buoyancy source or by changes in mineral assemblages and volatile solubility in melts (Giuffrida, Viccaro, & Ottolini, 2018). Analogously, Girona et al. (2015) suggested that volatile loss by passive degassing can trigger an eruption by promoting melt flow towards shallower depths by maintaining a differential pressure.

Secondly, the thermo-poro-elastic framework discussed in this study is useful for modeling not only the crustal deformation field but also the other two (multi) phase systems such as melt-mush systems. The various couplings between temperature, pressure, and stress field can be particularly crucial in a mush system with separate magma batches. As a concrete example, we can consider the boundary condition from Figure 2, Panel A where we imposed a change in temperature at the cavity edge. We found that this leads to large thermal pore pressure which slowly diffuses away. If there were additional magma bodies in the vicinity of the first magma reservoir, they would be perturbed by the diffusing pressure (and stress) wave and might be rapidly destabilized if they are close to critical states for eruption (i.e., have internal pressures close to P_c). Tarasewicz, Brandsdóttir, White, Hensch, and Thorbjarnardóttir (2012) observed a downward propagation of seismicity during the 2010 Eyjafjallajokull eruptions in Iceland and described it in a conceptual model with downward propagation of a pressure wave releasing melts from deeper crustal sills (see also R. S. White, Edmonds, Maclennan, Greenfield, and Agustsdottir (2019) and references therein).

Additionally, the thermo-poro-elastic process exerts a strong control on the stress state of the crustal (or mush zones) surrounding magma bodies. As we showed in Figures 4 and 5, these couplings can lead to localized regions of tensile stresses. The resulting stress field also affects the location of dike formation, plastic failure, and the flow directions of the degassed magmatic volatiles. We expect that using an ellipsoidal geometry for a magma body, as is more representative of natural systems, may also have a significant effect on this spatial field with potentially interesting coupling effects.

3.9 Conclusions

We have shown that there exists an important two-way coupling between the magmatic and overlying hydrothermal systems. The time-averaged permeability permeability of the crust in volcanic systems, as evidenced by extensive passive degassing, is likely to be non-zero.

We develop a fully coupled poro-thermo-elastic framework and derive an analytical solution for a spherical geometry. Using the analytical results, we find that the crustal fluid pore pressure is strongly coupled to the temperature and the stress field inside the magma reservoir (and likely vice-versa). We combined our analytical solution with a magma chamber box model, (modified from Degruyter and Huber (2014)) to assess how volatile loss affects magma eruptibility. We found that there is an additional controlling time-scale for the magmatic system - the magmatic volatile pore-pressure diffusion timescale (analogous to a similar timescale for melt percolation in Liao et al. (2018)). Pore pressure diffusion effectively acts as another pressure relaxation, akin to viscous relaxation of stresses. Furthermore, we find that under some circumstance, even relatively low permeabilities of order $10^{-18} - 10^{-19}$ m^2 may be sufficient for pore pressure diffusion to play an important role in modulating the frequency of volcanic eruptions.

Chapter 4

Magmatic architecture of continental flood basalts - a Deccan Traps perspective

4.1 Introduction

Continental flood basalt provinces (CFBs) are cataclysmic magmatic events, whose brief "main-phases" (durations $\sim$ 1 Ma; V. E. Courtillot & Renne, 2003; Bryan et al., 2010; V. Courtillot & Fluteau, 2014; R. E. Ernst & Youbi, 2017; H. Svensen et al., 2018) are associated with eruption of millions of km^3 of dominantly pāhoehoe basaltic lava flows over vast areas (e.g., Self, Keszthelyi, & Thordarson, 1998; J. J. Mahoney & Coffin, 1997; Bryan & Ferrari, 2013; R. E. Ernst, 2014, and references therein). CFBs are commonly associated with a large degree of mantle melting due to the arrival of a deep mantle plume head at the base of the lithosphere (e.g., M. A. Richards, Duncan, & Courtillot, 1989; Campbell & Griffiths, 1990; Farnetani & Richards, 1994; R. E. Ernst, 2014; R. E. Ernst, Liikane, Jowitt, Buchan, & Blanchard, 2019). Typically, full CFB sequences have an overall duration of about 5-15 Ma (V. E. Courtillot & Renne, 2003; V. Courtillot & Fluteau, 2014; H. Svensen et al., 2018), with the much briefer main-phase eruptions accounting for the majority of the erupted volume (e.g., $>$ 60% for the Deccan Traps, M. A. Richards et al. (2015), $\approx$ 87 % for the Columbia River Basalt, Kasbohm and Schoene (2018)). CFBs are also important events for solid earth-climate interaction, since they are frequently temporally correlated with significant environmental perturbations on a global scale, including major mass extinctions and rapid climate change (e.g., Wignall, 2001; M. T. Jones, Jerram, Svensen, & Grove, 2016; R. E. Ernst & Youbi, 2017; Clapham & Renne, 2019).

The main phase of each CFB is composed of hundreds of individual eruptive episodes, each representing almost continuous eruptions from a single or set of connected vents (Self, Schmidt, & Mather, 2014). In the field, each eruptive episode comprises a flow-field built up of one or several lava flows (See Thordarson & Self, 1998; Self et al., 1998; Jay, Mac Niocaill,

Widdowson, Self, & Turner, 2009, for more discussion of the terminology). Analysis of typical CFB flow fields, especially for the well-studied Columbia River Basalt province, suggest that they were emplaced over at least a decade, and likely over multiple centuries (Vye-Brown, Self, & Barry, 2013). Individual flow fields in CFBs have lava volumes ranging from 10^3- 10^4 km^3 (Self, Jay, Widdowson, & Keszthelyi, 2008; Bryan et al., 2010; Self et al., 2014).

By comparison with present-day basaltic volcanism (e.g., Kilauea, Laki, Piton de la Fournaise), individual CFB eruptive episodes represent a separate class of basaltic volcanism in terms of both volume (1000s of km^3 vs. 19.6 km^3 for Eldgjá 939 eruption, the largest known lava eruption in human history) and areal extent (10^5 km^2 vs. 780 km^2 for Eldgjá 939 eruption) (Thordarson, Miller, Larsen, Self, & Sigurdsson, 2001; Oppenheimer et al., 2018). Hence, the term "flood" basalt. *These huge erupted volumes, combined with relatively homogeneous magma compositions during eruptive episodes, pose significant challenges to understanding magma crustal transport, underscoring a fundamental question: What is the crustal plumbing system of CFBs that permits these large, repeated individual eruptive events? This magmatic architecture is related to a related key question: why do flood basalts erupt persistently in such large eruptive episodes?*

In this study, we explore the hypothesis that the unique character of "flood" basalt eruptions is a consequence of the crustal magmatic architecture, which acts as the transfer function between the quasi-continuous, extraordinarily large magma flux distributed over a broad region at the base of the lithosphere, but which also controls spatially and temporally localized individual eruptive episodes. Melt transport through the mantle lithosphere may act as an additional control on this behavior. However, once the melt pathways (dikes or two-phase channelization instabilities) are established, the timescale for magma transport through this system is expected to be relatively fast, continuous, and long-lived (Lister & Kerr, 1991; Rubin, 1995; Fowler, 2011).

The CFB magmatic system must consist of an interconnected network of sills or magma reservoirs (layered mafic intrusions) throughout the crust, Moho depth (magmatic underplating), and within the mantle lithosphere (R. E. Ernst et al., 2019, and references therein). This magmatic plumbing network transport millions of km^3 of magma from the underlying mantle plume sources and distributes it as intrusions, and onto the Earth's surface as flood basalts (e.g., R. E. Ernst, 2014). However, there is significant uncertainty on how large these components are and how they combine into a crustal magma system geometry that enables efficient transfer of large magma volumes from a mantle plume source to the surface (Jerram & Widdowson, 2005; R. E. Ernst, 2014; Cruden & Weinberg, 2018; Coetzee & Kisters, 2018; Magee et al., 2018; Magee, Ernst, Muirhead, Phillips, & Jackson, 2019). The only quantitative models for CFB magmatic architecture (Karlstrom & Richards, 2011; Black & Manga, 2017, see more description in Section 4.2.2) assume that the large eruptive episodes are fed from correspondingly large magma reservoirs ($> 10^4$-10^6 km^3) within the crust and/or at Moho depth through dikes. As we show in later sections of this paper, this assumption is not well-founded in terms of available constraints.

In order to test possible models, we must rely upon observations of erupted CFBs since

there is no modern-day active CFB province where the magmatic architecture can be inferred from direct geophysical methods. However, one of the primary difficulties with this approach is that we seldom have exposure of both the sub-crustal magmatic system and the overlying lava flow system in the same setting. For example, layered mafic intrusions (e.g., the Bushveld complex) and giant radiating dike swarms (e.g., McKenzie dike swarm) are interpreted to represent the crustal magma system and the feeders for massive overlying volcanic provinces (R. Ernst, Srivastava, Bleeker, & Hamilton, 2010; Buchan & Ernst, 2019; R. E. Ernst et al., 2019). However, in most of these cases, there are either no remaining lava flows or geochronologic constraints on the eruptive fluxes or volumes of lava flows (e.g., Bushveld complex Lenhardt & Eriksson, 2012). Additionally, there is the additional complexity that we are observing the final integrated system after solidification, and it is difficult to infer the temporal history vis-a-vis surface eruptions.

Conversely, for most Phanerozoic flood basalts with good temporal constraints on eruption rate for individual flow units, there are limited direct observations (exposures) of the trans-crustal magmatic system. In a few CFBs such as the Siberian Traps, North Atlantic Magmatic Province, and Karoo-Ferrar Traps (all with a thick sedimentary basin overlying the basement and underlying the lavas), multiple studies have analyzed the numerous interconnected stacked sill-dike complexes to provide constraints on very shallow (< 3 km) CFB plumbing systems (e.g., H. Svensen, Corfu, Polteau, Hammer, & Planke, 2012; S. M. Jones, Hoggett, Greene, & Jones, 2019; Hoggett, 2019; Magee, Ernst, et al., 2019, and references therein). Analogously, extensive geophysical and geochemical analysis of the dike swarms feeding surface lava flows has helped develop our understanding of the shallow CFB plumbing system (e.g., Vanderkluysen, Mahoney, Hooper, Sheth, & Ray, 2011; Rivalta, Taisne, Bunger, & Katz, 2015; Kavanagh, 2018; Magee, Ernst, et al., 2019; Buchan & Ernst, 2019). However, the magma transport relationship between dike swarms, sills, mid-crustal, and Moho depth magma reservoirs, and the mantle melt generation region remains unclear due to limited observational constraints (e.g., D. H. Elliot & Fleming, 2018, and references therein for the Karoo CFB). The primary direct observational support for the large magma reservoir model comes from the presence of thick ($\sim$ 5-15 km) high-velocity features above the Moho location in multiple CFBs (Emeishan, Deccan, Siberian, and Columbia River flood basalt provinces K. G. Cox, 1993; Ridley & Richards, 2010) as expected from the presence of solidified olivine- and clinopyroxene-rich cumulates in deep magma reservoirs (Farnetani, Richards, & Ghiorso, 1996). However, it is difficult to distinguish lower velocity crustal magma bodies from seismic data alone. Similar to layered mafic intrusions, geophysically observed mafic-ultramafic bodies represent the final time-integrated igneous evolution of mantle-generated melts with no information whether the features represent a single magma reservoir that was molten at the same time or was constructed incrementally (R. B. Larsen et al., 2018; Robb & Mungall, 2020).

An alternative method to test the validity of models for CFB magmatic architecture is to use the tempo of eruptive episodes. Specifically, this requires constraints on three key variables: the duration, volume, and frequency of individual eruptive episodes. *The pri-*

mary process that controls the eruptive tempo must be the magmatic architecture of CFBs. For example, the analysis by Black and Manga (2017) shows that in a magmatic architecture consisting of two large magma reservoirs (Moho and shallow-crustal levels), buoyancy overpressure is the primary mechanism for triggering CFB eruptions. This buoyancy overpressure is, in turn, controlled by the volatile content of the primary magmas. Due to the incompatible nature of magmatic volatiles (CO_2 and H_2O) during mantle melting, the initial low degree partial melts will be volatile-rich and are expected to erupt in frequent, low volume eruptive episodes. By contrast, subsequent higher degree of partial melts will accumulate in a large magma reservoir and become eruptible by volatile buoyancy over 10^5 - 10^6 years. Thus, the expected eruptive tempo during the main volumetric phase of CFBs is a few brief ($\sim 10^4$ yr) eruptive episodes with long (10^5 - 10^6 year) hiatuses in surface eruptions in-between them, again incompatible with observations, as discussed in detail below.

In this study, we use a compilation of recent datasets from the Deccan Traps CFB to estimate the eruptive tempo of eruptive episodes, in order to test the models for CFB magmatic architecture. The Deccan Traps (DT) are a continental flood basalt province (primarily tholeiitic) occupying an area of over 500,000 sq. km. in Western India, whose main-phase eruptions spanned ∼1 Ma beginning at about 66.3 Ma (e.g., Sprain et al., 2019; Schoene et al., 2019). The primary source of erupted magma was likely decompression melting in a large plume head (hundreds of km across) marking the arrival of the Reunion plume (M. A. Richards et al., 1989; Campbell & Griffiths, 1990). Due to extensive research over the past few decades, there are high-resolution constraints on eruption rate based on geochronology (Renne et al., 2015; Schoene et al., 2015; Sprain et al., 2019; Schoene et al., 2019), paleomagnetic directional groups (Chenet, Fluteau, Courtillot, Gérard, & Subbarao, 2008; Chenet et al., 2009), as well as Hg chemostratigraphy (Percival et al., 2018; I. M. Fendley et al., 2019) along with extensive geochemical characterization of the lava flows (e.g., K. G. Cox & Hawkesworth, 1984; Beane, Turner, Hooper, Subbarao, & Walsh, 1986; Lightfoot & Hawkesworth, 1988; J. J. Mahoney, 1988; Z. Peng, Mahoney, Hooper, Harris, & Beane, 1994; Z. Peng, Mahoney, Hooper, Macdougall, & Krishnamurthy, 1998; Sano, Fujii, Deshmukh, Fukuoka, & Aramaki, 2001). Additionally, the many geophysical datasets from gravity, seismic, and magnetotelluric observations provide constraints on the sub-surface magmatic structure feeding the lava flows (e.g., Patro, Raju, & Sarma, 2018). The Deccan Traps have a clear geophysical, as well as geochemical (and isotopic) signature associated with melt production from a mantle plume head, which also provides some constraints on the rate of melt input into the crustal column.

In aggregate, the available data sets constraining eruptive tempo for the Deccan Traps are unique among all CFBs. The closest CFB with comparable data sets is the Miocene Columbia River Basalts (CRB) with extensive geochemical and volcanological studies (P. Hooper, 1988a; P. Hooper & Hawkesworth, 1993; Barry et al., 2013; Wolff & Ramos, 2013). However, the total erupted volume of CRB is much smaller ($\geq$ 210,000 km^3; S. P. Reidel, Camp, Tolan, & Martin, 2013) is much smaller than for other CFBs. Additionally, the onset of the largest phase of Deccan volcanism, responsible for about 2/3 of the total erupted known DT

volume, is coincident, within Ar-Ar age precision, with the Cretaceous-Paleogene boundary (M. A. Richards et al., 2015; Sprain et al., 2019). This temporal coincidence makes the understanding the magmatic architecture of the Deccan Traps of special interest, given the recent hypothesis that this most voluminous phase of Deccan eruptions were accelerated ("triggered") by the strong ground motion from the Mw∼11 Chicxulub impact (M. A. Richards et al., 2015).

In Section 4.2, we review published conceptual and physical models for CFBs to illustrate the predictions from previous models. In Section 4.3, we provide a summary of the various observational constraints from the Deccan Traps (along with some additional data sets from other well studied flood basalt provinces such as the Columbia River Basalts and Siberian Traps). In Section 4.4, we describe a sequence of new models for fissure-style eruptions fed from either a single or multiple coupled magma reservoirs, as well as thermal models to assess how the crustal properties will evolve over the lifetime of a CFB event. These models allow us to predict the erupted fluxes, total erupted volumes (or equivalently the duration of eruptions), and frequency of eruptions for different CFB magmatic architectures and reservoir sizes. In Section 4.5, we describe the results of these models, emphasizing their consistency with various observational constraints and inferences regarding the required CFB magmatic plumbing system. Finally, in Section 4.6, we discuss the implications of our model results in terms of a new model for magmatic architecture for CFBs, emphasizing the importance of small multiple connected magma reservoirs for feeding the large volume basaltic lava flows.

4.2 Proposed Models for CFB magmatic architecture

Upon reviewing the literature on CFBs it becomes apparent that there have been remarkably few quantitative models, much less well-accepted models, proposed to explain the uniquely large total erupted volumes (typically $> 10^6$ km^3), or the large volumes of individual eruptive episodes, compared to contemporary basaltic volcanism. To first order, it has been proposed that a CFBs are just a consequence of the larger mantle melt flux from a mantle plume head with this melt erupting to the surface through some process. Nevertheless, we feel that it is important here to review the basics of the models that have been put forward previously in order to provide a fuller context for understanding our focus on the question: How are the processes of melt generation and lithosphere-crustal melt transport different for CFBs?

Regarding melt generation, the conclusion based on a large number of studies analyzing extensive geochemical data sets for major CFBs, seismic imaging, plate reconstruction models, and geodynamic models is that CFB melts are derived from three potential sources: partial melting of hot mantle plume heads (e.g., M. A. Richards et al., 1989; J. J. Mahoney, 1988; R. White & McKenzie, 1995; Lassiter & DePaolo, 1997; S. A. Gibson, 2002; Sobolev et al., 2011; G. Sen & Chandrasekharam, 2011; E. S. Jennings, Gibson, & Maclennan, 2019, and references therein), melting of the overlying metasomatized lithospheric mantle material due to the plume thermal anomaly (Arndt & Christensen, 1992; J. S. Marsh, 1987; Lightfoot &

Hawkesworth, 1988; Mckenzie & Bickle, 1988; Lightfoot et al., 1993; Turner & Hawkesworth, 1995; Natali, Beccaluva, Bianchini, Siena, et al., 2017; Black & Gibson, 2019; S. A. Gibson, Rooks, Day, Petrone, & Leat, 2020, and references therein), and other crustal-asthenospheric melting processes (e.g., Arndt, 1989; J. S. Marsh, 1989; Lassiter & DePaolo, 1997; Kempton & Harmon, 1992; H. C. Sheth, 2005). Of these, the plume head model is by far the most widely accepted. Nevertheless, irrespective of the specific source, the large volume of buoyant partial melts must migrate through the lithosphere via a combination of dikes and/or two-phase channelization instabilities to feed the crustal CFB magmatic system (Rabinowicz & Ceuleneer, 2005; Schiemenz, Liang, & Parmentier, 2011; J. M. S. Solano, Jackson, Sparks, Blundy, & Annen, 2012; T. Keller et al., 2013; Madrigal et al., 2015; Yarushina, Podladchikov, & Connolly, 2015b; Schmeling, Marquart, & Grebe, 2018; Schmeling, Marquart, Weinberg, & Wallner, 2019).

Rising CFB melts encounter a rheological contrast at or above the Moho since, depending on the geotherm and the fluid saturation state, the lower crust is either weaker than the upper crust, and lithospheric mantle or is stronger than the underlying lithospheric mantle (e.g., Bürgmann & Dresen, 2008; Fyfe, 1992; K. G. Cox, 1993). In both cases, the CFB magmas are expected to accumulate at Moho depth by magmatic underplating. Additionally, depending on the volatile content of the melt, the Moho may also be a density barrier leading to melt accumulation at these depths. Thus there are physical reasons to expect the formation of magmatic reservoirs at Moho depths beneath flood basalt provinces. These conclusions are further supported by various geophysical observations for crustal underplating in flood basalts (K. G. Cox, 1993; Bryan et al., 2010; Ridley & Richards, 2010; M. A. Richards et al., 2015; Farnetani et al., 1996, See Section 4.3.4 for more discussion). Finally, melt accumulated in these Moho-depth magma reservoirs, as well additional shallow crustal magma bodies, feed large, dike-fed fissure eruptions (e.g., R. Ernst, Grosfils, & Mège, 2001; R. E. Ernst et al., 2019; Magee et al., 2018, and references therein).

Besides this general framework, it remains unclear how the large individual magma reservoirs are if they also exist at shallower depths, and how the magmatic system supplies vast volumes of magma to large individual eruptions. So far, only a few models have been advanced for crustal magmatic processes specific to CFBs despite decades of geochemical studies on these systems. These models are primarily conceptual in nature, and largely motivated by petrological observations. There are only two published (to the best of the authors' knowledge) quantitative or physical models for crustal magmatic processes specific to CFBs which seems curious for one of the major occurrences of igneous rock on our Earth.

In this study, our focus is on the crustal magma transport system for CFBs. Hence we are largely agnostic about the actual source of primary melting as well as the processes of melt transport through the lithosphere.*Additionally, we use the term "magma reservoir" to refer to a well-mixed magma body which can be represented by a volume-averaged temperature, melt and volatile composition.* We choose this definition not to imply that individual magma bodies of any size must be necessarily compositionally, thermally, and rheologically well mixed (see discussion in B. D. Marsh (2013) about the relevant processes), but rather for

model consistency. Typically, most petrological models and magma physics models (including the new models in this study), assume that the magma bodies have a single representative temperature, pressure, and melt composition, such that a single very large magma chamber with significant spatial variations in thermal, chemical, and rheological properties (e.g., mush zones) will be represented as multiple magma reservoirs with a high degree of connectivity in between them.

In the following, we first describe the various conceptual CFB models followed by a description of the two quantitative models. We specifically highlight the magmatic architecture proposed by these models, especially the size of individual magma reservoirs, along with the observational motivation.

4.2.1 Conceptual Models

The first conceptual magmatic models for continental flood basalts was proposed by K. G. Cox (1980). He envisioned that the CFB magmatic system consists of a large (multi-km thick) crustal sill complex at/or close to Moho depth as the primary melt accumulation location, along with an elaborate network of dikes and sills for feeding surface lava flows. In K. G. Cox (1980) model, the parental picritic magma (MgO >15 wt.%) undergoes extensive fractional crystallization in the lower crustal sill complex with progressive fractionation of an ultramafic cumulate phase, and with a residual lower density evolved basaltic magma (MgO contents <8 wt.%, also see K. G. Cox & Hawkesworth, 1984). If the density of this magma were sufficiently lower than the overlying crustal column, the consequent buoyancy overpressure was hypothesized to lead to surface eruptions with some short-duration storage in an upper sill complex. A key feature of this model is that the relatively homogeneous composition of flood basalts is explained as a consequence of compositional buffering due to the crystallization of olivine, clinopyroxene, and plagioclase. In addition,K. G. Cox (1980) proposed that the observed small scale variation within this relatively homogeneous basaltic composition can be explained by small contributions of trans-crustal polybaric fractionation during magma ascent through the dike-sill network (See also K. Cox and Hawkesworth (1985), and H. Sheth (2016) for variants of this model).

More recently, R. E. Ernst et al. (2019) proposed a similar structural model for a CFB magmatic system with an extensive primary underplated magma reservoir(s) spanning hundreds of km laterally and up to 20 km in thickness. The magma is then envisioned to ascend both laterally outward and vertically through the crust via a large number of dikes (radiating, linear, or circumferential). During this transport, the magma can periodically accumulate in mafic-ultramafic intrusions of various shapes (e.g., multiple-km wide dikes: 2580 Ma Great dike of Zimbabwe; multiple km thick upper-to-mid crustal sills: 2060 Ma Bushveld and 2710 Ma Stillwater complexes; funnel-shaped intrusions: Rum and Skye igneous complexes associated with 56 Ma North Atlantic Magmatic province), and in sill complexes in sedimentary basins.

Another class of related models has been proposed by Heinonen, Luttinen, Spera, and

Bohrson (2019a), and Neumann, Svensen, Galerne, and Planke (2011) (and references cited therein) for CFB magma transport, specifically focused upon explaining the range of lava major and trace element compositions and mineralogy. These studies use a combination of Assimilation Fractional Crystallization (AFC) and energy-constrained AFC (EC-AFC) models (Spera & Bohrson, 2001; Bohrson & Spera, 2001; Spera & Bohrson, 2002; Bohrson & Spera, 2007) to assess what P-T conditions can match measured compositions. They suggest that the flood basalt magmatic plumbing system consists of a two-stage network wherein the magma undergoes AFC first at deep crustal depths ($\sim$ 10-30 km), followed by Fractional Crystallization (FC) in a shallow magma reservoir (3-5 km depth). A vital feature of this model is that of order 10-20 % assimilation of crustal material into the parental magma only occurs at a deeper depth. The Heinonen, Luttinen, Spera, and Bohrson (2019b) study proposes that the lack of shallow crustal assimilation is a consequence of sufficiently limited melt transport in individual dikes emplaced in a cold upper crust so as to prevent significant wall-rock melt back as required by observations of CFB dikes (H. L. Petcovic & Dufek, 2005; H. Petcovic & Grunder, 2003; H. C. Sheth & Cañón-Tapia, 2015). Additionally, if the same dike is used again for vertical melt transport, the chilled margins in the dike would provide a chemical barrier to reduce mixing between deep crustal melts and country-rock. Finally, the overall magmatic system is hypothesized to be in a quasi-steady state through active RTF processes (periodically Replenished and Tapped, continuously Fractionating O'Hara & Mathews, 1981). This model is essentially equivalent to REFC - Recharge FC model, (DePaolo, 1981; C.-T. A. Lee, Lee, & Wu, 2014) in individual magma reservoirs. This provides a mechanism for buffering magma compositions to explain the relative homogeneity of flood basalt lava compositions (e.g., K. Cox, 1988; Luttinen & Furnes, 2000).

Yu, Lee, Chen, and Zeng (2015) proposed a very similar conceptual CFB magmatic architecture model to explain the variations in lava compositions in continuous stratigraphic sequences. They propose that since the earliest magmas of a magma reservoir are emplaced in the colder crust, they will rapidly cool and form a compositional boundary plating layer (a high crystallinity solidification front B. D. Marsh, 2013), which progressively helps reduce crustal assimilation for subsequent magmas emplaced into the reservoir. Similar to other models, Yu et al. (2015) find that REAFC (REFC with crustal Assimilation C.-T. A. Lee et al., 2014) processes are necessary to explain the range and pattern of lava flow compositions (See discussion in Section 4.3.6).

A final class of conceptual models for LIP systems describe the long-term evolution of the CFB magmatic system from the initiation of the flood basalt province to its termination. As a representative example, we briefly describe a model presented by S. R. Krans, Rooney, Kappelman, Yirgu, and Ayalew (2018) based on the petrological analysis of continuous 1635 m-thick lava flow sequence of the Ethiopian Traps. The principal observational basis for this model is relative changes in phase assemblages (specifically olivine, clinopyroxene, ortho-pyroxene, and plagioclase) as a function of depth (e.g., Morse, 1980; Albarede, 1992; M. Richards, Contreras-Reyes, Lithgow-Bertelloni, Ghiorso, & Stixrude, 2013). S. R. Krans et al. (2018) propose that initially, the parental mantle melts accumulate in the Moho depth

magma reservoirs that periodically feed ol-phyric surface flows with minimal intermediate storage. Over time, a shallower magmatic plumbing system is established, leading to magma stalling and differentiation, as evidenced by a higher fraction of plag-phyric lava flows. This evolution in the magmatic plumbing network naturally leads to polybaric crystal fractionation (as argued by other conceptual models discussed above). Eventually, decreasing partial melt flux from the lithosphere leads to freezing of an increasing fraction of crustal magma reservoirs and increasing fractionation of the magmas that do erupt. Finally, the termination of the flood basalt activity in Ethiopian Traps is followed by a transition to much lower volume, localized shield building (Kieffer et al., 2004). S. R. Krans et al. (2018) posited that atop this general evolution of the magmatic system, there are variations in magmatic flux into the shallow crustal system. These include multiple pulses of magma recharge and brief hiatuses (as indicated by weathering horizons). Since there are no evident systematic mineralogical or volcanological variations on a flow-by-flow scale to these variations, they propose that the complex response is indicative of a complex magma plumbing system with multiple reservoirs. Depending on their pathway through the magmatic system, different melt batches will have varying storage times before eruption and hence experience different amounts of magma mixing and fractionation.

As additional evidence for this inference, S. R. Krans et al. (2018) interpret the occurrence of the few plagioclase-megacrystic basalt flows as indicative of a well established shallow magmatic mush zone. Based on the presence of complex zoning patterns and high An-content in plagioclase megacrysts, they propose that frequent recharge of deep melt into the magma reservoirs is required to explain these flows, with some of the larger influxes leading to large scale re-mobilizing the mush zone and eruption. A critical feature of this class of conceptual models is the presence of a complex magmatic plumbing network and the presence of multiple magma reservoirs and eruptive pathways in the system.

In summary, the various conceptual models all propose the presence of a deep crustal/Moho depth magma reservoir as well as some significant upper crustal plumbing network, which is continuously replenished in order to explain both the overall geochemical homogeneity as well as inter-flow variations in a stratigraphic section. Although these models do not explicitly discuss the size of individual magma reservoirs, it appears to be generally assumed that they are large enough to feed individual eruptive episodes (a size concomitant with volumes in excess of 1000 km^3 per eruption). The one exception to this is H. C. Sheth and Cañón-Tapia (2015) who explained geochemical variations within composite dikes in Deccan Traps with a model wherein individual CFB eruptive episodes are fed by multiple interacting magma reservoirs.

4.2.2 Quantitative Models

4.2.2.1 Recharge-crystallization model

A first quantitative models for CFB magmatic systems was proposed by Karlstrom and Richards (2011). Akin to the conceptual models described above, they assumed that the

parental ultramafic melt forms ellipsoidal intrusions at Moho depth or in the lower crust, since they are denser than the overlying crust. With subsequent fractional crystallization (up to $\sim$ 30% crystallinity), CO_2 exsolution from the melt makes the melt - volatile mixture buoyant and eruptible. Using thermo-mechanical models, they showed that during the early phases of a CFB, melt in a magma reservoir of volume comparable to the size of a single eruptive episode (10^3 - 10^4 km^3, $\sim$ 10-30 km semi-major axis horizontal length, 1-5 km vertical length) cools sufficiently to become buoyant on a timescale shorter than viscous stress relaxation timescale. Consequently, buoyant melt from each of these reservoirs feeds an individual surface eruption through dikes initiated by elastic stresses in the lower crust caused by the growth of the magma reservoirs (recharge). Continued magma flux will progressively heats the lower crust, leading to faster viscous stress relaxation and dominantly intrusive magma bodies instead of surface lava flow eruptions. For representative melt fluxes and crustal rheology, Karlstrom and Richards (2011) found that this transition occurs on a timescale order 1 Ma, which is comparable to the duration of the main phase of CFB emplacement.

The Karlstrom and Richards (2011) model envisions the formation of a dense network of intrusions in the lower crust. Due to melt buoyancy and background tectonic stresses, these magma reservoirs are expected to progress upward into colder, more elastic crust. The model also proposes that the maximum size of individual reservoirs is similar to the depth from the surface. This restriction is a consequence of free-surface shear stress and dike initiation at the edges of reservoirs for laterally extensive CFB magma bodies. Based on analog experiments and seismic datasets for sill complexes in Karoo Basin and North Atlantic magmatic province, the typical total diameter of sills is 1.5- 15 times the depth of the emplacement (e.g., Hoggett, 2019, and references therein), with a median value of 2.5 consistent with theoretical expectations (Malthe-Sørenssen et al., 2004; Manga & Michaut, 2017; Galland, Planke, Neumann, & Malthe-Sørenssen, 2009). We would however note that there are some very large sills (e.g., Basement Sill with $\sim$ 10,000 km^2 area, 400 m thickness) exposed in a 3-4 km deep surface section of the magmatic plumbing structure of the Karoo-Ferrar CFB in McMurdo Dry Valleys, Antarctica (B. D. Marsh, 2004). Thus, in practice, the concentration of free-surface shear stress may not be a strong limit on the spatial size of magma bodies due to visco-plastic deformation processes (Schofield et al., 2012; Galland et al., 2019). Finally, the eruption frequency is controlled by the melt recharge timescale, which determines the rate of deviatoric stress buildup in the lower crust and cooling timescale for buoyancy production by CO_2 exsolution. Since the lower crustal temperature will rapidly increase during the course of a CFB event, the first-order prediction from this model is that the time period between individual eruptive episodes will increase during generation of a CFB province, potentially with larger eruptive volumes later (e.g., Deccan Traps) due to expanding magma reservoirs.

4.2.2.2 Buoyancy overpressure model

Another quantitative model for CFBs was proposed by Black and Manga (2017) with a focus on explaining the available geochronological constraints and paleo-proxy inferred en-

vironmental changes for the Siberian Traps. They model the CFB plumbing architecture as composed of two magma chambers, one at Moho-depth and another at upper crustal depth. The reservoir sizes dynamically evolve in the model with melt influx from the underlying magma reservoir (mantle) and outflux to surface eruptions (overlying chamber) for the crustal-depth (Moho-depth) reservoir. The critical feature of this model is that the brittle tensional failure of large magma reservoirs is hypothesized to be a consequence of the buoyancy of the magma-volatile mixture. This buoyancy w.r.t to the surrounding country rock (δ_{rho}) leads to a buoyancy overpressure ($\Delta P_{buoy} = \delta_{rho} g h$; h is the magma reservoir thickness). This buoyancy overpressure cannot be relaxed by the viscous stress relaxation. Hence, ΔP_{buoy} can slowly accumulate over time without dissipation except by fluid flow into the surrounding crust.

Black and Manga (2017) used a 1D thermo-chemical model of the two magma reservoirs with thermal evolution, volatile exsolution, crustal assimilation of carbon-rich crust, bubble coalescence, and diffusive volatile escape into the country rock, and found that buoyancy overpressure alone is sufficient for the failure of large magma reservoirs. With regard to the eruptive tempo of CFBs, they find three primary eruptive regimes. At the start of a flood basalt sequence, the low-degree melts are volatile-rich and hence highly buoyant due to volatile exsolution during decompression. Consequently, the melt rises rapidly from the Moho-depth magma reservoir to surface eruptions with minimal storage in the crustal reservoirs. Additionally, the size of individual magma reservoirs is small ($\sim$ 1-2 km in height) since most of the mantle melt erupts rather than accumulating. With time, volatile content in the higher-degree mantle melts decreases, reducing magma buoyancy. As buoyancy slowly builds up slowly with volatile-exsolution as well as thicker/larger magma chambers (since $\Delta P_{buoy} \propto h$, the typical thickness is 8-15 km), the eruption frequency decreases along with a larger volume of individual eruptions. The eruptions are further inhibited by volatile loss to the surrounding medium during this accumulation phase. As a result, crustal permeability around the magma reservoir needs to be reduced sufficiently by thermal annealing of fractures, and crustal compaction before overpressure can build up and lead to crustal failure. These processes are repeated in the upper-crustal reservoir, which has an additional source of volatiles from the assimilation of carbon-rich crust (typically organic sediments in sedimentary basins, e.g., Karoo sills and Siberian Trap Sills H. H. Svensen et al., 2018), but also higher crustal permeability (S. Ingebritsen & Manning, 2010; Mittal & Richards, 2019). Finally, in the third stage, the decrease in parental flux prevents the buildup of sufficient ΔP_{buoy} in the magma reservoirs, and the reservoirs remain molten with some overpressure for 10^5 - 10^6 yr before eventual solidification.

During the second eruptive regime, Black and Manga (2017) found that the eruptive tempo of surface volcanism is very pulsed with perhaps just 2-4 eruptive events. Each eruptive pulse is expected to last 10^3 - 5x10^4 yrs with long hiatus of 2x10^5 - 5x10^5 yrs. Since each failure event at the Moho depth transfers a large volume of magma to the upper crustal system, the size of the upper crustal magma reservoirs feeding each eruptive episode is large (typical thickness is 2-4 km). Extrapolating from the 1D calculations, Black and

Manga (2017) propose that a full continental flood basalt sequence is fed by order 1-10 pairs of Moho and upper crustal magma reservoirs each with a melt source in the mantle of order 100-300 km (compaction lengthscale). Thus, on a province scale, the hiatuses between eruptive pulse may be shorter of order 10^5 - $5x10^5$ yrs, whereas individual stratigraphic sections would have longer hiatus since the erupted lava is expected to have been sourced from the same localized eruptive plumbing system in the crust.

4.2.2.3 Difficulties associated with large magma reservoirs

Although assuming that each large eruptive episode is fed from a correspondingly large magma reservoir makes logical sense, at least as a starting point, the description of the two models described above (Black & Manga, 2017; Karlstrom & Richards, 2011) illustrate that both the assembly and eruption of large magma reservoirs is challenging. In addition, the results illustrate that the presence of larger magma reservoirs naturally leads to more prolonged hiatus between eruptive episodes.

Among the two primary mechanisms for triggering eruptions, the efficiency of recharge associated overpressure decreases for a large reservoir for the following reasons. First, since the recharge associated overpressure is inversely proportional to the volume of the magma reservoir, it becomes progressively harder to erupt large magma bodies (Jellinek & DePaolo, 2003; Karlstrom, Dufek, & Manga, 2010; M. Townsend et al., 2019). Second, with the progressive assembly of lower crustal magma bodies, the increasing crustal temperature leads to faster visco-elastic stress relaxation of any accumulated recharge associated overpressure (Jellinek & DePaolo, 2003; Karlstrom, Paterson, & Jellinek, 2017). Additionally, in order to assemble the large magma bodies in the first place, the magma recharge rates needed to be low enough to prevent an eruption. Thus, using recharge-induced over-pressurization for the assembled larger magma bodies requires special, likely unreasonable, co-incidence of significant changes in melt influx into the magma reservoir. Although there may be some physical feedbacks for melt focusing (e.g., Karlstrom, Dufek, & Manga, 2009b; Karlstrom, Wright, & Bacon, 2015), it would seem unlikely that these would counteract the negative feedbacks described above.

As a consequence, recharge associated elastic stresses alone become inefficient as triggers for the eruption of large magma bodies, so that additional mechanisms such as buoyancy overpressure (e.g., Caricchi, Annen, Blundy, Simpson, & Pinel, 2014b; Black & Manga, 2017) or roof failure (e.g., de Silva & Gregg, 2014; Gudmundsson, 2016) are required. However, if buoyancy overpressure is the eruption trigger, a long eruption hiatus is a natural consequence due to the timescale for vertically assembly of the magma body (which would be slowed by lateral viscous flow), the timescale for crustal permeability reduction, and the timescale for sufficient solidification for volatile exsolution (Karlstrom et al., 2010; Black & Manga, 2017; Mittal & Richards, 2019). Thus, we contend that if individual eruptive episodes are indeed fed by large magma reservoirs, the eruptive tempo is naturally expected to be very pulsatory with hiatus of order 10^5 - 10^6 yrs, completely contrary to observations. Additionally, a

large magma reservoir will lead to large melt fluxes into the upper crustal reservoir when crustal failure does happen, and hence naturally leads to very large crustal magma reservoirs. Finally, since crustal assimilation of carbon rich country rock is an important source of volatiles for the upper-crustal magma reservoir, the eruptive tempo will be expected to be different for CFBs emplaced into a granitic upper crust instead of a thick sedimentary basin (e.g., Siberian Traps). Specifically, one would expect that the hiatus time between eruptive episodes is longer for CFBs with granitic upper crust (e.g.,Deccan Traps) along with overall reduced likelihood of eruption.

4.3 Observational constraints on magmatic architecture

In order to test the predictions from the previous models for CFB architecture, we use the Deccan Traps flood basalt as a representative example. Since the 1980s, the DT has been extensively studied and consequently has the most extensive geochemical, geochronological, and volcanological datasets among the large ($>$ 1 Million km^3 erupted volume) CFBs. In the following, we first give a brief geological overview of the Deccan Traps with a special emphasis on the chemo-stratigraphic framework and contribution of different crustal, lithospheric, and mantle sources to the erupted lava flows. We then summarize the direct constraints on the eruptive tempo of individual eruptive episodes for the DT main phase using geochronology, paleomagnetic secular variation, Mercury proxy records, and lava flow morphology. Next, we discuss the direct observations of the crustal magmatic architecture of Deccan Traps, particularly the dike swarms, sills, and geophysical estimates of Intrusive/Extrusive ratio for the DT. Finally, we describe some indirect constraints on DT magmatic architecture based on the stratigraphic pattern of geochemical variations in lava flows. Although our primary focus for this study is the DT, we include some complementary observations from other CFBs, layered mafic intrusions, and modern flood basalt analogs (e.g., the 1783 Laki eruption) to assess whether our DT observations are representative of CFBs in general.

4.3.1 Geological Background - Deccan Traps

The Deccan Traps is a late Cretaceous–Paleogene continental flood basalt province covering more than 500,000 km^2 of peninsular India (J. J. Mahoney, 1988; Verma & Khosla, 2019; Kale, Dole, Shandilya, & Pande, 2019; Manu Prasanth, Hari, & Santosh, 2019, and references therein). The Deccan Traps mark the beginning of the Réunion hotspot track and are associated with partial melting due to the arrival of a deep mantle plume under the Indian subcontinent (presently beneath Réunion) (e.g., M. A. Richards et al., 1989); see Peters et al. (2017) for discussion of isotopic evidence). The present-day subaerial volume of the DT lava flows is about 600,000 km^3 (Jay & Widdowson, 2008; M. A. Richards et al., 2015) along with a significant volume offshore in the Arabian Sea (Gombos Jr, Powell, & Norton, 1995; Calvès et al., 2011; D. Pandey, Pandey, & Rajan, 2011; Fainstein, Richards, & Kalra,

2019) and some small-volume Deccan-related intrusions in Seychelles (Devey & Stephens, 1991; Ganerød et al., 2011; T. M. Owen-Smith et al., 2013; Shellnutt et al., 2017). Estimates of the total pre-erosional DT lava flow volume range from 1 to 2 x 10^6 km^3 (Sukheswala, 1981; G. Sen, 2001; Jay & Widdowson, 2008).

Based on observed structural discontinuities as well as different geochemical and isotopic compositions of the lava flows, the Deccan Traps CFB is typically subdivided into four separate subprovinces each with potentially different eruptive history and corresponding magmatic system (Figure 4.1). These four subprovinces are the Western Ghat-Central Indian Volcanic province (WVP), the Mandla Lobe province, Malwa plateau province (including the volcanic sequences in the Narmada-Tapti rift zone), and the Saurashtra-Kutchh province (Z. X. Peng, Mahoney, Vanderkluysen, & Hooper, 2014; Kale et al., 2019). Among these, the WVP hosts some of the thickest continuous basalt flow sections for DT along the Western Ghats Escarpment (WGE) along the Western Coast of India (J. J. Mahoney, 1988). With a $\sim$ 3.5 km composite section of 10-50 m thick basalt flows emplaced atop Neoarchean basement (e.g., 1251 m thick Koyna core Mishra et al., 2017) easily logistically accessible, WGE sections have been extensively studied geochemically with detailed analysis of major and trace elements and isotopic composition (Sr, Pb, and Nd).

4.3.1.1 Western Ghats Geochemical Formations

On the basis of these measurements and volcanological features, the Western Ghats (WG) section has been grouped into three subgroups which are further subdivided into 12 geochemical formations each with several 100 m thicknesses (Deshmukh, 1977; J. Mahoney et al., 1982; K. Cox & Hawkesworth, 1985; Devey & Lightfoot, 1986; Beane et al., 1986; K. V. Subbarao, 1988; K. Subbarao, Bodas, Hooper, & Walsh, 1988; Beane & Hooper, 1988; Bodas, Khadri, & Subbarao, 1988; Khadri, Subbarao, Hooper, & Walsh, 1988; Lightfoot, Hawkesworth, Devey, Rogers, & Calsteren, 1990; C. Mitchell & Widdowson, 1991; Z. Peng et al., 1994; Choudhary & Jadhav, 2014; Hegde, Koti, & Kruger, 2014). The three subgroups of the WG (Wai, Lonavala, and Kalsubai, top to bottom) together represent more than 70 % of the total erupted volume of the DT and hence are the "main volumetric component" (M. A. Richards et al. (2015) and references therein).

The Kalsubai subgroup, consisting of the Jawhar, Igatpuri, Neral, Thakurwadi, and Bhimashanker formations, exhibits a large range of compositions ranging from picritic flows to evolved flows (Mg # <36, Beane et al. (1986)). The Lonavala subgroup, consisting of the Khandala and Bushe formations, includes flows in the Bushe formation with significant crustal assimilation. Finally, the Wai subgroup, comprising the Poladpur, Ambenali, Mahabaleshwar, Panhala, and Desur formations, are the most evolved lavas with regards to fractional crystallization. The Ambenali Formation records the lowest $^{87}Sr/^{86}Sr$ and the highest εNd values among the WG flows, indicative of minimal crustal assimilation (J. J. Mahoney, 1988; Lightfoot & Hawkesworth, 1988; Z. Peng et al., 1994). Geochemical analysis of lava flow sections in the Indian Deccan plateau has shown that the WG geochemical

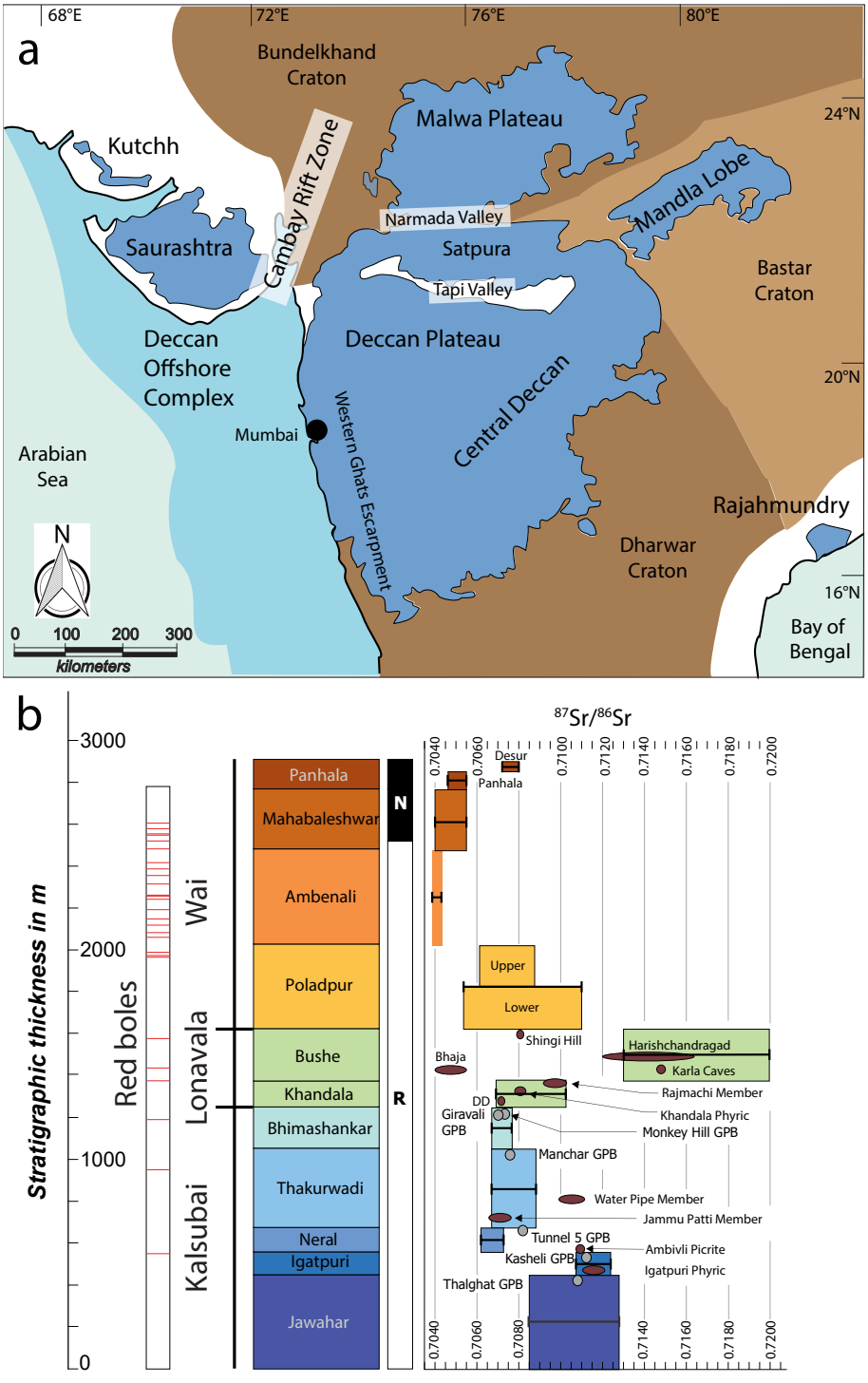
a
68°E
72°E
76°E
80°E
24°N
20°N
16°N
Bundelkhand Craton
Malwa Plateau
Kutchh
Cambay Rift Zone
Narmada Valley
Mandla Lobe
Saurashtra
Satpura
Tapi Valley
Bastar Craton
Deccan Offshore Complex
Deccan Plateau
Central Deccan
Mumbai
Western Ghats Escarpment
Arabian Sea
Rajahmundry
Dharwar Craton
Bay of Bengal
N
0 100 200 300
kilometers
b
Stratigraphic thickness in m
3000
2000
1000
0
Red boles
Wai
Lonavala
Kalsubai
Panhala
Mahabaleshwar
Ambenali
Poladpur
Bushe
Khandala
Bhimashankar
Thakurwadi
Neral
Igatpuri
Jawahar
N
R
87Sr/86Sr
0.7040
0.7060
0.7080
0.7100
0.7120
0.7140
0.7160
0.7180
0.7200
Desur
Panhala
Upper
Lower
Shingi Hill
Harishchandragad
Karla Caves
Bhaja
Rajmachi Member
DD
Giravali GPB
Khandala Phyric
Monkey Hill GPB
Manchar GPB
Water Pipe Member
Jammu Patti Member
Tunnel 5 GPB
Ambivli Picrite
Kasheli GPB
Igatpuri Phyric
Thalghat GPB

Figure 4.1 *(previous page)*: A) : Outline of the Deccan Traps Volcanic Province India including the offshore Deccan complex (modified from Kale et al., (2019) and Jay & Widdowson (2008)). The whole subaerial Deccan province is subdivided into four main subprovinces : Western Ghat-Central Indian Volcanic province (WVP), the Mandla Lobe province, the Malwa plateau province (including the volcanic sequences in the Narmada-Tapti rift zone), and the Saurashtra-Kutchh province. The southern edge of the Malwa province is typically the Narmada Tapi zone though some of the lava flows in the Satpura region may have been sourced from the central Deccan region. The Saurashtra-Kutchh and the Malwa subprovinces are divided by the Cambay rift zone. B) : A composite stratigraphic sections for the Western Ghats region showing the chemostratigraphic formations, magnetostratigraphic with the chron C29N and C29R boundary, and the locations of red boles in the section (following Sprain et al., 2019; Chenet et al., 2008). We show the range of $^{87}Sr/^{86}Sr$ for each geochemical formation (using compilation from Vanderkluysen et al., 2011; Sheth et al., 2016). The gray ellipses show the values for some selected Giant Plagioclase basalts while the brown ellipses show the values of some other Central Deccan chemical types (Figure modified from Kale et al., 2019).

formations can potentially be extended 100s of km laterally into the central Deccan (e.g., the Khandala and Poladpur formations Z. Peng et al., 1998; Melluso, Barbieri, & Beccaluva, 2004), the south-eastern Deccan (e.g., the Poladpur, Ambenali, and Mahabaleshwar formations C. Mitchell & Widdowson, 1991; Jay & Widdowson, 2008; Kaotekwar, Meshram, Sathyanarayanan, Krishna, & Charan, 2014), and the Rajamundry Traps (about 1000 km from the WG Baksi, 2001; Self et al., 2008). These results illustrate that the DT was typically associated with individual lava flows 100s of km long, and hence large individual eruptive episodes of order 1000s of km^3.

In the other DT subprovinces, lava flow major and trace element compositions similar to the WG geochemical formations have been found. For example, Z. Peng et al. (1998) (also see J. J. Mahoney, 1988; J. Mahoney, Sheth, Chandrasekharam, & Peng, 2000) found Poladpur formation type lava flows in a Malwa plateau province section about 1000 km from the WG Poladpur outcrops. However, these Poladpur-like lava flows have a very different Pb isotopic composition than the WG Poladpur geochemical formation. Thus, they could not be fed overland by the same magmatic plumbing system as the Poladpur flows. Instead, they must have a different crustal magmatic eruptive system interacting with different crustal assimilant (see discussion in the next section). There are similar examples of lava flows from the Saurashtra and Mandla lobe provinces, which have isotopic mismatches with WG formations despite similar major and trace element characteristics (e.g., Z. Peng, Walter, Aster, & Nyblade, 2014; Vanderkluysen et al., 2011; H. Sheth, Vanderkluysen, Demonterova, Ivanov, & Savatenkov, 2018). In addition to isotopic mismatches, there are also temporal differences between similar geochemical chemo-type lava flows across the different

DT subprovinces (e.g., H. Sheth et al., 2018, and references therein). A particularly illustrative case is the presence of the Bushe chemo-type (both isotopic and major/trace element composition) in lava flows and dikes in Saurashtra (Melluso et al., 1995; Melluso, Mahoney, & Dallai, 2006; H. C. Sheth, Zellmer, Kshirsagar, & Cucciniello, 2013), the Mandla Lobe (Shrivastava, Mahoney, & Kashyap, 2014), the Malwa Plateau subprovinces (Z. Peng et al., 1998; P. Hooper & Subbarao, 1999; J. Mahoney et al., 2000; H. Sheth, Mahoney, & Chandrasekharam, 2004), and Seychelles Island dikes (Devey & Stephens, 1991). However, given the chronostratigraphic and volcanologic constraints, these flows can not represent the same Bushe Formation of the Western Ghats (See the cited references for details). As described in Section 4.3.2.2, these subprovinces over a multiple Ma time-period with some provinces predating the WG sequence (e.g. Saurashtra, Malwa Plateau), while the other post-dating the WG Bushe flows (Mandla Lobe). In aggregate, these observations illustrate that the magmatic plumbing system for these subprovinces, at least the upper crustal transport network, is different.

Nevertheless, the repeated occurrence of lava chemically similar to the WG formations suggests a common sub-continental magma source and that specific petrologic processes occurred multiple times across the CFB magmatic system (Z. Peng et al., 1998; J. Mahoney et al., 2000; Haase, Regelous, Schöbel, Günther, & de Wall, 2019). Because of the complexities in magmatic architecture across multiple DT subprovinces described above, in this study we principally focus on the most voluminous Western Ghat-Central Deccan province. There is a broad consensus that most of this province represents eruptions from a single magmatic plumbing system, barring some components of the Central Deccan Plateau in the Narmada-Tapi rift valley (See Fig.1, discussion in Kale et al., 2019).

4.3.1.2 Magma composition and melt components

The dominant lava flow composition in the Deccan Traps is tholeiitic (> 95% of the exposed area) with minor volumes of carbonatitic, felsic, and alkaline eruptive products and intrusions (e.g. , Krishnamurthy & Cox, 1977, 1980; Devey & Cox, 1987; J. J. Mahoney, 1988; K. V. Subbarao, 1988; Z. Peng et al., 1994; Shrivastava & Pattanayak, 2002; Melluso, Sethna, d'Antonio, Javeri, & Bennio, 2002; Jay & Widdowson, 2008; Talusani, 2010; A. Ray, Paul, Patil, Das, & Biswas, 2010; Chandra, Paul, Stracke, Chabaux, & Granet, 2019; Prasanth, Hari, & Santosh, 2019, and references therein). Picritic lava flows are most abundant in the Saurashtra region and the northern part of the WG (Krishnamurthy & Cox, 1977; K. Cox & Hawkesworth, 1985; Beane & Hooper, 1988; Melluso et al., 1995; Sano et al., 2001). These olivine-phyric picritic lava flows are generally erupted in the early part of the lava flow sequence along with some alkali basalts (e.g., Krishnamurthy, Gopalan, & Macdougall, 2000, and references therein). In the Western Ghats section, picritic basalts constitute less than 10% of the total volume and are mostly reported in the lower formations (Igatpuri, Neral, Thakurvadi, Bushe, and Poladpur Beane & Hooper, 1988; Krishnamurthy et al., 2000). The reduced occurrence of picritic flows in younger DT sections has been typically interpreted as a sign of a steady-state magmatic plumbing system with progressively more fractionation

and ponding of picritic magmas (Krishnamurthy et al., 2000).

The geochemical diversity of WG lava flows suggests a complex petrologic evolution, involving significant fractional crystallization of plagioclase, clinopyroxene, and olivine as well as crustal assimilation and magma mixing (J. Mahoney et al., 1982; J. J. Mahoney, 1984; K. G. Cox & Hawkesworth, 1984; K. Cox & Hawkesworth, 1985; J. J. Mahoney, 1988; Chatterjee & Bhattacharji, 2008). The initial parental magma for the WG lava flows (the Ambenali Formation end-member) is a high-degree partial melt from the Réunion plume source along with some asthenospheric and lithospheric mantle contributions (Z. Peng et al., 1994; Z. Peng & Mahoney, 1995). K. G. Cox (1980) proposed that these high degree partial melts are initially picritic but undergo extensive fractional crystallization in the crustal system to form basalts with < 8 % MgO before surface eruptions (K. G. Cox & Hawkesworth, 1984; Herzberg & Gazel, 2009). Based on rare-earth element (REE) inversions (McKenzie & O'nions, 1991; S. Gibson & Geist, 2010), M. A. Richards et al. (2015) concluded that the top of the asthenospheric melt column was at about 60 km depth during the WG eruptive sequence.

Several different assimilates have been proposed for the DT lavas, including granitic upper crust (J. Mahoney et al., 1982; K. G. Cox & Hawkesworth, 1984; Lightfoot & Hawkesworth, 1988; Lightfoot, Hawkesworth, et al., 1990; Z. Peng et al., 1994; Dessai, Downes, López-Moro, & López-Plaza, 2008), lower granulitic continental crust (K. G. Cox & Hawkesworth, 1984; Z. Peng et al., 1994; Peters et al., 2017), and partial melting of subcontinental lithospheric mantle (Lightfoot & Hawkesworth, 1988) either individually or in sequence (Z. Peng et al., 1994). Some of the geochemical variations in lava flows have also been suggested to be indicative of partial melt from the lithospheric, asthenospheric, and deep plume components (e.g., J. J. Mahoney, 1988; K. V. Subbarao, 1988; E. S. Jennings, Gibson, Maclennan, & Heinonen, 2017; Hari, Swarnkar, & Prasanth, 2018; R. E. Ernst, 2014, and references therein). Furthermore, the crust beneath each subprovince is compositionally different due to the pre-Deccan structure of the Indian craton (See Figure 4.1). For instance, the WG region is underlain by continental crust similar to the Dharwar craton while the central DT is emplaced atop Archaen Bastar craton (Dessai & Vaselli, 1999; Y. B. Rao et al., 2017; Kale, Dole, Upasani, & Pillai, 2017). In contrast, the Mandla subprovince is underlain by the Bastor craton and some Proterozoic mobile belts (J. S. Ray & Parthasarathy, 2019; Kale et al., 2019, and references therein) while the crust under the Mandla province includes the Bundelkhand craton, Proterozoic Vindhyan Supergroup (sandstone, shale, and carbonates), and a Late Archean-Proterozoic collisional mobile belt (R. Ray et al., 2008; Ramakrishnan & Vaidyanadhan, 2010; L. Ray, Nagaraju, Singh, Ravi, & Roy, 2016). As a consequence, the isotopic and geochemical composition of the crustal contaminants in each of the DT subprovinces can vary significantly.

It is clear that the assimilates can vary rapidly between geochemical formations, despite their uncertain composition, or even their crustal vs. lithospheric–mantle nature (e.g., (J. J. Mahoney, 1988; Lightfoot, Hawkesworth, et al., 1990; Gallagher & Hawkesworth, 1992; Arndt, Czamanske, Wooden, & Fedorenko, 1993; Hawkesworth & Gallagher, 1993;

Z. Peng et al., 1994; Turner & Hawkesworth, 1995; Lassiter & DePaolo, 1997; H. Sheth & Chandrasekharam, 1997; Allegre, Birck, Capmas, & Courtillot, 1999; G. Sen, 2001; Chandrasekharam, Vaselli, Sheth, & Keshav, 2000). For instance, the crustal assimilation component for the highly contaminated Bushe Formation is isotopically different from the assimilate for the Mahabaleshwar Formation (e.g., K. Cox & Hawkesworth, 1985; Beane et al., 1986; Lightfoot & Hawkesworth, 1988; Z. Peng et al., 1994; J. Mahoney et al., 2000; Gangopadhyay, Sen, & Keshav, 2003; Melluso et al., 2006). Similarly, the main WG geochemical formations show abrupt changes in $^{87}Sr/^{86}Sr$ ratios, sometimes across even a single sheet flow boundary. These changes are indicative of rapid changes in the source components for the erupted magma (Beane et al. (1986), Figure 1b modified from Kale et al. (2019), Haase et al. (2019) for Mandla Lobe). Hence, the magmatic plumbing system for the DT is complex, with multiple assimilates, but also dynamic, with the ability to rapidly switch magma compositions. The geochemical memory of the magmatic system is relatively small. This is difficult to do in a magmatic plumbing system composed of only a few large well stirred magma chambers where each eruptive episode typically integrates magma compositions over multiple 100s of kyr (Black & Manga, 2017).

4.3.2 Deccan Traps Geochronology

The total DT eruptive sequence lasted about 10 Ma, with the oldest alkalic lava flows in Pakistan around 72-73 Ma (Khan, McCormick, & Reagan, 1999; J. Mahoney, Duncan, Khan, Gnos, & McCormick, 2002), and the youngest lava flows around 60-61 Ma in the Mumbai sequence (H. C. Sheth, Pande, & Bhutani, 2001a, 2001b; Pande, Yatheesh, & Sheth, 2017). However, the majority ($> 90\%$) of volcanism occurred during a $\sim$ 1 Ma time-interval from 66.3 to 65.3 Ma (Renne et al., 2015; Schoene et al., 2015; Parisio et al., 2016; Sprain et al., 2019; Schoene et al., 2019). This interval includes almost all of the Western Ghats eruptive sequence and hence constitutes the "main phase" of DT volcanism (Sprain et al., 2019; Schoene et al., 2019).

In the following section, we first discuss the geochronological datasets from the Western Ghats, since they represent the primary volumetric component of the Deccan Traps and have the best constraints on eruptive tempo. We then briefly describe the available geochronological constraints for the DT subprovinces, with a focus on their implications for the overall magmatic activity of the DT flood basalt province.

4.3.2.1 Western Ghats geochronology

Our best direct constraints on the eruptive rates for the Deccan Traps comes from the high-precision $^{40}Ar/^{39}Ar$ dating of lava flows and U-Pb dating of inter-flow horizons in the Western Ghats region (Renne et al., 2015; Schoene et al., 2015; Sprain et al., 2019; Schoene et al., 2019). Using their new ages with previously published high-precision dates, Sprain et al. (2019) concluded that the DT lava flows in the Western Ghats-Central Deccan province erupted continuously (within age precision) for a total duration of 0.991 Ma from $\sim$ 66.413

Ma (Jawahar Formation) to ∼ 65.422 Ma (Upper Mahabaleshwar Formation). This time period spans the Cretaceous-Paleogene Boundary (KPB; 66.052 Ma Sprain, Renne, Clemens, & Wilson, 2018) with more than 75 % of the DT volume erupted within 650 kyr of the KPB. The zircon U-Pb dates in Schoene et al. (2019) are consistent with the ^{40} Ar/^{39}Ar results with respect to the overall duration of the WG although their exact location of the KPB within the WG section is slightly different.

However, these recent studies do differ with respect to eruptive tempo. Sprain et al. (2019) found no evidence for a long hiatus (> 150 kyr) between individual lava flows or geochemical formations, and the mean magma eruption rate for the Kalsubai and Lonavala (0.4 ± 0.1 km/year) subgroups is statistically similar to that of the Wai subgroup (0.6 ± 0.2 km/year). In contrast, Schoene et al. (2019) proposed multiple hiatuses within the WG stratigraphy: a ∼ 100 kyr hiatus between Poladpur and Ambenali, and a ∼ 250 kyr hiatus between Ambenali and Mahabaleshwar formations. Correspondingly, they conclude that the eruptive rates were also pulsed with the Ambenali and Poladpur Formations each having an eruptive pulse of 6-10 km^3/year with a ∼ 100 kyr duration.

Although ascertaining why the results of the two studies differ is an area of ongoing work, we can use volcanological features to assess if there is any evidence for the proposed long hiatuses. Since sub-continental India was located in the equatorial belt around 66 Ma with potentially high rainfall and weathering rates (e.g., Dessert, Dupré, Gaillardet, François, & Allegre, 2003; Johansson, Zahirovic, & Müller, 2018), a long hiatus would be expected to correspond to a thick weathering horizon in between basaltic flows. Indeed, multiple Western Ghats sections have red weathering horizons (red boles, typically ≤ 1 m thick) in between basaltic flows (e.g., stratigraphic sections in Jay, 2005, Steve Self personal comm.). However, there is no evidence of a stratigraphically continuous, extraordinarily thick red-bole between the Poladpur and Ambenali formations (Jay, 2005; Jay et al., 2009; Chenet et al., 2009). Furthermore, some of the Ambenali-Poladpur transition sections do not have any red boles (Jay et al., 2009; Chenet et al., 2009; Sprain et al., 2019, ; also See Figure 4.1). Finally, red boles are frequently found between lava flows within the Ambenali formation, suggesting some hiatus time-period between individual eruptive episodes. Thus, we conclude that the eruptive tempo of the Western Ghats sequence does not show any evidence for multiple 100 kyr hiatuses between eruptive time-periods contrary to expectations of a large magma reservoir model (See Section 4.2.2.3).

4.3.2.2 Constraints for other DT subprovinces

Volcanism in the Saurashtra-Kutchh province (including some erupted products in Rajasthan) is generally considered to be the oldest in the Deccan stratigraphy. The largest silicic complexes in the DT - Barda Hills and Alech Hills in Saurashtra - and the overlying basalts in the region were emplaced between 69.5- 68.5 Ma based on the ^{40}Ar/^{39}Ar ages and field relationships (Dave, 1971; "Acid ring dykes and lava flows in Deccan trap basalt, Alech hills, Saurashtra, Gujarat", 1984; Shukla et al., 2001; A. Sen et al., 2012; Cucciniello,

Demonterova, Sheth, Pande, & Vijayan, 2015; Cucciniello, Choudhary, Pande, & Sheth, 2019). Additionally, although $^{40}Ar/^{39}Ar$ dates on two alkaline complexes (Sarnu-Dandali and Mundwara) in the Cambay graben suggest a multi-phase emplacement spanning 90 to 60 Ma (H. Sheth, Pande, Vijayan, Sharma, & Cucciniello, 2017; Pande, Cucciniello, et al., 2017), the oldest DT associated components have ages of 69.62 ± 0.08 Ma and 69.58 ± 0.16 Ma (Basu, Renne, DasGupta, Teichmann, and Poreda (1993); recalculated to Renne, Balco, Ludwig, Mundil, and Min (2011) standards by Parisio et al. (2016)). Finally, there were subaerial/submarine eruptions on the Saurashtra Volcanic Platform between 75-68 Ma (Calvès et al., 2011; G. Bhattacharya & Yatheesh, 2015) and the Anjar Traps in Kutchh erupted between 67.47 ± 0.30 and 67.67 ± 0.60 (V. Courtillot et al. (2000); recalculated to Renne et al. (2011) standards by Parisio et al. (2016)). It is noteworthy that Central Saurashtra mafic dikes have $^{40}Ar/^{39}Ar$ ages spanning 66.6 Ma to 62.4 Ma (Cucciniello et al., 2015), younger than any published ages of the lava flows in the region. Additionally, Paul, Ray, Das, Patil, and Biswas (2008) used paleomagnetic data to conclude that magmatism in the Kutchh basin (dominantly tholeiitic, though with a significant alkaline component) occurred across chrons C30N, C29R, and C29N (i.e., across the KPB boundary) although the data does permit older ages. In summary, the available geochronological datasets suggest that the magmatic activity in the Saurashtra-Kutchh province is among the oldest in any DT province and may have had large time-gaps between periods of activity (G. Sen et al., 2009).

For the Malwa plateau subprovince, Parisio et al. (2016) found that the alkaline and tholeiitic rocks were emplaced around the same time (within the age precision) with $^{40}Ar/^{39}Ar$ ages between 66.60 ± 0.35 to 65.25 ± 0.29 Ma for the Phenai Mata intrusive complex (also Basu et al. (1993) found similar ages) and 66.40 ± 2.80 to 64.90 ± 0.80 Ma for the Mount Pavagadh region. Based on paleomagnetic data as well as some $^{40}Ar/^{39}Ar$ dates (Schöbel, de Wall, Ganerød, Pandit, & Rolf, 2014, oldest date of 67.73 ± 0.22 Ma), the volcanism in the Malwa plateau may have been long-lived, spanning the chron C30N-C29R-C29N transitions.

In contrast to both the Saurashtra-Kutchh and Malwa Plateau provinces, the lava flows in the Mandla lobe are generally younger, with ages around 64.42 ± 0.33 Ma (Shrivastava, Duncan, & Kashyap, 2015; Pathak, Patil, & Shrivastava, 2017). However, some of the dikes in the region are older than published lava flow ages (e.g., 66.56 ± 0.42 Ma Shrivastava, Kumar, & Rani, 2017) suggesting the potential presence of older lava flows in the sequence.

The youngest section in the DT is the Mumbai sequence in the WG (along with some intrusive dikes in Goa). The Mumbai sequence includes a much wider compositional diversity than the rest of the DT, containing tholeiitic basalts, rhyolites, trachytes, and pyroclastics (Melluso et al., 2002). The $^{40}Ar/^{39}Ar$ ages for this sequence are typically between 61.5 and 63 Ma (Widdowson, Pringle, & Fernandez, 2000; H. C. Sheth et al., 2014; Samant, Patel, Pande, Sheth, & Jagadeesan, 2019; Duraiswami, Jutzeler, Karve, Gadpallu, & Kale, 2019) with some volcanism ranging from 64.55 Ma to 60.8 Ma (H. C. Sheth et al., 2001b, 2001a; P. Hooper, Widdowson, & Kelley, 2010). The main phase of Laxmi Ridge-India-Seychelles continental rifting and voluminous offshore magmatism (Misra, Bhattacharya, Mukherjee,

& Bose, 2014; Pande, Yatheesh, & Sheth, 2017; Samant et al., 2019) as well as intrusions in Seychelles (Shellnutt et al., 2017), also have an age around 62.5 Ma, suggesting a possible association.

In summary, there is a general progression of younger Deccan Trap ages moving southward, consistent with the northward motion of the Indian plate over a quasi-stationary mantle plume head. With a typical Indian plate motion of $\sim$ 15-20 cm/yr during Late Cretaceous-Early Paleogene (Cande & Patriat, 2015), the northward plate motion over 2 Ma is 300 - 400 km comparable to the distance between the Saurashtra region and the Mumbai-Pune region. However, the geochronology also suggests additional complexities, principally associated with the role of pre-existing tectonic features on the Indian sub-continent such as the Narmada-Tapi and the Cambay rift zone (See Figure 4.1). Petrologically, observations from each subprovince show that the silicic lavas and intrusions were typically emplaced after the local primary flood basalt sequence (e.g., Mount Pavagadh, Parisio et al. (2016); Mumbai : H. C. Sheth et al. (2014)). With a few exceptions, the alkaline rocks in the DT are generally emplaced both prior to and post the main phase of tholeiitic lava flows (e.g., Parisio et al., 2016), analogous to some other CFBs (e.g., S. Gibson, Thompson, & Day, 2006; R. E. Ernst & Bell, 2010; R. B. Larsen et al., 2018). This is consistent with an initial lower degree melt that quickly traverses the crust, potentially with minimal assimilation (e.g., Malwa plateau, Haase et al., 2019). This is followed by an increasing degree of partial melting in the mantle plume head and more extensive fractionation (K. G. Cox & Mitchell, 1988). Eventually, the system reverts back to a lower degree, alkalic melt, along with some silicic melts, coincident with progressive plate motion away from the plume (M. A. Richards et al., 1989).

With regards to eruptive tempo, the subprovinces appear to typically have a much more extended period of volcanic activity compared to the Western Ghats sections. However, with the available geochronological constraints, it is unclear whether the eruptive activity is pulsed with long hiatuses in between or if the typical time between individual eruptive episodes is simply longer.

4.3.2.3 Geochronological Constraints for other CFBs

Most CFBs, including the DT, show evidence for a short duration $\sim$ 0.5-1 Ma long "main phase" of volcanic activity wherein the majority of the CFB volume is erupted (e.g., V. E. Courtillot & Renne, 2003; Bryan et al., 2010; R. E. Ernst & Youbi, 2017; Wilkinson, Ganerød, Hendriks, & Eide, 2017; H. Svensen et al., 2018, and references therein). However, most of them lack a robust chemostratigraphic framework, or as abundant surface exposure of lava flows as the DT. Thus, at present, it is unclear based on geochronology alone whether the majority of eruptive episodes in other CFBs are further clustered into pulses within the main phase volcanism.

The two exceptions to this are the Columbia River Basalts (CRB) and the Siberian Traps. For the CRB, Kasbohm and Schoene (2018) used high precision zircon U-Pb geochronology

on volcanic ash beds between basaltic flows to constrain the duration of the main volcanic phase (> 95% of CRB volume) to about 800 kyr (16.7 to 15.9 Ma). These results, in combination with the magnetostratigraphy, show no evidence for a > 50-100 kyr hiatus between eruptions.

For the Siberian Traps, high-resolution U-Pb geochronology (S. D. Burgess & Bowring, 2015; S. Burgess, Muirhead, & Bowring, 2017) suggests that the volcanic sequence should be divided into three stages. More than two thirds of the extrusive volume was erupted in the first stage, which lasted 700 kyr (252.2 to 251.9 Ma). This was followed by a $\sim$ 420 kyr period of emplacement of mostly intrusives across the Siberian platform (also see Jerram, Svensen, Planke, Polozov, & Torsvik, 2016; Augland et al., 2019), potentially due to the volcanic load of the overlying lava flows (S. Burgess et al., 2017). Finally, in stage 3, a combination of extrusive and intrusive volcanism occurred for another 300-500 kyr. As there are only four dates for the basaltic lavas (two in Stage 1, and one each in Stage 2 and 3), it is not possible to assess if there were any eruptive hiatuses within each stage of extrusive lava flows. The intrusions continued throughout Stage 2 without any resolvable hiatus (> 100 kyr). It is important to note that the U-Pb dates are from intrusions emplaced within the lava flow stratigraphy or exposed on the periphery of lavas and volcaniclastic rock. This suggests that these intrusions were likely emplaced at shallow depths (< 2 km, also see Tomshin, Kopylova, and Tyan (2005); Tomshin, Kopylova, Vasilyeva, and Zaitsev (2014) for petrographic data suggesting shallow emplacement). Consequently, we would argue that the Stage 1-Stage 2 transition from extrusive eruptions to shallow intrusive magmatic activity for $\sim$ 420 kyr does not represent a hiatus for the crustal magmatic system. In addition, the sill complex does not correspond to a single well-mixed large magma reservoir, as the intrusions have varying geochemical compositions and emplacement ages (e.g., N. A. Krivolutskaya et al., 2018, see Description of a magma reservoir in Section 4.2). Hence, the frequency of crustal diking will be controlled by the timescale of pressure buildup in the upper crustal magma reservoir, regardless of whether each dike feeds a shallow sill complex or eruptions at the surface.

In conclusion, there is no clear evidence of long (> 100 kyr) eruptive (including shallow sill emplacement) hiatuses for either the Siberian Traps or Columbia River Basalts given the available datasets. These observations are inconsistent with the expectations of the large magma reservoir model (See Section 4.2.2.3).

4.3.3 Paleomagnetic constraints on eruptive tempo

Although there have been significant improvements in analytical techniques and consequent improvements in the precision of geochronological age precision to order 0.1 - 0.01%, the absolute age uncertainity is still of order 10,000 kyr (for KPB age samples Sprain et al., 2019; Schoene et al., 2019). In order to obtain a higher resolution eruptive tempo, multiple studies have utilized the record of paleo-secular variation recorded in successive lava flows (directional groups, DGs) to constrain lava flow eruption rates at $\sim$ 100 yr resolution (Riisager, Riisager, & Pedersen, 2003; Knight et al., 2004; Chenet et al., 2008, 2009; V. Cour-

tillot & Fluteau, 2014; Moulin et al., 2017; Pavlov et al., 2019). The Earth's magnetic field experiences secular variation, i.e. it naturally moves slightly over time. The paleomagnetic directions recorded in rocks accordingly display these variations in field position. Sets of lava flows with indistinguishable or very similar field directions are assigned to a directional group, which is commonly assumed to have been emplaced very rapidly (within $\sim$ 400 years) based on estimates of modern secular variation. The number and distribution of directional groups is thus an estimate of the temporal frequency of eruptions. Although this method has been used in studies for multiple decades, the relationship between the correlation of paleomagnetic directions to eruptive timescales has been based on strongly simplifying assumptions about secular variation. In particular, the quasi-cyclic nature of paleosecular variation can introduce spurious correlations wherein lava flows separated by multiple secular variation cycles still have a small difference in paleomagnetic directions.

We addressed these challenges by developing a generalized forward modeling approach to compare synthetic eruptive histories with field datasets in a Bayesian inversion framework (Mittal et al., 2019, Mittal et al. in prep). Since the real paleomagnetic field has a complex temporal structure with excursions and changing timescales for secular variation, we use a multi-million year long, low latitude deep sea sedimentary record of field variations for our forward model (Ohneiser et al., 2013). Additionally, we utilize the full statistical properties of the flow-by-flow records (e.g., fraction of lava flows in DGs and mean number of lava flows in DGs) instead of just the number of DGs to constrain permissible models. Using the same paleomagnetic dataset as Chenet et al. (2008, 2009), we find that the observations for the WG composite section (spanning Kalsubai, Lonavala, and Wai subgroups) is most consistent with continuous eruptions every 6,000-12,000 years (Figure 4.2). It does not show any evidence for highly pulsed eruption rate, contrary to the large magma chamber model predictions (Figure 4.2). Considering that the number of lava flows within DGs reported in previous studies is greater for the Siberian Traps and CAMP than for the Deccan Traps, we expect that the eruption frequency for these two CFBs was faster than DT but a full quantitative analysis is beyond the scope of this study.

4.3.4 Hg eruptive tempo estimates

Another indirect method to estimate the eruptive tempo of the DT at a 1000 yr resolution is the use of mercury (Hg) chemostratigraphy (e.g., Sial et al., 2013; Font et al., 2016; G. Keller et al., 2018; Percival et al., 2018; I. M. Fendley et al., 2019). Hg is emitted as a vapor during volcanic eruptions, as well as through passive degassing, and volcanism is the dominant source of Hg to the environment (See I. M. Fendley et al. (2019) for more discussion). Increases in Hg concentration, therefore, may indicate inflation of the global Hg budget due to flood basalt eruptions. However, to compare Hg concentration records from different locations and depositional environments, one must account for differences in sedimentation rate, sampling resolution, and sedimentary conditions such as organic carbon and sulfur concentration. We have developed a new statistical framework that uses an

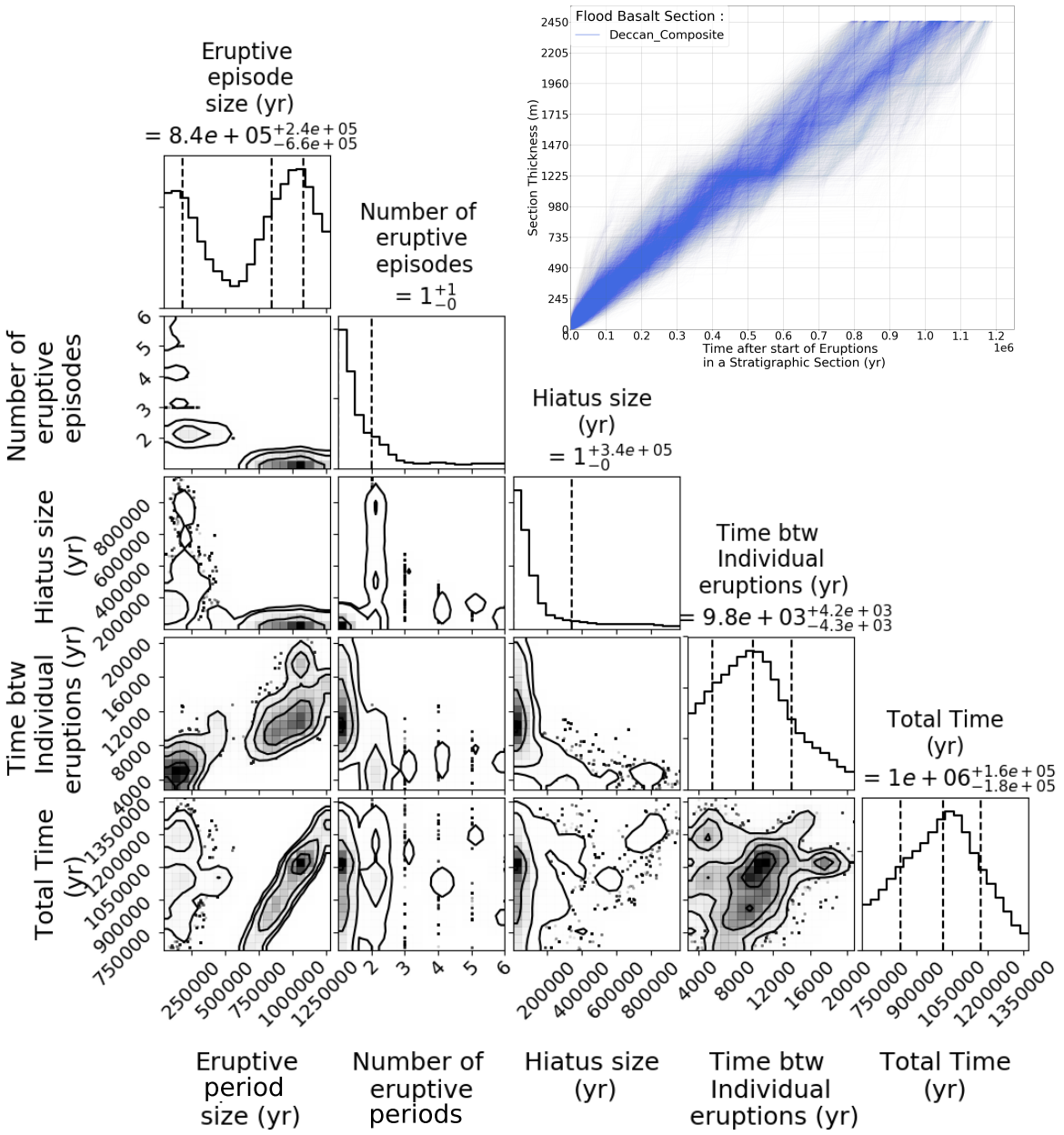
Flood Basalt Section :
Deccan_Composite
Section Thickness (m)
Time after start of Eruptions in a Stratigraphic Section (yr)
1e6
Eruptive episode size (yr)
$= 8.4e+05^{+2.4e+05}_{-6.6e+05}$
Number of eruptive episodes
$= 1^{+1}_{-0}$
Hiatus size (yr)
$= 1^{+3.4e+05}_{-0}$
Time btw Individual eruptions (yr)
$= 9.8e+03^{+4.2e+03}_{-4.3e+03}$
Total Time (yr)
$= 1e+06^{+1.6e+05}_{-1.8e+05}$
Eruptive period size (yr)
Number of eruptive periods
Hiatus size (yr)
Time btw Individual eruptions (yr)
Total Time (yr)

Figure 4.2 *(previous page)*: Bayesian parameter estimates for paleo-secular variation analysis for Eruptive period size (yr), Number of eruptive periods, Hiatus size (yr), Time between individual eruptive episodes (yr), and the Total time for the Composite Deccan Section. We use the flow-by-flow dataset from Chenet et al. (2008), and Chenet et al. (2009 for this analysis. The top right panel shows possible emplacement histories for the composite section based on the range of permissible inversion results. The lava lobe thickness are sampled from the distribution of the lobe thickness for the WG composite section and the total height of each composite record is equal to the height of the composite section.

environmental Hg cycle box model (Amos, Jacob, Streets, & Sunderland, 2013) to estimate eruptive rates and volumes by quantitatively evaluating the changes in global mercury budget indicated by varying concentrations in sedimentary records.

To do this analysis, we created many model eruptive time series with a variety of eruptive rates and durations. The main model parameters are the size and duration of each eruptive episode, the time between individual eruptive episodes, number and duration of eruptive events (each composed of multiple eruptive episodes), and the hiatus time between eruptive events. We set the cumulative volume to be less than 10 million km^3, and the total amount of time no more than $\sim$ 1 million years, matching the Deccan volumes (allowing some uncertainty) and geochronological constraints. We then use each permissible Hg input record as an input into the Amos et al. (2013) Hg box model to create synthetic sediment Hg records. Then we "sample" each synthetic record at the same sampling resolution as the data and include a time-smoothing to account for sedimentation rate, bioturbation and diffusion, as well as the physical sample size. These model records are then statistically compared with actual Hg records from the KPB interval by matching the mean and distributions of Hg peak amplitude, width, and time between peaks between each model output and a long terrestrial Hg record (I. M. Fendley et al., 2019; I. Fendley, Mittal, Renne, & Marvin-DiPasquale, 2019, Fendley et al. in prep).

Comparing with millions of potential eruptive histories, we find that the model parameters most consistent with the full dataset (DT main phase interval, blue curves) are those with individual eruptive episodes which lasted approximately 100 to 1000 years, occurred every 2500-4500 thousand years, and erupted around 20-80 cubic kilometers of basalt per year (Figure 4.3 I. M. Fendley et al., 2019; I. Fendley et al., 2019, Fendley et al. in prep). All of these estimates are averaged over the duration of the eruptive episode. Additionally, we do not find any support for a long ($>$ 50 kyr) hiatus throughout the "main-phase" DT volcanism, between $\sim$ 66.3 - 65.6 Ma. For the time-period near the KPB boundary (IRA-NV section: $\sim$ 40kyr before and $\sim$ 80kyr after the KPB boundary I. M. Fendley et al., 2019), we find that for each eruptive episode, eruption rate was slightly higher: 50-125 km^3/year, shorter eruptive episodes (50-250 years), and more frequent eruptions (every 2000 - 2500 yrs, Figure 4.3). We would emphasize that at present, the available Hg datasets do not have

sufficiently uniform high resolution to reconstruct a time-varying eruptive history for the DT. Consequently, it is unclear if the IRA-NV section eruption rates are representative of the whole Wai subgroup, or just the Khandala-Bushe-Poladpur formations. Based on the available datasets (e.g., Percival et al., 2018, Fendley et al. in prep), individual eruptive episodes during the Ambenali formation had similar eruptions rates as the full DT main phase interval results, but with a longer eruption duration. However, more data is needed to confirm this preliminary conclusion. Nevertheless, we do not find any evidence for a significant increase in the time-period between eruptive intervals with the Hg dataset. This is in direct contrast to the model expectations for a larger magma reservoir wherein eruptions are expected to become less frequent during a CFB sequence.

It is also important to note that the Hg proxy integrates eruptions over the whole of the Deccan Traps instead of a single stratigraphic lava flow section. Thus, the results are not biased by local hiatus in a particular lava flow stratigraphic section. Based on modern CFB analogs, a $\sim$ 20 m thick lava flow may not cover the topography uniformly and completely (e.g., Thordarson & Self, 1993; C. Neal et al., 2019). Consequently, a single stratigraphic CFB section would probably not record all the lava flows in the region, especially for spatially extensive flows, e.g., Wai sub-group flows. We hence naturally expect that the eruptive tempo from paleo-secular variation measurements is slower than that from Hg. This process also helps explain the more frequent occurrence of weathering horizons (red boles) in the Wai subgroup flows vis-a-vis Kalsubai and Lonavala subgroups (Figure 4.1). In the field (WGE sections), most of the red boles are spatially heterogeneous and are, in most cases, not continuous across 10s of km. Our Hg eruptive rates are thus very compatible with results from geochronology (Section 4.3.2) and paleo-secular variation analysis (Section 4.3.3).

Our overall results are also consistent with the lava flow eruption rate estimates based on flow morphology (e.g., Vye-Brown, Self, & Barry, 2013, Section 4.3.4). In conclusion, Hg chemostratigraphy also does not provide any evidence for a prolonged province-wide eruptive hiatus, contrary to expectations from the large magma reservoir model (See Section 4.2.2.2).

4.3.5 Eruptive estimates based on lava flow morphology

Every CFB is comprised of 100-1000s of individual eruptive episodes, each of which is associated with a dominantly pahoehoe lava flow field (Self et al., 1998) with exceedingly rare fully developed a'a lava flows (Self, Thordarson, & Keszthelyi, 1997; N. R. Bondre, Duraiswami, & Dole, 2004; Waichel, de Lima, Lubachesky, & Sommer, 2006; Sengupta & Ray, 2006; Passey & Bell, 2007; Duraiswami, Bondre, & Managave, 2008; R. J. Brown, Blake, Bondre, Phadnis, & Self, 2011; El Hachimi et al., 2011; Vye-Brown, Self, & Barry, 2013; Braz Machado, Reis Viana Rocha-Júnior, Soares Marques, & Ranalli Nardy, 2015). Early studies of CFB flow fields proposed that individual flow fields were emplaced within a few days to weeks timescale with a correspondingly large eruption rate (Shaw & Swanson, 1970; M. T. Mangan, Wright, Swanson, & Byerly, 1986; Tolan, 1989). However, extensive work on the lava flow fields in the Columbia River Basalt (Self et al., 1998; Vye-Brown, Self,

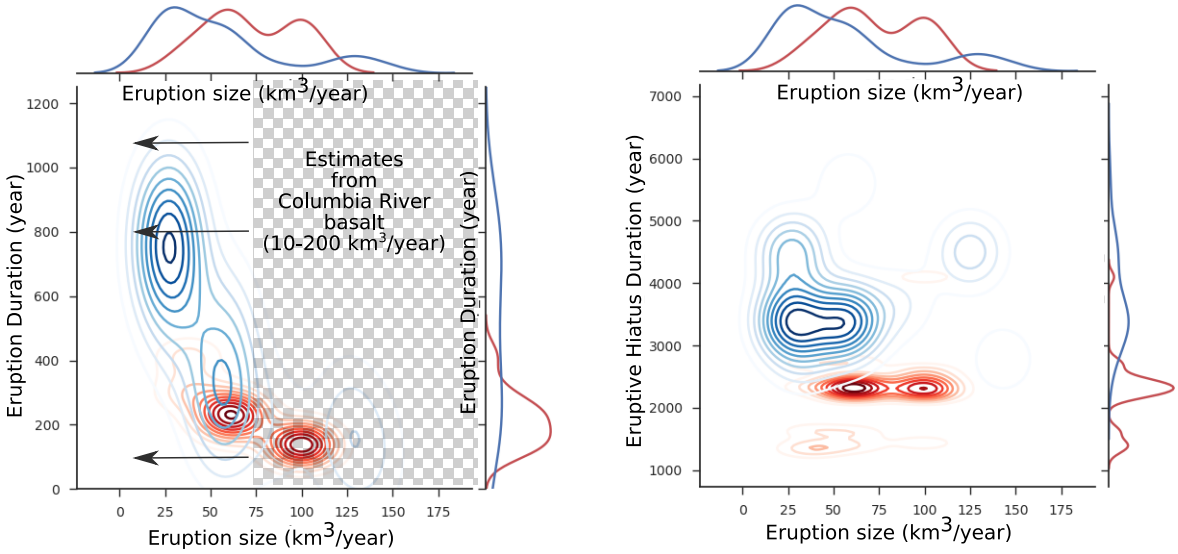

Figure 4.3: Estimates of Eruptive Volume Fluxes (km^3/year), Eruptive Duration (years) and Hiatus time between Individual eruptions (years) for Deccan Traps using statistical inversion of terrestrial Hg chemo-stratigraphic records (I. Fendley et al., 2019; I. M. Fendley et al., 2019). The blue curves show the result of the analysis for the section spanning a time period which includes the full "main phase" Deccan Trap eruptive period (Sprain et al., 2019) which the red curve considers the analysis for a time-period only spanning $\sim$ 120 kyr across the K-Pg boundary (IRA-NV section, I. M. Fendley et al., 2019). The estimates for the Columbia River Basalt shown as the grey pattern are based on observations of Columbia River Basalt flow fields(Self et al.,1998; Vye-Brown, Self, & Barry, 2013)

& Barry, 2013, and references therein) has illustrated a strong similarity between CFB lava flows and modern Hawaiian and Icelandic lava flows despite the significantly different spatial scale. As a consequence, the CFB flows were emplaced as inflated compound pahoehoe flow fields with eruption rates similar to the highest observed for Iceland (e.g., Laki 1783; 8,700 m^3/s Thordarson & Self, 1993; Guilbaud, Self, Thordarson, & Blake, 2005) and Hawaii (e.g., Kilauea 2018: 130-200 m^3/s C. Neal et al. (2019), Mauna Loa a'a flow: 1,179-1,769 m^3/s Finch and Macdonald (1953)), but sustained over years to decades (e.g., Ho & Cashman, 1997; Keszthelyi & Self, 1998; Self et al., 1998; S. Anderson, Stofan, Smrekar, Guest, & Wood, 1999; Bryan et al., 2010; Keszthelyi, Self, & Thordarson, 2006); See S. Reidel, Tolan, and Camp (2018) for an alternative viewpoint).

This conclusion is supported by the observations that the typical thickness of individual flow lobes in the Deccan Traps is $\sim$ 15-20 m (Jay, 2005; Jay et al., 2009) with only a few thicker lobes (up to 100 m) in the Wai subgroup formation (Koyna Core Mishra et al., 2017). Although this lobe thickness is larger than the typical value for Hawaiian pahoehoe

flow fields ($\sim$ 5 m lobes, HSDP2 core M. G. Katz & Cashman, 2003), the Laki 1783 eruption are associated with 15-25 m thick basaltic flows Thordarson and Self (1993).

Finally, the lack of a'a flow fields in CFBs provides an upper limit for permissible effusion rate. Hawaiian a'a flow fields form when emplacement is rapid (days to weeks, average effusion rates $\geq$10 m^3/s Rowland & Walker, 1990) with open lava channels near the fissure vents (e.g., Lipman & Banks, 1987; Wolff & Ramos, 2013). Since there is no clear evidence of such processes in most CFB flow fields (Self et al., 1998), we conclude that these flow fields (with much larger volumes than Hawaiian flows) must be emplaced over a long time-period (decades-centuries) rather than days-weeks. For the DT in particular, no clear lava tubes have been identified (Duraiswami, Bondre, & Dole, 2004; Pawar et al., 2015). However, the lack of unequivocally identified eruptive vents potentially allow for more frequent lava tubes and open channels. We also acknowledge that we do not preclude the possibility for some short-lived high effusion rate pulses that have been proposed to explain the rubbly pahoehoe structure in some CFB flows (N. R. Bondre et al., 2004; Duraiswami et al., 2008; B. Sen, 2017). In fact, Rader, Vanderkluysen, and Clarke (2017) have argued that effusive flux variations (of factor $\sim$ 2-5) are a necessary requirement for the formation of inflated sheet lobes. In both Columbia River Flood Basalts and Deccan Traps, the presence of multiple vesicle horizons in a single flow lobe may be evidence of this cyclic inflation (Hon, Kauahikaua, Denlinger, & Mackay, 1994; Cashman & Kauahikaua, 1997).

One potential challenge with using constraints on the effusion rate at the vent location to the estimate the duration of a CFB flow field is that each flow field may be fed by a long fissure system (e.g., $\sim$ 150 km for the CRB Rosa flow Self et al., 1998). If this fissure is active along a significant fraction of its length, the total time-period for a CFB emplacement will be short despite the restricted effusion rate. This hypothesis can be tested by using the thickness of a flow lobe's upper vesicular crust to constrain the duration of active inflation of the thickest flow lobe in a flow field. For the $\sim$ 1300 km^3 Roza flow field in the CRB, Thordarson and Self (1998) estimated a minimum duration of 5 to 14 years (using the (Hon et al., 1994) $\sqrt{t}$ scaling for the thickness of the flow's upper crust). Using a similar method, Vye-Brown, Self, and Barry (2013) estimated similar minimum emplacement durations for other CRB flow fields: Palouse Falls (233 km^3, 19.3 years), Ginkgo (1570 km^3, 8.3 years), and Sand Hollow (2,660 km^3,16.9 years). These estimates are minimum estimates for the duration of a CFB field since they assume that the thickest flow was inflating throughout an eruption. If instead, different lobes undergo inflation at different times and/or have some time-hiatus between them, the total duration of a CFB field would be longer (order centuries) (See Vye-Brown, Self, and Barry (2013) for a more detailed discussion of other model uncertainties). Thus, we can conclude that individual CFB fields are emplaced over a long time-period ($\sim$ centuries) by sustained eruptions.

Another dataset supporting a multi-year to decadal-scale of CFB field emplacement is the low and high-temperature thermo-chronology around CRB dike segments ($\sim$ 1 km long) from the Chief Joseph dike Swarm (H. L. Petcovic & Dufek, 2005; Karlstrom, Murray, & Reiners, 2019). The active duration of the $\sim$ 10 m thick Maxwell dike is constrained to be 1.4–5.4

years (H. L. Petcovic & Dufek, 2005; Karlstrom et al., 2019) while the $\sim$ 10 m Lee dike was active for 1.7 - 4.1 years with a long flow unsteadiness scale of 3.9 - 11.3 years (Karlstrom et al., 2019). Although more observations are needed to assess how representative these values are for other CRB dikes, as well as DT dikes, the general lack of melt-back in CRB dike swarm (Grunder & Taubeneck, 1997) suggest that analogous to Laki 1783 eruption, different parts of the fissure may have been active at different times during an eruption (Thordarson & Self, 1993). Summarizing the various observations, we conclude the CFB flow fields were most likely emplaced over a decade to centuries with eruption rates comparable to the peak Laki 1783 eruption rate.

4.3.6 Geochemical characteristics - Implications for magmatic system

Since the Deccan magmas underwent a complex sequence involving fractionation (potentially at multiple depths), assimilation of multiple components, and periodic replenishment of parental magmas before surface eruption, it is difficult to confidently ascertain the volume of cumulate material or their precise P-T histories and storage locations (See discussion in O'Hara and Herzberg (2002) and references therein). However, we can use stratigraphic changes in major, minor, and isotopic compositions to constrain the nature of magmatic plumbing structure, especially whether an open system with constant recharge is required.

With regards to Deccan magma across all subprovinces, there is a general consensus that the AFC processes occur first in a lower crust reservoir(s) followed by shallow ($<$ 2 kbar) fractionation and mixing (and in some cases assimilation) in upper crustal magma reservoir(s) (K. Cox & Devey, 1987; Devey & Cox, 1987; J. J. Mahoney, 1988; Hawkesworth, Kempton, Rogers, Ellam, & Van Calsteren, 1990; Lightfoot, Hawkesworth, et al., 1990; Z. Peng et al., 1994; J. Mahoney et al., 2000; G. Sen, 2001; Chatterjee & Bhattacharji, 2008; H. C. Sheth & Melluso, 2008; Natali et al., 2017). However, within with the general framework, is the magmatic plumbing system primarily a closed system with pulsed inputs of melts into the upper crustal system followed by closed system fractionation and assimilation?

4.3.6.1 Open System behavior

Firstly, many geochemical formations (e.g., Ambenali, Beane et al., 1986) as well various individual sections in other DT provinces (e.g., Malwa Plateau, Haase et al., 2019) typically have a restricted major and minor element composition. This observation can be explained by either of the two-model end-members: a quasi-steady state open magmatic system with reservoirs undergoing Recharge, Tapping via eruptions, Fractionation, and Assimilation (RTF, O'Hara & Mathews, 1981; Leeman & Hawkesworth, 1986; K. Cox, 1988; Arndt et al., 1993), or a thermally buffered, quasi-closed magma reservoir undergoing minimal chemical evolution (as suggested in Black & Manga, 2017). Similarly, continuous stratigraphic changes (e.g., from Poladpur to Ambenali) in ratios between incompatible elements (e.g., Ba and Zr) and isotopes can be explained by either of the scenarios since the observation-only requires some

form of mixing between different magma bodies (K. Cox & Hawkesworth, 1985). However, if the system undergoes a sudden change in lava composition (e.g., Bushe to Poladpur), a model with large lower and upper crustal reservoirs will have challenges since it is difficult to change bulk compositions with a large volume of pre-existing melt without drastic amounts of contamination. Instead, it is easier to explain these transitions in a magmatic system with multiple chambers coupled with changes in lower crustal magma compositions (K. Cox & Hawkesworth, 1985).

Finally, the Black and Manga (2017) style model predicts an increasing contribution from crustal assimilation with increasing thermal maturity of the upper crust. In contrast, the least contaminated DT lava flows are the Ambenali formation, which erupts towards the end of the sequence. We note that over time, the increasing size of the crustal magma reservoir due to the addition of lower crustal melt (Black & Manga, 2017) will partly modulating this effect. However, without quantitative calculations, it is unclear how much this will buffer compositions. For the DT, multiple authors have proposed that minimal crustal assimilation of the Ambenali flows (even though they have undergone extensive fractionation) is a consequence of geochemical buffering due to plating of the reservoir by previous solidification zones (e.g., J. J. Mahoney, 1988; Devey & Cox, 1987). If this process were to be relevant for the large magma reservoir also, it could explain the Ambenali formation composition within that model context. However, it will also further increase the hiatus time between eruptive episodes since the crustal volatile source will be removed unless the parental magma has sufficient volatile content to be buoyant.

4.3.6.2 Intra-geochemical formation variability

Another avenue to distinguish among the two model end-members is to use the small but resolvable geochemical (e.g., Sr isotopes, Ni and Ti, Cr and Zr, Mg and Fe; J. J. Mahoney, 1988, and references therein) and petrological variations (e.g., phenocryst fraction and modal percentages of ol, plag, and cpx; Beane et al., 1986; Pattanayak & Shrivastava, 1999; G. Sen, 2001) within a geochemical formation. As illustrated by almost all sections in WG, the stratigraphic variation in a formation is not smooth even after accounting for possible biases due to surface alteration and lava flow fractionation (J. J. Mahoney, 1988; K. Cox & Hawkesworth, 1985). In Figure 4.4, we show a few representative sections from the Deccan Traps illustrating this behavior. In Figure 4.4a, we show the $^{87}Sr/^{86}Sr$ variation for a composite WG section with geochemical formations from Neral to Mahabaleshwar as well as an inset with just Ambenali, Mahabaleshwar, Panhala formations (Beane et al., 1986; Lightfoot & Hawkesworth, 1988). Figure 4.4b shows the dataset for Zr in a 480 m section spanning almost the whole Ambenali Formation section (the Torna hill-fort Devey & Lightfoot, 1986). Both these datasets clearly illustrate quasi-oscillatory variations within a single geochemical formation.

As another example, we show the geochemical data for the 282 m Bhir section located about 300 km east of WGE in the Central Deccan province Talusani (2010) in Figure 4.4c.

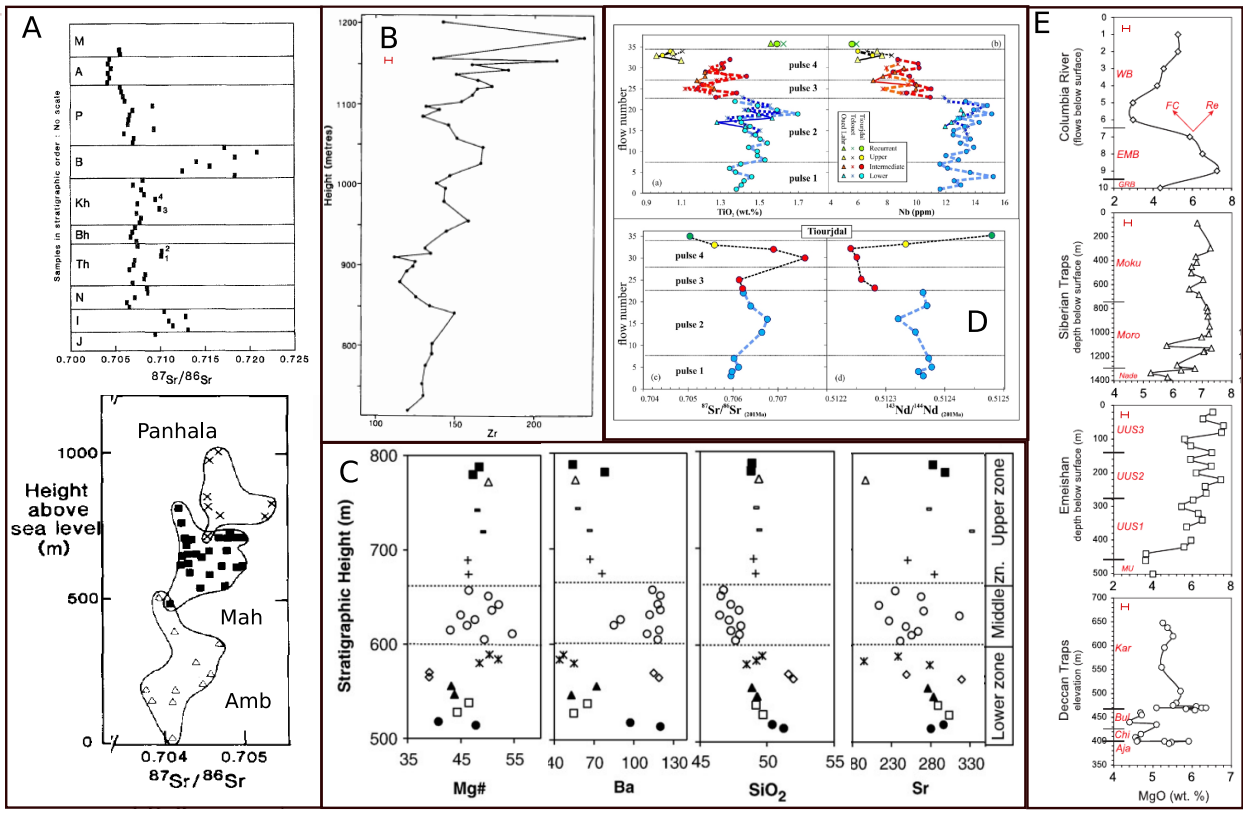

Based on the trace element ratios (e.g., Zr/Nb, Ba/Y) most diagnostic of different WG geochemical formations as well as regional stratigraphy (Jay & Widdowson, 2008), the Bhir section lavas have Ambenali-type geochemistry (Talusani, 2010). However, within this section (10 flows), the middle flow is alkalic with a very different composition compared to the other tholeiitic basalt flows in the section. Additionally, the Bhir basalts show a wide range of chemical compositions for incompatible elements (e.g., Nb, Zr, Y, and Rare Earth Elements) between individual flows as well as within a single flow (e.g., the middle alkalic flow). Since the difference between alkalic and tholeiitic basalt is explained as a different degree of partial melt in the mantle, the presence of the flow in the same geochemical formation is indicative of a magmatic plumbing system that does not homogenize the melt in a large magma reservoir (Talusani, 2010).

We show another Central Deccan Trap stratigraphic section in Figure 4.4e (lowermost panel) where the local geochemical formations are correlative to the Ambenali and Poladpur formations (K. V. Kumar et al., 2010). Similar to the other examples, there is clear evidence of oscillations in MgO concentration within the same formation. We would emphasize that these examples are not unique and are instead representative of a large number of DT studies

Figure 4.4 *(previous page)*: Representative sections showing geochemical variations within a stratigraphic section for Deccan Traps and some other continental flood basalts. A) $^{87}Sr/^{86}Sr$ variation for a composite WG section with geochemical formations from Neral to Mahabaleshwa(from Beane et al., 1986) with a zoomed inset showing the variations for the Ambenali, Mahabaleshwar, Panhala formations (from Lightfoot & Hawkesworth, 1988). B) Variation in Zr in a 480 m section spanning almost the whole Ambenali Formation section (the Torna hill-fort, Devey and Lightfoot (1986); K. Cox (1988)). C) Geochemical data from the Bhir section located about 300 km east of WGE in the Central Deccan province (from Talusani, 2010) with alkalic middle flow (this section has been correlated with the Ambenali formation). D) Geochemical datasets from the CAMP sections from Morrocco. The Nb (ppm), TiO_2 (wt %) data is shown for three sections from the Central High Atlas Mountains - Tiourjdal, Telouet, Oued Lahr while the isotopic dataset are from Tiourjdal section only. The Figure also shows the 4 eruptive pulses defined based on classical Directional Group analysis by Knight et al. (2004)(from Marzoli et al., 2019) E) MgO (wt %) for stratigraphic sections for stratigraphic sections for various flood basalts (from Yu et al., 2015). The dataset for Columbia River basalt include Eckler Mountain Basalt (EMB) and Wanapum Basalt (WB) flows. The Deccan Traps section is from K. V. Kumar et al. (2010) showing the Ajanta (Aja), Buldhana (Bul), Chikhli (Chi) formations (correlative to the Poladpur formation), and Karanja (Kar) formation (correlative to the Ambenali formation). The Yangliuping basaltic sequence from Emeishan large igneous province has been divided into four units by Song et al. (2006). Finally, the Siberian Traps section consists of three formations Mokulaevky (Moku), Morongovsky (Moro), and Nadezhdinsky (Nade) (Lightfoot, Hawkesworth, et al., 1990). The FC and Re arrows indicate the effect of Fractional Crystallization and magma recharge in an REAFC (REcharge Assimilation Fractional Crystallization) model. The typical error bar for each panel is of the size of the symbol unless otherwise specified. All of these datasets clearly illustrate quasi-oscillatory variations within a single geochemical formation across CFBs.

both within WGE as well as other subprovinces (e.g., K. Cox & Hawkesworth, 1985; Devey & Cox, 1987; Devey & Lightfoot, 1986; Lightfoot, Hawkesworth, et al., 1990; Z. Peng et al., 1998; J. Mahoney et al., 2000; Sengupta & Ray, 2011; S. K. Bhattacharya, Ma, & Matsuhisa, 2013; Z. X. Peng et al., 2014; Haase et al., 2019). This conclusion is also illustrated by the fact that each geochemical formation typically traces out an extended region (much larger than analytical uncertainty) in the Sr, Pb, and Nd isotope parameter space instead of a single point (e.g., Vanderkluysen et al., 2011).

Our conclusion of continuous magma recharge and mixing during the eruption of a geochemical formation is further supported by the common occurrence of various zoning patterns (normal, oscillatory, reverse, complex) in plagioclase and clinopyroxenes phenocrysts in lavas. These zoning patterns are indicative quasi-continuous mixing between primitive

and evolved magmas (Lightfoot, Hawkesworth, & Sethna, 1987; Pattanayak & Shrivastava, 1999; N. R. Bondre et al., 2004; Talusani, 2010). Similar to other geochemical variations, both the type of zoning patterns as well as phenocryst mineral composition (e.g., anorthite content of plagioclase) show clear changes in a stratigraphic section but without any smooth pattern (Lightfoot, Hawkesworth, et al., 1990).

4.3.6.3 Geochemical variability - Model

K. Cox (1988) proposed that these kinds of variations can be explained using a RTF-type magma reservoir with stochastic melt influx (z, in units of initial magma reservoir mass/model cycle), eruption rate(y, in units of magma reservoir mass/model cycle), and crystallization rates (x, in units of magma reservoir mass/model cycle) around the steady-state values. K. Cox (1988) showed that a WG Ambenali section (Figure 4.4c) could be statistically reproduced by the model with x/y $\sim$ 1, z random chosen between 0-5, and x $\sim$ 0.05 along with a slow increase in x up-section (to produce the long term trend). Each lava flow is considered the output of one model cycle and the lava's trace element composition oscillates around a steady-state value. Although this is a reasonable model to explain the data, it requires that a significant mass influx (up to five times the original magma reservoir mass) into the system throughout the eruption of a geochemical formation (i.e. an open system). This is extremely difficult to do for a large magma reservoir, especially the upper crustal reservoir where the expected influx is expected to be large (z $\sim$ 1-3) but only occur a few times at most during the eruption of a geochemical cycle (Black & Manga, 2017).

In order to explore more range of values for z (and corresponding values of x and y) can explain the geochemical datasets, we use a modified version of the Recharge-Eruption-Fractional crystallization model (ignoring assimilation to be consistent with K. Cox, 1988). Following C.-T. A. Lee et al. (2014); Yu et al. (2015), and K. Cox (1988), the rate of change of the total mass M and elemental mass m_{ch} of a magma reservoir per eruptive cycle (dN_c) is :

$$\frac{dM}{dN_c} = \frac{dM_{re}}{dN_c} + \frac{dM_e}{dN_c} + \frac{dM_{cc}}{dN_c} + \frac{dM_x}{dN_c} \tag{4.1}$$

$$dm_{ch} = dM_x DC_{ch} + dM_e C_{ch} + dM_{cc} C_{cc} + dM_{re} C_{re} \tag{4.2}$$

$$\frac{dM_{re}}{dN_c} = z * M_{initial} \tag{4.3}$$

$$\frac{dM_e}{dN_c} = y * M \tag{4.4}$$

$$\frac{dM_x}{dN_c} = x * M \tag{4.5}$$

Here, the magma reservoir mass changes due to eruption (dM_e, negative), assimilation (dM_{cc}, positive), recharge (dM_{re}, positive), and fractional crystallization (dM_x, negative) during an eruptive cycle (dN_c). For the elemental mass balance term, C_{ch} is the element's concentration in the magma reservoir, C_{cc} is the wall-rock composition, and C_{re} is the recharge

composition. D is the equilibrium partition coefficient between crystals and melt during fractional crystallization. For our calculations here, we set $dM_{cc} = 0$ to prevent crustal assimilation and x/y =1. Following Yu et al. (2015) and K. Cox (1988), we set bulk partition coefficients for Mg and Zr as 2 and 0.001 respectively. Since the actual composition of the magma recharge is not known, we assume a primitive magma composition with MgO = 9 wt % and Zr = 85 ppm (see K. Cox, 1988; J. J. Mahoney, 1988). We would emphasize our focus with these calculations is to look at broad features and hence the exact parameter choices are not important. For the starting magma composition in the magma reservoir, we set MgO = 5.8 wt % and Zr = 160 ppm, a range typical for the Ambenali formation (Beane et al., 1986; K. Cox, 1988). We randomly choose the value of x,y,and z between 0 and the maximal values x^m,y^m,and z^m.

In Figure 4.5, we show the results of the calculations for three sets of values : $x^m = y^m$: 0.03 (red), 0.02 (black), 0.01 (blue), and z^m : 0.06 (red), 0.04 (black), 0.02 (blue). The values have been chosen such that the magma reservoir is in quasi-steady state over 100s of eruptive cycles. The key result from this analysis is that sufficiently large values of z^m (and corresponding x^m and y^m) $\sim$ 0.06 are required to produce the amplitude of variations in Figure 4.4b and 4.4e (ignoring any long term trends). Although the precise threshold value will be dependent on the exact parameter choice for recharge magma, the result that recharge must be at least a few percentages of the reservoir size is a robust conclusion. In Figure 4.6A and 4.6B, we show model results where we have set either recharge (z, Figure 4.6A) or crystallization (x, Figure 4.6B) to be zero. We set the other parameters at $x^m = y^m = 0.03$ and $z^m = 0.06$ with the three lines in Figure 4.6A and 4.6B showing three model realizations each with the same input parameters. These results clearly illustrate that without all three processes in REFC, we do not get the oscillatory pattern of geochemical variation but instead only a persistent trend.

Based on the model results, there are two primary requirements for explaining the observations: a) a combination of fractional crystallization, recharge, and eruption together in a RTF/REAFC (or a variant of these, see O'Hara & Herzberg, 2002) type magma reservoir, b) a magma recharge volume at least a few percent of the reservoir mass.

4.3.6.4 Intra-Flow compositional variations

Although typically individual lava flows in a CFB are considered to be geochemical homogeneous, a few studies have illustrated that this may not always be the case (e.g., Philpotts, 1998; S. P. Reidel, 2005, 1998; N. R. Bondre & Hart, 2008); Passmore, Maclennan, Fitton, and Thordarson (2012) for Laki 1783 eruption). The results of Vye-Brown, Gannoun, Barry, Self, and Burton (2013) and Vye-Brown, Barry, and Self (2018) provide especially clear examples of the geochemical variations in products of a single eruption in the Columbia River Basalts.

Through the detailed mapping of the Sand Hollow ($\sim$ 2660 km^3) and Palouse Falls ($\sim$ 233 km^3) flow fields (Vye-Brown, Self, & Barry, 2013), these studies ensured that any observed

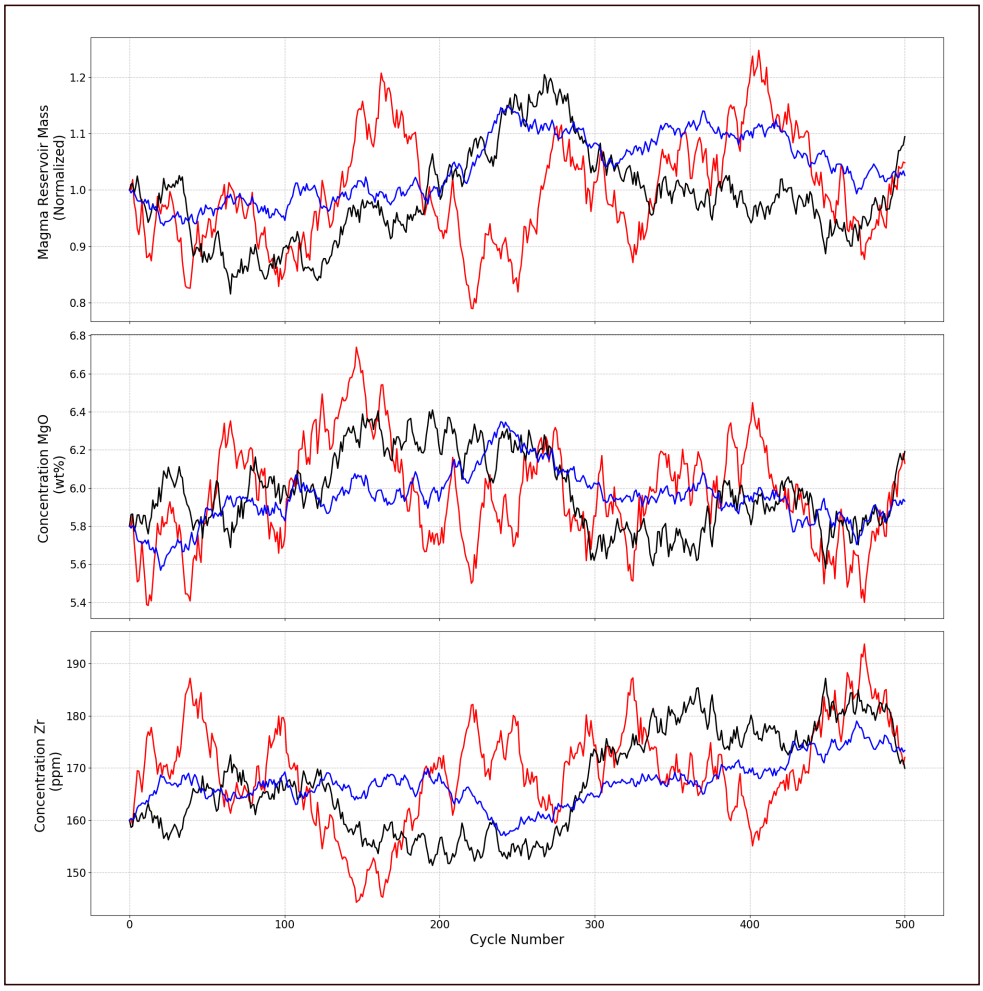

Figure 4.5: Results of REAFC model for Normalized magma reservoir mass, MgO (wt %), and Zr concentration (ppm). Calculations for three sets of values : $x^m = y^m$: 0.03 (red), 0.02 (black), 0.01 (blue), and z^m : 0.06 (red), 0.04 (black), 0.02 (blue) with stochastic variation around the mean value.

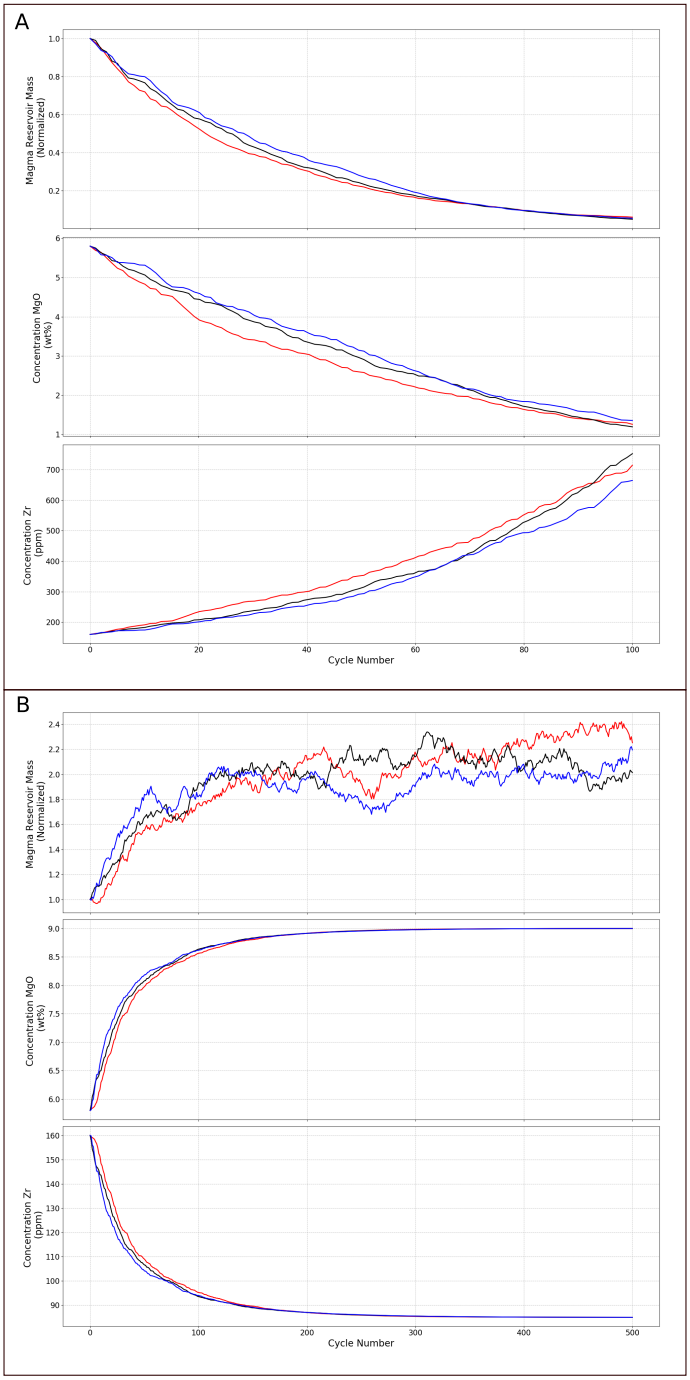
A
Magma Reservoir Mass (Normalized)
Concentration MgO (wt%)
Concentration Zr (ppm)
Cycle Number
B
Magma Reservoir Mass (Normalized)
Concentration MgO (wt%)
Concentration Zr (ppm)
Cycle Number

Figure 4.6

Figure 4.6 *(previous page)*: Results of REAFC model for Normalized magma reservoir mass, MgO (wt %), and Zr concentration (ppm). A) Calculations with no recharge (z = 0) B) Calculations with no crystallization (x = 0). We set the other parameters at $x^m = y^m = 0.03$ and $z^m = 0.06$ with the three lines each panel showing three model realizations each with the same input parameters.

variations were within a single eruption unit and not due to stratigraphic errors. In both cases (Sand Hallow and Palouse Falls), there is clear geochemical heterogeneity (major and minor elements) within both a single flow lobe, as well as laterally between different flow lobes of a single flow field. Based on the pattern of change across multiple elements, these studies concluded that either chemical weathering or post-emplacement fractionation could not have produced the observed variations. Instead, the intra-lobe and inter-lobe variations are indicative of heterogeneity within the magmatic system feeding the eruption. This conclusion is further supported by variations in $^{187}Os/^{188}Os$ isotopes across a 35 m Sand Hallow flow lobe that require different amounts of crustal assimilation in the erupted melt (Vye-Brown, Gannoun, et al., 2013). These observations are inconsistent with a compositionally homogeneous magma reservoir feeding an individual eruptive episode (See Section 4.2.2.3). Instead, each eruptive episode is likely sourced from a magmatic system consists of a network of magma reservoirs with more primitive compositions over time (potentially from deeper magma bodies).

Nevertheless, with the limited number of studies at present, it is unclear how common these intra-flow variations are for CFBs in general. In particular, no systematic stratigraphically controlled analysis of intra-flow variations has been done for lava flows in the Deccan Traps. Nevertheless, there are some potential examples from DT suggestive of geochemical differences within a single eruptive unit. For instance, K. Cox and Hawkesworth (1985) noted that the Kelghar Mafic Unit in the Mahabaleshwar Formation is restricted to only a single WG section. However, less mafic, but geochemically related Mahabaleshwar flows, are present at the same stratigraphic height in sections less than 40 km. Thus, one potential explanation for the Kelghar Mafic Unit is that it represents a small magma batch within the eruption of a larger, spatially extensive flow field. A similar interpretation has also been proposed for the DT lava flows with a large concentrations of multi-cm long plagioclase phenocrysts - giant phenocryst basalts (GPBs P. Hooper, 1988b; Higgins & Chandrasekharam, 2007b; H. Sheth, 2016). These flows occur at multiple stratigraphic heights within the WG sections though they are more common during the Kalsubai subgroup (e.g., Beane et al., 1986). They are also found in some of the other Deccan subprovinces (e.g., Talusani, 2012; Alexander & Purohit, 2019). Since GPBs are sometimes not continuous within a single physical eruptive unit, this suggests that is intra-flow variation within a single eruptive epsiode (Paul Renne and Steve Self, personal comm.).

Other potential evidence for geochemical variations within an eruptive event comes from

compositional (including isotopic) differences along a single dike (N. Bondre, Hart, & Sheth, 2006; R. Ray, Sheth, & Mallik, 2007; H. C. Sheth et al., 2009, 2013; Vanderkluysen et al., 2011; Cucciniello et al., 2015; H. Sheth et al., 2018). Additionally, closely spaced dikes in a dike swarm don't always have the same chemical compositions (N. Bondre et al., 2006; H. Sheth, Vanderkluysen, Demonterova, Ivanov, & Savatenkov, 2019).

Finally, a substantial fraction of dikes in the Deccan Traps have multiple columnar jointed layers due to several magma injections (H. C. Sheth & Cañón-Tapia, 2015, and references therein). Frequently, each of these layers has a different geochemical composition indicative of a different batch of magma (H. C. Sheth & Cañón-Tapia, 2015; Cucciniello et al., 2015; Gadgil, Viegas, & Iyer, 2019). A typical time-period for the emplacement of these composite dikes can be estimated based on the requirement that dike needs to cool sufficiently between each injection to form and preserve layered columnar joints. Using this principle, H. C. Sheth and Cañón-Tapia (2015) estimated that a multiple large dike (20-m-thick with ten columnar rows) would be emplaced over a minimum of several years and more likely up to a 100 years after accounting for latent heat of crystallization as well as the increasing country-rock temperature after emplacement of each dike segment (Evelyne, Annelore, François, & Sébastien, 2018). We readily acknowledge that there are counter-examples to this with DT dikes that are compositionally homogeneous over 10s of km (e.g., Vanderkluysen et al. (2011), see Kalsbeek and Taylor (1986); R. E. Ernst (2014); Buchan and Ernst (2019) for examples from other CFBs) and that some of the compositional differences may be due to dike-wall rock interactions. With existing literature, we cannot assess how ubiquitous intra-dike geochemical variations are. Still, observations from even a few dikes, along with physical evidence for multiple injections, suggests that a homogeneous, well-mixed magma reservoir does not always feed individual eruptive episodes. Additionally, the presence of multiple dikes in Deccan Traps hints at a long duration ($\sim$ 100 years) for each eruptive episode consistent with other datasets described in this section.

4.3.6.5 Geochemical variability - Implications for magmatic architecture

Considering the observations and the model results, we contend that it is very difficult to explain these with a large magma reservoir end-member. Firstly, this model predicts that a single geochemical formation with 10s of eruptive episodes is erupted very rapidly (order 100s to a few 1000 yrs, Black & Manga, 2017). Hence, there is generally not enough time-period between individual eruptive episodes for significant crystal fractionation or assimilation to change magma composition based on diffusion and crystal growth time-scales (Borges, Sen, Hart, Wolff, & Chandrasekharam, 2014; H. Sheth, 2016). The large compositional inertia of the system due to the large magma volume makes this even challenging. Secondly, the oscillatory stratigraphic, geochemical changes require an influx of some primitive melt input along with fractionation based on our calculations. The recharge into the crustal magma reservoir needs to quasi-continuous, which is contrary to the model results for a large magma reservoir model wherein there are generally very large but very sparse magma inputs for upper crustal reservoirs (Black & Manga, 2017, See description in Section 4.2.2.2, 4.2.2.3).

The observations are best explained by a smaller (order 5 %) continuous melt input into the magma reservoir (s). Thus, we conclude that the pattern of geochemical variations strongly suggests that the large magma reservoir end-member is not realistic. Instead, these variations are a natural outcome in a RTF/REAFC model with one or multiple magma reservoirs (K. Cox & Hawkesworth, 1985; Yu et al., 2015).

4.3.6.6 Observations from other CFBs

The stratigraphic section in many other CFBs shows the same characteristic geochemical variability features as described above for DT (inter and intra-geochemical formation variations). In Figure 4.4d and 4e, we show a few example cases for the Central Atlantic Magmatic Province (Figure 4.4d, CAMP Marzoli et al., 2019), Siberian Traps (Lightfoot, Naldrett, Gorbachev, Doherty, & Fedorenko, 1990), Columbia River Basalts (P. Hooper, 1988a; P. R. Hooper, 2000), and Emeishan CFB (all Figure 4.4e, Song et al., 2006). All of these cases have the same oscillatory features within a single geochemical formation as in DT. Many similar examples have been described for most CFBs: CAMP (e.g., Tegner et al., 2019; Marzoli et al., 2019, and references therein) , Karoo-Ferrar CFB (Fleming, Elliot, Jones, Bowman, & Siders, 1992; D. Elliot, Fleming, Haban, & Siders, 1995; Fleming, 1995; J. Marsh, Hooper, Rehacek, Duncan, & Duncan, 1997; Luttinen & Furnes, 2000), Siberian Traps (Lightfoot, Naldrett, et al., 1990; Fedorenko et al., 1996; Reichow, Saunders, White, Al'Mukhamedov, & Medvedev, 2005; N. A. Krivolutskaya & Sobolev, 2016; N. Krivolutskaya et al., 2018; N. A. Krivolutskaya et al., 2018), North Atlantic Magmatic Province (NAMP, Andreasen, Peate, & Brooks, 2004; Peate, Barker, Riishuus, & Andreasen, 2008; L. M. Larsen & Pedersen, 2009; Millett, Hole, Jolley, Schofield, & Campbell, 2016; Millett, Hole, Jolley, & Passey, 2017), Parana-Etendeka (Peate & Hawkesworth, 1996; Machado et al., 2018), Ethiopian Traps (Kieffer et al., 2004; S. Krans, Rooney, Kappelman, Yirgu, & Ayalew, 2018), and Columbia River Basalts (CRB, Brueseke, Heizler, Hart, & Mertzman, 2007; Wolff & Ramos, 2013; N. Moore, Grunder, & Bohrson, 2018). The CAMP section shown in Figure 4.4d is particularly illustrative since the stratigraphic section is divided into four individual pulses based on paleo-secular variation analysis each of which has been interpreted to have been erupted within a few hundred years (Knight et al., 2004; Font et al., 2011; Marzoli et al., 2019, , although see the discussion in Section 4.3.3). Nevertheless, the individual lava flows in a "pulse" have different major and minor elements, as well as Sr and Nd isotopes with the same quasi-oscillatory oscillations as the DT examples. These variations are characteristic of continuous magma mixing, recharge, assimilation, and fractionation (Section 4.3.6.3) and are hence inconsistent with expectations from a single large homogeneous upper crustal magma reservoir (See Section 4.2.2.2, 4.3.6.3). We readily acknowledge that precise REAFC characteristics (w.r.t values of x,y,z) for each CFB province are different and a careful examination of each CFB, and the corresponding magmatic architecture constraints, is beyond the scope of this study. Nevertheless, the general prevalence of flow-by-flow geochemical variations is a robust feature.

In many CFBs, a significant component of the magmatic system is the shallow ($<$ 4

km, See Magee, Ernst, et al., 2019; Hoggett, 2019; S. M. Jones et al., 2019) sill complexes emplaced in cratonic and passive margin sedimentary basins. The typical sill radius, area, and thickness in these complex as illustrated by a dataset from NAMP are 1-7.5 km, 1-100 km^2, and 100-500 m respectively (S. M. Jones et al., 2019; Magee et al., 2018; Magee, Ernst, et al., 2019). Nevertheless, the volumes of some of the largest sills can be similar to a single DT eruptive episode e.g., CAMP Palisades Sill (1500- 5000 km^3, Husch, 1990), Karoo-Ferrar associated Peneplain Sill (4750 km^3, Gunn & Warren, 1962), and Basement Sill in McMurdo Dry Valleys (1050 km^3, B. Marsh, 2004; Petford & Mirhadizadeh, 2017), Karoo Basin sills (upto 3000 km^3, H. Svensen et al., 2012), and the Karoo-Ferrar Dufek-Forrestal intrusions (10,200-11,880 km^3, Ferris, Johnson, & Storey, 1998). Since most sill complexes have been discovered and characterized primarily through seismic datasets (with some boreholes) (e.g., Magee et al., 2018; Galland et al., 2018; Magee, Ernst, et al., 2019), any geochemical variation between individual sills is difficult to ascertain.

The one exception to this is the Karoo Basin where a large number of sills are exposed and accessible. Through careful sampling of 5 sills and a dike over 125 km^2 area (Golden Valley Sill Complex, Karoo basin, South Africa), Galerne, Neumann, and Planke (2008); Galerne, Galland, Neumann, and Planke (2011) found that each of the sill, barring two, have different geochemical signatures and hence were fed by a different magma batch. This conclusion is supported by the few studies of larger sills which show evidence for multiple magma injections based on stratigraphic geochemical and petrological analysis e.g., the Beacon Sill (M. Zieg & Marsh, 2012), Palisades Sill (Husch, 1990; Gorring & Naslund, 1995), the Basement Sill (B. D. Marsh, 2004; Bédard, Marsh, Hersum, Naslund, & Mukasa, 2007), the Doros Complex (T. Owen-Smith & Ashwal, 2015), and the Black Sturgeon Sill (M. J. Zieg & Wallrich, 2018). Thus, these results suggest that large sills and sill complexes were emplaced as multiple magma batches over time (potentially within 10-100s of years to prevent sill solidification) with some of the magma injections having different compositions. We contend that it is difficult to get these eruption characteristics if the magma is sourced from a single, large well mixed magma reservoir especially considering the eruption rate results described later in this study.

4.3.7 Magmatic Architecture observations - Deccan Traps

In CFB provinces, the primary mechanism for magma transport from crustal reservoirs to the surface is a combination of mafic dike swarms, sills - both deep crustal sills (Wrona et al., 2019; Buntin et al., 2019) as well as shallow sill complexes (Maccaferri et al., 2011; Magee, Ernst, et al., 2019). Since the Deccan Traps were emplaced primarily atop Archean cratons, there are no large scale sill complexes hosted within sedimentary basins like many other CFBs e.g., Karoo-Ferrar province, Siberian Traps, North Atlantic Magmatic Province, and Central Atlantic Magmatic Province (See H. Svensen et al., 2018; Magee, Ernst, et al., 2019, and references therein). The sills in Deccan are generally restricted to the outlying regions of the province with sedimentary basins e.g., Jurassic sedimentary rocks in Kutchh (Biswas,

1982, 1987; Karkare & Srivastava, 1990; Duraiswami et al., 2008; Karmalkar et al., 2016) and Gondwana sediments in Central Indian Satpura Range (Crookshank, 1936; Sengupta & Ray, 2011). In addition, a small lopolith is emplaced in an intertrappean at Amboli hill, Mumbai (Tolia & Sethna, 1990), after the main DT eruptive phase (See discussion in Section 4.3.3.2 about Mumbai section).

The saucer-shaped Mahad sill (Duraiswami & Shaikh, 2013) in the south-western Deccan Traps is one of the few DT sills within the main DT section along with the olivine-gabbro Khopoli intrusion (Cucciniello et al., 2014). The Mahad sill, the larger of the two, is 7.1-km x 5.3 km long and is intruded into a Bushe Formation flow. Since the sill is geochemically associated with either the Poladpur- or Ambenali Formation, the sill was emplaced at < 1 km depth from the surface (Duraiswami & Shaikh, 2013). Based on existing work, none of these sills feed subaerial lava flows. The only known basaltic sill in DT that may have been responsible for magma transport to an overlying lava flow is the ~ 200 m Chakhla-Delakhari Intrusive Complex (CDIC) in the Central Deccan region (Crookshank, 1936; Shrivastava, MUKTA, & RAJU, 2008; H. C. Sheth et al., 2009). CDIC is the largest DT basaltic sill complex with an area of about 150 km^2 and is emplaced primarily in the Gondwana sandstone. The complex stratigraphic shape, spatially variable thickness, the mineralogical as well as chemical heterogeneity, and textural features of the CDIC strongly suggest that it is composed of multiple individual intrusions with different compositions (Crookshank, 1936; H. C. Sheth et al., 2009). Finally, We note that there are a number of small primarily alkaline intrusive complexes in the Saurashtra and Malwa Plateau subprovinces of DT such as Girnar, Osham, Barda (dominantly granophyre), Alech hills (dominantly rhyolite) of Saurashtra as well as the Pavagadh and the Phenai-mata igneous complexes in the Narmada-Tapti Tectonic Zone (Auden, 1949; Greenough, Hari, Chatterjee, & Santosh, 1998; B. Singh, Rao, Prajapati, & Swarnapriya, 2014a; Cucciniello et al., 2019). Although a number of these intrusions (e.g., Phenai-mata and Pavagadh) are associated with local tholeiitic and alkaline magmatism, there is as yet no geochemical, geochronological, or volcanological evidence suggesting that these intrusive complexes fed large DT lava flow units, especially any of the main phase WG flows.

The large Deccan Traps eruptive episodes are instead hypothesized to have been fed by tholeiitic dike swarms (Vanderkluysen et al., 2011). The three main DT dike swarms are the Narmada-Tapi dike swarm extending across from Mandla Lobe region to Saurashtra (Sant & Karanth, 1990; Bhattacharji, Chatterjee, Wampler, Nayak, & Deshmukh, 1996; Melluso, Sethna, Morra, Khateeb, & Javeri, 1999; R. Ray et al., 2007; H. C. Sheth et al., 2013; Cucciniello et al., 2015; H. Sheth et al., 2019), the Western Ghats Coastal dike swarm (Widdowson et al., 2000; P. Hooper et al., 2010; H. C. Sheth et al., 2014), and the Nasik-Pune dike swarm located to the east of the WGE (N. Bondre et al., 2006; Vanderkluysen et al., 2011). Based on similar major and minor element geochemistry as well as Pb-Nd-Sr isotopes, the three major dike swarms have been correlated with individual geochemical formations across the Deccan Traps (e.g., Vanderkluysen et al., 2011, and references therein). Vanderkluysen et al. (2011) concluded that lower and middle subgroups were most likely fed

by the oriented Narmada-Tapi and Coastal dike swarms while the Upper subgroup lavas were predominantly fed by Nasik-Pune dike swarm. There is no concensus if individual eruptive episodes were fed by a single dike (with sequentially active fissure segments like 1783 Laki eruption, Thordarson & Self, 1993), a set of dikes fed from the same magmatic system, or eruptive centers 100s of km apart that all feed the same flow field (Self et al., 1998; Vanderkluysen et al., 2011; Óskarsson & Riishuus, 2014; Kale et al., 2019). Without a detailed field analysis of individual flow fields along with complementary geochemical and isotopic analyses, each of these models may be applicable for Deccan eruptive episodes with potentially different styles for different DT regions, subprovinces, and/or geochemical formations.

Each of the three dike swarms is typically composed of a number of sub-swarms of 100s of dike segments each (Vanderkluysen et al., 2011; H. C. Sheth & Cañón-Tapia, 2015) with a wide range of thickness from 1 to 62 m (median of $\sim$ 10-20 m for different subswarms) and lengths (1 km to 79 km R. Ray et al., 2007; N. Bondre et al., 2006; H. Sheth et al., 2019) except the shorter ($<$ 200 m) and thinner (average $\sim$ 6 m) Goa dike swarm (Gadgil et al., 2019). A significant fraction of these dikes show evidence of multiple magma injections in the form of multiple columnar-jointed rows (2-5 injections) (See discussion in H. C. Sheth & Cañón-Tapia, 2015). Due to surface erosion, the dike tops in DT are typically truncated. Consequently, it is unclear if the dikes terminated in the crust/lava flow pile or if they fed lava flows directly. In typical shield volcanoes, only 30 % of the dikes are feeders (Galindo & Gudmundsson, 2012). Even if the number is higher for DTs (e.g., 50-50 ratio, H. C. Sheth & Cañón-Tapia, 2015), a large number of observed dike segments (e.g., Misra et al., 2014; Misra & Mukherjee, 2017) suggests magma reservoir failed even more frequently to form dykes (Kavanagh, 2018) than the rate of eruptive episodes. This observation makes it even more difficult for a single large magma reservoir to feed the surface eruptions given the various constraints on eruptive tempo described above (See Section 4.2.2.3).

4.3.8 Deccan Traps Intrusive structure - Geophysical Observations

Given the lack of direct observations of intrusive structures in Deccan Traps, we compiled results from various studies using a variety of geophysical methods (gravity, magnetics, magnetotelluric, and Deep seismic sounding) to constrain the crustal intrusive structure. Since the 1980s, geophysical methods have been used to image continental crustal structures, especially in Saurashtra and the Narmada-Tapi Rift zone, along with a few studies across the central Deccan Plateau and the WGE. If mafic magmatic bodies are emplaced at deep depths, they can be converted to a basic garnet-pyroxene-plagioclase-bearing granulite facies assemblage, which are good seismic reflectors (e.g., K. G. Cox, 1980). Similarly, the higher density of intrusive mafic bodies, especially mafic and ultra-mafic cumulates, would naturally lead to a signal in the gravity field as well as the change in seismic velocity (Ridley & Richards, 2010; M. Richards et al., 2013). We note that the high density of the mafic and ultramafic intrusions can lead to post-emplacement deformation and downward crustal flow

and potentially crustal delamination if the surrounding crust has sufficiently low viscosity (Roman & Jaupart, 2016, 2017; Gorczyk & Vogt, 2018). However, the presence of the upper crustal Bushveld complex (Eales & Cawthorn, 1996) and the lower crustal Seiland Igneous Province (R. B. Larsen et al., 2018) suggests that this process does not have completely remove the crustal intrusives. Thus, the present-day geophysically imaged intrusive bodies represent a lower bound on the total DT intrusives, especially at the Moho depth.

For our compilation, we have mostly followed the interpretation of the original studies to delineate the extent of intrusive mafic bodies vis-a-vis continental crust and sediments. Ideally, a re-analysis of all the datasets using the same model and set of assumptions would lead to more robust results. However, in most cases, the raw datasets are not publicly available for us to be able to do the analysis. In order to reduce biases, we have filtered our compilation only to include studies that utilize more than a single geophysical dataset, and preferably other geological observations, in the model inversion in order to reduce the non-uniqueness of the solutions. Another challenge with the available datasets is that they typically for 2D sections except for some MT studies. Consequently, our results are not very informative about the full 3D geometry of intrusive bodies. Finally, we expect our calculated to typically be a lower limit for the true intrusive volumes since geophysical methods may not detect small crustal intrusive bodies below the typical model resolution of 1-5 km (e.g., Patro & Sarma, 2016a). Although we have a complementary reduction in the volume of the surface lava flows due to erosion, we expect this would to be a smaller bias than the undetected small intrusive bodies.

The other, potentially much larger error in our compilation, comes from the interpretation of the inversion results with respect to the presence of an intrusive body vis-a-vis crustal faults, fluids, and background crustal structure. We refer the reader to individual studies in our compilation for the inversion method and interpretation of the results. In the end, we use results from 19 individual studies for a total of 53 individual measurements (Table 1). In Figure 4.7, we show the distribution of estimated Intrusive/Extrusive ratio for datasets with only large scale Moho-depth underplating (median of 5.5, 25th to 75th percentile of 2.5-8.5, 18 measurements), datasets include only upper crustal magma bodies (median of 1.3, 25th to 75th percentile of 0.5-2.0, 17 measurements), and datasets which include magmatic bodies throughout the crustal column (median of 8.5, 25th to 75th percentile of 5-14.0, 17 measurements). The primary result of this compilation is the absence of significant upper crustal magma bodies in the Deccan Traps with most of the intrusive volume in the lower crustal region. In the following, we describe the results of this analysis for Deccan Traps as well as some supporting datasets from other CFBs.

4.3.8.1 Mafic Underplating

In almost all the DT sections with geophysical datasets, we find a significant (multiple km thick) layers of underplating in the lower crust. Typically, the Extrusive to Intrusive ratio is an average value of 6 and a large range between $\sim$ 0.5 to 15.5. Even in datasets with some

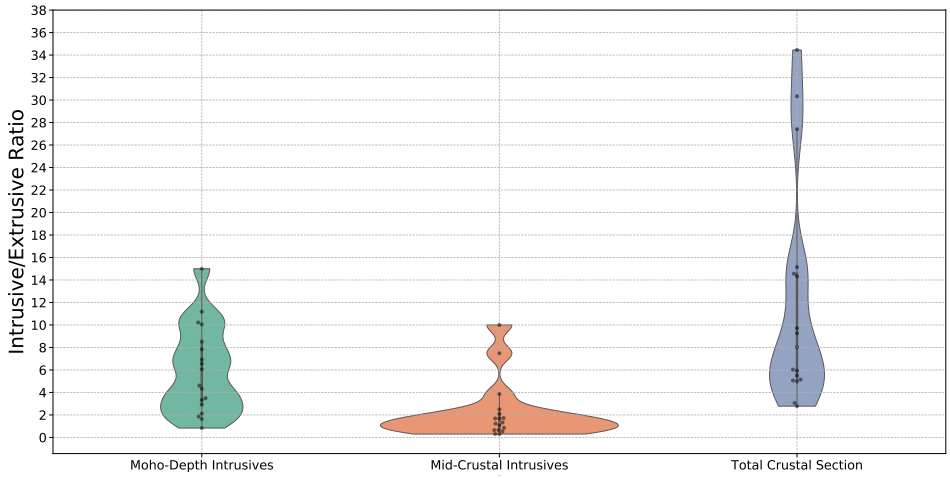

Figure 4.7: Kernel density estimates of Intrusive to Extrusive (I/E) Ratio for Deccan Traps using a literature compilation of gravity, seismic, and MT observations spanning the Western Ghats, Saurashtra, and Narmada Rift Valley in India (Table 1). The observations are divided into three groups based on whether the compiled datasets observed only Moho-depth intrusives, only mid/upper crustal intrusives, or mafic/ultramafic bodies across the whole crustal section (Moho plus crust). For each category, the individual measurements are plotted as circles while the bar plot shows the 25th to 75th percentile range. The high values for the I/E ratio (> 20) are the Phenai-mata and Pavagadh intrusive complexes. The range of I/E ratio for the whole crustal sections is approximately equivalent to the sum of distributions of the Moho-depth underplating and mid/upper crustal intrusives.

upper crustal magma bodies (full crustal column, Figure 4.7), most of the mafic intrusives are still at Moho depth (except the Phenaimata and Pavagardh intrusion described in the next section). A large value for Moho depth intrusions is consistent with the models of K. G. Cox (1980) as well as Black and Manga (2017) who proposed that at least 30-40 % of the parental melt is emplaced at the base of the crust as mafic cumulates. Existing gravity and seismic data suggest that similarly, thick Moho/lower-crust mafic underplates are common for both oceanic and continental flood basalts (Furlong & Fountain, 1986; K. G. Cox, 1993; R. White & McKenzie, 1989; Coffin & Eldholm, 1994; Ridley & Richards, 2010; M. Richards et al., 2013; Mammo, 2013; Thybo & Artemieva, 2013; Deng et al., 2016). Thus, there is significant observational support for models of flood basalt volcanism (See Section 4.2.1 for details) with deep crustal ponding and fractionation of ultramafic primary melts (Farnetani et al., 1996).

We note that the common presence of a thick ($\sim$ 5-15 km) underplated layer does not necessarily equate to a single magma body of equivalent size. Instead, frequent mafic intru-

sions(sills) at lower crustal depths along with visco-elastic deformation of the cumulate bodies can also lead to the formation of a large seismic underplate layer (J. D. White, Bryan, Ross, Self, & Thordarson, 2009; Roman & Jaupart, 2016, 2017; Gorczyk & Vogt, 2018; Galland et al., 2018). We have observational support for this hypothesis from an exhumed lower crustal LIP section - the Seiland Igneous Province (SIP, R. B. Larsen et al., 2018, and references therein). The $\sim$ 5000 km^2 SIP is a dominantly mafic and ultramafic intrusive complex that was emplaced at the 25-35 km depths and represents the deep magmatic plumbing system of the Ediacaran age Central Iapetus Magmatic Province (e.g., Higgins & Breemen, 1998). With a total preserved volume of 17000 km^3 (Pastore, Fichler, & McEnroe, 2018), the SIP is made up of a number of multiple layered mafic plutons (85 % area, each $\sim$ 10-50 km^2), deep-rooted four ultramafic complexes (8-10 % area, each $\sim$ 20-100 km^2 and roots up to 9 km), as well as 2-5% carbonatitic rocks and alkaline and dioritic plutons. Based on field relationships, especially various chill margins between the mafic-ultramafic units and mafic-country rock metasediments (See R. B. Larsen et al., 2018, and references therein), SIP was clearly emplaced sequentially. The first mafic (and alkalic) magmas were intruded into lower crustal metasediments. Subsequent parental melts were emplaced into mafic gabbros, which were still close to solidus temperature. This is clearly evidenced in the field by extensive wall rock melting and assimilation between the gabbros and ultramafic intrusions (Griffin, Sturt, O'Neill, Kirkland, & O'Reilly, 2013). The thermo-chemical insulation of emplacement into hot mafic rocks likely enabled the ultramafic melts to retain their parental composition with the deep ultra-mafic complexes acting as de facto LIP conduits for the shallow system (Grant et al., 2016; Degli Alessandrini, Menegon, Malaspina, Dijkstra, & Anderson, 2017).

In conclusion, observations from SIP clearly illustrate that the SIP magmatic system was never molten in total at the same time as a large lower crustal magma chamber but was rather assembled from multiple bodies. Additional support for this interpretation is provided by the seismic detection of a large (97 x 62 km) but thin (180 $\pm$ 40 m) igneous sill in the North Sea lower crust (17.5-22 km depths, Wrona et al., 2019) associated with the NAMP. As illustrated by a large number of intrusive steps and seismic reflection amplitude anomalies, the sill was formed sequentially with a complex pattern of lateral flow within the sill (Wrona et al. (2019), See Magee, Ernst, et al. (2019) for aerial examples of these features).

4.3.8.2 Upper Crustal Intrusive Bodies

With regards to upper crustal magma bodies, we do not find any evidence in the compiled sections for a large, continuous, upper crustal magma reservoir as hypothesized (See Section 4.2). Instead, the individual magma bodies, when detected, are typically small (5-15 km across and a few km thick, e.g., Patro & Sarma, 2016a; Prasad, Singh, & Tiwari, 2018), are prismatic in shape, and are distributed in complex pattern depending on the pre-existing crustal structure. Since smaller magma bodies of this size are close to the resolution limit for many studies, our estimated Intrusive/Extrusive ratio may be biased to smaller values. We posit that, in reality, the upper crust may have more small magma bodies as petrolog-

ically required based on ubiquitous shallow fractionation (See Section 4.3.4.2 for details). A common feature across many studies, especially in the Narmada-Tapi rift zone region, is that the intrusive bodies are typically associated with pre-existing Precambrian age crustal and lithospheric fault zones (and other weak zones) (Kale et al., 2017, 2019). This suggests that Deccan Traps parental magma and magmatic volatiles utilized these pathways for melt transport to and through the crust (e.g., Bhattacharji et al., 1996; Naganjaneyulu & Santosh, 2010; Azeez, Unsworth, Patro, Harinarayana, & Sastry, 2013; Patro & Sarma, 2016a; Azeez, Patro, Harinarayana, & Sarma, 2017a; G. P. Kumar et al., 2017; Patro et al., 2018). This is further reflected in the vertical magmatic features associated with fault zones. These magma bodies may have acted as conduits for upward transportation of magmatic material to other intrusive bodies (Patro & Sarma, 2016a; Naganjaneyulu & Santosh, 2011).

A number of other studies in LIPs and other magmatic systems have illustrated that pre-existing zones of lithospheric and crustal weakness play a critical role in magma transport (e.g., Begg, Hronsky, Griffin, & O'Reilly, 2018; Peace et al., 2018; Alghamdi, Aitken, & Dentith, 2018; Latyshev, Krivolutskaya, Ulyahina, Bychkova, & Gongalsky, 2019; Magee, Muirhead, et al., 2019). We note that the conclusions of our compilation w.r.t the size of individual upper crustal magma bodies differs strongly from the results in Bhattacharji, Sharma, and Chatterjee (2004) (based on 2d and 3D gravity analysis). They inferred the presence of an extremely large (12 km thick, 300 x 30 km) magma upper crustal (6 km depth) body. However, G. S. Rao, Kumar, and Radhakrishna (2018) used gravity datasets in combination with constraints from seismic observations, as well as magnetic datasets, and found that the observation can be better explained with much smaller crustal magma bodies along with a Moho depth underplate. Analogously, Patro and Sarma (2016a); Prasad et al. (2018) find that using higher-resolution datasets, the magma bodies in Narmada-Tapi Rift Zone are smaller and connected (if at all) thorough narrow zones instead of a larger, thicker, single magma body proposed originally by Bhattacharji et al. (2004).

Within our data compilation, the Phenai-mata and Pavagadh intrusive complexes in the Narmada-Tapti Rift Zone region are clear outliers (with very high intrusive/extrusive ratio, Figure 4.7). The Phenai-Mata complex consists of dominantly basaltic flows (2/3 by volume) along with alkaline plutonic rocks (1/3 by volume) and some orthopyroxene layered gabbro (Hari, Rao, & Swarnkar, 2011; Hari, Prasanth, Swarnkar, Kumar, & Randive, 2018). B. Singh et al. (2014a) used a combination of gravity and magnetic datasets to infer the presence of a large (11 km x 52 km) mafic body extending all the way from the surface to lower crustal depths ($\sim$ 20 km). The strong orientation of the intrusive body along the rift zone axis indicates the importance of a pre-existing tectonic structure for facilitating magma transport to the surface. The Pavagadh intrusive complex comprises of twelve flows with a wide compositional range from olivine basalts and andesites to rhyolites (H. C. Sheth & Melluso, 2008; Hari et al., 2011). With similar gravity-magnetic analysis, B. Singh et al. (2014a) found a low-density rhyolitic body (3x 5 km) extending to about 10 km from the surface. This rhyolitic plug is, in turn, emplaced within a larger mafic intrusive body (20 km x 13 km x 10 km depth). Finally, both the rhyolite and the mafic rocks are underlain

by an ultra-mafic body (20 km x 16 km) up to a depth of 20 km (and potentially larger). Thus, both the Phenai-Mata and Pavagadh intrusive complexes exhibit a trans-crustal DT magmatic system. Based on the different magnetization direction of the ultra-mafic and the rhyolitic magma bodies, B. Singh, Rao, Prajapati, and Swarnapriya (2014b) proposed that the Pavagadh complex may have been active between Chron 30N to Chron 29N/28N and was hence a long-lived system. Since most of the large WG flows are inferred to have been fed by dike swarms, we do not think that these igneous complexes are representative of the majority of DT magmatic architecture.

4.3.8.3 Relationship with Layered Mafic Intrusions

Another interesting conclusion of our data compilation is the lack of any intrusive bodies akin to large layered mafic intrusions such as the Rustenburg Layered Suite (RLS) of the Bushveld Igneous Complex. The RLS is the world's largest layered mafic intrusion that was emplaced about 2.06 Billion years ago. With an area of $\sim$ 65,000 km^2, a thickness of 7-9 km (Eales & Cawthorn, 1996; Cawthorn, 2015), and a shallow emplacement depth (0.15-0.25 GPa: Pitra & De Waal, 2001), R. E. Ernst et al. (2019) (and references therein) have suggested that RLS may be archetype for a typical CFB upper crustal magma reservoir. It has been typically assumed that the RLS represents a single, long-lived magma reservoir of the same size as its present-day extent with rapid assembly through multiple magma injections followed by a long period of closed system fractionation (Wager & Brown, 1968; Cawthorn & Walraven, 1998; Kruger, 2005). Such an interpretation serves as one of the original motivations for the large magma reservoir models discussed in Section 4.2. However, Robb and Mungall (2020) used a combination of high-precision U-Pb dates, plagioclase zoning observations, and thermal models to illustrate that RLS was instead accreted as an out-of-sequence stack of sills corresponding to individual magma intrusions over a 1.2 Ma time-period (C. Lee & Butcher, 1990; A. A. Mitchell & Scoon, 2007; Mungall, Kamo, & McQuade, 2016; Scoon & Costin, 2018; Hayes, Bybee, Mawela, Nex, & van Niekerk, 2018; Scoon & Costin, 2018; A. Mitchell, Scoon, & Sharpe, 2019). Thus, instead of a single magma reservoir, RLS more likely represents a region of extensive sill emplacement and subsequent thermo-chemical insulation of individual magma bodies akin to Seiland Igneous Province (as described in the previous sections). Thus, the presence of a large Bushveld sized intrusive body does not necessarily correspond to a large, well-mixed crustal magma reservoir. In fact, based on field observations, RLS was emplaced after the surface eruptions of the basaltic-rhyolitic Rooiberg Group (Lenhardt & Eriksson, 2012). Thus, the RLS was not an upper crustal magma body feeding the surface lavas, but was instead accreted as a set of sills under a lithostatic load.

For the CFBs in the past 200 Ma, we are not aware of any large upper crustal magnetic or gravity anomalies of the spatial scale and amplitude expected for a Bushveld sized large magma reservoir (or crustal deformation features suggesting their presence and subsequent delamination). Although there are layered mafic intrusions associated with recent CFBs such as the Doros Complex ($\sim$ 20 km^3, Parana–Etendeka CFB, T. Owen-Smith & Ashwal,

2015), NAMP associated central complexes such as Rum, Mull, Skye (< 100 km^3, O'Driscoll, Troll, Reavy, & Turner, 2006; O'driscoll, 2007; Namur et al., 2010), the Skaergaard intrusion (~ 280 km^3, NAMP, Nielsen, 2004), and the Graveyard Point Intrusion (Snake River Plain Basalt, C. M. White, 2007), they are much much smaller than RLS. In conclusion, we posit that a Bushveld layered mafic intrusion does not represent a typical upper crustal magma reservoir for Deccan Traps definitely, and potentially for many other CFBs in the last 200 Ma.

4.3.8.4 Implications for Magmatic Architecture

The main conclusions from the Deccan geophysical compilation of the Intrusive/Extrusive ratio are that there is a significant volume of intrusives: 5-15 with a few outliers. Additionally, the majority of the intrusive magmatic volume is in the lower crust with no clear evidence for a large spatially homogeneous upper crustal magma body. To first order, the lack of an upper crustal large magma reservoir is inconsistent with the buoyancy-driven magmatic eruption model (See section 4.2.2.2, 4.2.2.3), whereas the large underplated layer is consistent. Nevertheless, the observations from Seiland Igneous Province, as well as observations from various Layered Mafic Intrusions, show that the presence of a large magmatic intrusive body does not imply that it was necessarily molten at the same time as a well-mixed magma reservoir.

Another added complication with the geophysical observations is that we see the end-result of the system. Since there are no geochronological constraints for most of the intrusive bodies, it is not clear if they were emplaced prior to or post the main phase of volcanism. A particularly illustrative example is the McMurdo Dry Valleys sill complex (B. D. Marsh, 2004) with four large sills (from top to bottom): the Mt. Fleming Sill, the Asgard Sill, the Peneplain Sill, and the Basement Sill. The sill system is capped by the Kirkpatrick flood basalts on top. Although the bottom-up sequence of intrusions for the system makes logical sense, at least as a first guess, B. D. Marsh (2004) used a variety of field, petrological, and textural observations to demonstrate that the system was instead formed top-down. The sills were emplaced after the eruption of the flood basalt lava flows instead of feeding the lava flows through sill-edge dikes (B. D. Marsh (2004); Jerram, Davis, Mock, Charrier, and Marsh (2010), see D. H. Elliot and Fleming (2018) for a detailed comparison with alternative scenarios). With an increasing lithostatic weight of the flood basalt sequence, the magma was emplaced in a progressively stepped down sills first through the Karoo sedimentary sequence (Mt. Fleming, Asgard, Peneplain Sill), and finally in the granitic basement (Basement Sill). This relationship is not unique for the McMurdo Dry Valleys and has been in multiple CFBs (e.g., Hansen, Jerram, McCaffrey, & Passey, 2011; S. Burgess et al., 2017; Jerram, Dobson, Morgan, & Pankhurst, 2018) and has also been proposed for some CFB associate layered mafic intrusions (e.g., Higgins, 2005, Sept Iles intrusive Suite). Thus the intrusive structures and Intrusive/Extrusive Ratio calculated above should be considered as an upper limit (neglecting the methodological uncertainties) integrating over the whole CFB sequence.

4.3.9 Summary - Key observations

In summary, the primary observations that strongly argue against the single, large magma reservoir model are as follows :

- Deccan Geochemistry (Section 4.3.1, 4.3.6) : In the Western Ghats sections for Deccan Traps, the crustal and lithospheric assimilates can vary rapidly between geochemical formations. Even within individual flows of a geochemical formation, there are quasi-oscillatory geochemical and petrological variations. Thus, the magmatic system has a relatively short geochemical memory. This is difficult to explain within a magmatic plumbing system is composed of only a few large magma chambers which integrate magma compositions over multiple 100s of kyr (Black & Manga, 2017). Additionally, the model result for a REAFC/RTF type shows that the intra-flow variations require a continuous recharge of at least a few percent of the reservoir mass which is inconsistent with large reservoir model (Section 4.2.2.3). We find evidence for similar geochemical features in other CFBs including CAMP, Siberian Traps, Columbia River Basalts, and Karoo-Ferrar flood baslts. Finally, the Black and Manga (2017) style model predicts an increasing contribution from crustal assimilation with increasing thermal maturity of the upper crust. In contrast, the least contaminated DT lava flows are the Ambenali formation, which erupts towards the end of the sequence.

- Geochronology, Paleomagnetic, Mercury, Lava flow morphology (Section 4.3.2, 4.3.3, 4.3.4, 4.3.5) : The eruptive tempo of the Western Ghats sequence does not show any evidence for multiple 100 kyr hiatuses between eruptive time-periods contrary to expectations of a large magma reservoir model. For a single WG composite section (spanning Kalsubai, Lonavala, and Wai subgroups), the typical time-period between eruptions is every 4000-6000 years (Section 4.3.3). Using Hg results, which integrate over the whole DT province, we find that individual eruptive episodes lasted approximately 100 to 1000 years, occurred every 2500-4500 thousand years, and erupted around 20-80 cubic kilometers of basalt per year. This conclusion is supported by eruptive estimates from lava flow morphology from Columbia River Basalt. These observational constraints on eruptive tempo do not match the large magma chamber model predictions. Furthermore, there is no clear eruptive/shallow sill emplacement hiatus for other CFBs with sufficiently high resolution datasets (Siberian Traps, Columbia River Basalts).

- Intra-Flow variation (Section 4.3.6.4) : Based on a few studies, there is evidence for isotopic, geochemical, and petrological variations within a single flow as well as composite dikes in Deccan Traps as well as Columbia River Basalts. These observations clearly suggest that a single eruptive episode was not necessarily fed by a homogeneous, well-mixed magma reservoir.

- Geophysical datasets (Section 4.3.7, 4.3.8) : No geophysical evidence for a large, connected, upper crustal magma reservoir. We do find evidence for a large Moho-depth

mafic underplating layer consistent with the presence of a large Moho-depth magma reservoir. However, based on the exposed section of analogous systems (e.g., Seiland Igneous Province), we conclude that a thick mafic layer inferred using geophysical methods does not necessarily imply a single magma body of equivalent size.

We posit that the most plausible magmatic structure that may be able to explain these (and other) observations is a multiply-connected magma reservoir model each undergoing REAFC-type processes. However, with existing studies, it is unclear if this system can quantitatively explain the eruptive tempo associated with CFBs. In the following sections, we address this using a variety of magma reservoir models.

4.4 Magmatic system Model

The three primary "quantitative" physical constraints with regards to CFB eruptive episodes are : a) the eruptive volume fluxes (km^3/year, Section 4.3.4 and 4.3.5), b) the total erupted volumes of each flow unit (or equivalently the typical duration of each eruptive event, Section 4.3.4 and 4.3.5), and c) the frequency of eruptive intervals (Section 4.3.2-4.3.5). In order to assess how these parameters vary as a function of reservoir geometry and crustal properties for a single reservoir, as well as a set of connected reservoirs, we use a set of two model frameworks. Firstly, we use a volume-averaged visco-elastic mechanical model for an ellipsoidal magma reservoir coupled to a dike-shaped erodible conduit to calculate eruption rates and duration (Section 4.1). We then use idealized 1D thermal models with time-varying plume associated melt influx. In combination with characteristic timescales for magma reservoir evolution (Degruyter & Huber, 2014; Mittal & Richards, 2019), these model results allow us to assess how evolving crustal visco-elastic properties affect the likelihood of crustal magma accumulation vs. surface eruption (Section 4.3.4.2).

4.4.1 Magma Reservoir Model

4.4.1.1 Model Setup and assumptions

We start with a magma reservoir of a chosen geometry emplaced within a visco-elastic crustal half-space. We assume that the reservoir has reached the critical overpressure ($\Delta P \sim$ 20-40 MPa, Rubin, 1995; Caricchi et al., 2014a; Degruyter & Huber, 2014; Mittal & Richards, 2019) for crustal tensile failure and has just been connected to the surface through a dike-shaped conduit (See Fig.7). With this initial condition, we use a mechanical model (described in subsequent sections) to calculate the surface eruption rate and the total erupted volume before the dike closes due to magma solidification. Additionally, we allow for the scenario that the magma reservoir is connected to additional crustal reservoirs through conductive magma pathways (Figure 4.8). For these calculations, we are agnostic about both how long it took to assemble the magma body and if the ΔP was achieved through recharge, buoyancy overpressure, or volatile over-pressurization (e.g., Degruyter & Huber, 2014). Additionally,

we do not use a full thermo-mechanical box model for the magma reservoir evolution (e.g., Degruyter & Huber, 2014; Mittal & Richards, 2019) since the cooling timescale for even a 1 km radius magma reservoir ($L^2/\kappa_{thermal} \sim 30,000$ years, thermal diffusivity $\kappa_{thermal} \sim 10^{-6}$ m^2/s, Karlstrom et al. (2017)) takes much longer than the time duration of individual CFB eruptive episodes (100s to few 1000s years, Section 4.3.4, 4.3.5).

The primary components of our magma reservoir model are a) compressible ellipsoidal magma reservoir with influx from another reservoir, b) visco-elastic crust, and c) erodible dike-shaped conduit feeding surface eruption. Initially, the overpressure and buoyancy of the melt-crystal-magmatic volatile (MVP, CO_2 and H_2O) magma mixture drives surface eruption through the dike. With mass flux out of the reservoir, the overpressure in the magma reservoir progressively decreases, leading to a reduced eruption rate. The rate of overpressure change is modulated by the visco-elastic response of the surrounding crust as well as magma influx from other reservoirs. Eventually, the magma overpressure and buoyancy are insufficient to drive fast enough magma flow rate through the dike to prevent solidification. Throughout the eruptive period, we allow the dike width to increase at a rate proportional to the shear traction on the dike walls to approximate the process of thermal and mechanical erosion and plastic deformation (following Piombo, Tallarico, & Dragoni, 2016). This additional process approximates the rapid initial increase and subsequent slow decay in discharge rates that has been documented for many basaltic fissure eruptions, such as Stromboli (Italy), Holhuraun (Iceland), Piton de la Fournaise (La Réunion), Kilauea (Hawaii) (e.g., Wadge, 1981; Hon et al., 1994; Pedersen et al., 2017; Harris, Dehn, & Calvari, 2007; Calvari, 2019, and references therein).

For mathematical simplicity, we make several simplifying assumptions in our model. Firstly, we do not have the initial diking phase in our model calculations. Even if a magma reservoir reaches critical overpressure, the consequent dike may not always reach the surface to feed eruptions. Secondly, our dike-shaped conduit model does not include the multi-physics processes in the conduit, especially the rheological changes associated with vapor exsolution, crystallization, and bubble growth in ascending melts (e.g., H. Gonnermann & Manga, 2012; H. M. Gonnermann, 2015; Cassidy, Manga, Cashman, & Bachmann, 2018; A. Aravena, Cioni, de' Michieli Vitturi, et al., 2018). Additionally, we do include a very parameterized form of melt transport into the magma reservoir from other reservoirs. Thirdly, we do not model any potential migration of active fissures along a dike during an eruption (See Section 4.3.7 for CFB observations). For instance, the ten dike-fed fissures in the Laki 1783 eruption opened in sequence, with each individual dike segment only active for a short time (days - months, Thordarson & Self, 1993). A similar, well-characterized recent analog of this process is the Kilauea 2018 eruption (C. Neal et al., 2019) wherein the feeder dike kept propagating during the early phases of the eruption with multiple active vents. Finally, we do not allow changes in crystal, melt, and volatile-gas volume fractions in the magma reservoir due to magma mixing, preferential loss of vapor phase during an eruption, or fractional crystallization. We do allow changes in the MVP volume fraction and magma mixture density in the magma reservoir due to pressure-dependent CO_2- H_2O solubility and vapor

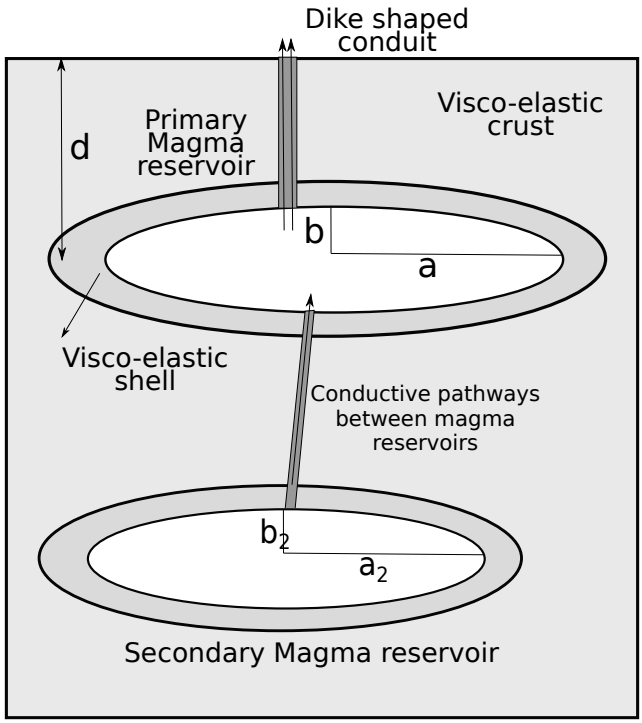

Figure 4.8: Schematic of the the magma reservoir model (Section 4.1). The primary magma reservoir is connected to the surface through a dike-shaped conduit and it can also be connected to one or multiple secondary reservoirs at depth.

phase density.

Although the physical processes mentioned above are important for understanding the full dynamics of CFB eruptions, our interest in this study is to obtain first-order estimates of eruption rates and duration (within a factor of 2 at best). Our constraints for CFB eruption are not sufficiently precise to warrant a more complicated model with additional unconstrained model parameters. Furthermore, the physical mechanisms associated with vent localization as well as fissure transition during a basaltic fissure eruption are not well understood even for modern basaltic eruptions. We anticipate that the unmodeled processes will principally introduce additional short timescale variability to the eruption rate (e.g., Patrick et al., 2019) but will not qualitatively change our conclusions (A. Aravena, Cioni, de' Michieli Vitturi, et al., 2018). We would also note that for magma reservoirs having a volume of at least ~ 10 km^3 (much smaller than what we consider in our calculations), dikes can reach the surface even from ~ 10 km depths (M. Townsend & Huber, 2020a). Thus, although our model is simplified vis-a-vis a real flood basalt eruption, a more complex model is beyond the scope of this present study. We can also perform a much larger parameter space exploration with our model compared to a full multi-physics conduit model.

In the subsequent sections, we first describe the basic model framework followed by analytical solutions for spherical and ellipsoidal magma reservoirs under simplifications. We then add additional complexity to develop the full numerical ODE model for a single magma reservoir and subsequently multiple coupled magma reservoirs.

4.4.1.2 Conservation Equations

The chamber averaged mass conversation equation for the magma reservoir is :

$$\frac{dM_{res}}{dt} = V\frac{d\rho_{res}}{dt} + \rho_{res}\frac{dV}{dt} + R_{in} - R_{out} \tag{4.6}$$

where M_{res}, ρ_{res}, and V are respectively the mass, density, and volume of the magmatic reservoir. R_{in} and R_{out} represent flux into and out of the magma reservoir. P is the over-pressure in the magma reservoir with respect to a lithostatic pressure at the same depth. Using the combined compressibility of the magmatic mixture (crystal + magmatic volatiles + magma) in the reservoir (β_{res}), we can write an equation for the change in density of the magmatic mixture in the reservoir :

$$\frac{d\rho_{res}}{dt} = \rho_{res}\beta_{res}\frac{dP}{dt} \tag{4.7}$$

Analogously, we can use the following equation for $\frac{dV}{dt}$:

$$\frac{dV}{dt} = V\beta_{cr}\frac{dP}{dt} + V\frac{P}{\eta_{cr}} \tag{4.8}$$

Here, β_{cr} is the elastic compressibility and η_{cr} is the viscosity of the surrounding crust. We have added an extra term for the change in reservoir volume (VP/η_{cr}) to provide a first order approximation for the crustal response, akin to many other lumped parameter magma chamber models (e.g., Degruyter & Huber, 2014). For a spherical magma chamber, $\beta_{cr} = \frac{3}{4K_{cr}}$ where K_{cr} is the effective elastic modulus of the crust (K. Anderson & Segall, 2011; Degruyter & Huber, 2014; Rivalta & Segall, 2008; Rivalta, 2010).

Using these relationships, we can re-write the mass conservation equation :

$$\implies \frac{dM_{res}}{dt} = \rho_{res}V\beta_{res}\frac{dP}{dt} + \rho_{res}\Big[V\beta_{cr}\frac{dP}{dt} + V\frac{P}{\eta_{cr}}\Big] \tag{4.9}$$

$$\implies \frac{dM_{res}}{dt} = \rho_{res}V\Big[\beta_{res} + \beta_{cr}\Big]\frac{dP}{dt} + \rho_{res}V\frac{P}{\eta_{cr}} \tag{4.10}$$

.

We assume an ellipsoidal shape for the magma reservoir with semi-major $a_c = c_c$ and semi-minor axis b_c and hence eccentricity $e = (1/a_c)\sqrt{a_c^2 + b_c^2}$. An ellipsoidal geometry

enables us to model large spatially extensive magma chambers wherein the $a_c > b_c$. The volume and surface area of the oblate ellipsoid is Weisstein (2003):

$$V = \frac{4\pi}{3} a_c^2 b_c \tag{4.11}$$

$$S_{res} = 2\pi a_c^2 + \pi \frac{b_c^2}{e} ln\Big(\frac{1+e}{1-e}\Big) \tag{4.12}$$

As magma is drained from the reservoir, the volume of the reservoir, and hence its dimensions will evolve with time. For mathematical simplicity, we assume that the aspect ratio of the magma reservoir ($O_{res} = b_c/a_c$) will remain constant. Although in practice, this assumption will likely not exactly hold, we expect that to first order this is reasonable for moderate aspect ratios given the expectation for the end-member case of a sphere wherein the magma reservoir will shrink/expand symmetrically. The consequent time evolution of the reservoir volume is :

$$\frac{dV}{dt} = 4O_{res}\pi a_c^2 \frac{da_c}{dt} \tag{4.13}$$

$$\text{Substituting the definition of } \frac{\mathrm{dV}}{\mathrm{dt}} \text{in Eqn 4.8, we have :} \tag{4.14}$$

$$4O_{res}\pi a_c^2 \frac{da_c}{dt} = \frac{4O_{res}\pi}{3} a_c^3 \Big[\beta_{cr}\frac{dP}{dt} + \frac{P}{\eta_{cr}}\Big] \tag{4.15}$$

$$\implies \frac{da_c}{dt} = \frac{a_c}{3}\Big[\beta_{cr}\frac{dP}{dt} + \frac{P}{\eta_{cr}}\Big] \tag{4.16}$$

The mass flux into the magma reservoir (R_{in}) is modeled as follows, similar to the analysis in Segall (2016); K. Anderson and Segall (2011) :

$$\frac{dM_{in,res}}{dt} = \Omega(t)(P^{\infty} - P + B_2^1)^n \tag{4.17}$$

where $\Omega(t)$ is a time dependent conductivity (with units of Kg/Pa s) between the two magma reservoirs 1 & 2 and P^{∞} is the over-pressure in the secondary magma reservoir w.r.t to its local lithostatic pressure. B_2^1 is the buoyancy overpressure due to the magma buoyancy between the two chambers if they are at different depths. B_2^1 is defined as :

$$B_2^1 = (\rho_{c,2} - \rho_{res,2})g d_{res,2} - (\rho_{c,1} - \rho_{res,1})g d_{res,1} \tag{4.18}$$

where $d_{res,1}, \rho_{res,1}$ and $d_{res,2}, \rho_{res,2}$ are respectively the depths and mixture densities of reservoirs 1 & 2. This term is added to ensure that when the two magma reservoirs reach a magmastatic pressure condition, there is no mass flux between them. This implies that $P^{\infty}_{mgst} = -(\rho_{c,2} - \rho_{res,2})g d_{res,2}$, $P_{mgst} = -(\rho_{c,1} - \rho_{res,1})g d_{res,1}$, and $P^{\infty}_{mgst} - P_{mgst} + B_2^1 = 0$. If $(P^{\infty} - P + B_2^1) > 0$, there is a magma flux into the primary magma reservoir from the secondary reservoir and vice-versa. We readily acknowledge that this is a significant

simplification of the physical processes of diking and other processes through which melt is transferred between different magmatic reservoirs. In addition, the value of n can be greater than unity for non-linear magma rheology as discussed in Segall (2019). However, this introduces additional, fairly unconstrained free parameters into the model. Consequently, we choose to set $n = 1$ with an exploration of non-linear rheological analysis beyond the scope of the present study. We parameterize the time-dependent conductivity as :

$$\Omega(t) = \Omega_0\Big(1 - e^{-t/t_{cond}}\Big) \tag{4.19}$$

where t_{cond} is the conductivity timescale and Ω_0 is the conductivity amplitude. We readily acknowledge that in reality, the connectivity between individual magma bodies is more complicated and can include anastomosing fault zones, vein networks, dikes, and segmented bridges as illustrated by various field examples (Pollard et al., 1975; Schofield et al., 2012; Magee, Muirhead, et al., 2016b; Magee, O'Driscoll, Petronis, & Stevenson, 2016; Schofield et al., 2017; Magee, Muirhead, et al., 2019; Galland et al., 2019, and references therein). However, these physical processes are very challenging to model accurately even in a simple system. Thus, we have chosen a simplified, but commonly used form for melt conductivity between magma reservoirs.

The magma flux out of the magma reservoir is modeled as a dike shaped conduit with semi-major axis a and semi-minor axis b ($b << a$). The volume flux out from the magma reservoir is :

$$Q_{out,res} = \frac{\pi}{4}\Big[\frac{P(t) + (\rho_c - \rho_{res})gd_{res}}{d_{res}}\Big]\frac{1}{\eta_{res}}\frac{a^3b^3}{a^2 + b^2} \tag{4.20}$$

$$\text{and consequently the mass flux out is } : \frac{dM_{out,res}}{dt} = -\rho_{res}Q_{out,res}(t) \tag{4.21}$$

where η_{res} is the viscosity of the magma mixture erupting at the surface, g is the acceleration due to gravity, and ρ_c is the crustal density at the depth of the magma reservoir.

Combining Equations 4.21, 4.17, and 4.10, we have the following mass conservation equation with influx and outflux:

$$\rho_{res}V\Big[\beta_{res} + \beta_{cr}\Big]\frac{dP}{dt} + \rho_{res}V\frac{P}{\eta_{cr}} \tag{4.22}$$
$$= -\rho_{res}\frac{\pi}{4}\Big[\frac{P(t) + (\rho_c - \rho_{res})gd_{res}}{d_{res}}\Big]\frac{1}{\eta_{res}}\frac{a^3b^3}{a^2 + b^2} + \Omega(t)(P^\infty - P + B_2^1)$$

$$\text{where } \frac{dP}{dt} = -\frac{P}{\eta_{cr}(\beta_{res} + \beta_{cr})} - \frac{\pi}{4V}\Big[\frac{P(t) + (\rho_c - \rho_{res})gd_{res}}{d_{res}}\Big]\frac{1}{\eta_{res}(\beta_{res} + \beta_{cr})}\frac{a^3b^3}{a^2 + b^2} + \tag{4.23}$$
$$\Omega(t)(P^\infty - P + B_2^1)\frac{1}{\rho_{res}V(\beta_{res} + \beta_{cr})}$$

We define a non-dimensional compressibility $\tilde{\beta}_s = (\beta_{res} + \beta_{cr})/\beta_{sph}$ where the net compressibility is scaled with the value for a spherical crustal reservoir ($\beta_{sph} = \frac{3}{4K_{cr}}$). Substituting

this into the equation set above, we get :

$$\frac{dP}{dt} = -\frac{4K_{cr}P}{3\eta_{cr}\tilde{\beta}_s} - \frac{K_{cr}}{4d_{res}\eta_{res}}\Big[\frac{P(t)+(\rho_c-\rho_{res})gd_{res}}{\tilde{\beta}_s a_c^2 b_c}\Big]\frac{a^3b^3}{a^2+b^2} + \Omega(t)(P^\infty - P + B_2^1)\frac{K_{cr}}{\pi a_c^2 b_c \tilde{\beta}_s \rho_{res}} \tag{4.24}$$

The typical timescales in this pressure evolution equation are (assuming $a >> b$):

$$t_{Maxwell} = \frac{\eta_{cr}\tilde{\beta}_s}{K_{cr}} \tag{4.25}$$

$$t_{flux} = \frac{4d_{res}a_c^2 b_c}{ab^3}\frac{\eta_{res}\tilde{\beta}_s}{K_{cr}} \tag{4.26}$$

$$t_{repres} = \frac{\pi a_c^2 b_c \tilde{\beta}_s \rho_{res}}{\Omega K_{cr}} \tag{4.27}$$

Here $t_{Maxwell}$ is the viscous stress relaxation timescale, t_{repres} is the timescale to re-pressurize the magma reservoir by recharge, and t_{flux} is the timescale to relax the magma overpressure by dike-fed eruptions.

Following the model presented in Piombo et al. (2016) to explain the observed transient increase in volume flux in dike fed basaltic eruptions, we allow the dike semi-minor axis to evolve over time due to mechanical erosion (according to Dragoni & Santini, 2007). The erosion rate is assumed to be proportional to the shear traction on the conduit walls :

$$\tau \sim \frac{\eta_{res}Q}{(\pi ab)b} \tag{4.28}$$

$$\implies \tau \sim \Big[\frac{P(t)+(\rho_c-\rho_{res})gd_{res}}{d_{res}}\Big]b \tag{4.29}$$

.

The wall of the conduit maintains an elliptical shape despite erosion. We keep the semi-major axis (a) constant with time since $a >> b$ and it is much easier for dikes to accommodate increased flux by elastic deformation of the semi-major axis b (Dragoni & Tallarico, 2018). Hence, we have the following time evolution equation for b :

$$\frac{db}{dt} = \frac{k}{d_{res}}\Big[P(t)+(\rho_c-\rho_{res})gd_{res}\Big]\frac{a^2 b}{a^2+b^2} \tag{4.30}$$

$$\frac{db}{dt} \approx \frac{k}{d_{res}}\Big[P(t)+(\rho_c-\rho_{res})gd_{res}\Big]b \tag{4.31}$$

where k is the erosion rate per unit traction (m/Pa-s). A. Aravena, Cioni, de' Michieli Vitturi, et al. (2018) show that to first order, the results of this model are consistent with the more complex conduit model with elastic deformation, depth dependent viscosity, and multi-phase processes. The permanent plastic deformation of the conduit (represented by the erosion term) is much larger than conduit shape variation by elastic deformation except at the very end of the eruption (See Fig. S6 A. Aravena, Cioni, de' Michieli Vitturi, et al., 2018).

4.4.1.3 Spherical Magma Chamber

First, we consider a visco-elastic mechanical model for a spherical chamber modified from Segall (2016). The primary feature of this model is the inclusion of a visco-elastic shell with an outer radius of R_2 surrounding the magma chamber of radius R_1. Additionally, we include a melt flux into the magma chamber as well a melt flux out due to a dike fed surface eruption. Since the magma reservoir geometry is spherical, $a_c = b_c = R_1$. The new mass conservation equation is :

$$\frac{dM_{res}}{dt} = V\frac{d\rho_{res}}{dt} + \rho_{res}\frac{dV}{dt} \tag{4.32}$$

$$\implies \frac{dM_{res}}{dt} = \rho_{res}V\beta_{res}\frac{dP}{dt} + \rho_{res}\Big[4\pi R_1^2\frac{du_r}{dt}(r = R_1) + V\frac{P}{\eta_{cr,fr}}\Big] \tag{4.33}$$

where $u_r(r = R_1)$ is the radial displacement at the edge of the magma reservoir and $\eta_{cr,fr}$ is the viscosity of the far-field crust. The first term for the volume displacement is due to the deformation of the visco-elastic shell embedded in an elastic medium, whereas the other term represents deformation back to lithostatic pressure from far field longer duration viscous relaxation. Combining with the mass flux terms into and out of the primary chamber, we get :

$$\begin{aligned} -\rho_{res}\frac{\pi}{4}\Big[\frac{P(t) + (\rho_c - \rho_{res})gd_{res}}{d_{res}}\Big]\frac{1}{\eta_{res}}\frac{a^3b^3}{a^2+b^2} + \Omega(t)(P^\infty - P + B_2^1) \\ = \rho_{res}V\beta_{res}\frac{dP}{dt} + \rho_{res}\Big[4\pi R_1^2\frac{du_r}{dt}(r = R_1) + V\frac{P}{\eta_{cr,fr}}\Big] \end{aligned} \tag{4.34}$$

For notational convenience, we define a few additional variables as follows :

$$B^1 = (\rho_c - \rho_{res})gd_{res} \tag{4.35}$$

$$Q^1 = \rho_{res}\frac{\pi}{4d_{res}}\frac{1}{\eta_{res}}\frac{a^3b^3}{a^2+b^2} \tag{4.36}$$

$$Q^{rl} = \frac{V}{\eta_{cr,fr}} \tag{4.37}$$

Consequently, we can re-write the mass conservation equation as :

$$-\frac{Q^1}{\rho_{res}}(P + B^1) + \frac{\Omega}{\rho_{res}}(P^\infty - P + B_2^1) - Q^{rl}P = V\beta_{res}\frac{dP}{dt} + 4\pi R_1^2\frac{du_r}{dt}(r = R_1) \tag{4.38}$$

We can analytically solve this equation set assuming that the terms such as b, ρ_{res}, Ω, and $P^\infty$are not functions of time. Consequently, we can use the Laplace transform to solve the linear equation set. We refer to the reader to the Appendix in Segall (2016) for the full description of the mathematical details and only describe the solution steps here that differ

from their analysis. Firstly, the Laplace transformed mass conservation equation is (with the Laplace transform form of P(t) being $\hat{P}$(s)):

$$-Q^1(\hat{P}+\frac{B^1}{s})+\Omega(\frac{P^\infty}{s}-\hat{P}+\frac{B_2^1}{s})-Q^{rl}\rho_{res}\hat{P} \tag{4.39}$$

$$=\rho_{res}V\beta_{res}(s\hat{P}-P_0^+)+\rho_{res}V\beta_{cr}\Big[s\hat{P}\Big(\frac{s+(\alpha+1)t_R^{-1}}{s+t_R^{-1}}\Big)-P_0^+\Big]$$

$$\text{with}:\ \alpha=\frac{3(1-\nu)}{(1+\nu)}\Big[\Big(\frac{R_2}{R_1}\Big)^3-1\Big] \tag{4.40}$$

$$t_R=\Big[\frac{3\eta_{cr,1}(1-\nu)}{K_{cr}(1+\nu)}\Big]\Big(\frac{R_2}{R_1}\Big)^3 \tag{4.41}$$

where we have used the solution from Dragoni and Magnanensi (1989) for a spherical magma chamber surrounded by a Maxwell viscoelastic shell in a full space (See Appendix of Segall (2016) for details). Here $\eta_{cr,1}$ is the viscosity in the visco-elastic shell between radius R_1 and R_2 and ν is the Poisson's ratio. Due to the presence of a finite thickness visco-elastic shell, one of the viscous relaxation timescales in this model setup is t_R (Dragoni & Magnanensi, 1989). P_0^+ is the initial value of overpressure at t=0. Substituting the expression for t_{repres} with $a_c=b_c=R_1$, and defining the timescale $\tau_{rl}=t_{repres}(a_c=b_c=R_1)$, we get :

$$-\hat{P}L_1+\frac{1}{s}L_2=\tau_{rl}\Big(s\hat{P}-P_0^+ +\beta s\hat{P}\frac{\alpha t_R^{-1}}{s+t_R^{-1}}\Big) \tag{4.42}$$

$$\text{with}:\ \beta=\frac{\beta_{cr}}{\beta_{cr}+\beta_{res}} \tag{4.43}$$

$$L_1=\frac{Q^1+\Omega+Q^{rl}\rho_{res}}{\Omega} \tag{4.44}$$

$$L_2=\frac{-Q^1B^1+\Omega(P^\infty+B_2^1))}{\Omega} \tag{4.45}$$

$$\tau_{rl}=\Big[\frac{\pi R_1^3\tilde{\beta}_s\rho_{res}}{\Omega K_{cr}}\Big] \tag{4.46}$$

We can re-arrange the equation to get :

$$\hat{P}=\frac{(L_2+s\tau_{rl}P_0^+)(s+t_R^{-1})}{s[\beta s\tau_{rl}\alpha t_R^{-1}+(s+t_R^{-1})(s\tau_{rl}+L_1)]} \tag{4.47}$$

The time domain solution of the over-pressure evolution P(t) is :

$$P(t) = \frac{L_2 t_R^{-1}}{\tau_{rl} s_1 s_2} + \frac{(L_2 + s_1\tau_{rl}P_0^+)(s_1 + t_R^{-1})}{s_1\tau_{rl}(s_1 - s_2)} e^{s_1 t} + \frac{(L_2 + s_2\tau_{rl}P_0^+)(s_2 + t_R^{-1})}{s_2\tau_{rl}(s_2 - s_1)} e^{s_2 t} \quad (4.48)$$

$$\text{where : } s_1 = \frac{-1}{2}\Big(t_R^{-1}(1+\beta\alpha) + \frac{L_1}{\tau_{rl}}\Big) + \frac{1}{2}\sqrt{[t_R^{-1}(1+\beta\alpha) + \frac{L_1}{\tau_{rl}}]^2 - 4\frac{L_1 t_R^{-1}}{\tau_{rl}}} \quad (4.49)$$

$$s_2 = \frac{-1}{2}\Big(t_R^{-1}(1+\beta\alpha) + \frac{L_1}{\tau_{rl}}\Big) - \frac{1}{2}\sqrt{[t_R^{-1}(1+\beta\alpha) + \frac{L_1}{\tau_{rl}}]^2 - 4\frac{L_1 t_R^{-1}}{\tau_{rl}}} \quad (4.50)$$

In the limit of no recharge (i.e $\tau_{rl} -> \infty$) and no flux out of the magma chamber ($Q^1 = 0$), we get :

$$P(t) = \frac{P_0^+}{1+\beta\alpha}(1 + \beta\alpha \exp[-t_R^{-1}(1+\beta\alpha)t] \quad (4.51)$$

$$(4.52)$$

with a characteristic timescale of $t_{R,relax\ compress} = t_R/(1+\beta\alpha)$ with eventually $P(t)_{lim\ t->\infty} = P_0^+/(1+\beta\alpha)$.

Using the analytical solution, we can also calculate the crustal stress field surrounding the magma chamber. The hoop stress term is defined as follows for regions 1 (visco-elastic shell) and region 2 (elastic region) :

$$\sigma_{\theta\theta}^{(1)}(r,t) = -\frac{L_2 t_R^{-1}}{\tau_{rl} s_1 s_2} + \frac{(L_2 + s_1\tau_{rl}P_0^+)}{s_1\tau_{rl}(s_1 - s_2)}\Big(\frac{s_1 R_1^3}{2r^3} - t_R^{-1}\Big)e^{s_1 t} + \frac{(L_2 + s_2\tau_{rl}P_0^+)}{s_2\tau_{rl}(s_2 - s_1)}\Big(\frac{s_2 R_1^3}{2r^3} - t_R^{-1}\Big)e^{s_2 t} \quad (4.53)$$

$$\sigma_{\theta\theta}^{(2)}(r,t) = \frac{L_2 t_R^{-1}}{\tau_{rl} s_1 s_2}\Big(\frac{R_2}{2r}\Big)^3 + \Big(\frac{R_1^3}{2r^3}\Big)\Big[\frac{(L_2 + s_1\tau_{rl}P_0^+)}{s_1\tau_{rl}(s_1 - s_2)}\Big(s_1 + t_R^{-1}\Big(\frac{R_2}{R_1}\Big)^3\Big)e^{s_1 t} + \frac{(L_2 + s_2\tau_{rl}P_0^+)}{s_2\tau_{rl}(s_2 - s_1)}\Big(s_2 + t_R^{-1}\Big(\frac{R_2}{R_1}\Big)^3\Big)e^{s_2 t}\Big] \quad (4.54)$$

Here, positive values represent tension while negative values imply compression.

4.4.1.4 Ellipsoidal Magma Chamber

Although the spherical magma chamber model provides a nice theoretical framework to analyze the coupled interaction of magma recharge, dike-fed eruption, and crustal visco-elastic deformation, there are some significant limitations of the model making it difficult to quantitatively use for flood basalt eruptions. In particular, the choice of spherical geometry is a very strong limitation with the maximum volume of magma chambers of order 550 km^3 (for a 5 km Radius chamber) which is significantly smaller than typical flood basalt eruptive

volumes of 2000 - 10,000 km^3. In addition, the conductivity between the magma reservoirs 1 & 2, semi-major and semi-minor axis (a_c and b_c), and dike semi-minor axis (b) are fixed in order to use the Laplace transform method for the analytical solution. The latter is especially critical since an evolution of b is one potential mechanism to explain the observed time-evolution of volume fluxes from basaltic eruptions (Piombo et al., 2016; Calvari, 2019).

We hence modify and extend the eruption model presented in (Piombo et al., 2016). The conservation equations are :

$$\frac{dP}{dt} = -\frac{4K_{cr}P}{3\eta_{cr}\tilde{\beta}_s} - \frac{K_{cr}}{4d_{res}\eta_{res}}\Big[\frac{P(t)+(\rho_c-\rho_{res})gd_{res}}{\tilde{\beta}_s a_c^2 b_c}\Big]\frac{a^3b^3}{a^2+b^2} + \Omega(t)(P^\infty - P + B_2^1)\frac{K_{cr}}{\pi a_c^2 b_c \tilde{\beta}_s \rho_{res}} \tag{4.55}$$

$$\frac{db}{dt} \approx \frac{k}{d_{res}}\Big[P(t)+(\rho_c-\rho_{res})gd_{res}\Big]b \tag{4.56}$$

$$\frac{da_c}{dt} = \frac{a_c}{3}\Big[\beta_{cr}\frac{dP}{dt} + \frac{P}{\eta_{cr}}\Big] \tag{4.57}$$

$$\frac{d\rho_{res}}{dt} = \rho_{res}\beta_{res}\frac{dP}{dt} \tag{4.58}$$

We first consider an elastic end-member model wherein we set influx equal to zero and ignore crustal viscous stress relaxation as well as changes in a_c and ρ_{res}. We hence have a coupled non-linear ODE system :

$$\frac{dP}{dt} = -\frac{K_{cr}}{4d_{res}\eta_{res}}\Big[\frac{P(t)+(\rho_c-\rho_{res})gd_{res}}{\tilde{\beta}_s a_c^2 b_c}\Big](ab^3) \tag{4.59}$$

$$\frac{db}{dt} \approx \frac{k}{d_{res}}\Big[P(t)+(\rho_c-\rho_{res})gd_{res}\Big]b \tag{4.60}$$

The solution of this coupled ODE equation set is :

$$P(t) = C_1 - W_3[B^1 + C_1]e^{W_1}\frac{1}{W_3e^{W_1}+1} \tag{4.61}$$

$$b^3(t) = \frac{3W_2e^{W_1}}{W_3e^{W_1}+1}(B^1+C_1) \tag{4.62}$$

$$\text{with : } W_1 = 3W_2(B^1+C_1)(t-3C_2) \tag{4.63}$$

$$W_2 = \frac{k}{d_{res}} \tag{4.64}$$

$$W_3 = \frac{1}{t_{flux}b_0^3} \tag{4.65}$$

Here C_1 and C_2 are the integration constants. Using the initial conditions for P and b at t = 0 :

$$P(t=0) = P_0^+ \tag{4.66}$$

$$b(t=0) = b_0 \tag{4.67}$$

we get the following solution :

$$b(t) = \left[e^{(\alpha_{el}+1)t/t_{flux}} \frac{\alpha_{el}+1}{e^{(\alpha_{el}+1)t/t_{flux}} + \alpha_{el}}\right]^{1/3} b_0 \tag{4.68}$$

$$P(t) = \frac{(\alpha_{el}+1)(P_0^+ + B^1)}{e^{(\alpha_{el}+1)t/t_{flux}} + \alpha_{el}} \tag{4.69}$$

$$\alpha_{el} = 12(P_0^+ + B^1)\frac{\eta_{res} k}{K_{cr} a b_0^3} \hat{\beta}_s a_c^2 b_c \tag{4.70}$$

$$t_{flux} = \frac{4 d_{res} a_c^2 b_c}{a b_0^3} \frac{\eta_{res} \tilde{\beta}_s}{K_{cr}} \tag{4.71}$$

Additionally, the volume flow rate is given by :

$$Q(t) = Q_0(1+\alpha_{el})^2 \frac{e^{(\alpha_{el}+1)t/t_{flux}}}{\left[e^{(\alpha_{el}+1)t/t_{flux}} + \alpha_{el}\right]^2} \tag{4.72}$$

$$\text{with} \ : \ Q_0 = a b_0^3 \frac{\pi}{4\eta_{res} d_{res}} (P_0^+ + B^1) \tag{4.73}$$

and peak flux (Q_{max}) and peak flux time (t_{max}) being :

$$Q_{max} = \frac{Q_0}{4} \frac{(1+\alpha_{el})^2}{\alpha_{el}} \tag{4.74}$$

$$t_{max} = \frac{t_{flux}}{1+\alpha_{el}} log(\alpha_{el}) \tag{4.75}$$

For large magma chambers ($a_c, b_c >$ 1km), the value of α_{el} is much larger than 1. Hence, we can simplify the Q_{max} relationship as follows :

$$Q_{max} \approx \frac{Q_0}{4} \alpha_{el} \tag{4.76}$$

$$\implies Q_{max} \approx 3\pi (P_0^+ + B^1)^2 \frac{k \hat{\beta}_s}{K_{cr} d_{res}} a_c^2 b_c \tag{4.77}$$

$$\tag{4.78}$$

Interestingly, this relationship is independent of the initial shape of the dike as well as magma mixture viscosity. Using typical values for $K_{cr} \sim 10^{10}$ Pa, $\beta_s \sim 5$, k$\sim 10^{-10}$ m/Pa-s, $P_0^+ \sim$ 20MPa, $\Delta\rho \sim$ 300km/m^3, and a depth of 5 km (See discussion of parameter values in Section 4.3), the constraint on the magma reservoir geometry can be expressed as :

$$a_c^2 b_c \approx 27.5 (\frac{Q_{max}}{100 km^3/yr}) km^3 \tag{4.79}$$

Thus, a typical magma reservoir semi-major axis for an individual flood basalt eruption required to match the observed eruptive volume fluxes is $\sim$ 5km for an aspect ratio $b_c/a_c \sim 0.2$.

We next include a time-dependent flux from a secondary reservoir as well as viscous relaxation by numerically solving the coupled ODE system for the two (or more) reservoirs. In order to include the effect of a low-viscosity ($\eta_{cr,shell}$) visco-elastic shell in our analysis, we have included an additional faster viscous relaxation term from a visco-elastic shell surrounding the magma reservoirs analogous to the far field pressure relaxation term. The effective viscosities of the shell for magma reservoirs 1 & 2 are $\tilde{\eta}_{cr,shell,1}$ and $\tilde{\eta}_{cr,shell,2}$ respectively. These viscosities have been defined in order to provide an analog of the characteristic timescale for stress relaxation in the no recharge limit $t_{R,relax\,compress}$- $t_R/(1+\beta\alpha)$ (Segall, 2016, See results in previous section). The final set of equations are as follows :

$$\frac{dP}{dt} = -\frac{4K_{cr}P}{3\eta_{cr,1}\tilde{\beta}_{s,1}} - \frac{K_{cr}}{4d_{res,1}\eta_{res,1}}\Big[\frac{P(t)+(\rho_c-\rho_{res,1})gd_{res,1}}{\tilde{\beta}_{s,1}a_{c,1}^2 b_{c,1}}\Big]\frac{a^3b^3}{a^2+b^2} + \Omega(t)(P^\infty - P + B_2^1)\frac{K_{cr}}{\pi a_{c,1}^2 b_{c,1}\tilde{\beta}_{s,1}\rho_{res,1}} - \frac{4K_{cr}P}{3\tilde{\eta}_{cr,shell,1}\tilde{\beta}_{s,1}} \tag{4.80}$$

$$\frac{dP^\infty}{dt} = -\frac{4K_{cr}P^\infty}{3\eta_{cr,2}\tilde{\beta}_{s,2}} - \Omega(t)(P^\infty - P + B_2^1)\frac{K_{cr}}{\pi a_{c,2}^2 b_{c,2}\tilde{\beta}_{s,2}\rho_{res,2}} - \frac{4K_{cr}P^\infty}{3\tilde{\eta}_{cr,shell,2}\tilde{\beta}_{s,2}} \tag{4.81}$$

$$\frac{db}{dt} \approx \frac{k}{d_{res,1}}\Big[P(t)+(\rho_c-\rho_{res,1})gd_{res,1}\Big]b \tag{4.82}$$

$$\frac{da_{c,1}}{dt} = \frac{a_{c,1}}{3}\Big[\beta_{cr,1}\frac{dP}{dt} + \frac{P}{\eta_{cr,1}} + \frac{P}{\tilde{\eta}_{cr,shell,1}}\Big] \tag{4.83}$$

$$\frac{da_{c,2}}{dt} = \frac{a_{c,2}}{3}\Big[\beta_{cr,2}\frac{dP^\infty}{dt} + \frac{P^\infty}{\eta_{cr,2}} + \frac{P^\infty}{\tilde{\eta}_{cr,shell,2}}\Big] \tag{4.84}$$

$$\frac{d\rho_{res,1}}{dt} = \rho_{res,1}\beta_{res,1}\frac{dP}{dt} \tag{4.85}$$

$$\frac{d\rho_{res,2}}{dt} = \rho_{res,2}\beta_{res,2}\frac{dP^\infty}{dt} \tag{4.86}$$

$$\tilde{\eta}_{cr,shell,1} = \eta_{cr,shell,1}\Big[\frac{3(1-\nu)}{(1+\nu)}\Big]\frac{1}{1+\beta_1\alpha_1}\Big(\frac{a_{c,out,1}}{a_{c,1}}\Big)^3 \tag{4.87}$$

$$\tilde{\eta}_{cr,shell,2} = \eta_{cr,shell,2}\Big[\frac{3(1-\nu)}{(1+\nu)}\Big]\frac{1}{1+\beta_2\alpha_2}\Big(\frac{a_{c,out,2}}{a_{c,2}}\Big)^3 \tag{4.88}$$

$$\alpha_1 = \frac{3(1-\nu)}{(1+\nu)}\Big[\Big(\frac{a_{c,out,1}}{a_{c,1}}\Big)^3 - 1\Big] \tag{4.89}$$

$$\alpha_2 = \frac{3(1-\nu)}{(1+\nu)}\Big[\Big(\frac{a_{c,out,2}}{a_{c,2}}\Big)^3 - 1\Big] \tag{4.90}$$

$$\beta_1 = \frac{\beta_{cr,1}}{\beta_{cr,1}+\beta_{res,1}} \tag{4.91}$$

$$\beta_2 = \frac{\beta_{cr,2}}{\beta_{cr,2}+\beta_{res,2}} \tag{4.92}$$

Here, $a_{c,out,1}$ and $a_{c,out,2}$ are the semi-major axis of the crustal viscous shell. We readily

acknowledge that this additional term only qualitatively captures the behavior of the system in an ellipsoidal geometry, the spatial pattern of stress relaxation and timescale will not be exactly the same, especially near the free surface (Karlstrom & Richards, 2011). Additionally, as illustrated in the no-recharge limit for the visco-elastic shell model, the maximum relaxation of the over-pressure from the viscous relaxation is $P(t)_{lim\, t->\infty} = P_0^+/(1+\beta\alpha)$ as opposed to the formalism here. Nevertheless, the addition of this term allows us to first order capture a short term response of the system. An eruption will stop when the advective heat flux through the dike is insufficient to keep it open. Thus, we terminate the calculation when the Peclet number (the ratio of timescales for diffusive to advective heat transport) reduces to less than unity. Mathematically, this implies that $\mathrm{Pe} = (b^2/\kappa)/(d_{res}/v_{dike}) < 1$ where κ is the thermal diffusivity and v_{dike} is the magma flow rate in the dike. Finally, analogous to the REAFC model above, the rate of change of the elemental mass m_{ch} of a magma reservoir is :

$$dm_{ch} = dM_e C_{ch} + dM_{re} C_{re} \tag{4.93}$$

Here, C_{ch} is the element's concentration in the magma reservoir and C_{re} is the element's concentration in the magma recharge. dM_e (negative) and dM_{re} (positive) are the mass changes due to eruption and recharge from other magma reservoirs, respectively.

4.4.2 1D thermal model

4.4.2.1 Model setup and assumptions

We use a 1-D thermal diffusion model to calculate the time-evolving background crustal temperature structure due to the emplacement of vertical dike-shaped crustal magma bodies following Karlstrom et al. (2017) (note that given the 1D model horizontal sills will be just a single point). The melt is emplaced over a stochastic range of depths with the total heat input dependent on the specified melt flux rate at the base of the crust. Over time, the increasing crustal temperature leads to a reduction in crustal viscosity and permeability as well as slower cooling of magma bodies. Using the framework of a thermo-chemical magma reservoir box model and associated timescales (Degruyter & Huber, 2014; Mittal & Richards, 2019), we assess how these changes impact the likelihood of different size magma bodies to accumulate melt or erupt to the surface. In addition, the timescales help illustrate the dominant mechanism for the build-up of the critical overpressure for the reservoirs that may erupt. We also systematically assess how this likelihood changes as a function of crustal depth.

Given our 1D model, we cannot directly include a number of important physical processes such as 3D viscous deformation around magma bodies, emplacement, and growth of laterally extensive magma bodies, and the role of pre-existing crustal structure and heterogeneity (Karakas & Dufek, 2015; Karakas, Degruyter, Bachmann, & Dufek, 2017; Colón, Bindeman, & Gerya, 2019). Following Karlstrom et al. (2017), our 1D thermal model does not include an explicit melt component in the crust with individual dikes instantaneously transfer their heat

content into the crust upon emplacement. Finally, we do not explicitly model the thermo-chemical evolution of the magma reservoir and the corresponding changes in the melt, crystal, and volatile content, as well as crustal assimilation and the associated release of volatiles (e.g., Black & Manga, 2017). Although the inclusion of these processes is essential for a full magmatic system model (e.g., Black & Manga, 2017), it would introduce additional, not well constrained, model parameters, choices about magmatic architecture, as well as significant numerical complexity. Since our primary focus in this analysis is calculating how the crustal thermal structure evolves over time, we contend that our 1D model framework provides a reasonable first-order estimate. Furthermore, our model framework permits a broad parameter space exploration. Thus, despite simplifications, the 1D thermal model coupled with magmatic timescale (Degruyter & Huber, 2014; Mittal & Richards, 2019) helps constrain the conditions required for frequent magma eruptions and the crustal location of the corresponding magma bodies.

4.4.2.2 Magmatic timescales

We calculate the crustal thermal evolution using a 1D finite difference method (Langtangen & Linge, 2017) allowing a depth dependent thermal conductivity profile with continuous dike intrusions in a specified depth range (L^{rng}_{dike}). The crustal thermal profile evolves from a steady state geotherm to an elevated temperature due to the additional heat input from dikes. We follow Karlstrom et al. (2017) for the model setup and parameters and refer the reader to their paper for details and model justifications. Following Roland et al. (2010); Cao, Lee, Yang, and Zuza (2019), we implement the effect of hydrothermal cooling in the upper crust (top 8 km) by modifying the thermal conductivity based on a Nusselt number (See the respective papers for details). Given the significant thermal input associated with a CFB, we choose Nu = 8 for all our calculations. The primary variables for the 1D model are the input melt volume flux and the time-period (T_{period}) of the sinusoidal variation in the volume flux, with the volume flux defined as $Q_{melt}(t) = Q_0\pi \sin(2\pi\, t/T_{period})$. We can define two characteristic non-dimensional numbers for this system

$$\mathrm{De}_{Maxwell} = t^c_{Maxwell}/t^c_{fill} \tag{4.94}$$

$$\mathrm{Tr}^{cr} = T_{period}/t^c_{diff,intr} = T_{period}/[(L^{rng}_{dike})^2/\kappa_{cr}] \tag{4.95}$$

$$\tag{4.96}$$

Here Tr^{cr} quantifies the variability in melt supply to the crust by scaling it with a thermal diffusion time for the vertical length-scale L^{rng}_{dike} over which volume flux Q_0 is uniformly distributed (Karlstrom et al., 2017). On a crustal scale if $\mathrm{De}_{Maxwell} > 1$, the magma reservoir can erupt before the stresses viscously relax, whereas $\mathrm{De}_{Maxwell} < 1$ implies a regime where magma accumulation is favored (Karlstrom et al., 2017). If Tr^{cr} is much greater than one, i.e., the magma supply varies significantly with time, the thermal cooling between successive dike intrusions is appreciable and as a result, the crustal heating by intrusions is reduced.

The eruptive dynamics of a magma reservoir can be defined, to first-order, by a set of characteristic timescales (Degruyter & Huber, 2014; Mittal & Richards, 2019; M. Townsend et al., 2019) : a timescale for viscous relaxation ($t^c_{viscous}$), timescale for pressurization by melt recharge t^c_{fill}, timescale for cooling and crystallization t^c_{cool} to a typical crystal fraction (ϵ_0) based on an energy balance (Karlstrom & Richards, 2011) and a pore pressure diffusion timescale $t^c_{press\,diff}$ (Mittal & Richards, 2019). These timescales characterize the likelihood of magma eruptibility as well as the physical mechanism leading to magma overpressure (See discussion in Mittal & Richards, 2019). The timescales are defined as :

$$t^c_{viscous} = \eta_{crust}/(\Delta P) \tag{4.97}$$

$$t^c_{fill} = V/Q_0 \tag{4.98}$$

$$t^c_{cool} = \epsilon_0 V \Big(\frac{\oint_{res} q(\Delta T) dA}{\rho_{res} L_f} - \frac{Q_0 c_p \Delta T}{L_f} \Big)^{-1} \tag{4.99}$$

$$t^c_{press\,diff} = \frac{b_c^2}{4\kappa_{pd}} \tag{4.100}$$

where η_{crust} is temperature dependent viscosity defined as follows $\eta_{crust}(T) = A \exp(G/RT)$ with A = 4.25 x 10^7, R = 8.31 (gas constant), G = 141 x 10^3 (activation energy), and T the temperature in Kelvin (Karlstrom et al., 2017). Q_0 is the melt flux into the magma reservoir which is calculated by integrating the linear melt flux at the base of the mantle over an area equal to the square of the crustal thickness (Karlstrom et al., 2017). In the cooling timescale, ΔT is the magma temperature decrease below the liquidus , $q(\Delta T)$ is the heat flux from the magma reservoir into the surrounding crust, $\oint_{res} q(\Delta T) dA$ is the heat flux integrated over the area of the magma reservoir, c_p is the specific heat capacity, and L_f is the latent heat of fusion. For the pressure diffusion timescale, we choose the typical lengthscale for diffusion to be $b_c/2$ as the shell outside the reservoir and κ_{pd} is the pore-pressure diffusivity. As described in Mittal and Richards (2019), the pressure diffusivity is defined as $\kappa_{pd} = k^m M_B/\eta_{fluid}$ where k^m is the crustal permeability, η_{fluid} is the fluid viscosity ($\sim 10^{-4}$ Pa s), and M_B is the crustal Biot modulus (= 5.59 x 10^{10} Pa for Westerley granite). Since crustal permeability is expected to be smaller at depth due to higher temperatures and increasing lithostatic pressure (S. Ingebritsen & Gleeson, 2017) as well as be decreased with higher temperatures due to ductile flow, we approximate the time-varying permeability around a magma reservoir using the following functional form with exponential temperature and depth dependence (e-folding distance of 5 km, S. Ingebritsen & Manning, 2010):

$$k^m(T, d_{res}) = k^m_0 [1 - \exp(-20/T)] \exp(-d_{res}/5000) \tag{4.101}$$

with $k^m_0 = 1$ x10^{-18} m^2 and temperature T in ^{o}C. Although the permeability around a magma reservoir can have significant transient variations associated with loss of exsolved magma fluids, eruptions and dike formation as well as tectonic and far field stress perturbations, the processes involved are complex and require a full multi-physics analysis (See Mittal & Richards, 2019, and references therein). Consequently, we have chosen the above form as

a first order approximation to illustrate the importance of passive volatile loss on magma eruptibility. In addition, we use the solubility calculations to ensure that the there are sufficient exsolved volatiles (volatile volume fraction $\epsilon_g > 0.0075$) in the magma system for this mechanism to be applicable. Otherwise, the permeability value is set to zero. We emphasize that our parameter choice is fairly conservative, both with regards to temperature and depth scaling, given available permeability measurements for geothermal-metamorphic regions (S. Ingebritsen & Manning, 2010; Stober & Bucher, 2015).

The heat flux around an ellipsoidal magma chamber can be estimated using spatial gradients for a steady state temperature profile (Moons & Spencer, 1988; Karlstrom & Richards, 2011) :

$$q(\xi,\phi) = \frac{k\Delta T}{cot^{-1}(\xi_0)(1+\xi^2)}\sqrt{\frac{1+\xi^2}{(a_c^2-b_c^2)(\xi^2+\phi^2)}} \tag{4.102}$$

Here ϕ is the scaled polar co-ordinate ($=\sin\chi$) and ξ ($=\sinh\mu$) is a scaled distance from the reservoir wall with μ and χ ($\in[\pi/2,\pi/2]$) being the radial and polar coordinate the oblate spheroidal coordinate system. The surface of the oblate ellipsoid is defined by $\mu=\mu_0$ with $\tanh(\mu_0) = b_c/a_c$ For our calculations, we integrate the heat flux over the ellipsoid surface at the reservoir-crust interface ($\xi=\xi_0$). Consequently, the integral flux term $\oint_{res} q(\Delta T)dA$ is :

$$\oint_{res} q(\Delta T)dA = 2\pi a_c \int_{-c}^{c} q(\Delta T,\xi_0,z/b_c)\sqrt{1+\frac{(a_c-b_c)(a_c+b_c)z^2}{b_c^4}}dz \tag{4.103}$$

$$= \frac{2\pi a_c k\Delta T}{cot^{-1}(\xi_0)(1+\xi_0^2)}\sqrt{\frac{1+\xi_0^2}{(a_c^2-b_c^2)}}\int_{-c}^{c}\sqrt{1+\frac{(a_c-b_c)(a_c+b_c)z^2}{b_c^4}}\frac{1}{\sqrt{\xi_0^2+(z/b_c)^2}}dz \tag{4.104}$$

where we have used the surface integral equation for an oblate spheroid and the relationship between ϕ and the Cartesian co-ordinate z ($\phi = z/b_c$). We numerically calculate this integral to calculate the total heat flux from the surface of the magma reservoir.

4.4.3 Model Parameters

4.4.3.1 Elastic Compressiblity

We calculate the elastic compressibility for ellipsoidal magma reservoirs using the results of the numerical finite element calculations from K. Anderson and Segall (2011) in an elastic half space as a function of aspect ratio b_c/a_c. We use the numerical results for the medium-deep regime when the depth of the magma reservoir is larger than the semi-major axis a_c and shallow results otherwise. We also extrapolate to lower aspect ratios (< 0.5) outside the numerical calculations using the analytical expressions from Amoruso and Crescentini (2009) for full elastic space - $\beta_{cr} = 3/(4K_{cr})[(a_c/b_c)(2/\pi) - 4/5]$. Although the free surface

effects are likely important for spatially extensive magma reservoirs, the lack of simple analytical expressions makes it difficult to accurately model within our framework and using the analytical solution in the regions outside the numerical region enable us to capture the first order behavior.

4.4.3.2 Magmatic volatile solubility

Since the magmatic volatiles have a strong impact on the magma compressibility (e.g., Rivalta & Segall, 2008), it is important to include the presence of magmatic volatiles (CO_2 and H_2O) in the magma mixture. We calculate the joint solubility of the magmatic volatiles (CO_2 and H_2O) in the melt using the equations described in Iacono-Marziano, Morizet, Le Trong, and Gaillard (2012). If the volume fraction of the magmatic volatiles in the magmatic mixture is very high, the volatiles will likely be passively lost from the reservoir even without any eruption due to their high buoyancy w.r.t the surrounding crust (See discussion in Mittal & Richards, 2019). Hence, we cap the maximum volume fraction of volatiles in the magmatic reservoir to 20 % as an upper limit (Aarnes, Podladchikov, & Svensen, 2012). In order to calculate the exsolved magmatic volatiles at a given magma reservoir depth, we either assume a closed system degassing path wherein exsolved volatiles remain in the system (upto a maximum of 20% volume fraction) or a partial open system degassing where some fraction of the exsolved volatiles at each depth are lost from the system and passively degassed. These different exsolution paths affect both the depth when water starts exsolving from the melt as well as the bulk density and compressibility of the magma reservoir.

We calculate the initial concentrations of water and CO_2 in the melt by starting with a chosen mantle source composition and using partition coefficients to calculate the volatile content (X_{melt}) in the melt given a degree of partial melting (F):

$$X_{melt} = \frac{X_{mantle}}{D + F(1 - D)} \tag{4.105}$$

Following (Black & Manga, 2017), we set the bulk partition coefficient D to be 0.01 for water (R. F. Katz, Spiegelman, & Langmuir, 2003) and 10^{-4} for CO_2 (Hauri, Gaetani, & Green, 2006) assuming oxidizing redox conditions (Rohrbach & Schmidt, 2011; Stagno, Ojwang, McCammon, & Frost, 2013). Although there is considerable uncertainty regarding the initial mantle volatile (CO_2, H_2O) composition (e.g., Self et al., 2014) and references therein), there is increasing evidence that the mantle source of Phanerozoic LIPs is volatile enriched compared to the background mantle (Gu et al., 2019). The typical range of water content ranges from 0.1 to 0.6 wt % (X.-C. Wang, Wilde, Xu, & Pang, 2016; Liu, Xia, Kuritani, Hanski, & Yu, 2017; Ivanov et al., 2018; Gu et al., 2019) with the real values closer to the upper end since measurements are biased by pre-eruptive degassing. With regards to mantle CO_2 contents, K. R. Anderson and Poland (2017) estimated that the Hawaiian mantle plume has a CO_2 content of 964 ppm (with a 68 % range from 740 to 1230 ppm) while Matthews, Shorttle, Maclennan, and Rudge (2019) infered that the Iceland plume has

a CO_2 concentration of $\sim$ 2.2 wt% ($\pm$1.5 wt %). These results are broadly consistent with estimates from Lange (2002) arguing for more than 4 wt % concentration of CO_2 and H_2O in the CRB melt (for a typical melt fraction of 5-15%) in order to ensure their buoyancy. The frequent presence of mantle composition sulphides, as well as carbonatitic and hydrous assemblages in the SIP ultramafic intrusions also support the presence of a significant volatile flux into the system throughout the CFB event (R. B. Larsen et al., 2018). Additionally, the metasomatized mantle lithosphere may also contribute significant C to the parental melt reaching the crustal system (e.g., Black & Gibson, 2019; S. A. Gibson et al., 2020). Based on these results, we assume a higher mantle volatile composition than Black and Manga (2017) with a conservative value of 750 ppm CO_2, and 0.23 wt % H_2O. This parameter set ensures that the partial melt water content for 10 % degree partial melting is $\sim$ 2 wt %, consistent with some melt inclusions results from the Deccan Trap Wai sub-group (Choudhary, Santosh, De Vivo, Jadhav, & Babu, 2019) and some estimates from the Reunion lava flows (Boudoire, Rizzo, Di Muro, Grassa, & Liuzzo, 2018).

As discussed in Section 4.3.1, there is a general consensus that the primary plume derived melt was picritic (K. G. Cox, 1980; G. Sen & Chandrasekharam, 2011; Chatterjee & Sheth, 2015; K. V. Kumar, Laxman, & Nagaraju, 2018; Dongre, Viljoen, & Rathod, 2018). Consequently, we use the estimate of the primary melt composition modeled from the most primitive picrite from Deccan Traps (Pavagadh Picrite) as well a Deccan lava flow average for our solubility calculations (G. Sen & Chandrasekharam, 2011; K. V. Kumar et al., 2018). We acknowledge that actual magma compositions will evolve through REAFC processes in the magmatic system. However, a comprehensive analysis of different magma compositions is beyond the scope of this study and does not influence our primary results. Additionally, the dominance of a tholeiitic composition in Deccan Traps suggest that although fractional crystallization was extensive, only small volumes of intermediate and high silicic rocks (e.g., rhyolites) were produced. In the Fig.8, we show the solubility curves (for different choices of open system degassing fraction, See (Mittal & Richards, 2019) for a discussion of passive degassing observations and mechanisms) for two different melt compositions (Deccan average vs Pavagadh Picrite) and two different mantle volatile contents (F = 10% M. Richards et al., 2013). The main feature of note with these calculations is that CO_2 can exsolve from the melt at fairly deep depths (order 20-30 km) whereas H_2O can remain soluble up until shallow depths (order 3-6 km). Thus, any buoyancy driven over-pressurization due to H_2O volatiles will be a significant process only in the upper crust whereas the CO_2 associated buoyancy dominates for the deeper crustal reservoirs. The upper limit on the amount of magmatic volatiles in these calculations is set by the requirement that the volatile volume fraction is always less than 20%. With decreasing lithostatic pressure, the decrease in density of the volatile phase leads to a strong reduction in the total CO_2 and H_2O. Additionally, we show the results for a range of degassing efficiency from 0 (closed system) to 80 % in Figure 4.9 for each scenario. The results illustrate that the choice of open system degassing fraction can have a substantial impact on the melt solubility through differences in the amount of the exsolved volatile phase which is in equilibrium with the melt. For the rest of our analysis, we

use the Deccan primitive composition (Pavagadh Picrite) and a mantle volatile composition of 750 ppm CO_2 and 0.23 wt % H_2O with a relatively closed system configuration (degassing efficiency of less about 5 %) unless otherwise noted.

4.4.3.3 Other parameters

To calculate the melt-crystal-exsolved fluid mixture density and compressiblity, we use the modified Redlich-Kwong equation of state for magmatic fluids from Halbach and Chatterjee (1982) (See Degruyter and Huber (2014) for details). The density of the melt and the crytals depend on the melt compostion as well as depth, and volatile content, all of which will be evolving during the magmatic system evolution. However, to first order, we can use a simplified, conservative constant melt density linearly increasing from 2500 kg/m^3 from shallow depths (5 km depth, constant for depths less than 5 km) to 2700 kg/m^3 for deeper depths (30 km) based on the pMELTS calculations from Karlstrom and Richards (2011) for approximately 30 % crystal fraction (as well as typical parameters from Piombo et al., 2016; A. Aravena, Cioni, de' Michieli Vitturi, et al., 2018) while we conservatively set crystal density to be 3000 kg/m^3 to represent ultramafic crystalized cumulate. Similarly, for simplicity, we set the compressibility of melt and crystals to 2 x 10^{-10} Pa^{-1} and 2 x 10^{-11} Pa^{-1} respectively (K. Anderson & Segall, 2011). We emphasize that these simplifications significantly reduce the model complexity and allow a more clear physical analysis of the model, thus allowing us to capture the first order behavior. A fully coupled petrological analysis, though important, is beyond the scope of this study and does not affect the primary conclusions of our analysis. We set the crustal effective elastic modulus to 10 GPa and Poisson's ratio to 0.25 (Karlstrom et al., 2017).

For the crustal density and conductivity structure, we use a simplified piecewise linear relationship using the results from S. Jennings, Hasterok, and Payne (2019) and DeBari and Greene (2011) for a typical continental crustal section. We set the viscosity of the basaltic magma at $\sim$ 1000 Pa-s based on field based measurements for Hawaiian lava flows which are reasonable analogs for flood basalt lava flows both in terms of composition and eruptive style (Chevrel, Pinkerton, & Harris, 2019).

For all our calculations, we set the dike semi-major axis (a)to 500 m and the initial dike semi-minor axis (b) to be equivalent to that required for an initial Peclet number of 2. For a typical magma reservoir depth of 5 km (and other parameters described above), the initial dike width is 0.25-1 m. These values are very consistent with the lower range of DT dike thickness (Section 4.3.7) representing the single injection dikes. With regards to dike length, our chosen value of a 1 km long active segment is broadly consistent with modern CFB analogs such as Laki 1783 eruption (Thordarson & Self, 1993) when accounting for flow localization within the dikes and the region of active magma flow within a dike segment (Bruce & Huppert, 1990; Fialko & Rubin, 1999; Wylie, Helfrich, Dade, Lister, & Salzig, 1999; R. Brown et al., 2007; Taisne & Tait, 2011; Parcheta, Fagents, Swanson, Houghton, & Ericksen, 2015). We find that changing the dike shape within reasonable ranges does

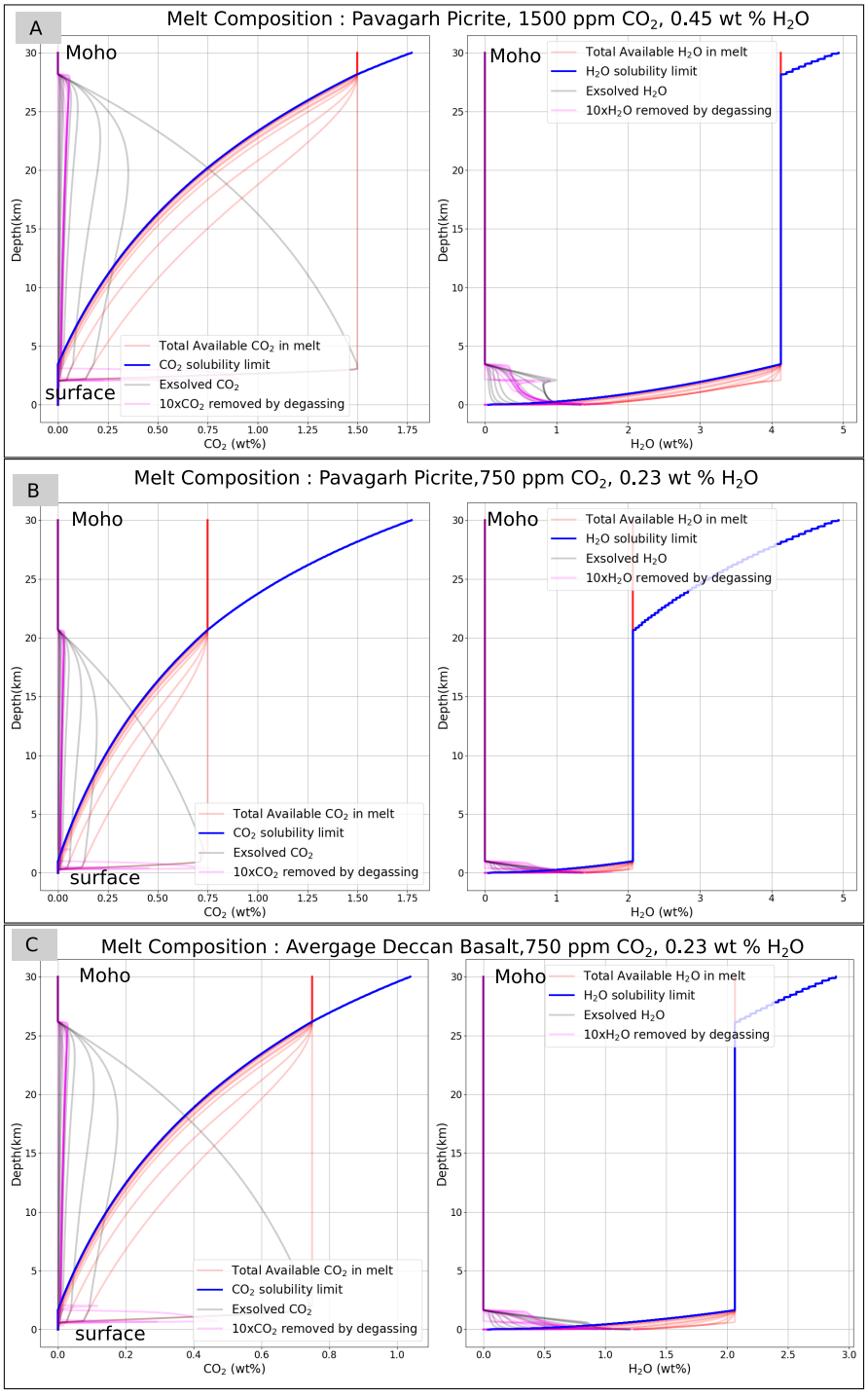
A
Melt Composition : Pavagarh Picrite, 1500 ppm CO_2, 0.45 wt % H_2O
Moho
surface
Depth(km)
CO_2 (wt%)
H_2O (wt%)
Total Available CO_2 in melt
CO_2 solubility limit
Exsolved CO_2
10xCO_2 removed by degassing
Total Available H_2O in melt
H_2O solubility limit
Exsolved H_2O
10xH_2O removed by degassing
B
Melt Composition : Pavagarh Picrite,750 ppm CO_2, 0.23 wt % H_2O
C
Melt Composition : Avergage Deccan Basalt,750 ppm CO_2, 0.23 wt % H_2O

Figure 4.9

Figure 4.9 *(previous page)*: Joint solubility of the magmatic volatiles (CO_2 - Left panels, and H_2O- Right panels) in the melt for 2 different primitive melt composition estimates (Panel B and C) as well as two different initial mantle volatile compositions (Panel A and B). The initial concentrations of water and CO_2 in the melt are calculated for 10% degree of partial melting. In the plots, the degree of magmatic volatiles lost at each depth increases from 0% to 80 % (different gray lines) illustrating how the magmatic volatile content changes as the system moves from a closed system to an unbuffered open-system behavior. The exsolution of CO_2 occurs fairly deep in the crustal column whereas H_2O comes out from the melt at shallow depths for all compositions.

not significantly change our results, especially given other parameter uncertainties. A more comprehensive analysis of the whole parameter space is beyond the scope of this study.

4.5 Model results - Magma Reservoir Model

We use our new visco-elastic mechanical model for an ellipsoidal magma reservoir described in Section 4.1 to calculate how eruptive volume fluxes (km^3/year) and the total erupted volumes of each flow unit (or equivalently the typical duration of each eruptive event) depend on reservoir geometry, and the crustal properties. We are particularly interested in finding what magmatic architecture is required to match the CFB observations constraints (Section 4.3.4 & 4.3.5). The typical ranges of eruptive fluxes and volumes of individual CFB eruptive episodes are 30-300 (km^3/year) and 1,000 - 10,000 km^3. The absence of significant a'a flows in most CFB provinces suggest that the eruption rates did not exceed more than a few thousand km^3/year at best (Section 4.3.5). In the following, we first discuss results for a spherical magma reservoir followed by the ellipsoidal reservoir.

4.5.1 Spherical Reservoir Model

Typical magma reservoirs associated with CFBs are expected to have a high aspect ratio, especially for the hypothesized large (> 100 km long) magma reservoirs (e.g., Section 4.2, 4.3.6 & 4.3.7). Thus, the choice of a spherical geometry seems an unreasonable choice. Nevertheless, starting with a spherical reservoir model enables us to directly compare and contrast our results with those from previous studies (Huppert & Woods, 2002; Woods & Huppert, 2003; Piombo et al., 2016; M. Townsend et al., 2019; M. Townsend & Huber, 2020b).

In Figures 9 and 10, we show model calculations for a range of magma reservoir radius. The depth of all the reservoirs is 5 km, representative of an upper crustal magma body. We note that for most of the reservoir sizes, a 5 km depth is not physical since the top of the magma body will exceed the free surface. However, changing the magma reservoir depth for

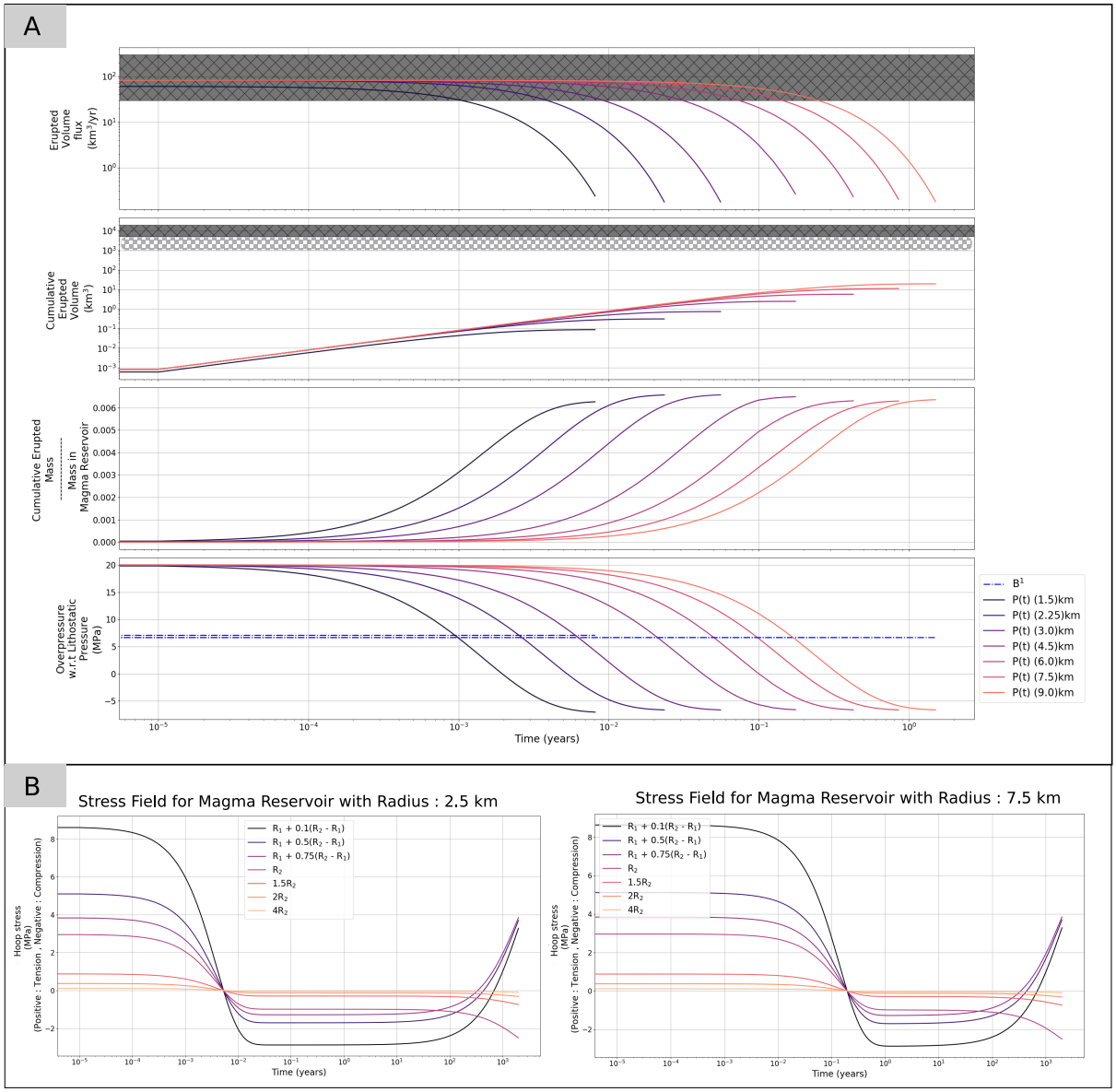

Figure 4.10

each reservoir size would make it more complicated to compare the results since the volatile exsolution, magma mixture buoyancy, and crustal properties are all depth-dependent. Thus, for these calculations, we keep the nominal reservoir depth the same. We consider more physical magma reservoirs in the subsequent section (Section 4.5.2). In order to match the observational constraint for eruptive volume flux (Figure 4.10A, top panel), we set the dike width to be 1 m. The far-field crustal viscosity and the visco-elastic shell radius is fixed at 10^{21} Pa-s and $R_2 = 1.5R_1$ (Segall, 2016) for all results shown here.

Figure 4.10 *(previous page)*: Model Results for Spherical Reservoir Model : Erupted volume flux (km^3/yr), total erupted volume (km^3), fraction of magma chamber mass erupted, and magma reservoir overpressure (Pa), for different reservoir radius (Panel A, see legend in the figure) at a typical upper crustal depth of 5 km. The viscosity of the surrounding crust is set to 10^{20} Pa-s and the conductivity is set to 10^{-6} Kg/Pa-s. A range of eruptive volume fluxes (30-300 km^3/year) and total erupted volumes (1,000 - 5,000 km^3 : hashed region & 5,000 - 10,000 km^3 : shaded hashed region) for flood basalts based on observational constraints is shown on the figure. The Panel B show the time-evolving total pressure for 2 different radius magma reservoirs at different distances outward from the reservoir wall in the visco-elastic shell. The B^1 curve shows the magma buoyancy overpressure in the conduit. At the termination of the eruption, the total overpressure is zero : $P(t) + B^1 \sim 0$.

First, we consider the case of no magma recharge from the underlying reservoir (conductivity = 10^{-6} Kg/Pa-s) and a relatively cold visco-elastic shell ($\eta_{cr,1} = 10^{20}$ Pa-s). The total duration of the eruption is set by the t_{flux} (Eqn. 26, Table 1), which is proportional to the magma reservoir volume. For our chosen parameters, the eruption duration is less than a year, much shorter than CFB observations. Additionally, the erupted volume is too low for model parameters chosen to obtain reasonable eruption rates. This result is a direct consequence of the low eruption efficiency of a spherical magma reservoir (Figure 4.10A, cumulative erupted mass/mass in magma reservoir curves). Huppert and Woods (2002) showed that the typical erupted volume from an over-pressurized magma reservoir is $\sim V_{res}\beta_{res}\Delta P$ (Also see M. Townsend & Huber, 2020b). For a typical compressibility of 1-3 x 10^{-10} Pa for a magma mixture with some exsolved volatiles (Rivalta, 2010; Degruyter & Huber, 2014) and $\Delta P \sim 20MPa$ (Rubin, 1995), the erupted volume $\sim 0.002 - 0.006V_{res}$. Even if this value is increased by a factor of 10 with progressive crystallization, higher initial melt volatile content or shallower magma body (Edmonds & Wallace, 2017, also See Figure 8), only a few percent of reservoir volume can erupt. Consequently, an eruption of $\sim$ 5000 km^3 magma volume requires a magma reservoir size of 100,000 - 10^6 km^3 (30-60 km radius) inconsistent with various observational constraints (see section 4.3). We note that the efficiency of eruption can potentially be significantly enhanced when accounting for pressurization by caldera and graben subsidence during the eruption (Gudmundsson, 2016). We also note that in most CFBs, there is no evidence any caldera collapse type features on the surface (See Section 4.3.7, 4.3.8).

A corollary of the typical low eruption efficiency is that it makes explaining CFB volcanism by the large magma reservoir model (with failure by buoyancy overpressure) even more challenging. Black and Manga (2017) assumed that all the whole fraction of the magma body that is both molten and buoyant erupt once the critical buoyancy, overpressure is reached. However, if only a few percent of the mass erupts, many more reservoir failure events would be required to explain the total CFB volumes. However, each eruption would still be as-

sociated with a crustal permeability increase due to fracturing (S. Ingebritsen & Manning, 2010) and consequent volatile loss. Thus, there should not be a significant reduction in the timescale between individual eruptions if the failure is due to buoyancy overpressure.

An interesting conclusion from our model calculations is that the eruptions do not stop when the magma overpressure reduces back to lithostatic conditions, as is generally assumed in box models (K. Anderson & Segall, 2011; Degruyter & Huber, 2014; Mittal & Richards, 2019; M. Townsend et al., 2019). Instead, we find that our eruptions end with the magma reservoir under-pressurized w.r.t lithostatic conditions (akin to results in Karlstrom, Rudolph, & Manga, 2012). This result is a consequence of the buoyancy of the magma. A magma reservoir erupts mass to the surface until it reaches the magmastatic condition rather than the lithostatic condition. Consequently, in Figure 4.10A, the sum of magma overpressure and buoyancy term (B^1) is close to zero when eruptions terminate due to insufficient melt flux through the dike. This under-pressure can help increase the magma reservoir eruption efficiency by volatile exsolution driven magmatic siphoning (Karlstrom & Manga, 2009). For some parameter choices, the continued exsolution (and consequent magma buoyancy) can sustain eruptions for a long period. In our model calculations, we include this effect by calculating CO_2 - H_2O solubility and magma density during an eruption. The difference in the magma pressure evolution (i.e. magma under-pressurization rather than zero overpressure) also has a strong influence on the stress pattern in the visco-elastic shell surrounding the reservoir (Figure 4.10B, top panel).

Initially, the hoop stress ($\sigma^{(1)}_{\theta\theta}$) is positive (tension) due to the initial ΔP. With continuing surface eruptions, the magma overpressure decreases to a negative value, which in turn leads to compressional hoop stresses. With no further melt influx, the eruption eventually stops, but the shear stresses within the shell continue relaxing. This stress relaxation eventually leads to a change in sign of the hoop stress in order to match the radial stress (which is tensional due to magma under-pressure) (timescale of $t_{R,relax\,compress}$; See Segall (2016) for a more detailed discussion). Eventually, on a much longer timescale ($t_{R,Maxwell}$) related to the far-field crustal viscosity (not shown in the figure), all the stresses in the reservoir will relax. Since the viscous shell is coupled to a surrounding viscoelastic medium (with much higher viscosity), any tensional hoop stress in the shell leads to a corresponding compressional stress in the surrounding crust (curves with $r > R_2$, Figure 4.10B).

The hoop stresses in the viscous shell are particularly interesting with regards to how the connectivity between magma reservoirs is established. For a dike to propagate into the magma reservoir, the dike's magma pressure within the dike must exceed the least compressive stress tangential to the chamber wall. Thus, with respect to an initial lithostatic stress condition, the excess pressure defined as $\sigma_{\theta\theta} + P_{dike}(t)$ measures the difference between the circumferential compressive stress and magma over-pressure. The condition of tensile failure at a given radial distance from the magma reservoir is when either $\sigma^{(1)}_{\theta\theta}(r,t) + P_{dike}(t) = \Delta P$ (for r $< R_2$) or $\sigma^{(2)}_{\theta\theta}(r = R_2, t) + P_{dike}(t) = \Delta P$ (for r $\geq R_2$). Our results suggest that initially, the rapid under-pressurization will lead to a stress pattern that inhibits fracture propagation both out of and into the magma reservoir. Over time, the hoop stresses become

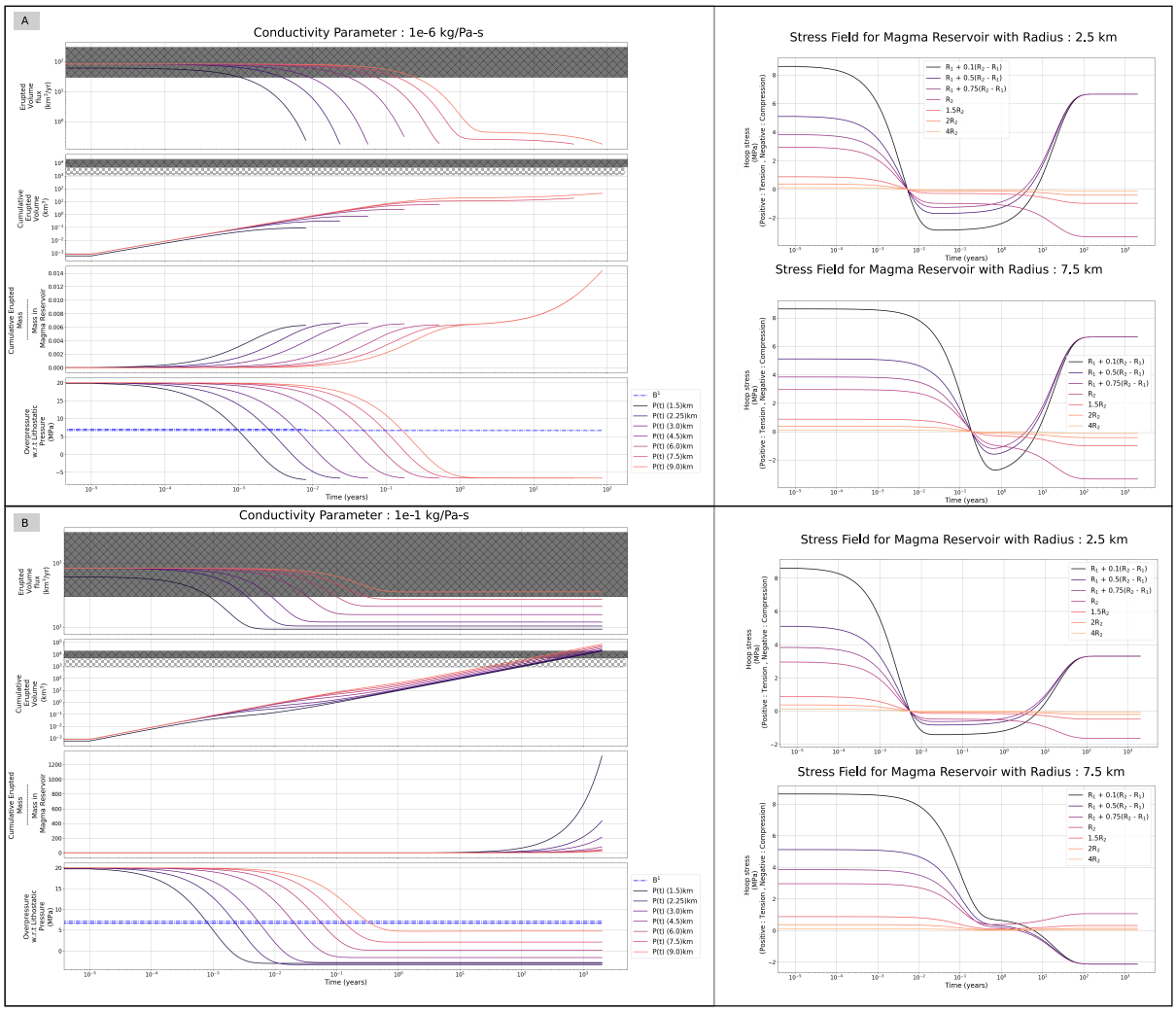

Figure 4.11

tensional, thus making dike propagation more favorable. In the visco-elastic crust coupled to the shell, there is a similar, but opposite effect. We posit that these stress variations may lead to natural timescales for enhanced connectivity between different magma bodies.

Next, we show some model results where we allow faster stress relaxation in the visco-elastic shell ($\eta_{cr,1} = 10^{18}$ Pa-s; Figure 4.11A, Left Panel). With lower shell viscosity, stress relaxation in the viscous shell leads to pressurization if the magma mixture is not infinitely compressible (Segall, 2016). This pressurization, in turn, enables continued melt flux into the dike and longer, larger eruptions. We find this process is responsible for the much longer eruption duration, total erupted volume, as well as a higher eruption efficiency of large magma reservoirs (Figure 4.11A). In contrast, the eruptions from a smaller magma reservoir cease before this mechanism can act (timescale of $t_{R,relax\ compress}$). However, the eruption

Figure 4.11 *(previous page)*: Model Results for Spherical Reservoir Model : Erupted volume flux (km^3/yr), total erupted volume (km^3), fraction of magma chamber mass erupted, and magma reservoir overpressure (Pa), for different reservoir radius (See legend in the figure) at a depth of 5 km. The viscosity of the surrounding crust is set to $\mathbf{10^{18}}$ **Pa-s** and the conductivity is set to 10^{-6} Kg/Pa-s (Part A) and 10^{-1} Kg/Pa-s(Part B). A range of eruptive volume fluxes (30-300 km^3/year) and total erupted volumes (1,000 - 5,000 km^3 : hashed region & 5,000 - 10,000 km^3 : shaded hashed region) for flood basalts based on observational constraints is shown on the figure. The Right Panels for each Part show the time-evolving total pressure for two different radius magma reservoirs at different distances outward from the reservoir wall in the visco-elastic shell. The B^1 curve shows the magma buoyancy overpressure in the conduit. At the termination of the eruption, the total overpressure is zero : $P(t) + B^1 \sim 0$.

rate is still to small compared to observational constraints.

Finally, we increase the melt influx into the magma reservoir from a deeper magma body (conductivity $\Omega = 10^{-1}$ Kg/Pa-s, $\eta_{cr,1} = 10^{18}$ Pa-s; Figure 4.11B, Left Panel). The lower magma reservoir is assumed to be quasi-infinite with a constant lithostatic magma pressure and a depth equal to 5 km plus twice the semi-major axis of the primary reservoir. This depth choice approximates the growing region of influence of a larger magma reservoir (e.g., Karlstrom et al., 2009b, 2015). With this model configuration, we do find that many magma reservoirs can satisfy both the eruptive flux and the erupted volume constraints. Physically, melt influx helps maintain magma pressurization (with an associated timescale of t_{repres}, Eqn. 27) akin to the visco-elastic shell. Since the magma-overpressure never decreases below zero for the largest magma reservoir, the hoop stresses remain compressional in contrast to the results for smaller magma bodies (Figure 4.11B top and bottom panels).

Considering different magma reservoir depths, initial volatile content, and depth of the secondary reservoir, we find a qualitatively similar model behavior as described above. A continuous melt influx from an additional magma reservoir is necessary for feeding an individual eruptive episode from the smaller magma reservoir. There are, however, some critical physical processes that are missing in the spherical reservoir model, e.g., changing dike widths, appropriate reservoir geometry, and a quasi-infinite lower reservoir (See Section 4.2.4). Since we do not model pressure evolution in the secondary reservoir, magma transport from the reservoir does not lead to an under-pressurization. Consequently, an extensive secondary reservoir with high conductivity and buoyancy acts as an infinite magma source for the primary reservoir feeding surface eruptions. We relax all of these model assumptions with the results from the Ellipsoidal reservoir model described in the next section.

4.5.2 Ellipsoidal Reservoir Model

In the following, we describe our results for the Ellipsoidal reservoir model. We start with the simplest case - an elastic reservoir. We then sequentially add a crustal visco-elastic response, melt influx from a single secondary reservoir, and finally melt influx from four additional reservoirs. The semi-minor axis and depth of the primary reservoir is set to 3 km and 5 km, respectively, for all results unless otherwise noted. We show the model results for a maximum of 10,000 years or when the eruption stops, whichever is faster. The maximum eruption length should be smaller than 10,000 years given the observational constraints on the duration of individual eruptive episodes (Section 4.3.2, 4.3.3, 4.3.4, 4.3.5).

4.5.2.1 Elastic end-member

We first consider an elastic Ellipsoidal magma reservoir in an elastic half-space connected to the surface with an erodible dike-shaped conduit. Using the analytical solutions described in Section 4.2.4, we show the model results for a wide range of reservoir sizes ranging from 2.5 to 75 km (semi-major axis a_c) in Figure 4.12. These results do not include any crustal stress relaxation or melt influx from other magma reservoirs. In contrast to the spherical reservoir model, the eruption flux initially increases, followed by a subsequent decline and shutdown of eruptions. This difference is a direct consequence of evolving dike widths, which changes both the eruption rate as well as the timescale to relax overpressure by mass loss (t_{flux}; Eqn. 26, Table 1). For instance, the dike width increases from 0.25 m to 20 m by the end of the eruption for the 150 km long magma reservoir (Figure 4.12, orange curve). The elastic compressibility of a low aspect ratio magma reservoir is much larger than for an equivalent spherical magma body. Thus, the total erupted mass fraction for the largest magma reservoir is about 15 % as opposed to less than a percent in Figure 4.10.

Still, despite the different model geometry, we find that it is not possible to satisfy the observational constraints on eruptive rate and total volume with a given model geometry. In Figure 4.13, the results of a wide parameter space exploration show that we need a magma reservoir with semi-major axis $\sim$ 5-10 km to match the eruptive flux estimates of 30-300 km^3/year. But, magma reservoirs that can erupt volumes equivalent to individual CFB eruptive episodes have sizes $a_c \sim 60 - 100$ km (for a total erupted volume of 5,000-20,000 km^3). The required reservoir size typically increases with decreasing aspect ratios since for the same semi-major axis, smaller aspect ratio implies a smaller total magma reservoir volume. The inversion of this trend at small aspect ratios is due to the rapid increase in elastic compressibility, which in turn increases the eruption efficiency and total erupted volume despite smaller reservoir size.

4.5.2.2 Visco-elastic crust and melt influx

Next, we enable far-field crustal stress relaxation with the crustal viscosity set to either 10^{19} Pa-s (Figure 4.14A) or 10^{21} Pa-s (Figure 4.14B). We find that a lower crustal viscosity

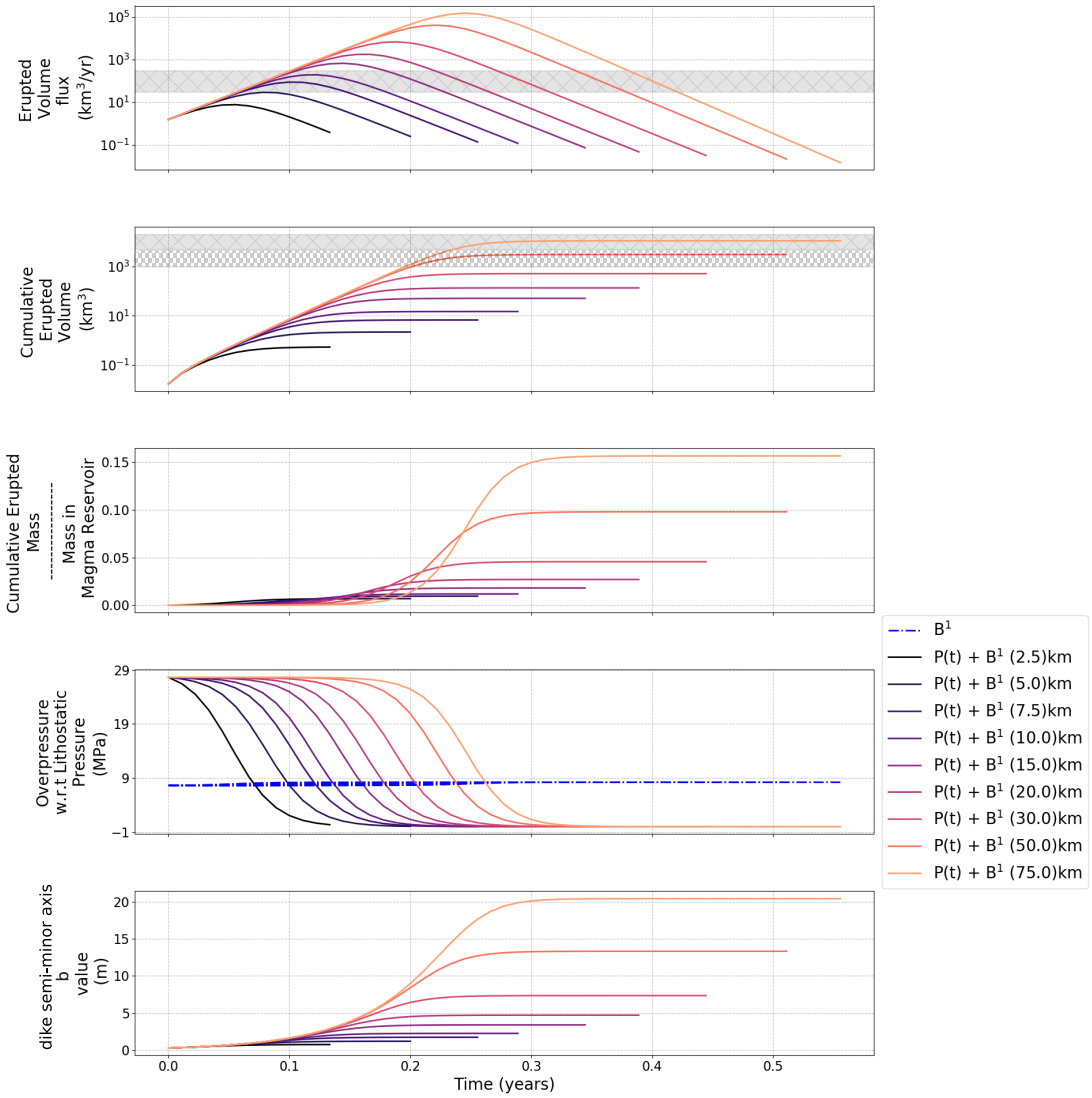

Figure 4.12: Model Results for Elastic Ellipsoidal Reservoir Model : Erupted volume flux (km^3/yr), total erupted volume (km^3), fraction of magma chamber mass erupted, and magma reservoir overpressure (Pa), and dike width (b). The results are shown for different reservoir semi-major axis sizes (See legend in the figure) with a constant semi-minor axis ($b^c = 3$ km). In this calculation, the crustal stress relaxation and melt influx from additional magma reservoirs is not included. The depth of all the reservoirs is set to 5 km. A range of eruptive volume fluxes (30-300 km^3/year) and total erupted volumes (1,000 - 5,000 km^3 : hashed region & 5,000 - 10,000 km^3 : shaded hashed region) for flood basalts based on observational constraints is shown on the figure.The B^1 curve shows the magma buoyancy overpressure in the conduit. At the termination of the eruption, the total overpressure is zero : $P(t)+B^1 \sim 0$.

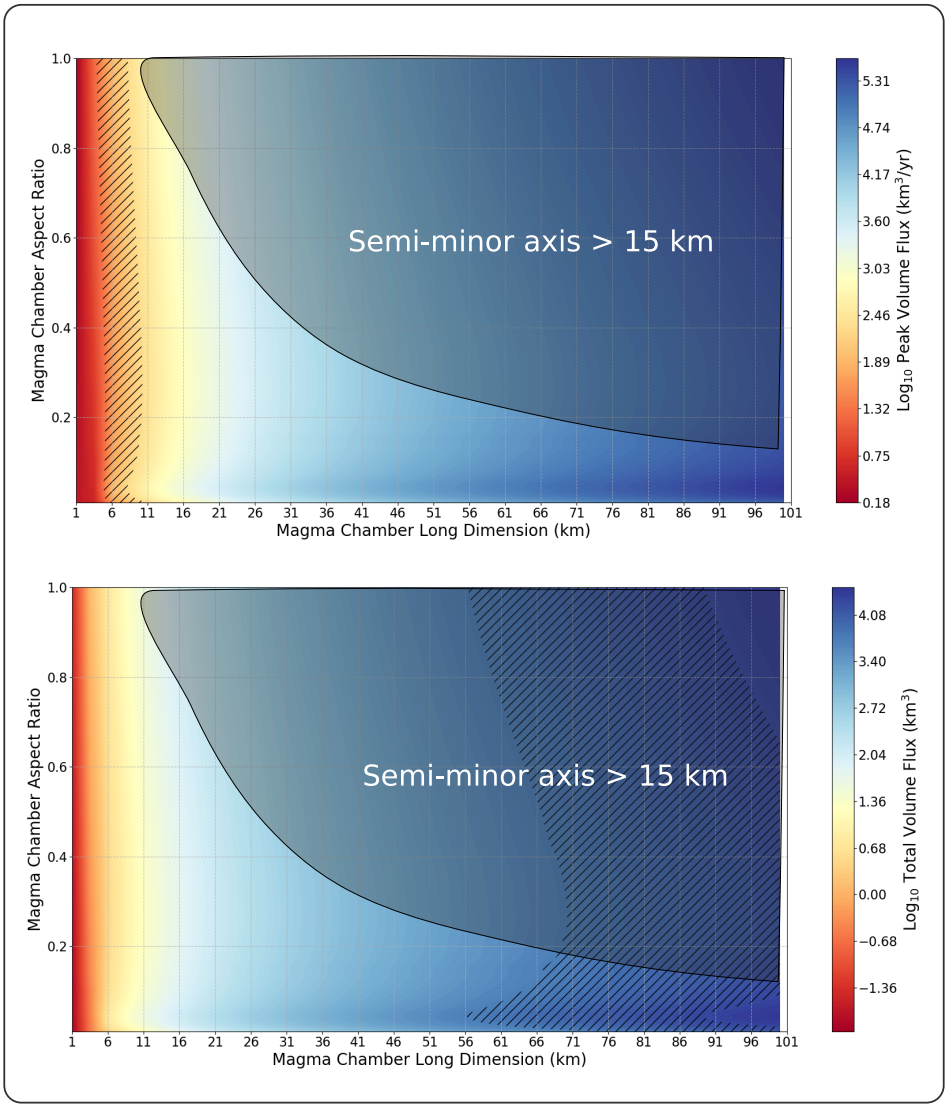

Figure 4.13: Parameter Space plot for Elastic Ellipsoidal Reservoir Model. A range of eruptive volume fluxes (30-300 km^3/year, Top Panel) and total erupted volumes (5,000 - 10,000 km^3, Bottom Panel) for flood basalts is shaded on the plots. These results clearly illustrate that there is no magma reservoir geometry that can simultaneously satisfy both the constraints.

allows more rapid relaxation of the magma over/under-pressure akin to the Spherical Reservoir Model results (See Figure 4.11). This process, in turn, enables longer, larger eruptions with a prolonged low eruption phase. Although this additional eruptive phase decreases the required reservoir size to 30-70 km (for a total erupted volume of 5000-20,000 km^3), this still does not overlap with eruptive rate estimates (Figure 4.15, crustal viscosity = 10^{19} Pa-s). Additionally, the total duration of an eruptive episode is too long to be consistent with observations. We find a qualitatively similar model behavior when we use lower viscous shell viscosity instead of a lower far-field crustal viscosity.

In order to further increase the erupted mass and decrease the eruption duration, we enable melt influx into the primary magma reservoir from an additional large reservoir ($a_{c,2}, b_{c,2}$: 60 km, 4 km) located at 11 km (3 km plus 2 x semi-major axis of the primary reservoir). In Figure 4.16, we show the results of models calculations for a range of primary reservoir sizes (a_c between 5 - 20 km) and conductivity timescales ranging from 0.5 to 100 years (t_{cond}, 4.19). For all the model results, the amplitude of the conductivity (Ω_0), once it is active, is 0.1 kg/Pa-s. In these calculations, we include far-field crustal stress relaxation in a cold crust with the viscosity set to 10^{21} Pa-s for the primary magma reservoir and 10^{20} Pa-s for the secondary (deeper) magma reservoir. The viscosity of the viscous shell surrounding both the magma reservoirs is set to 5 x 10^{18} Pa-s (Degruyter & Huber, 2014).

Analogous to the results from the Spherical Reservoir Model (Figure 4.11B), we find that a variety of magma reservoir sizes can match both the erupted volume flux and total erupted volume constraints with small t_{cond} (Figure 4.16A) even though the far-field crust is relatively high viscosity. However, in contrast to results in Figure 4.11B, the secondary reservoir magma pressure decreases due to mass outflux, and the secondary reservoir becomes under-pressurized over time. This, in turn, reduces the rate in mass flux into the primary reservoir and, consequently, the rate of surface eruptions. In these scenarios, most of the erupted mass is sourced from the deeper magma reservoir directly as illustrated by a 10 km decrease in the semi-major axis of the secondary reservoir. The combination of a large initial reservoir size, as well as lower crustal viscosity, naturally leads to a long-lived eruption. The shape of the primary reservoir geometry only determines the initial eruption rates and the subsequent system behavior is entirely determined by the secondary reservoir dynamics (e.g., Figure 4.16A, same eruption rates and dike widths at $>$ 10 years) as long as the conductivity timescale is short ($t_{cond} \sim 0.5 - 10$ years). The only exception to this is if t_{cond} is large (e.g., 100 years). In this case, the eruptions from the small reservoir stop before the mass influx can begin (Figure 4.16C). In reality, this influx may re-pressurize the primary reservoir sufficiently to lead to tensile failure for the small reservoirs.

Although, these results illustrate one potential magma architecture that can produce appropriate eruptive parameters, the choice of an extensive deep magma reservoir is potentially problematic. In particular, it is unclear if the deep magma system is directly activated in each flood basalt eruption given the geochemical evidence for significant shallow fractionation, especially for the Wai subgroup flow (e.g., plagioclase as the dominant phenocryst, See Section 4.3.1). A large upper crustal magma reservoir is ruled out by geophysical observa-

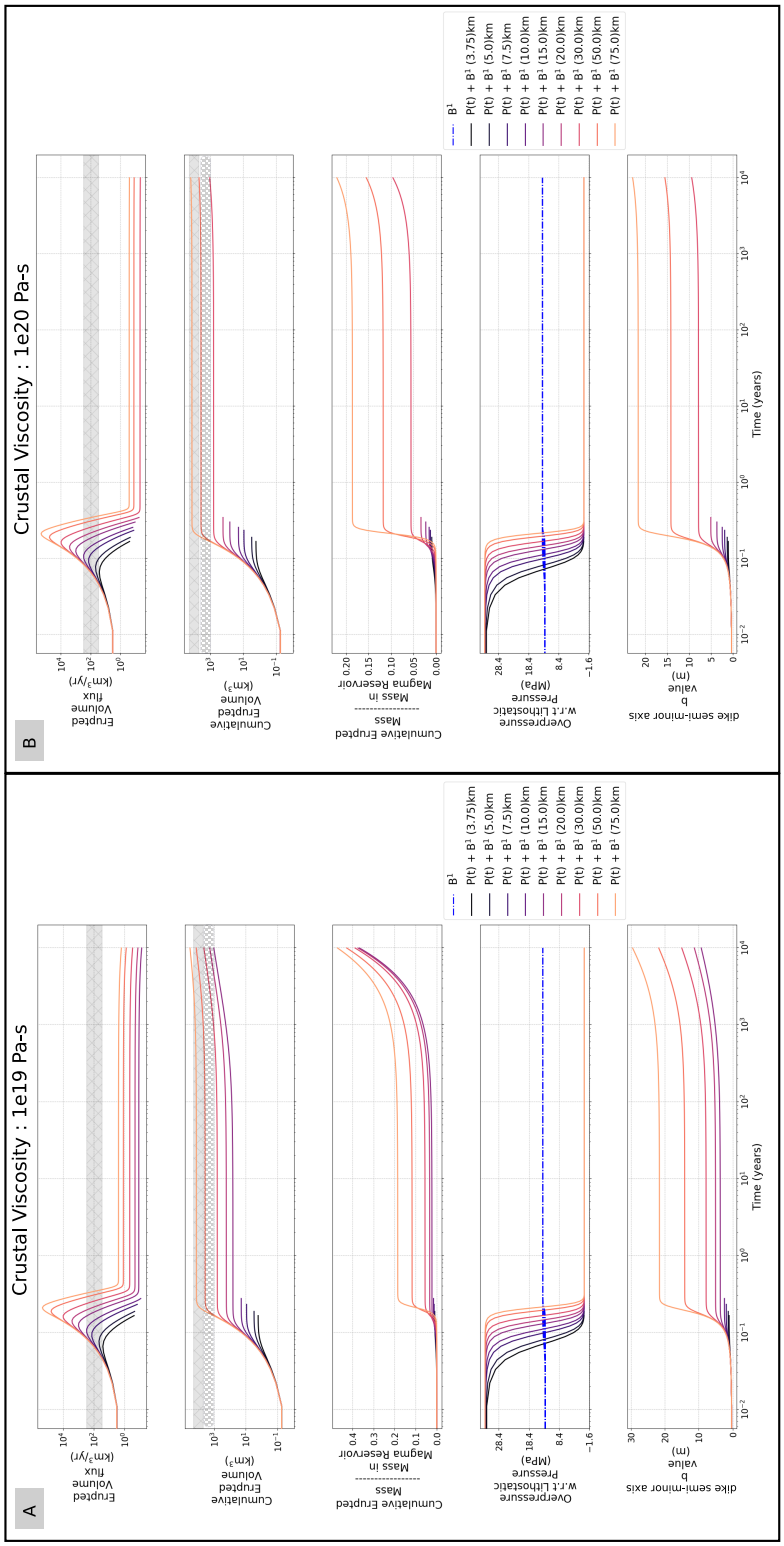
A
Crustal Viscosity : 1e19 Pa-s
B
Crustal Viscosity : 1e20 Pa-s
Erupted Volume flux (km³/yr)
Cumulative Erupted Volume (km³)
Cumulative Erupted Mass ---------- Mass in Magma Reservoir
Overpressure w.r.t Lithostatic Pressure (MPa)
dike semi-minor axis b value (m)
Time (years)
B¹
P(t) + B¹ (3.75)km
P(t) + B¹ (5.0)km
P(t) + B¹ (7.5)km
P(t) + B¹ (10.0)km
P(t) + B¹ (15.0)km
P(t) + B¹ (20.0)km
P(t) + B¹ (30.0)km
P(t) + B¹ (50.0)km
P(t) + B¹ (75.0)km

Figure 4.14

Figure 4.14 *(previous page)*: Model Results for Ellipsoidal Reservoir Model : Erupted volume flux (km^3/yr), total erupted volume (km^3), fraction of magma chamber mass erupted, and magma reservoir overpressure (Pa), and dike width (b). The results are shown for different reservoir semi-major axis sizes (See legend in the figure) and semi-minor axis set to 3 km. In this calculation, we include far-field crustal stress relaxation with the viscosity set to either 10^{19} Pa-s (Panel A) or 10^{20} Pa-s (Panel B) and with no viscous shell relaxation. The depth of all the reservoirs is set to 5 km. A range of eruptive volume fluxes (30-300 km^3/year) and total erupted volumes (1,000 - 5,000 km^3 : hashed region & 5,000 - 10,000 km^3 : shaded hashed region) for flood basalts based on observational constraints is shown on the figure. The B^1 curve shows the magma buoyancy overpressure in the conduit. At the termination of the eruption, the total overpressure is zero : $P(t) + B^1 \sim 0$.

tions (Section 4.3.8). Additionally, if every eruptive episode involves the same large secondary reservoir, it is challenging to explain the geochemical and isotopic changes between successive eruptive events (Section 4.3.6). Finally, the challenges with building enough overpressure within large magma reservoirs (Section 4.2.2.3) make it difficult to argue for the rapid establishment of a high conductivity between the primary and a large secondary reservoir for each eruptive episode. In addition, we find in our model, eruptions from a large secondary reservoir continue for 10,000 years (and potentially even longer). Given the estimates of the typical time between individual eruptive episodes (Section 4.3.3, 4.3.4, 4.3.5), this duration is too long.

Thus, we explore a large parameter space with different conductivity amplitudes (Ω_0) and secondary reservoir sizes. We show the results for a few representative calculations in Figure 4.17 with a smaller reservoir size ($a_{c,2}, b_{c,2}$: 6 km, 2 km) and lower conductivity ($\Omega_0 = 0.001$ Kg/Pa-s). Except for the parameters from Figure 4.16B, none of the other parameter choices can match the eruption rate and erupted volume constraints. For a small reservoir with high conductivity, the faster under-pressurization of the secondary magma reservoir reduces the total erupted volume (Figure 4.17A vs. Figure 4.17C). Similarly, a lower conductivity for the large secondary reservoir leads to a much slower eruption rate (Figure 4.17C vs. Figure 4.17D, Figure 4.17A vs. Figure 4.17B). We find the same qualitative conclusions irrespective of the reservoir depth and volatile content. The higher buoyancy of a more volatile-rich magma mixture leads to slightly higher ($10 - 15\%$) erupted volumes due to higher compressibility as well as the higher underpressure of the primary magma reservoir due to buoyancy. Nevertheless, these processes do not increase the erupted volume for the small secondary reservoir enough to reproduce the observed CFB values. We note that decreasing the far field crustal viscosity does not qualitatively change the results since the viscous stress relaxation is primarily controlled by the low-viscosity visco-elastic shell surrounding the magma reservoir.

It is also noteworthy that even with a small magma reservoir, the eruptive duration in

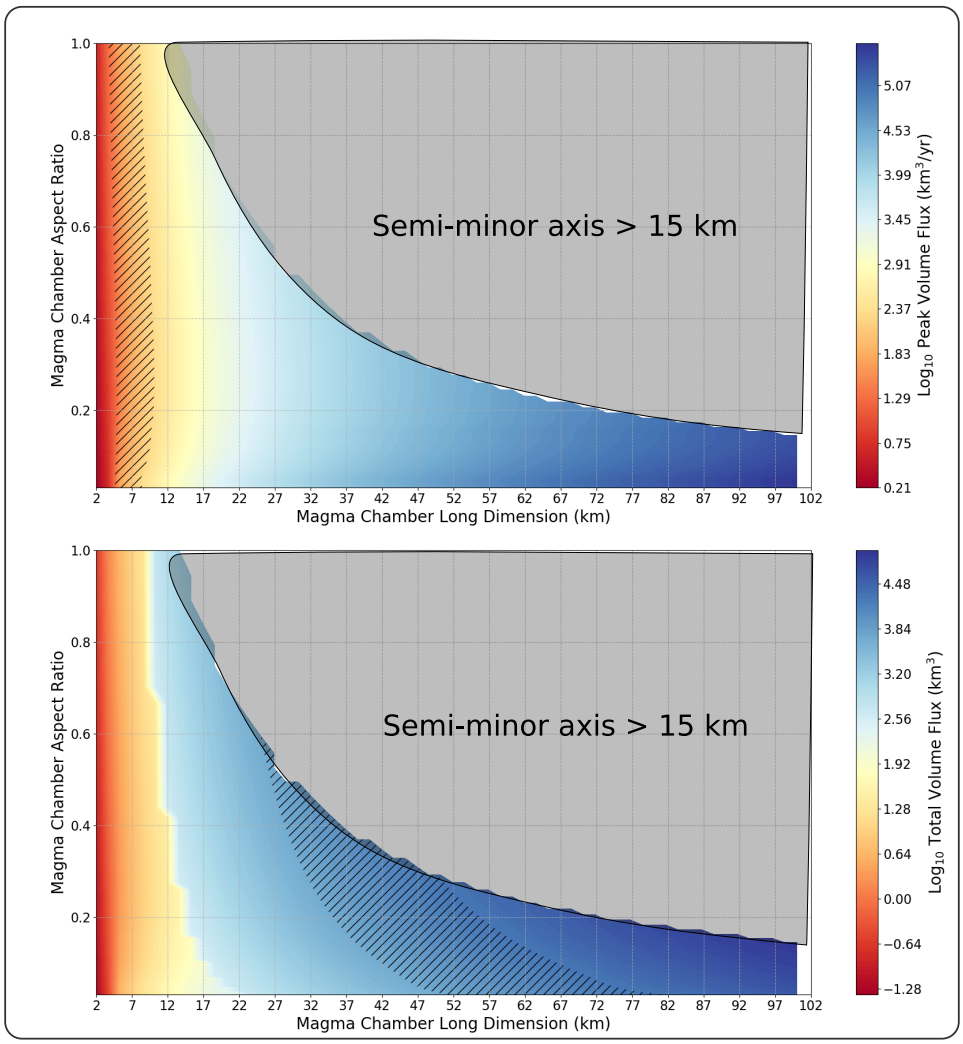

Figure 4.15: Parameter Space plot for Ellipsoidal Reservoir Model with crustal viscous relaxation (viscosity set to $\mathbf{10}^{19}$ **Pa-s**). A range of eruptive volume fluxes (30-300 km^3/year, Top Panel) and total erupted volumes (5,000 - 10,000 km^3, Bottom Panel) for flood basalts is shaded on the plots. These results clearly illustrate that there is no magma reservoir geometry that can simultaneously satisfy both the constraints.

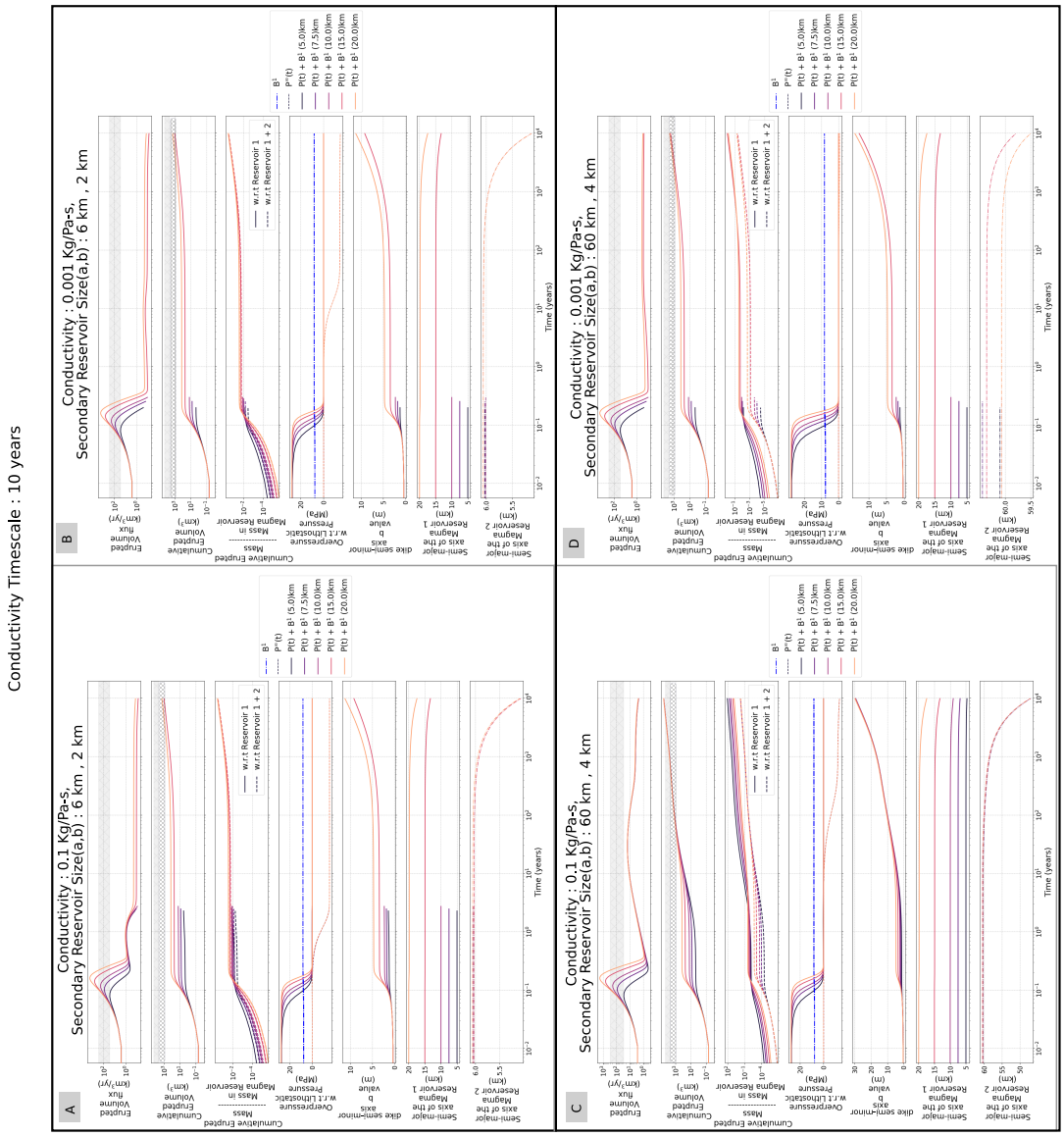
Conductivity Timescale : 10 years
A
Conductivity : 0.1 Kg/Pa-s,
Secondary Reservoir Size(a,b) : 6 km , 2 km
B
Conductivity : 0.001 Kg/Pa-s,
Secondary Reservoir Size(a,b) : 6 km , 2 km
C
Conductivity : 0.1 Kg/Pa-s,
Secondary Reservoir Size(a,b) : 60 km , 4 km
D
Conductivity : 0.001 Kg/Pa-s,
Secondary Reservoir Size(a,b) : 60 km , 4 km
Time (years)

Figure 4.16

Figure 4.16 *(previous page)*: Model Results for the two Ellipsoidal Reservoir Model with different primary reservoir semi-major axis sizes (See legend in the figure) and semi-minor axis set to 3 km. In this calculation, we include far-field crustal stress relaxation with the viscosity set to 10^{21} Pa-s for the primary magma reservoir and 10^{20} Pa-s for the secondary (deeper) magma reservoir. The viscosity of the viscous shell surrounding both the magma reservoir is set to 5 x 10^{18} Pa-s. The depth of primary reservoirs is set to 5 km while the secondary reservoir is at 11 km depth. The conductivity value and secondary reservoir sizes are fixed to 0.1 kg/Pa-s and 60 km, 4 km respectively. The conductivity time-scale for the calculations varies from 0.5 years (Panel A), 10 years (Panel B), and 100 years (Panel C). A range of eruptive volume fluxes and total erupted volumes for flood basalts based on observational constraints is shaded on the plots.

our model is too long to match observations. This is a direct consequence of two physical processes in our model. Firstly, the increase in dike width reduces the magma flux required to reach a unit Peclet number. Thus, even eruptions rates lower than a km^3/year do not terminate the eruption (Figure 4.17A). Secondly, the viscous stress relaxation in the visco-elastic shell and associated magma re-pressurization provides the small pressure gradient to keep low volume eruptions ongoing, potentially until the magma reservoir is almost fully erupted. This behavior is analogous to the volatile driven siphoning proposed for flood basalt eruptions (Karlstrom & Manga, 2009).

We posit that part of this model behavior may not be physical due to missing physics in our model. Following Piombo et al. (2016), the dike width in our model only evolves due to mechanical erosion or plastic deformation. We have not included any elastic response of the dike-shaped conduit or large scale conduit failure, both of which are potentially key processes for restricting eruption duration. Specifically, the low overpressure within the hydrofracture during the later stages of the eruption may elastically reduce the conduit aperture and shut-off the eruption by faster solidification (Pollard & Segall, 1987; Gudmundsson, 2002). A. Aravena, Cioni, de' Michieli Vitturi, et al. (2018) included an elastic deformation component in their model following Costa, Melnik, and Sparks (2007) and found that its net impact on the conduit width is small for typical values of erosion rate (A. Aravena, Cioni, de' Michieli Vitturi, et al., 2018, , See Figure S6). However, the efficiency of this process can be enhanced by reducing the host rock rigidity during an eruption as the country rock heats up and plastically deforms. Since the magma overpressure is negative towards the end of the later stages of eruption, the conduit walls may collapse/elastically close and consequently increase the melt flux required for the critical Peclet number = 2. In the following, we include a first order representation of this behavior by including an addition term to the dike semi-minor axis (b) evolution equation (see Eqns. 4.31). Following Costa et al. (2007); A. Aravena, Cioni, de' Michieli Vitturi, et al. (2018), we calculate the influence of elastic

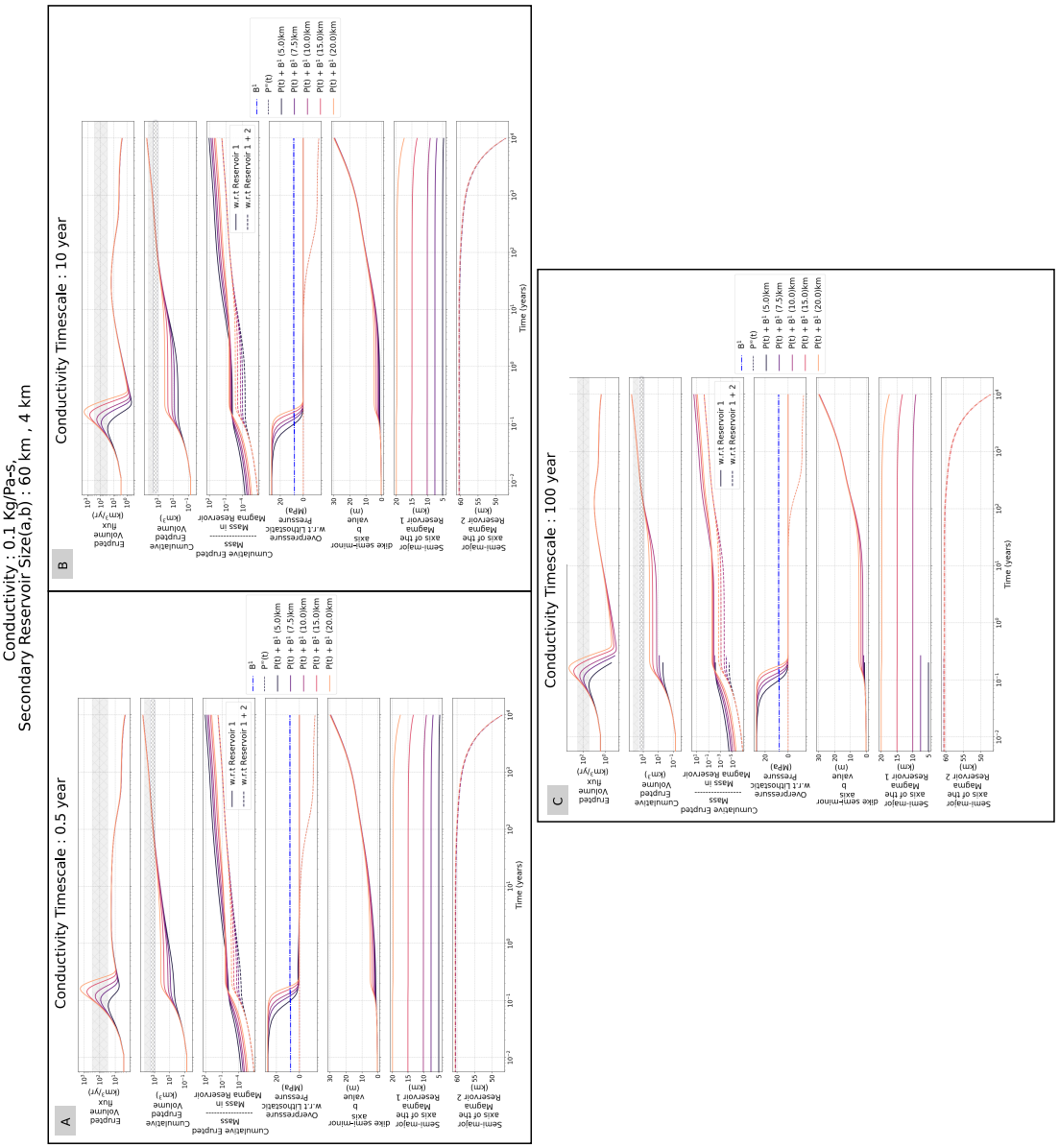
Conductivity : 0.1 Kg/Pa-s
Secondary Reservoir Size(a,b) : 60 km , 4 km
A
Conductivity Timescale : 0.5 year
B
Conductivity Timescale : 10 year
C
Conductivity Timescale : 100 year
Time (years)
w.r.t Reservoir 1
w.r.t Reservoir 1 + 2

Figure 4.17

Figure 4.17 *(previous page)*: Model Results for two Ellipsoidal Reservoir Model for different primary reservoir semi-major axis sizes (See legend in the figure) and semi-minor axis set to 3 km. In this calculation, we include far-field crustal stress relaxation with the viscosity set to 10^{21} Pa-s for the primary magma reservoir and 10^{20} Pa-s for the secondary (deeper) magma reservoir. The viscosity of the viscous shell surrounding both the magma reservoirs is set to 5 x 10^{18} Pa-s. The depth of primary reservoirs is set to 5 km while the secondary reservoir is at 11 km depth.. The conductivity time-scale for all the calculations is fixed to 10 years with two different conductivity values (Panels A & B; Panels C & D), and two different secondary reservoir sizes (Panels A & C; Panels B & D). A range of eruptive volume fluxes and total erupted volumes for flood basalts based on observational constraints is shaded on the plots.

deformation on b as :

$$b_{steady}(t) = b(t) + P(t)(f_2(t)a + f_1(t)b) \tag{4.106}$$
$$f_1(t) = (2 * \nu_r - 1)/(2\mu_r(t)) \tag{4.107}$$
$$f_2(t) = (1 - \nu_r)/(\mu_r(t)) \tag{4.108}$$
$$\mu_r(t) = [10exp^{-t/t_{cool,b}} + 0.5\,]\text{GPa} \tag{4.109}$$

Here ν_r (= 0.3) and $\mu_r(t)$ (in GPa) are the Poisson ratio and the rigidity of the host rock respectively. We allow evolution of μ_r over a cooling timescale $\sim 5(b^2/\kappa_{thermal})$ to model the thermal weakening of the conduit with continued magma flux. Thus, the ability of a conduit to remain stable during under-pressurization will progressively decrease (see more discussion in Á. Aravena, Cioni, Vitturi, & Neri, 2018, and references therein). Using the difference between the present conduit shape (b) and the steady state elastic shape b_{steady}, we write a relaxation term $b_{elast,relx}$:

$$b_{elast,relx} = (b_{new} - b)/t_{relax,elast} \tag{4.110}$$

We set $t_{relax,elast} \sim 10$ years (decreasing to 1 year if $b_{elast,relx}$ is negative). We acknowledge that this parameter is extremely uncertain and can potentially be much smaller than a year (e.g., kilauea eruption C. Neal et al., 2019) or very long considering the crustal Maxwell time-scale. Here, we chose an intermediate value assuming a low crustal rigidity and low crustal viscosity near the conduit.

In our model, the net evolution of the dike semi-minor axis (b) is :

$$\frac{db}{dt} = \frac{k}{d_{res}}\Big[P(t) + (\rho_c - \rho_{res})gd_{res}\Big]b + b_{elast,relx} \tag{4.111}$$

We acknowledge that our model is highly idealized and introduces additional not well constrained model parameters. In the following, we have typically chosen model parameters

that prevent continued eruptions with eruption rates less than ~ 0.5 km^3/year in order to be consistent with the lower end of estimates from Section 4.3.5 (also see A. Aravena, Cioni, de' Michieli Vitturi, et al., 2018). To first order, the additional dike semi-major axis evolution model helps terminate eruptions much earlier for the small magma reservoirs.

4.5.2.3 Multiple Secondary Reservoirs

Given the challenges with a single reservoir model, we next consider a model scenario where the primary reservoir is connected to multiple secondary reservoirs. This model setup approximates the idea of a magmatic architecture composed of a set of magma reservoirs interconnected through multiple magma transport pathways analogous to what has been proposed for modern-day arc and hotspot volcanism (e.g., B. D. Marsh, 2013; Cashman et al., 2017, see Figure 4.29B for a cartoon illustration). A particularly relevant example is the Icelandic Eyjafjallajokull 2010 eruption where there is seismic and petrological evidence of stress interaction between sill-shaped magma lenses over weeks and consequent failure to feed the eruptive conduit (Tarasewicz, White, Woods, Brandsdóttir, & Gudmundsson, 2012; R. S. White et al., 2019).

To illustrate the model behavior with this configuration, we show a set of representative calculations in Figure 4.18. For these calculations, the primary reservoir (a_c, b_c: 7.5km, 2 km; 5 km depth) is connected to five additional secondary reservoirs with semi-major axes between 15-25 km and a 3 km semi-minor axis (depth of 11 km). The crustal viscosity is 10^{21} Pa-s for the primary reservoir and 10^{20} Pa-s for the secondary reservoirs. We initialize the system with an overpressure of 20 MPa in the primary reservoir and between 5-20 MPa for the secondary reservoirs (to represent various stages of magmatic evolution). The viscosity of the viscous shell surrounding each of the magma reservoirs is set to 1 x 10^{19} Pa-s (Figure 4.18A) or 2 x 10^{19} Pa-s (Figure 4.18B). We also calculate the erupted magma composition based on a simple mixing model for the primary magma reservoir (Eqn. 91). The initial compositions of all the reservoirs are chosen at random between 4 to 6 wt % MgO (a range typical of Wai subgroup flows, Beane et al., 1986, Figure 4.4e)/

In Figure 4.18, we show the results for two representative calculations with different conductivity timescales (t_{cond}) and amplitude (Ω_0). In Figure 4.18A, we use a high $\Omega_0 = 0.3$ Kg/Pa-s and a range of conductivity timescales (t_{cond} = 0.1, 0.2, 0.5, 2, and 5 years). This model case represents a more mature magmatic system with high inter-connectivity. For Figure 4.18B, we choose a lower conductivity (Ω_0 = 0.01 Kg/Pa-s) as well as longer conductivity timescales (t_{cond} = 0.1, 0.5, 5, 10, and 20 years). Not surprisingly, we can better match the eruptive flux and volume constraints, especially for the parameters in Figure 4.18A. With a less mature magmatic system (e.g., Figure 4.18B), the time-averaged eruptive flux is lower and a longer eruption duration is required to reach the appropriate erupted volumes. Also, the range of conductivity timescales naturally introduces variable surface eruption rates, which have been hypothesized to be a requirement for the formation of inflated sheet lobes (e.g., Rader et al., 2017). The bottom panels of Figure 4.18A and

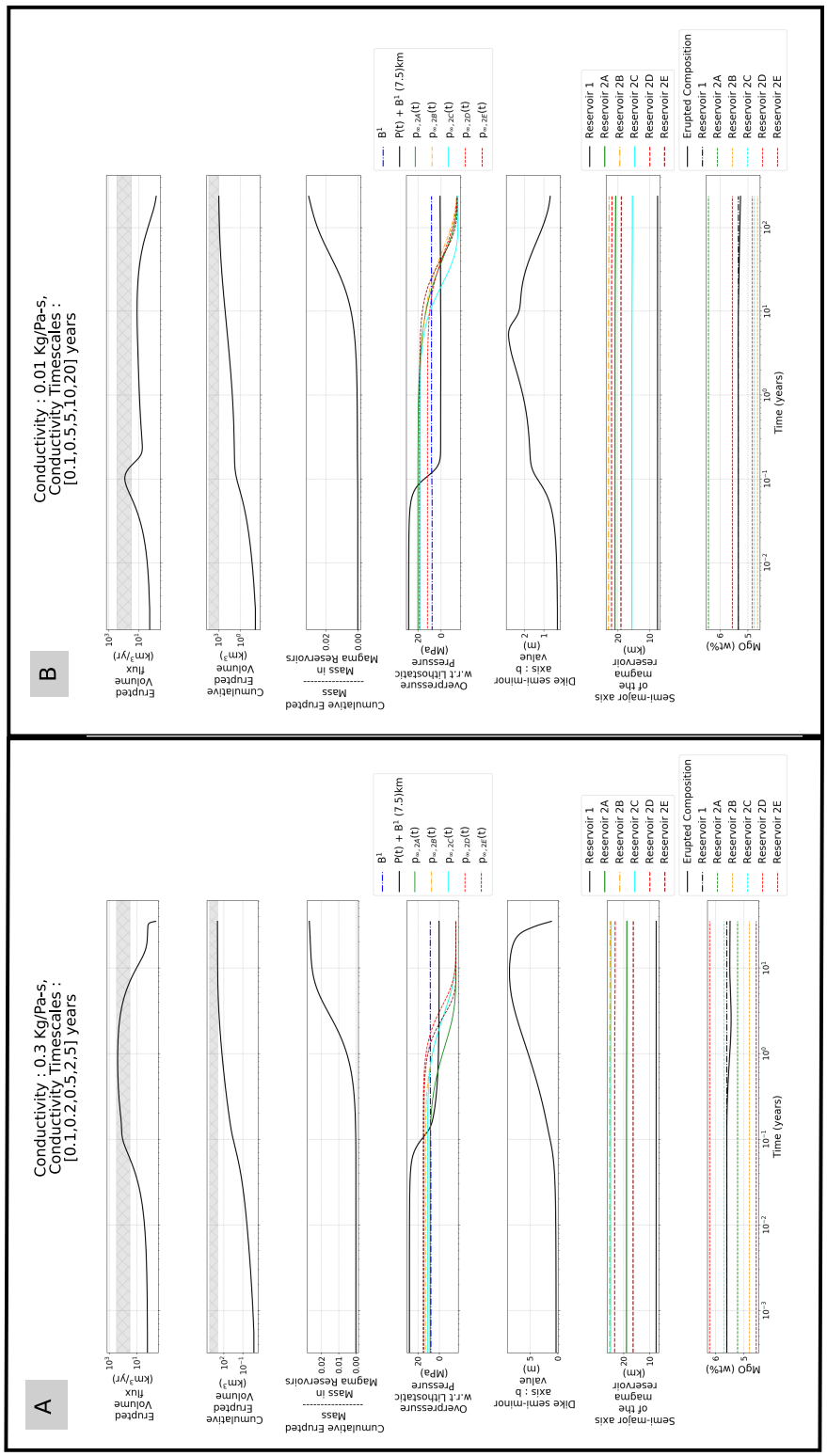
A
Conductivity : 0.3 Kg/Pa-s,
Conductivity Timescales :
[0.1,0.2,0.5,2,5] years
B
Conductivity : 0.01 Kg/Pa-s,
Conductivity Timescales :
[0.1,0.5,5,10,20] years
Erupted Volume flux (km³/yr)
Cumulative Erupted Volume (km³)
Cumulative Erupted Mass
Mass in Magma Reservoirs
Overpressure w.r.t Lithostatic Pressure (MPa)
Dike semi-minor axis : b value (m)
Semi-major axis of the magma reservoir (km)
MgO (wt%)
Time (years)
B¹
P(t) + B¹ (7.5)km
Reservoir 1
Reservoir 2A
Reservoir 2B
Reservoir 2C
Reservoir 2D
Reservoir 2E
Erupted Composition

Figure 4.18

Figure 4.18 *(previous page)*: Model Results for multiple Ellipsoidal Reservoir Model : Erupted volume flux (km^3/yr), total erupted volume (km^3), fraction of magma chamber mass erupted, and magma reservoir overpressure (Pa), and dike width (b), and MgO wt %. The primary reservoir has a semi-major axis 7.5 km, semi-minor axis 2 km at 5 km depth connected to 5 secondary reservoirs with different conductivity values and conductivity timescales (See in Figure title). The initial size of each of the secondary reservoir is 15-25 km (semi-major axis), 3 km (semi-minor axis), 11 km depth with the crustal viscosity of 10^{21} Pa-s for the primary reservoir and 10^{20} Pa-s for the secondary reservoirs. The viscosity of the viscous shell surrounding both the magma reservoirs is set to 1 x 10^{19} Pa-s (Panel A), and 2 x 10^{19} Pa-s (Panel B). A range of eruptive volume fluxes and total erupted volumes for flood basalts based on observational constraints is shaded on the plots. Panel A represents the higher inter-reservoir conductivity scenario while the Panel B shows the impact of longer conductive times and lower conductive amplitude.

17B show the erupted composition will have some intra-flow variation due to the different compositions of secondary reservoirs and varying levels of mixing. Finally, a final dike width of $\sim$ 10 m is very consistent with the range of feeder dike widths in Deccan Traps, especially the active portions of a multiple dike (Section 4.3.7).

We want to emphasize that our parameter choices are not unique and it is possible to obtain the same time-averaged eruptive flux and total volume with different parameters. Additionally, it is not difficult to sustain higher eruptive fluxes and/or longer eruptions by changing the conductivity timescales, conductivity amplitude, as well as the number of secondary reservoirs. At present, it is difficult to infer how the eruptive style and rates evolved during a CFB eruptive episode based on the lava flow morphology or geochemical variations due to lack of systematic observations (See Section 3.5 and 3.6). Thus, we are not trying to match a specific eruptive history with these calculations. Instead, these results show that the properties of a CFB eruptive episode can be explained by a multiply connected magmatic system.

4.5.3 Timescale analysis

We can summarize the key features of the Magma Reservoir Models using a few key characteristic timescales for the primary magma reservoir : timescale for re-pressurization by recharge ($t_{repress}$), crustal and visco-elastic shell relaxation (t_{relax}), establishment of significant conductivity between reservoirs (t_{cond}), and the timescale for overpressure relaxation by eruptions (t_{flux}, Eqns. 19, 25-27, Table 1). We define t_{relax} as the minimum of $t_{Maxwell}$ and $t_{R,relax\,compress}$ since both of them represent viscous stress relaxation in the surrounding

crust. Using t_{flux} to non-dimensionalize the timescales, we get :

$$\Theta_1 = t_{flux}(t=0)/t_{relax} \tag{4.112}$$

$$\Theta_2 = t_{flux}(t=0)/t_{cond} \tag{4.113}$$

$$\Theta_3 = t_{repress}/t_{flux}(t=0) \tag{4.114}$$

We show a regime diagram with these non-dimensional numbers in Figure 4.19. With two or more magma reservoirs, the full system behavior is controlled by an analogous set of non-dimensional numbers for the secondary reservoir. These additional numbers are necessary to fully describe the model results, especially the absolute values of the erupted volume and eruption rates. Additionally, the conduit width can significantly change (by a factor of 100 in some of the calculations) leading to a significant time-evolution of the t_{flux}. A full analysis of this system is beyond the scope of this study. We do, however, find that Θ_1, Θ_2, and Θ_3 provide a "qualitative" description of the model behavior.

We first consider the case of high reservoir conductivity such that $t_{repress}$ and t_{flux} are comparable or t_{flux} is smaller (i.e. $\Theta_3 < 10$, Figure 4.19A). If both the timescales for magma recharge and crustal viscous stress relaxation are significantly longer than the t_{flux} ($\Theta_1 << 1$, $\Theta_2 << 1$), then the erupted mass is sourced only from the primary magma reservoir with a high initial eruption rate and short eruptions (elastic limit, Figure 4.12). As the viscosity of the visco-elastic shell decreases, the rapid relaxation of magma underpressure allows a continuous eruption at a low eruption rate (Figure 4.14). Consequently, the time-averaged eruption rate (over the eruption duration) for the system decreases. Since the magma eruption is long-lived, the recharge can contribute to the erupted mass even for $\Theta_2 < 1$ (e.g., Figure 4.16C). This further increases the total erupted volume.

At the other end-member, if the crust is elastic ($\Theta_1 << 1$) but the timescale for recharge is large, i.e., $\Theta_2 > 1$, the recharge from the secondary reservoir will ensure a high continuous eruption rate. Since the crustal response (for both magma reservoirs) is primarily elastic, the eruptions will stop when both the magma reservoirs are underpressurized. If instead, the crust has a lower viscosity (larger Θ_1), eruptions will be long-lived but with lower eruption rates. Thus maximum erupted mass in the system is in the top right parameter space ($\Theta_2 > 1$, $\Theta_2 > 1$). The maximum time-averaged eruption rates are for the lower right part of parameter space ($\Theta_2 > 1$, $\Theta_2 < 1$). A larger primary magma reservoir will increase the t_{flux} for the same dike width, thus moving us towards the top right of the parameter space. Given the model results and the observational constraints, we anticipate that the optimal parameter space for CFB eruptions is in the center-right part of the parameter space (Figure 4.19A). However, the specific region of parameter space would depend on the parameters of the secondary reservoirs.

If the size of the secondary magma reservoir is increased, the maximum eruption rate, as well as the erupted volume, will increase along with potentially a small increased time-averaged eruption rate (e.g., Figure 4.17A, 16C). We illustrate this in Figure 4.19B with the blue arrow direction chosen to represent these characteristics. On the other hand, if the

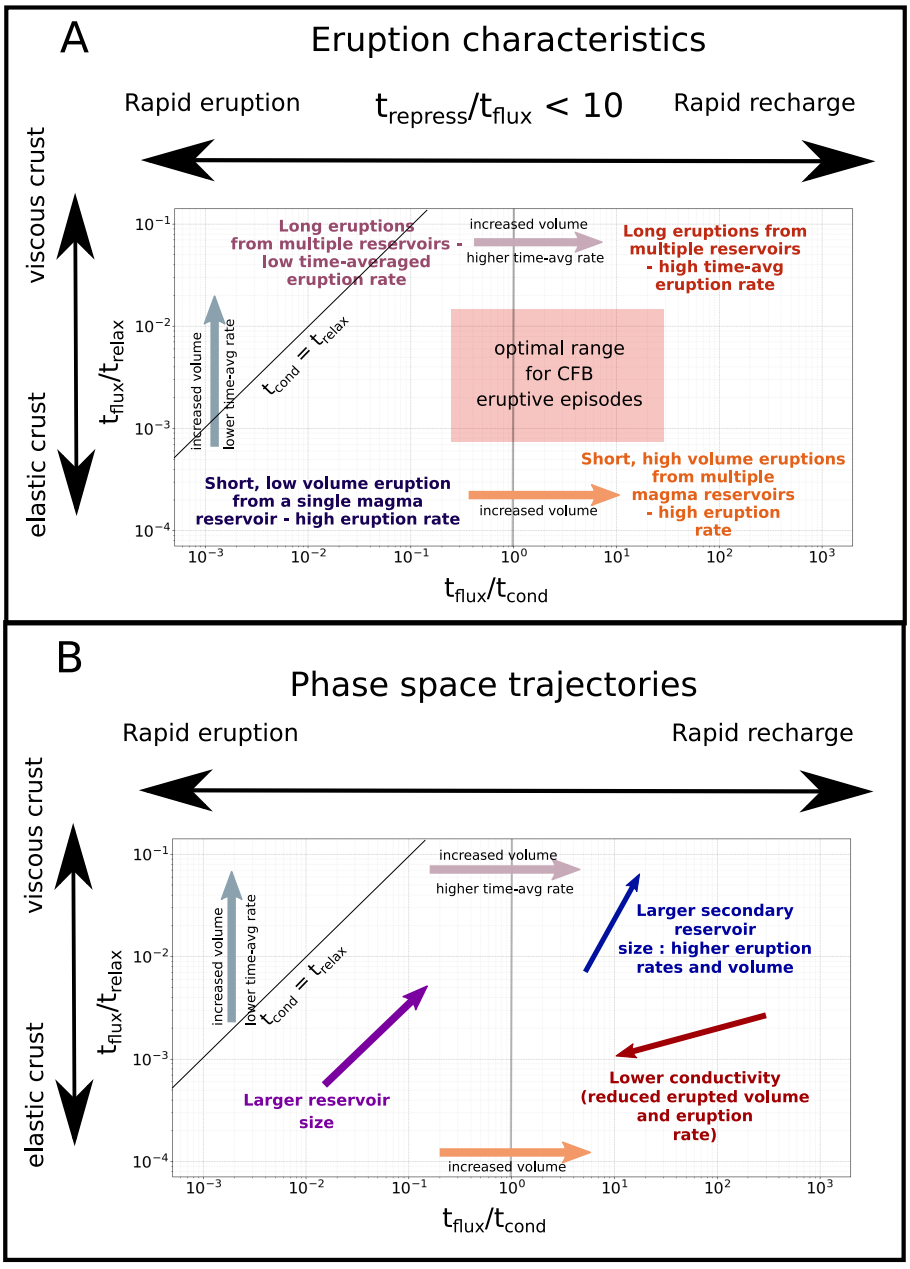

Figure 4.19: Regime diagram for the two Ellipsoidal Reservoir Model. Using results from Section 4.5.2, the changes in eruption fluxes and duration are illustrated on the regime diagram (Panel A). In Panel B, we show how changes in physical properties of the reservoirs as well as other characteristic timescale translate to movement in this regime space. We also highlight a potential region for optimal continental flood basalt eruptions in Panel A.

reservoir conductivity decreases, both $t_{repress}$ and Θ_3 will increase. As illustrated by Figure 4.17C & 16D, this would typically lead to reduced erupted volume as well as eruption rates (red arrow in Figure 4.19B).

4.5.3.1 Implications for CFB architecture

In conclusion, our model results clearly illustrate that eruptions from a single large magma reservoir do not match the observational constraints on DT eruption rates and eruption durations. Instead, magma recharge during the eruption from secondary magma reservoirs is a key requirement. We posit that based on a variety of observations, this secondary magma reservoir cannot just be a large lower crustal magma body (See Section 4.5.2). Instead, our preferred model architecture for CFBs is the presence of several small ($\sim 10^2$ - $10^{3.5}$ km^3) interconnected magma reservoirs present throughout the crust. As illustrated in Figure 4.18 (with potentially even more coupled reservoirs), such a magmatic architecture can help explain both the properties of individual eruptive episodes as well as the intra-flow geochemical variability (Section 4.3.7).

4.6 Model results - Thermal Model

We next assess how the crustal thermal evolution affects the ability of different magma bodies to erupt vs. accumulate and grow. We first briefly describe the phase space, how it relates to eruption frequency, and how changing reservoir and crustal properties translate to the phase space. We then present model results for first a constant time-averaged melt flux followed by a melt flux representative of a melts from a mantle plume head.

4.6.1 Magmatic Timescales

We can define a magma reservoir's eruptive dynamics using a set of four characteristic timescales : $t^c_{viscous}$, t^c_{cool}, t^c_{fill}, and $t^c_{press\,diff}$ (Eqns 92-95, Degruyter & Huber, 2014; Mittal & Richards, 2019). In order to compare these timescales, we define the following non-dimensional Deborah timescales (ratios of two different characteristic times) :

$$De_{visc} = t^c_{viscous}/t^c_{fill} \tag{4.115}$$

$$De_{cool} = t^c_{cool}/t^c_{fill} \tag{4.116}$$

$$De_{pd} = t^c_{press\,diff}/t^c_{fill} \tag{4.117}$$

$$\tag{4.118}$$

In Figure 4.20A, we show the 2D regime diagram (assuming $De_{pd} >> 1$). When $De_{viscous} < 1$, the viscous relaxation will prevent a magma reservoir for reaching sufficient overpressure to initiate diking to the surface (Degruyter & Huber, 2014). If $De_{cool} < 1$ but $De_{visc} > De_{cool}$, eruptions can still occur due to pressurization by secondary volatile exsolution during cooling (Region 1) whereas in the converse, no eruptions occur and the magma

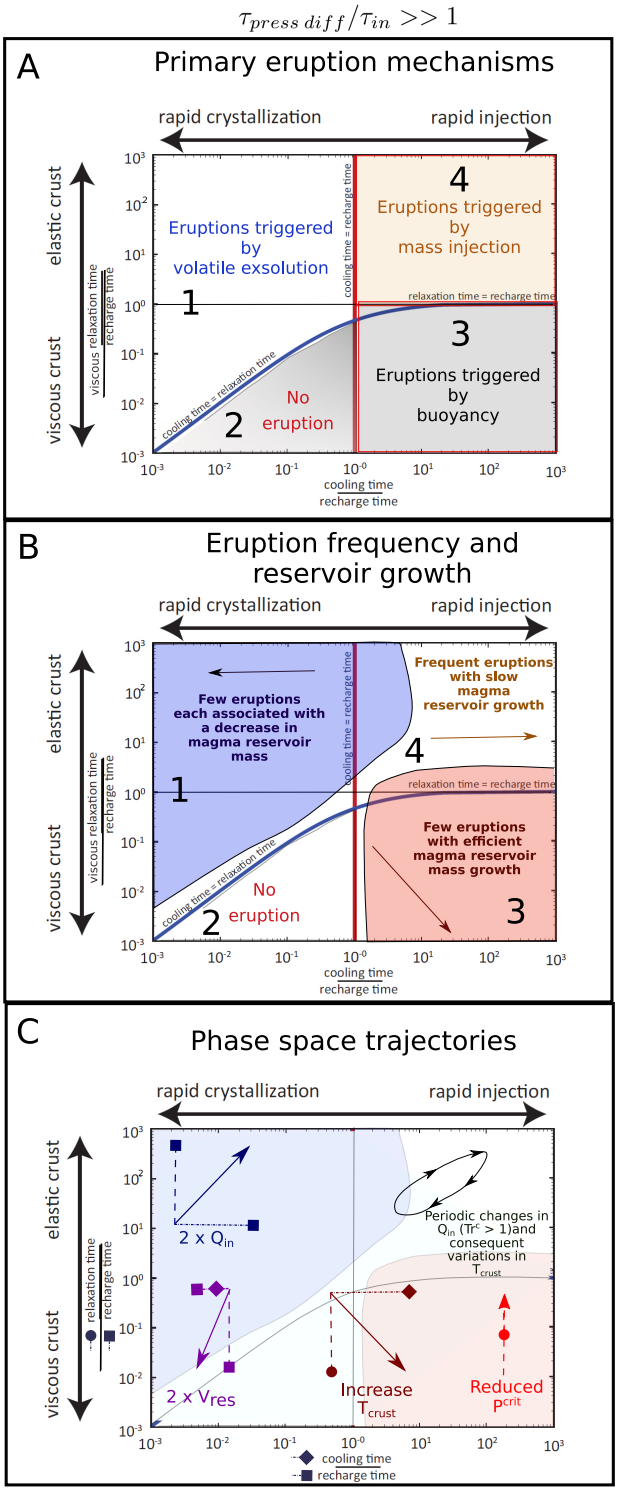
$\tau_{press\ diff}/\tau_{in} >> 1$
A
Primary eruption mechanisms
rapid crystallization
rapid injection
elastic crust
viscous crust
viscous relaxation time
recharge time
Eruptions triggered by volatile exsolution
1
4
Eruptions triggered by mass injection
cooling time = recharge time
relaxation time = recharge time
3
Eruptions triggered by buoyancy
cooling time = relaxation time
2
No eruption
cooling time
recharge time
B
Eruption frequency and reservoir growth
Few eruptions each associated with a decrease in magma reservoir mass
Frequent eruptions with slow magma reservoir growth
Few eruptions with efficient magma reservoir mass growth
C
Phase space trajectories
2 x Q_{in}
Periodic changes in Q_{in} (Ti^c > 1)and consequent variations in T_{crust}
2 x V_{res}
Increase T_{crust}
Reduced P^{crit}

Figure 4.20

Figure 4.20 *(previous page)*: Regime diagram for the non-dimensional magmatic timescales (Degruyter & Huber, 2014; Mittal & Richards, 2019) when pressure diffusion is not important. In Panel A, we show how the eruptibility changes as a function of non-dimensional parameters as well as which eruption mechanism dominates. In Panel B, we used results from Townsend et al. (2019) and Black and Manga (2017) to illustrate regions of reservoir growth vs shrinkage and how the eruption frequency changes across the phase space. In Panel C, we illustrate the direction of translation in the phase space based on potential changes in crustal and reservoir properties (Arrow line). The dashed and dotted lines illustrate how different components - filling timescale (square), cooling time (diamond), and viscous timescales (circle) contribute to the net motion in the phase space.

will accumulate as intrusions (Region 2). On the other hand, $De_{cool} > 1$ and $De_{viscous} > 1$ allows buildup of magma overpressure by recharge (Region 4). Finally, if $De_{cool} > 1$ and $De_{viscous} < 1$, the magma reservoir will not cool rapidly enough to crystallize but any elastic stress accumulation is relaxed too rapidly (Region 3). Thus, the only viable mechanism to initiate tensile failure is buoyancy overpressure (See Section 4.2.2) or external triggers (de Silva & Gregg, 2014; Gudmundsson, 2016). When $De_{pd} < 1$ (not shown here, see Mittal & Richards, 2019), pressure diffusion of volatiles will reduce the ability of a magma reservoir to pressurize and erupt. We show a couple of other orthogonal projections of the phase space in Figure 4.21 (bottom right panel). In the limit of $De_{viscous} >> 1$, the phase space behavior is similar with De_{pd} being the stress relaxation mechanism instead of $De_{viscous}$. Finally, when $De_{viscous} > De_{pd}$, pore pressure diffusion is the relevant relaxation mechanism while viscous stress relaxation dominates in the opposite case.

Within this 3D phase space, the eruption frequency and the reservoir growth rate also vary. Based on the results from M. Townsend et al. (2019) and Black and Manga (2017), we show the various regimes in Figure 4.20B for a 2-D slice of the full phase space assuming De_{pd} much larger than 1. In Region 1 (along with a small fraction of Region 2), individual eruptions are associated with a net mass loss since volatile exsolution increases the magma compressibility and hence the efficiency of the eruption. Additionally, a single magma reservoir does not erupt very frequently or many times before solidification (Degruyter & Huber, 2014). This result is a direct consequence of the fact that volatile exsolution would generally require a significant amount of cooling per cycle, and this is not very efficient to sustain frequently erupting long-lived magma bodies.

In Region 3, on the other hand, the cooling timescale is much longer than the recharge timescale leading to reservoir growth. Since buoyancy overpressure is the primary mechanism for eruption, individual eruptions, if they occur, are large but very infrequent (Black & Manga, 2017, Section 4.2.2.3). Finally, in Region 4, recharge is an efficient mechanism for eruptions. Consequently, the magma reservoir can erupt frequently but does not accumulate much mass over multiple eruption cycles. We note these results have been calculated

using a much more simplified eruption model than presented in the previous section. Specifically, an eruption in this model stops when the magma pressure reaches lithostatic rather than the magmastatic condition (See discussion in Section 4.5.1 Degruyter & Huber, 2014; Mittal & Richards, 2019). Additionally, the magma reservoir geometry can also influence the eruption frequency. Nevertheless, we still expect that the overall pattern of eruption frequency and reservoir growth vs. shrinkage is a robust conclusion given the underlying physical mechanisms described above.

The primary focus of our subsequent analysis is to assess how changes in magma reservoir size, as well as crustal temperature, affect the likelihood of eruptibility. In Figure 4.20C, we illustrate how these changes translate to the phase space (2D slice with $De_{pd} >> 1$). Firstly, an increase in magma reservoir size leads to a decrease in De_{cool} since $t^c_{cool} \propto R^2$ (diamond in Figure 4.20C) while $t^c_{fill} \propto R^3$ (square in Figure 4.20C). Similarly, De_{visc} as well as De_{pd} decrease as well. Thus, in conclusion, an increase in reservoir size is a net left-downward direction (Purple color). Since the buoyancy overpressure is proportional to the reservoir's height, an increase in the size of the magma body would also increase the likelihood of buoyancy-driven eruption.

An increase in crustal temperature decreases the crustal viscosity (and hence t^c_{visc} - circle symbol in Figure 4.20C) and crustal permeability (De_{pd} increase) while increasing the cooling timescale t^c_{cool}. In aggregate, the hotter crust is characterized by a right-downward arrow in the 2D phase space (Brown color). A reduction in critical overpressure ΔP increases the t^c_{visc} without affecting any of the other timescales. Hence, it is represented by an upward arrow (Red color). Finally, an increase in the recharge rate decreases the t^c_{fill} and is thus represented by the right-upward arrow (Blue color).

Besides the Deborah numbers described above, there is one additional characteristic timescale in our 1D thermal model. Following Karlstrom et al. (2017), we allow variability in the input melt flux with a time period T_{period} (Section 4.2.2). Non-dimensionalizing this with the reservoir recharge timescale, we get another non-dimension number :

$$\mathrm{Tr}^c = T_{period}/t^c_{fill} \tag{4.119}$$

Here Tr^c is the crustal transport number, which quantifies whether variability in melt supply is significant compared to the mean recharge rate for a given magma reservoir. Typically, an increase in parental melt flux would be associated with crustal temperature increase (since not all the melt may be directly emplaced in the magma body) and vice-versa. Thus, in the phase space (Figure 4.20C), periodic variations in melt flux can trace a loop oriented along the right-upward arrow direction (Black color, Figure 4.20C). The larger the Tr^c value, the larger the amplitude of the corresponding loop.

4.6.2 Constant Melt flux

We first consider a constant time-averaged melt flux of 10^{-6} (km^3/year)/km^2 at the base of the 30 km crustal section with a dike injection lengthscale (L^{rng}_{dike}) of 15 km (See Section

4.2 and 4.3 for other parameter choices) and $\mathrm{Tr}^{cr} \sim 0.05$ (Figure 4.21, top panel). Integrated over the mantle plume head with a radius of $\sim$ 500 km (e.g., Farnetani, Hofmann, Duvernay, & Limare, 2018) also approximately equivalent to the circular area of DT), our chosen flux represents a total melt flux of 0.75 km^3/year. Since we do not model explicitly regions of melt accumulation in our model, all input crustal melt is emplaced stochastically as dikes. Consequently, our chosen parameter value is, to first order, reasonable since a substantial fraction of the plume melt will accumulate in magma bodies and feed surface eruptions. The total duration of all our model calculations is 2 Ma.

We show the results for this parameter set in Figure 4.21. In the top panel, we plot the input melt flux at the base of the crust. The bottom left panel of Figure 4.21 shows the results of the thermal calculation over time along with the corresponding values of various De numbers for a small magma body (a_c, b_c: 2 km, 600 m) as well as the Buoyancy overpressure w.r.t local lithostatic pressure. We find that with continued melt emplacement into the crust, the lower crustal temperature increases rapidly while the upper crust remains cold due to hydrothermal circulation and L^{rng}_{dike} of 15 km. Because of the increase in temperature and a corresponding decrease in crustal viscosity, both the Maxwell and the viscous relaxation times decrease. There is also a corresponding increase in the cooling timescale due to higher background temperature. Finally, the crustal permeability at great depths is too low to significantly affect pore pressure diffusion. Coupled with the low volume fraction of magmatic volatile phase at depth, De_{pd} is very large in the lower crust but is much less than 1 in the top $\sim$ 5 km of the crust. Since the magma reservoir is only 600 m depth, the buoyancy overpressure is negligible for all depths.

The bottom right panel of Figure 4.21 shows three projections of the De number phase space (described in the previous section). In this phase space, we show the temporal De number trajectories for magma bodies emplaced at a few different depths. The De_{pd} vs. De_{visc} phase space (Panel III) shows that the dominant stress relaxation process at shallow depths (5 km and 9 km depths) is pore pressure diffusion. In contrast, viscous stress relaxation is more important for deeper magma bodies. Thus, the appropriate 2D phase space for the shallow bodies is De_{pd} vs. De_{cool} (Panel II) while De_{visc} vs. De_{cool} (Panel I) is the relevant phase for the deeper magma reservoirs.

Due to the high crustal permeability, the 5 km depth magma body is likely to never erupt. In contrast, the same sized magma body at the 9 km depth can erupt due to volatile exsolution throughout the 2 Ma time interval (if the melt has sufficient volatiles). We find that although even deeper magma bodies can initially erupt via volatile exsolution, the temperature increase eventually shuts off eruptions with buoyancy overpressure being the only viable eruption mechanism. In Figures 4.22, 4.23, 4.24, we show the results for the same thermal model for three different magma reservoir sizes (a^c, b^c): 2km, 600m; 5 km, 1.5 km; and 20 km, 5 km. The pattern for all three magma bodies in their respective panel I are essentially the same except that the trajectories are translated to the left for larger magma bodies. This result is consistent with the conclusions from the previous section (and illustrated by the purple arrow in Figure 4.20C). It is interesting to note that the larger

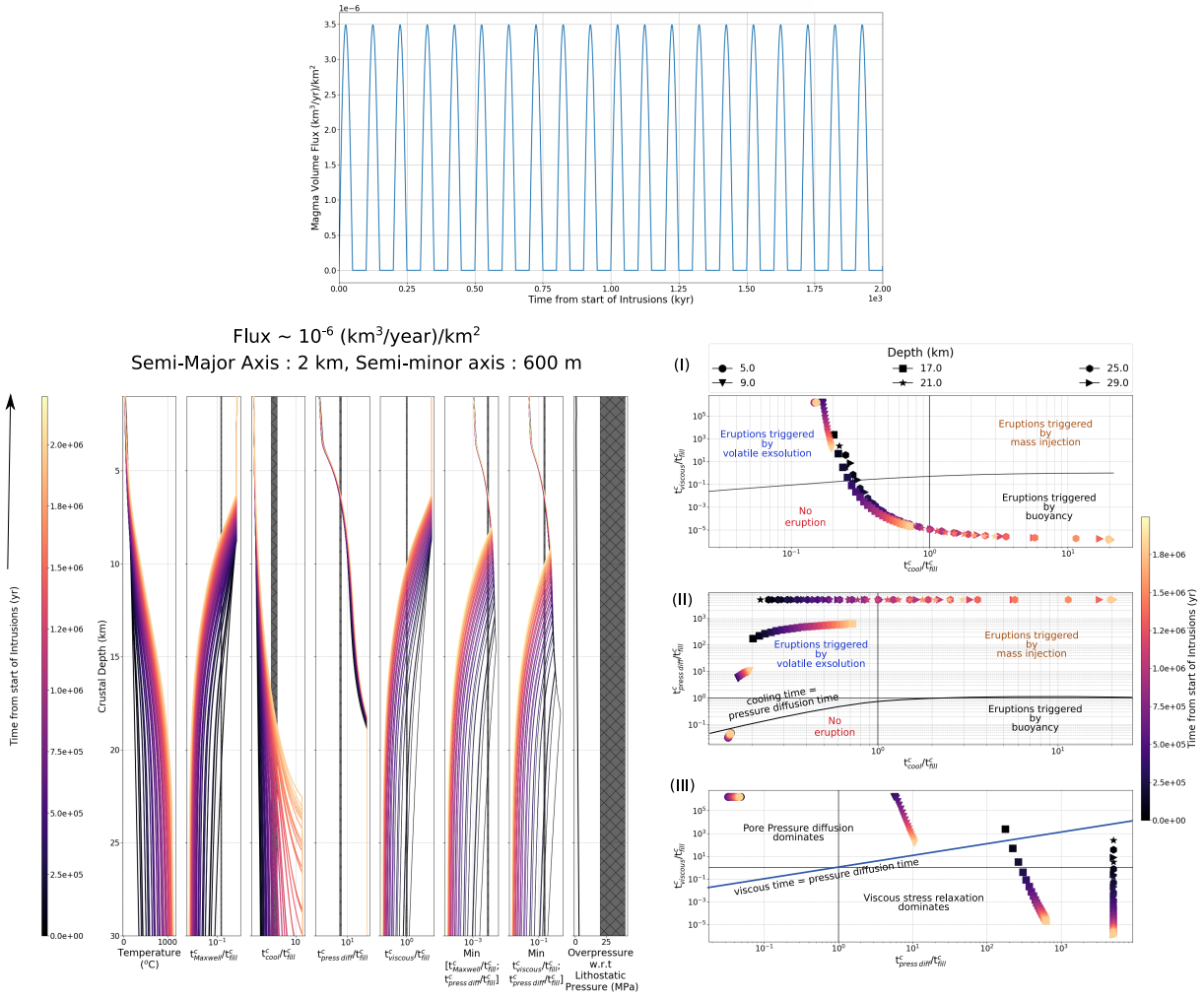

Figure 4.21: 1D thermal evolution model with constant melt input with a dike length-scale of 15 km (w.r.t the base of the crust). The Figure panel on the top shows the time-history of melt flux into the crustal column, the middle figure shows the thermal evolution of the crustal column as well as various non-dimensional timescales (Degruyter & Huber, 2014; Mittal & Richards, 2019) while the third figure shows the magmatic regime diagram for ascertaining the eruptibility of magma for reservoirs at different depths. The initial concentrations of water and CO_2 in the melt is calculated for 10% degree of partial melting with a mantle source composition of 750 ppm CO_2 and 0.23 wt % H_2O.

magma bodies are typically in the no eruption phase space as opposed to the smaller bodies which transit that phase space quickly with changing temperatures (See Figure 4.22 vs. Figure 4.24).

Next, we show the results with a more volatile-rich mantle composition: 1500 ppm CO_2 and 0.46 wt % H_2O (See discussion in Section 4.3.2) in Figure 4.25B. The main consequence of this change vis-a-vis the standard case (Figure 4.22) is the deeper volatile exsolution of CO_2 and smaller pressure diffusion timescale. As a result, the primary stress relaxation mechanism for some of the mid-crustal magma bodies (17, 21 km depths) is initially not viscous relaxation. Thus, with higher initial volatile content, the relevance of pore pressure diffusion increases to greater crustal depths.

Finally, in Figure 4.25A, we show the model results for a 10x higher input melt flux: 10^{-5} $(km^3/year)/km^2$. Unsurprisingly, the crustal temperature increases much more rapidly with the larger melt flux. The larger melt flux (and the consequent decrease in recharge timescale) translates the trajectories towards the upper right part of the phase space in Figure 4.25A, Panel I (also see blue arrow in Figure 4.20C). Consequently, some of the upper to mid-crustal magma bodies can initially erupt due to recharge associated over-pressurization and have frequent eruptions. Eventually, the increasing crustal temperature translates most magma bodies to the buoyancy overpressure part of the phase space.

In conclusion, we find that smaller magma bodies typically are easier to erupt than larger magma bodies. We find that pore pressure diffusion is an important process for the upper crustal magma bodies, and this can significantly inhibit eruption likelihood. A magma body may eventually lose enough volatiles to the crust and/or trap low volume fraction magmatic volatiles by capillary trapping (e.g., Parmigiani et al., 2016) to become volatile depleted and eruptible by other mechanisms. Additionally, the formation of a thermal aureole around the magma reservoir may also decrease the efficiency of pore pressure diffusion (See discussion in Mittal & Richards, 2019). Nevertheless, volatile loss by passive degassing is likely a significant stress relaxation process in the upper crust. For mid-crustal magma bodies, we find that the eruption mechanism and hence eruption frequency depend sensitively to the mass influx rate as well as melt volatile content. In particular, higher melt flux allows recharge-driven frequent eruptions for a 5 km x 1.5 km magma body at 9-15 km depths (Figure 4.25A). In contrast, the higher crustal temperature and corresponding lower viscosity make buoyancy overpressure the only viable mechanism for eruptions.

4.6.3 Plume-type melt flux

Since there are significant changes in both input melt flux and the degree of partial melting during a CFB event, we represent the crustal melt input as a Weibull distribution function with some additional noise following Black and Manga (2017) (Figure 4.26A). The degree of partial melting also follows the same functional form with a maximum of 10 % (e.g., J. J. Mahoney, 1988). To first order, this functional form approximates the observed pattern of alkali melts at the start and the end of the Deccan Traps main phase volcanism (Section

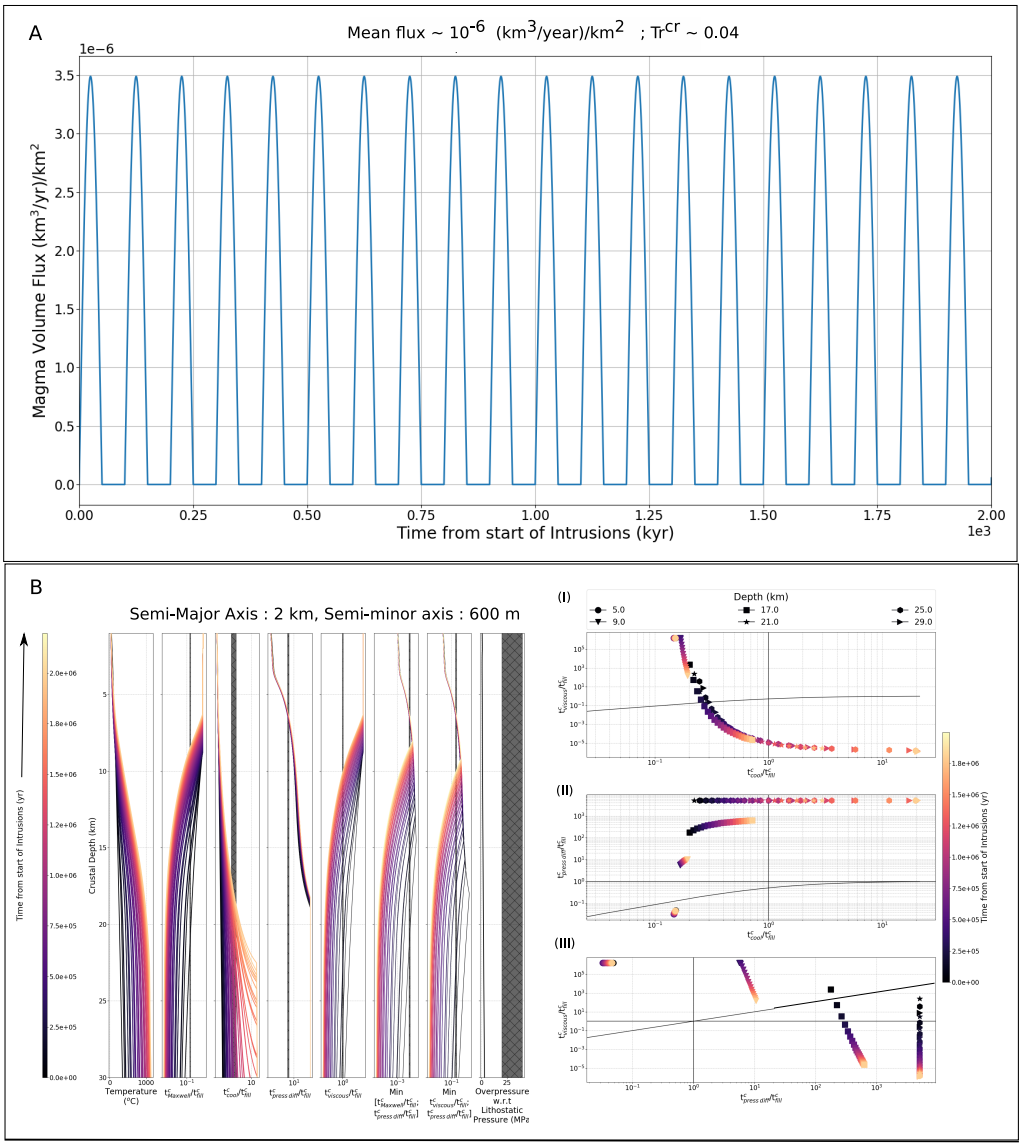

Figure 4.22: 1D thermal evolution model with constant melt input with a dike length-scale of 15 km (w.r.t the base of the crust) for a small magma reservoir. The Figure panel on the top (Panel A) shows the time-history of melt flux into the crustal column. For each panel, the middle figure shows the thermal evolution of the crustal column as well as various non-dimensional timescales (Degruyter & Huber, 2014; Mittal & Richards, 2019) while the third figure shows the magmatic regime diagram for ascertaining the eruptibility of magma for reservoirs at different depths. The initial concentrations of water and CO_2 in the melt is calculated for 10% degree of partial melting with a mantle source composition of 750 ppm CO_2 and 0.23 wt % H_2O.

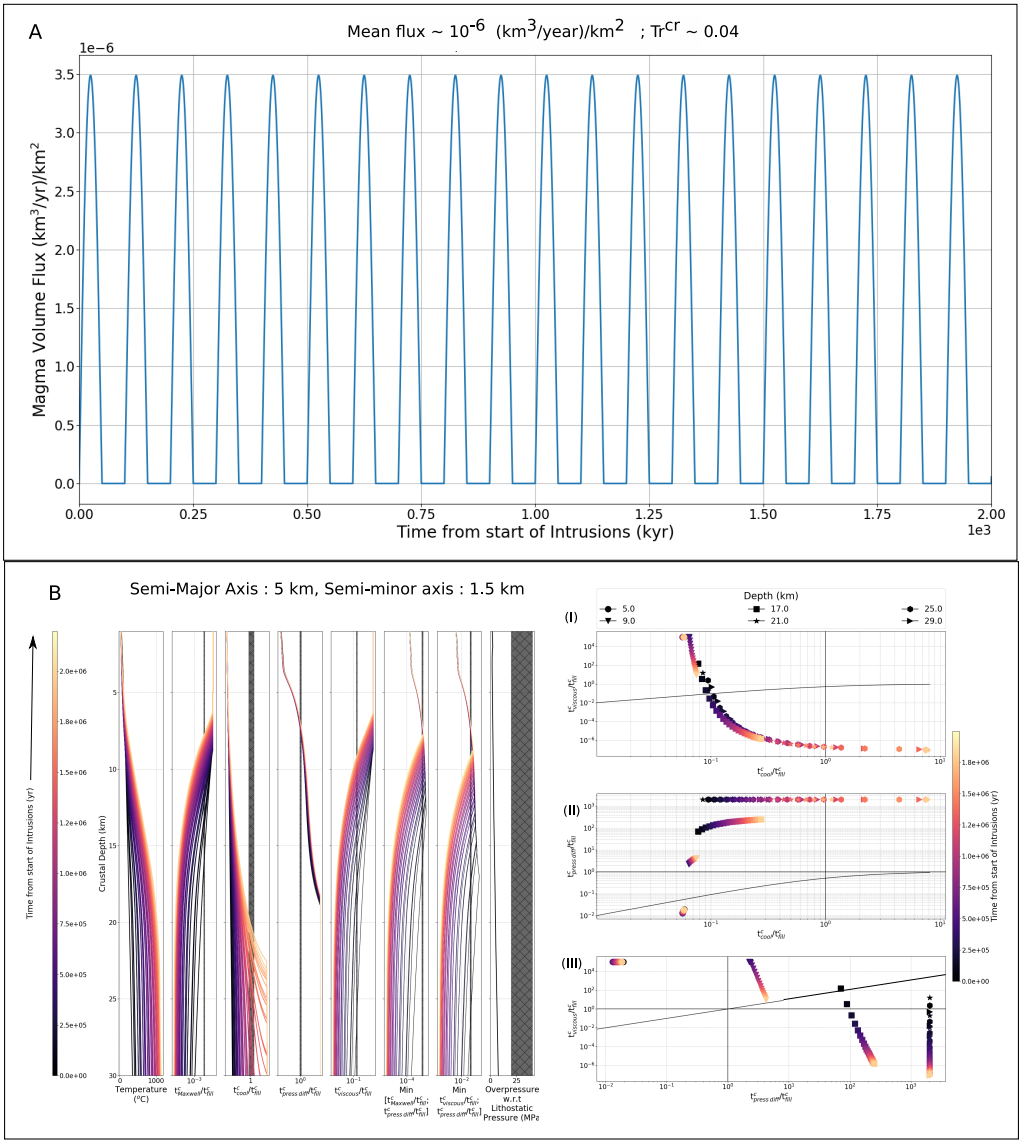

Figure 4.23: 1D thermal evolution model with constant melt input with a dike length-scale of 15 km (w.r.t the base of the crust) for a medium magma reservoir. The Figure panel on the top (Panel A) shows the time-history of melt flux into the crustal column. For each panel, the middle figure shows the thermal evolution of the crustal column as well as various non-dimensional timescales (Degruyter & Huber, 2014; Mittal & Richards, 2019) while the third figure shows the magmatic regime diagram for ascertaining the eruptibility of magma for reservoirs at different depths. The initial concentrations of water and CO_2 in the melt is calculated for 10% degree of partial melting with a mantle source composition of 750 ppm CO_2 and 0.23 wt % H_2O.

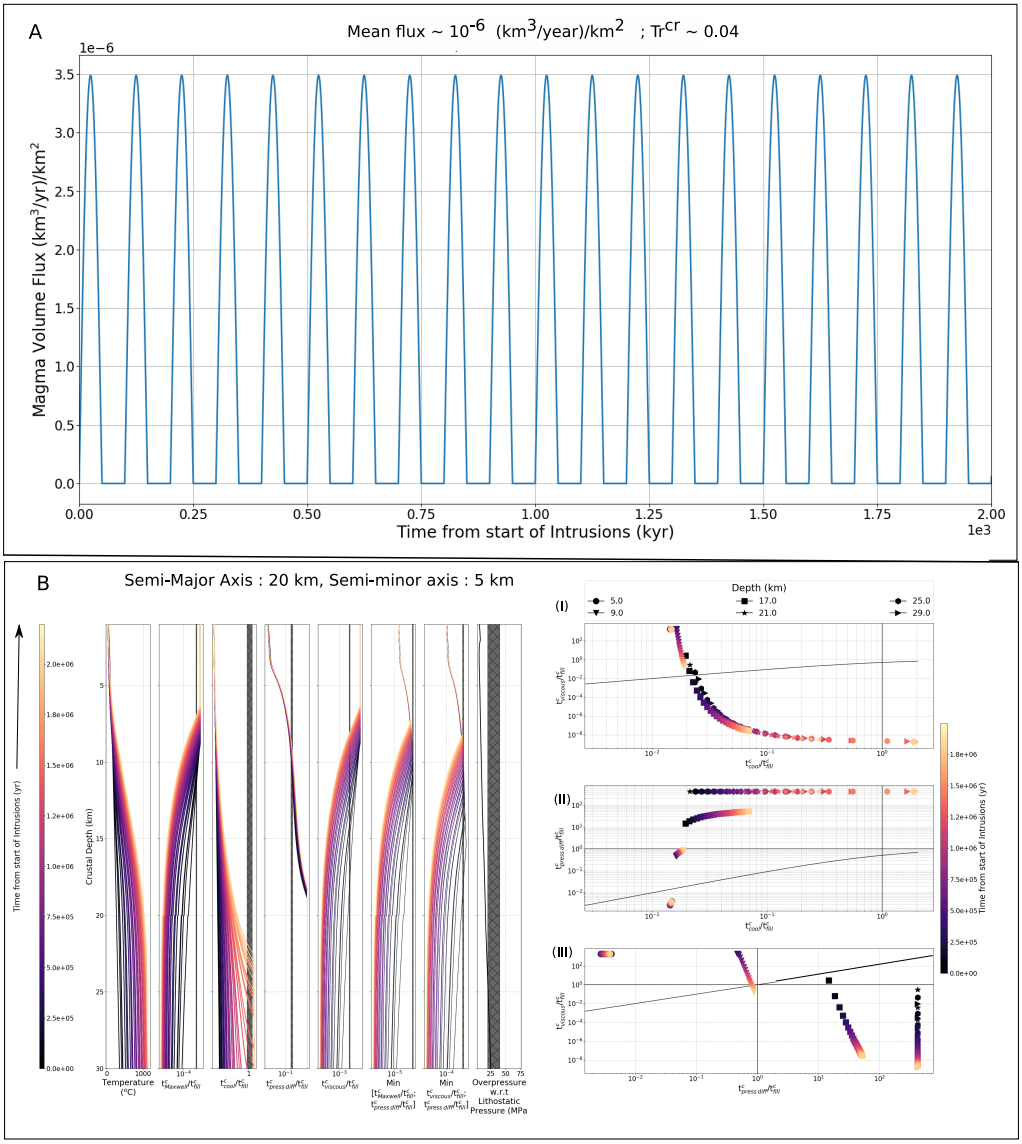

Figure 4.24: 1D thermal evolution model with constant melt input with a dike length-scale of 15 km (w.r.t the base of the crust) for a large magma reservoir. The Figure panel on the top (Panel A) shows the time-history of melt flux into the crustal column. For each panel, the middle figure shows the thermal evolution of the crustal column as well as various non-dimensional timescales (Degruyter & Huber, 2014; Mittal & Richards, 2019) while the third figure shows the magmatic regime diagram for ascertaining the eruptibility of magma for reservoirs at different depths. The initial concentrations of water and CO_2 in the melt is calculated for 10% degree of partial melting with a mantle source composition of 750 ppm CO_2 and 0.23 wt % H_2O.

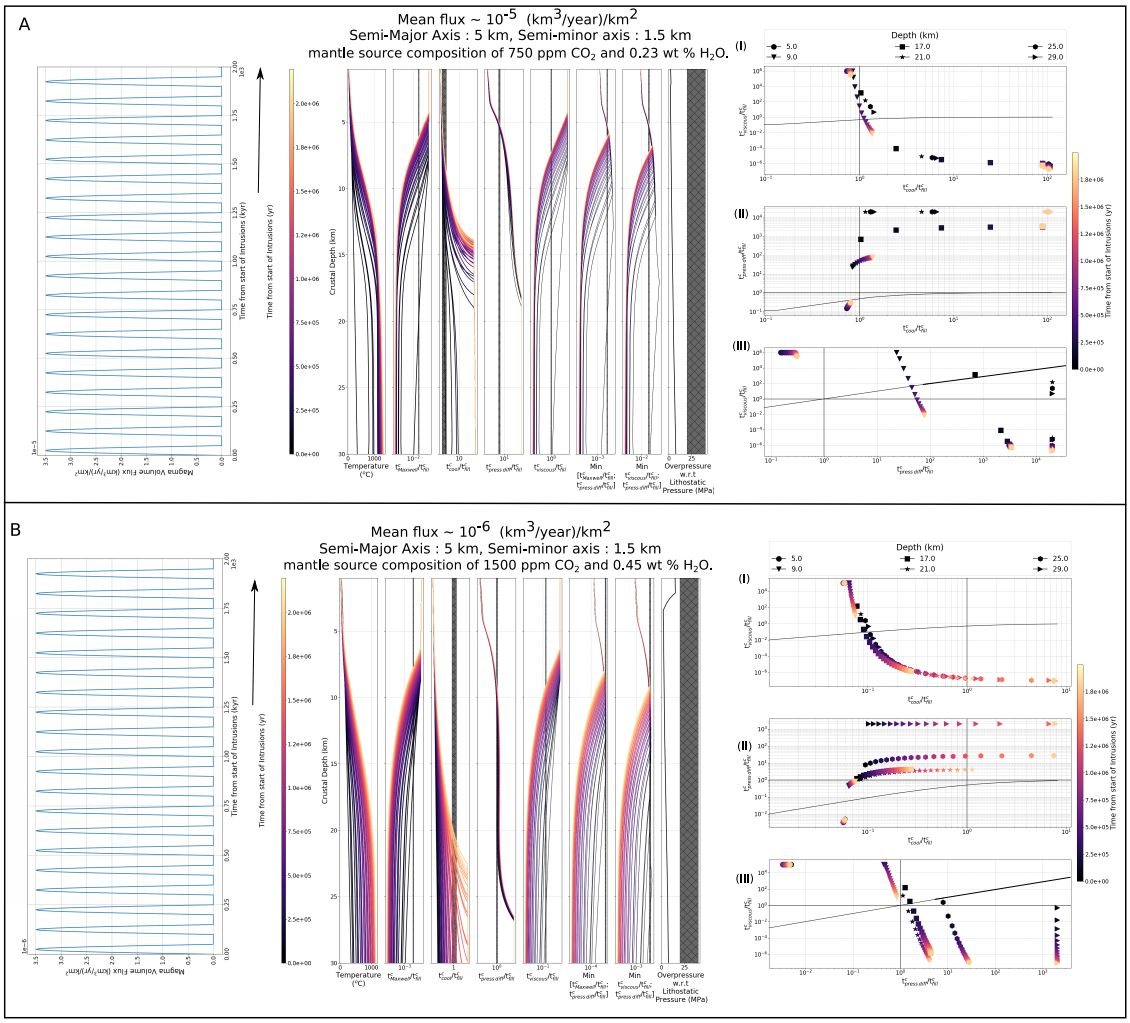

Figure 4.25: 1D thermal evolution model with constant melt input with a dike length-scale of 15 km (w.r.t the base of the crust). For each Panel, the Figure panel on the left shows the time-history of melt flux into the crustal column, the middle figure shows the thermal evolution of the crustal column as well as various non-dimensional timescales (Degruyter & Huber, 2014; Mittal & Richards, 2019) while the third figure shows the magmatic regime diagram for ascertaining the eruptibility of magma for reservoirs at different depths. The two sets of figure panels show the calculations for a same sized magma reservoir - 5 km semi-major axis, 1.5 km semi-minor axis, with different melt input fluxes and mantle volatile composition (Panel A, B, also see Figure 4.23). The initial concentrations of water and CO_2 in the melt is calculated for 10% degree of partial melting with a mantle source composition of 750 ppm CO_2 and 0.23 wt % H_2O (Panel A) and 1500 ppm and CO_2 and 0.46 wt % H_2O (Panel B)

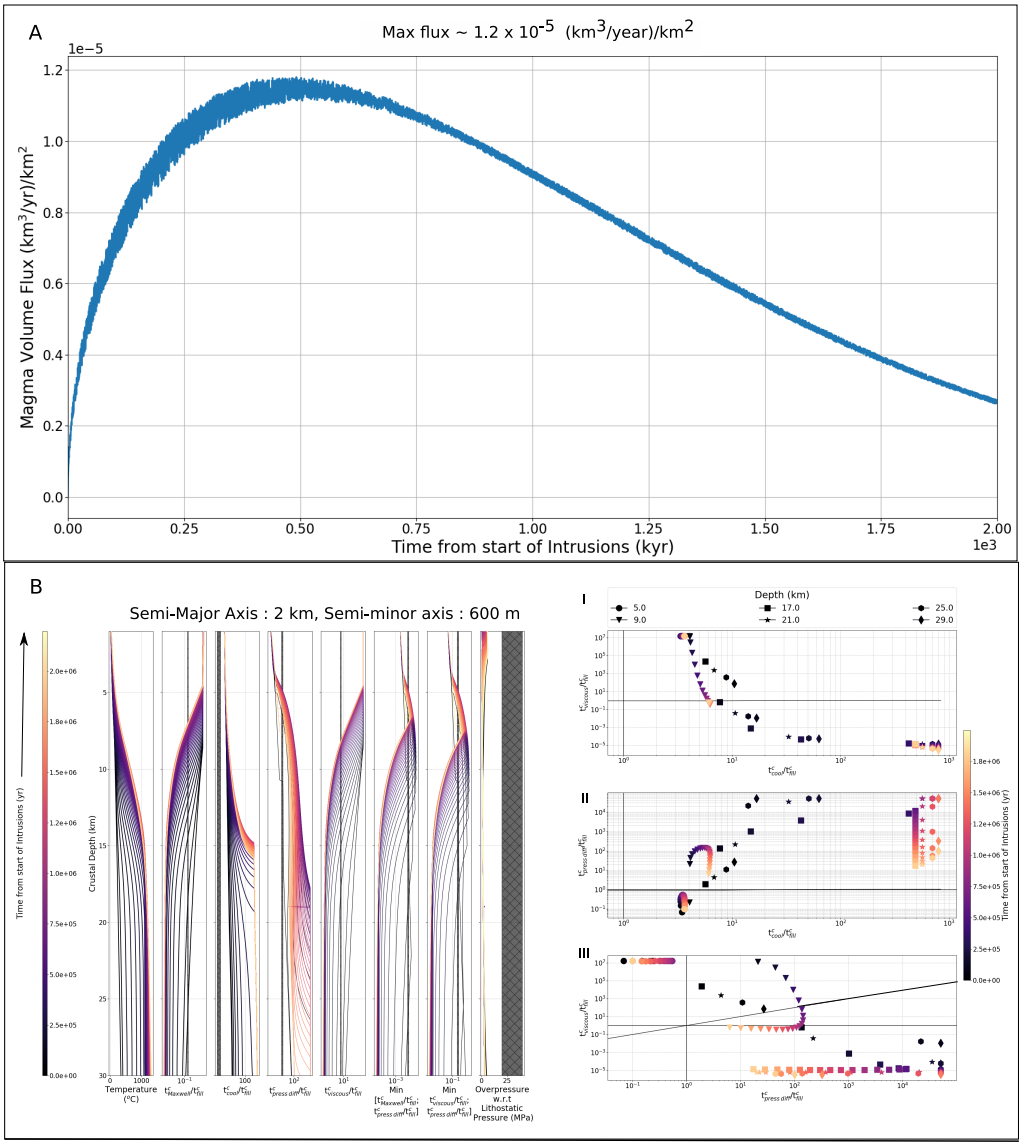

Figure 4.26: 1D thermal evolution model with time-varying melt input and a dike length-scale of 15 km (w.r.t the base of the crust) for a small magma reservoir. The input melt flux as well the degree of partial melting follow a weibull distribution (as shown the top figure panel A) to approximate the melting history from a flood basalt event. The initial concentrations of water and CO_2 in the melt is calculated for temporally varying degree of partial melting (maximum of 10 %) with a mantle source composition of 750 ppm CO_2 and 0.23 wt % H_2O.

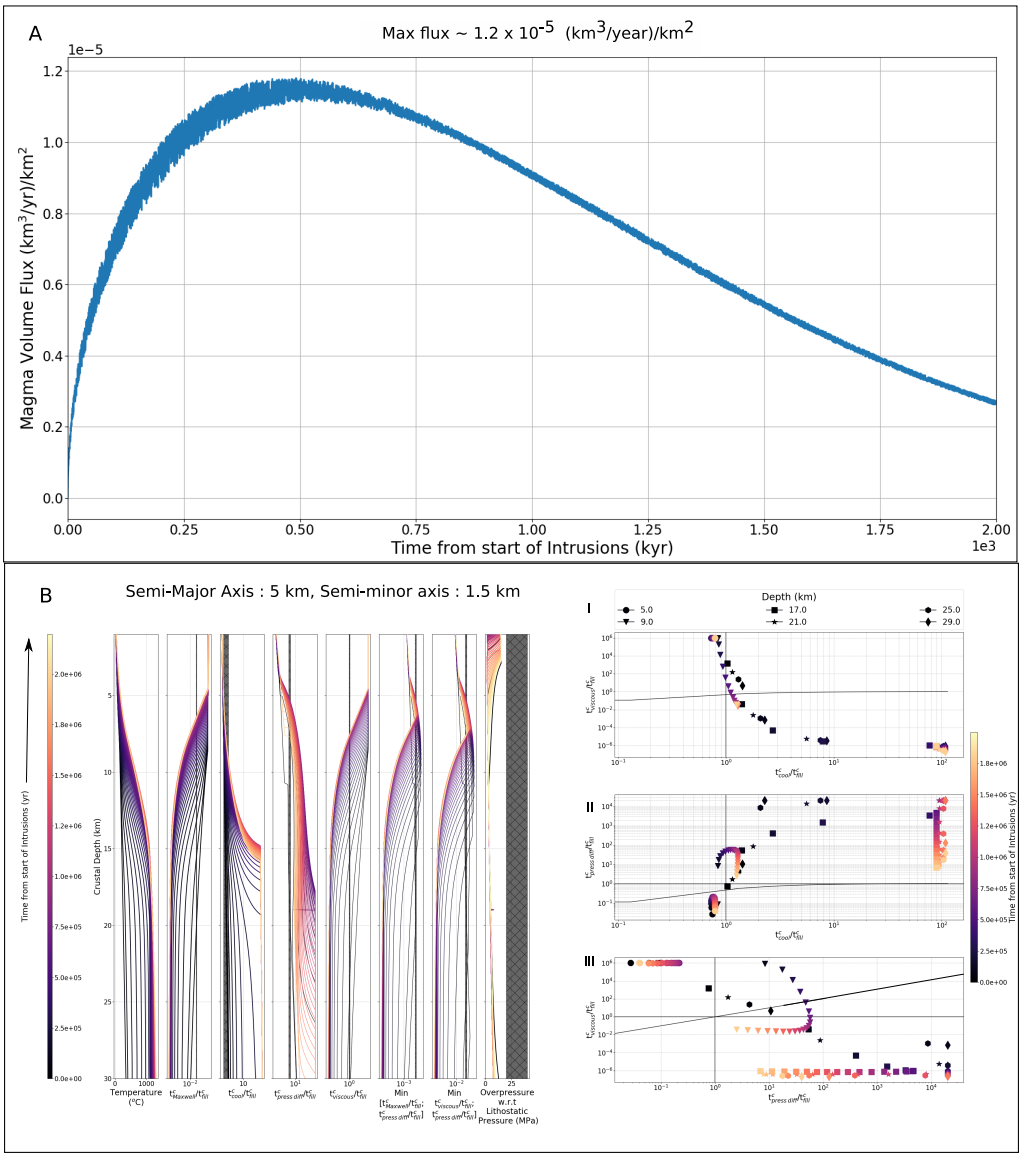

Figure 4.27: 1D thermal evolution model with time-varying melt input and a dike length-scale of 15 km (w.r.t the base of the crust) for a medium magma reservoir. The input melt flux as well the degree of partial melting follow a weibull distribution (as shown the top figure panel A) to approximate the melting history from a flood basalt event. The initial concentrations of water and CO_2 in the melt is calculated for temporally varying degree of partial melting (maximum of 10 %) with a mantle source composition of 750 ppm CO_2 and 0.23 wt % H_2O.

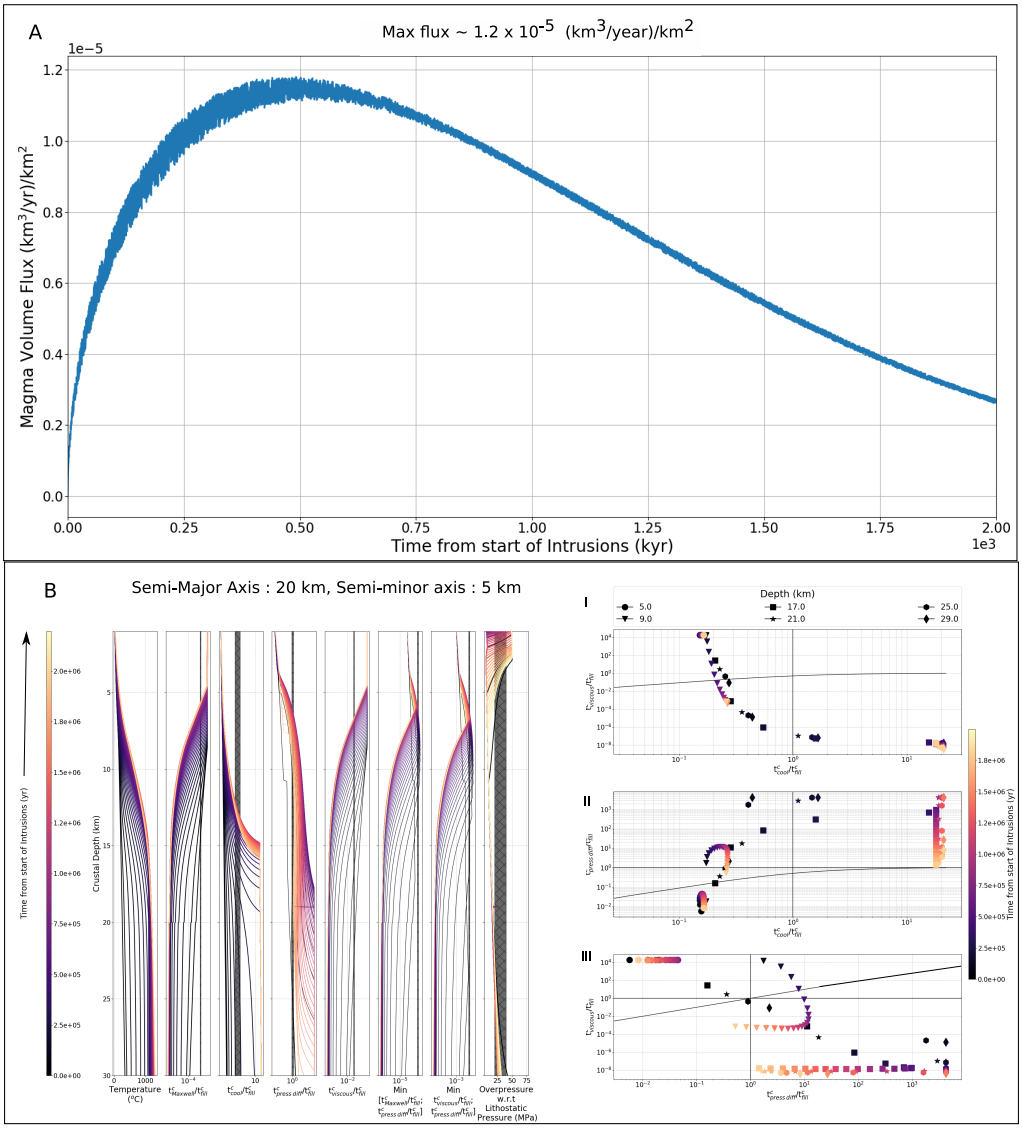

Figure 4.28: 1D thermal evolution model with time-varying melt input and a dike length-scale of 15 km (w.r.t the base of the crust) for a large magma reservoir. The input melt flux as well the degree of partial melting follow a weibull distribution (as shown the top figure panel A) to approximate the melting history from a flood basalt event. The initial concentrations of water and CO_2 in the melt is calculated for temporally varying degree of partial melting (maximum of 10 %) with a mantle source composition of 750 ppm CO_2 and 0.23 wt % H_2O.

4.3.1, Section 4.3.2). The peak melt crustal melt flux is about 10^{-5} (km^3/year)/km^2, equating to about 7.5 km^3/year over a 500 km radius plume head (or equivalently $\sim$ 1.5 km^3/year for a 200 km radius). In Figures 4.26, 4.27, and 4.28 we show the results of this model set up for a small, medium, and large magma reservoir size (a^c, b^c): 2km, 600m; 5 km, 1.5 km; and 20 km, 5 km respectively.

Compared to the results in Figure 4.25A, the main difference is that initially the degree of melting is very small ($\sim$ 1 %), leading to very volatile-rich initial melts. Consequently, significant CO_2 exsolution occurs in the lower crust, which in turn ensures a non-zero crustal permeability in the cold crust. With an increasing degree of melting, the volatile content decreases with a consequent increase of De_{pd} in the lower crust. Eventually, the degree of melting decreases and the melt's volatile content increases again. The strong effect of changing degrees of partial melting can be seen in the De_{pd} vs. De_{visc} phase space panels in Figures 4.26, 4.27, and 4.28. Since the crustal viscosity progressively decreases during a CFB event, the trajectories loop back but are not closed loops.

For the small sill shaped magma body (a^c, b^c - 2 km, 600 m), pore-pressure diffusion is the primary stress relaxation mechanism at upper crustal depths (5 km) throughout the calculations and the mid-crustal depths (9 & 17 km) for the initial part (Figure 4.26B, Right Panel III). Analyzing the corresponding phase space plot (Figure 4.26B, Right Panel II) for these magma bodies, we find that the shallow depth reservoir remains within the buoyancy overpressure regime. In contrast, the others are in the recharge-dominated regime permitting frequent eruptions. Given the small vertical extent of the magma body, the buoyancy overpressure is small even with high volatile content (Figure 4.26B). Consequently, the eruption of the shallowest magma reservoir seems potentially tricky. However, we posit that since these magma bodies are close to the region of recharge dominated eruptions, stochastic variations in the input melt flux (loops in the phase space, Figure 4.20C) may be sufficient to enable eruptions.

Furthermore, if we account for a potentially larger fraction of the plume melt flux feeding the magma reservoirs instead of being emplaced in the crust as dikes, we can further translate the trajectories towards the top right corner. Considering depths where viscous stress relaxation dominates, we find that mid-crustal magma bodies typically start in the recharge-dominated regime before transitioning at various times to the buoyancy regime with increasing temperature (Figure 4.26B, Right Panel I). Thus, while small sized mid-crustal bodies can frequently erupt with minimal growth rate, lower crustal bodies will typically erupt very infrequently and accumulate mass over time.

We find broadly similar results for the larger magma reservoir (a^c, b^c - 5 km, 1.5 km) with recharge associated eruptions likely for upper-crustal and mid-crustal magma bodies, especially after including some melt influx variability (Figure 4.27B, Left Panels I & II). The eruption likelihood is further enhanced by the larger buoyancy overpressure (due to the larger vertical extent of the magma body) for the upper crustal bodies. Thus, the additional elastic overpressure required for an eruption is lower. Consequently, all the trajectories will be translated upward further, making recharge or volatile-exsolution associated eruptions likely

(Figure 4.20C, red arrow). In contrast, medium sized magma reservoirs are not expected to erupt frequently in the lower crust and will instead grow rapidly over time.

Finally, for the largest magma body (a^c, b^c - 20 km, 5 km), the right downward translation of phase space trajectories (Figure 4.28B, Left Panel I; Figure 4.20C) moves several magma bodies into either the no-eruption regime or the volatile exsolution regime. Thus, we expect infrequent eruptions if at all in this scenario. We note that the buoyancy overpressure is much higher, especially in the upper crust due to the coupled CO_2- H_2O exsolution as well as in the lower crust due to higher crustal density. Thus, some of the shallow, as well as lower crustal bodies, would likely be eruptible (B. D. Marsh, 1989).

4.6.4 Implications for CFB architecture

In conclusion, we find that at upper and mid-crustal depths, a medium-sized magma body ($a^c, b^c \sim 5$ km, 1.5 km) is the optimal geometry given the requirement for frequent eruptions as well as being able to erupt sufficient volume in each eruptive episode (e.g., Figure 4.13, Section 4.3). Additionally, we have some direct evidence of similarly sized intruded magma bodies in the DT geophysical datasets (Section 4.3.8).

In the lower crust, however, viscous stress relaxation is too rapid to permit any other eruption mechanism (among the ones considered here) besides buoyancy overpressure. This result is, however, very challenging to reconcile with the requirement for frequent surface eruptions. The results from Black and Manga (2017) clearly illustrate that large magma reservoirs with failure due to buoyancy overpressure have a long hiatus between eruptions (also see Section 4.2.2.3, Figure 4.20B). Furthermore, there is clear geochemical evidence for significant lower crustal assimilation - fractional crystallization in the erupted lavas (e.g., J. J. Mahoney, 1988; G. Sen, 2001, and references therein, Section 4.3.1). Thus, the erupted magmas spent some time in lower crustal magma reservoirs.

In order to address these challenges, we posit that we are missing a critical physical process in our model framework - the viscous flow of the surrounding country rock and formation of vertically extensive but spatially limited melt pathways (Cao, Kaus, & Paterson, 2016; Rummel et al., 2018; Colón et al., 2019). We envision that initially, the parental melt is stochastically emplaced in the lower crust with infrequent recharge into a single magma body (large Tr^c). As long is $T_{period}/t^c_{cool} \sim 0.1$ - 1, individual magma bodies can cool sufficiently to produce buoyancy overpressure but still remain eruptible (B. D. Marsh, 1989, 2013). This buoyancy overpressure, in turn, leads to magma flow towards the top of the magma reservoir along (and associated crustal deformation) with the potential formation of non-elastic weak shear zones as well as brittle-ductile or ductile dikes (Scheibert, Galland, & Hafver, 2017; Bertelsen, Rogers, Galland, Dumazer, & Abbana Benanni, 2018; Haug et al., 2018; Kjøll, Galland, Labrousse, & Andersen, 2019). These deformation pathways can be used by the magma body to ascend to shallower depths. Typically, the critical overpressure is lower for these mechanisms in comparison to tensile failure (Cao et al., 2016). Thus, over time, the magma body would become vertically extended with larger column-integrated buoyancy

which further promotes deformation/tensile failure. Due to decreasing crustal temperature, as well as changes in the upper crustal rheology, the efficiency of this process will eventually decrease, and magma reservoir failure would become dominated by brittle tensile failure (Cao et al., 2016; Rummel et al., 2018) at mid-crustal depths. Additionally, the lower density of the middle crust reduces the magma-crustal density difference (e.g., Figure 4.28B). Since this cannot be compensated by increased volatile exsolution until shallower depths, the overall driving buoyancy pressure will also decrease (Figure 8).

We hypothesize that a combination of larger buoyancy overpressure, shorter absolute cooling timescales for a small reservoir, and periodic large melt influx (leading to more elongated Tr^c loops, Figure 4.20C) allow frequent eruptions from the lower crust. As the CFB magmatic system matures, we envision that the lower crustal magmatic system develops quasi-connected conduit style pathways analogous to the four ultramafic intrusions in the Seiland igneous province (R. B. Larsen et al., 2018). The area of each of these intrusions is only a few 100 km^2, but they have roots of up to 9 km. We note that a variety of physical mechanisms can form ductile shear zones. These include shear heating and thermal softening by small shear strains leading to spontaneous ductile shear zone generation (e.g., Kiss, Podladchikov, Duretz, & Schmalholz, 2019), reaction-weakening caused by infiltration of fluids (Mancktelow & Pennacchioni, 2005; Sørensen, Grant, Ryan, & Larsen, 2019), or fabric development in rock with significant mechanical heterogeneities (Montési, 2013). Thus, the formation of weak zones can occur under a wide variety of thermo-mechanical conditions for the lower crust and is observed in some exhumed rift margins and magmatic bodies (Wenker & Beaumont, 2018; Tetreault & Buiter, 2018; Koptev et al., 2018; Francois, Koptev, Cloetingh, Burov, & Gerya, 2018; Korchinski, Rey, Mondy, Teyssier, & Whitney, 2018; Kjøll et al., 2019; Sørensen et al., 2019; A. L. Lee, Lloyd, Torvela, & Walker, 2020).

4.7 New Conceptual Model for CFB magmatic system

Based on the observational constraints as well as the results from the magma reservoir model and thermal model, we propose a new conceptual model for CFB volcanism. *The key feature of this model is that individual CFB eruptive episodes are fed by a series of small interconnected trans-crustal magma reservoirs instead of a single large magma reservoir.* In Figure 4.29, we show a schematic representation of this model with three stages of CFB volcanism: Early phase, Main phase, and Late-stage continental flood basalt volcanism. Our proposed model structure builds upon various conceptual CFB magmatic architectures (Section 4.2.1). In particular, our results closely resemble the proposed model for Ethiopian Traps by S. R. Krans et al. (2018) as well as H. C. Sheth and Cañón-Tapia (2015) to explain composite Deccan Trap dikes. However, we can constrain the magmatic structure more quantitatively, especially with regards to the size of individual magma reservoirs and the physical processes driving eruptions. We acknowledge that a real continental flood basalt

such as the Deccan Traps likely had multiple eruptive centers (e.g., Section 4.3.2) as well as different sources of parental melt source compositions (Section 4.3.1). In the following, we do not attempt to explain this full geochemical complexity. Instead, our conceptual model is focused on explaining the overall eruptive tempo and some key geochemical features of CFBs (See Section 4.3.9).

4.7.1 Stage 1a : Early Phase Flood Basalt

Initially, low-degree melts from partial melting in the mantle plume head and the metasomatized mantle lithosphere ascend through some combination of brittle-ductile dikes (Havlin et al., 2013; Kjøll et al., 2019), diapiric melt bodies, and two-phase melt channelization (Aharonov et al., 1997; R. F. Katz, Spiegelman, & Holtzman, 2006; J. M. S. Solano et al., 2012; Weatherley & Katz, 2012; T. Keller et al., 2013; Weatherley & Katz, 2015; Schmeling et al., 2018, 2019). Since these melts are highly volatile enriched (R. F. Katz et al., 2003; Black & Gibson, 2019), they can exsolve significant CO_2 during decompression even at lower crustal depths (1st boiling, Edmonds & Wallace, 2017, Figure 4.26B). These melts are thus expected to be very buoyant, highly compressible, and have a lower solidus temperature (Black & Gibson, 2019; Yaxley et al., 2019). As a consequence, these melts can erupt to the surface from deep crustal reservoirs by buoyancy overpressure alone without much mid/upper crustal storage (Black & Manga, 2017). The typical magma reservoirs feeding these eruptions are expected to be either medium-sized ellipsoidal bodies or small but vertically elongated magma bodies. In some cases, the erupted melts ascend through the crust rapidly enough to carry mantle and lower crustal xenoliths (e.g., A. Ray et al. (2016); alkali basaltic lava flows and dikes in Kutchh subprovince). Additionally, the pre-existing crustal tectonic structure, such as old faults and shear zones, serve as important controls on the melt transport, volatile degassing, and the location of eruptions (e.g., Latyshev, Veselovskiy, & Ivanov, 2018) Siberian Traps, Section 4.3.7 for Deccan Traps observations, Gettysburg Sill associated with CAMP (M. Mangan, Marsh, Froelich, & Gottfried, 1993), and the Franklin sills (Bédard et al., 2012)).

4.7.2 Stage 1b : Early Phase Flood Basalt

Over time ($\sim 10^5$ - 10^6 years), the melt's volatile content will decrease due to increasing degrees of partial melting. Thus, individual Moho-depth magma reservoirs will not have enough buoyancy overpressure due to decompression alone. Also, the magmatism will progressively heat the lower crust. As a consequence of these two effects, parental melts will start accumulating at depth in several small-medium sized bodies rather than erupting. With progressive cooling and differentiation and associated volatile exsolution (Karlstrom & Richards, 2011), the buoyancy overpressure will increase. Coupled with non-tensile failure mechanisms, the higher buoyancy pressure will enable the development of small but vertically extensive magma bodies (See Section 4.6.4). We posit that eventually these processes will lead to an efficient conduit style lower crustal transport system.

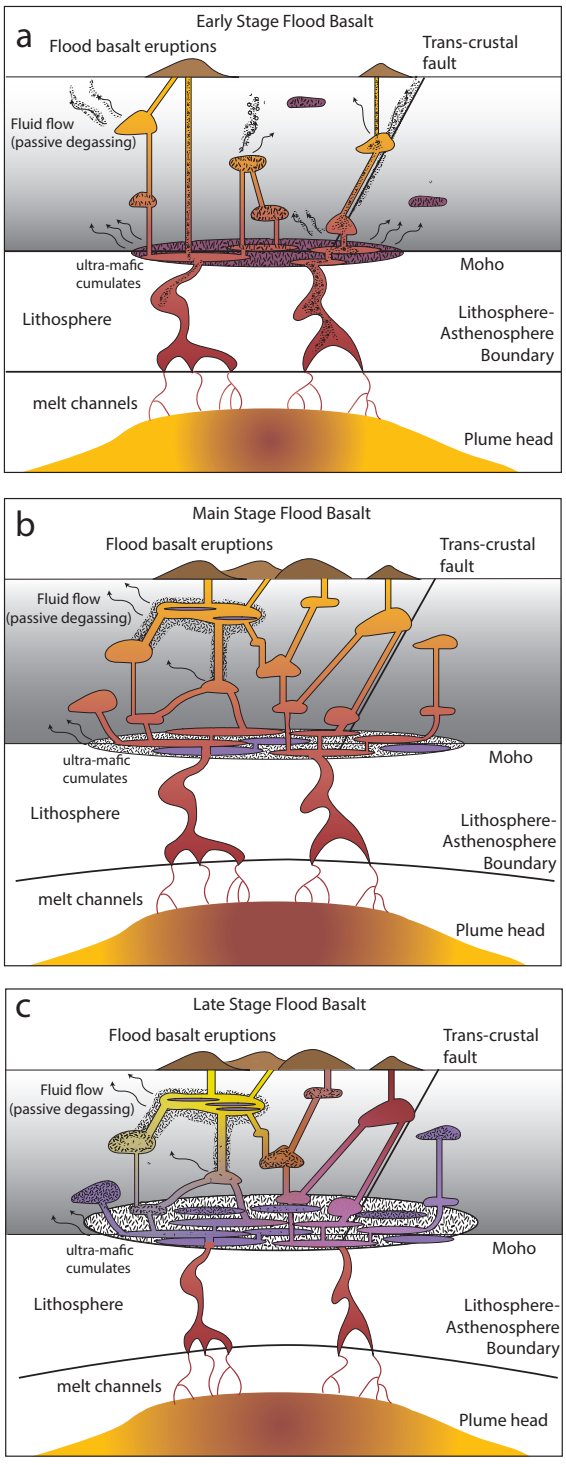
a
Early Stage Flood Basalt
Flood basalt eruptions
Trans-crustal fault
Fluid flow (passive degassing)
ultra-mafic cumulates
Moho
Lithosphere
Lithosphere-Asthenosphere Boundary
melt channels
Plume head
b
Main Stage Flood Basalt
Flood basalt eruptions
Trans-crustal fault
Fluid flow (passive degassing)
ultra-mafic cumulates
Moho
Lithosphere
Lithosphere-Asthenosphere Boundary
melt channels
Plume head
c
Late Stage Flood Basalt
Flood basalt eruptions
Trans-crustal fault
Fluid flow (passive degassing)
ultra-mafic cumulates
Moho
Lithosphere
Lithosphere-Asthenosphere Boundary
melt channels
Plume head

Figure 4.29

Figure 4.29 *(previous page)*: Conceptual model for the magmatic structure of a continental flood basalt sequence in three stages : Early Stage Flood Basalts (Panel A), Main Stage Flood Basalts (Panel B), and Late Stage Flood Basalts (Panel C). The most voluminous surface eruptions occur during the Main Stage Flood Basalts while the maximum passive degassing typically occurs towards the end of Early Stage CFBs. The darker colors in the plume head signify the degree of partial melting which increases from Early stage to Main stage and decreases again in the Late Stage. In the crustal magmatic system, the light yellow color (Late Stage Panel C) indicates the presence of a rhyolitic magma reservoir. In all the panels, the shaded crustal grayscale colors represent the background geotherm.

In conclusion, we propose that during Stage 1, the initial eruption efficiency (and frequency) from the lower crust will be very high. It will subsequently decrease before increasing again towards the end of Stage 1. To have this increase (as well as match observations), it is critical that the lower crustal magmatic system is not a single large magma reservoir but is instead comprised of a small-medium sized magma body embedded in a mush zone (Section 4.2.2.3, 4.3.9, 4.3.6.4). We propose a similar time progression for the mid and upper crustal magma bodies. Initially, the shallower crust is both colder and has high permeability. Thus, there is initially a high likelihood for the magma reservoir to freeze in place and lose most of its volatiles to the surrounding crust. Over time, both the mantle melt flux and the lower crustal melt transport efficiency will increase along with higher crustal temperatures. These changes will enable mid-upper crustal magma to remain eruptible for longer, reduce the effectiveness of pore pressure diffusion, and permit eruptions by recharge associated overpressure (See Section 4.6.3 and 4.6.4). Additionally, the presence of potentially more eruptible magma bodies will permit an individual eruption to include more secondary reservoirs with progressively decreasing conductivity timescales and higher conductivity (Sections 5.2.3, 5.3.1). Thus, we expect that both the eruption frequency as well as the volume of individual eruptive episodes would increase towards the end of Stage 1.

We emphasize that the same set of magma reservoirs do not need to feed each eruptive episode. Instead, each eruption represents a stochastic network of magma reservoirs that can connect depending on the crustal stress state, their internal overpressure, and eruptive history. Conceptually, this is similar to the idea of an open-system trans-crustal magamatic system that has been proposed for present-day arc volcanism (B. D. Marsh, 2013; Cashman et al., 2017; Bergantz, Schleicher, & Burgisser, 2015). Typically, a given magma reservoir will only be part of an eruption episode every 0.5-5 kyr. Thus, there is sufficient time for shallow plagioclase fractionation despite relatively frequent eruptive episodes (Section 4.3.3, 4.3.4, 4.3.5). The crustal residence time for some of the upper crustal magma bodies erupted towards the end of Stage 1b may be particularly long (e.g., 2-10 kyr) since the system is transitioning from a low to a high eruption probability. Thus, recharge driven individual eruptive episodes may entrain the magmatic mushes (both the melt and the large plagioclase

crystals) from the primary or secondary reservoirs in some cases. Mush disaggregation and entrainment by a carrier melt has been geochemically shown to be an important process during the Laki 1783 eruption, a modern CFB analog (Passmore et al., 2012; Neave, Buisman, & Maclennan, 2017). Similar processes have also suggested explaining the occurrence of GPB flows with a large concentrations and sizes of plagioclase phenocrysts in the Deccan Traps (Beane et al., 1986; Higgins & Chandrasekharam, 2007a; Krishnamurthy, 2019) as well as the Iceland Neogene flood basalts (Óskarsson, Andersen, Riishuus, Sørensen, & Tegner, 2017) and the Emeishan province (L. Cheng, Zeng, Ren, Wang, & Luo, 2014; L.-L. Cheng, Yang, Zeng, Wang, & Luo, 2014). Based on Sr isotope zoning in plagioclase crystals as well as crystal size distributions, Higgins and Chandrasekharam (2007a); L. Cheng et al. (2014); Borges et al. (2014) inferred a GPB growth timescale of up to a few thousand years (See H. Sheth (2016) for more discussion and alternative models). Concerning the DT, we envision that the Kalsubai formation with several GPBs represents the end of Stage 1 of the CFB magmatic system.

Finally, with regards to passive degassing of magmatic volatiles, we expect an initial increase in degassing efficiency due to crustal melt storage and high permeability followed by a decline due to thermal maturation of the crust. The total volume of magmatic volatiles degassed depends on both the efficiency of degassing as well as the shallow melt volume. Thus, we anticipate that the peak passive degassing will be shifted closer towards the end of stage 1 coincident with increasing surface eruptions. We readily acknowledge that this temporal pattern does not include any potential carbon release from heating and assimilation of country rocks. Multiple studies have suggested that this additional carbon source, primarily due to crustal heating by shallow sill complexes, is critical for CFBs such as Siberian Traps, Karoo, CAMP, and NAMP (H. Svensen et al., 2018, and references therein). Since the shallow sill network may be emplaced after the lava flows (Section 4.3.2.3, 4.3.8.4) due to the mechanical loading at the surface, the temporal rate of passive degassing can be significantly modified.

4.7.3 Stage 2: Main Stage Flood Basalt

With increasing mantle melt flux, shallowing lithosphere-asthenosphere boundary (N. Kumar, Zeyen, Singh, & Singh, 2013; H. Wang, van Hunen, & Pearson, 2015; Maurya et al., 2016), along with a higher degree of partial melting and the development of vertically integrated melt pathways in the lower crust, the CFB system transitions to Stage 2- Main stage flood basalt sequence. During this time period, the mid-upper crustal magmatic system is composed of a set of small-medium (5-15 km semi-major axis) magma bodies that progressively become more connected over time (higher conductivity and lower conductivity timescale). This, in turn, leads to both larger and potentially shorter eruptions since the conductivity timescales are faster (e.g., Wai subgroup flows, especially Poladpur, see Section 4.3.3 and 4.5.2.3). Additionally, with increasing magma mixing and rapid eruptions, the magmatic system becomes geochemically homogenized through REAFC/RTF style processes

(e.g., K. Cox, 1988, Section 4.2.2). The geochemical variations are further reduced by less crustal interaction due to basaltic plating as well as a similar themo-chemical environment for the different crustal magma bodies (J. J. Mahoney, 1988; Chatterjee & Bhattacharji, 2008; Yu et al., 2015; R. B. Larsen et al., 2018; Heinonen et al., 2019a). Due to the high rate of magma recharge as well as restricted reservoir size, eruptions are frequent and primarily recharge drate of magma riven.

We hypothesize that during Stage 2, the magmatic stresses determine the crustal stress field instead of far-field tectonic stress. For the DT, this is potentially illustrated by changes in the orientation of dike swarms over time from being more oriented (and feeding the lower Formations) to less oriented (feeding Wai subgroup, see Vanderkluysen et al. (2011); M. A. Richards et al. (2015) for discussion). Towards the end of Stage 2, the decreasing crustal viscosity (due to higher temperatures) will potentially lead to longer and larger individual eruptive episodes but with slightly reduced eruption rates (e.g., Ambenali flows, see Section 4.3.3 and 5.2.2). We note that within our conceptual model, the rapid transitions between geochemical formations is a bit challenging to explain. These abrupt changes may be indicative of either state transitions in the magmatic system due to "thermo-poro-chemo-elastic" interactions between magma reservoirs (Parks et al., 2017; Elshaafi & Gudmundsson, 2018; Albino, Biggs, & Syahbana, 2019; Mittal & Richards, 2019; Belardinelli, Bonafede, & Nespoli, 2019) or spatial changes in eruptive centers with a separate plumbing system (e.g., Wolff & Ramos, 2013, for Columbia River Basalts).

4.7.4 Stage 3: Late Stage Flood Basalt

Eventually, the mantle melt flux into the system decreases along with a lower degree of melting of a depleted mantle plume head. Thus, although the volatile content of the magmas is potentially higher than "main-phase" CFBs, it is insufficient to allow frequent eruptions (akin to Stage 1a) through a hot crust. Additionally, over time, the deep crustal rheology also evolves due to metamorphic reactions as well as the continued influx of CO_2 rich fluids and magma (e.g., R. B. Larsen et al., 2018). Typically, these processes would lead to a weaker lower crust (Black & Gibson, 2019; Bürgmann & Dresen, 2008; Karlstrom & Richards, 2011). The lower crustal viscosity is further reduced due to the lower viscosity of the large cumulate ultramafic region (composed primarily of clinopyroxene and olivine, M. Richards et al., 2013) vis-a-vis a typical continental crust (some anorthite and clinopyroxene, Figure 4.7 from Karlstrom & Richards, 2011). Thus consequent faster viscous relaxation leads to both faster lower crustal flow (disrupting melt transport pathways) as well as reduced efficiency of recharge to trigger eruptions. In aggregate, the eruption efficiency in the system progressively decreases. Some of the larger lower and upper crustal magma bodies can persist for a long time, slowly building up buoyancy but never being sufficient to erupt to the surface. Furthermore, continued crystallization and solidification front instabilities (B. D. Marsh, 2002) can generate rhyolitic magmas that erupt towards the end of the DT eruptive sequence (Section 4.3.2). If there is some continental rifting in this time-period,

the eruption of both shallow and deep melts become easier (e.g., the Mumbai sequence, P. Hooper et al., 2010)

Within our conceptual model framework, the typical one million year duration of "main phase" CFB volcanism is a consequence of two related processes. Firstly, the thermal maturity of the crust decreases due to reduced melt flux with plate motion over the mantle plume. Thus, it is difficult for smaller magma bodies to remain eruptible. Secondly, with an increase in the size of the connected magma reservoirs (Biggs & Annen, 2019), especially in the lower crust, the eruption efficiency by any mechanism other than buoyancy becomes harder. As illustrated by Black and Manga (2017), there is a long hiatus time before large magma bodies can build up buoyancy overpressure and erupt. We posit that towards the end of the CFB sequence, this overpressure condition may never be achieved due to decreasing melt input.

4.8 Discussion

4.8.1 What makes CFB eruptive episodes unique ?

Individual eruptive episodes in continental flood basalts are unique compared to any modern basaltic volcanic system (e.g., Hawaii and Iceland), with much larger erupted volumes and eruption durations. Nevertheless, we propose that a CFB magmatic system can still be considered as a scaled-up version of these modern analogs with one key difference. The larger magma flux from a mantle plume head (and the consequent thermal input) allows multiple magma bodies to remain thermally viable with a high likelihood of inter-reservoir connectivity due to thermo-poro-mechanical processes (e.g., Section 4.5.1, Belardinelli et al., 2019; Mittal & Richards, 2019). This larger flux enables larger, longer CFB eruptions over a large distributed region rather than the formation of a single surface volcano and associated upper crustal conduit system.

We note that we do not expect that the magmatic architecture of each CFB will be the same. Variations in plume composition, crustal and lithospheric structure and composition, and background tectonics all play a critical role in determining the magmatic plumbing structure of a given CFB. For instance, the eruption styles, as well as the volume of silicic components, vary significantly between CFBs. The Parana-Etendeka, Columbia River Basalts, and the Ethiopian Trap flood basalts have a significant silicic component, unlike Deccan Traps and Siberian Traps (Bryan et al., 2010). As described in Section 4.3.6, many CFBs are associated with large sill complexes that may have fed the overlying lava flows (Muirhead, Airoldi, Rowland, & White, 2012; Muirhead, Airoldi, White, & Rowland, 2014; D. H. Elliot & Fleming, 2018; Coetzee, Kisters, & Chevallier, 2019; Magee, Ernst, et al., 2019) and facilitated both long-distance lateral magma transport (Leat, 2008; Magee, Muirhead, et al., 2016b) as well as magma transport vertically through the sill complex (Angkasa et al., 2017; H. Svensen et al., 2018; Galland et al., 2019; Magee, Ernst, et al., 2019).

Nevertheless, our results suggest that all these systems still need some form of a multiply-

connected magmatic system to match constraints on the eruptive tempo and volume of individual eruptive episodes. In this work, we have exclusively focused on Continental Flood Basalts and not discussed their oceanic counterparts, such as the Ontong Java Plateau. Due to the different crustal structure and rheology, we anticipate that the magmatic architecture of the oceanic Large Igneous Provinces is probably a bit different (Karlstrom & Richards, 2011). Without additional geochronological, geophysical, and volcanological constraints for these systems, it is difficult to ascertain how similar eruptive episodes for oceanic LIPs are those for CFBs (e.g., A. C. Kerr, Tarney, Marriner, Nivia, & Saunders, 1997; Geldmacher, van den Bogaard, Heydolph, & Hoernle, 2014; Pietsch & Uenzelmann-Neben, 2015; Hochmuth, Gohl, & Uenzelmann-Neben, 2015; Sager et al., 2019; Zhang, Chen, & Huang, 2019; C. R. Neal, Coffin, & Sager, 2019, and references therein). Thus, we can not rule out the possibility that oceanic LIPs are erupted from large magma reservoirs with long hiatus.

4.8.2 Testing the proposed CFB model

Our proposed CFB magmatic architecture model is principally based on observations from the Deccan Traps, particularly the Western Ghats region (Section 4.3). Thus, additional high-precision geochronology and paleomagnetic datasets from other parts of the Deccan Traps, especially the Central Deccan region, would be very useful to better constrain the volume, number, and hiatus intervals between individual eruptive episodes. Additionally, improved constraints on the eruptive tempo - duration, flux rate, and frequency of eruptive episodes for other CFBs would help assess if our conceptual model is generally applicable or not.

Another useful test for our proposed model would be a combined analysis of lava flow geochemistry (major, minor, trace element & isotopic compositions, petrology, diffusion timescales), paleo-secular variation, and flow morphology in a single stratigraphic section with high precision Ar-Ar flow dates. Such an analysis would help temporally constrain the timescale for intra-flow variations as well as the eruptive rates and eruption frequency. In particular, differences in isotopic and geochemical compositions can be used to directly constrain the timescale of magma mixing, fractionation, and the input of more deep-seated melt flux/fluids between eruptive events. A similar analysis for a spatially extensive single physically traced flow unit (Vye-Brown, Gannoun, et al., 2013) will help test how homogeneous individual eruptive units are and if that is consistent with a multiply connected magmatic architecture.

Finally, we expect that the pattern of deformation due to recharge and eruption of an interconnected magma reservoir network will be different compared to a single large upper crustal magma reservoir. This topographic difference may impact the pattern of lava flow distribution and the spatial coverage of individual lava flows. Also, on a more local scale, the pattern of deformation may manifest itself in 5-50 km scale changes in relative elevation of a single flow as well as changes in flow morphology due to changes in slope (N. R. Bondre & Hart, 2008; Richardson & Karlstrom, 2019). At present, these variations are challenging

to discern given the limited datasets and complexities associated with inflated sheet lobe formation (Vye-Brown, Self, & Barry, 2013; Rader et al., 2017). However, systematic studies can potentially help distinguish between single vs. multiple magma chamber models. Additionally, recent studies (O'Hara, Karlstrom, & Roering, 2019; Karlstrom, Richardson, O'Hara, & Ebmeier, 2018) have illustrated that magmatic systems may imprint a strong signature on the overlying landscape with regards to the surface topography and erosion rates. We thus posit that a careful topographic analysis of CFBs may help constrain the structure of the shallow magmatic system.

4.8.3 Quantitative model of CFB magmatism

In this study, we use a set of idealized models (Section 4.4) to constrain the conditions required for CFB eruptive episodes. However, to self-consistently calculate how the eruptive tempo varies throughout a CFB event, a full thermo-chemo-physical model is required. Our results illustrate that such a model needs to have a few key features. Firstly, the magmatic system should be comprised of a multi-level network of small-medium sized magma bodies which interact through crustal thermo-poro-visco-elastic processes (e.g., Taron et al., 2009; Liao et al., 2018; Mittal & Richards, 2019) as well as direct recharge of melt and volatiles and their associated evolution (Snyder & Tait, 1995; Montagna et al., 2015; Papale et al., 2017; Calogero, Hetland, & Lange, 2020). It is also essential to account for pre-existing tectonic structures and specific crustal properties since these strongly influence the location of magma bodies and their ability to ascend (e.g., presence or absence of a sedimentary basin). One should also include non-magmatic stresses due to uplift from the mantle plume head, continental rifting, and surface loading by lava flows (Hieronymus & Bercovici, 2001; Saunders et al., 2007; Karlstrom et al., 2009b; Rooney et al., 2014; McGovern et al., 2015; Tibaldi, 2015; J. A. Blanchard, Ernst, & Samson, 2017; R. E. Ernst et al., 2019).

Secondly, the importance of magmatic volatiles for the eruptibility of a magma reservoir suggests that processes associated with magmatic fluid transport in the magmatic mush and the crust are critical (Mittal & Richards, 2019; Lamy-Chappuis, Heinrich, Driesner, & Weis, 2020). Additionally, influx or outflux of just the magmatic vapor phase can significantly affect the thermochemical properties of the magma reservoir (e.g., B. D. Marsh & Coleman, 2009; Caricchi, Sheldrake, & Blundy, 2018). Since magma reservoirs likely have spatially variable amounts of melt, crystals and exsolved volatiles along with various layered and banded structures (e.g., Jerram et al., 2018, and references therein), it is challenging to model the volatile transport and mechanical response adequately with a volume averaged approximation and a single rheology (B. D. Marsh, 1996; Hildreth & Wilson, 2007; Bachmann & Bergantz, 2008; B. D. Marsh, 2013; R. Sparks et al., 2019; Carrara, Burgisser, & Bergantz, 2019; Burgisser, Carrara, & Annen, 2020; Carrara, Burgisser, & Bergantz, 2020). To accurately model the visco-elastic rheological response of a magma reservoir, it also important to consider changes in crustal assimilant due to thermal and fluid-driven metamorphic reactions (Aarnes et al., 2012). Lavecchia, Clark, Beekman, Cloetingh, and Burov (2016) showed that

depending on the P-T conditions, crustal strength in the proximity of the magmatic bodies could both increase and decrease along with changes in crustal density. Since a CFB event is associated with a large crustal-scale thermo-chemical perturbation, these processes are important to model the temporal evolution of the magmatic system (Lavecchia, Beekman, Clark, & Cloetingh, 2016).

Finally, our results and observations suggest that a quantitative CFB model should include some mechanisms for visco-elastoplastic crustal deformation and the formation of shear zones/ductile fracture/two-phase flow channelization instabilities (Colón et al., 2019; Schmeling et al., 2018, 2019). This introduces significant model complexity and high numerical resolution (Calogero et al., 2020). However without such processes, it is challenging to transport melt from lower crustal magma reservoirs into the upper crust without a long time hiatus. Since, we do not find evidence for such hiatuses in Deccan Traps and other CFBs (Section 4.3.2, 4.3.5), we contend that a realistic flood basalt model should include, either directly or in a parametrized form, some non-tensile failure mechanisms (Kjøll et al., 2019).

4.9 Conclusions

Continental flood basalt provinces (CFB) are some of the largest magmatic events in Earth's history and are typically associated with global-scale environmental perturbations (Clapham & Renne, 2019). Individual eruptive episodes for CFBs have lava volumes much larger than any modern-day counterpart. The commonly accepted model to explain this observation is that individual eruptive episodes are fed by correspondingly large magma reservoirs that erupt due to buoyancy overpressure (Black & Manga, 2017, see Section 4.2). However, it is difficult to validate this model due to the lack of surface exposure of these hypothesized magma bodies. In this study, we use constraints, both direct (geochronology - Section 4.3.2; paleo-secular variation - Section 4.3.3) and indirect (Hg chemostratigraphy - Section 4.3.4; lava flow morphology- Section 4.3.5), on the eruptive tempo of the Deccan Traps flood basalt province to show that the observations do not match the large magma reservoir model predictions. This conclusion is further supported by the pattern of inter- and intra-flow geochemical variations, as well as the absence of a large upper crustal magma reservoir in geophysical datasets.

Using a set of simplified magma reservoir mechanical models and 1D thermal calculations (Section 4.5 & 4.6), we find that most plausible the crustal plumbing system of CFBs is a multiply connected magmatic architecture with small-medium sized magma reservoirs (3-10 km semi-major axis, each a few hundred km^3 in volume). Individual eruptions are fed from a stochastic network of connected magma reservoirs, and this setup can help explain the eruptive flux, duration, and frequency of individual eruptive episodes. We propose that these small magma reservoirs are distributed throughout the crust and erupt due to recharge associated overpressure (for upper and middle crust). In contrast, buoyancy, along with non-tensile failure mechanisms, are responsible for the development of a vertically extended, but spatially limited, melt transport network in the lower crust. Based on these results, we

propose an updated conceptual model for continental flood basalt volcanism (Section 4.7).

We find observational constraints from other CFBs, especially Columbia River Basalts and Siberian Traps, to support our proposed model. In particular, that most of the CFBs show similar geochemical variations as the Deccan Traps strongly suggests a multiple magma reservoir magmatic architecture. Our study provides a framework to combine various disparate observations with theoretical calculations and can be used with future measurements for the Deccan Traps and other CFBs to both test and refine our model. A better understanding of the CFB magmatic architecture is critical for making quantitative predictions for the rate of volatile release (CO_2 and SO_2) during eruptions as well as the volume that is passively degassed. These inputs, along with magma volume flux and duration of individual eruptive episodes, are critical for quantitatively assessing the environmental consequences of flood basalt events and comparing with paleo-climate proxy observations (Self, Widdowson, Thordarson, & Jay, 2006; Schmidt et al., 2016; Glaze, Self, Schmidt, & Hunter, 2017; Suarez, Edmonds, & Jones, 2019; Hull et al., 2020).

Count	Paper reference	Deccan Traps Region	Category	I/E ratio
1	O. Pandey, Chandrakala, Parthasarathy, Reddy, and Reddy (2009)	Western Ghats	Moho-Depth Intrusives	4.34
2	O. Pandey et al. (2009)	Central Deccan	Moho-Depth Intrusives	0.83
3	Vedanti, Malkoti, Pandey, and Shrivastava (2018)	Central Deccan	Moho-Depth Intrusives	3.33
4	Vedanti et al. (2018)	Central Deccan	Mid-Crustal Intrusives	10.00
5	G. S. Rao et al. (2018)	Western Ghats	Moho-Depth Intrusives	3.49
6	G. S. Rao et al. (2018)	Western Ghats	Moho-Depth Intrusives	2.12
7	G. S. Rao et al. (2018)	Saurashtra	Moho-Depth Intrusives	6.07
8	P. V. Kumar et al. (2018)	Saurashtra	Total Crustal Section	2.78

9	Tewari, Prasad, and Kumar (2018a)	Narmada Son Lineament-Central India	Mid-Crustal Intrusives	7.48
10	Tewari et al. (2018a)	Narmada Son Lineament-Central India	Total Crustal Section	14.56
11	Tewari et al. (2018a)	Narmada Son Lineament-Central India	Total Crustal Section	14.32
12	Tewari et al. (2018a)	Narmada Son Lineament-Central India	Moho-Depth Intrusives	15.00
13	Tewari, Prasad, and Kumar (2018b)	Western Ghats	Total Crustal Section	3.06
14	Tewari et al. (2018b)	Western Ghats	Moho-Depth Intrusives	1.64
15	Seshu, Rao, and Nagan-janeyulu (2016)	Kutchh	Mid-Crustal Intrusives	0.65
16	Seshu et al. (2016)	Kutchh	Mid-Crustal Intrusives	0.30
17	Seshu et al. (2016)	Kutchh	Mid-Crustal Intrusives	0.54
18	Seshu et al. (2016)	Kutchh	Mid-Crustal Intrusives	0.30
19	A. Singh, Singh, and Kennett (2015)	Narmada Son Lineament Central India	Total Crustal Section	27.41
20	Rajaram, Anand, Erram, and Shinde (2016)	Koyna Central India	Moho-Depth Intrusives	1.86
21	Tewari et al. (2018b)	Saurashtra	Total Crustal Section	9.27

22	Tewari et al. (2018b)	Cambay Rift Zone	Moho-Depth Intrusives	6.92
23	Tewari et al. (2018b)	Cambay Rift Zone	Moho-Depth Intrusives	6.55
24	Tewari et al. (2018b)	Cambay Rift Zone	Moho-Depth Intrusives	4.61
25	Naganjaneyulu and Santosh (2010)	Cambay Rift Zone	Total Crustal Section	5.15
26	Naganjaneyulu and Santosh (2010)	Narmada Son Lineament Central india	Total Crustal Section	4.97
27	Azeez, Patro, Harinarayana, and Sarma (2017b)	Narmada Son Lineament Central india	Total Crustal Section	9.71
28	Naidu and Harinarayana (2009)	Narmada Son Lineament Central india	Moho-Depth Intrusives	7.83
29	Patro and Sarma (2016b)	Narmada Son Lineament Central india	Total Crustal Section	5.06
30	Patro and Sarma (2016b)	Narmada Son Lineament Central india	Total Crustal Section	8.05
31	Patro and Sarma (2016b)	Narmada Son Lineament Central india	Total Crustal Section	6.03
32	Prasad et al. (2018)	Narmada Son Lineament Central india	Mid-Crustal Intrusives	2.50
33	Prasad et al. (2018)	Narmada Son Lineament Central india	Mid-Crustal Intrusives	0.85
34	Prasad et al. (2018)	Narmada Son Lineament Central india	Mid-Crustal Intrusives	1.69

35	Prasad et al. (2018)	Narmada Son Lineament Central india	Mid-Crustal Intrusives	1.72
36	Prasad et al. (2018)	Narmada Son Lineament Central india	Mid-Crustal Intrusives	2.10
37	Prasad et al. (2018)	Narmada Son Lineament Central india	Mid-Crustal Intrusives	1.33
38	Prasad et al. (2018)	Narmada Son Lineament Central india	Mid-Crustal Intrusives	1.23
39	Prasad et al. (2018)	Narmada Son Lineament Central india	Mid-Crustal Intrusives	0.65
40	Prasad et al. (2018)	Narmada Son Lineament Central india	Mid-Crustal Intrusives	1.10
41	Prasad et al. (2018)	Narmada Son Lineament Central india	Mid-Crustal Intrusives	3.86
42	Prasad et al. (2018)	Narmada Son Lineament Central india	Mid-Crustal Intrusives	1.68
43	Krishna, Verma, and Purushotham (2002)	Western Ghats	Moho-Depth Intrusives	2.90
44	Krishna et al. (2002)	Saurashtra	Moho-Depth Intrusives	8.54
45	B. Singh et al. (2014b)	Saurashtra	Total Crustal Section	15.14
46	B. Singh et al. (2014b)	Saurashtra	Total Crustal Section	34.45
47	B. Singh et al. (2014b)	Saurashtra	Mid-Crustal Intrusives	5.94
48	B. Singh et al. (2014b)	Saurashtra	Total Crustal Section	30.33

49	J. Blanchard, Ernst, and Samson (2017)	Saurashtra	Total Crustal Section	5.51
50	Chouhan, Choudhury, and Pal (2020)	Cambay Rift Zone	Moho-Depth Intrusives	10.22
51	Chouhan et al. (2020)	Cambay Rift Zone	Moho-Depth Intrusives	10.05
52	Chouhan et al. (2020)	Cambay Rift Zone	Moho-Depth Intrusives	11.18

Table 4.1: Geophysical Estimates of Intrusive/Extrusive Ratio for Deccan Traps

Timescale	Expression
$t_{Maxwell}$	$\frac{\eta_{cr}\tilde{\beta}_s}{K_{cr}}$
t_{flux}	$\frac{4d_{res}a_c^2b_c}{ab^3}\frac{\eta_{res}\tilde{\beta}_s}{K_{cr}}$
t_{repres}	$\frac{\pi a_c^2 b_c \tilde{\beta}_s \rho_{res}}{\Omega K_{cr}}$
$t_{R,spherical\ shell}$	$\left[\frac{3\eta_{cr,1}(1-\nu)}{K_{cr}(1+\nu)}\right]\left(\frac{R_2}{R_1}\right)^3$
$t_{R,relax\ compress}$	$t_{R,spherical\ shell}/(1+\beta\alpha)$
$t^c_{viscous}$	$\eta_{crust}/(\Delta P)$
t^c_{fill}	V/Q_0
t^c_{cool}	$\epsilon_0 V\left(\frac{\oint_{res} q(\Delta T)dA}{\rho_{res}L_f} - \frac{Q_0 c_p \Delta T}{L_f}\right)^{-1}$
$t^c_{press\ diff}$	$\frac{b_c^2}{4\kappa_{pd}}$

Table 4.2: Summary of characteristic timescale for the magma reservoir model and the thermo-chemical box model.

In the following, I summarize the main results from the previous three chapters.

Plume-ridge interaction is commonly modeled in terms of interaction between solid-state plume flow and divergent ridge flow, but such models do not likely lead to the kind of solid-state flow-channelization that might explain narrow features such as the Wolf-Darwin lineament (WDL) at Galápagos and the Rodrigues Ridge (RR). Likewise, models involving tapping of anomalously hot and/or fertile asthenosphere between the plume and ridge due to lithospheric faulting appear to be inconsistent with a variety of evidence. We propose an alternative model in which the lineaments are the surface expressions of localized melt channels in the asthenosphere formed due to instabilities in a two-phase partially-molten system. A thermodynamic analysis shows that given the magma fluxes inferred to be associated with structures such as WDL and RR, these melt channels can be maintained over plume-ridge distances up to $\sim$ 1000 km. These results suggest that plume-ridge interaction in general, possibly including transport of plume-derived material along ridge axes (e.g., Iceland), may involve transport in high-melt-fraction channels, as opposed to just solid-state mantle flow.

The loss of volatiles from a magma reservoir affects the magmatic overpressure responsible for driving ground deformation and eruptions. I developed a fully coupled poro-thermo-elastic framework to account for both the flow of volatiles as well as associated effects on the stress state of the crust and calculate an analytical solution for spherical geometry. I then combined a magma chamber box model with these solutions to analyze eruption dynamics in magmatic systems. I found that in addition to viscous relaxation, magma recharge, and cooling time scales, the pore-pressure diffusion timescale exerts a first-order control on volcanic eruptions with moderately high crustal permeabilities of order 10^{-17} to 10^{-19} m^2. I described a parameter space to identify which components dominate in different regimes for volcanic eruptions according to these different time-scales.

I used a new volume-averaged visco-elastic mechanical model for an ellipsoidal magma reservoir coupled to a dike-shaped erodible conduit to calculate how eruptive fluxes (km^3/year) and volumes vary as a function of reservoir geometry and crustal properties for a single magma reservoir, as well as multiple connected reservoirs. I used a 1D thermal model with characteristic timescales for magma reservoir evolution to model how crustal visco-elastic properties evolve over time during the emplacement history of a CFB event, and how they impact magma eruptibility. Using the well-studied Deccan Traps as an archetype for CFB systems, I compiled multiple lines of evidence - geochronology, eruption tempo, intrusive-extrusive ratio, geochemical variations, and volcanological observations - to assess the viability of previous models. I found that the presence of just a few large crustal magma reservoirs is inconsistent with these constraints. Instead, I propose that CFB eruptions are fed from a number of smaller ($\sim 10^2$ - $10^{3.5}$ km^3) interconnected magma reservoirs present throughout the crust consistent with the paradigm of a trans-crustal magmatic system. This magmatic plumbing architecture permits; (a) large volume efficient eruptive episodes with durations of tens to hundreds of years; (b) relatively short time-periods separating eruptive episodes (thousands of years) since multiple mechanisms can trigger eruptions (via magma recharge or volatile exsolution, as opposed to long term (10^5 - 10^6 year) accumulation of buoyancy

overpressure); (c) lack of large upper-crustal intrusive bodies in various geophysical datasets; and (d) marked geochemical changes between and within individual eruptive episodes as observed in various CFB sections. Although observations from the Deccan Traps primarily motivate our model, I discussed constraints from other CFBs to illustrate that our model may be broadly applicable, with important implications for interpreting CFB geochemical datasets as well as the timing and volumes of climate-altering volatile emissions associated with CFBs.

Bibliography

Aarnes, I., Podladchikov, Y., & Svensen, H. (2012). Devolatilization-induced pressure build-up: Implications for reaction front movement and breccia pipe formation. *Geofluids*, *12*(4), 265–279.

Achtziger-Zupančič, P., Loew, S., & Hiller, A. (2017). Factors controlling the permeability distribution in fault vein zones surrounding granitic intrusions (ore mountains/germany). *Journal of Geophysical Research: Solid Earth*, *122*(3), 1876–1899.

Achtziger-Zupančič, P., Loew, S., & Mariéthoz, G. (2017). A new global database to improve predictions of permeability distribution in crystalline rocks at site scale. *Journal of Geophysical Research: Solid Earth*, *122*(5), 3513–3539.

Acid ring dykes and lava flows in deccan trap basalt, alech hills, saurashtra, gujarat. (1984). *Spec. Publ. Ser.-Geol. Surv. India*.

Afanasyev, A., Blundy, J., Melnik, O., & Sparks, S. (2018). Formation of magmatic brine lenses via focussed fluid-flow beneath volcanoes. *Earth and Planetary Science Letters*, *486*, 119–128.

Aharonov, E., Spiegelman, M., & Kelemen, P. (1997). Three-dimensional flow and reaction in porous media: Implications for the earth's mantle and sedimentary basins. *Journal of Geophysical Research: Solid Earth*, *102*(B7), 14821–14833.

Aharonov, E., Whitehead, J. A., Kelemen, P. B., & Spiegelman, M. (1995). Channeling instability of upwelling melt in the mantle. *Journal of Geophysical Research*, *100*(B10), 20433. doi: 10.1029/95JB01307

Albarede, F. (1992). How deep do common basaltic magmas form and differentiate? *Journal of Geophysical Research: Solid Earth*, *97*(B7), 10997–11009.

Albers, M., & Christensen, U. R. (2001). Channeling of plume flow beneath mid-ocean ridges. *Earth and Planetary Science Letters*, *187*(1-2), 207–220. doi: 10.1016/S0012-821X(01)00276-X

Albino, F., Biggs, J., & Syahbana, D. K. (2019). Dyke intrusion between neighbouring arc volcanoes responsible for 2017 pre-eruptive seismic swarm at agung. *Nature communications*, *10*(1), 1–11.

Alexander, P. O., & Purohit, M. (2019). Giant plagioclase basalt from the deccan volcanic province (dvp), sagar district, madhya pradesh, india: First report and implications. *Journal of the Geological Society of India*, *94*(2), 139–141.

Alghamdi, A. H., Aitken, A. R., & Dentith, M. C. (2018, apr). The deep crustal structure

of the warakurna LIP, and insights on proterozoic LIP processes and mineralisation. *Gondwana Research*, *56*, 1–11. doi: 10.1016/j.gr.2017.12.001

Allegre, C., Birck, J., Capmas, F., & Courtillot, V. (1999). Age of the deccan traps using 187re–187os systematics. *Earth and Planetary Science Letters*, *170*(3), 197–204.

Amoruso, A., & Crescentini, L. (2009). Shape and volume change of pressurized ellipsoidal cavities from deformation and seismic data. *Journal of Geophysical Research: Solid Earth*, *114*(B2).

Amos, H. M., Jacob, D. J., Streets, D. G., & Sunderland, E. M. (2013). Legacy impacts of all-time anthropogenic emissions on the global mercury cycle. *Global Biogeochemical Cycles*, *27*(2), 410–421.

Anderson, K., & Segall, P. (2011). Physics-based models of ground deformation and extrusion rate at effusively erupting volcanoes. *Journal of Geophysical Research: Solid Earth*, *116*(B7).

Anderson, K. R., & Poland, M. P. (2017). Abundant carbon in the mantle beneath hawai 'i. *Nature Geoscience*, *10*(9), 704–708.

Anderson, S., Stofan, E., Smrekar, S., Guest, J., & Wood, B. (1999). Pulsed inflation of pahoehoe lava flows: implications for flood basalt emplacement. *Earth and Planetary Science Letters*, *168*(1-2), 7–18.

Andersson, C., Führer, C., & Åkesson, J. (2015). Assimulo: A unified framework for {ODE} solvers. *Mathematics and Computers in Simulation*, *116*(0), 26 - 43. doi: http://dx.doi.org/10.1016/j.matcom.2015.04.007

Andreasen, R., Peate, D. W., & Brooks, C. K. (2004). Magma plumbing systems in large igneous provinces: inferences from cyclical variations in palaeogene east greenland basalts. *Contributions to Mineralogy and Petrology*, *147*(4), 438–452.

Angkasa, S. S., Jerram, D. A., Millett, J. M., Svensen, H. H., Planke, S., Taylor, R. A., ... Howell, J. (2017). Mafic intrusions, hydrothermal venting, and the basalt-sediment transition: Linking onshore and offshore examples from the north atlantic igneous province. *Interpretation*, *5*(3), SK83–SK101.

Aravena, A., Cioni, R., de' Michieli Vitturi, M., Pistolesi, M., Ripepe, M., & Neri, A. (2018, aug). Evolution of conduit geometry and eruptive parameters during effusive events. *Geophysical Research Letters*, *45*(15), 7471–7480. doi: 10.1029/2018gl077806

Aravena, A., Cioni, R., de' Michieli Vitturi, M., Pistolesi, M., Ripepe, M., & Neri, A. (2018). Evolution of conduit geometry and eruptive parameters during effusive events. *Geophysical Research Letters*, *45*(15), 7471–7480.

Aravena, Á., Cioni, R., Vitturi, M. d., & Neri, A. (2018). Conduit stability effects on intensity and steadiness of explosive eruptions. *Scientific reports*, *8*(1), 1–9.

Armstrong, R. T., McClure, J. E., Berrill, M. A., Rücker, M., Schlüter, S., & Berg, S. (2016). Beyond darcy's law: The role of phase topology and ganglion dynamics for two-fluid flow. *Physical Review E*, *94*(4), 043113.

Arndt, N. T. (1989). An open boundary between lower continental crust and mantle : its role in crust formation and crustal recycling. *Tectonophysics*, *161*, 201–212.

Arndt, N. T., & Christensen, U. (1992). The role of lithospheric mantle in continental flood

volcanism: thermal and geochemical constraints. *Journal of Geophysical Research: Solid Earth*, *97*(B7), 10967–10981.

Arndt, N. T., Czamanske, G. K., Wooden, J. L., & Fedorenko, V. A. (1993). Mantle and crustal contributions to continental flood volcanism. *Tectonophysics*, *223*(1-2), 39–52.

Auden, J. (1949). Dykes in western india-a discussion on their relationships with the deccan traps. *Trans. Nat. Inst. Sci. India*, *3*, 123–157.

Augland, L., Ryabov, V., Vernikovsky, V., Planke, S., Polozov, A., Callegaro, S., ... Svensen, H. (2019). The main pulse of the siberian traps expanded in size and composition. *Scientific Reports*, *9*(1), 1–12.

Azeez, K. A., Patro, P. K., Harinarayana, T., & Sarma, S. (2017a, sep). Magnetotelluric imaging across the tectonic structures in the eastern segment of the central indian tectonic zone: Preserved imprints of polyphase tectonics and evidence for suture status of the tan shear. *Precambrian Research*, *298*, 325–340. doi: 10.1016/j.precamres.2017.06.018

Azeez, K. A., Patro, P. K., Harinarayana, T., & Sarma, S. (2017b, sep). Magnetotelluric imaging across the tectonic structures in the eastern segment of the central indian tectonic zone: Preserved imprints of polyphase tectonics and evidence for suture status of the tan shear. *Precambrian Research*, *298*, 325–340. doi: 10.1016/j.precamres.2017.06.018

Azeez, K. A., Unsworth, M. J., Patro, P. K., Harinarayana, T., & Sastry, R. (2013). Resistivity structure of the central indian tectonic zone (citz) from multiple magnetotelluric (mt) profiles and tectonic implications. *Pure and Applied Geophysics*, *170*(12), 2231–2256.

Bachmann, O., & Bergantz, G. (2008). The magma reservoirs that feed supereruptions. *Elements*, *4*(1), 17–21.

Bachmann, O., & Bergantz, G. W. (2006). Gas percolation in upper-crustal silicic crystal mushes as a mechanism for upward heat advection and rejuvenation of near-solidus magma bodies. *Journal of Volcanology and Geothermal research*, *149*(1-2), 85–102.

Bai, B. (2006). Response of saturated porous media subjected to local thermal loading on the surface of semi-infinite space. *Acta Mechanica Sinica*, *22*(1), 54–61.

Bai, H., & Montési, L. G. (2015). Slip-rate-dependent melt extraction at mid-ocean ridges. *Geochem. Geophys. Geosyst.*, *16*, 1–19. doi: 10.1002/2014GC005579.Received

Baksi, A. K. (2001). The rajahmundry traps, andhra pradesh: evaluation of their petrogenesis relative to the deccan traps. *Journal of Earth System Science*, *110*(4), 397–407.

Ballmer, M. D., Conrad, C. P., Smith, E. I., & Harmon, N. (2013). Non-hotspot volcano chains produced by migration of shear-driven upwelling toward the East Pacific Rise. *Geology*, *41*(4), 479–482. doi: 10.1130/G33804.1

Baltzell, C., Parmentier, E. M., Liang, Y., & Tirupathi, S. (2015, nov). A high-order numerical study of reactive dissolution in an upwelling heterogeneous mantle: 2. Effect of shear deformation. *Geochemistry, Geophysics, Geosystems*, *16*(11), 3855–3869. doi: 10.1002/2015GC006038

Barbier, E. (2002). Geothermal energy technology and current status: an overview. *Renewable and sustainable energy reviews*, *6*(1-2), 3–65.

Barry, T., Kelley, S. P., Reidel, S. P., Camp, V. E., Self, S., Jarboe, N., ... Wolff, J. (2013). Eruption chronology of the columbia river basalt group. *The Columbia River Flood Basalt Province: Geological Society of America Special Paper*, *497*, 45–66.

Barton, C. A., Zoback, M. D., & Moos, D. (1995). Fluid flow along potentially active faults in crystalline rock. *Geology*, *23*(8), 683–686.

Basu, A. R., Renne, P. R., DasGupta, D. K., Teichmann, F., & Poreda, R. J. (1993). Early and late alkali igneous pulses and a high-3he plume origin for the deccan flood basalts. *Science*, *261*(5123), 902–906.

Beane, J., & Hooper, P. (1988). A note on the picrite basalts of the western ghats, deccan trap, india. *Memoir-Geological Society of India*(10), 117–133.

Beane, J., Turner, C., Hooper, P., Subbarao, K., & Walsh, J. (1986). Stratigraphy, composition and form of the deccan basalts, western ghats, india. *Bulletin of Volcanology*, *48*(1), 61–83.

Bédard, J. H., Marsh, B. D., Hersum, T. G., Naslund, H. R., & Mukasa, S. B. (2007). Large-scale mechanical redistribution of orthopyroxene and plagioclase in the basement sill, ferrar dolerites, mcmurdo dry valleys, antarctica: petrological, mineral-chemical and field evidence for channelized movement of crystals and melt. *Journal of Petrology*, *48*(12), 2289–2326.

Bédard, J. H., Naslund, H. R., Nabelek, P., Winpenny, A., Hryciuk, M., Macdonald, W., ... others (2012). Fault-mediated melt ascent in a neoproterozoic continental flood basalt province, the franklin sills, victoria island, canada. *Bulletin*, *124*(5-6), 723–736.

Begg, G. C., Hronsky, J. M., Griffin, W. L., & O'Reilly, S. Y. (2018). Global-to deposit-scale controls on orthomagmatic ni-cu (-pge) and pge reef ore formation. In *Processes and ore deposits of ultramafic-mafic magmas through space and time* (pp. 1–46). Elsevier.

Belardinelli, M., Bonafede, M., & Nespoli, M. (2019). Stress heterogeneities and failure mechanisms induced by temperature and pore-pressure increase in volcanic regions. *Earth and Planetary Science Letters*, *525*, 115765.

Benson, P. M., Heap, M. J., Lavallee, Y., Flaws, A., Hess, K.-U., Selvadurai, A., ... Schillinger, B. (2012). Laboratory simulations of tensile fracture development in a volcanic conduit via cyclic magma pressurisation. *Earth and Planetary Science Letters*, *349*, 231–239.

Bergantz, G., Schleicher, J., & Burgisser, A. (2015). Open-system dynamics and mixing in magma mushes. *Nature Geoscience*, *8*(10), 793–796.

Bertelsen, H. S., Rogers, B. D., Galland, O., Dumazer, G., & Abbana Benanni, A. (2018). Laboratory modeling of coeval brittle and ductile deformation during magma emplacement into viscoelastic rocks. *Frontiers in Earth Science*, *6*, 199.

Bhattacharji, S., Chatterjee, N., Wampler, J., Nayak, P., & Deshmukh, S. (1996). Indian intraplate and continental margin rifting, lithospheric extension, and mantle upwelling in deccan flood basalt volcanism near the k/t boundary: evidence from mafic dike swarms. *The Journal of Geology*, *104*(4), 379–398.

Bhattacharji, S., Sharma, R., & Chatterjee, N. (2004). Two-and three-dimensional gravity modeling along western continental margin and intraplate narmada-tapti rifts: Its relevance to deccan flood basalt volcanism. *Journal of Earth System Science*, *113*(4), 771–784.

Bhattacharya, G., & Yatheesh, V. (2015). Plate-tectonic evolution of the deep ocean basins adjoining the western continental margin of india—a proposed model for the early opening scenario. In *Petroleum geosciences: Indian contexts* (pp. 1–61). Springer.

Bhattacharya, S. K., Ma, G. S.-K., & Matsuhisa, Y. (2013, mar). Oxygen isotope evidence for crustal contamination in deccan basalts. *Geochemistry*, *73*(1), 105–112. doi: 10.1016/j.chemer.2012.11.007

Biggs, J., & Annen, C. (2019, jan). The lateral growth and coalesence of magma systems. *Philosophical Transactions of the Royal Society A: Mathematical, Physical and Engineering Sciences*, *377*(2139), 20180005. doi: 10.1098/rsta.2018.0005

Bistacchi, A., Tibaldi, A., Pasquarè, F. A., & Rust, D. (2012). The association of cone-sheets and radial dykes: Data from the Isle of Skye (UK), numerical modelling, and implications for shallow magma chambers. *Earth and Planetary Science Letters*, *339-340*, 46–56. doi: 10.1016/j.epsl.2012.05.020

Biswas, S. (1982). Rift basins in western margin of india and their hydrocarbon prospects with special reference to kutch basin. *AAPG Bulletin*, *66*(10), 1497–1513.

Biswas, S. (1987). Regional tectonic framework, structure and evolution of the western marginal basins of india. *Tectonophysics*, *135*(4), 307–327.

Blacic, T. M., Ito, G., Canales, J. P., Detrick, R. S., & Sinton, J. (2004). Constructing the crust along the Galapagos Spreading Center 91.3o-95.5oW: Correlation of seismic layer 2A with axial magma lens and topographic characteristics. *Journal of Geophysical Research B: Solid Earth*, *109*(10), B10310. doi: 10.1029/2004JB003066

Blacic, T. M., Ito, G., Shah, A. K., Canales, J. P., & Lin, J. (2008). Axial high topography and partial melt in the crust and mantle beneath the western Galápagos spreading center. *Geochemistry, Geophysics, Geosystems*, *9*(12). doi: 10.1029/2008GC002100

Black, B. A., & Gibson, S. A. (2019). Deep carbon and the life cycle of large igneous provinces. *Elements: An International Magazine of Mineralogy, Geochemistry, and Petrology*, *15*(5), 319–324.

Black, B. A., & Manga, M. (2017). Volatiles and the tempo of flood basalt magmatism. *Earth and Planetary Science Letters*, *458*, 130–140.

Blanchard, J., Ernst, R., & Samson, C. (2017, mar). Gravity and magnetic modelling of layered mafic–ultramafic intrusions in large igneous province plume centre regions: case studies from the 1.27 ga mackenzie, 1.38 ga kunene–kibaran, 0.06 ga deccan, and 0.13–0.08 ga high arctic events. *Canadian Journal of Earth Sciences*, *54*(3), 290–310. doi: 10.1139/cjes-2016-0132

Blanchard, J. A., Ernst, R. E., & Samson, C. (2017). Gravity and magnetic modelling of layered mafic–ultramafic intrusions in large igneous province plume centre regions: case studies from the 1.27 ga mackenzie, 1.38 ga kunene–kibaran, 0.06 ga deccan, and 0.13–0.08 ga high arctic events. *Canadian Journal of Earth Sciences*, *54*(3), 290–310.

Bodas, M., Khadri, S., & Subbarao, K. (1988). Stratigraphy of the jawhar and igatpuri formations, western ghat lava pile, india. *Memoir-Geological Society of India*(10).

Bohrson, W. A., & Spera, F. J. (2001). Energy-constrained open-system magmatic processes ii: application of energy-constrained assimilation–fractional crystallization (ec-afc) model to magmatic systems. *Journal of Petrology*, *42*(5), 1019–1041.

Bohrson, W. A., & Spera, F. J. (2007). Energy-constrained recharge, assimilation, and fractional crystallization (ec-raχfc): A visual basic computer code for calculating trace element and isotope variations of open-system magmatic systems. *Geochemistry, Geophysics, Geosystems*, *8*(11).

Bondre, N., Hart, W., & Sheth, H. (2006). Geology and geochemistry of the sangamner mafic dike swarm, western deccan volcanic province, india: implications for regional stratigraphy. *The Journal of geology*, *114*(2), 155–170.

Bondre, N. R., Duraiswami, R. A., & Dole, G. (2004). Morphology and emplacement of flows from the deccan volcanic province, india. *Bulletin of Volcanology*, *66*(1), 29–45.

Bondre, N. R., & Hart, W. K. (2008). Morphological and textural diversity of the steens basalt lava flows, southeastern oregon, usa: implications for emplacement style and nature of eruptive episodes. *Bulletin of Volcanology*, *70*(8), 999–1019.

Borges, M. R., Sen, G., Hart, G. L., Wolff, J. A., & Chandrasekharam, D. (2014). Plagioclase as recorder of magma chamber processes in the deccan traps: Sr-isotope zoning and implications for deccan eruptive event. *Journal of Asian Earth Sciences*, *84*, 95–101.

Boudoire, G., Rizzo, A. L., Di Muro, A., Grassa, F., & Liuzzo, M. (2018). Extensive co2 degassing in the upper mantle beneath oceanic basaltic volcanoes: First insights from piton de la fournaise volcano (la réunion island). *Geochimica et Cosmochimica Acta*, *235*, 376–401.

Braun, M. G., & Kelemen, P. B. (2002, nov). Dunite distribution in the Oman Ophiolite: Implications for melt flux through porous dunite conduits. *Geochemistry, Geophysics, Geosystems*, *3*(11), 1–21. doi: 10.1029/2001GC000289

Braun, M. G., & Sohn, R. A. (2003). Melt migration in plume-ridge systems. *Earth and Planetary Science Letters*, *213*(3-4), 417–430. doi: 10.1016/S0012-821X(03)00279-6

Braz Machado, F., Reis Viana Rocha-Júnior, E., Soares Marques, L., & Ranalli Nardy, A. (2015). Volcanological aspects of the northwest region of paraná continental flood basalts (brazil). *Solid Earth*, 227–241.

Brown, R., Kavanagh, J., Sparks, R., Tait, M., & Field, M. (2007). Mechanically disrupted and chemically weakened zones in segmented dike systems cause vent localization: Evidence from kimberlite volcanic systems. *Geology*, *35*(9), 815–818.

Brown, R. J., Blake, S., Bondre, N., Phadnis, V., & Self, S. (2011). ´ a´ ā lava flows in the deccan volcanic province, india, and their significance for the nature of continental flood basalt eruptions. *Bulletin of Volcanology*, *73*(6), 737–752.

Bruce, P. M., & Huppert, H. E. (1990). Solidification and melting along dykes by the laminar flow of basaltic magma. *Magma transport and storage*, 87–101.

Brueseke, M. E., Heizler, M. T., Hart, W. K., & Mertzman, S. A. (2007). Distribution and geochronology of oregon plateau (usa) flood basalt volcanism: The steens basalt

revisited. *Journal of Volcanology and Geothermal Research*, *161*(3), 187–214.

Bryan, S. E., & Ferrari, L. (2013). Large igneous provinces and silicic large igneous provinces: Progress in our understanding over the last 25 years. *GSA Bulletin*, *125*(7-8), 1053–1078.

Bryan, S. E., Peate, I. U., Peate, D. W., Self, S., Jerram, D. A., Mawby, M. R., ... Miller, J. A. (2010). The largest volcanic eruptions on earth. *Earth-Science Reviews*, *102*(3-4), 207–229.

Buchan, K. L., & Ernst, R. E. (2019). Giant circumferential dyke swarms: catalogue and characteristics. In *Dyke swarms of the world: A modern perspective* (pp. 1–44). Springer.

Buntin, S., Malehmir, A., Koyi, H., Högdahl, K., Malinowski, M., Larsson, S. Å., ... Górszczyk, A. (2019). Emplacement and 3d geometry of crustal-scale saucer-shaped intrusions in the fennoscandian shield. *Scientific reports*, *9*(1), 1–11.

Burgess, S., Muirhead, J., & Bowring, S. (2017). Initial pulse of siberian traps sills as the trigger of the end-permian mass extinction. *Nature Communications*, *8*(1), 1–6.

Burgess, S. D., & Bowring, S. A. (2015). High-precision geochronology confirms voluminous magmatism before, during, and after earth's most severe extinction. *Science Advances*, *1*(7), e1500470.

Burgisser, A., Carrara, A., & Annen, C. (2020). Numerical simulations of magmatic enclave deformation. *Journal of Volcanology and Geothermal Research*, *392*, 106790.

Burgisser, A., Chevalier, L., Gardner, J. E., & Castro, J. M. (2017). The percolation threshold and permeability evolution of ascending magmas. *Earth and Planetary Science Letters*, *470*, 37–47.

Bürgmann, R., & Dresen, G. (2008). Rheology of the lower crust and upper mantle: Evidence from rock mechanics, geodesy, and field observations. *Annu. Rev. Earth Planet. Sci.*, *36*, 531–567.

Burton, M. R., Sawyer, G. M., & Granieri, D. (2013). Deep carbon emissions from volcanoes. *Reviews in Mineralogy and Geochemistry*, *75*(1), 323–354.

Busby-Spera, C. J., & White, J. D. (1987). Variation in peperite textures associated with differing host-sediment properties. *Bulletin of Volcanology*, *49*(6), 765–776.

Cai, Z., & Bercovici, D. (2016). Two-dimensional magmons with damage and the transition to magma-fracturing. *Physics of the Earth and Planetary Interiors*, *256*, 13–25.

Calogero, M., Hetland, E., & Lange, R. (2020). High-resolution numerical modeling of heat and volatile transfer from basalt to wall rock: Application to the crustal column beneath long valley caldera, ca. *Journal of Geophysical Research: Solid Earth*, *n/a*(n/a), e54059. Retrieved from `https://agupubs.onlinelibrary.wiley.com/doi/abs/10.1029/2018JB016773` (e54059 2018JB016773) doi: 10.1029/2018JB016773

Calvari, S. (2019). Understanding basaltic lava flow morphologies and structures for hazard assessment. *Annals of Geophysics*.

Calvès, G., Schwab, A. M., Huuse, M., Clift, P. D., Gaina, C., Jolley, D., ... Inam, A. (2011). Seismic volcanostratigraphy of the western indian rifted margin: The pre-

deccan igneous province. *Journal of Geophysical Research: Solid Earth*, *116*(B1).

Campbell, I. H., & Griffiths, R. W. (1990). Implications of mantle plume structure for the evolution of flood basalts. *Earth and Planetary Science Letters*, *99*(1-2), 79–93.

Canales, J., Ito, G., Detrick, R. S., & Sinton, J. (2002, oct). Crustal thickness along the western Galápagos Spreading Center and the compensation of the Galápagos hotspot swell. *Earth and Planetary Science Letters*, *203*(1), 311–327. doi: 10.1016/S0012-821X(02)00843-9

Canales, J. P., Dunn, R. A., Ito, G., Detrick, R. S., & Sallares, V. (2014). Effect of variations in magma supply on the crustal structure of mid-ocean ridges: Insights from the western Galápagos Spreading Center. *The Galapagos: A Natural Laboratory for the Earth Sciences*, 363–391. doi: 10.1002/9781118852538.ch17

Cande, S. C., & Patriat, P. (2015). The anticorrelated velocities of africa and india in the late cretaceous and early cenozoic. *Geophysical Journal International*, *200*(1), 227–243.

Cannat, M., Briais, A., Deplus, C., Escartin, J., Georgen, J., Lin, J., ... da Silva, P. (1999, nov). Mid-Atlantic Ridge–Azores hotspot interactions: along-axis migration of a hotspot-derived event of enhanced magmatism 10 to 4 Ma ago. *Earth and Planetary Science Letters*, *173*(3), 257–269. doi: 10.1016/S0012-821X(99)00234-4

Cao, W., Kaus, B. J., & Paterson, S. (2016). Intrusion of granitic magma into the continental crust facilitated by magma pulsing and dike-diapir interactions: Numerical simulations. *Tectonics*, *35*(6), 1575–1594.

Cao, W., Lee, C.-T. A., Yang, J., & Zuza, A. V. (2019, jun). Hydrothermal circulation cools continental crust under exhumation. *Earth and Planetary Science Letters*, *515*, 248–259. doi: 10.1016/j.epsl.2019.03.029

Caricchi, L., Annen, C., Blundy, J., Simpson, G., & Pinel, V. (2014a). Frequency and magnitude of volcanic eruptions controlled by magma injection and buoyancy. *Nature Geoscience*, *7*(2), 126.

Caricchi, L., Annen, C., Blundy, J., Simpson, G., & Pinel, V. (2014b). Frequency and magnitude of volcanic eruptions controlled by magma injection and buoyancy. *Nature Geoscience*, *7*(2), 126–130. doi: 10.1038/ngeo2041

Caricchi, L., Sheldrake, T. E., & Blundy, J. (2018). Modulation of magmatic processes by co2 flushing. *Earth and Planetary Science Letters*, *491*, 160–171.

Carn, S., Fioletov, V., McLinden, C., Li, C., & Krotkov, N. (2017). A decade of global volcanic so 2 emissions measured from space. *Scientific reports*, *7*, 44095.

Carrara, A., Burgisser, A., & Bergantz, G. W. (2019). Lubrication effects on magmatic mush dynamics. *Journal of Volcanology and Geothermal Research*, *380*, 19–30.

Carrara, A., Burgisser, A., & Bergantz, G. W. (2020). The architecture of an intrusion in magmatic mush.

Carslaw, H. S., & Jaeger, J. C. (1959). Conduction of heat in solids. *Oxford: Clarendon Press, 1959, 2nd ed.*.

Cashman, K. V., & Kauahikaua, J. P. (1997). Reevaluation of vesicle distributions in basaltic lava flows. *Geology*, *25*(5), 419–422.

Cashman, K. V., Sparks, R. S. J., & Blundy, J. D. (2017). Vertically extensive and unstable magmatic systems: a unified view of igneous processes. *Science*, *355*(6331), eaag3055.

Cassidy, M., Manga, M., Cashman, K., & Bachmann, O. (2018). Controls on explosive-effusive volcanic eruption styles. *Nature communications*, *9*(1), 1–16.

Castillo, P. R., Natland, J. H., Niu, Y., & Lonsdale, P. F. (1998). Sr, Nd and Pb isotopic variation along the Pacific–Antarctic risecrest, 53–57oS: Implications for the composition and dynamics of the South Pacific upper mantle. *Earth and Planetary Science Letters*, *154*(1-4), 109–125. doi: 10.1016/S0012-821X(97)00172-6

Cathles, L. (1977). An analysis of the cooling of intrusives by ground-water convection which includes boiling. *Economic Geology*, *72*(5), 804–826.

Cathles, L., & Adams, J. J. (2005). Fluid flow and petroleum and mineral resources in the upper (¡ 20 km) continental crust. *Economic Geology 100th Anniversary Volume*, 77–110.

Cawthorn, R. G. (2015). The bushveld complex, south africa. In *Layered intrusions* (pp. 517–587). Springer.

Cawthorn, R. G., & Walraven, F. (1998). Emplacement and crystallization time for the bushveld complex. *Journal of Petrology*, *39*(9), 1669–1687.

Chadam, J., Merino, E., & Ortoleva, P. (1986). Reactive Infiltration Instabilities. *IMA Journal of Applied Mathematics*, 207–221.

Chandra, J., Paul, D., Stracke, A., Chabaux, F., & Granet, M. (2019, may). The origin of carbonatites from amba dongar within the deccan large igneous province. *Journal of Petrology*, *60*(6), 1119–1134. doi: 10.1093/petrology/egz026

Chandrasekharam, D., Vaselli, O., Sheth, H., & Keshav, S. (2000). Petrogenetic significance of ferro-enstatite orthopyroxene in basaltic dikes from the tapi rift, deccan flood basalt province, india. *Earth and Planetary Science Letters*, *179*(3-4), 469–476.

Chatterjee, N., & Bhattacharji, S. (2008). Trace element variations in deccan basalts: roles of mantle melting, fractional crystallization and crustal assimilation. *Journal of the Geological Society of India*, *71*(2), 171.

Chatterjee, N., & Sheth, H. (2015). Origin of the powai ankaramite, and the composition, p–t conditions of equilibration and evolution of the primary magmas of the deccan tholeiites. *Contributions to Mineralogy and Petrology*, *169*(3), 32.

Chenet, A.-L., Courtillot, V., Fluteau, F., Gérard, M., Quidelleur, X., Khadri, S., ... Thordarson, T. (2009). Determination of rapid deccan eruptions across the cretaceous-tertiary boundary using paleomagnetic secular variation: 2. constraints from analysis of eight new sections and synthesis for a 3500-m-thick composite section. *Journal of Geophysical Research: Solid Earth*, *114*(B6).

Chenet, A.-L., Fluteau, F., Courtillot, V., Gérard, M., & Subbarao, K. (2008). Determination of rapid deccan eruptions across the cretaceous-tertiary boundary using paleomagnetic secular variation: Results from a 1200-m-thick section in the mahabaleshwar escarpment. *Journal of Geophysical Research: Solid Earth*, *113*(B4).

Cheng, A. (2016). Porothermoelasticity. In *Poroelasticity* (pp. 599–701). Cham: Springer International Publishing.

Cheng, L., Zeng, L., Ren, Z., Wang, Y., & Luo, Z. (2014). Timescale of emplacement of the panzhihua gabbroic layered intrusion recorded in giant plagioclase at sichuan province, sw china. *Lithos*, *204*, 203–219.

Cheng, L.-L., Yang, Z.-F., Zeng, L., Wang, Y., & Luo, Z.-H. (2014). Giant plagioclase growth during storage of basaltic magma in emeishan large igneous province, sw china. *Contributions to Mineralogy and Petrology*, *167*(2), 971.

Chevrel, M. O., Pinkerton, H., & Harris, A. J. (2019). Measuring the viscosity of lava in the field: A review. *Earth-Science Reviews*.

Chiaradia, M., Schaltegger, U., & Spikings, R. A. (2014). Time scales of mineral systems-advances in understanding over the past decade. *Soc. Econ. Geol. Spec. Publ.*, *18*, 37–58.

Chiodini, G., Cardellini, C., Amato, A., Boschi, E., Caliro, S., Frondini, F., & Ventura, G. (2004). Carbon dioxide earth degassing and seismogenesis in central and southern italy. *Geophysical Research Letters*, *31*(7).

Chiodini, G., Paonita, A., Aiuppa, A., Costa, A., Caliro, S., De Martino, P., ... Vandemeulebrouck, J. (2016). Magmas near the critical degassing pressure drive volcanic unrest towards a critical state. *Nature communications*, *7*, 13712.

Chiodini, G., Selva, J., Pezzo, E., Marsan, D., Siena, L., D'auria, L., ... others (2017). Clues on the origin of post-2000 earthquakes at campi flegrei caldera (italy). *Scientific reports*, *7*(1), 4472.

Choudhary, B. R., & Jadhav, G. N. (2014). Petrogenesis of fractionated basaltic lava flows of poladpur-mahabaleshwar formation around mahabaleshwar, western ghats, india. *Journal of the Geological Society of India*, *84*(2), 197–208.

Choudhary, B. R., Santosh, M., De Vivo, B., Jadhav, G., & Babu, E. (2019). Melt inclusion evidence for mantle heterogeneity and magma degassing in the deccan large igneous province, india. *Lithos*, *346*, 105135.

Chouhan, A. K., Choudhury, P., & Pal, S. K. (2020, feb). New evidence for a thin crust and magmatic underplating beneath the cambay rift basin, western india through modelling of EIGEN-6c4 gravity data. *Journal of Earth System Science*, *129*(1). doi: 10.1007/s12040-019-1335-y

Christie, D. M., Werner, R., Hauff, F., Hoernle, K., & Hanan, B. B. (2005, jan). Morphological and geochemical variations along the eastern Galápagos Spreading Center. *Geochemistry, Geophysics, Geosystems*, *6*(1), n/a–n/a. doi: 10.1029/2004GC000714

Christopher, T., Blundy, J., Cashman, K., Cole, P., Edmonds, M., Smith, P., ... Stinton, A. (2015). Crustal-scale degassing due to magma system destabilization and magma-gas decoupling at soufrière hills volcano, montserrat. *Geochemistry, Geophysics, Geosystems*, *16*(9), 2797–2811.

Clapham, M. E., & Renne, P. R. (2019). Flood basalts and mass extinctions. *Annual Review of Earth and Planetary Sciences*, *47*, 275–303.

Coetzee, A., Kisters, A., & Chevallier, L. (2019). Sill complexes in the karoo lip: Emplacement controls and regional implications. *Journal of African Earth Sciences*, *158*, 103517.

Coetzee, A., & Kisters, A. F. (2018). The elusive feeders of the karoo large igneous province and their structural controls. *Tectonophysics*, *747*, 146–162.

Coffin, M. F., & Eldholm, O. (1994). Large igneous provinces: crustal structure, dimensions, and external consequences. *Reviews of Geophysics*, *32*(1), 1–36.

Coleman, D. S., Gray, W., & Glazner, A. F. (2004). Rethinking the emplacement and evolution of zoned plutons: Geochronologic evidence for incremental assembly of the tuolumne intrusive suite, california. *Geology*, *32*(5), 433–436.

Colman, A., Sinton, J. M., White, S. M., McClinton, J. T., Bowles, J. A., Rubin, K. H., ... Russo, C. (2012, aug). Effects of variable magma supply on mid-ocean ridge eruptions: Constraints from mapped lava flow fields along the Galápagos Spreading Center. *Geochemistry, Geophysics, Geosystems*, *13*(8), n/a–n/a. doi: 10.1029/2012GC004163

Colombier, M., Wadsworth, F. B., Gurioli, L., Scheu, B., Kueppers, U., Di Muro, A., & Dingwell, D. B. (2017). The evolution of pore connectivity in volcanic rocks. *Earth and Planetary Science Letters*, *462*, 99–109.

Colón, D. P., Bindeman, I. N., & Gerya, T. V. (2019). Understanding the isotopic and chemical evolution of yellowstone hot spot magmatism using magmatic-thermomechanical modeling. *Journal of Volcanology and Geothermal Research*, *370*, 13–30.

Connolly, J. (2009). The geodynamic equation of state: what and how. *Geochemistry, Geophysics, Geosystems*, *10*(10).

Connolly, J. A., & Podladchikov, Y. Y. (2015). An analytical solution for solitary porosity waves: dynamic permeability and fluidization of nonlinear viscous and viscoplastic rock. *Geofluids*, *15*(1-2), 269–292.

Connolly, J. A. D., & Podladchikov, Y. Y. (2007). Decompaction weakening and channeling instability in ductile porous media: Implications for asthenospheric melt segregation. *Journal of Geophysical Research: Solid Earth*, *112*(10), 1–15. doi: 10.1029/2005JB004213

Connolly, J. A. D., & Podladchikov, Y. Y. (2015). An analytical solution for solitary porosity waves: Dynamic permeability and fluidization of nonlinear viscous and viscoplastic rock. *Geofluids*, *15*(1-2), 269–292. doi: 10.1111/gfl.12110

Costa, A., Melnik, O., & Sparks, R. (2007). Controls of conduit geometry and wallrock elasticity on lava dome eruptions. *Earth and Planetary Science Letters*, *260*(1-2), 137–151.

Courtillot, V., & Fluteau, F. (2014). A review of the embedded time scales of flood basalt volcanism with special emphasis on dramatically short magmatic pulses. *Geological Society of America Special Papers*, *505*, SPE505–15.

Courtillot, V., Gallet, Y., Rocchia, R., Féraud, G., Robin, E., Hofmann, C., ... Ghevariya, Z. (2000). Cosmic markers, 40ar/39ar dating and paleomagnetism of the kt sections in the anjar area of the deccan large igneous province. *Earth and Planetary Science Letters*, *182*(2), 137–156.

Courtillot, V. E., & Renne, P. R. (2003). On the ages of flood basalt events. *Comptes Rendus Geoscience*, *335*(1), 113–140.

Cox, K. (1988). Numerical modelling of a randomized rtf magma chamber: a comparison

with continental flood basalt sequences. *Journal of Petrology*, *29*(3), 681–697.

Cox, K., & Devey, C. W. (1987). Fractionation processes in deccan traps magmas: Comments on the paper by g. sen? mineralogy and petrogenesis of the deccan trap lava flows around mahabaleshwar, india. *Journal of Petrology*, *28*(1), 235–238.

Cox, K., & Hawkesworth, C. (1985). Geochemical stratigraphy of the deccan traps at mahabaleshwar, western ghats, india, with implications for open system magmatic processes. *Journal of Petrology*, *26*(2), 355–377.

Cox, K. G. (1980). A model for flood basalt volcanism. *Journal of Petrology*, *21*(4), 629–650. doi: 10.1093/petrology/21.4.629

Cox, K. G. (1993). Continental magmatic underplating. *Philosophical Transactions of the Royal Society of London. Series A: Physical and Engineering Sciences*, *342*(1663), 155–166.

Cox, K. G., & Hawkesworth, C. J. (1984). Relative contribution of crust and mantle to flood basalt magmatism, mahabaleshwar area, deccan traps. *Philosophical Transactions of the Royal Society of London. Series A, Mathematical and Physical Sciences*, *310*(1514), 627–641.

Cox, K. G., & Mitchell, C. (1988). Importance of crystal settling in the differentiation of deccan trap basaltic magmas. *Nature*, *333*(6172), 447–449.

Cox, S. F. (2002). Fluid flow in mid-to deep crustal shear systems. *Earth, planets and space*, *54*(11), 1121–1125.

Crankshaw, I., Archfield, S., Newman, A., Bergfeld, D., Clor, L., Spicer, K., ... Ingebritsen, S. (2018). Multi-year high-frequency hydrothermal monitoring of selected high-threat cascade range volcanoes. *Journal of Volcanology and Geothermal Research*, *356*, 24–35.

Crisp, J. A. (1984). Rates of magma emplacement and volcanic output. *Journal of Volcanology and Geothermal Research*, *20*(3-4), 177–211.

Crookshank, H. (1936). Geology of the northern slopes of the satpuras between morand and sher rivers-mem. *Geol. Sur. of India*, *66*(Pt 2).

Crowley, J. W., Katz, R. F., Huybers, P., Langmuir, C. H., & Park, S.-h. (2015). Production of Oceanic Crust. *Science*, *347*(6227), 1237–1240.

Cruden, A. R., & Weinberg, R. F. (2018). Mechanisms of magma transport and storage in the lower and middle crust—magma segregation, ascent and emplacement. In *Volcanic and igneous plumbing systems* (pp. 13–53). Elsevier.

Cucci, L., Di Luccio, F., Esposito, A., & Ventura, G. (2017). Vein networks in hydrothermal systems provide constraints for the monitoring of active volcanoes. *Scientific reports*, *7*(1), 146.

Cucciniello, C., Choudhary, A. K., Pande, K., & Sheth, H. (2019). Mineralogy, geochemistry and 40 ar–39 ar geochronology of the barda and alech complexes, saurashtra, northwestern deccan traps: early silicic magmas derived by flood basalt fractionation. *Geological Magazine*, *156*(10), 1668–1690.

Cucciniello, C., Choudhary, A. K., Zanetti, A., Sheth, H. C., Vichare, S., & Pereira, R. (2014). Mineralogy, geochemistry and petrogenesis of the khopoli mafic intrusion,

deccan traps, india. *Mineralogy and Petrology*, *108*(3), 333–351.

Cucciniello, C., Demonterova, E. I., Sheth, H., Pande, K., & Vijayan, A. (2015). 40ar/39ar geochronology and geochemistry of the central saurashtra mafic dyke swarm: insights into magmatic evolution, magma transport, and dyke-flow relationships in the northwestern deccan traps. *Bulletin of Volcanology*, *77*(5), 45.

Cushman, B., Sinton, J., Ito, G., & Eaby Dixon, J. (2004, aug). Glass compositions, plume-ridge interaction, and hydrous melting along the Galápagos Spreading Center, 90.5oW to 98oW. *Geochemistry, Geophysics, Geosystems*, *5*(8), n/a–n/a. doi: 10.1029/2004GC000709

Dahm, T. (2000). On the shape and velocity of fluid-filled fractures in the Earth. *Geophysical Journal International*, *142*(1), 181–192. doi: 10.1046/j.1365-246X.2000.00148.x

Das, R., Zhang, Y., Schaubs, P., & Cleary, P. (2014). Modelling rock fracturing caused by magma intrusion using the smoothed particle hydrodynamics method. *Computational Geosciences*, *18*(6), 927–947.

Dasgupta, R., Hirschmann, M. M., & Smith, N. D. (2007). Partial melting experiments of peridotite + CO2 at 3 GPa and genesis of alkalic ocean island basalts. *Journal of Petrology*, *48*(11), 2093–2124. doi: 10.1093/petrology/egm053

Dave, S. (1971). The geology of the igneous complex of the barda hills, saurashtra, gujarat state (india). *Bulletin Volcanologique*, *35*(3), 619–632.

DeBari, S. M., & Greene, A. R. (2011). Vertical stratification of composition, density, and inferred magmatic processes in exposed arc crustal sections. In *Arc-continent collision* (pp. 121–144). Springer.

Degli Alessandrini, G., Menegon, L., Malaspina, N., Dijkstra, A., & Anderson, M. (2017). Creep of mafic dykes infiltrated by melt in the lower continental crust (seiland igneous province, norway). *Lithos*, *274*, 169–187.

Degruyter, W., & Huber, C. (2014). A model for eruption frequency of upper crustal silicic magma chambers. *Earth and Planetary Science Letters*, *403*, 117–130.

Degruyter, W., Huber, C., Bachmann, O., Cooper, K. M., & Kent, A. J. (2017). Influence of exsolved volatiles on reheating silicic magmas by recharge and consequences for eruptive style at volcán quizapu (chile). *Geochemistry, Geophysics, Geosystems*, *18*(11), 4123–4135.

Degruyter, W., Parmigiani, A., Huber, C., & Bachmann, O. (2019). How do volatiles escape their shallow magmatic hearth? *Philosophical Transactions of the Royal Society A*, *377*(2139), 20180017.

Delaney, P. T. (1982). Rapid intrusion of magma into wet rock: groundwater flow due to pore pressure increases. *Journal of Geophysical Research: Solid Earth*, *87*(B9), 7739–7756.

Delaney, P. T., & Pollard, D. D. (1981). *Deformation of host rocks and flow of magma during growth of minette dikes and breccia-bearing intrusions near ship rock, new mexico* (Tech. Rep.). USGPO,.

De Moor, J., Aiuppa, A., Pacheco, J., Avard, G., Kern, C., Liuzzo, M., ... Fischer, T. P. (2016). Short-period volcanic gas precursors to phreatic eruptions: Insights from poás

volcano, costa rica. *Earth and Planetary Science Letters*, *442*, 218–227.

Deng, Y., Chen, Y., Wang, P., Essa, K. S., Xu, T., Liang, X., & Badal, J. (2016). Magmatic underplating beneath the emeishan large igneous province (south china) revealed by the comgra-elip experiment. *Tectonophysics*, *672*, 16–23.

DePaolo, D. J. (1981). Trace element and isotopic effects of combined wallrock assimilation and fractional crystallization. *Earth and planetary science letters*, *53*(2), 189–202.

Deshmukh, S. (1977). *A critical petrological study of the deccan basalts and associated high level laterites in parts of the western ghats, maharashtra state* (Unpublished doctoral dissertation). PhD thesis, Nagpur University, p 306.

de Silva, S. L., & Gregg, P. M. (2014). Thermomechanical feedbacks in magmatic systems: Implications for growth, longevity, and evolution of large caldera-forming magma reservoirs and their supereruptions. *Journal of Volcanology and Geothermal Research*, *282*, 77–91.

Dessai, A., Downes, H., López-Moro, F.-J., & López-Plaza, M. (2008). Lower crustal contamination of deccan traps magmas: evidence from tholeiitic dykes and granulite xenoliths from western india. *Mineralogy and Petrology*, *93*(3-4), 243–272.

Dessai, A., & Vaselli, O. (1999). Petrology and geochemistry of xenoliths in lamprophyres from the deccan traps: implications for the nature of the deep crust boundary in western india. *Mineralogical Magazine*, *63*(5), 703–722.

Dessert, C., Dupré, B., Gaillardet, J., François, L. M., & Allegre, C. J. (2003). Basalt weathering laws and the impact of basalt weathering on the global carbon cycle. *Chemical Geology*, *202*(3-4), 257–273.

Devey, C. W., & Cox, K. (1987). Relationships between crustal contamination and crystallisation in continental flood basalt magmas with special reference to the deccan traps of the western ghats, india. *Earth and Planetary Science Letters*, *84*(1), 59–68.

Devey, C. W., & Lightfoot, P. (1986). Volcanological and tectonic control of stratigraphy and structure in the western deccan traps. *Bulletin of Volcanology*, *48*(4), 195–207.

Devey, C. W., & Stephens, W. (1991). Tholeiitic dykes in the seychelles and the original spatial extent of the deccan. *Journal of the Geological Society*, *148*(6), 979–983.

Dipple, G. M., & Ferry, J. M. (1992). Metasomatism and fluid flow in ductile fault zones. *Contributions to Mineralogy and Petrology*, *112*(2-3), 149–164.

Dongre, A., Viljoen, K., & Rathod, A. (2018). Mineralogy and geochemistry of picrodolerite dykes from the central deccan traps flood basaltic province, india, and their geodynamic significance. *Mineralogy and Petrology*, *112*(2), 267–277.

Dragoni, M., & Magnanensi, C. (1989). Displacement and stress produced by a pressurized, spherical magma chamber, surrounded by a viscoelastic shell. *Physics of the Earth and Planetary Interiors*, *56*(3-4), 316–328.

Dragoni, M., & Santini, S. (2007). Lava flow in tubes with elliptical cross sections. *Journal of volcanology and geothermal research*, *160*(3-4), 239–248.

Dragoni, M., & Tallarico, A. (2018). Changes in lava effusion rate from a volcanic fissure due to pressure changes in the conduit. *Geophysical Journal International*, *216*(1), 692–702.

Duncan, R. A. (1990). The volcanic record of the Reunion Hotspot. *Proc. Ocean Drill. Program Sci. Results*, *115*(1987), 3–10.

Duraiswami, R. A., Bondre, N. R., & Dole, G. (2004). Possible lava tube system in a hummocky lava flow at daund, western deccan volcanic province, india. *Journal of Earth System Science*, *113*(4), 819–829.

Duraiswami, R. A., Bondre, N. R., & Managave, S. (2008). Morphology of rubbly pahoehoe (simple) flows from the deccan volcanic province: Implications for style of emplacement. *Journal of Volcanology and Geothermal Research*, *177*(4), 822–836.

Duraiswami, R. A., Jutzeler, M., Karve, A. V., Gadpallu, P., & Kale, M. G. (2019). Subaqueous effusive and explosive phases of late deccan volcanism: evidence from mumbai islands, india. *Arabian Journal of Geosciences*, *12*(23), 703.

Duraiswami, R. A., & Shaikh, T. N. (2013, jun). Geology of the saucer-shaped sill near mahad, western deccan traps, india, and its significance to the flood basalt model. *Bulletin of Volcanology*, *75*(7). doi: 10.1007/s00445-013-0731-4

Dutrow, B., & Norton, D. (1995). Evolution of fluid pressure and fracture propagation during contact metamorphism. *Journal of Metamorphic Geology*, *13*(6), 677–686.

Dyment, J., Hémond, C., Guillou, H., Maia, M., Briais, A., & Gente, P. (2001). Central indian ridge and reunion hotspot in rodrigues area: Another type of ridge-hotspot interaction? In *Agu fall meeting abstracts* (Vol. 1, p. 05).

Dyment, J., Lin, J., & Baker, E. (2007). Ridge-Hotspot Interactions: What Mid-Ocean Ridges Tell Us About Deep Earth Processes. *Oceanography*, *20*(1), 102–115. doi: 10.5670/oceanog.2007.84

Eales, H., & Cawthorn, R. (1996). The bushveld complex. In *Developments in petrology* (Vol. 15, pp. 181–229). Elsevier.

Edmonds, M., Cashman, K. V., Holness, M., & Jackson, M. (2019). *Architecture and dynamics of magma reservoirs.* The Royal Society Publishing.

Edmonds, M., & Wallace, P. J. (2017). Volatiles and exsolved vapor in volcanic systems. *Elements*, *13*(1), 29–34.

Edmonds, M., & Woods, A. W. (2018). Exsolved volatiles in magma reservoirs. *Journal of Volcanology and Geothermal Research*.

El Hachimi, H., Youbi, N., Madeira, J., Bensalah, M. K., Martins, L., Mata, J., ... others (2011). Morphology, internal architecture and emplacement mechanisms of lava flows from the central atlantic magmatic province (camp) of argana basin (morocco). *Geological Society, London, Special Publications*, *357*(1), 167–193.

Elliot, D., Fleming, T., Haban, M., & Siders, M. (1995). Petrology and mineralogy of the kirkpatrick basalt and ferrar dolerite, mesa range region, north victoria land, antarctica. *Contributions to Antarctic Research IV*, *67*, 103–141.

Elliot, D. H., & Fleming, T. H. (2018). The ferrar large igneous province: field and geochemical constraints on supra-crustal (high-level) emplacement of the magmatic system. *Geological Society, London, Special Publications*, *463*(1), 41–58.

Elliott, T., & Spiegelman, M. (2013). Melt Migration in Oceanic Crustal Production: A U-Series Perspective. In *Treatise on geochemistry: Second edition* (2nd ed., Vol. 4, pp.

543–581). Elsevier Ltd. doi: 10.1016/B978-0-08-095975-7.00317-X

Elshaafi, A., & Gudmundsson, A. (2018). Mechanical interaction between volcanic systems in libya. *Tectonophysics*, *722*, 549–565.

Elsworth, D., & Voight, B. (1996). Evaluation of volcano flank instability triggered by dyke intrusion. *Geological Society, London, Special Publications*, *110*(1), 45–53.

Ernst, R., Grosfils, E., & Mège, D. (2001, may). Giant Dike Swarms : Earth, Venus, and Mars. *Annual Review of Earth and Planetary Sciences*, *29*(1), 489–534. doi: 10.1146/annurev.earth.29.1.489

Ernst, R., Srivastava, R., Bleeker, W., & Hamilton, M. (2010). Precambrian large igneous provinces (lips) and their dyke swarms: new insights from high-precision geochronology integrated with paleomagnetism and geochemistry. *Precambrian Research*, *3*(183), vii–xi.

Ernst, R. E. (2014). *Large igneous provinces*. Cambridge University Press.

Ernst, R. E., & Bell, K. (2010). Large igneous provinces (lips) and carbonatites. *Mineralogy and Petrology*, *98*(1-4), 55–76.

Ernst, R. E., Liikane, D. A., Jowitt, S. M., Buchan, K., & Blanchard, J. (2019). A new plumbing system framework for mantle plume-related continental large igneous provinces and their mafic-ultramafic intrusions. *Journal of Volcanology and Geothermal Research*, *384*, 75–84.

Ernst, R. E., & Youbi, N. (2017). How large igneous provinces affect global climate, sometimes cause mass extinctions, and represent natural markers in the geological record. *Palaeogeography, Palaeoclimatology, Palaeoecology*, *478*, 30–52.

Evelyne, T., Annelore, B., François, B., & Sébastien, P. (2018, dec). Thermal model of successive dike injections and implications for the development of intraplate volcanoes. *Lithos*, *322*, 129–147. doi: 10.1016/j.lithos.2018.10.007

Fainstein, R., Richards, M., & Kalra, R. (2019). Seismic imaging of deccan-related lava flows at the kt boundary, deepwater west india. *The Leading Edge*, *38*(4), 286–290.

Farnetani, C. G., Hofmann, A. W., Duvernay, T., & Limare, A. (2018). Dynamics of rheological heterogeneities in mantle plumes. *Earth and Planetary Science Letters*, *499*, 74–82.

Farnetani, C. G., & Richards, M. A. (1994). Numerical investigations of the mantle plume initiation model for flood basalt events. *Journal of Geophysical Research: Solid Earth*, *99*(B7), 13813–13833.

Farnetani, C. G., Richards, M. A., & Ghiorso, M. S. (1996). Petrological models of magma evolution and deep crustal structure beneath hotspots and flood basalt provinces. *Earth and Planetary Science Letters*, *143*(1-4), 81–94.

Fedorenko, V. A., Lightfoot, P. C., Naldrett, A. J., Czamanske, G. K., Hawkesworth, C. J., Wooden, J. L., & Ebel, D. S. (1996). Petrogenesis of the flood-basalt sequence at noril'sk, north central siberia. *International Geology Review*, *38*(2), 99–135.

Feighner, M. A., & Richards, M. A. (1995, jan). The fluid dynamics of plume-ridge and plume-plate interactions: An experimental investigation. *Earth and Planetary Science Letters*, *129*(1-4), 171–182. doi: 10.1016/0012-821X(94)00247-V

Fendley, I., Mittal, T., Renne, P. R., & Marvin-DiPasquale, M. C. (2019). Mercury chemostratigraphy and geochemical box model constraints on large igneous province eruption rates: Case studies from the deccan and siberian traps. In *Agu fall meeting 2019.*

Fendley, I. M., Mittal, T., Sprain, C. J., Marvin-DiPasquale, M., Tobin, T. S., & Renne, P. R. (2019). Constraints on the volume and rate of deccan traps flood basalt eruptions using a combination of high-resolution terrestrial mercury records and geochemical box models. *Earth and Planetary Science Letters*, *524*, 115721.

Ferris, J., Johnson, A., & Storey, B. (1998). Form and extent of the dufek intrusion, antarctica, from newly compiled aeromagnetic data. *Earth and Planetary Science Letters*, *154*(1-4), 185–202.

Fialko, Y. A., & Rubin, A. M. (1998). Thermodynamics of lateral dike propagation: Implications for crustal accretion at slow spreading mid-ocean ridges. *Journal of Geophysical Research-Solid Earth*, *103*(B2), 2501–2514. doi: 10.1029/97JB03105

Fialko, Y. A., & Rubin, A. M. (1999). Thermal and mechanical aspects of magma emplacement in giant dike swarms. *Journal of Geophysical Research: Solid Earth*, *104*(B10), 23033–23049. doi: 10.1029/1999JB900213

Finch, R., & Macdonald, G. A. (1953). *Hawaiian volcanoes during 1950* (Tech. Rep.). US Govt. Print. Off.,.

Fleming, T. H. (1995). *Isotopic and chemical evolution of the ferrar group, beardmore glacier region, antarctica* (Unpublished doctoral dissertation). The Ohio State University.

Fleming, T. H., Elliot, D. H., Jones, L. M., Bowman, J. R., & Siders, M. A. (1992). Chemical and isotopic variations in an iron-rich lava flow from the kirkpatrick basalt, north victoria land, antarctica: implications for low-temperature alteration. *Contrib Mineral Petrol*, *1111440*, 45.

Font, E., Adatte, T., Sial, A. N., Drude de Lacerda, L., Keller, G., & Punekar, J. (2016). Mercury anomaly, deccan volcanism, and the end-cretaceous mass extinction. *Geology*, *44*(2), 171–174.

Font, E., Youbi, N., Fernandes, S., El Hachimi, H., Kratinova, Z., & Hamim, Y. (2011). Revisiting the magnetostratigraphy of the central atlantic magmatic province (camp) in morocco. *Earth and Planetary Science Letters*, *309*(3-4), 302–317.

Fournier, R. O. (1999). Hydrothermal processes related to movement of fluid from plastic into brittle rock in the magmatic-epithermal environment. *Economic Geology*, *94*(8), 1193–1211.

Fowler, a. C. (2011). *Mathematical Geoscience* (Vol. 36). doi: 10.1007/978-0-85729-721-1

Francois, T., Koptev, A., Cloetingh, S., Burov, E., & Gerya, T. (2018). Plume-lithosphere interactions in rifted margin tectonic settings: Inferences from thermo-mechanical modelling. *Tectonophysics*, *746*, 138–154.

Fridhleifsson, G. Ó., Elders, W. A., Zierenberg, R. A., Stefánsson, A., Fowler, A. P., Weisenberger, T. B., ... Mesfin, K. G. (2017). The iceland deep drilling project 4.5 km deep well, iddp-2, in the seawater-recharged reykjanes geothermal field in sw iceland has successfully reached its supercritical target. *Scientific Drilling*, *23*, 1.

Füri, E., Hilton, D. R., Murton, B. J., Hémond, C., Dyment, J., & Day, J. M. (2011). Helium isotope variations between réunion island and the central indian ridge (17–21 s): New evidence for ridge–hot spot interaction. *Journal of Geophysical Research: Solid Earth*, *116*(B2).

Furlong, K. P., & Fountain, D. M. (1986). Continental crustal underplating: Thermal considerations and seismic-petrologic consequences. *Journal of Geophysical Research: Solid Earth*, *91*(B8), 8285–8294.

Fyfe, W. (1992). Magma underplating of continental crust. *Journal of Volcanology and Geothermal Research*, *50*(1-2), 33–40.

Gadgil, R., Viegas, A., & Iyer, S. D. (2019). Structure and emplacement of the coastal deccan tholeiitic dyke swarm in goa, on the western indian rifted margin. *Bulletin of Volcanology*, *81*(6), 35.

Gal, F., Leconte, S., & Gadalia, A. (2018). The "escarot" gas seep, french massif central: Co2 discharge from a quiescent volcanic system–characterization and quantification of gas emissions. *Journal of Volcanology and Geothermal Research*, *353*, 68–82.

Galerne, C. Y., Galland, O., Neumann, E.-R., & Planke, S. (2011). 3d relationships between sills and their feeders: evidence from the golden valley sill complex (karoo basin) and experimental modelling. *Journal of Volcanology and Geothermal Research*, *202*(3-4), 189–199.

Galerne, C. Y., Neumann, E.-R., & Planke, S. (2008, oct). Emplacement mechanisms of sill complexes: Information from the geochemical architecture of the golden valley sill complex, south africa. *Journal of Volcanology and Geothermal Research*, *177*(2), 425–440. doi: 10.1016/j.jvolgeores.2008.06.004

Galindo, I., & Gudmundsson, A. (2012). Basaltic feeder dykes in rift zones: geometry, emplacement, and effusion rates. *Natural Hazards and Earth System Sciences*, *12*(12), 3683.

Gallagher, K., & Hawkesworth, C. (1992). Dehydration melting and the generation of continental flood basalts. *Nature*, *358*(6381), 57–59.

Galland, O., Bertelsen, H., Eide, C., Guldstrand, F., Haug, Ø., Leanza, H. A., ... others (2018). Storage and transport of magma in the layered crust—formation of sills and related flat-lying intrusions. In *Volcanic and igneous plumbing systems* (pp. 113–138). Elsevier.

Galland, O., Planke, S., Neumann, E.-R., & Malthe-Sørenssen, A. (2009). Experimental modelling of shallow magma emplacement: Application to saucer-shaped intrusions. *Earth and Planetary Science Letters*, *277*(3-4), 373–383.

Galland, O., Spacapan, J. B., Rabbel, O., Mair, K., Soto, F. G., Eiken, T., ... Leanza, H. A. (2019). Structure, emplacement mechanism and magma-flow significance of igneous fingers–implications for sill emplacement in sedimentary basins. *Journal of Structural Geology*, *124*, 120–135.

Ganerød, M., Torsvik, T. H., van Hinsbergen, D. J. J., Gaina, C., Corfu, F., Werner, S., ... Hendriks, B. W. H. (2011). Palaeoposition of the seychelles microcontinent in relation to the deccan traps and the plume generation zone in late cretaceous-early

palaeogene time. *Geological Society, London, Special Publications*, *357*(1), 229–252. doi: 10.1144/sp357.12

Gangopadhyay, A., Sen, G., & Keshav, S. (2003). Experimental crystallization of deccan basalts at low pressure: effect of contamination on phase equilibrium. *Indian Journal of Geology*, *75*(1/4), 54.

Geldmacher, J., van den Bogaard, P., Heydolph, K., & Hoernle, K. (2014, nov). The age of Earth's largest volcano: Tamu Massif on Shatsky Rise (northwest Pacific Ocean). *International Journal of Earth Sciences*, *103*(8), 2351–2357. doi: 10.1007/s00531-014-1078-6

Géli, L., Aslanian, D., Olivet, J. L., Vlastelic, I., Dosso, L., Guillou, H., & Bougault, H. (1998). Location of Louisville hotspot and origin of Hollister Ridge: Geophysical constraints. *Earth and Planetary Science Letters*, *164*(1-2), 31–40. doi: 10.1016/S0012-821X(98)00217-9

Gerdes, M. L., Baumgartner, L. P., & Person, M. (1995). Stochastic permeability models of fluid flow during contact metamorphism. *Geology*, *23*(10), 945–948.

Gerdes, M. L., Baumgartner, L. P., & Person, M. (1998). Convective fluid flow through heterogeneous country rocks during contact metamorphism. *Journal of Geophysical Research: Solid Earth*, *103*(B10), 23983–24003.

Germanovich, L. N., Lowell, R. P., & Astakhov, D. K. (2001). Temperature-dependent permeability and bifurcations in hydrothermal flow. *Journal of Geophysical Research: Solid Earth*, *106*(B1), 473–495.

Ghassemi, A., Nygren, A., & Cheng, A. (2008). Effects of heat extraction on fracture aperture: A poro–thermoelastic analysis. *Geothermics*, *37*(5), 525–539.

Ghiorso, M. S., Hirschmann, M. M., Reiners, P. W., & Kress, V. C. (2002). The pmelts: A revision of melts for improved calculation of phase relations and major element partitioning related to partial melting of the mantle to 3 gpa. *Geochemistry, Geophysics, Geosystems*, *3*(5), 1–35.

Ghods, A., & Arkani-Hamed, J. (2000). Melt migration beneath mid-ocean ridges. *Geophysical Journal International*, *140*(3), 687–697. doi: 10.1046/j.1365-246X.2000.00032.x

Gibson, S., & Geist, D. (2010). Geochemical and geophysical estimates of lithospheric thickness variation beneath galápagos. *Earth and Planetary Science Letters*, *300*(3-4), 275–286.

Gibson, S., Thompson, R., & Day, J. (2006). Timescales and mechanisms of plume–lithosphere interactions: 40ar/39ar geochronology and geochemistry of alkaline igneous rocks from the paraná–etendeka large igneous province. *Earth and Planetary Science Letters*, *251*(1-2), 1–17.

Gibson, S. A. (2002). Major element heterogeneity in archean to recent mantle plume starting-heads. *Earth and Planetary Science Letters*, *195*(1-2), 59–74.

Gibson, S. A., & Geist, D. (2010). Geochemical and geophysical estimates of lithospheric thickness variation beneath Galápagos. *Earth and Planetary Science Letters*, *300*(3-4), 275–286. doi: 10.1016/j.epsl.2010.10.002

Gibson, S. A., Geist, D. J., & Richards, M. A. (2015, may). Mantle plume capture, anchoring,

and outflow during Galápagos plume-ridge interaction. *Geochemistry, Geophysics, Geosystems*, *16*(5), 1634–1655. doi: 10.1002/2015GC005723

Gibson, S. A., Rooks, E. E., Day, J. A., Petrone, C. M., & Leat, P. T. (2020). The role of sub-continental mantle as both "sink" and "source" in deep earth volatile cycles. *Geochimica et Cosmochimica Acta*. doi: https://doi.org/10.1016/j.gca.2020.02.018

Girona, T., Costa, F., Newhall, C., & Taisne, B. (2014). On depressurization of volcanic magma reservoirs by passive degassing. *Journal of Geophysical Research: Solid Earth*, *119*(12), 8667–8687.

Girona, T., Costa, F., & Schubert, G. (2015). Degassing during quiescence as a trigger of magma ascent and volcanic eruptions. *Scientific reports*, *5*, 18212.

Giuffrida, M., Viccaro, M., & Ottolini, L. (2018). Ultrafast syn-eruptive degassing and ascent trigger high-energy basic eruptions. *Scientific reports*, *8*(1), 147.

Glaze, L. S., Self, S., Schmidt, A., & Hunter, S. J. (2017). Assessing eruption column height in ancient flood basalt eruptions. *Earth and Planetary Science Letters*, *457*, 263–270.

Gombos Jr, A. M., Powell, W. G., & Norton, I. O. (1995). The tectonic evolution of western india and its impact on hydrocarbon occurrences: an overview. *Sedimentary Geology*, *96*(1-2), 119–129.

Gomila, R., Arancibia, G., Mitchell, T. M., Cembrano, J. M., & Faulkner, D. R. (2016). Palaeopermeability structure within fault-damage zones: A snap-shot from microfracture analyses in a strike-slip system. *Journal of Structural Geology*, *83*, 103–120.

Gonnermann, H., & Manga, M. (2012). *Dynamics of magma ascent in the volcanic conduit, modeling volcanic processes: The physics and mathematics of volcanism, eds. sarah a. fagents, tracy kp gregg, and rosaly mc lopes.* Cambridge University Press.

Gonnermann, H. M. (2015). Magma fragmentation. *Annual Review of Earth and Planetary Sciences*, *43*, 431–458.

Gorczyk, W., & Vogt, K. (2018). Intrusion of magmatic bodies into the continental crust: 3-d numerical models. *Tectonics*, *37*(3), 705–723.

Gorring, M. L., & Naslund, H. (1995). Geochemical reversals within the lower 100 m of the palisades sill, new jersey. *Contributions to Mineralogy and Petrology*, *119*(2-3), 263–276.

Graham, D. W., Hanan, B. B., Lupton, J. E., Hoernle, K., Werner, R., Christie, D. M., & Sinton, J. M. (2014). Helium isotope variations and mantle plume-spreading ridge interactions along the Galápagos Spreading Center. In *The galápagos: A natural laboratory for the earth sciences* (pp. 393–414). doi: 10.1002/9781118852538.ch18

Grant, T. B., Larsen, R. B., Anker-Rasch, L., Grannes, K. R., Iljina, M., McEnroe, S., ... Øen, E. (2016). Anatomy of a deep crustal volcanic conduit system; the reinfjord ultramafic complex, seiland igneous province, northern norway. *Lithos*, *252*, 200–215.

Greenough, J. D., Hari, K., Chatterjee, A., & Santosh, M. (1998). Mildly alkaline basalts from pavagadh hill, india: Deccan flood basalts with an asthenospheric origin. *Mineralogy and Petrology*, *62*(3-4), 223–245.

Griffin, W., Sturt, B., O'Neill, C., Kirkland, C., & O'Reilly, S. Y. (2013). Intrusion and contamination of high-temperature dunitic magma: the nordre bumandsfjord pluton,

seiland, arctic norway. *Contributions to Mineralogy and Petrology*, *165*(5), 903–930.

Gruen, G., Heinrich, C. A., & Schroeder, K. (2010). The bingham canyon porphyry cu-mo-au deposit. ii. vein geometry and ore shell formation by pressure-driven rock extension. *Economic Geology*, *105*(1), 69–90.

Grunder, A., & Taubeneck, W. (1997). Partial melting of tonalite at the margins of columbia river basalt group dikes, wallowa mountains, oregon. In *Geol. soc. am. abstr. prog* (Vol. 29, p. 18).

Gu, X.-Y., Wang, P.-Y., Kuritani, T., Hanski, E., Xia, Q.-K., & Wang, Q.-Y. (2019). Low water content in the mantle source of the hainan plume as a factor inhibiting the formation of a large igneous province. *Earth and Planetary Science Letters*, *515*, 221–230.

Gudmundsson, A. (2002). Emplacement and arrest of sheets and dykes in central volcanoes. *Journal of Volcanology and Geothermal Research*, *116*(3-4), 279–298.

Gudmundsson, A. (2011). Deflection of dykes into sills at discontinuities and magma-chamber formation. *Tectonophysics*, *500*(1-4), 50–64.

Gudmundsson, A. (2016). The mechanics of large volcanic eruptions. *Earth-science reviews*, *163*, 72–93.

Gudmundsson, A., Lecoeur, N., Mohajeri, N., & Thordarson, T. (2014). Dike emplacement at bardarbunga, iceland, induces unusual stress changes, caldera deformation, and earthquakes. *Bulletin of Volcanology*, *76*(10), 869.

Guilbaud, M.-N., Self, S., Thordarson, T., & Blake, S. (2005). Morphology, surface structures, and emplacement of lavas produced by laki, ad 1783–1784. *Geological Society of America Special Papers*, *396*, 81–102.

Gunn, B. M., & Warren, G. (1962). *Geology of victoria land between the mawson and mulock glaciers, antarctica* (No. 70-71). Trans-Antarctic Expedition Committee.

Haase, K., Regelous, M., Schöbel, S., Günther, T., & de Wall, H. (2019). Variation of melting processes and magma sources of the early deccan flood basalts, malwa plateau, india. *Earth and Planetary Science Letters*, *524*, 115711.

Hager, B. H., & O'Connell, R. J. (1981). A simple global model of plate dynamics and mantle convection. *Journal of Geophysical Research*, *86*(B6), 4843. doi: 10.1029/JB086iB06p04843

Halbach, H., & Chatterjee, N. D. (1982). An empirical redlich-kwong-type equation of state for water to 1,000 c and 200 kbar. *Contributions to Mineralogy and Petrology*, *79*(3), 337–345.

Hansen, J., Jerram, D., McCaffrey, K., & Passey, S. (2011). Early cenozoic saucer-shaped sills of the faroe islands: an example of intrusive styles in basaltic lava piles. *Journal of the Geological Society*, *168*(1), 159–178.

Hanson, R. (1992). Effects of fluid production on fluid flow during regional and contact metamorphism. *Journal of Metamorphic Geology*, *10*(1), 87–97.

Hanson, R. B. (1996). Hydrodynamics of magmatic and meteoric fluids in the vicinity of granitic intrusions. *Earth and Environmental Science Transactions of The Royal Society of Edinburgh*, *87*(1-2), 251–259.

Hanson, R. B. (1997). Hydrodynamics of regional metamorphism due to continental collision. *Economic Geology*, *92*(7-8), 880–891.

Hari, K., Prasanth, M. M., Swarnkar, V., Kumar, J. V., & Randive, K. R. (2018). Evidence for the contrasting magmatic conditions in the petrogenesis of a-type granites of phenai mata igneous complex: implications for felsic magmatism in the deccan large igneous province. *Journal of the Indian Institute of Science*, *98*(4), 379–399.

Hari, K., Rao, N. C., & Swarnkar, V. (2011). Petrogenesis of gabbro and orthopyroxene gabbro from the phenai mata igneous complex, deccan volcanic province: Products of concurrent assimilation and fractional crystallization. *Journal of the Geological Society of India*, *78*(6), 501–509.

Hari, K., Swarnkar, V., & Prasanth, M. M. (2018). Significance of assimilation and fractional crystallization (afc) process in the generation of basaltic lava flows from chhotaudepur area, deccan large igneous province, nw india. *Journal of Earth System Science*, *127*(6), 85.

Harmon, N., Forsyth, D. W., & Scheirer, D. S. (2006). Analysis of gravity and topography in the GLIMPSE study region: Isostatic compensation and uplift of the Sojourn and Hotu Matua Ridge systems. *Journal of Geophysical Research: Solid Earth*, *111*(11). doi: 10.1029/2005JB004071

Harpp, K., & Geist, D. (2002). Wolf–darwin lineament and plume–ridge interaction in northern galápagos. *Geochemistry, Geophysics, Geosystems*, *3*(11), 1–19.

Harpp, K. S., Hall, P. S., & Jackson, M. G. (2014, aug). Galápagos and Easter. In *The galapagos: A natural laboratory for the earth sciences* (pp. 27–40). doi: 10.1002/9781118852538.ch3

Harpp, K. S., & White, W. M. (2001, jun). Tracing a mantle plume: Isotopic and trace element variations of Galápagos seamounts. *Geochemistry, Geophysics, Geosystems*, *2*(6). doi: 10.1029/2000GC000137

Harpp, K. S., Wirth, K. R., & Korich, D. J. (2002a). Northern Galápagos Province: Hotspot-induced, near-ridge volcanism at Genovesa Island. *Geology*, *30*(5), 399. doi: 10.1130/0091-7613(2002)030¡0399:NGPPHI¿2.0.CO;2

Harpp, K. S., Wirth, K. R., & Korich, D. J. (2002b). Northern galápagos province: hotspot-induced, near-ridge volcanism at genovesa island. *Geology*, *30*(5), 399–402.

Harpp, K. S., Wirth, K. R., Teasdale, R., Blair, S., Reed, L., Barr, J., ... Korich, D. (2014, aug). Plume-Ridge Interaction in the Galápagos. In (pp. 285–334). doi: 10.1002/9781118852538.ch15

Harris, A. J., Dehn, J., & Calvari, S. (2007). Lava effusion rate definition and measurement: a review. *Bulletin of Volcanology*, *70*(1), 1.

Haug, Ø., Galland, O., Souloumiac, P., Souche, A., Guldstrand, F., Schmiedel, T., & Maillot, B. (2018). Shear versus tensile failure mechanisms induced by sill intrusions: Implications for emplacement of conical and saucer-shaped intrusions. *Journal of Geophysical Research: Solid Earth*, *123*(5), 3430–3449.

Hauri, E. H., Gaetani, G. A., & Green, T. H. (2006). Partitioning of water during melting of the earth's upper mantle at h2o-undersaturated conditions. *Earth and Planetary*

Science Letters, *248*(3-4), 715–734.

Havlin, C., Parmentier, E., & Hirth, G. (2013, aug). Dike propagation driven by melt accumulation at the lithosphere–asthenosphere boundary. *Earth and Planetary Science Letters*, *376*, 20–28. doi: 10.1016/j.epsl.2013.06.010

Hawkesworth, C., & Gallagher, K. (1993). Mantle hotspots, plumes and regional tectonics as causes of intraplate magmatism. *Terra Nova*, *5*(6), 552–559.

Hawkesworth, C., Kempton, P., Rogers, N., Ellam, R., & Van Calsteren, P. (1990). Continental mantle lithosphere, and shallow level enrichment processes. *Earth and Planetary Science Letters*, *96*, 256–268.

Haxby, W., Melkonian, A., Coplan, J., Chan, S., & Ryan, W. (2010). *Geomapapp freeware software, v. 2.3. lamont-doherty earth observatory, palisades.*

Hayba, D. O., & Ingebritsen, S. E. (1997). Multiphase groundwater flow near cooling plutons. *Journal of Geophysical Research: Solid Earth*, *102*(B6), 12235–12252.

Hayes, B., Bybee, G. M., Mawela, M., Nex, P. A., & van Niekerk, D. (2018). Residual melt extraction and out-of-sequence differentiation in the bushveld complex, south africa. *Journal of Petrology*, *59*(12), 2413–2434.

Heap, M., Farquharson, J., Baud, P., Lavallée, Y., & Reuschlé, T. (2015). Fracture and compaction of andesite in a volcanic edifice. *Bulletin of volcanology*, *77*(6), 55.

Heap, M. J., & Kennedy, B. M. (2016). Exploring the scale-dependent permeability of fractured andesite. *Earth and Planetary Science Letters*, *447*, 139–150.

Heap, M. J., Violay, M., Wadsworth, F. B., & Vasseur, J. (2017). From rock to magma and back again: The evolution of temperature and deformation mechanism in conduit margin zones. *Earth and Planetary Science Letters*, *463*, 92–100.

Hebert, L. B., & Montési, L. G. (2011). Melt extraction pathways at segmented oceanic ridges: Application to the east pacific rise at the siqueiros transform. *Geophysical Research Letters*, *38*(11).

Hedenquist, J. W., Arribas, A., & Reynolds, T. J. (1998). Evolution of an intrusion-centered hydrothermal system; far southeast-lepanto porphyry and epithermal cu-au deposits, philippines. *Economic Geology*, *93*(4), 373–404.

Hegde, V., Koti, B., & Kruger, S. (2014). Geochemistry of the desur lavas, deccan traps: Case study from the vicinity of belgaum, karnataka and their petrogenetic inferences. *Journal of the Geological Society of India*, *83*(4), 363–375.

Heimisson, E. R., Hooper, A., & Sigmundsson, F. (2015, dec). Forecasting the path of a laterally propagating dike. *Journal of Geophysical Research: Solid Earth*, *120*(12), 8774–8792. Retrieved from `http://doi.wiley.com/10.1002/2014JB011237` `http://doi.wiley.com/10.1002/2015JB012402` doi: 10.1002/2015JB012402

Heinonen, J. S., Luttinen, A. V., Spera, F. J., & Bohrson, W. A. (2019a). Deep open storage and shallow closed transport system for a continental flood basalt sequence revealed with magma chamber simulator. *Contributions to Mineralogy and Petrology*, *174*(11), 87.

Heinonen, J. S., Luttinen, A. V., Spera, F. J., & Bohrson, W. A. (2019b, oct). Deep open storage and shallow closed transport system for a continental flood basalt sequence

revealed with magma chamber simulator. *Contributions to Mineralogy and Petrology*, *174*(11). doi: 10.1007/s00410-019-1624-0

Helfrich, K. R. (1995). Thermo-viscous fingering of flow in a thin gap: a model of magma flow in dikes and fissures. *Journal of fluid mechanics*, *305*, 219 – 238. doi: 10.1017/S0022112095004605

Henley, R., & McNabb, A. (1978). Magmatic vapor plumes and ground-water interaction in porphyry copper emplacement. *Economic Geology*, *73*(1), 1–20.

Hernández, P., Notsu, K., Salazar, J., Mori, T., Natale, G., Okada, H., ... Pérez, N. (2001). Carbon dioxide degassing by advective flow from usu volcano, japan. *Science*, *292*(5514), 83–86.

Herzberg, C., & Gazel, E. (2009). Petrological evidence for secular cooling in mantle plumes. *Nature*, *458*(7238), 619–622.

Hewitt, I. J. (2010). Modelling melting rates in upwelling mantle. *Earth and Planetary Science Letters*, *300*(3-4), 264–274. doi: 10.1016/j.epsl.2010.10.010

Hewitt, I. J., & Fowler, A. C. (2009). Melt channelization in ascending mantle. *Journal of Geophysical Research: Solid Earth*, *114*(6), 1–14. doi: 10.1029/2008JB006185

Hieronymus, C. F., & Bercovici, D. (2001). A theoretical model of hotspot volcanism: Control on volcanic spacing and patterns via magma dynamics and lithospheric stresses. *Journal of Geophysical Research-Solid Earth*, *106*, 683–702. doi: 10.1029/2000JB900355

Higgins, M. D. (2005). A new interpretation of the structure of the sept iles intrusive suite, canada. *Lithos*, *83*(3-4), 199–213.

Higgins, M. D., & Breemen, O. V. (1998). The age of the sept iles layered mafic intrusion, canada: implications for the late neoproterozoic/cambrian history of southeastern canada. *The Journal of Geology*, *106*(4), 421–432.

Higgins, M. D., & Chandrasekharam, D. (2007a). Nature of sub-volcanic magma chambers, deccan province, india: evidence from quantitative textural analysis of plagioclase megacrysts in the giant plagioclase basalts. *Journal of Petrology*, *48*(5), 885–900.

Higgins, M. D., & Chandrasekharam, D. (2007b, mar). Nature of sub-volcanic magma chambers, deccan province, india: Evidence from quantitative textural analysis of plagioclase megacrysts in the giant plagioclase basalts. *Journal of Petrology*, *48*(5), 885–900. doi: 10.1093/petrology/egm005

Hildreth, W. (1981). Gradients in silicic magma chambers: implications for lithospheric magmatism. *Journal of Geophysical Research: Solid Earth*, *86*(B11), 10153–10192.

Hildreth, W. (2017). Fluid-driven uplift at long valley caldera, california: Geologic perspectives. *Journal of Volcanology and Geothermal Research*, *341*, 269–286.

Hildreth, W., & Wilson, C. J. (2007). Compositional zoning of the bishop tuff. *Journal of Petrology*, *48*(5), 951–999.

Hindmarsh, A. C., Brown, P. N., Grant, K. E., Lee, S. L., Serban, R., Shumaker, D. E., & Woodward, C. S. (2005). SUNDIALS: Suite of nonlinear and differential/algebraic equation solvers. *ACM Transactions on Mathematical Software (TOMS)*, *31*(3), 363–396.

Hirschmann, M. M., Asimow, P. D., Ghiorso, M. S., & Stolper, E. M. (1999). Calculation

of Peridotite Partial Melting from Thermodynamic Models of Minerals and Melts. III. Controls on Isobaric Melt Production and the Effect of Water on Melt Production. *Journal of Petrology*, *40*(5), 831–851. doi: 10.1093/petroj/40.5.831

Ho, A. M., & Cashman, K. V. (1997). Temperature constraints on the ginkgo flow of the columbia river basalt group. *Geology*, *25*(5), 403–406.

Hochmuth, K., Gohl, K., & Uenzelmann-Neben, G. (2015). *Playing jigsaw with Large Igneous Provinces-A plate tectonic reconstruction of Ontong Java Nui, West Pacific.* doi: 10.1002/2015GC006036

Hoek, E., Carranza-Torres, C., & Corkum, B. (2002). Hoek-brown failure criterion-2002 edition. *Proceedings of NARMS-Tac*, *1*, 267–273.

Hoggett, M. (2019). *A global analysis of igneous sill dimensions and their effect on sedimentary basins and petroleum system-statistics and modelling of seismic observations* (Unpublished doctoral dissertation). University of Birmingham.

Holtzman, B., Groebner, N., Zimmerman, M., Ginsberg, S., & Kohlstedt, D. (2003). Stress-driven melt segregation in partially molten rocks. *Geochemistry, Geophysics, Geosystems*, *4*(5).

Hon, K., Kauahikaua, J., Denlinger, R., & Mackay, K. (1994). Emplacement and inflation of pahoehoe sheet flows: Observations and measurements of active lava flows on kilauea volcano, hawaii. *Geological Society of America Bulletin*, *106*(3), 351–370.

Hooper, P. (1988a). The columbia river basalt. In *Continental flood basalts* (pp. 1–33). Springer.

Hooper, P. (1988b). Crystal fractionation and recharge (rfc) in the american bar flows of the imnaha basalt, columbia river basalt group. *Journal of Petrology*, *29*(5), 1097–1118.

Hooper, P., & Hawkesworth, C. (1993). Isotopic and geochemical constraints on the origin and evolution of the columbia river basalt. *Journal of Petrology*, *34*(6), 1203–1246.

Hooper, P., & Subbarao, K. (1999). The deccan traps. *Deccan Volcanic Province: Geological Society of India Memoir*, *43*, 153–165.

Hooper, P., Widdowson, M., & Kelley, S. (2010). Tectonic setting and timing of the final deccan flood basalt eruptions. *Geology*, *38*(9), 839–842.

Hooper, P. R. (2000). Chemical discrimination of columbia river basalt flows. *Geochemistry, Geophysics, Geosystems*, *1*(6).

Hsieh, P. A., & Bredehoeft, J. D. (1981). A reservoir analysis of the denver earthquakes: A case of induced seismicity. *Journal of Geophysical Research: Solid Earth*, *86*(B2), 903–920.

Hull, P. M., Bornemann, A., Penman, D. E., Henehan, M. J., Norris, R. D., Wilson, P. A., ... others (2020). On impact and volcanism across the cretaceous-paleogene boundary. *Science*, *367*(6475), 266–272.

Hunt, J. A., Zafu, A., Mather, T. A., Pyle, D. M., & Barry, P. H. (2017). Spatially variable co2 degassing in the main ethiopian rift: Implications for magma storage, volatile transport, and rift-related emissions. *Geochemistry, Geophysics, Geosystems*, *18*(10), 3714–3737.

Huppert, H. E., & Woods, A. W. (2002). The role of volatiles in magma chamber dynamics. *Nature*, *420*(6915), 493–495.

Husch, J. M. (1990). Palisades sill: origin of the olivine zone by separate magmatic injection rather than gravity settling. *Geology*, *18*(8), 699–702.

Iacono-Marziano, G., Morizet, Y., Le Trong, E., & Gaillard, F. (2012). New experimental data and semi-empirical parameterization of h2o–co2 solubility in mafic melts. *Geochimica et Cosmochimica Acta*, *97*, 1–23.

Iguchi, M., Saito, E., Nishi, Y., & Tameguri, T. (2002). Evaluation of recent activity at satsuma-iwojima-felt earthquake on june 8, 1996. *Earth, planets and space*, *54*(3), 187–195.

Ikeda, R., Kajiwara, T., Omura, K., & Hickman, S. (2008). Physical rock properties in and around a conduit zone by well-logging in the unzen scientific drilling project, japan. *Journal of Volcanology and Geothermal Research*, *175*(1-2), 13–19.

Ilyinskaya, E., Mobbs, S., Burton, R., Burton, M., Pardini, F., Pfeffer, M. A., ... others (2018). Globally significant co2 emissions from katla, a subglacial volcano in iceland. *Geophysical Research Letters*, *45*(19), 10–332.

Ingebritsen, S., & Gleeson, T. (2017). Crustal permeability. *Hydrogeology Journal*, *25*(8), 2221–2224.

Ingebritsen, S., & Manning, C. E. (2010). Permeability of the continental crust: dynamic variations inferred from seismicity and metamorphism. *Geofluids*, *10*(1-2), 193–205.

Ingebritsen, S., & Sanford, W. (1999). *Groundwater in geologic processes*. Cambridge University Press.

Ingebritsen, S. E., & Appold, M. (2012). The physical hydrogeology of ore deposits. *Economic Geology*, *107*(4), 559–584.

Ingle, S., Ito, G., Mahoney, J. J., Chazey, W., Sinton, J., Rotella, M., & Christie, D. M. (2010, apr). Mechanisms of geochemical and geophysical variations along the western Galápagos Spreading Center. *Geochemistry, Geophysics, Geosystems*, *11*(4), n/a–n/a. doi: 10.1029/2009GC002694

Inguaggiato, S., Paz, M. J., Mazot, A., Granados, H. D., Inguaggiato, C., & Vita, F. (2013). Co2 output discharged from stromboli island (italy). *Chemical geology*, *339*, 52–60.

International Seismological Centre. (2013). On-line bulletin [Computer software manual]. Thatcham, United Kingdom. (http://www.isc.ac.uk)

Ito, G., & Bianco, T. (2014, aug). Patterns in Galápagos Magmatism Arising from the Upper Mantle Dynamics of Plume-Ridge Interaction. In *The galapagos: A natural laboratory for the earth sciences* (pp. 245–261). doi: 10.1002/9781118852538.ch13

Ito, G., & Lin, J. (1995). Oceanic spreading center - hotspot interactions: constraints from along-isochron bathymetry and gravity anomalies. *Geology*, *23*(7), 657–660. doi: 10.1130/0091-7613(1995)023¡0657

Ito, G., Lin, J., & Gable, C. W. (1997). Interaction of mantle plumes and migrating mid-ocean ridges: Implications for the Galápagos plume-ridge system. *Journal of Geophysical Research*, *102417*(10), 403–15. doi: 10.1029/97JB01049

Ito, G., Lin, J., & Graham, D. (2003). Observational and theoretical studies of the dynamics

of mantle plume-mid-ocean ridge interaction. *Reviews of Geophysics*, *41*(4), 24. doi: 10.1029/2002rg000117

Ivanov, A. V., Mukasa, S. B., Kamenetsky, V. S., Ackerson, M., Demonterova, E. I., Pokrovsky, B. G., ... Zedgenizov, D. A. (2018). Volatile concentrations in olivine-hosted melt inclusions from meimechite and melanephelinite lavas of the siberian traps large igneous province: Evidence for flux-related high-ti, high-mg magmatism. *Chemical Geology*, *483*, 442–462.

Jackson, M., Blundy, J., & Sparks, R. (2018). Chemical differentiation, cold storage and remobilization of magma in the earth's crust. *Nature*, *564*(7736), 405.

Jay, A. E. (2005). *Volcanic architecture of the deccan traps, western maharashtra, india: an integrated chemostratigraphic and paleomagnetic study* (Unpublished doctoral dissertation). The Open University.

Jay, A. E., Mac Niocaill, C., Widdowson, M., Self, S., & Turner, W. (2009). New palaeomagnetic data from the mahabaleshwar plateau, deccan flood basalt province, india: implications for the volcanostratigraphic architecture of continental flood basalt provinces. *Journal of the Geological Society*, *166*(1), 13–24.

Jay, A. E., & Widdowson, M. (2008). Stratigraphy, structure and volcanology of the se deccan continental flood basalt province: implications for eruptive extent and volumes. *Journal of the Geological Society*, *165*(1), 177–188.

Jellinek, A. M., & DePaolo, D. J. (2003). A model for the origin of large silicic magma chambers: precursors of caldera-forming eruptions. *Bulletin of Volcanology*, *65*(5), 363–381.

Jennings, E. S., Gibson, S. A., & Maclennan, J. (2019). Hot primary melts and mantle source for the paraná-etendeka flood basalt province: New constraints from al-in-olivine thermometry. *Chemical Geology*, *529*, 119287.

Jennings, E. S., Gibson, S. A., Maclennan, J., & Heinonen, J. S. (2017). Deep mixing of mantle melts beneath continental flood basalt provinces: Constraints from olivine-hosted melt inclusions in primitive magmas. *Geochimica et Cosmochimica Acta*, *196*, 36–57.

Jennings, S., Hasterok, D., & Payne, J. (2019). A new compositionally based thermal conductivity model for plutonic rocks. *Geophysical Journal International*, *219*(2), 1377–1394.

Jerram, D. A., Davis, G. R., Mock, A., Charrier, A., & Marsh, B. D. (2010). Quantifying 3d crystal populations, packing and layering in shallow intrusions: a case study from the basement sill, dry valleys, antarctica. *Geosphere*, *6*(5), 537–548.

Jerram, D. A., Dobson, K. J., Morgan, D. J., & Pankhurst, M. J. (2018). The petrogenesis of magmatic systems: Using igneous textures to understand magmatic processes. In *Volcanic and igneous plumbing systems* (pp. 191–229). Elsevier.

Jerram, D. A., Svensen, H. H., Planke, S., Polozov, A. G., & Torsvik, T. H. (2016). The onset of flood volcanism in the north-western part of the siberian traps: Explosive volcanism versus effusive lava flows. *Palaeogeography, Palaeoclimatology, Palaeoecology*, *441*, 38–50.

Jerram, D. A., & Widdowson, M. (2005). The anatomy of continental flood basalt provinces: geological constraints on the processes and products of flood volcanism. *Lithos*, *79*(3-4), 385–405.

Joanne, F., & Teng-fong, W. (1986). Micromechanics of thermally induced cracking in three crustal rocks. *Journal of Geophysical Research: Solid Earth*, *91*(B12), 12743-12764. Retrieved from https://agupubs.onlinelibrary.wiley.com/doi/abs/10.1029/JB091iB12p12743 doi: 10.1029/JB091iB12p12743

Johansson, L., Zahirovic, S., & Müller, R. D. (2018). The interplay between the eruption and weathering of large igneous provinces and the deep-time carbon cycle. *Geophysical Research Letters*, *45*(11), 5380–5389.

Jones, M. T., Jerram, D. A., Svensen, H. H., & Grove, C. (2016). The effects of large igneous provinces on the global carbon and sulphur cycles. *Palaeogeography, Palaeoclimatology, Palaeoecology*, *441*, 4–21.

Jones, S. M., Hoggett, M., Greene, S. E., & Jones, T. D. (2019). Large igneous province thermogenic greenhouse gas flux could have initiated paleocene-eocene thermal maximum climate change. *Nature Communications*, *10*(1), 1–16.

Jones, T. A., & Detwiler, R. L. (2016). Fracture sealing by mineral precipitation: The role of small-scale mineral heterogeneity. *Geophysical Research Letters*, *43*(14), 7564–7571.

Kale, V. S., Dole, G., Shandilya, P., & Pande, K. (2019). Stratigraphy and correlations in deccan volcanic province, india: Quo vadis? *Geological Society of America Bulletin*.

Kale, V. S., Dole, G., Upasani, D., & Pillai, S. P. (2017). Deccan plateau uplift: insights from parts of western uplands, maharashtra, india. *Geological Society, London, Special Publications*, *445*(1), 11–46.

Kalsbeek, F., & Taylor, P. N. (1986). Chemical and isotopic homogeneity of a 400 km long basic dyke in central west greenland. *Contributions to Mineralogy and Petrology*, *93*(4), 439–448.

Kaotekwar, A. B., Meshram, R. R., Sathyanarayanan, M., Krishna, A. K., & Charan, S. (2014). Structures, petrography and geochemistry of deccan basalts at anantagiri hills, andhra pradesh. *Journal of the Geological Society of India*, *84*(6), 675–685.

Karakas, O., Degruyter, W., Bachmann, O., & Dufek, J. (2017). Lifetime and size of shallow magma bodies controlled by crustal-scale magmatism. *Nature Geoscience*, *10*(6), 446–450.

Karakas, O., & Dufek, J. (2015). Melt evolution and residence in extending crust: Thermal modeling of the crust and crustal magmas. *Earth and Planetary Science Letters*, *425*, 131–144. doi: 10.1016/j.epsl.2015.06.001

Karkare, S., & Srivastava, R. K. (1990). Regional dyke swarms related to the deccan trap alkaline province, india. In *International dyke conference. 2* (pp. 335–347).

Karlstrom, L., Dufek, J., & Manga, M. (2009a). Organization of volcanic plumbing through magmatic lensing by magma chambers and volcanic loads. *Journal of Geophysical Research: Solid Earth*, *114*(10), 1–16. doi: 10.1029/2009JB006339

Karlstrom, L., Dufek, J., & Manga, M. (2009b). Organization of volcanic plumbing through

magmatic lensing by magma chambers and volcanic loads. *Journal of Geophysical Research: Solid Earth*, *114*(B10).

Karlstrom, L., Dufek, J., & Manga, M. (2010). Magma chamber stability in arc and continental crust. *Journal of Volcanology and Geothermal Research*, *190*(3-4), 249–270.

Karlstrom, L., & Manga, M. (2009, 12). Magma siphoning and the mechanics of large igneous province eruptions. *AGU Fall Meeting Abstracts*.

Karlstrom, L., Murray, K. E., & Reiners, P. W. (2019, apr). Bayesian markov-chain monte carlo inversion of low-temperature thermochronology around two 8 - 10 m wide columbia river flood basalt dikes. *Frontiers in Earth Science*, *7*. doi: 10.3389/feart.2019.00090

Karlstrom, L., Paterson, S. R., & Jellinek, A. M. (2017). A reverse energy cascade for crustal magma transport. *Nature Geoscience*, *10*(8), 604.

Karlstrom, L., & Richards, M. (2011). On the evolution of large ultramafic magma chambers and timescales for flood basalt eruptions. *Journal of Geophysical Research: Solid Earth*, *116*(B8).

Karlstrom, L., Richardson, P. W., O'Hara, D., & Ebmeier, S. K. (2018). Magmatic landscape construction. *Journal of Geophysical Research: Earth Surface*, *123*(8), 1710–1730.

Karlstrom, L., Rudolph, M. L., & Manga, M. (2012). Caldera size modulated by the yield stress within a crystal-rich magma reservoir. *Nature Geoscience*, *5*(6), 402–405.

Karlstrom, L., Wright, H. M., & Bacon, C. R. (2015). The effect of pressurized magma chamber growth on melt migration and pre-caldera vent locations through time at Mount Mazama, Crater Lake, Oregon. *Earth and Planetary Science Letters*, *412*, 209–219. doi: 10.1016/j.epsl.2014.12.001

Karmalkar, N., Duraiswami, R., Jonnalagadda, M., Griffin, W., Gregoire, M., Benoit, M., & Delpech, G. (2016). Magma types and source characterization of the early deccan magmatism, kutch region, nw india: Insights from geochemistry of igneous intrusions. *J Geol Soc India Spl Pub*, *6*, 193–208.

Kasbohm, J., & Schoene, B. (2018). Rapid eruption of the columbia river flood basalt and correlation with the mid-miocene climate optimum. *Science advances*, *4*(9), eaat8223.

Katz, M. G., & Cashman, K. V. (2003). Hawaiian lava flows in the third dimension: Identification and interpretation of pahoehoe and a'a distribution in the kp-1 and soh-4 cores. *Geochemistry, Geophysics, Geosystems*, *4*(2).

Katz, R. F., Spiegelman, M., & Holtzman, B. (2006). The dynamics of melt and shear localization in partially molten aggregates. *Nature*, *442*(7103), 676–9. doi: 10.1038/nature05039

Katz, R. F., Spiegelman, M., & Langmuir, C. H. (2003). A new parameterization of hydrous mantle melting. *Geochemistry, Geophysics, Geosystems*, *4*(9).

Katz, R. F., & Weatherley, S. M. (2012). Consequences of mantle heterogeneity for melt extraction at mid-ocean ridges. *Earth and Planetary Science Letters*, *335-336*, 226–237. doi: 10.1016/j.epsl.2012.04.042

Kavanagh, J. L. (2018). Mechanisms of magma transport in the upper crust—dyking. In *Volcanic and igneous plumbing systems* (pp. 55–88). Elsevier.

Kelemen, P. B., Hirth, G., Shimizu, N., Spiegelman, M., & Dick, H. J. (1997). A review of melt migration processes in the adiabatically upwelling mantle beneath oceanic spreading ridges. *Philosophical Transactions of the Royal Society A: Mathematical, Physical and Engineering Sciences*, *355*(1723), 283–318. doi: 10.1098/rsta.1997.0010

Keller, G., Mateo, P., Punekar, J., Khozyem, H., Gertsch, B., Spangenberg, J., ... Adatte, T. (2018). Environmental changes during the cretaceous-paleogene mass extinction and paleocene-eocene thermal maximum: Implications for the anthropocene. *Gondwana Research*, *56*, 69–89.

Keller, T., & Katz, R. F. (2016). The role of volatiles in reactive melt transport in the asthenosphere. *Journal of Petrology*, *57*(6), 1073–1108.

Keller, T., Katz, R. F., & Hirschmann, M. M. (2017). Volatiles beneath mid-ocean ridges: Deep melting, channelised transport, focusing, and metasomatism. *Earth and Planetary Science Letters*, *464*, 55–68.

Keller, T., May, D. A., & Kaus, B. J. P. (2013). Numerical modelling of magma dynamics coupled to tectonic deformation of lithosphere and crust. *Geophysical Journal International*, *195*(3), 1406–1442. doi: 10.1093/gji/ggt306

Kelley, K. A., Kingsley, R., & Schilling, J.-g. (2013). Composition of plume-influenced mid-ocean ridge lavas and glasses from the Mid-Atlantic Ridge, East Pacific Rise, Galápagos Spreading Center, and Gulf of Aden. *Geochemistry, Geophysics, Geosystems*, *14*(doi:10.1029/2002GC000320). doi: 10.1029/2012GC004415

Kempton, P. D., & Harmon, R. S. (1992). Oxygen isotope evidence for large-scale hybridization of the lower crust during magmatic underplating. *Geochimica et Cosmochimica Acta*, *56*(3), 971–986.

Kerr, A. C., Tarney, J., Marriner, G. F., Nivia, A., & Saunders, A. D. (1997). The Caribbean-Colombian Cretaceous Igneous Province: The internal anatomy of an oceanic plateau. *Geophysical Monograph*, *100*, 123–144. doi: 10.1029/GM100p0123

Kerr, R. C., Meriaux, C., & Lister, J. R. (2008). Effect of thermal diffusion on the stability of strongly tilted mantle plume tails. *Journal of Geophysical Research: Solid Earth*, *113*(9), 1–12. doi: 10.1029/2007JB005510

Keszthelyi, L., & Self, S. (1998). Some physical requirements for the emplacement of long basaltic lava flows. *Journal of Geophysical Research: Solid Earth*, *103*(B11), 27447–27464.

Keszthelyi, L., Self, S., & Thordarson, T. (2006). Flood lavas on earth, io and mars. *Journal of the geological society*, *163*(2), 253–264.

Khadri, S., Subbarao, K., Hooper, P., & Walsh, J. (1988). Stratigraphy of thakurvadi formation, western deccan basalt province, india. *Memoir-Geological Society of India*(10), 281–304.

Khan, W., McCormick, G. R., & Reagan, M. K. (1999). Parh group basalts of northeastern balochistan, pakistan: precursors to the deccan traps. *Special Papers-Geological Society of America*, 59–74.

Kieffer, B., Arndt, N., Lapierre, H., Bastien, F., Bosch, D., Pecher, A., ... others (2004). Flood and shield basalts from ethiopia: magmas from the african superswell. *Journal*

of Petrology, *45*(4), 793–834.

Kingsley, R. H., & Schilling, J. G. (1998). Plume-Ridge Interaction In the Easter Salas Y Gomez Seamount Chain Easter Microplate System - Pb Isotope Evidence. *Journal of Geophysical Research-Solid Earth*, *103*, 24159–24177. doi: 10.1029/98JB01496

Kiss, D., Podladchikov, Y., Duretz, T., & Schmalholz, S. M. (2019, aug). Spontaneous generation of ductile shear zones by thermal softening: Localization criterion, 1d to 3d modelling and application to the lithosphere. *Earth and Planetary Science Letters*, *519*, 284–296. doi: 10.1016/j.epsl.2019.05.026

Kjøll, H. J., Galland, O., Labrousse, L., & Andersen, T. B. (2019, jul). Emplacement mechanisms of a dyke swarm across the brittle-ductile transition and the geodynamic implications for magma-rich margins. *Earth and Planetary Science Letters*, *518*, 223–235. doi: 10.1016/j.epsl.2019.04.016

Knight, K., Nomade, S., Renne, P., Marzoli, A., Bertrand, H., & Youbi, N. (2004). The central atlantic magmatic province at the triassic–jurassic boundary: paleomagnetic and 40ar/39ar evidence from morocco for brief, episodic volcanism. *Earth and Planetary Science Letters*, *228*(1-2), 143–160.

Kohlstedt, D. L., & Holtzman, B. K. (2009). Shearing melt out of the earth: An experimentalist's perspective on the influence of deformation on melt extraction. *Annual Review of Earth and Planetary Sciences*, *37*, 561–593.

Kohlstedt, D. L., Zimmerman, M. E., & Mackwell, S. J. (2009). Stress-driven melt segregation in partially molten feldspathic rocks. *Journal of Petrology*, *51*(1-2), 9–19. doi: 10.1093/petrology/egp043

Koide, H., & Bhattacharji, S. (1975). Formation of fractures around magmatic intrusions and their role in ore localization. *Economic Geology*, *70*(4), 781–799.

Kokfelt, T. F., Lundstrom, C., Hoernle, K., Hauff, F., & Werner, R. (2005). Plume-ridge interaction studied at the Galápagos spreading center: Evidence from 226Ra-230Th-238U and 231Pa-235U isotopic disequilibria. *Earth and Planetary Science Letters*, *234*(1-2), 165–187. doi: 10.1016/j.epsl.2005.02.031

Koptev, A., Burov, E., Gerya, T., Le Pourhiet, L., Leroy, S., Calais, E., & Jolivet, L. (2018). Plume-induced continental rifting and break-up in ultra-slow extension context: Insights from 3d numerical modeling. *Tectonophysics*, *746*, 121–137.

Korchinski, M., Rey, P. F., Mondy, L., Teyssier, C., & Whitney, D. L. (2018). Numerical investigation of deep-crust behavior under lithospheric extension. *Tectonophysics*, *726*, 137–146.

Krans, S., Rooney, T., Kappelman, J., Yirgu, G., & Ayalew, D. (2018). From initiation to termination: a petrostratigraphic tour of the ethiopian low-ti flood basalt province. *Contributions to Mineralogy and Petrology*, *173*(5), 37.

Krans, S. R., Rooney, T. O., Kappelman, J., Yirgu, G., & Ayalew, D. (2018, apr). From initiation to termination: a petrostratigraphic tour of the ethiopian low-ti flood basalt province. *Contributions to Mineralogy and Petrology*, *173*(5). doi: 10.1007/s00410-018-1460-7

Krishna, M. R., Verma, R., & Purushotham, A. K. (2002). Lithospheric structure below the

eastern arabian sea and adjoining west coast of india based on integrated analysis of gravity and seismic data. *Marine Geophysical Researches*, *23*(1), 25–42.

Krishnamurthy, P. (2019). Giant plagioclase basalts (gpbs) from the deccan volcanic province (dvp) and the deccan volcanic cycle (dvc), india. *Journal of the Geological Society of India*, *94*(3), 223–226.

Krishnamurthy, P., & Cox, K. (1977). Picrite basalts and related lavas from the deccan traps of western india. *Contributions to Mineralogy and Petrology*, *62*(1), 53–75.

Krishnamurthy, P., & Cox, K. (1980). A potassium-rich alkalic suite from the deccan traps, rajpipla, india. *Contributions to Mineralogy and Petrology*, *73*(2), 179–189.

Krishnamurthy, P., Gopalan, K., & Macdougall, J. (2000). Olivine compositions in picrite basalts and the deccan volcanic cycle. *Journal of Petrology*, *41*(7), 1057–1069.

Krivolutskaya, N., Kuzmin, D., Gongalsky, B., Roshchina, I., Kononkova, N., Svirskaya, N., & Romashova, T. (2018). Stages of trap magmatism in the norilsk area: New data on the structure and geochemistry of the volcanic rocks. *Geochemistry International*, *56*(5), 419–437.

Krivolutskaya, N. A., Kuzmin, D. V., Gongalsky, B. I., Roshchina, I. A., Kononkova, N. N., Svirskaya, N. M., & Romashova, T. V. (2018, may). Stages of trap magmatism in the norilsk area: New data on the structure and geochemistry of the volcanic rocks. *Geochemistry International*, *56*(5), 419–437. doi: 10.1134/s0016702918050026

Krivolutskaya, N. A., & Sobolev, A. I. (2016). *Siberian traps and pt-cu-ni deposits in the noril'sk area*. Springer.

Kruger, F. J. (2005). Filling the bushveld complex magma chamber: lateral expansion, roof and floor interaction, magmatic unconformities, and the formation of giant chromitite, pge and ti-v-magnetitite deposits. *Mineralium Deposita*, *40*(5), 451–472.

Kumar, G. P., Mahesh, P., Nagar, M., Mahender, E., Kumar, V., Mohan, K., & Kumar, M. R. (2017, may). Role of deep crustal fluids in the genesis of intraplate earthquakes in the kachchh region, northwestern india. *Geophysical Research Letters*, *44*(9), 4054–4063. doi: 10.1002/2017gl072936

Kumar, K. V., Chavan, C., Sawant, S., Raju, K. N., Kanakdande, P., Patode, S., ... Balaram, V. (2010). Geochemical investigation of a semi-continuous extrusive basaltic section from the deccan volcanic province, india: implications for the mantle and magma chamber processes. *Contributions to Mineralogy and Petrology*, *159*(6), 839–862.

Kumar, K. V., Laxman, M. B., & Nagaraju, K. (2018). Mantle source heterogeneity in continental mafic large igneous provinces: insights from the panjal, rajmahal and deccan basalts, india. *Geological Society, London, Special Publications*, *463*(1), 87–116.

Kumar, N., Zeyen, H., Singh, A., & Singh, B. (2013). Lithospheric structure of southern indian shield and adjoining oceans: integrated modelling of topography, gravity, geoid and heat flow data. *Geophysical Journal International*, *194*(1), 30–44.

Kumar, P. V., Patro, P. K., Rao, P. S., Singh, A., Kumar, A., & Nagarjuna, D. (2018). Electrical resistivity cross-section across northern part of saurashtra region: An insight to crystallized magma and fluids. *Tectonophysics*, *744*, 205–214.

Kushnir, A. R., Martel, C., Champallier, R., & Arbaret, L. (2017). In situ confirmation of permeability development in shearing bubble-bearing melts and implications for volcanic outgassing. *Earth and Planetary Science Letters*, *458*, 315–326.

Lamur, A., Kendrick, J., Eggertsson, G., Wall, R., Ashworth, J., & Lavallée, Y. (2017). The permeability of fractured rocks in pressurised volcanic and geothermal systems. *Scientific Reports*, *7*(1), 6173.

Lamy-Chappuis, B., Heinrich, C. A., Driesner, T., & Weis, P. (2020). Mechanisms and patterns of magmatic fluid transport in cooling hydrous intrusions. *Earth and Planetary Science Letters*, *535*, 116111.

Lange, R. A. (2002). Constraints on the preeruptive volatile concentrations in the columbia river flood basalts. *Geology*, *30*(2), 179–182.

Langtangen, H., & Linge, S. (2017). *Finite difference computing with pdes, texts in computational science and engineering.* Springer International Publishing, Cham. https://doi.org/10.1007/978-3-319 ....

Larsen, L. M., & Pedersen, A. K. (2009). Petrology of the paleocene picrites and flood basalts on disko and nuussuaq, west greenland. *Journal of Petrology*, *50*(9), 1667–1711.

Larsen, R. B., Grant, T., Sørensen, B. E., Tegner, C., McEnroe, S., Pastore, Z., ... others (2018). Portrait of a giant deep-seated magmatic conduit system: The seiland igneous province. *Lithos*, *296*, 600–622.

Larson, B., Houghton, J., Lowell, R., Farough, A., & Meile, C. (2015). Subsurface conditions in hydrothermal vents inferred from diffuse flow composition, and models of reaction and transport. *Earth and Planetary Science Letters*, *424*, 245–255.

Lassiter, J. C., & DePaolo, D. J. (1997). Plume/lithosphere interaction in the generation of continental and oceanic flood basalts: chemical and isotopic constraints. *Geophysical Monograph-American Geophysical Union*, *100*, 335–356.

Latyshev, A., Krivolutskaya, N., Ulyahina, P., Bychkova, Y. V., & Gongalsky, B. (2019). Intrusions of the kulumbe river valley, nw siberian traps province: Paleomagnetism, magnetic fabric and geochemistry. In *Recent advances in rock magnetism, environmental magnetism and paleomagnetism* (pp. 67–82). Springer.

Latyshev, A., Veselovskiy, R., & Ivanov, A. (2018, jan). Paleomagnetism of the permian-triassic intrusions from the tunguska syncline and the angara-taseeva depression, siberian traps large igneous province: Evidence of contrasting styles of magmatism. *Tectonophysics*, *723*, 41–55. doi: 10.1016/j.tecto.2017.11.035

Lavecchia, A., Beekman, F., Clark, S. R., & Cloetingh, S. A. (2016). Thermo-rheological aspects of crustal evolution during continental breakup and melt intrusion: The main ethiopian rift, east africa. *Tectonophysics*, *686*, 51–62.

Lavecchia, A., Clark, S. R., Beekman, F., Cloetingh, S. A., & Burov, E. (2016). Thermal perturbation, mineral assemblages, and rheology variations induced by dyke emplacement in the crust. *Tectonics*, *35*(5), 1137–1152.

Leat, P. T. (2008). On the long-distance transport of ferrar magmas. *Geological Society, London, Special Publications*, *302*(1), 45–61.

Lee, A. L., Lloyd, G. E., Torvela, T., & Walker, A. M. (2020). Evolution of a shear zone

before, during and after melting. *Journal of the Geological Society*.

Lee, C., & Butcher, A. (1990). Cyclicity in the sr isotope stratigraphy through the merensky and bastard reef units, atok section, eastern bushveld complex. *Economic Geology*, *85*(4), 877–883.

Lee, C.-T. A., Lee, T. C., & Wu, C.-T. (2014). Modeling the compositional evolution of recharging, evacuating, and fractionating (refc) magma chambers: Implications for differentiation of arc magmas. *Geochimica et Cosmochimica Acta*, *143*, 8–22.

Lee, H., Muirhead, J. D., Fischer, T. P., Ebinger, C. J., Kattenhorn, S. A., Sharp, Z. D., & Kianji, G. (2016). Massive and prolonged deep carbon emissions associated with continental rifting. *Nature Geoscience*, *9*(2), 145.

Leeman, W., & Hawkesworth, C. (1986). Open magma systems: trace element and isotopic constraints. *Journal of Geophysical Research: Solid Earth*, *91*(B6), 5901–5912.

Lénat, J. F., Merle, O., & Lespagnol, L. (2009). La réunion: An example of channeled hot spot plume. *Journal of Volcanology and Geothermal Research*, *184*(1-2), 1–13. doi: 10.1016/j.jvolgeores.2008.12.001

Lenhardt, N., & Eriksson, P. G. (2012). Volcanism of the palaeoproterozoic bushveld large igneous province: the rooiberg group, kaapvaal craton, south africa. *Precambrian Research*, *214*, 82–94.

Lewicki, J. L., Hilley, G. E., Shelly, D. R., King, J. C., McGeehin, J. P., Mangan, M., & Evans, W. C. (2014). Crustal migration of co2-rich magmatic fluids recorded by tree-ring radiocarbon and seismicity at mammoth mountain, ca, usa. *Earth and Planetary Science Letters*, *390*, 52–58.

Liang, Y., & Peng, Q. (2010). Non-modal melting in an upwelling mantle column: Steady-state models with applications to REE depletion in abyssal peridotites and the dynamics of melt migration in the mantle. *Geochimica et Cosmochimica Acta*, *74*(1), 321–339. doi: 10.1016/j.gca.2009.09.029

Liao, Y., Soule, S. A., & Jones, M. (2018). On the mechanical effects of poroelastic crystal mush in classical magma chamber models. *Journal of Geophysical Research: Solid Earth*, *123*(11), 9376–9406.

Lightfoot, P., & Hawkesworth, C. (1988). Origin of deccan trap lavas: evidence from combined trace element and sr-, nd-and pb-isotope studies. *Earth and Planetary Science Letters*, *91*(1-2), 89–104.

Lightfoot, P., Hawkesworth, C., Devey, C. W., Rogers, N., & Calsteren, P. V. (1990). Source and differentiation of deccan trap lavas: implications of geochemical and mineral chemical variations. *Journal of Petrology*, *31*(5), 1165–1200.

Lightfoot, P., Hawkesworth, C., Hergt, J., Naldrett, A., Gorbachev, N., Fedorenko, V., & Doherty, W. (1993). Remobilisation of the continental lithosphere by a mantle plume: major-, trace-element, and sr-, nd-, and pb-isotope evidence from picritic and tholeiitic lavas of the noril'sk district, siberian trap, russia. *Contributions to Mineralogy and Petrology*, *114*(2), 171–188.

Lightfoot, P., Hawkesworth, C., & Sethna, S. (1987). Petrogenesis of rhyolites and trachytes from the deccan trap: Sr, nd and pb isotope and trace element evidence. *Contributions*

to Mineralogy and Petrology, *95*(1), 44–54.

Lightfoot, P., Naldrett, A., Gorbachev, N., Doherty, W., & Fedorenko, V. (1990). Geochemistry of the siberian trap of the noril'sk area, ussr, with implications for the relative contributions of crust and mantle to flood basalt magmatism. *Contributions to Mineralogy and Petrology*, *104*(6), 631–644.

Lipman, P. W., & Banks, N. G. (1987). Aa flow dynamics, mauna loa 1984. *US Geol Surv Prof Pap*, *1350*, 1527–1567.

Lister, J. R., & Dellar, P. J. (1996). Solidification of pressure-driven flow in a finite rigid channel with application to volcanic eruptions. *Journal of Fluid Mechanics*, *323*(-1), 267. doi: 10.1017/S0022112096000912

Lister, J. R., & Kerr, R. C. (1991). Fluid-mechanical models of crack propagation and their application to magma transport in dykes. *Journal of Geophysical Research: Solid Earth*, *96*(B6), 10049–10077.

Liu, J., Xia, Q.-K., Kuritani, T., Hanski, E., & Yu, H.-R. (2017). Mantle hydration and the role of water in the generation of large igneous provinces. *Nature communications*, *8*(1), 1–8.

Lowell, R. P., Van Cappellen, P., & Germanovich, L. N. (1993). Silica precipitation in fractures and the evolution of permeability in hydrothermal upflow zones. *Science*, *260*(5105), 192–194.

Luttinen, A. V., & Furnes, H. (2000). Flood basalts of vestfjella: Jurassic magmatism across an archaean–proterozoic lithospheric boundary in dronning maud land, antarctica. *Journal of Petrology*, *41*(8), 1271–1305.

Maccaferri, F., Bonafede, M., & Rivalta, E. (2011). A quantitative study of the mechanisms governing dike propagation, dike arrest and sill formation. *Journal of Volcanology and Geothermal Research*, *208*(1-2), 39–50. doi: 10.1016/j.jvolgeores.2011.09.001

Machado, F. B., Rocha-Júnior, E. R. V., Marques, L. S., Nardy, A. J. R., Zezzo, L. V., & Marteleto, N. S. (2018). Geochemistry of the northern paraná continental flood basalt (pcfb) province: implications for regional chemostratigraphy. *Brazilian Journal of Geology*, *48*(2), 177–199.

Madrigal, P., Gazel, E., Denyer, P., Smith, I., Jicha, B., Flores, K. E., ... Snow, J. (2015). A melt-focusing zone in the lithospheric mantle preserved in the Santa Elena Ophiolite, Costa Rica. *Lithos*, *230*, 189–205. doi: 10.1016/j.lithos.2015.04.015

Magee, C., Ernst, R. E., Muirhead, J., Phillips, T., & Jackson, C. A.-L. (2019). Magma transport pathways in large igneous provinces: Lessons from combining field observations and seismic reflection data. In *Dyke swarms of the world: A modern perspective* (pp. 45–85). Springer.

Magee, C., Muirhead, J., Schofield, N., Walker, R. J., Galland, O., Holford, S., ... McCarthy, W. (2019). Structural signatures of igneous sheet intrusion propagation. *Journal of Structural Geology*, *125*, 148–154.

Magee, C., Muirhead, J. D., Karvelas, A., Holford, S. P., Jackson, C. A., Bastow, I. D., ... others (2016a). Lateral magma flow in mafic sill complexes. *Geosphere*, GES01256–1.

Magee, C., Muirhead, J. D., Karvelas, A., Holford, S. P., Jackson, C. A., Bastow, I. D.,

... others (2016b). Lateral magma flow in mafic sill complexes. *Geosphere*, *12*(3), 809–841.

Magee, C., O'Driscoll, B., Petronis, M., & Stevenson, C. (2016, apr). Three-dimensional magma flow dynamics within subvolcanic sheet intrusions. *Geosphere*, *12*(3), 842–866. doi: 10.1130/ges01270.1

Magee, C., Stevenson, C. T., Ebmeier, S. K., Keir, D., Hammond, J. O., Gottsmann, J. H., ... others (2018). Magma plumbing systems: a geophysical perspective. *Journal of Petrology*, *59*(6), 1217–1251.

Mahoney, J., Duncan, R., Khan, W., Gnos, E., & McCormick, G. (2002). Cretaceous volcanic rocks of the south tethyan suture zone, pakistan: implications for the réunion hotspot and deccan traps. *Earth and Planetary Science Letters*, *203*(1), 295–310.

Mahoney, J., Macdougall, J., Lugmair, G., Murali, A., Das, M. S., & Gopalan, K. (1982). Origin of the deccan trap flows at mahabaleshwar inferred from nd and sr isotopic and chemical evidence. *Earth and Planetary Science Letters*, *60*(1), 47–60.

Mahoney, J., Sheth, H., Chandrasekharam, D., & Peng, Z. (2000). Geochemistry of flood basalts of the toranmal section, northern deccan traps, india: implications for regional deccan stratigraphy. *Journal of Petrology*, *41*(7), 1099–1120.

Mahoney, J. J. (1984). *Isotopic and chemical studies of the deccan and rajmahal traps, india: mantle sources and petrogenesis* (Unpublished doctoral dissertation).

Mahoney, J. J. (1988). Deccan traps. In *Continental flood basalts* (pp. 151–194). Springer.

Mahoney, J. J., & Coffin, M. F. (1997). *Large igneous provinces: continental, oceanic, and planetary flood volcanism* (Vol. 100). American Geophysical Union.

Maia, M., Dyment, J., & Jouannetaud, D. (2005). Constraints on age and construction process of the Foundation chain submarine volcanoes from magnetic modeling. *Earth and Planetary Science Letters*, *235*(1-2), 183–199. doi: 10.1016/j.epsl.2005.02.044

Mair, J. L., Goldfarb, R. J., Johnson, C. A., Hart, C. J., & Marsh, E. E. (2006). Geochemical constraints on the genesis of the scheelite dome intrusion-related gold deposit, tombstone gold belt, yukon, canada. *Economic Geology*, *101*(3), 523–553.

Malthe-Sørenssen, A., Planke, S., Svensen, H., Jamtveit, B., Breitkreuz, C., & Petford, N. (2004). Formation of saucer-shaped sills. *Physical geology of high-level magmatic systems. Geological Society, London, Special Publications*, *234*, 215–227.

Mammo, T. (2013). Crustal structure of the flood basalt province of ethiopia from constrained 3-d gravity inversion. *Pure and Applied Geophysics*, *170*(12), 2185–2206.

Mancktelow, N. S., & Pennacchioni, G. (2005). The control of precursor brittle fracture and fluid–rock interaction on the development of single and paired ductile shear zones. *Journal of Structural Geology*, *27*(4), 645–661.

Manga, M., Beresnev, I., Brodsky, E. E., Elkhoury, J. E., Elsworth, D., Ingebritsen, S. E., ... Wang, C.-Y. (2012). Changes in permeability caused by transient stresses: Field observations, experiments, and mechanisms. *Reviews of Geophysics*, *50*(2).

Manga, M., & Michaut, C. (2017). Formation of lenticulae on europa by saucer-shaped sills. *Icarus*, *286*, 261–269.

Mangan, M., Marsh, B., Froelich, A., & Gottfried, D. (1993). Emplacement and differ-

entiation of the york haven diabase sheet, pennsylvania. *Journal of Petrology*, *34*, 1271–1302.

Mangan, M. T., Wright, T. L., Swanson, D. A., & Byerly, G. R. (1986). Regional correlation of grande ronde basalt flows, columbia river basalt group, washington, oregon, and idaho. *Geological Society of America Bulletin*, *97*(11), 1300–1318.

Manning, C. E. (2018). Fluids of the lower crust: Deep is different. *Annual Review of Earth and Planetary Sciences*, *46*, 67–97.

Manu Prasanth, M., Hari, K., & Santosh, M. (2019). Tholeiitic basalts of deccan large igneous province, india: An overview. *Geological Journal*, *54*(5), 2980–2993.

Marsh, B. (2004). A magmatic mush column rosetta stone: The McMurdo Dry Valleys of Antarctica. *Eos, Transactions American Geophysical Union*, *85*(47), 497. doi: 10.1029/2004EO470001

Marsh, B. D. (1989). Magma chambers. *Annual Review of Earth and Planetary Sciences*, *17*(1), 439–472.

Marsh, B. D. (1996). Solidification fronts and magmatic evolution. *Mineralogical Magazine*, *60*(398), 5–40.

Marsh, B. D. (2002). On bimodal differentiation by solidification front instability in basaltic magmas, part 1: basic mechanics. *Geochimica et Cosmochimica Acta*, *66*(12), 2211–2229.

Marsh, B. D. (2004). A magmatic mush column rosetta stone: the mcmurdo dry valleys of antarctica. *Eos, Transactions American Geophysical Union*, *85*(47), 497–502.

Marsh, B. D. (2013, aug). On some fundamentals of igneous petrology. *Contributions to Mineralogy and Petrology*, *166*(3), 665–690. doi: 10.1007/s00410-013-0892-3

Marsh, B. D., & Coleman, N. M. (2009). Magma flow and interaction with waste packages in a geologic repository at yucca mountain, nevada. *Journal of volcanology and geothermal research*, *182*(1-2), 76–96.

Marsh, J., Hooper, P., Rehacek, J., Duncan, R., & Duncan, A. (1997). Stratigraphy and age of karoo basalts of lesotho and implications for correlations within the karoo igneous province. *Geophysical Monograph-American Geophysical Union*, *100*, 247–272.

Marsh, J. S. (1987). Basalt geochemistry and tectonic discrimination within continental flood basalt provinces. *Journal of Volcanology and Geothermal Research*, *32*(1-3), 35–49.

Marsh, J. S. (1989). Geochemical constraints on coupled assimilation and fractional crystallization involving upper crustal compositions and continental tholeiitic magma. *Earth and Planetary Science Letters*, *92*(1), 70–80.

Marzoli, A., Bertrand, H., Youbi, N., Callegaro, S., Merle, R., Reisberg, L., ... others (2019). The central atlantic magmatic province (camp) in morocco. *Journal of Petrology*, *60*(5), 945–996.

Matter, J. M., Goldberg, D., Morin, R. H., & Stute, M. (2006). Contact zone permeability at intrusion boundaries: new results from hydraulic testing and geophysical logging in the newark rift basin, new york, usa. *Hydrogeology Journal*, *14*(5), 689.

Matter, J. M., Stute, M., Snæbjörnsdottir, S. Ó., Oelkers, E. H., Gislason, S. R., Aradottir,

E. S., ... others (2016). Rapid carbon mineralization for permanent disposal of anthropogenic carbon dioxide emissions. *Science*, *352*(6291), 1312–1314.

Matthews, S., Shorttle, O., Maclennan, J., & Rudge, J. F. (2019). Melt inclusion constraints on mantle carbon heterogeneity within an individual mantle plume and at the global scale.

Maurya, S., Montagner, J.-P., Kumar, M. R., Stutzmann, E., Kiselev, S., Burgos, G., ... Srinagesh, D. (2016, oct). Imaging the lithospheric structure beneath the indian continent. *Journal of Geophysical Research: Solid Earth*, *121*(10), 7450–7468. doi: 10.1002/2016jb012948

Mayer, K., Scheu, B., Gilg, H. A., Heap, M. J., Kennedy, B. M., Lavallée, Y., ... Dingwell, D. B. (2015). Experimental constraints on phreatic eruption processes at whakaari (white island volcano). *Journal of Volcanology and Geothermal Research*, *302*, 150–162.

McClinton, T., White, S. M., Colman, A., & Sinton, J. M. (2013, aug). Reconstructing lava flow emplacement processes at the hot spot-affected Galápagos Spreading Center, 95 o W and 92 o W. *Geochemistry, Geophysics, Geosystems*, *14*(8), 2731–2756. doi: 10.1002/ggge.20157

McDougall, I. (1971, mar). The geochronology and evolution of the young volcanic island of Réunion, Indian Ocean. *Geochimica et Cosmochimica Acta*, *35*(3), 261–288. Retrieved from `http://linkinghub.elsevier.com/retrieve/pii/0016703771900378` doi: 10.1016/0016-7037(71)90037-8

McDougall, I., Upton, B. G. J., & Wadsworth, W. J. (1965, apr). A Geological Reconnaissance of Rodriguez Island, Indian Ocean. *Nature*, *206*(4979), 26–27. Retrieved from `http://dx.doi.org/10.1038/206026a0` `http://www.nature.com/doifinder/10.1038/206026a0` doi: 10.1038/206026a0

McGovern, P. J., Grosfils, E. B., Galgana, G. A., Morgan, J. K., Rumpf, M. E., Smith, J. R., & Zimbelman, J. R. (2015, jan). Lithospheric flexure and volcano basal boundary conditions: keys to the structural evolution of large volcanic edifices on the terrestrial planets. *Geological Society, London, Special Publications*, *401*(1), 219–237. doi: 10.1144/SP401.7

McKenzie, D. (1984). the Generation and Compaction of Partially Molten Rock. *Journal of Petrology*, *25*(3), 713–765.

Mckenzie, D., & Bickle, M. (1988). The volume and composition of melt generated by extension of the lithosphere. *Journal of petrology*, *29*(3), 625–679.

McKenzie, D., & O'nions, R. (1991). Partial melt distributions from inversion of rare earth element concentrations. *Journal of Petrology*, *32*(5), 1021–1091.

Melluso, L., Barbieri, M., & Beccaluva, L. (2004). Chemical evolution, petrogenesis, and regional chemical correlations of the flood basalt sequence in the central deccan traps, india. *Journal of Earth System Science*, *113*(4), 587–603.

Melluso, L., Beccaluva, L., Brotzu, P., Gregnanin, A., Gupta, A., Morbidelli, L., & Traversa, G. (1995). Constraints on the mantle sources of the deccan traps from the petrology and geochemistry of the basalts of gujarat state (western india). *Journal of Petrology*,

36(5), 1393–1432.

Melluso, L., Mahoney, J. J., & Dallai, L. (2006). Mantle sources and crustal input as recorded in high-mg deccan traps basalts of gujarat (india). *Lithos*, *89*(3-4), 259–274.

Melluso, L., Sethna, S., d'Antonio, M., Javeri, P., & Bennio, L. (2002). Geochemistry and petrogenesis of sodic and potassic mafic alkaline rocks in the deccan volcanic province, mumbai area (india). *Mineralogy and Petrology*, *74*(2-4), 323–342.

Melluso, L., Sethna, S., Morra, V., Khateeb, A., & Javeri, P. (1999). Petrology of mafic dyke swarm of the tapti river in the nandurbar area. *Deccan volcanic province*, *3*(1), 735–738.

Menand, T., Annen, C., & de Saint Blanquat, M. (2015). Rates of magma transfer in the crust: Insights into magma reservoir recharge and pluton growth. *Geology*, *43*(3), 199–202.

Meschede, M., & Barckhausen, U. (2000). Plate tectonic evolution of the Cocos-Nazca Spreading Center. *Proceedings of the Ocean Drilling Program, Scientific Results*, *170*(January), 10.

Millett, J., Hole, M., Jolley, D., & Passey, S. (2017). Geochemical stratigraphy and correlation within large igneous provinces: the final preserved stages of the faroe islands basalt group. *Lithos*, *286*, 1–15.

Millett, J., Hole, M., Jolley, D., Schofield, N., & Campbell, E. (2016). Frontier exploration and the north atlantic igneous province: new insights from a 2.6 km offshore volcanic sequence in the ne faroe–shetland basin. *Journal of the Geological Society*, *173*(2), 320–336.

Mishra, S., Misra, S., Vyas, D., Nikalje, D., Warhade, A., & Roy, S. (2017). A 1251m-thick deccan flood basalt pile recovered by scientific drilling in the koyna region, western india. *Journal of the Geological Society of India*, *90*(6), 788–794.

Misra, A. A., Bhattacharya, G., Mukherjee, S., & Bose, N. (2014). Near n–s paleo-extension in the western deccan region, india: does it link strike-slip tectonics with india–seychelles rifting? *International Journal of Earth Sciences*, *103*(6), 1645–1680.

Misra, A. A., & Mukherjee, S. (2017). Dyke–brittle shear relationships in the western deccan strike-slip zone around mumbai (maharashtra, india). *Geological Society, London, Special Publications*, *445*(1), 269–295.

Mitchell, A., Scoon, R., & Sharpe, M. (2019). The upper critical zone in the swartklip sector, north-western bushveld complex, on the farm wilgerspruit 2jq: Ii. origin by intrusion of ultramafic sills with concomitant partial melting of host norite-anorthosite cumulates. *South African Journal of Geology 2019*, *122*(2), 143–162.

Mitchell, A. A., & Scoon, R. N. (2007). The merensky reef at winnaarshoek, eastern bushveld complex: a primary magmatic hypothesis based on a wide reef facies. *Economic Geology*, *102*(5), 971–1009.

Mitchell, C., & Widdowson, M. (1991). A geological map of the southern deccan traps, india and its structural implications. *Journal of the Geological Society*, *148*(3), 495–505.

Mittal, T., & Richards, M. A. (2019). Volatile degassing from magma chambers as a control on volcanic eruptions. *Journal of Geophysical Research: Solid Earth*.

Mittal, T., Sprain, C. J., Fendley, I., Self, S., Renne, P. R., & Richards, M. A. (2019). Constraining the eruptive tempo of the deccan traps to understand potential climate consequences. In *Agu fall meeting 2019.*

Mittelstaedt, E., & Ito, G. (2005). Plume-ridge interaction, lithospheric stresses, and the origin of near-ridge volcanic lineaments. *Geochemistry, Geophysics, Geosystems*, *6*(6). doi: 10.1029/2004GC000860

Mittelstaedt, E., Ito, G., & Van Hunen, J. (2011). Repeat ridge jumps associated with plume-ridge interaction, melt transport, and ridge migration. *Journal of Geophysical Research: Solid Earth*, *116*(1), 1–20. doi: 10.1029/2010JB007504

Mittelstaedt, E., Soule, A. S., Harpp, K. S., & Fornari, D. (2014). Variations in Crustal Thickness, Plate Rigidity, and Volcanic Processes Throughout the Northern Galápagos Volcanic Province. *The Galapagos: A Natural Laboratory for the Earth Sciences*, 263–284. doi: 10.1002/9781118852538.ch14

Mittelstaedt, E., Soule, S., Harpp, K., Fornari, D., McKee, C., Tivey, M., ... Mello, C. (2012). Multiple expressions of plume-ridge interaction in the Galápagos: Volcanic lineaments and ridge jumps. *Geochemistry, Geophysics, Geosystems*, *13*(5). doi: 10.1029/2012GC004093

Molins, S., Trebotich, D., Steefel, C. I., & Shen, C. (2012). An investigation of the effect of pore scale flow on average geochemical reaction rates using direct numerical simulation. *Water Resources Research*, *48*(3).

Montagna, C., Papale, P., & Longo, A. (2015). Timescales of mingling in shallow magmatic reservoirs. *Geological Society, London, Special Publications*, *422*(1), 131–140.

Montési, L. G. (2013). Fabric development as the key for forming ductile shear zones and enabling plate tectonics. *Journal of Structural Geology*, *50*, 254–266.

Montesi, L. G., Behn, M. D., Hebert, L. B., Lin, J., & Barry, J. L. (2011). Controls on melt migration and extraction at the ultraslow southwest indian ridge 10–16 e. *Journal of Geophysical Research: Solid Earth*, *116*(B10).

Moons, P., & Spencer, D. (1988). Field theory handbook: including coordinate systems, differential equations, and their solutions. *Eleven Coordinate Systems*, 1–48.

Moore, J., White, W. M., Paul, D., Duncan, R. A., Abouchami, W., & Galer, S. J. G. (2011). Evolution of shield-building and rejuvenescent volcanism of Mauritius. *Journal of Volcanology and Geothermal Research*, *207*(1-2), 47–66. doi: 10.1016/j.jvolgeores.2011.07.005

Moore, N., Grunder, A., & Bohrson, W. (2018). The three-stage petrochemical evolution of the steens basalt (southeast oregon, usa) compared to large igneous provinces and layered mafic intrusions. *Geosphere*, *14*(6), 2505–2532.

Moos, D., & Zoback, M. D. (1993). State of stress in the long valley caldera, california. *Geology*, *21*(9), 837–840.

Morgan, W. J. (1978). Rodriguez, Darwin, Amsterdam, ..., A second type of Hotspot Island. *Journal of Geophysical Research*, *83*(B11), 5355. doi: 10.1029/JB083iB11p05355

Morgan, W. J., & Morgan, J. P. (2007). Plate velocities in the hotspot reference frame. *Geological Society of America Bulletin*, *2430*(04), 65–78. doi: 10.1130/2007.2430(04).

Morse, S. A. (1980). *Basalts and phase diagrams: an introduction to the quantitative use of phase diagrams in igneous petrology*. Springer-Verlag.

Moulin, M., Fluteau, F., Courtillot, V., Marsh, J., Delpech, G., Quidelleur, X., & Gérard, M. (2017, feb). Eruptive history of the karoo lava flows and their impact on early jurassic environmental change. *Journal of Geophysical Research: Solid Earth*, *122*(2), 738–772. doi: 10.1002/2016jb013354

Muirhead, J. D., Airoldi, G., Rowland, J. V., & White, J. D. (2012). Interconnected sills and inclined sheet intrusions control shallow magma transport in the ferrar large igneous province, antarctica. *Bulletin*, *124*(1-2), 162–180.

Muirhead, J. D., Airoldi, G., White, J. D., & Rowland, J. V. (2014). Cracking the lid: Sill-fed dikes are the likely feeders of flood basalt eruptions. *Earth and Planetary Science Letters*, *406*, 187–197.

Müller, R. D., Seton, M., Zahirovic, S., Williams, S. E., Matthews, K. J., Wright, N. M., ... Cannon, J. (2016). Ocean basin evolution and global-scale reorganization events since Pangea breakup. *Annual Review of Earth and Planetary Science Letters*.

Mungall, J. E., Kamo, S. L., & McQuade, S. (2016). U–pb geochronology documents out-of-sequence emplacement of ultramafic layers in the bushveld igneous complex of south africa. *Nature Communications*, *7*(1), 1–13.

Muraoka, H., Uchida, T., Sasada, M., Yagi, M., Akaku, K., Sasaki, M., ... others (1998). Deep geothermal resources survey program: igneous, metamorphic and hydrothermal processes in a well encountering 500 c at 3729 m depth, kakkonda, japan. *Geothermics*, *27*(5-6), 507–534.

Murrell, S. (1964). The theory of the propagation of elliptical griffith cracks under various conditions of plane strain or plane stress: Parts ii and iii. *British Journal of Applied Physics*, *15*(10), 1211.

Murton, B. J., Tindle, A. G., Milton, J. A., & Sauter, D. (2005). Heterogeneity in southern central indian ridge morb: implications for ridge–hot spot interaction. *Geochemistry, Geophysics, Geosystems*, *6*(3).

Nabelek, P. I. (2009). Numerical simulation of kinetically-controlled calc-silicate reactions and fluid flow with transient permeability around crystallizing plutons. *American Journal of Science*, *309*(7), 517–548.

Nabelek, P. I., Bédard, J. H., & Rainbird, R. H. (2014). Numerical constraints on degassing of metamorphic co2 during the neoproterozoic franklin large igneous event, arctic canada. *Bulletin*, *126*(5-6), 759–772.

Naganjaneyulu, K., & Santosh, M. (2010, nov). The central india tectonic zone: A geophysical perspective on continental amalgamation along a mesoproterozoic suture. *Gondwana Research*, *18*(4), 547–564. doi: 10.1016/j.gr.2010.02.017

Naganjaneyulu, K., & Santosh, M. (2011, jul). Geophysical signatures of fluids in a reactivated precambrian collisional suture in central india. *Geoscience Frontiers*, *2*(3), 289–301. doi: 10.1016/j.gsf.2011.06.001

Naidu, G. D., & Harinarayana, T. (2009, oct). Deep electrical imaging of the narmada–tapti region, central india from magnetotellurics. *Tectonophysics*, *476*(3-4), 538–549. doi:

10.1016/j.tecto.2009.07.010

Namur, O., Charlier, B., Toplis, M. J., Higgins, M. D., Liégeois, J.-P., & Vander Auwera, J. (2010). Crystallization sequence and magma chamber processes in the ferrobasaltic sept iles layered intrusion, canada. *Journal of Petrology*, *51*(6), 1203–1236.

Natali, C., Beccaluva, L., Bianchini, G., Siena, F., et al. (2017). Comparison among ethiopia-yemen, deccan, and karoo continental flood basalts of central gondwana: Insights on lithosphere versus asthenosphere contributions in compositionally zoned magmatic provinces. *The Crust-Mantle and lithosphere-asthenosphere boundaries: insights from xenoliths, orogenic deep sections, and geophysical studies*, *526*, 191–215.

Nauret, F., Abouchami, W., Galer, S., Hofmann, A., Hémond, C., Chauvel, C., & Dyment, J. (2006). Correlated trace element-pb isotope enrichments in indian morb along 18–20 s, central indian ridge. *Earth and Planetary Science Letters*, *245*(1), 137–152.

Neal, C., Brantley, S., Antolik, L., Babb, J., Burgess, M., Calles, K., ... others (2019). The 2018 rift eruption and summit collapse of kīlauea volcano. *Science*, *363*(6425), 367–374.

Neal, C. R., Coffin, M. F., & Sager, W. W. (2019). Contributions of scientific ocean drilling to understanding the emplacement of submarine large igneous provinces and their effects on the environment. *Oceanography*, *32*(1), 176–192.

Neave, D. A., Buisman, I., & Maclennan, J. (2017). Continuous mush disaggregation during the long-lasting laki fissure eruption, iceland. *American Mineralogist: Journal of Earth and Planetary Materials*, *102*(10), 2007–2021.

Neumann, E.-R., Svensen, H., Galerne, C. Y., & Planke, S. (2011). Multistage evolution of dolerites in the karoo large igneous province, central south africa. *Journal of Petrology*, *52*(5), 959–984.

Nielsen, T. F. (2004). The shape and volume of the skaergaard intrusion, greenland: implications for mass balance and bulk composition. *Journal of Petrology*, *45*(3), 507–530.

Nippress, S., & Rietbrock, A. (2007). Seismogenic zone high permeability in the central andes inferred from relocations of micro-earthquakes. *Earth and Planetary Science Letters*, *263*(3-4), 235–245.

Nissanka, U. S., Weeraratne, D. S., & Parmentier, E. M. (2014). Viscous fingering in miscible fluids and the oceanic asthenosphere: significance for the formation of intraplate seamount chains. *AGU Fall Meeting Abstracts*.

Norton, D., & Knight, J. (1977). Transport phenomena in hydrothermal systems: cooling plutons. *Am. J. Sci.;(United States)*, *277*.

Norton, D., & Taylor Jr, H. (1979). Quantitative simulation of the hydrothermal systems of crystallizing magmas on the basis of transport theory and oxygen isotope data: An analysis of the skaergaard intrusion. *Journal of Petrology*, *20*(3), 421–486.

Norton, D. L. (1984). Theory of hydrothermal systems. *Annual Review of Earth and Planetary Sciences*, *12*(1), 155–177.

O'Driscoll, B., Troll, V. R., Reavy, R. J., & Turner, P. (2006). The great eucrite intrusion of ardnamurchan, scotland: Reevaluating the ring-dike concept. *Geology*, *34*(3), 189–192.

O'Hara, D., Karlstrom, L., & Roering, J. J. (2019). Distributed landscape response to localized uplift and the fragility of steady states. *Earth and Planetary Science Letters*, *506*, 243–254.

Ohneiser, C., Acton, G., Channell, J. E., Wilson, G. S., Yamamoto, Y., & Yamazaki, T. (2013). A middle miocene relative paleointensity record from the equatorial pacific. *Earth and Planetary Science Letters*, *374*, 227–238.

Olive, J.-A., & Crone, T. J. (2018). Smoke without fire: How long can thermal cracking sustain hydrothermal circulation in the absence of magmatic heat? *Journal of Geophysical Research: Solid Earth*, *123*(6), 4561–4581.

Oppenheimer, C., Orchard, A., Stoffel, M., Newfield, T. P., Guillet, S., Corona, C., ... Büntgen, U. (2018). The eldgjá eruption: timing, long-range impacts and influence on the christianisation of iceland. *Climatic change*, *147*(3-4), 369–381.

Ortoleva, P., Chadam, J., Merino, E., & Sen, A. (1987). *Geochemical self-organization II; the reactive-infiltration instability* (Vol. 287) (No. 10). doi: 10.2475/ajs.287.10.1008

Óskarsson, B. V., Andersen, C. B., Riishuus, M. S., Sørensen, E. V., & Tegner, C. (2017). The mode of emplacement of neogene flood basalts in eastern iceland: The plagioclase ultraphyric basalts in the grænavatn group. *Journal of Volcanology and Geothermal Research*, *332*, 26–50.

Óskarsson, B. V., & Riishuus, M. S. (2014, dec). The mode of emplacement of neogene flood basalts in eastern iceland: Facies architecture and structure of simple aphyric basalt groups. *Journal of Volcanology and Geothermal Research*, *289*, 170–192. doi: 10.1016/j.jvolgeores.2014.11.009

Owen-Smith, T., & Ashwal, L. (2015). Evidence for multiple pulses of crystal-bearing magma during emplacement of the doros layered intrusion, namibia. *Lithos*, *238*, 120–139.

Owen-Smith, T. M., Ashwal, L. D., Torsvik, T. H., Ganerød, M., Nebel, O., Webb, S. J., & Werner, S. C. (2013). Seychelles alkaline suite records the culmination of deccan traps continental flood volcanism. *Lithos*, *182*, 33–47.

O'Connor, J. M., Stoffers, P., & Wijbrans, J. R. (2004). The Foundation Chain: Inferring Hotspot-Plate Interaction from a Weak Seamount Trail. In *Oceanic hotspots* (Vol. 6, pp. 349–374). Berlin, Heidelberg: Springer Berlin Heidelberg. doi: 10.1007/978-3-642-18782-7_12

O'driscoll, B. (2007). The centre 3 layered gabbro intrusion, ardnamurchan, nw scotland. *Geological Magazine*, *144*(6), 897–908.

O'Hara, M., & Herzberg, C. (2002). Interpretation of trace element and isotope features of basalts: relevance of field relations, petrology, major element data, phase equilibria, and magma chamber modeling in basalt petrogenesis. *Geochimica et Cosmochimica Acta*, *66*(12), 2167–2191.

O'Hara, M., & Mathews, R. (1981). Geochemical evolution in an advancing, periodically replenished, periodically tapped, continuously fractionated magma chamber. *Journal of the Geological Society*, *138*(3), 237–277.

Pande, K., Cucciniello, C., Sheth, H., Vijayan, A., Sharma, K. K., Purohit, R., ... Shinde, S. (2017). Polychronous (early cretaceous to palaeogene) emplacement of the mundwara

alkaline complex, rajasthan, india: 40 ar/39 ar geochronology, petrochemistry and geodynamics. *International Journal of Earth Sciences*, *106*(5), 1487–1504.

Pande, K., Yatheesh, V., & Sheth, H. (2017). 40ar/39ar dating of the mumbai tholeiites and panvel flexure: intense 62.5 ma onshore–offshore deccan magmatism during india-laxmi ridge–seychelles breakup. *Geophysical Journal International*, *210*(2), 1160–1170.

Pandey, D., Pandey, A., & Rajan, S. (2011). Offshore extension of deccan traps in kachchh, central western india: implications for geological sequestration studies. *Natural resources research*, *20*(1), 33–43.

Pandey, O., Chandrakala, K., Parthasarathy, G., Reddy, P., & Reddy, G. K. (2009). Upwarped high velocity mafic crust, subsurface tectonics and causes of intraplate laturkillari (m 6.2) and koyna (m 6.3) earthquakes, india–a comparative study. *Journal of Asian Earth Sciences*, *34*(6), 781–795.

Paonita, A., Caracausi, A., Martelli, M., & Rizzo, A. L. (2016). Temporal variations of helium isotopes in volcanic gases quantify pre-eruptive refill and pressurization in magma reservoirs: The mount etna case. *Geology*, *44*(7), 499–502.

Papale, P., Montagna, C. P., & Longo, A. (2017). Pressure evolution in shallow magma chambers upon buoyancy-driven replenishment. *Geochemistry, Geophysics, Geosystems*, *18*(3), 1214–1224.

Parcheta, C., Fagents, S., Swanson, D. A., Houghton, B. F., & Ericksen, T. (2015). Hawaiian fissure fountains: quantifying vent and shallow conduit geometry, episode 1 of the 1969–1974 mauna ulu eruption. *Hawaiian Volcanoes: From Source to Surface: American Geophysical Union Geophysical Monograph*, *208*, 369–391.

Parisio, L., Jourdan, F., Marzoli, A., Melluso, L., Sethna, S. F., & Bellieni, G. (2016). 40ar/39ar ages of alkaline and tholeiitic rocks from the northern deccan traps: implications for magmatic processes and the k–pg boundary. *Journal of the Geological Society*, *173*(4), 679–688.

Parks, M. M., Heimisson, E. R., Sigmundsson, F., Hooper, A., Vogfjörd, K. S., Árnadóttir, T., ... others (2017). Evolution of deformation and stress changes during the caldera collapse and dyking at bárdarbunga, 2014–2015: Implication for triggering of seismicity at nearby tungnafellsjökull volcano. *Earth and Planetary Science Letters*, *462*, 212–223.

Parmigiani, A., Degruyter, W., Leclaire, S., Huber, C., & Bachmann, O. (2017). The mechanics of shallow magma reservoir outgassing. *Geochemistry, Geophysics, Geosystems*, *18*(8), 2887–2905.

Parmigiani, A., Faroughi, S., Huber, C., Bachmann, O., & Su, Y. (2016). Bubble accumulation and its role in the evolution of magma reservoirs in the upper crust. *Nature*, *532*(7600), 492.

Passey, S. R., & Bell, B. R. (2007). Morphologies and emplacement mechanisms of the lava flows of the Faroe Islands Basalt Group, Faroe Islands, NE Atlantic Ocean. *Bulletin of Volcanology*, *70*(2), 139–156. doi: 10.1007/s00445-007-0125-6

Passmore, E., Maclennan, J., Fitton, G., & Thordarson, T. (2012, sep). Mush disaggregation in basaltic magma chambers: Evidence from the ad 1783 laki eruption. *Journal of*

Petrology, *53*(12), 2593–2623. doi: 10.1093/petrology/egs061

Pastore, Z., Fichler, C., & McEnroe, S. A. (2018, apr). Magnetic anomalies of the mafic/ultramafic seiland igneous province. *Norwegian Journal of Geology*. doi: 10.17850/njg98-1-06

Paterson, M. S., & Wong, T.-f. (2005). *Experimental rock deformation-the brittle field*. Springer Science & Business Media.

Pathak, V., Patil, S., & Shrivastava, J. (2017). Tectonomagmatic setting of lava packages in the mandla lobe of the eastern deccan volcanic province, india: palaeomagnetism and magnetostratigraphic evidence. *Geological Society, London, Special Publications*, *445*(1), 69–94.

Patrick, M., Dietterich, H., Lyons, J., Diefenbach, A., Parcheta, C., Anderson, K., ... Kauahikaua, J. (2019). Cyclic lava effusion during the 2018 eruption of kīlauea volcano. *Science*, *366*(6470).

Patro, P. K., Raju, K., & Sarma, S. (2018). Some insights into the lithospheric electrical structure in the western ghat region from magnetotelluric studies. *Journal of the Geological Society of India*, *92*(5), 529–532.

Patro, P. K., & Sarma, S. (2016a, oct). Evidence for an extensive intrusive component of the deccan large igneous province in the narmada son lineament region, india from three dimensional magnetotelluric studies. *Earth and Planetary Science Letters*, *451*, 168–176. doi: 10.1016/j.epsl.2016.07.005

Patro, P. K., & Sarma, S. (2016b, oct). Evidence for an extensive intrusive component of the deccan large igneous province in the narmada son lineament region, india from three dimensional magnetotelluric studies. *Earth and Planetary Science Letters*, *451*, 168–176. doi: 10.1016/j.epsl.2016.07.005

Pattanayak, S., & Shrivastava, J. (1999). Petrography and major-oxide geochemistry of basalts from the eastern deccan volcanic province, india. *Memoirs-Geological Society of India*(2), 233–270.

Paul, D. K., Ray, A., Das, B., Patil, S. K., & Biswas, S. K. (2008). Petrology, geochemistry and paleomagnetism of the earliest magmatic rocks of deccan volcanic province, kutch, northwest india. *Lithos*, *102*(1-2), 237–259.

Pavlov, V. E., Fluteau, F., Latyshev, A. V., Fetisova, A. M., Elkins-Tanton, L. T., Black, B. A., ... Veselovskiy, R. V. (2019). Geomagnetic secular variations at the permian-triassic boundary and pulsed magmatism during eruption of the siberian traps. *Geochemistry, Geophysics, Geosystems*, *20*(2), 773–791.

Pawar, N. R., Katikar, A. H., Vaddadi, S., Shinde, S. H., Rajaguru, S. N., Joshi, S. V., & Eksambekar, S. P. (2015). The genesis of a lava cave in the deccan volcanic province (maharashtra, india). *International Journal of Speleology*, *45*(1), 6.

Peace, A., McCaffrey, K., Imber, J., van Hunen, J., Hobbs, R., & Wilson, R. (2018). The role of pre-existing structures during rifting, continental breakup and transform system development, offshore west greenland. *Basin Research*, *30*(3), 373–394.

Peacock, J. R., Mangan, M. T., McPhee, D., & Wannamaker, P. E. (2016). Three-dimensional electrical resistivity model of the hydrothermal system in long valley

caldera, california, from magnetotellurics. *Geophysical Research Letters*, *43*(15), 7953–7962.

Peate, D. W., Barker, A. K., Riishuus, M. S., & Andreasen, R. (2008). Temporal variations in crustal assimilation of magma suites in the east greenland flood basalt province: Tracking the evolution of magmatic plumbing systems. *Lithos*, *102*(1-2), 179–197.

Peate, D. W., & Hawkesworth, C. J. (1996). Lithospheric to asthenospheric transition in low-ti flood basalts from southern parana, brazil. *Chemical Geology*, *127*(1-3), 1–24.

Peate, D. W., & Hawkesworth, C. J. (2005). *U series disequilibria: Insights into mantle melting and the timescales of magma differentiation* (Vol. 43) (No. 1). doi: 10.1029/2004RG000154

Pec, M., Holtzman, B. K., Zimmerman, M., & Kohlstedt, D. L. (2015). Reaction infiltration instabilities in experiments on partially molten mantle rocks. *Geology*, *43*(7), 575–578. doi: 10.1130/G36611.1

Pedersen, G., Höskuldsson, A., Dürig, T., Thordarson, T., Jonsdottir, I., Riishuus, M. S., ... others (2017). Lava field evolution and emplacement dynamics of the 2014–2015 basaltic fissure eruption at holuhraun, iceland. *Journal of Volcanology and Geothermal Research*, *340*, 155–169.

Peiffer, L., Wanner, C., & Lewicki, J. L. (2018). Unraveling the dynamics of magmatic co 2 degassing at mammoth mountain, california. *Earth and planetary science letters*, *484*, 318–328.

Peng, Z., & Mahoney, J. (1995). Drillhole lavas from the northwestern deccan traps, and the evolution of réunion hotspot mantle. *Earth and Planetary Science Letters*, *134*(1-2), 169–185.

Peng, Z., Mahoney, J., Hooper, P., Harris, C., & Beane, J. (1994). A role for lower continental crust in flood basalt genesis? isotopic and incompatible element study of the lower six formations of the western deccan traps. *Geochimica et Cosmochimica Acta*, *58*(1), 267–288.

Peng, Z., Mahoney, J., Hooper, P., Macdougall, J., & Krishnamurthy, P. (1998). Basalts of the northeastern deccan traps, india: isotopic and elemental geochemistry and relation to southwestern deccan stratigraphy. *Journal of Geophysical Research: Solid Earth*, *103*(B12), 29843–29865.

Peng, Z., Walter, J., Aster, R., & Nyblade, A. (2014). Antarctic icequakes triggered by the 2010 Maule earthquake in Chile. *Nature ...*, *7*(August), 1–5. doi: 10.1038/NGEO2212

Peng, Z. X., Mahoney, J. J., Vanderkluysen, L., & Hooper, P. R. (2014). Sr, nd and pb isotopic and chemical compositions of central deccan traps lavas and relation to southwestern deccan stratigraphy. *Journal of Asian Earth Sciences*, *84*, 83–94.

Percival, L. M., Jenkyns, H. C., Mather, T. A., Dickson, A. J., Batenburg, S. J., Ruhl, M., ... others (2018). Does large igneous province volcanism always perturb the mercury cycle? comparing the records of oceanic anoxic event 2 and the end-cretaceous to other mesozoic events. *American Journal of Science*, *318*(8), 799–860.

Petcovic, H., & Grunder, A. (2003). Textural and thermal history of partial melting in

tonalitic wallrock at the margin of a basalt dike, wallowa mountains, oregon. *Journal of Petrology*, *44*(12), 2287–2312.

Petcovic, H. L., & Dufek, J. D. (2005). Modeling magma flow and cooling in dikes: Implications for emplacement of columbia river flood basalts. *Journal of Geophysical Research: Solid Earth*, *110*(B10).

Peters, B. J., Day, J. M., Greenwood, R. C., Hilton, D. R., Gibson, J., & Franchi, I. A. (2017). Helium–oxygen–osmium isotopic and elemental constraints on the mantle sources of the deccan traps. *Earth and Planetary Science Letters*, *478*, 245–257.

Petford, N., & Mirhadizadeh, S. (2017). Image-based modelling of lateral magma flow: the basement sill, antarctica. *Royal Society open science*, *4*(5), 161083.

Phillips, O. M. (1991). *Flow and reactions in permeable rocks*. Cambridge University Press.

Philpotts, A. R. (1998). Nature of a flood-basalt-magma reservoir based on the compositional variation in a single flood-basalt flow and its feeder dike in the mesozoic hartford basin, connecticut. *Contributions to mineralogy and petrology*, *133*(1-2), 69–82.

Pichavant, M., Le Gall, N., & Scaillet, B. (2018). Gases as precursory signals: Experimental simulations, new concepts and models of magma degassing.

Pietsch, R., & Uenzelmann-Neben, G. (2015). The manihiki plateau—a multistage volcanic emplacement history. *Geochemistry, Geophysics, Geosystems*, *16*(8), 2480–2498.

Pimienta, L., Sarout, J., Esteban, L., David, C., & Clennell, M. B. (2017). Pressure-dependent elastic and transport properties of porous and permeable rocks: Microstructural control. *Journal of Geophysical Research: Solid Earth*, *122*(11), 8952–8968.

Piombo, A., Tallarico, A., & Dragoni, M. (2016). Role of mechanical erosion in controlling the effusion rate of basaltic eruptions. *Geophysical Research Letters*, *43*(17), 8970–8977.

Pirajno, F., & Van Kranendonk, M. (2005). Review of hydrothermal processes and systems on earth and implications for martian analogues. *Australian Journal of Earth Sciences*, *52*(3), 329–351.

Pitra, P., & De Waal, S. (2001). High-temperature, low-pressure metamorphism and development of prograde symplectites, marble hall fragment, bushveld complex (south africa). *Journal of Metamorphic Geology*, *19*(3), 311–325.

Pollard, D. D., Muller, O. H., & Dockstader, D. R. (1975). The form and growth of fingered sheet intrusions. *Bulletin of the Geological Society of America*, *86*(3), 351–363.

Pollard, D. D., & Segall, P. (1987). Theoretical displacements and stresses near fractures in rock: with applications to faults, joints, veins, dikes, and solution surfaces. In *Fracture mechanics of rock* (pp. 277–347).

Prasad, K., Singh, A., & Tiwari, V. (2018, aug). 3d upper crustal density structure of the deccan syneclise, central india. *Geophysical Prospecting*, *66*(8), 1625–1640. doi: 10.1111/1365-2478.12675

Prasanth, M. M., Hari, K., & Santosh, M. (2019, mar). Tholeiitic basalts of deccan large igneous province, india: An overview. *Geological Journal*. doi: 10.1002/gj.3497

Rabinowicz, M., & Ceuleneer, G. (2005). The effect of sloped isotherms on melt migration in the shallow mantle: A physical and numerical model based on observations

in the Oman ophiolite. *Earth and Planetary Science Letters*, *229*(3-4), 231–246. doi: 10.1016/j.epsl.2004.09.039

Rader, E., Vanderkluysen, L., & Clarke, A. (2017). The role of unsteady effusion rates on inflation in long-lived lava flow fields. *Earth and Planetary Science Letters*, *477*, 73–83.

Rajaram, M., Anand, S. P., Erram, V. C., & Shinde, B. N. (2016, sep). Insight into the structures below the deccan trap-covered region of maharashtra, india from geopotential data. *Geological Society, London, Special Publications*, *445*(1), 219–236. doi: 10.1144/sp445.8

Ramakrishnan, M., & Vaidyanadhan, R. (2010). Geology of india (vol. 1 & 2). *GSI Publications*, *2*(1).

Rao, G. S., Kumar, M., & Radhakrishna, M. (2018, feb). Structure, mechanical properties and evolution of the lithosphere below the northwest continental margin of india. *International Journal of Earth Sciences*, *107*(6), 2191–2207. doi: 10.1007/s00531-018-1594-x

Rao, Y. B., Sreenivas, B., Kumar, T. V., Khadke, N., Krishna, A. K., & Babu, E. (2017). Evidence for neoarchean basement for the deccan volcanic flows around koyna-warna region, western india: Zircon u-pb age and hf-isotopic results. *Journal of the Geological Society of India*, *90*(6), 752–760.

Ray, A., Hatui, K., Paul, D. K., Sen, G., Biswas, S., & Das, B. (2016, feb). Mantle xenolith-xenocryst-bearing monogenetic alkali basaltic lava field from kutch basin, gujarat, western india: Estimation of magma ascent rate. *Journal of Volcanology and Geothermal Research*, *312*, 40–52. doi: 10.1016/j.jvolgeores.2016.01.015

Ray, A., Paul, D., Patil, S., Das, B., & Biswas, S. (2010). Petrology, geochemistry and petrogenesis of the magmatic rocks of pachcham island, kutch, northwestern india. *Origin and Evolution of Deep Continental Crust. Narosa Publishing House Pvt. Ltd, New Delhi*, 217–236.

Ray, J. S., & Parthasarathy, G. (2019). Recent advancement in studies of deccan trap and its basement; carbonatites and kimberlites–an indian perspective in last five years. *Proceedings of the Indian National Science Academy*, *85*(2), 481–492.

Ray, L., Nagaraju, P., Singh, S., Ravi, G., & Roy, S. (2016). Radioelemental, petrological and geochemical characterization of the bundelkhand craton, central india: implication in the archaean geodynamic evolution. *International Journal of Earth Sciences*, *105*(4), 1087–1107.

Ray, R., Sheth, H. C., & Mallik, J. (2007). Structure and emplacement of the nandurbar–dhule mafic dyke swarm, deccan traps, and the tectonomagmatic evolution of flood basalts. *Bulletin of Volcanology*, *69*(5), 537.

Ray, R., Shukla, A. D., Sheth, H. C., Ray, J. S., Duraiswami, R. A., Vanderkluysen, L., ... Mallik, J. (2008). Highly heterogeneous precambrian basement under the central deccan traps, india: direct evidence from xenoliths in dykes. *Gondwana Research*, *13*(3), 375–385.

Redmond, P. B., & Einaudi, M. T. (2010). The bingham canyon porphyry cu-mo-au deposit.

i. sequence of intrusions, vein formation, and sulfide deposition. *Economic Geology*, *105*(1), 43–68.

Regenauer-Lieb, K., & Yuen, D. (2004). Positive feedback of interacting ductile faults from coupling of equation of state, rheology and thermal-mechanics. *Physics of the Earth and Planetary Interiors*, *142*(1-2), 113–135.

Reichow, M. K., Saunders, A., White, R., Al'Mukhamedov, A., & Medvedev, A. Y. (2005). Geochemistry and petrogenesis of basalts from the west siberian basin: an extension of the permo–triassic siberian traps, russia. *Lithos*, *79*(3-4), 425–452.

Reidel, S., Tolan, T., & Camp, V. (2018). Columbia river flood basalt flow emplacement rates—fast, slow, or variable. *Field Volcanology: A Tribute to the Distinguished Career of Don Swanson: Geological Society of America Special Paper*, *538*, 1–19.

Reidel, S. P. (1998). Emplacement of columbia river flood basalt. *Journal of Geophysical Research: Solid Earth*, *103*(B11), 27393–27410.

Reidel, S. P. (2005). A lava flow without a source: The cohassett flow and its compositional components, sentinel bluffs member, columbia river basalt group. *The Journal of geology*, *113*(1), 1–21.

Reidel, S. P., Camp, V. E., Tolan, T. L., & Martin, B. S. (2013). The columbia river flood basalt province: Stratigraphy, areal extent, volume, and physical volcanology. *The Columbia River flood basalt province: geological society of America special paper*, *497*, 1–43.

Reinsch, T., Dobson, P., Asanuma, H., Huenges, E., Poletto, F., & Sanjuan, B. (2017). Utilizing supercritical geothermal systems: a review of past ventures and ongoing research activities. *Geothermal Energy*, *5*(1), 16.

Renne, P. R., Balco, G., Ludwig, K. R., Mundil, R., & Min, K. (2011). Response to the comment by wh schwarz et al. on "joint determination of 40k decay constants and 40ar/40k for the fish canyon sanidine standard, and improved accuracy for 40ar/39ar geochronology" by pr renne et al.(2010). *Geochimica et Cosmochimica Acta*, *75*(17), 5097–5100.

Renne, P. R., Sprain, C. J., Richards, M. A., Self, S., Vanderkluysen, L., & Pande, K. (2015). State shift in deccan volcanism at the cretaceous-paleogene boundary, possibly induced by impact. *Science*, *350*(6256), 76–78.

Ribe, N. M. (1986). Melt segregation driven by dynamic forcing. *Geophysical Research Letters*, *13*(13), 1462–1465.

Ribe, N. M. (1996, jul). The dynamics of plume-ridge interaction: 2. Off-ridge plumes. *Journal of Geophysical Research: Solid Earth*, *101*(B7), 16195–16204. doi: 10.1029/96JB01187

Richards, M., Contreras-Reyes, E., Lithgow-Bertelloni, C., Ghiorso, M., & Stixrude, L. (2013). Petrological interpretation of deep crustal intrusive bodies beneath oceanic hotspot provinces. *Geochemistry, Geophysics, Geosystems*, *14*(3), 604–619. doi: 10.1029/2012GC004448

Richards, M. A., Alvarez, W., Self, S., Karlstrom, L., Renne, P. R., Manga, M., ... Gibson, S. A. (2015). Triggering of the largest deccan eruptions by the chicxulub impact. *GSA*

Bulletin, *127*(11-12), 1507–1520.

Richards, M. A., Duncan, R. A., & Courtillot, V. E. (1989). Flood basalts and hot-spot tracks: plume heads and tails. *Science*, *246*(4926), 103–107.

Richards, M. A., & Griffiths, R. W. (1988). Deflection of plumes by mantle shear flow: experimental results and a simple theory. *Geophysical Journal*, *94*(September), 367–376. doi: 10.1111/j.1365-246X.1988.tb02260.x

Richardson, P., & Karlstrom, L. (2019). The multi-scale influence of topography on lava flow morphology. *Bulletin of Volcanology*, *81*(4), 21.

Richter, F. M., & McKenzie, D. (1984, nov). Dynamical Models for Melt Segregation from a Deformable Matrix. *The Journal of Geology*, *92*(6), 729–740. Retrieved from `http://www.journals.uchicago.edu/doi/10.1086/628908` doi: 10.1086/628908

Ridley, V. A., & Richards, M. A. (2010). Deep crustal structure beneath large igneous provinces and the petrologic evolution of flood basalts. *Geochemistry, Geophysics, Geosystems*, *11*(9), 1–21. doi: 10.1029/2009GC002935

Riisager, J., Riisager, P., & Pedersen, A. K. (2003). Paleomagnetism of large igneous provinces: case-study from west greenland, north atlantic igneous province. *Earth and Planetary Science Letters*, *214*(3-4), 409–425.

Rivalta, E. (2010). Evidence that coupling to magma chambers controls the volume history and velocity of laterally propagating intrusions. *Journal of Geophysical Research: Solid Earth*, *115*(B7).

Rivalta, E., & Segall, P. (2008). Magma compressibility and the missing source for some dike intrusions. *Geophysical Research Letters*, *35*(4).

Rivalta, E., Taisne, B., Bunger, A. P., & Katz, R. F. (2015). A review of mechanical models of dike propagation: Schools of thought, results and future directions. *Tectonophysics*, *638*(C), 1–42. doi: 10.1016/j.tecto.2014.10.003

Robb, S. J., & Mungall, J. E. (2020). Testing emplacement models for the rustenburg layered suite of the bushveld complex with numerical heat flow models and plagioclase geospeedometry. *Earth and Planetary Science Letters*, *534*, 116084.

Rogie, J. D., Kerrick, D. M., Sorey, M. L., Chiodini, G., & Galloway, D. L. (2001). Dynamics of carbon dioxide emission at mammoth mountain, california. *Earth and Planetary Science Letters*, *188*(3-4), 535–541.

Rohrbach, A., & Schmidt, M. W. (2011). Redox freezing and melting in the earth's deep mantle resulting from carbon–iron redox coupling. *Nature*, *472*(7342), 209–212.

Roland, E., Behn, M. D., & Hirth, G. (2010). Thermal-mechanical behavior of oceanic transform faults: Implications for the spatial distribution of seismicity. *Geochemistry, Geophysics, Geosystems*, *11*(7). doi: 10.1029/2010GC003034

Roman, A., & Jaupart, C. (2016, nov). The fate of mafic and ultramafic intrusions in the continental crust. *Earth and Planetary Science Letters*, *453*, 131–140. doi: 10.1016/j.epsl.2016.07.048

Roman, A., & Jaupart, C. (2017). Postemplacement dynamics of basaltic intrusions in the continental crust. *Journal of Geophysical Research: Solid Earth*, *122*(2), 966–987.

Rooney, T. O., Bastow, I. D., Keir, D., Mazzarini, F., Movsesian, E., Grosfils, E. B., ...

Yirgu, G. (2014, jun). The protracted development of focused magmatic intrusion during continental rifting. *Tectonics*, *33*(6), 875–897. doi: 10.1002/2013TC003514

Rowland, S. K., & Walker, G. P. (1990). Pahoehoe and aa in hawaii: volumetric flow rate controls the lava structure. *Bulletin of Volcanology*, *52*(8), 615–628.

Rozhko, A., Podladchikov, Y., & Renard, F. (2007). Failure patterns caused by localized rise in pore-fluid overpressure and effective strength of rocks. *Geophysical Research Letters*, *34*(22).

Rubin, A. M. (1995). Propagation of magma-filled cracks. *Annual Review of Earth and Planetary Sciences*, *23*(1), 287–336.

Rummel, L., Kaus, B. J., White, R. W., Mertz, D. F., Yang, J., & Baumann, T. S. (2018). Coupled petrological-geodynamical modeling of a compositionally heterogeneous mantle plume. *Tectonophysics*, *723*, 242–260.

Ryan, W. B., Carbotte, S. M., Coplan, J. O., O'Hara, S., Melkonian, A., Arko, R., ... others (2009). Global multi-resolution topography synthesis. *Geochemistry, Geophysics, Geosystems*, *10*(3).

Saffman, P., & Taylor, G. (1958, may). The penetration of a fluid into a porous medium or Hele-Shaw cell containing a .... *Proceedings of the Royal Society of London. ....*

Sager, W. W., Huang, Y., Tominaga, M., Greene, J. A., Nakanishi, M., & Zhang, J. (2019). Oceanic plateau formation by seafloor spreading implied by tamu massif magnetic anomalies. *Nature Geoscience*, *12*(8), 661–666.

Samant, H., Patel, V., Pande, K., Sheth, H., & Jagadeesan, K. (2019). 40ar/39ar dating of tholeiitic flows and dykes of elephanta island, panvel flexure zone, western deccan traps: A five-million-year record of magmatism preceding india-laxmi ridge-seychelles breakup. *Journal of Volcanology and Geothermal Research*, *379*, 12–22.

Sano, T., Fujii, T., Deshmukh, S., Fukuoka, T., & Aramaki, S. (2001). Differentiation processes of deccan trap basalts: contribution from geochemistry and experimental petrology. *Journal of Petrology*, *42*(12), 2175–2195.

Sant, D., & Karanth, R. (1990). Emplacement of dyke swarms in lower narmada valley, western india. In *International dyke conference. 2* (pp. 383–389).

Saunders, A., Jones, S., Morgan, L., Pierce, K., Widdowson, M., & Xu, Y. (2007). Regional uplift associated with continental large igneous provinces: the roles of mantle plumes and the lithosphere. *Chemical Geology*, *241*(3-4), 282–318.

Scheibert, J., Galland, O., & Hafver, A. (2017). Inelastic deformation during sill and laccolith emplacement: Insights from an analytic elastoplastic model. *Journal of Geophysical Research: Solid Earth*, *122*(2), 923–945.

Schiemenz, A., Liang, Y., & Parmentier, E. M. (2011). A high-order numerical study of reactive dissolution in an upwelling heterogeneous mantle-I. Channelization, channel lithology and channel geometry. *Geophysical Journal International*, *186*(2), 641–664. doi: 10.1111/j.1365-246X.2011.05065.x

Schilling, J. (1973, nov). Iceland mantle plume. *Nature*, *246*(16 November), 141–143. doi: 10.1038/246141a0

Schilling, J. (1991). Fluxes and excess temperatures of mantle plumes inferred from

their interaction with migrating mid-ocean ridges. *Nature*, *352*(1), 397–403. doi: 10.1038/352397a0

Schilling, J.-G., Fontignie, D., Blichert-Toft, J., Kingsley, R., & Tomza, U. (2003, oct). Pb-Hf-Nd-Sr isotope variations along the Galápagos Spreading Center (101o-83oW): Constraints on the dispersal of the Galápagos mantle plume. *Geochemistry, Geophysics, Geosystems*, *4*(10), n/a–n/a. doi: 10.1029/2002GC000495

Schilling, J.-G., Kingsley, R. H., & Devine, J. D. (1982). Galapagos Hot Spot-Spreading Center System 1. Spatial Petrological and Geochemical Variations (83W-101W). *Journal of Geophysical Research*, *87*, 5593–5610. doi: 10.1029/JB087iB07p05593

Schilling, J. G., Thompson, G., Kingsley, R., & Humphris, S. (1985). Hotspot—migrating ridge interaction in the South Atlantic. *Nature*, *313*(5999), 187–191. doi: 10.1038/313187a0

Schmeling, H., Marquart, G., & Grebe, M. (2018). A porous flow approach to model thermal non-equilibrium applicable to melt migration. *Geophysical Journal International*, *212*(1), 119–138.

Schmeling, H., Marquart, G., Weinberg, R., & Wallner, H. (2019, jan). Modelling melting and melt segregation by two-phase flow: new insights into the dynamics of magmatic systems in the continental crust. *Geophysical Journal International*, *217*(1), 422–450. doi: 10.1093/gji/ggz029

Schmidt, A., Skeffington, R. A., Thordarson, T., Self, S., Forster, P. M., Rap, A., ... others (2016). Selective environmental stress from sulphur emitted by continental flood basalt eruptions. *Nature Geoscience*, *9*(1), 77–82.

Schöbel, S., de Wall, H., Ganerød, M., Pandit, M. K., & Rolf, C. (2014). Magnetostratigraphy and 40ar–39ar geochronology of the malwa plateau region (northern deccan traps), central western india: Significance and correlation with the main deccan large igneous province sequences. *Journal of Asian Earth Sciences*, *89*, 28–45.

Schoene, B., Eddy, M. P., Samperton, K. M., Keller, C. B., Keller, G., Adatte, T., & Khadri, S. F. (2019). U-pb constraints on pulsed eruption of the deccan traps across the end-cretaceous mass extinction. *Science*, *363*(6429), 862–866.

Schoene, B., Samperton, K. M., Eddy, M. P., Keller, G., Adatte, T., Bowring, S. A., ... Gertsch, B. (2015). U-pb geochronology of the deccan traps and relation to the end-cretaceous mass extinction. *Science*, *347*(6218), 182–184.

Schofield, N., Brown, D. J., Magee, C., & Stevenson, C. T. (2012). Sill morphology and comparison of brittle and non-brittle emplacement mechanisms. *Journal of Structural Geology*, *169*(Baer 1995), 127–141. doi: 10.1144/0016-76492011-078.Sill

Schofield, N., Holford, S., Millett, J., Brown, D., Jolley, D., Passey, S. R., ... others (2017). Regional magma plumbing and emplacement mechanisms of the faroe-shetland sill complex: implications for magma transport and petroleum systems within sedimentary basins. *Basin Research*, *29*(1), 41–63.

Scoon, R. N., & Costin, G. (2018). Chemistry, morphology and origin of magmatic-reaction chromite stringers associated with anorthosite in the upper critical zone at winnaarshoek, eastern limb of the bushveld complex. *Journal of Petrology*, *59*(8),

1551–1578.

Scott, D. R., & Stevenson, D. J. (1984). Magma solitons. *Geophysical Research Letters*, *11*(11), 1161–1164. doi: 10.1029/GL011i011p01161

Segall, P. (2016). Repressurization following eruption from a magma chamber with a viscoelastic aureole. *Journal of Geophysical Research: Solid Earth*, *121*(12), 8501–8522.

Segall, P. (2019). Magma chambers: what we can, and cannot, learn from volcano geodesy. *Philosophical Transactions of the Royal Society A*, *377*(2139), 20180158.

Self, S., Jay, A. E., Widdowson, M., & Keszthelyi, L. P. (2008). Correlation of the deccan and rajahmundry trap lavas: Are these the longest and largest lava flows on earth? *Journal of Volcanology and Geothermal Research*, *172*(1-2), 3–19.

Self, S., Keszthelyi, L., & Thordarson, T. (1998). The importance of pāhoehoe. *Annual Review of Earth and Planetary Sciences*, *26*(1), 81–110.

Self, S., Schmidt, A., & Mather, T. (2014). Emplacement characteristics, time scales, and volcanic gas release rates of continental flood basalt eruptions on earth. *Geological Society of America Special Papers*, *505*.

Self, S., Thordarson, T., & Keszthelyi, L. (1997). Emplacement of continental flood basalt lava flows. *Geophysical Monograph - American Geophysical Union*, *100*, 381–410.

Self, S., Widdowson, M., Thordarson, T., & Jay, A. E. (2006). Volatile fluxes during flood basalt eruptions and potential effects on the global environment: A Deccan perspective. *Earth and Planetary Science Letters*, *248*(1-2), 517–531. doi: 10.1016/j.epsl.2006.05.041

Sen, A., Pande, K., Hegner, E., Sharma, K. K., Dayal, A., Sheth, H. C., & Mistry, H. (2012). Deccan volcanism in rajasthan: 40ar–39ar geochronology and geochemistry of the tavidar volcanic suite. *Journal of Asian Earth Sciences*, *59*, 127–140.

Sen, B. (2017). Lava flow transition in pāhoehoe-dominated lower pile of deccan traps from manmad-chandwad area, western maharashtra. *Journal of the Geological Society of India*, *89*(3), 281–290.

Sen, G. (2001). Generation of deccan trap magmas. *Journal of Earth System Science*, *110*(4), 409–431.

Sen, G., Bizimis, M., Das, R., Paul, D. K., Ray, A., & Biswas, S. (2009). Deccan plume, lithosphere rifting, and volcanism in kutch, india. *Earth and Planetary Science Letters*, *277*(1-2), 101–111.

Sen, G., & Chandrasekharam, D. (2011). Deccan traps flood basalt province: An evaluation of the thermochemical plume model. In *Topics in igneous petrology* (pp. 29–53). Springer.

Sengupta, P., & Ray, A. (2006). Primary volcanic structures from a type section of deccan trap flows around narsingpur-harrai-amarwara, central india: Implications for cooling history. *Journal of earth system science*, *115*(6), 631–642.

Sengupta, P., & Ray, J. (2011). Petrology of the mafic sill of narshingpur-lakhnadon section, eastern deccan volcanic province. *Journal of the Geological Society of India*, *77*(4), 309–327.

Seshu, D., Rao, P. R., & Naganjaneyulu, K. (2016, jan). Three-dimensional gravity mod-

elling of kutch region, india. *Journal of Asian Earth Sciences*, *115*, 16–28. doi: 10.1016/j.jseaes.2015.09.015

Shaw, H., & Swanson, D. A. (1970). Eruption and flow rates of flood basalts. In *Proceedings of the second columbia river basalt symposium* (pp. 271–299).

Shellnutt, J. G., Yeh, M.-W., Suga, K., Lee, T.-Y., Lee, H.-Y., & Lin, T.-H. (2017). Temporal and structural evolution of the early palaeogene rocks of the seychelles microcontinent. *Scientific reports*, *7*(1), 1–7.

Shelly, D. R., Ellsworth, W. L., & Hill, D. P. (2016). Fluid-faulting evolution in high definition: Connecting fault structure and frequency-magnitude variations during the 2014 long valley caldera, california, earthquake swarm. *Journal of Geophysical Research: Solid Earth*, *121*(3), 1776–1795.

Sheth, H. (2016). Giant plagioclase basalts: Continental flood basalt–induced remobilization of anorthositic mushes in a deep crustal sill complex. *Bulletin*, *128*(5-6), 916–925.

Sheth, H., & Chandrasekharam, D. (1997). Early alkaline magmatism in the deccan traps: implications for plume incubation and lithospheric rifting. *Physics of the Earth and Planetary Interiors*, *104*(4), 371–376.

Sheth, H., Mahoney, J., & Chandrasekharam, D. (2004). Geochemical stratigraphy of deccan flood basalts of the bijasan ghat section, satpura range, india. *Journal of Asian Earth Sciences*, *23*(1), 127–139.

Sheth, H., Pande, K., Vijayan, A., Sharma, K. K., & Cucciniello, C. (2017). Recurrent early cretaceous, indo-madagascar (89–86 ma) and deccan (66 ma) alkaline magmatism in the sarnu-dandali complex, rajasthan: 40ar/39ar age evidence and geodynamic significance. *Lithos*, *284*, 512–524.

Sheth, H., Vanderkluysen, L., Demonterova, E. I., Ivanov, A. V., & Savatenkov, V. M. (2018, mar). Geochemistry and 40 ar/39 ar geochronology of the nandurbar-dhule mafic dyke swarm: Dyke-sill-flow correlations and stratigraphic development across the deccan flood basalt province. *Geological Journal*, *54*(1), 157–176. doi: 10.1002/gj.3167

Sheth, H., Vanderkluysen, L., Demonterova, E. I., Ivanov, A. V., & Savatenkov, V. M. (2019). Geochemistry and 40ar/39ar geochronology of the nandurbar-dhule mafic dyke swarm: Dyke-sill-flow correlations and stratigraphic development across the deccan flood basalt province. *Geological Journal*, *54*(1), 157–176.

Sheth, H. C. (2005). Were the deccan flood basalts derived in part from ancient oceanic crust within the indian continental lithosphere? *Gondwana Research*, *8*(2), 109–127.

Sheth, H. C., & Cañón-Tapia, E. (2015). Are flood basalt eruptions monogenetic or polygenetic? *International Journal of Earth Sciences*, *104*(8), 2147–2162.

Sheth, H. C., & Melluso, L. (2008). The mount pavagadh volcanic suite, deccan traps: geochemical stratigraphy and magmatic evolution. *Journal of Asian Earth Sciences*, *32*(1), 5–21.

Sheth, H. C., Pande, K., & Bhutani, R. (2001a). 40 ar-39 ar age of a national geological monument: the gilbert hill basalt, deccan traps, bombay. *Current Science (Bangalore)*, *80*(11), 1437–1440.

Sheth, H. C., Pande, K., & Bhutani, R. (2001b). 40ar-39ar ages of bombay trachytes:

Evidence for a palaeocene phase of deccan volcanism. *Geophysical Research Letters*, *28*(18), 3513–3516.

Sheth, H. C., Ray, J. S., Ray, R., Vanderkluysen, L., Mahoney, J. J., Kumar, A., ... Jana, B. (2009). Geology and geochemistry of pachmarhi dykes and sills, satpura gondwana basin, central india: problems of dyke-sill-flow correlations in the deccan traps. *Contributions to Mineralogy and Petrology*, *158*(3), 357.

Sheth, H. C., Zellmer, G. F., Demonterova, E. I., Ivanov, A. V., Kumar, R., & Patel, R. K. (2014). The deccan tholeiite lavas and dykes of ghatkopar–powai area, mumbai, panvel flexure zone: geochemistry, stratigraphic status, and tectonic significance. *Journal of Asian Earth Sciences*, *84*, 69–82.

Sheth, H. C., Zellmer, G. F., Kshirsagar, P. V., & Cucciniello, C. (2013). Geochemistry of the palitana flood basalt sequence and the eastern saurashtra dykes, deccan traps: clues to petrogenesis, dyke–flow relationships, and regional lava stratigraphy. *Bulletin of Volcanology*, *75*(4), 701.

Shinohara, H. (2013). Volatile flux from subduction zone volcanoes: Insights from a detailed evaluation of the fluxes from volcanoes in japan. *Journal of Volcanology and Geothermal Research*, *268*, 46–63.

Shorttle, O., MacLennan, J., & Jones, S. M. (2010). Control of the symmetry of plume-ridge interaction by spreading ridge geometry. *Geochemistry, Geophysics, Geosystems*, *11*(7), 1–27. doi: 10.1029/2009GC002986

Shrivastava, J., Duncan, R. A., & Kashyap, M. (2015). Post-k/pb younger 40ar–39ar ages of the mandla lavas: implications for the duration of the deccan volcanism. *Lithos*, *224*, 214–224.

Shrivastava, J., Kumar, R., & Rani, N. (2017). Feeder and post deccan trap dyke activities in the northern slope of the satpura mountain: Evidence from new 40ar-39ar ages. *Geoscience Frontiers*, *8*(3), 483–492.

Shrivastava, J., Mahoney, J., & Kashyap, M. (2014). Trace elemental and nd-sr-pb isotopic compositional variation in 37 lava flows of the mandla lobe and their chemical relation to the western deccan stratigraphic succession, india. *Mineralogy and Petrology*, *108*(6), 801–817.

Shrivastava, J., MUKTA, G., & RAJU, K. (2008). Petrography, composition and petrogenesis of basalts from chakhla-delakhari intrusive complex, eastern deccan volcanic province, india. indian dykes: Geochemistry. *Geophysics and Geochronology*, 83–108.

Shrivastava, J., & Pattanayak, S. (2002). Basalts of the eastern deccan volcanic province, india. *Gondwana Research*, *5*(3), 649–665.

Shukla, A., Bhandari, N., Kusumgar, S., Shukla, P., Ghevariya, Z., Gopalan, K., & Balaram, V. (2001). Geochemistry and magnetostratigraphy of deccan flows at anjar, kutch. *Journal of Earth System Science*, *110*(2), 111–132.

Sial, A., Lacerda, L., Ferreira, V., Frei, R., Marquillas, R., Barbosa, J., ... Pereira, N. (2013). Mercury as a proxy for volcanic activity during extreme environmental turnover: The cretaceous–paleogene transition. *Palaeogeography, Palaeoclimatology, Palaeoecology*, *387*, 153–164.

Sibson, R., Moore, J. M. M., & Rankin, A. (1975). Seismic pumping—a hydrothermal fluid transport mechanism. *Journal of the Geological Society*, *131*(6), 653–659.

Sibson, R. H. (1987). Earthquake rupturing as a mineralizing agent in hydrothermal systems. *Geology*, *15*(8), 701–704.

Sibson, R. H. (2017). The edge of failure: critical stress overpressure states in different tectonic regimes. *Geological Society, London, Special Publications*, *458*(1), 131–141.

Simakin, A., & Botcharnikov, R. (2001). Degassing of stratified magma by compositional convection. *Journal of volcanology and geothermal research*, *105*(3), 207–224.

Singh, A., Singh, C., & Kennett, B. L. N. (2015). Tectonophysics A review of crust and upper mantle structure beneath the Indian subcontinent. *Tectonophysics*, *644-645*, 1–21. doi: 10.1016/j.tecto.2015.01.007

Singh, B., Rao, M. P., Prajapati, S., & Swarnapriya, C. (2014a). Combined gravity and magnetic modeling over pavagadh and phenaimata igneous complexes, gujarat, india: Inference on emplacement history of deccan volcanism. *Journal of Asian Earth Sciences*, *80*, 119–133.

Singh, B., Rao, M. P., Prajapati, S., & Swarnapriya, C. (2014b, feb). Combined gravity and magnetic modeling over pavagadh and phenaimata igneous complexes, gujarat, india: Inference on emplacement history of deccan volcanism. *Journal of Asian Earth Sciences*, *80*, 119–133. doi: 10.1016/j.jseaes.2013.11.005

Sinton, C. W., Christie, D. M., & Duncan, R. A. (1996). Geochronology of Galápagos seamounts. *Journal of Geophysical Research*, *101*(B6), 13689. doi: 10.1029/96JB00642

Sinton, J., Detrick, R., Canales, J. P., Ito, G., & Behn, M. (2003, dec). Morphology and segmentation of the western Galápagos Spreading Center, 90.5°-98°W: Plume-ridge interaction at an intermediate spreading ridge. *Geochemistry, Geophysics, Geosystems*, *4*(12), n/a–n/a. doi: 10.1029/2003GC000609

Sisson, T., & Bacon, C. (1999). Gas-driven filter pressing in magmas. *Geology*, *27*(7), 613–616.

Sleep, N. H. (2008). Channeling at the base of the lithosphere during the lateral flow of plume material beneath flow line hot spots. *Geochemistry, Geophysics, Geosystems*, *9*(8). doi: 10.1029/2008GC002090

Small, C. (1995). Observations of ridge-hotspot interactions in the Southern Ocean. *Journal of Geophysical Research*, *100946*(10), 931–17. doi: 10.1029/95JB01377

Smith, K., & Cann, R. (1992). The role of seamount volcanism in crustal construction at the mid-atlantic ridge (24-30 N). *Journal of Geophysical Research*, *97*, 1645–1658. doi: 10.1029/91JB02507

Snyder, D., & Tait, S. (1995). Replenishment of magma chambers: comparison of fluid-mechanic experiments with field relations. *Contributions to Mineralogy and Petrology*, *122*(3), 230–240. doi: 10.1007/s004100050123

Sobolev, S. V., Sobolev, A. V., Kuzmin, D. V., Krivolutskaya, N. a., Petrunin, A. G., Arndt, N. T., ... Vasiliev, Y. R. (2011). Linking mantle plumes, large igneous provinces and environmental catastrophes. *Nature*, *477*(7364), 312–316. doi: 10.1038/nature10385

Solano, J., Jackson, M., Sparks, R., Blundy, J., & Annen, C. (2012). Melt segregation in deep crustal hot zones: a mechanism for chemical differentiation, crustal assimilation and the formation of evolved magmas. *Journal of Petrology*, *53*(10), 1999–2026.

Solano, J. M. S., Jackson, M. D., Sparks, R. S. J., Blundy, J. D., & Annen, C. (2012). Melt segregation in deep crustal hot zones: A mechanism for chemical differentiation, crustal assimilation and the formation of evolved magmas. *Journal of Petrology*, *53*(10), 1999–2026. doi: 10.1093/petrology/egs041

Song, X.-Y., Zhou, M.-F., Keays, R. R., Cao, Z.-M., Sun, M., & Qi, L. (2006). Geochemistry of the emeishan flood basalts at yangliuping, sichuan, sw china: implications for sulfide segregation. *Contributions to Mineralogy and Petrology*, *152*(1), 53–74.

Sørensen, B. E., Grant, T., Ryan, E. J., & Larsen, R. B. (2019). In situ evidence of earthquakes near the crust mantle boundary initiated by mantle co2 fluxing and reaction-driven strain softening. *Earth and Planetary Science Letters*, *524*, 115713.

Sparks, D. W., & Parmentier, E. M. (1991). Melt extraction from the mantle beneath spreading centers. *Earth and Planetary Science Letters*, *105*(4), 368–377. doi: 10.1016/0012-821X(91)90178-K

Sparks, R., Annen, C., Blundy, J., Cashman, K., Rust, A., & Jackson, M. (2019). Formation and dynamics of magma reservoirs. *Philosophical Transactions of the Royal society A*, *377*(2139), 20180019.

Spera, F. J., & Bohrson, W. A. (2001). Energy-constrained open-system magmatic processes i: General model and energy-constrained assimilation and fractional crystallization (ec-afc) formulation. *Journal of Petrology*, *42*(5), 999–1018.

Spera, F. J., & Bohrson, W. A. (2002). Energy-constrained open-system magmatic processes 3. energy-constrained recharge, assimilation, and fractional crystallization (ec-rafc). *Geochemistry, Geophysics, Geosystems*, *3*(12), 1–20.

Spiegelman, M. (1993a). Flow in deformable porous media. Part 1 Simple analysis. *Journal of Fluid Mechanics*, *247*(-1), 17. doi: 10.1017/S0022112093000369

Spiegelman, M. (1993b). Physics of Melt Extraction: Theory, Implications and Applications. *Philosophical Transactions of the Royal Society A: Mathematical, Physical and Engineering Sciences*, *342*(1663), 23–41. doi: 10.1098/rsta.1993.0002

Spiegelman, M. (1993c, jan). Physics of Melt Extraction: Theory, Implications and Applications. *Philosophical Transactions of the Royal Society A: Mathematical, Physical and Engineering Sciences*, *342*(1663), 23–41. doi: 10.1098/rsta.1993.0002

Spiegelman, M., & Kelemen, P. B. (2003). Extreme chemical variability as a consequence of channelized melt transport. *Geochemistry, Geophysics, Geosystems*, *4*(7). doi: 10.1029/2002GC000336

Spiegelman, M., Kelemen, P. B., & Aharonov, E. (2001). *Causes and consequences of flow organization during melt transport: The reaction infiltration instability in compactible media* (Vol. 106) (No. B2). doi: 10.1029/2000JB900240

Spiegelman, M., & McKenzie, D. (1987). Simple 2-D models for melt extraction at mid-ocean ridges and island arcs. *Earth and Planetary Science Letters*, *83*(1-4), 137–152. doi: 10.1016/0012-821X(87)90057-4

Sprain, C. J., Renne, P. R., Clemens, W. A., & Wilson, G. P. (2018). Calibration of chron c29r: New high-precision geochronologic and paleomagnetic constraints from the hell creek region, montana. *Bulletin*, *130*(9-10), 1615–1644.

Sprain, C. J., Renne, P. R., Vanderkluysen, L., Pande, K., Self, S., & Mittal, T. (2019). The eruptive tempo of deccan volcanism in relation to the cretaceous-paleogene boundary. *Science*, *363*(6429), 866–870.

Sreejith, K. M., & Krishna, K. S. (2015). Magma production rate along the Ninetyeast Ridge and its relationship to Indian plate motion and Kerguelen hot spot activity. *Geophysical Research Letters*, *42*(4), 1105–1112. doi: 10.1002/2014GL062993

Stagno, V., Ojwang, D. O., McCammon, C. A., & Frost, D. J. (2013). The oxidation state of the mantle and the extraction of carbon from earth's interior. *Nature*, *493*(7430), 84–88.

Stein, C. A., & Stein, S. (1994). Constraints on hydrothermal heat flux through the oceanic lithosphere from global heat flow. *Journal of Geophysical Research: Solid Earth*, *99*(B2), 3081 - 3095.

Stevenson, D. J. (1989). Spontaneous small-scale melt segregation in partial melts undergoing deformation. *Geophysical Research Letters*, *16*(9), 1067. doi: 10.1029/GL016i009p01067

Stober, I., & Bucher, K. (2015). Hydraulic conductivity of fractured upper crust: insights from hydraulic tests in boreholes and fluid-rock interaction in crystalline basement rocks. *Geofluids*, *15*(1-2), 161–178.

Suarez, C. A., Edmonds, M., & Jones, A. P. (2019, oct). Earth catastrophes and their impact on the carbon cycle. *Elements*, *15*(5), 301–306. doi: 10.2138/gselements.15.5.301

Subbarao, K., Bodas, M., Hooper, P., & Walsh, J. (1988). Petrogenesis of jawhar and igatpuri formations, western deccan basalt province. *Memoir-Geological Society of India*(10), 253–280.

Subbarao, K. V. (1988). *Deccan flood basalts* (Vol. 10). Geological Society of India.

Sukheswala, R. (1981). Deccan basalt volcanism. *Memoir-Geological Society of India*(3), 8–18.

Svensen, H., Corfu, F., Polteau, S., Hammer, Ø., & Planke, S. (2012). Rapid magma emplacement in the karoo large igneous province. *Earth and Planetary Science Letters*, *325*, 1–9.

Svensen, H., Torsvik, T., Callegaro, S., Augland, L., Heimdal, T., Jerram, D., ... Pereira, E. (2018). Gondwana large igneous provinces: plate reconstructions, volcanic basins and sill volumes. *Geological Society, London, Special Publications*, *463*(1), 17–40.

Svensen, H. H., Frolov, S., Akhmanov, G. G., Polozov, A. G., Jerram, D. A., Shiganova, O. V., ... Planke, S. (2018). Sills and gas generation in the siberian traps. *Philosophical Transactions of the Royal Society A: Mathematical, Physical and Engineering Sciences*, *376*(2130), 20170080.

Taisne, B., & Tait, S. (2011). Effect of solidification on a propagating dike. *Journal of Geophysical Research: Solid Earth*, *116*(1), 1–14. doi: 10.1029/2009JB007058

Taisne, B., Tait, S., & Jaupart, C. (2011). Conditions for the arrest of a vertical propagating dyke. *Bulletin of Volcanology*, *73*(2), 191–204.

Takei, Y., & Katz, R. F. (2013, nov). Consequences of viscous anisotropy in a deforming, two-phase aggregate. Part 1. Governing equations and linearized analysis. *Journal of Fluid Mechanics*, *734*, 424–455. doi: 10.1017/jfm.2013.482

Taler, J., & Duda, P. (2006). *Solving Direct and Inverse Heat Conduction Problems*. Berlin, Heidelberg: Springer Berlin Heidelberg. doi: 10.1007/978-3-540-33471-2

Talusani, R. V. (2010). Bimodal tholeiitic and mildly alkalic basalts from bhir area, central deccan volcanic province, india: Geochemistry and petrogenesis. *Journal of Volcanology and Geothermal Research*, *189*(3-4), 278–290.

Talusani, R. V. (2012). Giant plagioclase basalts from northeastern deccan volcanic province, india: Implications for their origin and petrogenetic significance. *International Journal of Geosciences*, *3*, 1027–1032.

Tarasewicz, J., Brandsdóttir, B., White, R. S., Hensch, M., & Thorbjarnardóttir, B. (2012). Using microearthquakes to track repeated magma intrusions beneath the eyjafjallajökull stratovolcano, iceland. *Journal of Geophysical Research: Solid Earth*, *117*(B9).

Tarasewicz, J., White, R. S., Woods, A. W., Brandsdóttir, B., & Gudmundsson, M. T. (2012). Magma mobilization by downward-propagating decompression of the eyjafjallajökull volcanic plumbing system. *Geophysical Research Letters*, *39*(19).

Taron, J., & Elsworth, D. (2009). Thermal–hydrologic–mechanical–chemical processes in the evolution of engineered geothermal reservoirs. *International Journal of Rock Mechanics and Mining Sciences*, *46*(5), 855–864.

Taron, J., Elsworth, D., & Min, K.-B. (2009). Numerical simulation of thermal-hydrologic-mechanical-chemical processes in deformable, fractured porous media. *International Journal of Rock Mechanics and Mining Sciences*, *46*(5), 842–854.

Taylor, B., Crook, K., & Sinton, J. (1994). Extensional transform zones and oblique spreading centers. *Journal of Geophysical Research*, *99*(B10), 19707–19718. doi: 10.1029/94JB01662

Taylor-West, J., & Katz, R. F. (2015, nov). Melt-preferred orientation, anisotropic permeability and melt-band formation in a deforming, partially molten aggregate. *Geophysical Journal International*, *203*(2), 1253–1262. doi: 10.1093/gji/ggv372

Tegner, C., Michelis, S. A., McDonald, I., Brown, E. L., Youbi, N., Callegaro, S., ... Marzoli, A. (2019). Mantle dynamics of the central atlantic magmatic province (camp): Constraints from platinum group, gold and lithophile elements in flood basalts of morocco. *Journal of Petrology*, *60*(8), 1621–1652.

Tetreault, J., & Buiter, S. (2018). The influence of extension rate and crustal rheology on the evolution of passive margins from rifting to break-up. *Tectonophysics*, *746*, 155–172.

Tewari, H. C., Prasad, B. R., & Kumar, P. (2018a). Central indian region. In *Structure and tectonics of the indian continental crust and its adjoining region* (pp. 147–174). Elsevier. doi: 10.1016/b978-0-12-813685-0.00006-6

Tewari, H. C., Prasad, B. R., & Kumar, P. (2018b). Deccan volcanic province near the

west coast. In *Structure and tectonics of the indian continental crust and its adjoining region* (pp. 115–145). Elsevier. doi: 10.1016/b978-0-12-813685-0.00005-4

Thordarson, T., Miller, D., Larsen, G., Self, S., & Sigurdsson, H. (2001). New estimates of sulfur degassing and atmospheric mass-loading by the 934 ad eldgjá eruption, iceland. *Journal of Volcanology and Geothermal Research*, *108*(1-4), 33–54.

Thordarson, T., & Self, S. (1993). The laki (skaftár fires) and grímsvötn eruptions in 1783–1785. *Bulletin of Volcanology*, *55*(4), 233–263.

Thordarson, T., & Self, S. (1998). The roza member, columbia river basalt group: A gigantic pahoehoe lava flow field formed by endogenous processes? *Journal of Geophysical Research: Solid Earth*, *103*(B11), 27411–27445.

Thybo, H., & Artemieva, I. M. (2013). Moho and magmatic underplating in continental lithosphere. *Tectonophysics*, *609*, 605–619.

Tibaldi, A. (2008). Contractional tectonics and magma paths in volcanoes. *Journal of Volcanology and Geothermal Research*, *176*(2), 291–301. doi: 10.1016/j.jvolgeores.2008.04.008

Tibaldi, A. (2015). Structure of volcano plumbing systems: A review of multi-parametric effects. *Journal of Volcanology and Geothermal Research*, *298*, 85–135. doi: 10.1016/j.jvolgeores.2015.03.023

Titley, S. R. (1990). Evolution and style of fracture permeability in intrusion-centered hydrothermal systems. *The role of fluids in crustal processes*, 50–63.

Tolan, T. L. (1989). Revision on the extent and volume of the columbia river basalt group. *Geol. Soc. Am. Spec. Paper*, *239*, 1–20.

Tolia, N., & Sethna, S. (1990). Lopolithic intrusion of basalt in the intertrappeans at amboli hill, jogeshwari, bombay. *J. Geol. Soc. India*, *35*, 524–528.

Tomshin, M., Kopylova, A., & Tyan, O. (2005). Petrochemical variability of traps at the eastern periphery of the tungus basin. *Russ. Geol. Geophys*, *46*, 72–82.

Tomshin, M., Kopylova, A., Vasilyeva, A., & Zaitsev, A. (2014). Geochemical and isotope characteristics of intrusive traps in the eastern siberian platform. *International Multidisciplinary Scientific GeoConference: SGEM: Surveying Geology & mining Ecology Management*, *1*, 113.

Townsend, M., & Huber, C. (2020a). A critical magma chamber size for volcanic eruptions. *Geology*.

Townsend, M., & Huber, C. (2020b, feb). A critical magma chamber size for volcanic eruptions. *Geology*. doi: 10.1130/g47045.1

Townsend, M., Huber, C., Degruyter, W., & Bachmann, O. (2019). Magma chamber growth during inter-caldera periods: insights from thermo-mechanical modeling with applications to laguna del maule, campi flegrei, santorini, and aso. *Geochemistry, Geophysics, Geosystems*.

Townsend, M., Pollard, D. D., Johnson, K., & Culha, C. (2015). Jointing around magmatic dikes as a precursor to the development of volcanic plugs. *Bulletin of Volcanology*, *77*(10), 92.

Townsend, M. R. (2018). Modeling thermal pressurization around shallow dikes using

temperature-dependent hydraulic properties: implications for deformation around intrusions. *Journal of Geophysical Research: Solid Earth*.

Turner, S., & Hawkesworth, C. (1995). The nature of the sub-continental mantle: constraints from the major-element composition of continental flood basalts. *Chemical Geology*, *120*(3-4), 295–314.

Turner, S., Kokfelt, T., Hauff, F., Haase, K., Lundstrom, C., Hoernle, K., ... Devey, C. (2015). Mid-ocean ridge basalt generation along the slow-spreading, South Mid-Atlantic Ridge (5-11??S): Inferences from 238U-230Th-226Ra disequilibria. *Geochimica et Cosmochimica Acta*, *169*, 152–166. doi: 10.1016/j.gca.2015.07.036

Vanderkluysen, L., Mahoney, J. J., Hooper, P. R., Sheth, H. C., & Ray, R. (2011). The feeder system of the deccan traps (india): insights from dike geochemistry. *Journal of Petrology*, *52*(2), 315–343.

Vanorio, T., & Kanitpanyacharoen, W. (2015). Rock physics of fibrous rocks akin to roman concrete explains uplifts at campi flegrei caldera. *Science*, *349*(6248), 617–621.

Vasseur, J., & Wadsworth, F. B. (2017). Sphere models for pore geometry and fluid permeability in heterogeneous magmas. *Bulletin of Volcanology*, *79*(11), 77.

Vedanti, N., Malkoti, A., Pandey, O. P., & Shrivastava, J. P. (2018, mar). Ultrasonic p- and s-wave attenuation and petrophysical properties of deccan flood basalts, india, as revealed by borehole studies. *Pure and Applied Geophysics*, *175*(8), 2905–2930. doi: 10.1007/s00024-018-1817-x

Verma, O., & Khosla, A. (2019). Developments in the stratigraphy of the deccan volcanic province, peninsular india. *Comptes Rendus Geoscience*, *351*(7), 461–476.

Veveakis, E., Regenauer-Lieb, K., & Weinberg, R. F. (2015). Ductile compaction of partially molten rocks: The effect of non-linear viscous rheology on instability and segregation. *Geophysical Journal International*, *200*(1), 519–523. doi: 10.1093/gji/ggu412

Vidito, C., Herzberg, C., Gazel, E., Geist, D., & Harpp, K. (2013, oct). Lithological structure of the Galápagos Plume. *Geochemistry, Geophysics, Geosystems*, *14*(10), 4214–4240. doi: 10.1002/ggge.20270

Vignaroli, G., Aldega, L., Balsamo, F., Billi, A., De Benedetti, A. A., De Filippis, L., ... Rossetti, F. (2015). A way to hydrothermal paroxysm, colli albani volcano, italy. *Bulletin*, *127*(5-6), 672–687.

Villagómez, D. R., Toomey, D. R., Geist, D. J., Hooft, E. E. E., & Solomon, S. C. (2014). Mantle flow and multistage melting beneath the Galápagos hotspot revealed by seismic imaging. *Nature Geoscience*, *7*(2), 151–156. doi: 10.1038/ngeo2062

Villagomez, D. R., Toomey, D. R., Hooft, E. E. E., & Solomon, S. C. (2007). Upper mantle structure beneath the Galapagos Archipelago from surface wave tomography. *Journal of Geophysical Research-Solid Earth*, *112*(B7), 25. doi: B07303 Artn b07303

Violay, M., Heap, M., Acosta, M., & Madonna, C. (2017). Porosity evolution at the brittle-ductile transition in the continental crust: Implications for deep hydro-geothermal circulation. *Scientific reports*, *7*(1), 7705.

Viveiros, F., Cardellini, C., Ferreira, T., Caliro, S., Chiodini, G., & Silva, C. (2010). Soil co2 emissions at furnas volcano, são miguel island, azores archipelago: Volcano monitoring

perspectives, geomorphologic studies, and land use planning application. *Journal of Geophysical Research: Solid Earth*, *115*(B12).

Vlastélic, I., & Dosso, L. (2005, may). Initiation of a plume-ridge interaction in the South Pacific recorded by high-precision Pb isotopes along Hollister Ridge. *Geochemistry, Geophysics, Geosystems*, *6*(5), n/a–n/a. Retrieved from `http://doi.wiley.com/10.1029/2004GC000902` doi: 10.1029/2004GC000902

Vogt, P. R. (1974). The Iceland Phenomenon: Imprints of a Hot Spot on the Ocean Crust, and Implications for Flow Below the Plates. In *Geodynamics of iceland and the north atlantic area* (pp. 105–126). Dordrecht: Springer Netherlands. doi: 10.1007/978-94-010-2271-2_7

Vogt, P. R. (1976). Plumes, subaxial pipe flow, and topography along the Mid-Oceanic Ridge. *Earth and Planetary Science Letters*, *29*(2), 309–325. doi: 10.1016/0012-821X(76)90135-7

Vogt, P. R. (1983). The Iceland mantle plume: {S}tatus of the hypothesis after a decade of new work. In *Structure and development of the greenland-scotland ridge* (pp. 191–216).

Vye-Brown, C., Barry, T., & Self, S. (2018). Revealing emplacement dynamics of a simple flood basalt eruption unit using systematic compositional heterogeneities. *Field Volcanology: A Tribute to the Distinguished Career of Don Swanson*, *538*, 21.

Vye-Brown, C., Gannoun, A., Barry, T., Self, S., & Burton, K. (2013). Osmium isotope variations accompanying the eruption of a single lava flow field in the columbia river flood basalt province. *Earth and Planetary Science Letters*, *368*, 183–194.

Vye-Brown, C., Self, S., & Barry, T. (2013). Architecture and emplacement of flood basalt flow fields: case studies from the columbia river basalt group, nw usa. *Bulletin of Volcanology*, *75*(3), 697.

Wadge, G. (1981). The variation of magma discharge during basaltic eruptions. *Journal of Volcanology and Geothermal Research*, *11*(2-4), 139–168.

Wager, L., & Brown, G. (1968). Layered igneous intrusions. *Edinburgh and London: Oliver and Boyd*, 1–588.

Wagner, W., & Pruß, A. (2002). The iapws formulation 1995 for the thermodynamic properties of ordinary water substance for general and scientific use. *Journal of physical and chemical reference data*, *31*(2), 387–535.

Waichel, B. L., de Lima, E. F., Lubachesky, R., & Sommer, C. A. (2006). Pahoehoe flows from the central paraná continental flood basalts. *Bulletin of Volcanology*, *68*(7-8), 599–610.

Wang, H., van Hunen, J., & Pearson, D. G. (2015). The thinning of subcontinental lithosphere: The roles of plume impact and metasomatic weakening. *Geochemistry, Geophysics, Geosystems*. doi: 10.1002/2015GC005784

Wang, X.-C., Wilde, S. A., Xu, B., & Pang, C.-J. (2016). Origin of arc-like continental basalts: implications for deep-earth fluid cycling and tectonic discrimination. *Lithos*, *261*, 5–45.

Watanabe, N., Egawa, M., Sakaguchi, K., Ishibashi, T., & Tsuchiya, N. (2017). Hydraulic fracturing and permeability enhancement in granite from subcritical/brittle to super-

critical/ductile conditions. *Geophysical Research Letters*.

Watanabe, N., Numakura, T., Sakaguchi, K., Saishu, H., Okamoto, A., Ingebritsen, S. E., & Tsuchiya, N. (2017). Potentially exploitable supercritical geothermal resources in the ductile crust. *Nature Geoscience*, *10*(2), 140.

Weatherley, S. M., & Katz, R. F. (2010). Plate-driven mantle dynamics and global patterns of mid-ocean ridge bathymetry. *Geochemistry, Geophysics, Geosystems*, *11*(10). doi: 10.1029/2010GC003192

Weatherley, S. M., & Katz, R. F. (2012). Melting and channelized magmatic flow in chemically heterogeneous, upwelling mantle. *Geochemistry, Geophysics, Geosystems*, *13*(1), 1–23. doi: 10.1029/2011GC003989

Weatherley, S. M., & Katz, R. F. (2015). Melt transport rates in heterogeneous mantle beneath mid-ocean ridges. *Geochimica et Cosmochimica Acta*. doi: 10.1016/j.gca.2015.09.029

Weeraratne, D. S., Parmentier, E. M., & Forsyth, D. W. (2003). Viscous Fingering of Miscible Fluids in Laboratory Experiments and the Oceanic Mantle Asthenosphere. *AGU Fall Meeting Abstracts*.

Weinberger, R., Lyakhovsky, V., Baer, G., & Agnon, A. (2000). Damage zones around en echelon dike segments in porous sandstone. *Journal of Geophysical Research: Solid Earth*, *105*(B2), 3115–3133.

Weis, P. (2015). The dynamic interplay between saline fluid flow and rock permeability in magmatic-hydrothermal systems. *Geofluids*, *15*(1-2), 350–371.

Weis, P., Driesner, T., & Heinrich, C. (2012). Porphyry-copper ore shells form at stable pressure-temperature fronts within dynamic fluid plumes. *Science*, *338*(6114), 1613–1616.

Weisstein, E. W. (2002). Exponential integral, from mathworld–a wolfram web resource http://mathworld.wolfram.com/exponentialintegral.html.

Weisstein, E. W. (2003). Oblate spheroid.

Wenker, S., & Beaumont, C. (2018). Effects of lateral strength contrasts and inherited heterogeneities on necking and rifting of continents. *Tectonophysics*, *746*, 46–63.

Werner, C., Bergfeld, D., Farrar, C. D., Doukas, M. P., Kelly, P. J., & Kern, C. (2014). Decadal-scale variability of diffuse co2 emissions and seismicity revealed from long-term monitoring (1995–2013) at mammoth mountain, california, usa. *Journal of Volcanology and Geothermal Research*, *289*, 51–63.

Werner, R., Hoernle, K., Barckhausen, U., & Hauff, F. (2003). Geodynamic evolution of the Galápagos hot spot system (Central East Pacific) over the past 20 m.y.: Constraints from morphology, geochemistry, and magnetic anomalies. *Geochemistry, Geophysics, Geosystems*, *4*(12). doi: 10.1029/2003GC000576

White, C. M. (2007). The graveyard point intrusion: An example of extreme differentiation of snake river plain basalt in a shallow crustal pluton. *Journal of Petrology*, *48*(2), 303–325.

White, J. D., Bryan, S. E., Ross, P.-S., Self, S., & Thordarson, T. (2009). Physical volcanology of continental large igneous provinces: update and review. *Studies in volcanology:*

the legacy of George Walker. Special Publications of IAVCEI, *2*, 291–321.

White, R., & McKenzie, D. (1989). Magmatism at rift zones: The generation of volcanic continental margins and flood basalts. *Journal of Geophysical Research*, *94*(B6), 7685. doi: 10.1029/JB094iB06p07685

White, R., & McKenzie, D. (1995). Mantle plumes and flood basalts. *Journal of Geophysical Research: Solid Earth*, *100*(B9), 17543–17585.

White, R. S., Edmonds, M., Maclennan, J., Greenfield, T., & Agustsdottir, T. (2019). Melt movement through the icelandic crust. *Philosophical Transactions of the Royal Society A*, *377*(2139), 20180010.

White, S. M., Crisp, J. A., & Spera, F. J. (2006). Long-term volumetric eruption rates and magma budgets. *Geochemistry, Geophysics, Geosystems*, *7*(3).

White, S. M., Meyer, J. D., Haymon, R. M., Macdonald, K. C., Baker, E. T., & Resing, J. A. (2008, sep). High-resolution surveys along the hot spot-affected Galápagos Spreading Center: 2. Influence of magma supply on volcanic morphology. *Geochemistry, Geophysics, Geosystems*, *9*(9), n/a–n/a. doi: 10.1029/2008GC002036

White, W. M. (2010). Oceanic Island Basalts and Mantle Plumes: The Geochemical Perspective. *Annual Review of Earth and Planetary Sciences*, *38*(1), 133–160. doi: 10.1146/annurev-earth-040809-152450

White, W. M., McBirney, A. R., & Duncan, R. A. (1993, nov). Petrology and geochemistry of the Galápagos Islands: Portrait of a pathological mantle plume. *Journal of Geophysical Research: Solid Earth*, *98*(B11), 19533–19563. doi: 10.1029/93JB02018

Whittaker, J. M., Afonso, J. C., Masterton, S., Müller, R. D., Wessel, P., Williams, S. E., & Seton, M. (2015). Long-term interaction between mid-ocean ridges and mantle plumes. *Nature Geoscience*, *8*(May), 1–6. doi: 10.1038/ngeo2437

Widdowson, M., Pringle, M., & Fernandez, O. (2000). A post k–t boundary (early palaeocene) age for deccan-type feeder dykes, goa, india. *Journal of Petrology*, *41*(7), 1177–1194.

Wignall, P. B. (2001). Large igneous provinces and mass extinctions. *Earth-science reviews*, *53*(1-2), 1–33.

Wilkinson, C. M., Ganerød, M., Hendriks, B. W., & Eide, E. A. (2017). Compilation and appraisal of geochronological data from the north atlantic igneous province (naip). *Geological Society, London, Special Publications*, *447*(1), 69–103.

Wilson, C. J., Moore, D. H., Luzin, V., & Salvemini, F. (2017). Costerfield antimony-gold deposit, southeast australia: Coupling between brittle deformation and dissolution-precipitation reactions in the melbourne zone. *Ore Geology Reviews*, *91*, 741–764.

Wilson, D. S., & Hey, R. N. (1995). History of rift propagation and magnetization intensity for the Cocos-Nazca sspreading Center. *Journal of Geophysical Research*, *100*(95), 10041. doi: 10.1029/95JB00762

Wohletz, K. H. (1986). Explosive magma-water interactions: Thermodynamics, explosion mechanisms, and field studies. *Bulletin of Volcanology*, *48*(5), 245–264.

Wolff, J., & Ramos, F. (2013). Source materials for the main phase of the Columbia River Basalt Group: Geochemical evidence and implications for magma storage and

transport. *Geological Society of America Special Papers*, *497*(11), 273–291. doi: 10.1130/2013.2497(11)

Woods, A. W., & Huppert, H. E. (2003). On magma chamber evolution during slow effusive eruptions. *Journal of Geophysical Research*, *108*(B8), 2403. doi: 10.1029/2002JB002019

Wrona, T., Magee, C., Fossen, H., Gawthorpe, R. L., Bell, R., Jackson, C.-L., & Faleide, J. I. (2019). 3-d seismic images of an extensive igneous sill in the lower crust. *Geology*, *47*(8), 729–733.

Wylie, J. J., Helfrich, K. R., Dade, B., Lister, J. R., & Salzig, J. F. (1999). Flow localization in fissure eruptions. *Bulletin of Volcanology*, *60*(6), 432–440.

Yardley, B., Baumgartner, L., Handy, M., Hirth, G., & Hovius, N. (2007). Fluid processes in deep crustal fault zones. *Tectonic Faults–Agents of Change on a Dynamic Earth*, 295–318.

Yarushina, V. M., Podladchikov, Y. Y., & Connolly, J. a. D. (2015a, jul). (De)compaction of porous viscoelastoplastic media: Solitary porosity waves. *Journal of Geophysical Research: Solid Earth*, *120*(7), 4843–4862. doi: 10.1002/2014JB011260

Yarushina, V. M., Podladchikov, Y. Y., & Connolly, J. a. D. (2015b, jul). (De)compaction of porous viscoelastoplastic media: Solitary porosity waves. *Journal of Geophysical Research: Solid Earth*, *120*(7), 4843–4862. doi: 10.1002/2014JB011260

Yaxley, G. M., Ghosh, S., Kiseeva, E. S., Mallik, A., Spandler, C., Thomson, A. R., & Walter, M. J. (2019). Co2-rich melts in earth. In *Deep carbon: Past to present.* Cambridge University Press.

Yu, X., Lee, C.-T. A., Chen, L.-H., & Zeng, G. (2015). Magmatic recharge in continental flood basalts: Insights from the chifeng igneous province in inner mongolia. *Geochemistry, Geophysics, Geosystems*, *16*(7), 2082–2096.

Zencher, F., Bonafede, M., & Stefansson, R. (2006). Near-lithostatic pore pressure at seismogenic depths: a thermoporoelastic model. *Geophysical Journal International*, *166*(3), 1318–1334.

Zhang, J., Chen, J., & Huang, Y. (2019). Secondary cones of the shatsky rise and implications for late-stage volcanism atop oceanic plateaus. *Journal of Ocean University of China*, *18*(5), 1115–1122.

Zhao, C., Hobbs, B. E., & Ord, A. (2008). *Convective and advective heat transfer in geological systems*. Springer Science & Business Media.

Zieg, M., & Marsh, B. (2012). Multiple reinjections and crystal-mush compaction in the beacon sill, mcmurdo dry valleys, antarctica. *Journal of Petrology*, *53*(12), 2567–2591.

Zieg, M. J., & Wallrich, B. M. (2018). Emplacement and differentiation of the black sturgeon sill, nipigon, ontario: A principal component analysis. *Journal of Petrology*, *59*(12), 2385–2412.

Appendix A

Poro-thermo-visco-elastic constants

A.1 Microphysical constants

In the poro-thermo-visco-elastic equations, we have used a number of poro-elastic constants. These are defined as follows :

1. α_B : Biot-Willis factor ($\phi \leq \alpha_B \leq 1$):

$$\alpha_B \approx (1 - K_b/K_s) \tag{A.1}$$

2. $\alpha_{Th,terms}$: Various thermal expansivity terms :

$$\alpha_{Th,d} \approx \alpha_{Th,s} \tag{A.2}$$
$$\alpha_{Th,\nu} \approx \phi(\alpha_{Th,f} - \alpha_{Th,s}) \tag{A.3}$$
$$m_d'' = (1-\phi)\rho_s c_{p,s}/T_0 + \phi\rho_f c_{p,f}/T_0 - 9K_b(\alpha_{Th,d})^2 \tag{A.4}$$

   Here $\alpha_{Th,d}$ is the drained coefficient of linear thermal expansion for porous medium frame, and $\alpha_{Th,\nu}$ is a coefficient of volumetric thermal expansion for variation in fluid content. Additionally, $c_{p,s/f}$ is the drained specific heat, k_b^c is the effective bulk thermal conductivity.

3. $\alpha_{Th,p}$: Linear pore thermal expansivity –

$$\alpha_{Th,p} = [\alpha_{Th,b} - (1-\phi)\alpha_{Th,s}]/\phi \tag{A.5}$$

   This is generally considered to be much smaller than $\alpha_{Th,f}$ and is assumed to zero for the ideal porosity model.

4. $K_{b,d} = K_b$: drained bulk modulus. It represents the stiffness of a porous solid frame against volumetric deformation in a drained test (i.e. solid frame without fluid). Mathematically,

$$K_b = \left.\frac{\Delta P}{\Delta V/V}\right|_{drained} \tag{A.6}$$

5. B : Skempton's coefficient is the induced pore pressure due to a sudden change in the mean stress in the undrained limit (i.e. the change in pore pressure due to sudden external stress). An expression for B is :

$$B = \frac{1/K_b - 1/K_s}{(1/K_b - 1/K_s) + \phi(1/K_f - 1/K_\phi)} \tag{A.7}$$

where K_ϕ is the unjacketed pore bulk modulus. It is the modulus associated with the unjacketed pore compressibility which is the change in pore volume with change in pore pressure when the confining pressure is required to track with the pore pressure. Frequently, $K_\phi \sim K_s$.

6. $1/M_B$: Constrained Specific Storage. It is the volume of fluid released from the storage per unit control volume per unit pressure decline holding the control volume constant - $1/M_B = \left.\frac{\delta\zeta}{\delta P_f}\right|_{\epsilon=0}$. It is the reciprocal of Biot's modulus (M_B) and is equal to

   - $\frac{1}{M_B} = [\alpha_B(1 - \alpha_B B)]/[K_b B]$ (Wang 2000)
   - $\Leftrightarrow \frac{1}{M_B} = (1 - \alpha_B)(1/K_b - 1/K_s) + \phi(1/K_f - 1/K_s)$ if $K_\phi = K_s$ (S. Ingebritsen & Sanford, 1999)
   - $\Leftrightarrow \frac{1}{M_B} = \phi/K_f - \phi/K_s + \alpha_B/K_s$ (B. Bai, 2006)

7. $\alpha_{Th,e}$: It is a coefficient of linear thermal expansion for variation in fluid content at constant frame volume :

   - $\alpha_{Th,e} = \phi(\alpha_{Th,f} - \alpha_{Th,s}) + \alpha_B\alpha_{Th,s}$ (Ghassemi et al., 2008)
   - $\alpha_{Th,e} = K_b\alpha_{Th,b}(1/K_b - 1/K_s) + \phi\alpha_{Th,f} + (1 - \phi)\alpha_{Th,s} - 3\alpha_{Th,b}$ (S. Ingebritsen & Sanford, 1999)
     which simplifies to $\alpha_{Th,e} = -\alpha_{Th,b}(K_b/K_s) + \phi\alpha_{Th,f} + (1 - \phi)\alpha_{Th,s}$, i.e the same as other definition of $\alpha_{Th,e}$ if $\alpha_{Th,b} = \alpha_{Th,s}$.

As shown by a few examples above, there are multiple choices with regards to obtaining average parameters if the constants for individual phases is known. We discuss a few commonly used models in the following for the drained bulk modulus of the porous media using the values for solid bulk modulus (K_s) and shear modulus (G_s) :

1. Ideal porous medium condition - a porous medium made of homogeneous and isotropic solid material. Considering the Gassmann model, $\alpha_B = 1 - K_b/K_s$ along with the form of B, and $1/M_B$ defined above. Under an ideal porous medium condition, we hence get :

$$\frac{1}{K_b} = \frac{1}{K_s} + \frac{\phi}{K_p} \tag{A.8}$$

$$\tag{A.9}$$

where K_s and K_p are bulk modulus of the solid and the pore volume bulk modulus respectively ($K_p = \frac{\phi}{\alpha_B} K_b$ always).

A.2 Relationship between microphysical constants

We approximate our crustal medium as an ideal porous medium model with the material being microscopically homogeneous and isotropic and use a set of microphysical relationships for constitutive parameters. We refer the reader to A. Cheng (2016) (Poroelasticity, Ch 1-4) for derivations of these relationships.

$$\alpha_B = 1 - \frac{K}{K_s} \tag{A.10}$$

$$M_B = \frac{K_f K_s^2}{K_f(K_s - K) + \phi K_s(K_s - K_f))} \tag{A.11}$$

$$K_u = M * \alpha_B^2 + K \tag{A.12}$$

$$S = \frac{3K_u + 4G}{M(3K + 4G)} \tag{A.13}$$

$$c = \frac{k^m}{S\eta_{fl}} \tag{A.14}$$

$$k_T = \phi * k_{T,fl} + (1 - \phi) * k_{T,s} \tag{A.15}$$

$$\beta_\nu = \phi * (\beta_f - \beta_s) \tag{A.16}$$

$$\beta_e = (\alpha_B - \phi) * \beta_s + \phi * \beta_f \tag{A.17}$$

$$m_d = \frac{c_d}{T_{fl}} \tag{A.18}$$

$$\beta_c = \beta_e - \frac{3K\alpha_B}{3K + 4G}\beta_s \tag{A.19}$$

$$\alpha_e = \frac{\beta_c}{S} \tag{A.20}$$

$$\alpha_d = K\beta_s \tag{A.21}$$

$$\eta_d = \frac{3\alpha_d G}{3K + 4G} \tag{A.22}$$

$$\eta = 3\alpha_B G 3K + 4G \tag{A.23}$$

$$S_a = m_d + \alpha_d * \eta_d / G \tag{A.24}$$

$$c_a = m_d * \kappa_T / S_a \tag{A.25}$$

$$\alpha_p = \beta_c / S_a \tag{A.26}$$

$$C_Q = \sqrt{(c - c_a)^2 + 4 * c * c_a * \alpha_p * \alpha_e} \tag{A.27}$$

$$\lambda_1 = \sqrt{\frac{(c + c_a) + C_Q}{2cc_a}} \tag{A.28}$$

$$\lambda_2 = \sqrt{\frac{(c + c_a) - C_Q}{2cc_a}} \tag{A.29}$$